Computational and Experimental Methods in Structures – Vol. 2

Advances in Multiphysics Simulation and Experimental Testing of MEMS

Attilio Frangi
Carlo Cercignani
Subrata Mukherjee
Narayan Aluru
Editors

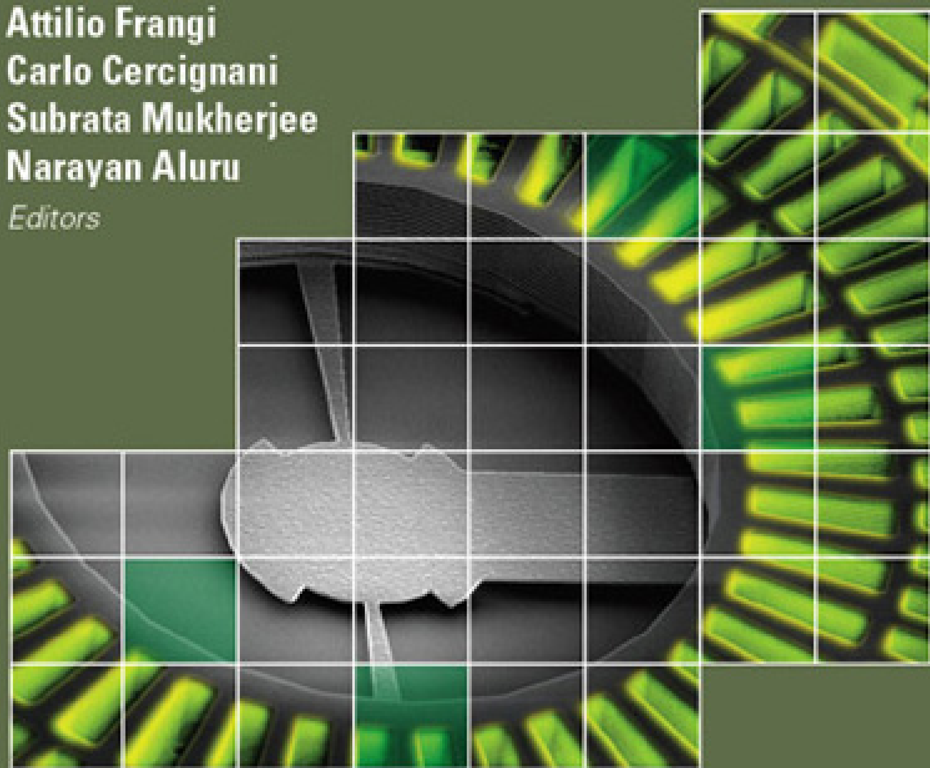

Imperial College Press

Advances in Multiphysics Simulation and Experimental Testing of MEMS

Computational and Experimental Methods in Structures

Series Editor: Ferri M. H. Aliabadi *(Imperial College London, UK)*

Vol. 1 Buckling and Postbuckling Structures: Experimental, Analytical and Numerical Studies
edited by B. G. Falzon and M. H. Aliabadi
(Imperial College London, UK)

Vol. 2 Advances in Multiphysics Simulation and Experimental Testing of MEMS
edited by A. Frangi, C. Cercignani (Politecnico di Milano, Italy), S. Mukherjee (Cornell University, USA) and N. Aluru (University of Illinois at Urbana Champaign, USA)

Computational and Experimental Methods in Structures – Vol. 2

Advances in Multiphysics Simulation and Experimental Testing of MEMS

Editors

Attilio Frangi
Carlo Cercignani
Politecnico di Milano, Italy

Subrata Mukherjee
Cornell University, USA

Narayan Aluru
University of Illinois at Urbana Champaign, USA

Imperial College Press

Published by

Imperial College Press
57 Shelton Street
Covent Garden
London WC2H 9HE

Distributed by

World Scientific Publishing Co. Pte. Ltd.

5 Toh Tuck Link, Singapore 596224

USA office: 27 Warren Street, Suite 401-402, Hackensack, NJ 07601

UK office: 57 Shelton Street, Covent Garden, London WC2H 9HE

British Library Cataloguing-in-Publication Data
A catalogue record for this book is available from the British Library.

ADVANCES IN MULTIPHYSICS SIMULATION AND EXPERIMENTAL TESTING OF MEMS

Copyright © 2008 by Imperial College Press

All rights reserved. This book, or parts thereof, may not be reproduced in any form or by any means, electronic or mechanical, including photocopying, recording or any information storage and retrieval system now known or to be invented, without written permission from the Publisher.

For photocopying of material in this volume, please pay a copying fee through the Copyright Clearance Center, Inc., 222 Rosewood Drive, Danvers, MA 01923, USA. In this case permission to photocopy is not required from the publisher.

ISBN-13 978-1-86094-862-6
ISBN-10 1-86094-862-6

Printed in Singapore.

Preface

Nearly three decades ago, it was uncovered that silicon can be an excellent mechanical material. The excellent electronic properties of silicon combined with the excellent mechanical properties led to revolutionary advances in the development of microelectromechanical technology. Microelectromechanical systems (MEMS) are miniaturized sensors, actuators, devices and systems with a critical dimension of the order of micrometers. Even though many initial concepts for MEMS were based on silicon, a variety of other materials and fabrication techniques have been developed over the last two decades for applications in mechanical, electrical, chemical, biological and other disciplines. MEMS devices such as accelerometers, gyroscopes, high performance mirror displays, pressure sensors, micro motors, micro engines, RF switches, valves, pumps, ultra sensitive membranes, single-chip microfluidic systems such as chemical analyzers or synthesizers, single-chip micro total analysis systems (also referred to as lab-on-a-chip) and many more devices and systems have been designed and fabricated over the last one to two decades. MEMS technology has already impacted many industries (*e.g.*, defense, aerospace, health care, etc.) even though a number of fundamental and practical challenges still remain. On the other hand, advances in nanotechnology as well as in nanomachining techniques over the last decade have enabled development of novel nanoelectromechanical systems (NEMS). Nanoelectromechanical systems (NEMS) are nanometer scale sensors, actuators, devices and systems with critical feature sizes ranging from 100 nanometers to a few nanometers. The effective masses, heat capacities and power consumption of NEMS are proportional to the critical feature size, either linearly or nonlinearly, while the fundamental frequencies, mass/force sensitivities, mechanical quality factors are inversely proportional to the critical feature size.

A number of experimental and fabrication approaches, and computational design tools have been developed over the last decade to accelerate progress in the area of MEMS. In the area of NEMS, fundamental aspects are slowly being understood and experimental measurement techniques and computational design tools are starting to emerge. While many NEMS devices can be modeled using MEMS

physical theories or MEMS computational tools, a large class of NEMS devices demand new simulation capabilities because of the new physics encountered at nanoscale. In addition, the break-down of a continuum approximation for some NEMS devices poses new challenges. As a result, the development of quantum, atomistic, multiscale and continuum simulation tools based on advanced physical theories becomes critical.

Covering at length computational techniques for both classes of devices in one single book is not realistic and we have chosen to focus on the more mature world of MEMS, with several openings towards the NEMS world. In particular, we privilege fundamental aspects and computational design tools. Moreover, a few chapters addressing experimental techniques for MEMS and NEMS have been included. Indeed, not only numerical models have to be validated against experiments, but it is also true that experiments at the micro/nanoscale often give access to the quantities of interest often in an indirect way and data-reduction procedures strongly relying on numerical simulations are required. The thin borderline between experiments and simulation becomes immaterial at these scales.

Many experts have written excellent chapters in this book summarizing the state-of-the-art, fundamental issues, computational methods, experimental measurements, validation and future challenges. In the first part of the book (Chapters 1-6) focus is set on micro/nanofluidics, while in the latter (Chapters 7-12) more emphasis is given to truly multiphysics analyses concerning mainly advanced topics of solid mechanics and electrostatics.

Microfluidics has deep roots in MEMS and NEMS. Microducts are used in infrared detectors, diode lasers, miniature gas chromatographs and high-frequency fluidic control systems. Micropumps are used for ink jet printing, environmental testing and electronic cooling. Potential medical applications for small pumps include controlled delivery and monitoring of minute amount of medication, manufacturing of nanoliters of chemicals and development of artificial pancreas. Moreover, microfluidics affects the dynamical behavior of almost all microsystems through dissipation even when it is not the mechanical phenomenon of direct interest. Hence, flows in micro and nanochannels have always attracted and deserved considerable attention in the scientific community, even though many open challenges remain, as stressed in Chapter 1. The customary continuum, Navier–Stokes modeling is ordinarily applicable for flows in macrodevices. Even for common fluids such as air or water, such modeling is bound to fail at sufficiently small scales, but the onset for such failure is different for the two forms of matter. Moreover, when the no-slip, quasi-equilibrium Navier–Stokes system is no longer applicable, the alternative modeling schemes are different for gases and liquids. For liquid flows, the dense nature of the matter precludes the use of the kinetic

theory of gases, and numerically intensive molecular dynamics simulations are the only alternative rooted in first principles, as discussed in Chapter 1.

For dilute gases, statistical methods are applied and the Boltzmann equation is the cornerstone of such approaches. This topic is addressed in Chapter 2. The application of kinetic theory methods is first illustrated by deriving a generalized Reynolds equation from the linearized Boltzmann equation. The analysis, valid for arbitrary Knudsen number, is based on two different kinetic models of the collisional operator: the Bhatnagar, Gross and Krook (BGK) model and the ellipsoidal statistical (ES) model. The semi-analytical results described also form the basis for the *modified viscosity approach*, a simplified technique discussed in Chapter 5 and frequently applied to extend the validity of continuum models to the transition regime. In Chapter 2 it also shown that gas flows occurring in inertial MEMS having a complex geometry can be successfully studied by numerical deterministic solution of linearized kinetic model equations (BGK) whose predictions are in very good agreement with the experimental data presented.

The most well-known numerical tool for the solution of the Boltzmann equation in general strongly nonequilibrium conditions is the Direct Simulation Monte Carlo (DSMC) approach, analysed in detail in Chapter 3. Even DSMC is computationally more demanding than most continuum CFD methods it is shown that this problem can be partially alleviated by its superior parallel performance. Another feature of DSMC is the lack of numerical instabilities even for the most physically and geometrically complicated problems which, together with its unmatched accuracy, makes DSMC a unique method to study physical phenomena at the mean-free-path level. Besides the cases for which DSMC is the only applicable method, DSMC can be used concurrently with continuum methods and analytical approaches to develop empirical models that can be implemented in engineering codes.

However, using DSMC for subsonic-flow MEMS simulations is not without issues. A problem arises when the characteristic velocities of the micro-gas flow become very small since the use of conventional DSMC in such instances often incur in large statistical errors. Unfortunately, the typical gas flow velocities in most MEMS devices are in the low velocity range. This issue has stimulated many investigation and novel numerical approaches, like the multiscale coarse-grain molecular block (or "big molecule") described in Chapter 4. Molecular blocks are used to replace the particles in the DSMC method, and a molecular block direct simulation Monte Carlo (MB-DSMC) method is established. As the mass of the molecular block is larger, the statistical error of the MB-DSMC method is expected to be sensibly smaller.

Even if all the approaches presented in these chapters are rooted in the molecular nature of fluids, the evaluation of gas damping for MEMS working at ambient pressure can be still conveniently addressed by means of continuum models. Estimating dissipation in air-packaged MEMS like inertial sensors seems, for several reasons, to be an ideal application for fast integral equation methods as shown in Chapter 5. First, the micromechanical structures are innately three-dimensional and geometrically complicated. Second, in order to provide an estimate of the mechanical dissipation, the only quantities of interest are velocities and forces on the structure surface. Surface-only integral equations have a dimensional advantage over volume methods in such a setting. Third, the velocities and displacements for many MEMS of interest are small enough, and the surrounding air is viscous enough, that the flow, at moderate frequencies, can be often described by a linear quasi-static Stokes model with slip boundary conditions. For the above reasons, there have been a number of experimentally-verified successes in evaluating gas damping for air-packaged MEMS as discussed at length in Chapter 5.

As a conclusion for the microfluidics section and as a transition towards the second part of the book, Chapter 6 reviews experimental techniques that are suitable for quality factor measurements of in-plane, out-of-plane and torsional vibrations of microresonators and comments on optical techniques applicable to nanoresonators.

Interestingly enough, one major open issue for MEMS working in near vacuum-conditions, is that dissipation predicted by experiments is much larger than expected for resonators having high aspect ratios and there is strong evidence that it should be linked to surface phenomena even if no reliable physical models are available. The classical theory of thermoelastic coupling can however explain intrinsic dissipation in specific conditions and is the object of several investigations and extensions, as done in Chapter 7. A full-Lagrangian multiphysics Newton method is proposed for the dynamic analysis of electrostatic MEMS in the presence of damping. This new scheme has several advantages over conventional MEMS simulation tools in terms of speed and convergence rates and is used to explore new nonlinear dynamic properties of electrostatic MEMS. Complex nonlinear oscillations and the period doubling route to chaos are observed under superharmonic excitations and the effect of these complex oscillations on thermoelastic damping in electrostatic MEMS is also studied.

A similar approach to electromechanical coupling is addressed in Chapter 8 which focuses on the quasi static response behavior of MEMS devices made up of very thin conducting plates. A convenient way to model such a problem is to assume plates with vanishing thickness, solve for sum of the charges on the upper

and lower surfaces of each plate and adopt a full-Lagrangian scheme both for the solid-mechanics and elecrostatics analysis.

One major and truly multiphysics issue in vibrating MEMS is pull-in instability, which is investigated in Chapter 9 for MEM membranes subjected to Coulomb and Casimir forces. The Casimir force represents the attraction between two uncharged material bodies due to modification of the zero-point energy associated with the electromagnetic modes in the space between them. An important feature of the Casimir effect is that even though its nature is quantistic, it predicts a force between macroscopic bodies. This nonlinear multiphysics problem is analyzed by the meshless local Petrov-Galerkin (MLPG) method. It is shown that beyond a critical size, the geometric effect modeled by the Casimir force becomes dominant over the Coulomb force, and the device collapses with zero applied voltage.

Dielectrophoresis, addressed in Chapter 10, is an effective tool for particle separation and manipulation which is increasingly used in various BioMEMS applications for the analysis and separation of biological particles, such as cells, bacteria, viruses and DNA. The term alternating current (AC) electrokinetics refers to the particle movement arising from the interaction of non-uniform AC electric field with polarizable particles. One of these techniques is the dielectrophoresis (DEP), which arises from the interaction of AC electric field and the induced dipole in a particle. One of the DEP techniques is the field flow fractionation (FFF) method, in which DEP force levitates different particles to different vertical heights above the surface, and hydrodynamic force drives the particles traveling at different speed according to their heights from the surface to achieve the separation. Another well-known DEP technique is the traveling wave dielectrophoresis (twDEP), in which the particle motion is induced by traveling electric field. Both these techniques are simulated by means of a novel meshfree method named the linearly conforming point interpolation method (LC-PIM).

Chapter 11, the last contribution of the book addressing specific numerical techniques, discusses topology optimization issues emerging in the context of MEMS and focuses, in particular, on two problems related to manufacturing constraints in surface-micromachined structures and in protein sequence design.

All the numerical methods detailed in previous chapters make indeed use of material parameters which have to be evaluated from experiments. As in other technologies, the ability to exploit materials in MEMS and NEMS is limited by our knowledge of their properties. In particular, the successful fabrication and the reliable use of micro/nanostructures is strongly contingent on a sufficiently rigorous understanding of their length scale-dependent and process-dependent mechanical properties. In turn, such understanding requires the ability to perform mechanical measurements on microstructures. Hence, the challenging task of

mechanical characterization requires an entirely new set of techniques to achieve the force and displacement resolution required. The issue of mechanical characterization of polysilicon often used in MEMS is discussed in Chapter 12. An innovative approach based on a fully on-chip testing procedure is described and three ad hoc designed electrostatically actuated microsystems are here used in order to determine experimentally the Young's modulus and the rupture strength of thin and thick polysilicon. The accurate data-reduction procedure relying on electromechanical numerical simulations is discussed. The rupture values are interpreted by means of the Weibull approach and statistical size effects and stress gradient effects are taken into account thus allowing for a direct comparison of the data obtained from the different test structures.

Curiously enough, MEMS can be adopted as test machine for nanostructures, as demonstrated in Chapter 13. The need to characterize nanometer-scale materials and structures has grown tremendously in the past decade and a brief review of some of the methods used in mechanical characterization of nanoscale specimens, is presented first, followed by a detailed description of a MEMS-based material testing system. This MEMS-based system allows for continuous observation of specimen deformation and failure with sub-nanometer resolution by scanning or transmission electron microscope while simultaneously measuring the applied load electronically with nano-Newton resolution. Special emphasis is placed on modeling and analysis of a thermal actuator used to apply a displacement-controlled load to the tensile specimen as well as the electrostatic load sensor. Finally, experimental results demonstrating the advantages of the MEMS-based system are presented.

N. Aluru
C. Cercignani
A. Frangi
S. Mukherjee

Contents

Preface v

1. Challenges in Modeling Liquid and Gas Flows in Micro/Nano Devices 1
M. Gad-el-Hak

2. Using the Kinetic Equations for MEMS and NEMS 37
C. Cercignani, A. Frezzotti and S. Lorenzani

3. Applying the Direct Simulation Monte Carlo (DSMC) Method to Gas-Filled MEMS Devices 81
M. A. Gallis

4. New Approaches for the Simulation of Micro-Fluidics in MEMS 121
T. Y. Ng, H. Li, L. S. Pan, D. Xu and K. Y. Lam

5. Evaluating Gas Damping in MEMS Using Fast Integral Equation Solvers 153
A. Frangi, W. Ye and J. White

6. Experimental Techniques for Damping Characterization of Micro and Nanostructures 183
A. Bosseboeuf and H. Mathias

7. Nonlinear Dynamics of Electrostatically Actuated MEMS 235

S. K. De and N. R. Aluru

8. Coupled Deformation Analysis of Thin MEMS Plates 287

S. Mukherjee and S. Telukunta

9. Pull-In Instability in Electrostatically Actuated MEMS due to Coulomb and Casimir Forces 329

R. C. Batra, M. Porfiri and D. Spinello

10. Numerical Simulation of BioMEMS with Dielectrophoresis 375

G. R. Liu and C. X. Song

11. Continuous Modeling of Multi-Physics Problems of Microsystems for Topology Optimization 399

G. K. Ananthasuresh

12. Mechanical Characterization of Polysilicon at the Micro-Scale Through On-Chip Tests 427

A. Corigliano, F. Cacchione, A. Frangi, S. Zerbini and M. Ferrera

13. Nano-Scale Testing of Nanowires and Carbon Nanotubes Using a Micro-Electro-Mechanical System 455

H. D. Espinosa, Y. Zhu, B. Peng and O. Loh

Chapter 1

Challenges in Modeling Liquid and Gas Flows in Micro/Nano Devices

Mohamed Gad-el-Hak

Department of Mechanical Engineering
Virginia Commonwealth University, Richmond, VA 23284, U.S.A.
gadelhak@vcu.edu

Traditional fluid mechanics edifies the indifference between liquid and gas flows as long as certain similarity parameters—most prominently the Reynolds number—are matched. This may or may not be the case for flows in nano- or microdevices. The customary continuum, Navier–Stokes modeling is ordinarily applicable for both air and water flowing in macrodevices. Even for common fluids such as air or water, such modeling is bound to fail at sufficiently small scales, but the onset for such failure is different for the two forms of matter. Moreover, when the no-slip, quasi-equilibrium Navier–Stokes system is no longer applicable, the alternative modeling schemes are different for gases and liquids. For dilute gases, statistical methods are applied and the Boltzmann equation is the cornerstone of such approaches. For liquid flows, the dense nature of the matter precludes the use of the kinetic theory of gases, and numerically intensive molecular dynamics simulations are the only alternative rooted in first principles. The present chapter discusses the above issues, emphasizing the differences between liquid and gas transport at the microscale and the physical phenomena unique to liquid flows in minute devices.

Contents

1.1 Introduction . . . 2
1.2 Fluid Mechanics Issues . . . 4
1.3 Fluid Modeling . . . 6
1.4 Gas Flows . . . 9
1.5 Liquid Flows . . . 12
1.6 Molecular Dynamics Simulations . . . 16
1.7 A Typical MD Result . . . 18
1.8 Hybrid Methods . . . 24
1.9 Surface Phenomena . . . 26
1.10 Conclusions . . . 31
References . . . 33

In a little time I felt something alive moving on my left leg, which advancing gently forward over my breast, came almost up to my chin; when bending my eyes downward as much as I could, I perceived it to be a human creature not six inches high, with a bow and arrow in his hands, and a quiver at his back. . . . I had the fortune to break the strings, and wrench out the pegs that fastened my left arm to the ground; for, by lifting it up to my face, I discovered the methods they had taken to bind me, and at the same time with a violent pull, which gave me excessive pain, I a little loosened the strings that tied down my hair on the left side, so that I was just able to turn my head about two inches. . . . These people are most excellent mathematicians, and arrived to a great perfection in mechanics by the countenance and encouragement of the emperor, who is a renowned patron of learning. This prince has several machines fixed on wheels, for the carriage of trees and other great weights.
(From "Gulliver's Travels—A Voyage to Lilliput," by Jonathan Swift, 1726.)

In the Nevada desert, an experiment has gone horribly wrong. A cloud of nanoparticles—micro-robots—has escaped from the laboratory. This cloud is self-sustaining and self-reproducing. It is intelligent and learns from experience. For all practical purposes, it is alive. It has been programmed as a predator. It is evolving swiftly, becoming more deadly with each passing hour.
Every attempt to destroy it has failed.
And we are the prey.
(From Michael Crichton's novel "Prey," HarperCollins Publishers, 2002.)

1.1. Introduction

Almost three centuries apart, the imaginative novelists quoted above contemplated the astonishing, at times frightening possibilities of living beings much bigger or much smaller than us. In 1959, the physicist Richard Feynman envisioned the fabrication of machines minutely small as compared to their makers. Tool making has always differentiated our species from all others on Earth. Aerodynamically correct wooden spears were carved by archaic Homo sapiens close to 400,000 years ago. Man builds things consistent with his size, typically in the range of two orders of magnitude larger or smaller than himself, as indicated in Fig. 1.1. But humans have always striven to explore, build and control the extremes of length and time scales. In the voyages to Lilliput and Brobdingnag of Gulliver's Travels, Jonathan Swift speculated on the remarkable possibilities which diminution or magnification of physical dimensions provides. The Great Pyramid of Khufu

was originally 147 m high when completed around 2600 B.C., while the Empire State Building, constructed in 1931, is presently—after the addition of a television antenna mast in 1950—449 m high. At the other end of the spectrum of man-made artifacts, a dime is slightly less than 2 cm in diameter. Watchmakers have practised the art of miniaturization since the thirteenth century. The invention of the microscope in the seventeenth century opened the way for direct observation of microbes and plant and animal cells. Smaller things were man-made in the latter half of the twentieth century. The transistor—invented in 1947—in today's integrated circuits has a gate length of 45 nanometers, and approaches 10 nm in research laboratories (source: International Technology Roadmap for Semiconductors <http://public.itrs.net>). But what about the miniaturization of mechanical parts—machines—envisioned by Richard Feynman[1] in a legendary lecture delivered in 1959?

Microelectromechanical systems (MEMS) refer to devices that have characteristic length of less than 1 mm but more than 1 micron, that combine electrical and mechanical components, and that are fabricated using integrated circuit batch-processing technologies. MEMS are finding an increasing number of applications in a variety of industrial and medical fields, with a potential worldwide market in the billions of dollars. Accelerometers for automobile airbags, keyless entry systems, dense arrays of micromirrors for high-definition optical displays, scanning electron microscope tips to image single atoms, micro-heat-exchangers for cooling of electronic circuits, reactors for separating biological cells, blood analyzers and pressure sensors for catheter tips are but a few examples of current usage. Microducts are used in infrared detectors, diode lasers, miniature gas chromatographs and high-frequency fluidic control systems. Micropumps are used for ink jet printing, environmental testing and electronic cooling. Potential medical applications for small pumps include controlled delivery and monitoring of minute amount of medication, manufacturing of nanoliters of chemicals and development of artificial pancreas. The much sought-after lab-on-a-chip is promising to automate biology and chemistry to the same extent the integrated circuit has allowed large-scale automation of computation.[2]

Not all MEMS devices involve fluid flows, but the present paper will focus on the ones that do. Gas flows will first be briefly discussed, but the emphasis of the paper will be on liquid flows. Microducts, micropumps, microturbines, microvalves, microcombustors, synthetic jets and lab-on-a-chip are examples of small devices involving the flow of liquids and gases. Because of length limitation, the present paper only touches on its broad subject matter, with particular emphasis on liquid flows and surface phenomena, and the reader is referred to several other sources for further details.[2–6]

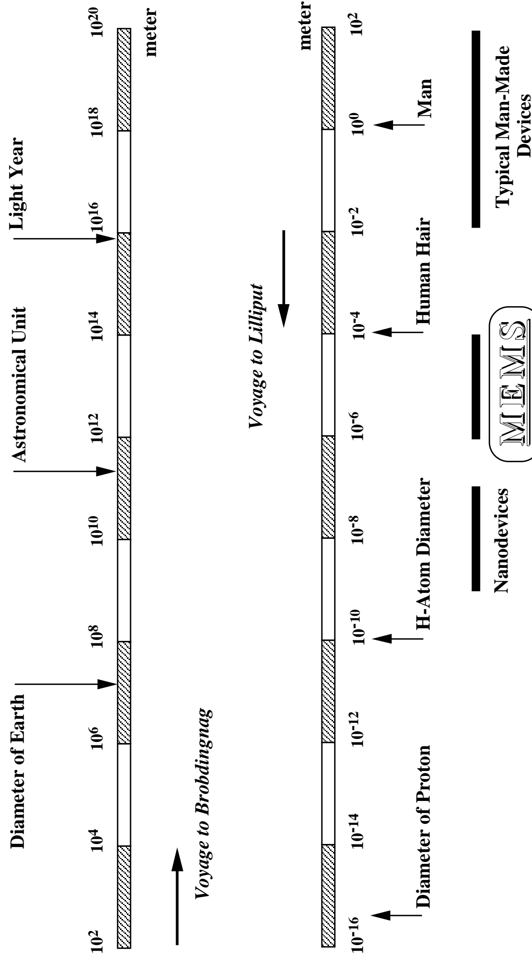

Fig. 1.1. The scale of things in meter. Lower scale continues in the upper bar from left to right. Reproduced with permission from Ref. [3].

1.2. Fluid Mechanics Issues

The rapid progress in fabricating and utilizing microelectromechanical systems during the last decade has not been matched by corresponding advances in our understanding of the unconventional physics involved in the operation and

manufacture of small devices. Providing such understanding is crucial to designing, optimizing, fabricating and operating improved MEMS devices.

Fluid flows in small devices differ from those in macroscopic machines. The operation of MEMS-based ducts, nozzles, valves, bearings, turbomachines, combustors, synthetic jets, *etc.*, cannot always be predicted from conventional flow models such as the Navier–Stokes equations with no-slip boundary condition at a fluid–solid interface, as routinely and successfully applied for larger flow devices. Many questions have been raised when the results of experiments with microdevices could not be explained via traditional flow modeling. The pressure gradient in a long microduct was observed to be non-constant and the measured flowrate was higher than that predicted from the conventional continuum flow model. Slip flow has been observed in microchannels. Load capacities of microbearings were diminished and electric currents needed to move micromotors were extraordinarily high. The dynamic response of micromachined accelerometers operating at atmospheric conditions was observed to be over-damped.

In the early stages of development of this exciting new field, the objective was to build MEMS devices as productively as possible. Microsensors were reading something, but not many researchers seemed to know exactly what. Microactuators were moving, but conventional modeling could not precisely predict their motion. After a decade of unprecedented progress in MEMS technology, perhaps the time is now ripe to take stock, slow down a bit and answer the many questions that arose. The ultimate aim of this long-term exercise is to achieve rational-design capability for useful microdevices and to be able to characterize definitively and with as little empiricism as possible the operations of microsensors and microactuators.

In dealing with fluid flow through microdevices, one is faced with the question of which model to use, which boundary condition to apply and how to proceed to obtain solutions to the problem at hand. Obviously surface effects dominate in small devices. The surface-to-volume ratio for a machine with a characteristic length of 1 m is 1 m^{-1}, while that for a MEMS device having a size of 1 μm is 10^6 m^{-1}. The million-fold increase in surface area relative to the mass of the minute device substantially affects the transport of mass, momentum and energy through the surface. The small length scale of microdevices may invalidate the continuum approximation altogether. Slip flow, thermal creep, rarefaction, viscous dissipation, compressibility, intermolecular forces and other unconventional effects may have to be taken into account, preferably using only first principles such as conservation of mass, Newton's second law, and conservation of energy.

In this chapter, I shall discuss liquid flows and surface phenomena. To place the topic in perspective, gas flows in microdevices will first be discussed briefly.

Microfluid mechanics of liquids is more complicated than that for gases. The liquid molecules are much more closely packed at normal pressures and temperatures, and the attractive or cohesive potential between the liquid molecules as well as between the liquid and solid ones plays a dominant role if the characteristic length of the flow is sufficiently small. In cases when the traditional continuum model fails to provide accurate predictions or postdictions, expensive molecular dynamics simulations seem to be the only first-principle approach available to rationally characterize liquid flows in microdevices. Such simulations are not yet feasible for realistic flow extent or number of molecules. As a consequence, the microfluid mechanics of liquids is much less developed than that for gases.

1.3. Fluid Modeling

There are basically two ways of modeling a flowfield. Either as the fluid really is—a collection of molecules—or as a continuum where the matter is assumed continuous and indefinitely divisible. The former modeling is subdivided into deterministic methods and probabilistic ones, while in the latter approach the velocity, density, pressure, *etc.*, are defined at every point in space and time, and conservation of mass, energy and momentum lead to a set of nonlinear partial differential equations (Euler, Navier–Stokes, Burnett, *etc.*). Fluid modeling classification is depicted schematically in Fig. 1.2.

Fluid and heat flows in conventional macrodevices is traditionally modeled using the principles of conservation of mass, momentum (Newton's second law), and energy (first law of thermodynamics). Additionally, all processes are constrained by the second law of thermodynamics. Those principles are typically expressed in the form of partial differential field equations, where the macroscopic quantities of interest such as velocity, temperature, pressure, *etc.*, depend on a continuum space and time. The first principles, as expressed to describe fluid-transport phenomena in conventional devices, are collectively called the Navier–Stokes equations, a system of nonlinear partial differential equations subject to a sufficient number of initial and boundary conditions, the latter is typically in the form of no velocity slip and no temperature jump at a fluid–solid interface.

There are three fundamental assumptions that must be satisfied in order for the Navier–Stokes equations to be valid:

- The Newtonian framework of mechanics—which specifies that mass and energy are conserved separately and that, in an inertial frame of reference, the sum of all forces is equal to the rate of change of momentum—is valid.

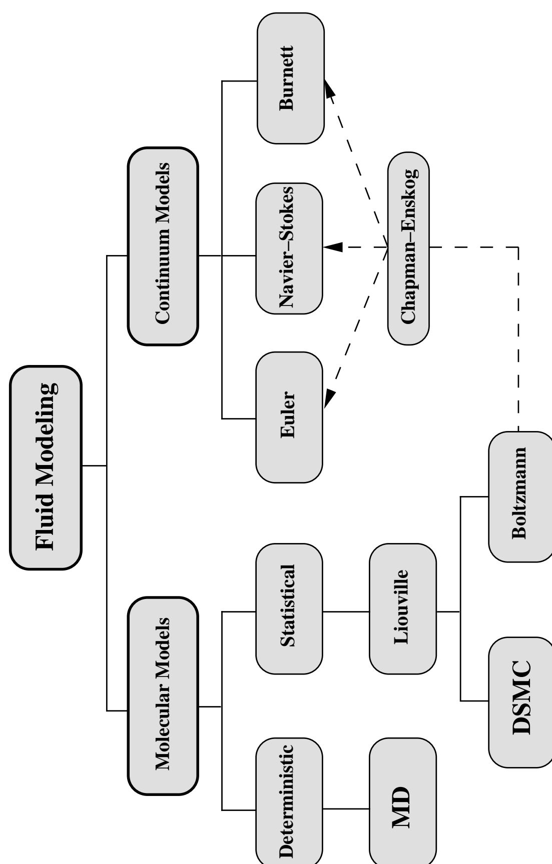

Fig. 1.2. Molecular and continuum flow models. Reproduced with permission from Ref. [3].

- The continuum approximation—which assumes that space and time are indefinitely divisible continuum—is applicable.
- Thermodynamic equilibrium or at least quasi-equilibrium—which permits linear relations between stress and rate of strain and between heat flux and temperature gradient—is assumed.

Fluid isotropy and stress tensor symmetry are also typically, albeit not always, assumed. Violation of any one of the three assumptions listed above invalidates the Navier–Stokes equations and alternative modeling is then called for. We elaborate on the three assumptions in turn.

Newtonian framework: The fluid motions under consideration are assumed non-relativistic, *i.e.*, their characteristic velocities are far below the speed of light. Thus, mass and energy are not interchangeable and each is separately conserved. As long as we are not dealing with atomic or subatomic particles or, at the other extreme of length scale, with stars and galaxies, the Newtonian framework is an excellent modeling tool for most problems in mechanics including those dealing with microelectromechanical systems. Quantum and relativistic mechanics are clearly beyond the scope of the present paper. Therefore, the Newtonian assumption is one that we no longer have to revisit for the rest of this article.

Continuum model: In both solid and fluid mechanics, the continuum approximation implies that the spatial and temporal derivatives of all the macroscopic dependent variables exist in some reasonable sense. In other words, local properties such as density, velocity, stress and heat flux are defined as averages over elements sufficiently large compared with the microscopic structure in order to guarantee a sufficiently large number of molecules inside each fluid element and thus to effect molecular chaos, but small enough in comparison with the scale of the macroscopic phenomena to permit the use of differential calculus to describe those properties. The continuum approximation is almost always met, but exceptions do exist. The resulting equations therefore cover a very broad range of situations, the exception being flows with spatial scales that are not much larger than the mean distance between the fluid molecules, as for example in the case of rarefied gases, shock waves that are thin relative to the molecular distances, and some flows in micro- and nanodevices. We will describe later the precise conditions under which the continuum approximation fails for certain minute devices.

It should be emphasized that the continuum approximation in and by itself leads to an indeterminate set of equations, *i.e.*, more unknowns than equations. To close the resulting system of partial differential equations, relations between the stress and rate of strain and between the heat flux and temperature gradient are needed. At least for compressible flows, two equations of state, relating density and internal energy each to pressure and temperature, are also required. The fact that the continuum approximation does not necessarily lead to the Navier–Stokes equations is a subtle point that is often confused in the literature.

Thermodynamic equilibrium: Thermodynamic equilibrium implies that the macroscopic quantities have sufficient time to adjust to their changing surroundings. In motion, exact thermodynamic equilibrium is impossible as each fluid

particle is continuously having volume, momentum or energy added or removed, and so in fluid dynamics and heat transfer we speak of quasi-equilibrium. The second law of thermodynamics imposes a tendency to revert to equilibrium state, and the defining issue here is whether or not the flow quantities are adjusting fast enough. The reversion rate will be very high if the molecular time and length scales are very small as compared to the corresponding macroscopic flow-scales. This will guarantee that numerous molecular collisions will occur in sufficiently short time to equilibrate fluid particles whose properties vary little over distances comparable to the molecular length scales. For gases, the characteristic length for molecular collision is the mean free path, $\mathcal{L}$, the average distance traveled by a molecule before colliding with another. When $\mathcal{L}$ is, say, one order of magnitude smaller than the flow length scale, L, macroscopic quantities such as velocity and temperature will have nearly linear gradients over molecular distances, and it is on these gradients alone that departure from equilibrium will depend. Therefore, the quasi-equilibrium assumption signifies that the stress is linearly related to the rate of strain (Newtonian fluids) and the heat flux is linearly related to the temperature gradient (Fourier fluids). These issues have been described quite eloquently by Lighthill.[8] Thermodynamic equilibrium additionally gives rise to the no-slip and no-temperature-jump boundary conditions.[8,9]

As is the case with the continuum approximation, the quasi-equilibrium assumption can be violated under certain circumstances relevant to microdevices. In these cases, alternatives to the no-slip condition or even to the Navier–Stokes equations themselves must be sought. We are now ready to quantify the conditions under which the continuum approximation or the quasi-equilibrium assumption can be made. For gases at least, the answer to both questions is well known from statistical thermodynamics particularly as was extensively applied to rarefied gas dynamics half a century ago.[9,10] For that reason we discuss gas flows first deferring the discussion of liquid flows to afterward.

1.4. Gas Flows

The well-known chart reproduced in Fig. 1.3 clearly illustrates the answer we are seeking. All scales in this plot are logarithmic. The bottom abscissa represents the density normalized with a reference density, ρ/ρ_0, or equivalently the normalized number density (number of molecules per unit volume), n/n_0. The top abscissa is the average distance between molecules normalized with the molecular diameter, δ/σ. Clearly, the density ratio is proportional to the inverse cube of δ/σ. The left ordinate represents a characteristic flow dimension, L, in meter. This can be computed from a characteristic macroscopic property, such as density, divided by

the absolute value of its gradient. The right ordinate is the length scale normalized with the molecular diameter, L/σ. The chart in Fig. 1.3 depicts a gas having a molecular diameter of $\sigma = 4 \times 10^{-10}$ m, which diameter very closely represents air modeled as rigid spheres. Similar charts can be drawn for other gases.

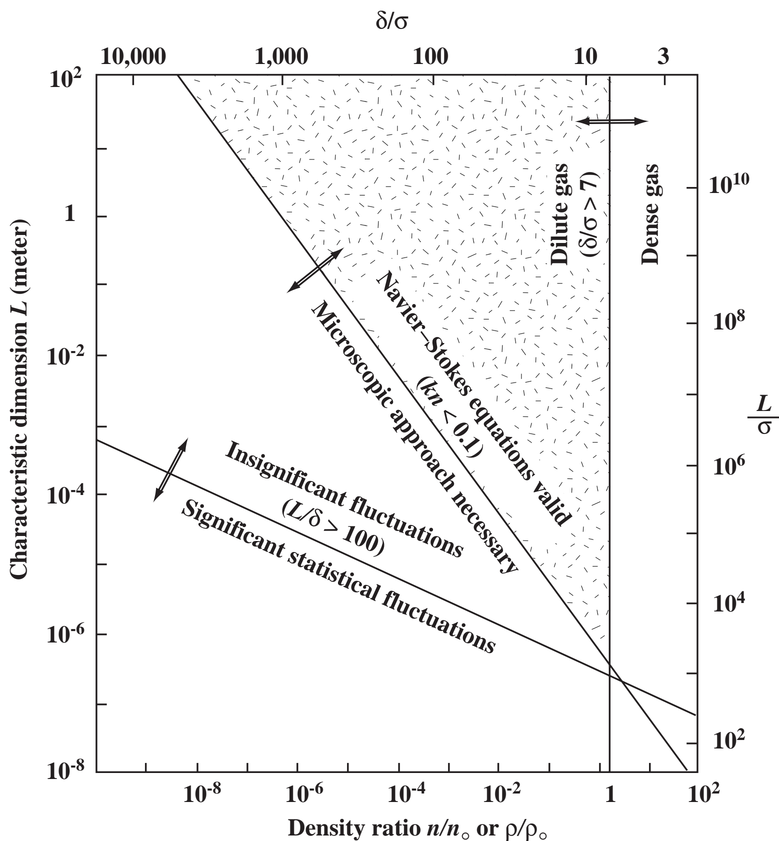

Fig. 1.3. Effective limits of different flow models. Reproduced with permission from Ref. [10].

The vertical line inserted in Fig. 1.3 represents the boundary between dilute gas and dense one. Dilute gas is to the left of this line where $\delta/\sigma > 7$. For such gas, intermolecular forces play no role and the molecules spend most of their time in free flight between brief collisions at which instances the molecules' direction and speed abruptly change. Additionally, the probability of more than two molecules colliding is minuscule. We then speak of only binary collisions,

and all the simplifications of the powerful kinetic theory of gases can be invoked when dealing with dilute gases. Dry air at standard conditions has a pressure of 1.01×10^5 N/m^2, temperature of 288 K, density ratio of 1, and $\delta/\sigma = 9$. Standard air is therefore a dilute, ideal gas, but barely.

The gently sloped line in Fig. 1.3 indicates the limit of molecular chaos. When averaging over many molecules to compute macroscopic quantities, insignificant statistical fluctuations occur when there is at least 100 molecules to the side $L/\sigma > 100$, in other words when at least 1 million molecules reside inside the smallest macroscopic fluid volume of interest. Therefore, the continuum approximation is valid only on top of that line. The molecular chaos restriction improves the accuracy of computing the macroscopic quantities from the microscopic information. In essence, the volume over which averages are computed has to have sufficient number of molecules to reduce statistical errors. It can be shown that computing macroscopic flow properties by averaging over a number of molecules will result in statistical fluctuations with a standard deviation of approximately 0.1% if one million molecules are used, around 3% if one thousand molecules are used, and so on.

The steeper line in Fig. 1.3 indicates the boundary of validity of the quasi-equilibrium assumption. This limit is governed by the Knudsen number, Kn $\equiv \mathcal{L}/L$, which is the ratio of the mean free path to the characteristic macroscopic length. Navier–Stokes equations are valid only if Kn < 0.1 (above the steeper line), although the no-slip condition demands the stricter limit of Kn < 0.001. The line corresponding to the stricter limit is parallel to the steeper line in Fig. 1.3 but shifted upward by two decades. The mean free path is proportional to n^{-1}, and therefore the slope of the quasi-equilibrium line, in the logarithmic plot, is three times steeper than that of the molecular chaos line. Much of that has been known since the classical experiments conducted by Knudsen.[11] These experiments have been recently repeated with great precision at the U.S. National Institute of Standards and Technology by Tison[12] and reported by Beskok *et al.*[13]

How does all that relate to microdevices? As density is reduced, the gas changes from dense to dilute. As size shrinks for a low-density gas, the flow slips, followed by a failure of the Navier–Stokes equation, followed by a failure of the continuum approximation altogether. For a dense gas, a reverse trend is observed as L is reduced: the continuum approximation fails first followed by a failure of the quasi-equilibrium assumption. Clearly, the continuum approximation and the quasi-equilibrium assumption are two different things. The two lines in Fig. 1.3 describing the two respective limits meet only at a single point.

To give a concrete example, for air at 1 atm, slip occurs if $L < 100$ microns, (stress)–(rate of strain) relation becomes nonlinear if $L < 1$ micron, and the

continuum approximation fails altogether if $L < 0.4$ micron. For air at 10^{-3} atm, slip occurs if $L < 100$ mm, (stress)–(rate of strain) relation becomes nonlinear if $L < 1$ mm, and the continuum approximation fails if $L < 4$ microns. Light gases such as Helium will reach those limits at considerably larger characteristic lengths. All of those conditions are well within the operating ranges of micro- and nanodevices. Thus, there are circumstances when transport in microdevices should not be modeled using the traditional equations.

The next step for both gas and liquid flows is to figure out what to do if conventional modeling fails. For gases at least, there are first-principles equations that give the precise amount of slip or temperature jump to include in case the Knudsen number exceeds the critical limit of 0.001.[3] Higher-order equations such as those of Burnett can replace the Navier–Stokes equations when Kn exceeds 0.1. Finally, if the continuum approximation fails altogether, the fluid can be modeled as it really is, a collection of molecules. There, one can use molecular dynamics simulations (for liquids), Boltzmann equation (for dilute gases), or direct simulations Monte Carlo (also for dilute gases). Subject to their own limitations, all the molecular-based models can also be used in lieu of higher-order momentum and energy equations, *i.e.*, for non-equilibrium, continuum situations. All the strategies listed here are schematically depicted in Fig. 1.2, and described in greater details in the books by Karniadakis and Beskok[6] and Gad-el-Hak.[5]

1.5. Liquid Flows

From the continuum point of view, liquids and gases are both fluids obeying the same equations of motion. For incompressible flows, for example, the Reynolds number is the primary dimensionless parameter that determines the character of the flowfield for a given geometry. True, water, for example, has density and viscosity that are, respectively, three and two orders of magnitude higher than those for air, but if the Reynolds number and geometry are matched, liquid and gas flows should be identical.[a] For MEMS applications, however, we anticipate the possibility of non-equilibrium flow conditions and the consequent invalidity of the Navier–Stokes equations and the no-slip boundary conditions. Such circumstances can best be researched using the molecular approach. This was discussed for gases in the previous section, and the corresponding arguments for liquids will be given in the present section. The literature on non-Newtonian fluids in general and polymers in particular is vast (for example, the bibliographic survey by Nadolink and Haigh[14] cites over 4,900 references on polymer drag reduction

[a]Barring phenomena unique to liquids such as cavitation, free surface flows, *etc.*

alone) and provides a rich source of information on the molecular approach for liquid flows.

Solids, liquids and gases are distinguished merely by the degree of proximity and the intensity of motions of their constituent molecules. In solids, the molecules are packed closely and confined, each hemmed in by its neighbors.[9] Only rarely would one solid molecule slip from its neighbors to join a new set. As the solid is heated, molecular motion becomes more violent and a slight thermal expansion takes place. At a certain temperature that depends on ambient pressure, sufficiently intense motion of the molecules enables them to pass freely from one set of neighbors to another. The molecules are no longer confined but are nevertheless still closely packed, and the substance is now considered a liquid. Further heating of the matter eventually releases the molecules altogether, allowing them to break the bonds of their mutual attractions. Unlike solids and liquids, the resulting gas expands to fill any volumeavailable to it.

Unlike solids, both liquids and gases cannot resist finite shear force without continuous deformation; that is the definition of a fluid medium. In contrast to the reversible, elastic, static deformation of a solid, the continuous deformation of a fluid resulting from the application of a shear stress results in an irreversible work that eventually becomes random thermal motion of the molecules; that is viscous dissipation. There are around 25 million molecules of STP air in a one-micron cube. The same cube would contain around 34 billion molecules of water. So, liquid flows are continuum even in extremely small devices through which gases would not be considered continuum. The average distance between molecules in the gas example is one order of magnitude higher than the diameter of its molecules, while that for the liquid phase approaches the molecular diameter. As a result, liquids are almost incompressible. Their isothermal compressibility coefficient α and bulk expansion coefficient β are much smaller compared to those for gases. For water, for example, a hundred-fold increase in pressure leads to less than 0.5% decrease in volume. Sound speeds through liquids are also high relative to those for gases, and as a result most liquid flows are incompressible.[b] Notable exceptions to that are propagation of ultra-high-frequency sound waves and cavitation phenomena.

The mechanisms through which liquids transport mass, momentum and energy must be very different from those of gases. In dilute gases, intermolecular forces play no role and the molecules spend most of their time in free flight between brief collisions at which instances the molecules' direction and speed abruptly change. The random molecular motions are responsible for gaseous transport

[b]Note that we distinguish between a fluid and a flow being compressible/incompressible. For example, the flow of the highly compressible air can be either compressible or incompressible.

processes. In liquids, on the other hand, the molecules are closely packed though not fixed in one position. In essence, the liquid molecules are always in a collision state. Applying a shear force must create a velocity gradient so that the molecules move relative to one another, *ad infinitum* as long as the stress is applied. For liquids, momentum transport due to the random molecular motion is negligible compared to that due to the intermolecular forces. The straining between liquid molecules causes some to separate from their original neighbors, bringing them into the force field of new molecules. Across the plane of the shear stress, the sum of all intermolecular forces must, on the average, balance the imposed shear. Liquids at rest transmit only normal force, but when a velocity gradient occurs, the net intermolecular force will have a tangential component.

The incompressible Navier–Stokes equations describe liquid flows under most circumstances. But what are the conditions for which the no-slip Navier–Stokes equations fail to adequately describe liquid flows? In other words, how small does a device have to be before a particular liquid flow starts slipping perceptibly and for the stress–strain relation to become nonlinear? Answering this question from first principles is the holy grail of microfluidic modeling. Liquids do not have a well-advanced molecular-based theory as that for dilute gases. The concept of mean free path is not very useful for liquids and the conditions under which a liquid flow fails to be in quasi-equilibrium state are not well defined. There is no Knudsen number for liquid flows to guide us through the maze. We do not know, from first principles, the conditions under which the no-slip boundary condition becomes inaccurate, or the point at which the (stress)–(rate of strain) relation or the (heat flux)–(temperature gradient) relation fails to be linear. Certain empirical observations indicate that those simple relations that we take for granted occasionally fail to accurately model liquid flows. For example, it has been shown in rheological studies[15] that non-Newtonian behavior commences when the strain rate approximately exceeds twice the molecular frequency-scale

$$\dot{\gamma} = \frac{\partial u}{\partial y} \geq 2\Im^{-1} \tag{1.1}$$

where the molecular time scale $\Im$ is given by

$$\Im = \left[\frac{m\sigma^2}{\epsilon}\right]^{\frac{1}{2}} \tag{1.2}$$

where m is the molecular mass, and σ and ϵ are respectively the characteristic length and energy scales for the molecules. For ordinary liquids such as water, this time scale is extremely small and the threshold shear rate for the onset of

non-Newtonian behavior is therefore extraordinarily high. For high-molecular-weight polymers, on the other hand, m and σ are both many orders of magnitude higher than their respective values for water, and the linear stress–strain relation breaks down at realistic values of the shear rate.

As is the case for gas flows, the threshold for the occurrence of measurable slip in liquid flows is expected to be higher (in terms of, say, channel height) than that necessary for the occurrence of nonlinear stress–strain relation. The moving contact line when a liquid spreads on a solid substrate is an example where slip flow must be allowed to avoid singular or unrealistic behavior in the Navier–Stokes solutions.[16–19] Other examples where slip-flow must be admitted include corner flows[20,21] and extrusion of polymer melts from capillary tubes.[22–24] Wall slip in polymer extrusion is discussed extensively by Den.[25] The recent chapter by Lauga, Brenner and Stone[26] provides a comprehensive treatment of the no-slip boundary condition for Newtonian and non-Newtonian fluids as well as for polar and non-polar liquids. These authors trace the issue to its 19th century roots, and survey both the experimental and analytical aspects of the problem.

Existing experimental results of liquid flow in microdevices are contradictory. This is not surprising given the difficulty of such experiments and the lack of a guiding rational theory. References [27–30] summarize the relevant literature. For small-length-scale flows, a phenomenological approach for analyzing the data is to define an apparent viscosity μ_a calculated so that if it were used in the traditional no-slip Navier–Stokes equations instead of the actual fluid viscosity μ, the results would be in agreement with experimental observations. Israelachvili[31] and Gee *et al.*[32] found that $\mu_a = \mu$ for thin-film flows as long as the film thickness exceeds 10 molecular layers ($\approx$ 5 nm). For thinner films, μ_a depends on the number of molecular layers and can be as much as 10^5 times larger than μ. Chan and Horn's results[33] are somewhat different: the apparent viscosity deviates from the fluid viscosity for films thinner than 50 nm.

In polar-liquid flows through capillaries, Migun and Prokhorenko[34] report that μ_a increases for tubes smaller than 1 micron in diameter. In contrast, Debye and Cleland[35] report μ_a smaller than μ for paraffin flow in porous glass with average pore size several times larger than the molecular length scale. Experimenting with microchannels ranging in depths from 0.5 micron to 50 microns, Pfahler *et al.*[27] found that μ_a is consistently smaller than μ for both liquid (isopropyl alcohol; silicone oil) and gas (nitrogen; helium) flows in microchannels. For liquids, the apparent viscosity decreases with decreasing channel depth. Other researchers using small capillaries report that μ_a is about the same as μ.[36–41]

More recently, Sharp[42] and Sharp *et al.*[43] asserted that, despite the significant inconsistencies in the literature regarding liquid flows in microchannels, such

flows are well predicted by macroscale continuum theory. A case can be made to the contrary, however, as will be seen at the end of Section 1.7, and the final verdict on this controversy is yet to come.

The above contradictory results point to the need for replacing phenomenological models by first-principles ones. The lack of molecular-based theory of liquids—despite extensive research by the rheology and polymer communities—leaves molecular dynamics simulations (MD) as the nearest weapon to first-principles arsenal. MD simulations offer a unique approach to checking the validity of the traditional continuum assumptions. However, as was pointed out earlier, such simulations are limited to exceedingly minute flow extent. Koplik and Banavar[21] offer a useful primer on the history, principles, applications and limitations of molecular dynamics simulations. We provide in the following section a brief discussion of MD simulations.

1.6. Molecular Dynamics Simulations

The molecular models recognize the fluid as a myriad of discrete particles: molecules, atoms, ions and electrons. The goal here is to determine the position, velocity and state of all particles at all times. The molecular approach is either deterministic or probabilistic (refer to Fig. 1.2), and the former is the most fundamental of the molecular approaches. The motion of the molecules are governed by the laws of classical mechanics, although, at the expense of greatly complicating the problem, the laws of quantum mechanics can also be considered in special circumstances. The modern molecular dynamics computer simulations have been pioneered by Alder and Wainwright,[44–46] and reviewed by Ciccotti and Hoover,[47] Allen and Tildesley,[48] Haile,[49] and Koplik and Banavar.[21]

The MD simulation begins with a set of N molecules in a region of space, each assigned a random velocity corresponding to a Boltzmann distribution at the temperature of interest. The interaction between the particles is prescribed typically in the form of a two-body potential energy and the time evolution of the molecular positions is determined by integrating Newton's equations of motion, one for each molecule. Because MD is based on the most basic set of equations, it is valid in principle for any flow extent and any range of parameters. The method is straightforward in principle but there are two hurdles: choosing a proper and convenient potential for particular fluid and solid combinations, and the colossal computer resources required to simulate a reasonable flowfield extent. A significant advantage of molecular dynamics simulations is that the relation between the stress and rate of strain as well as between the heat flux and temperature gradient comes out as part of the answer. In other words, whether the fluid is Newtonian/

non-Newtonian or Fourier/non-Fourier does not have to be assumed. Likewise, the presence/absence of momentum or energy slip at a solid wall comes out as part of the answer. The issue of thermodynamic equilibrium or lack thereof is therefore moot.

For purists, the difficulty of choosing a potential is a sticky one. Aside from computer-intensive quantum mechanics calculations, there is currently no totally rational methodology by which a convenient potential can be favored. Part of the art of molecular dynamics simulations is to pick an appropriate potential and validate the simulation results with experiments or other analytical/computational results. By astutely choosing the potential and its parameters, one can essentially obtain any desired result; a clear weakness of the MD approach. A commonly used potential between two molecules is the generalized Lennard-Jones 6–12 potential, to be used and further discussed in the sections.

The second difficulty, and by far the most serious limitation of molecular dynamics simulations, is the number of molecules N that can realistically be modeled on a digital computer. Since the computation of an element of trajectory for any particular molecule requires consideration of all other molecules as potential collision partners, the amount of computation required by the MD method is proportional to N^2. Some saving in computer time can be achieved by cutting off the weak tail of the potential (see Fig. 1.4) at, say, $r_c = 2.5\sigma$, and shifting the potential by a linear term in r so that the force goes smoothly to zero at the cutoff. As a result, only nearby molecules are treated as potential collision partners, and the computation time for N molecules no longer scales with N^2.

The state of the art of molecular dynamics simulations in the early 2000s is such that with a few hours of CPU time, general-purpose supercomputers can handle around 100,000 molecules. At enormous expense, the fastest parallel machine available can simulate around 10 million particles, although more recent reports of an order-of-magnitude higher number of molecules have been made (MIT's Nicolas G. Hadjiconstantinou; private communication). Because of the extreme diminution of molecular scales, the 10 million figure translates into regions of liquid flow of about 0.06 mm (600 Angstroms) in linear size, over time intervals of around 0.001 ms, enough for continuum behavior to set in for simple molecules. To simulate 1 s of real time for complex molecular interactions, *e.g.*, including vibration modes, reorientation of polymer molecules, collision of colloidal particles, *etc.*, requires unrealistic CPU time measured in hundreds of years.

MD simulations are highly inefficient for dilute gases where the molecular interactions are infrequent. The simulations are more suited for dense gases and liquids. Clearly, molecular dynamics simulations are reserved for situations where the continuum approach or the statistical methods are inadequate to compute from

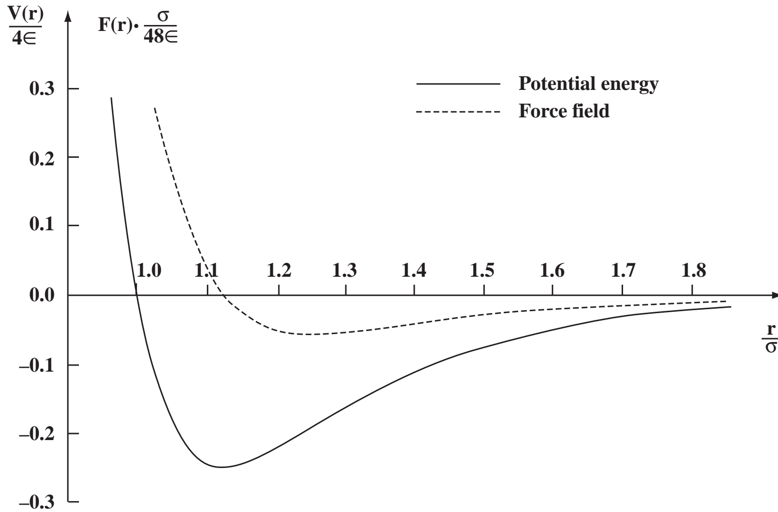

Fig. 1.4. Typical Lennard-Jones 6–12 potential and the intermolecular force field resulting from it. Only a small portion of the potential function is shown for clarity.

first principles important flow quantities. Slip boundary condition for a liquid flow in an extremely small device is such a case, as will be discussed in the following section.

1.7. A Typical MD Result

Thompson and Troian[50] provide molecular dynamics simulations to quantify the slip-flow boundary condition dependence on shear rate. Recall the linear Navier boundary condition introduced[51] in 1823,

$$\Delta u\big|_w = u_{\text{fluid}} - u_{\text{wall}} = L_s \frac{\partial u}{\partial y}\bigg|_w \tag{1.3}$$

where L_s is the constant slip length, and $(\partial u/\partial y)|_w$ is the strain rate computed at the wall. The goal of Thompson and Troian's simulations was to determine the degree of slip at a solid–liquid interface as the interfacial parameters and the shear rate change. In their simulations, a simple liquid underwent planar shear in a Couette cell as shown in Fig. 1.5. The typical cell measured $12.51 \times 7.22 \times h$, in units of molecular length scale σ, where the channel depth h varied in the range of 16.71σ–24.57σ, and the corresponding number of molecules simulated ranged from 1,152 to 1,728. The liquid is treated as an isothermal ensemble of

spherical molecules. A shifted Lennard-Jones 6–12 potential is used to model intermolecular interactions, with energy and length scales ϵ and σ, and cut-off distance $r_c = 2.2\sigma$:

$$V(r) = 4\epsilon \left[\left(\frac{r}{\sigma}\right)^{-12} - \left(\frac{r}{\sigma}\right)^{-6} - \left(\frac{r_c}{\sigma}\right)^{-12} + \left(\frac{r_c}{\sigma}\right)^{-6} \right] \tag{1.4}$$

The truncated potential is set to zero for $r > r_c$.

The fluid–solid interaction is also modeled with a truncated Lennard-Jones potential, with energy and length scales ϵ^{wf} and σ^{wf}, and cut-off distance r_c. The equilibrium state of the fluid is a well-defined liquid phase characterized by number density $n = 0.81\sigma^{-3}$ and temperature $T = 1.1\epsilon/k$, where k is the Boltzmann constant.

The steady state velocity profiles resulting from Thompson and Troian's MD simulations[50] are depicted in Fig. 1.5 for different values of the interfacial parameters ϵ^{wf}, σ^{wf} and n^w. Those parameters, shown in units of the corresponding fluid parameters ϵ, σ and n, characterize, respectively, the strength of the liquid–solid coupling, the thermal roughness of the interface and the commensurability of wall and liquid densities. The macroscopic velocity profiles recover the expected flow behavior from continuum hydrodynamics with boundary conditions involving varying degrees of slip. Note that when slip exists, the shear rate $\dot{\gamma}$ no longer equals U/h. The degree of slip increases (*i.e.*, the amount of momentum transfer at the wall–fluid interface decreases) as the relative wall density n^w increases or the strength of the wall–fluid coupling σ^{wf} decreases; in other words when the relative surface energy corrugation of the wall decreases. Conversely, the corrugation is maximized when the wall and fluid densities are commensurate and the strength of the wall–fluid coupling is large. In this case, the liquid feels the corrugations in the surface energy of the solid owing to the atomic close-packing. Consequently, there is efficient momentum transfer and the no-slip condition applies, or in extreme cases, a 'stick' boundary condition takes hold.

Variations of the slip length L_s and viscosity μ as functions of shear rate $\dot{\gamma}$ are shown in parts (a) and (b) of Fig. 1.6, for five different sets of interfacial parameters. For Couette flow, the slip length is computed from its definition, $\Delta u|_w / \dot{\gamma} = (U/\dot{\gamma} - h)/2$. The slip length, viscosity and shear rate are normalized in the figure using the respective molecular scales for length, viscosity, and inverse time. The viscosity of the fluid is constant over the entire range of shear rates (Fig. 1.6b), indicating Newtonian behavior. As indicated earlier, non-Newtonian behavior is expected for $\dot{\gamma} \geq 2\Im^{-1}$, well above the shear rates used in Thompson and Troian's simulations.

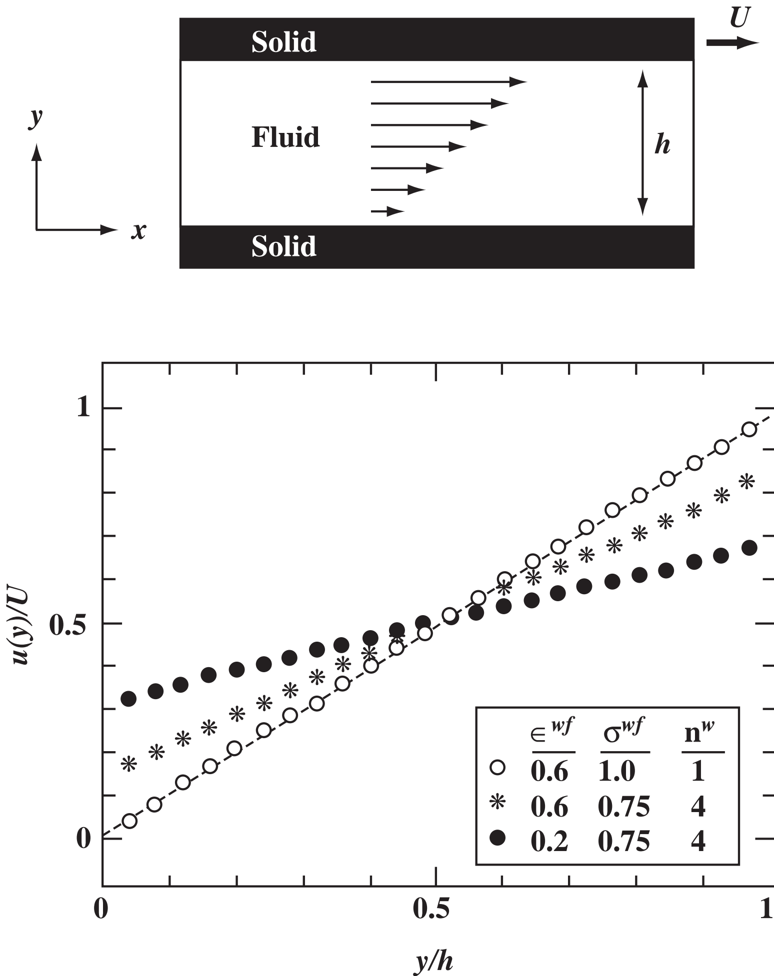

Fig. 1.5. Velocity profiles in a Couette flow geometry at different interfacial parameters. All three profiles are for $U = \sigma\Im^{-1}$, and $h = 2,457\sigma$. The dashed line is the no-slip Couette-flow solution. Reproduced with permission from Ref. [50].

At low shear rates, the slip length behavior is consistent with the Navier model, *i.e.*, is independent of the shear rate. Its limiting value ranges from 0 to $\sim 17\sigma$ for the range of interfacial parameters chosen (Fig. 1.6a). In general, the amount of slip increases with decreasing surface energy corrugation. Most interestingly, at high shear rates the Navier condition breaks down as the slip length increases rapidly with $\dot{\gamma}$. The critical shear-rate value for the slip length to diverge, $\dot{\gamma}_c$,

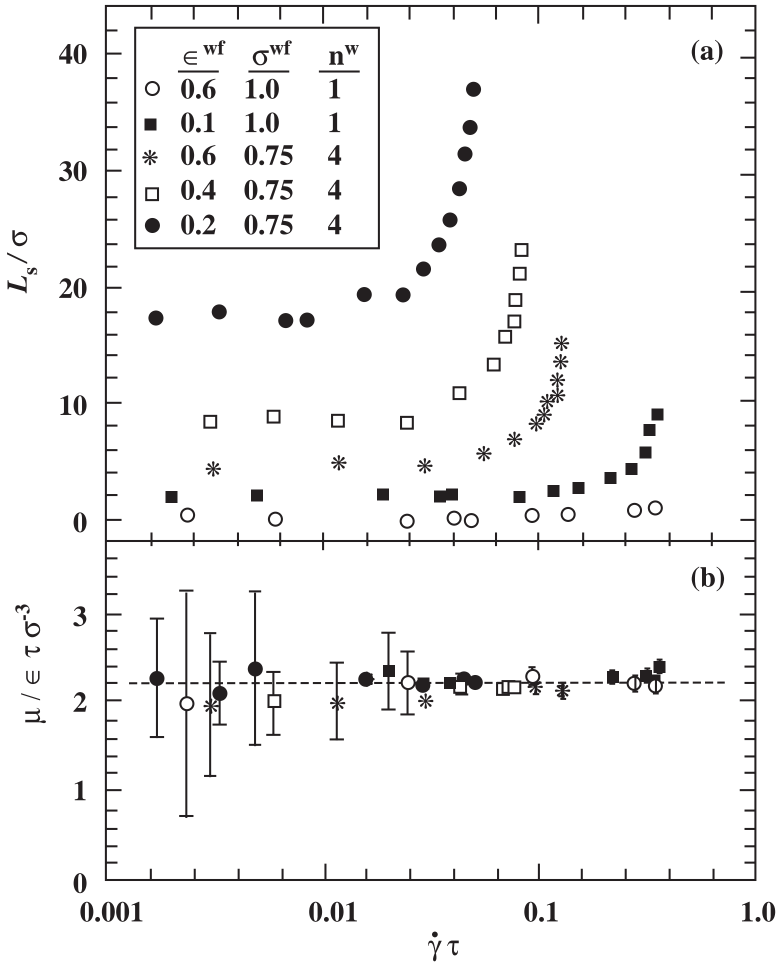

Fig. 1.6. Variation of slip length and viscosity as functions of shear rate. Reproduced with permission from Ref. [50].

decreases as the surface energy corrugation decreases. Surprisingly, the boundary condition is nonlinear even though the liquid is still Newtonian. In dilute gases, the linear slip condition and the Navier–Stokes equations, with their linear stress–strain relation, are both valid to the same order of approximation in Knudsen number. In other words, deviation from linearity is expected to take place at the same value of $\mathrm{Kn} = 0.1$. In liquids, in contrast, the slip length appears to become nonlinear and to diverge at a critical value of shear rate well below the shear

rate at which the linear stress–strain relation fails. Moreover, the boundary condition deviation from linearity is not gradual but is rather catastrophic. The critical value of shear rate $\dot{\gamma}_c$ signals the point at which the solid can no longer impart momentum to the liquid. This means that the same liquid molecules sheared against different substrates will experience varying amounts of slip and vice versa.

Based on the above results, Thompson and Troian[50] suggest a universal boundary condition at a solid–liquid interface. Scaling the slip length L_s by its asymptotic limiting value L_s^o and the shear rate $\dot{\gamma}$ by its critical value $\dot{\gamma}_c$, collapses the data in the single curve shown in Fig. 1.7. The data points are well described by the relation

$$L_s \;=\; L_s^o \left[1 - \frac{\dot{\gamma}}{\dot{\gamma}_c}\right]^{-\frac{1}{2}} \tag{1.5}$$

The nonlinear behavior close to a critical shear rate suggests that the boundary condition can significantly affect flow behavior at macroscopic distances from the wall. Experiments with polymers confirm this observation.[52] The rapid change in the slip length suggests that for flows in the vicinity of $\dot{\gamma}_c$, small changes in surface properties can lead to large fluctuations in the apparent boundary condition. Thompson and Troian[50] conclude that the Navier slip condition is but the low-shear-rate limit of a more generalized universal relationship which is nonlinear and divergent. Their relation provides a mechanism for relieving the stress singularity in spreading contact lines and corner flows, as it naturally allows for varying degrees of slip on approach to regions of higher rate of strain.

To place the above results in physical terms, consider water[c] at a temperature of $T = 288$ K. The energy-scale in the Lennard-Jones potential is then $\epsilon = 3.62 \times 10^{-21}$ J. For water, $m = 2.99 \times 10^{-26}$ kg, $\sigma = 2.89 \times 10^{-10}$ m, and at standard temperature $n = 3.35 \times 10^{28}$ molecules/m^3. The molecular time-scale can thus be computed,

$$\Im = \left[m\,\sigma^2/\epsilon\right]^{1/2} = 8.31 \times 10^{-13}\text{s} \tag{1.6}$$

For the third case depicted in Fig. 1.7 (the open squares), $\dot{\gamma}_c\,\Im = 0.1$, and the critical shear rate at which the slip condition diverges is thus $\dot{\gamma}_c = 1.2 \times 10^{11}\ \text{s}^{-1}$.

[c]Water molecules are complex ones, forming directional, short-range covalent bonds. Thus requiring a more complex potential than the Lennard-Jones to describe the intermolecular interactions. For the purpose of the qualitative example described here, however, we use the computational results of Thompson and Troian (1997) who employed the L-J potential.

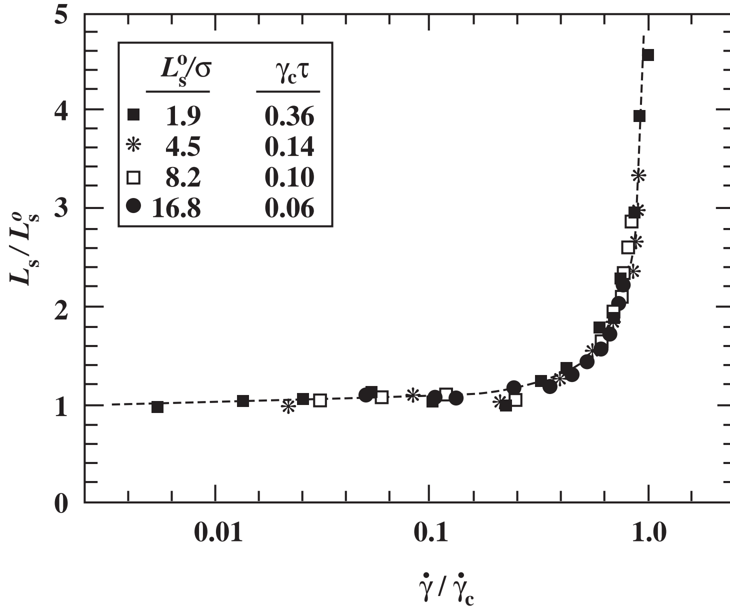

Fig. 1.7. Universal relation of slip length as a function of shear rate. Reproduced with permission from Ref. [50].

Such an enormous rate of strain[d] may be found in extremely small devices having extremely high speeds. On the other hand, the conditions to achieve a measurable slip of 17σ (the solid circles in Fig. 1.6) are not difficult to encounter in microdevices: density of solid four times that of liquid, and energy-scale for wall–fluid interaction that is one fifth of energy-scale for liquid.

The limiting value of slip length is independent of the shear rate and can be computed for water as $L_s^o = 17\,\sigma = 4.91 \times 10^{-9}$ m. Consider a water microbearing having a shaft diameter of 100 μm and rotation rate of 20,000 rpm and a minimum gap of $h = 1\,\mu$m. In this case, $U = 0.1$ m/s and the no-slip shear rate is $U/h = 10^5$ s^{-1}. When slip occurs at the limiting value just computed, the shear rate and the wall slip-velocity are computed as follows:

$$\dot{\gamma} \;=\; \frac{U}{h \,+\, 2\,L_s^o} \;=\; 9.90 \times 10^4 \ \mathrm{s}^{-1} \tag{1.7}$$

$$\Delta u\Big|_w \;=\; \dot{\gamma}\, L_s \;=\; 4.87 \times 10^{-4} \ \mathrm{m/s}. \tag{1.8}$$

[d]Note however that $\dot{\gamma}_c$ for high-molecular-weight polymers would be many orders of magnitude smaller than the value developed here for water.

As a result of the Navier slip, the shear rate is reduced by 1% from its no-slip value, and the slip velocity at the wall is about 0.5% of U, small but not insignificant.

1.8. Hybrid Methods

At sufficiently small device scale for both liquid and gas flows, the continuum and the quasi-equilibrium hypotheses eventually fail or at least yield increasingly inaccurate results. This is true even for simple fluids such as air or water where non-equilibrium effects, *e.g.*, velocity slip, temperature jump, non-Newtonian and non-Fourier behavior, are not ordinarily observed in macrodevices operating near room pressure and temperature. Because of widely different molecular spacings, the scale at which the traditional assumptions should no longer be made clearly differs for dilute gases and for dense gases and liquids.

Noting the difficulty of obtaining reliable experimental data at the micro/nano scales, the no-slip Navier–Stokes equations themselves should not be used to determine the scale at which those assumptions fail to provide accurate modeling of the flow under consideration, as that is clearly a circular argument. The kinetic theory of dilute gases provides powerful answers, and enables us to determine from first principles the scales at which the no-slip assumption, the linear stress–rate of strain relation, and the continuum hypothesis are no longer valid. Note that those three assumptions fail at progressively smaller device size, much the same as they do fail at progressively lower density or higher altitude. For dense gases and liquids, on the other hand, no such straightforward strategy as the kinetic theory exists, first to answer the question of whether or not the Navier–Stokes system is usable, and second to provide a more accurate alternative.

A molecular dynamics simulation offers a first-principles solution to the problem, but is limited to unrealistically small spatial and temporal scales. For example, the time step needed to simulate pure water with fixed O–H bonds and H–O–H angles is dictated by the fastest frequency needed to be resolved and is of the order of 2 fs. To simulate a mere 1 ms of real time, a whopping 500 million time steps are needed, requiring well above one year of CPU time. The physical phenomena investigated in a typical microdevice occur over a broad range of spatial and temporal scales. One way out of this conundrum is to use a hybrid method, where the expensive, high-resolution atomistic model is confined to flow regions in which it is needed, *e.g.*, near strong flow gradients and fluid–solid interfaces, and the continuum model is used in the rest of the computational domain. Such hybrid methods can in principle be used in solids,[53–55] dilute gases,[56–64] and liquids.[65–71] In all cases, however, the challenge is to choose the correct coupling

method and to properly match the interface between the atomistic and continuum regions. Coupling is done based on the physics of the particular flow problem investigated (whether the continuum flow is compressible or incompressible; steady or unsteady), and is considered more or less a solved problem.[69,70] On the other hand, passing information from the continuum to the molecular subdomain is a more subtle problem that at present has no satisfactory solution for dense gases and liquids. This is caused by our inability to unambiguously define and recreate the interacting molecular state for a dense gas (or a liquid) from knowledge of the continuum solution, which is essentially the first few moments of the non-equilibrium distribution function (Nicolas G. Hadjiconstantinou; private communication).

For dilute gases, the atomistic calculation of choice is the Boltzmann equation simulation tool known as the direct simulation Monte Carlo (DSMC).[69] Baker and Hadjiconstantinou[72] assert that considerable saving in computational time can be achieved by considering only the deviation from thermodynamic equilibrium. This is particularly important in the low Mach number limit where DSMC is slow to converge as it computes the Boltzmann collision integral. In this Mach number limit, important for typical MEMS flows, the deviation from equilibrium is modest and quicker convergence of the statistical sampling of macroscopic observables such as flow velocity is achieved by Baker and Hadjiconstantinou's variance reduction technique.

Continuum–DSMC hybrid methods allows the simulation of complex phenomena at the microscale without the prohibitive cost of a purely atomistic calculation. The two computational regimes are matched over a region of space where both are assumed to be valid. For compressible flows, the continuum and atomistic time steps are comparable, and explicit time integration with a finite-volume-type coupling technique is feasible. The adaptive mesh and algorithm refinement (AMAR) scheme proposed by Wijesinghe *et al.*[70] provides a robust flux-based method for coupling an atomistic fluid representation to a continuum model. The algorithm extends adaptive mesh refinement by introducing the molecular description at the finest level of refinement. This is not possible generally for incompressible, dilute gas flows, as explicit integration at the molecular time step becomes prohibitive. An implicit method, based on a domain decomposition approach known as the Schwarz alternating method, has been successfully demonstrated by Wijesinghe and Hadjiconstantinou.[69] This coupling method uses state variables instead of fluxes to achieve the matching, and provides time-scale decoupling between the very small atomistic time and the much larger Courant–Friedrich–Lewy (CFL) stability time step in the stiff continuum calculations. Convergence to the global problem steady state is reached via iteration between the steady state

solutions of the continuum and atomistic subdomains. Imposition of the boundary conditions on the molecular simulations is accomplished by extending the molecular subdomain through the artifice of a reservoir region in which molecules are generated using a Chapman–Enskog distribution that is parametrized by the Navier–Stokes flow field in the continuum subdomain.

For dense gases and liquids, molecular dynamics simulations are used in the very near proximity of rigid or compliant walls, while the Navier–Stokes equations are discretized in the bulk of the flow.[70] As mentioned earlier, the outstanding difficulty in such hybrid simulation is passing the information from the continuum to the molecular subdomain. We are simply unable to unambiguously define and recreate the liquid interacting molecular state from knowledge of the continuum solution. In that case, heuristic approaches inevitably replace first-principles strategies. Very recently, Werder *et al.*[71] proposed an MD simulation coupled to a finite volume discretization of the N–S equations. The two descriptions were combined in a domain decomposition formulation using the Schwarz alternating method. The method avoids direct imposition of fluxes but ensures flux continuity by matching the transport coefficients in the overlap region. Non-periodic velocity boundary conditions were imposed from the continuum to the atomistic domain based on an effective boundary potential, consistent body forces, particle insertion algorithm and specular walls. The strategy iteratively finds a consistent solution in the atomistic and continuum domains. An overlap region heuristically facilitates information exchange between the two subdomains in the form of state (Dirichlet) boundary conditions. Convergence is reached in successive Schwarz iterations when the solutions in the continuum and atomistic subdomains become identical in the overlap region. This technique was applied to the flow of liquid argon around a carbon nanotube and the resulting flow field was found to agree with a fully atomistic reference solution.

1.9. Surface Phenomena

The surface-to-volume ratio for a machine with a characteristic length of 1 m is 1 m^{-1}, while that for a MEMS device having a size of 1 μm is 10^6 m^{-1}. The million-fold increase in surface area relative to the mass of the minute device substantially affects the transport of mass, momentum and energy through the surface. Obviously surface effects dominate in small devices. The surface boundary conditions in MEMS flows have been discussed above and in the extensive literature cited in Refs. [26] and [73]. In microdevices, it has been shown that it is possible to have measurable slip-velocity and temperature jump at a solid–fluid interface. Liquids such as macromolecule polymers would slip even in minichannels (mm

scale).[25] In this section, we illustrate other ramifications of the large surface-to-volume ratio unique to MEMS, and provide a molecular viewpoint to surface forces.

In microdevices, both radiative and convective heat loss/gain are enhanced by the huge surface-to-volume ratio. Consider a device having a characteristic length L_s. Use of the lumped capacitance method to compute the rate of convective heat transfer, for example, is justified if the Biot number ($\equiv h\,L_s/\kappa_s$, where h is the convective heat transfer coefficient of the fluid and κ_s is the thermal conductivity of the solid) is less than 0.1. Small L_s implies small Biot number, and a nearly uniform temperature within the solid. Within this approximation, the rate at which heat is lost to the surrounding fluid is given by

$$\rho_s\,L_s^3\,c_s\,\frac{\mathrm{dT_s}}{\mathrm{dt}} \;=\; -\,h\,L_s^2\,(T_s\,-\,T_\infty) \tag{1.9}$$

where ρ_s and c_s are respectively the density and specific heat of the solid, T_s is its (uniform) temperature, and T_∞ is the ambient fluid temperature. Solution of the above equation is trivial, and the temperature of a hot surface drops exponentially with time from an initial temperature T_i,

$$\frac{T_s(t)\,-\,T_\infty}{T_i\,-\,T_\infty} \;=\; \exp\left[-\frac{t}{\mathcal{T}}\right] \tag{1.10}$$

where the time constant $\mathcal{T}$ is given by

$$\mathcal{T} \;=\; \frac{\rho_s\,L_s\,c_s}{h} \tag{1.11}$$

For small devices, the time it takes the solid to cool down is proportionally small. Clearly, the million-fold increase in surface-to-volume ratio implies a proportional increase in the rate at which heat escapes. Identical scaling arguments can be made regarding mass transfer.

Another effect of the diminished scale is the increased importance of surface forces and the waning importance of body forces. Based on biological studies, Went[74] concludes that the demarcation length scale is around 1 mm. Below that, surface forces dominate over gravitational forces. A 10 mm piece of paper will fall down when gently placed on a smooth, vertical wall, while a 0.1 mm piece will stick. Try it! *Stiction* is a major problem in MEMS applications. Certain structures such as long, thin polysilicon beams and large, thin comb drives have a propensity to stick to their substrates and thus fail to perform as designed.[75,76]

Conventional dry friction between two solids in relative motion is proportional to the normal force which is usually a component of the moving device weight. The friction is independent of the contact-surface area because the van der Waals cohesive forces are negligible relative to the weight of the macroscopic device. In MEMS applications, the cohesive intermolecular forces between two surfaces are significant and the stiction is independent of the device mass but is proportional to its surface area. The first micromotor did not move—despite large electric current through it—until the contact area between the 100 micron rotor and the substrate was reduced significantly by placing dimples on the rotor's surface.[77–79]

One last example of surface effects that to my knowledge has not been investigated for microflows is the adsorbed layer in gaseous wall-bounded flows. It is well known[8,80] that when a gas flows in a duct, the gas molecules are attracted to the solid surface by the van der Waals and other forces of cohesion. The potential energy of the gas molecules drops on reaching the surface. The adsorbed layer partakes the thermal vibrations of the solid, and the gas molecules can only escape when their energy exceeds the potential energy minimum. In equilibrium, at least part of the solid would be covered by a monomolecular layer of adsorbed gas molecules. Molecular species with significant partial pressure—relative to their vapor pressure—may locally form layers two or more molecules thick. Consider, for example, the flow of a mixture of dry air and water vapor at STP. The energy of adsorption of water is much larger than that for nitrogen and oxygen, making it more difficult for water molecules to escape the potential energy trap. It follows that the life time of water molecules in the adsorbed layer significantly exceeds that for the air molecules (by 60,000 folds, in fact) and, as a result, the thin surface layer would be mostly water. For example, if the proportion of water vapor in the ambient air is 1:1,000 (*i.e.*, very low humidity level), the ratio of water to air in the adsorbed layer would be 60:1. Microscopic roughness of the solid surface causes partial condensation of the water along portions having sufficiently strong concave curvature. So, surfaces exposed to non-dry airflows are mainly liquid water surfaces. In most applications, this thin adsorbed layer has little effect on the flow dynamics, despite the fact that the density and viscosity of liquid water are far greater than those for air. In MEMS applications, however, the layer thickness may not be an insignificant portion of the characteristic flow dimension and the water layer may have a measurable effect on the gas flow. A hybrid approach of molecular dynamics and continuum flow simulations or MD–Monte Carlo simulations may be used to investigate this issue.

It should be noted that recently, Majumdar and Mezic[81,82] have studied the stability and rupture into droplets of thin liquid films on solid surfaces. They point out that the free energy of a liquid film consists of a surface tension component

as well as highly nonlinear volumetric intermolecular forces resulting from van der Waals, electrostatic, hydration and elastic strain interactions. For water films on hydrophilic surfaces such as silica and mica, Majumdar and Mezic[81] estimate the equilibrium film thickness to be about 0.5 nm (2 monolayers) for a wide range of ambient-air relative humidities. The equilibrium thickness grows very sharply, however, as the relative humidity approaches 100%.

Majumdar and Mezic's results[81,82] open many questions. What are the stability characteristics of their water film in the presence of airflow above it? Would this water film affect the accommodation coefficient for microduct airflow? In a modern Winchester-type hard disk, the drive mechanism has a read/write head that floats 50 nm above the surface of the spinning platter. The head and platter together with the air layer in between form a slider bearing. Would the computer performance be affected adversely by the high relative humidity on a particular day when the adsorbed water film is no longer 'thin'? If a microduct hauls liquid water, would the water film adsorbed by the solid walls influence the effective viscosity of the water flow? Electrostatic forces can extend to almost 1 micron (the Debye length), and that length is known to be highly pH-dependent. Would the water flow be influenced by the surface and liquid chemistry? Would this explain the contradictory experimental results of liquid flows in microducts discussed earlier?

The few examples above illustrate the importance of surface effects in small devices. From the continuum viewpoint, forces at a solid–fluid interface are the limit of pressure and viscous forces acting on a parallel elementary area displaced into the fluid, when the displacement distance is allowed to tend to zero. From the molecular point of view, all macroscopic surface forces are ultimately traced to intermolecular forces, which subject is extensively covered in the book by Israelachvilli[83] and references therein. Here we provide a very brief introduction to the molecular viewpoint. The four forces in nature are (i) the strong and (ii) weak forces describing the interactions between neutrons, protons, electrons, *etc.*; (iii) the electromagnetic forces between atoms and molecules; and (iv) gravitational forces between masses. The range of action of the first two forces is around 10^{-5} nm, and hence neither concerns us overly in MEMS applications. The electromagnetic forces are effective over a much larger though still small distance on the order of the inter-atomic separations (0.1–0.2 nm). Effects over longer range—several orders of magnitude longer—can and do rise from the short-range intermolecular forces. For example, the rise of liquid column in capillaries and the action of detergent molecules in removing oily dirt from fabric are the result of intermolecular interactions. Gravitational forces decay with the distance to second power, while intermolecular forces decay much quicker, typically with the seventh power. Cohesive forces are therefore negligible once the distance between

molecules exceeds few molecular diameters, while massive bodies like stars and planets are still strongly interacting, via gravity, over astronomical distances.

Electromagnetic forces are the source of all intermolecular interactions and the cohesive forces holding atoms and molecules together in solids and liquids. They can be classified into (i) purely electrostatic arising from the Coulomb force between charges, interactions between charges, permanent dipoles, quadrupoles, *etc.*; (ii) polarization forces arising from the dipole moments induced in atoms and molecules by the electric field of nearby charges and permanent dipoles; and (iii) quantum mechanical forces that give rise to covalent or chemical bonding and to repulsive steric or exchange interactions that balance the attractive forces at very short distances. The Hellman–Feynman theorem of quantum mechanics states that once the spatial distribution of the electron clouds has been determined by solving the appropriate Schrdinger equation, intermolecular forces may be calculated on the basis of classical electrostatics, in effect reducing all intermolecular forces to Coulombic forces. Note however that intermolecular forces exist even when the molecules are totally neutral. Solutions of the Schrödinger equation for general atoms and molecules are not easy of course, and alternative modeling are sought to represent intermolecular forces. The van der Waals attractive forces are usually represented with a potential that varies as the inverse-sixth power of distance, while the repulsive forces are represented with either a power or an exponential potential.

A commonly used potential between two molecules is the generalized Lennard-Jones (L-J 6–12) pair potential given by

$$V_{ij}(r) \;=\; 4\,\epsilon \left[c_{ij} \left(\frac{r}{\sigma} \right)^{-12} - \; d_{ij} \left(\frac{r}{\sigma} \right)^{-6} \right] \tag{1.12}$$

where V_{ij} is the potential energy between two particles i and j, r is the distance between the two molecules, ϵ and σ are respectively characteristic energy- and length-scales, and c_{ij} and d_{ij} are parameters to be chosen for the particular fluid and solid combinations under consideration. The first term in the right-hand side is the strong repulsive force that is felt when two molecules are at extremely close range comparable to the molecular length-scale. That short-range repulsion prevents overlap of the molecules in physical space. The second term is the weaker, van der Waals attractive force that commences when the molecules are sufficiently close (several times σ). That negative part of the potential represents the attractive polarization interaction of neutral, spherically symmetric particles. The power of 6 associated with this term is derivable from quantum mechanics considerations, while the power of the repulsive part of the potential is found empirically. The

Lennard-Jones potential is zero at very large distances, has a weak negative peak at r slightly larger than σ, is zero at $r = \sigma$, and is infinite as $r \to 0$.

The force field resulting from this potential is given by

$$F_{ij}(r) = -\frac{\partial V_{ij}}{\partial r} = \frac{48\,\epsilon}{\sigma}\left[c_{ij}\left(\frac{r}{\sigma}\right)^{-13} - \frac{d_{ij}}{2}\left(\frac{r}{\sigma}\right)^{-7}\right] \tag{1.13}$$

A typical L-J 6-12 potential and force field was shown in Fig. 1.4, for $c = d = 1$. The minimum potential $V_{\text{min}} = -\epsilon$, corresponds to the equilibrium position (zero force) and occurs at $r = 1.12\,\sigma$. The attractive van der Waals contribution to the minimum potential is $-2\,\epsilon$, while the repulsive energy contribution is $+\epsilon$. Thus the inverse 12th-power repulsive force term decreases the strength of the binding energy at equilibrium by 50%.

The L-J potential is commonly used in molecular dynamics simulations to model intermolecular interactions between dense gas or liquid molecules and between fluid and solid molecules. As mentioned earlier, such potential is not accurate for complex substances such as water whose molecules form directional covalent bonds. As a result, MD simulations for water are much more involved.

1.10. Conclusions

The traditional Navier–Stokes model of fluid flows with no-slip boundary conditions works only for a certain range of the governing parameters. This model basically demands three conditions: (i) Newtonian mechanics, and not quantum or relativistic mechanics, applies; (ii) The fluid is a continuum, which is typically satisfied as there are usually more than 1 million molecules in the smallest volume in which appreciable macroscopic changes take place. This is the molecular chaos restriction, which can be violated for rarefied gas flows in macrodevices or for STP airflows in nanodevices; and (iii) The flow is not too far from thermodynamic equilibrium, which is satisfied if there is sufficient number of molecular encounters during a time period small compared to the smallest time scale for flow changes. During this time period the average molecule would have moved a distance small compared to the smallest flow length scale.

For gases, the Knudsen number determines the degree of rarefaction and the applicability of traditional flow models. As Kn $\to 0$, the time and length scales of molecular encounters are vanishingly small compared to those for the flow, and the velocity distribution of each element of the fluid instantaneously adjusts to the equilibrium thermodynamic state appropriate to the local macroscopic properties as this molecule moves through the flowfield. From the continuum viewpoint, the flow is isentropic and heat conduction and viscous diffusion and dissipation

vanish from the continuum conservation relations, leading to the Euler equations of motion. At small but finite Kn, the Navier–Stokes equations describe quasi-equilibrium, continuum flows.

Slip flow must be taken into account for Kn > 0.001. The slip boundary condition is at first linear in Knudsen number, then nonlinear effects take over beyond a Knudsen number of 0.1. At the same transition regime, *i.e.*, $0.1 <$ Kn < 10, the linear stress–rate of strain and heat flux–temperature gradient relations—needed to close the field equations—also break down, and alternative continuum equations (*e.g.*, Burnett or higher-order equations) or molecular-based models must be invoked. In the transition regime, provided that the dilute gas and molecular chaos assumptions hold, solutions to the difficult Boltzmann equation are sought, but physical simulations such as Monte Carlo methods are more readily executed in this range of Knudsen number. In the free-molecule flow regime, *i.e.*, Kn > 10, the nonlinear collision integral is negligible and the Boltzmann equation is drastically simplified. Analytical solutions are possible in this case for simple geometries and numerical integration of the Boltzmann equation is straightforward for arbitrary geometries, provided that the surface-reflection characteristics are accurately modeled.

Gaseous flows are often compressible in microdevices even at low Mach numbers. Viscous effects can cause sufficient pressure drop and density changes for the flow to behave as compressible. In a long, constant-area microduct, all Knudsen number regimes may be encountered and the degree of rarefaction increases along the tube. The pressure drop is nonlinear and the Mach number increases downstream, limited only by choked-flow condition.

Similar deviation and breakdown of the traditional Navier–Stokes equations occur for liquids as well, but at considerably smaller device scale. Existing experiments are contradictory, and the situation for dense gases and liquids is more murky than that for dilute gases. There is no kinetic theory of liquids, and first-principles prediction methods are scarce. Molecular dynamics simulations can be used, but they are limited to extremely small flow extents. Nevertheless, measurable slip is predicted from MD simulations at realistic shear rates in microdevices. Hybrid atomistic–continuum methods hold promise to provide first-principles solutions while remaining computationally affordable. Though requiring considerable numerical erudition, the use of hybrid strategies for dilute gases is within reach. Further development is needed for implementing hybrid methods for liquid and dense gas flows.

Much non-traditional physics is still to be learned and many exciting applications of microdevices are yet to be discovered. The future is bright for this emerging field of nanoscience and nanotechnology.

References

1. R. P. Feynman, There's plenty of room at the bottom, in *Miniaturization*, ed. H. D. Gilbert, pp. 282–296, New York: Reinhold Publishing (1961).
2. T. M. Squires, S. R. Quake, Microfluidics: fluid physics at the nanoliter scale. *Rev. Mod. Phys.* **77**, 977–1026 (2005).
3. M. Gad-el-Hak, The fluid mechanics of microdevices—the Freeman scholar lecture". *J. Fluids Eng.* **121**, 5–33 (1999).
4. H. A. Stone, A. D. Stroock, A. Ajdari, Engineering flows in small devices: microfluidics toward a lab-on-a-chip. *Annu. Rev. Fluid Mech.* **36**, 381–411 (2004).
5. M. Gad-el-Hak, ed., it The MEMS Handbook, second edition, volumes I–III, Boca Raton: CRC Press (2005).
6. G. Em Karniadakis, A. Beskok, *Microflows: Fundamentals and Simulation*, New York: Springer-Verlag (2002).
7. G. K. Batchelor, *An Introduction to Fluid Dynamics*, London: Cambridge University Press (1967).
8. M. J. Lighthill, Introduction. Real and ideal fluids, in *Laminar Boundary Layers*, ed. L. Rosenhead, pp. 1–45, Oxford: Clarendon Press (1963).
9. S. Chapman, T. G. Cowling, *The Mathematical Theory of Non-Uniform Gases*, third edition, London: Cambridge University Press (1970).
10. G. A. Bird, *Molecular Gas Dynamics and the Direct Simulation of Gas Flows*, Oxford: Clarendon Press (1994).
11. M. Knudsen, Die gesetze der molekularströmung und der inneren reibungsstrmung der gase durch röhren. *Annalen der Physik* **28**, 75–130 (1909).
12. S. A. Tison, Experimental data and theoretical modeling of gas flows through metal capillary leaks. *Vacuum* **44**, 1171–1175 (1993).
13. A. Beskok, G. E. Karniadakis, W. Trimmer, Rarefaction and compressibility effects in gas microflows. *J. Fluids Eng.* **118**, 448–456 (1996).
14. R. H. Nadolink, W. W. Haigh, Bibliography on skin friction reduction with polymers and other boundary-layer additives. *Appl. Mech. Rev.* **48**, 351–459 (1995).
15. W. Loose, S. Hess, Rheology of dense fluids via nonequilibrium molecular hydrodynamics: shear thinning and ordering transition. *Rheologica Acta* **28**, 91–101 (1989).
16. E. B. Dussan, S. H. Davis, On the motion of fluid–fluid interface along a solid surface. *J. Fluid Mech.* **65**, 71–95 (1974).
17. E. B. Dussan, The moving contact line: the slip boundary condition. *J. Fluid Mech.* **77**, 665–684 (1976).
18. E. B. Dussan, On the spreading of liquids on solid surfaces: static and dynamic contact lines. *Annu. Rev. Fluid Mech.* **11**, 371–400 (1976).
19. P. A. Thompson, M. O. Robbins, Simulations of contact line motion: slip and the dynamic contact angle. *Phys. Rev. Lett.* **63**, 766–769 (1989).
20. H. K. Moffatt, Viscous and resistive eddies near a sharp corner. *J. Fluid Mech.* **18**, 1–18 (1964).
21. J. Koplik, J. R. Banavar, Continuum deductions from molecular hydroynamics. *Annu. Rev. Fluid Mech.* **27**, 257–292 (1995).
22. J. R. A. Pearson, C. J. S. Petrie, On melt flow instability of extruded polymers, in *Polymer Systems: Deformation and Flow*, eds. R. E. Wetton, R. W. Whorlow, pp. 163–187, London: Macmillian (1968).

23. S. Richardson, On the no-slip boundary condition. *J. Fluid Mech.* **59**, 707–719 (1973).
24. M. M. Den, Issues in viscoelastic fluid mechanics. *Annu. Rev. Fluid Mech.* **22**, 13–34 (1990).
25. M .M. Den, Extrusion instabilities and wall slip. *Annu. Rev. Fluid Mech.* **33**, 265–287 (2001).
26. E. Lauga, M. P. Brenner, H. A. Stone, Microfluidics: the no-slip boundary condition, in *Handbook of Experimental Fluid Dynamics*, eds. J. Foss, C. Tropea, A. Yarin, chapter 15, New York: Springer (2006).
27. J. Pfahler, J. Harley, H.H. Bau, J.N. Zemel, Liquid transport in micron and submicron channels. *Sensors and Actuators* **21–23**, 431–434 (1990).
28. J. Pfahler, J. Harley, H. H. Bau, J. N. Zemel, Gas and liquid flow in small channels, in *Proc. Symp. on Micromechanical Systems, Sensors, and Actuators*, eds. D. Cho, R. Warrington, A. Pisano, H. H. Bau, C. Friedrich, J. Jara-Almonte, J. Liburdy, ASME DSC-Vol. 32, pp. 49–60, New York: ASME (1991).
29. J. Pfahler, Liquid transport in micron and submicron size channels, Ph.D. Thesis, University of Pennsylvania, Philadelphia, Pennsylvania (1992).
30. H. H. Bau, Transport processes associated with micro-devices. *Thermal Sci. Eng.* **2**, 172–178 (1994).
31. J. N. Israelachvili, Measurement of the viscosity of liquids in very thin films. *J. Colloid Interface Sci.* **110**, 263–271 (1986).
32. M. L. Gee, P. M. McGuiggan, J. N. Israelachvili, A. M. Homola, Liquid to solidlike transitions of molecularly thin films under shear. *J. Chemical Phys.* **93**, 1895–1906 (1990).
33. D. Y. C. Chan, R. G. Horn, Drainage of thin liquid films. *J. Chemical Phys.* **83**, 5311–5324 (1985).
34. N. P. Migun, P. P. Prokhorenko, Measurement of the viscosity of polar liquids in microcapillaries. *Colloid J. of the USSR* **49**, 894–897 (1987).
35. P. Debye, R. L. Cleland, Flow of liquid hydrocarbons in porous Vycor. *J. Appl. Phys.* **30**, 843–849 (1959).
36. J. L. Anderson, J. A. Quinn, Ionic mobility in microcapillaries. *J. Chemical Phys.* **27**, 1208–1209 (1972).
37. D. B. Tuckermann, R. F. W. Pease, High-performance heat sinking for VLSI. *IEEE Electron Device Lett.* **EDL-2**, 126–129 (1981).
38. D. B. Tuckermann, R. F. W. Pease, Optimized convective cooling using micromachined structures. *J. Electrochemical Soc.* **129**, C98, March (1982).
39. D. B. Tuckermann, Heat transfer microstructures for integrated circuits, Ph.D. Thesis, Stanford University, Palo Alto, California (1984).
40. M. G. Guvenc, V-groove capillary for low flow control and measurement, in *Micromachining and Micropackaging of Transducers* , eds. C. D. Fung, P. W. Cheung, W. H. Ko, D. G. Fleming, pp. 215–223, Amsterdam: Elsevier (1985).
41. S. Nakagawa, S. Shoji, M. Esashi, A micro-chemical analyzing system integrated on silicon chip, in *Proc. IEEE: Micro Electro Mechanical Systems*, Napa Valley, California, IEEE 90CH2832-4, New York: IEEE (1990).
42. K. V. Sharp, Experimental investigation of liquid and particle-laden flows in microtubes, Ph.D. Thesis, University of Illinois at Urbana–Champaign (2001).

43. K. V. Sharp, R. J. Adrian, J. G. Santiago, J. I. Molho, Liquid flow in microchannels, in *The MEMS Handbook*, vol. I, second edition, ed. M. Gad-el-Hak, pp. 10.1–10.45, Boca Raton: CRC Press (2006).
44. B. J. Alder, T. E. Wainwright, Studies in molecular dynamics. *J. Chemical Phys.* **27**, 1208–1209 (1957).
45. B. J. Alder, T. E. Wainwright, Molecular dynamics by electronic computers, in *Transport Processes in Statistical Mechanics*, ed. I. Prigogine, pp. 97–131, New York: Interscience (1958).
46. B. J. Alder, T. E. Wainwright, Decay of the velocity auto-correlation function. *Phys. Rev. A* **1**, 18–21 (1970).
47. G. Ciccotti, W. G. Hoover, eds., *Molecular Dynamics Simulation of Statistical Mechanics Systems*, Amsterdam: North Holland (1986).
48. M. P. Allen, D. J. Tildesley, *Computer Simulation of Liquids*, Oxford: Clarendon Press (1987).
49. J. M. Haile, *Molecular Dynamics Simulation: Elementary Methods*, New York: Wiley (1993).
50. P. A. Thompson, S. M. Troian, A general boundary condition for liquid flow at solid surfaces. *Nature* **389**, 360–362 (1997).
51. C. L. M. H. Navier, Mémoire sur les lois du mouvement des fluides. *Mémoires de l'Académie Royale des Sciences de l'Institute de France* **VI**, 389–440 (1823).
52. B. T. Atwood, W. R. Schowalter, Measurements of slip at the wall during flow of high-density polyethylene through a rectangular conduit. *Rheologica Acta* **28**, 134–146 (1989).
53. F. F. Abraham, J. Q. Broughton, N. Bernstein, E. Kaxiras, Spanning the continuum to quantum length scales in a dynamic simulation of brittle fracture. *Europhys. Lett.* **44**, 783–787 (1998).
54. V. B. Shenoy, R. Miller, E. B. Tadmor, D. Rodney, R. Phillips, M. Ortiz, An adaptive finite element approach to atomic-scale mechanics—the quasicontinuum method. *J. Mech. Phys. Solids* **47**, 611–642 (1999).
55. R. E. Rudd, J. Q. Broughton, Concurrent coupling of length scales in solid state systems. *Physica Status Solidi B* **217**, 251–291 (2000).
56. D. C. Wadsworth, D. A. Erwin, One-dimensional hybrid continuum/particle simulation approach for rarefied hypersonic flows. AIAA Paper Number 90-1690 (1990).
57. D. Hash, H. Hassan, A decoupled DSMC/Navier–Stokes analysis of a transitional flow experiment. AIAA Paper Number 96-353 (1996).
58. J. Bourgat, P. Le Tallec, M. Tidriri, Coupling Boltzmann and Navier–Stokes equations by friction. *J. Comput. Phys.* **127**, 227–245 (1996).
59. B. J. Alder, Highly discretized dynamics. *Physica A* **240**, 193–195 (1997).
60. P. Le Tallec, F. Mallinger, Coupling Boltzmann and Navier–Stokes Equations by half fluxes. *J. Comput. Phys.* **136**, 51–67 (1997).
61. S. Tiwari, A. Klar, Coupling of the Boltzmann and Euler equations with adaptive domain decomposition procedure. *J. Comput. Phys.* **144**, 710–726 (1998).
62. A. L. Garcia, J. Bell, W. Y. Crutchfield, B. J. Alder, Adaptive mesh and algorithm refinement using direct simulation Monte Carlo. *J. Comput. Phys.* **154**, 134–155 (1999).
63. O. Aktas, N. R. Aluru, A combined continuum/DSMC technique for multiscale analysis of microfluidic filters. *J. Comput. Phys.* **178**, 342–372 (2002).

64. R. Roveda, D. B. Goldstein, P. L. Varghese, Hybrid Euler/direct simulation Monte Carlo calculation of unsteady slit flow. *J. Spacecr. Rockets* **37**, 753–760 (2000).
65. S. T. O'Connell, P. A. Thompson, Molecular dynamics–continuum hybrid computations: a tool for studying complex fluid flows. *Phys. Rev. E* **52**, R5792–R5795 (1995).
66. J. Li, D. Liao, S. Yip, Coupling continuum to molecular-dynamics simulation: reflecting particle method and the field estimator. *Phys. Rev. E* **57**, 7259–7267 (1998).
67. N. G. Hadjiconstantinou, Hybrid atomistic–continuum formulations and the moving contact-line problem. *J. Comput. Phys.* **154**, 245–265 (1999).
68. E. G. Flekkoy, G. Wagner, J. Feder, Hybrid model for combined particle and continuum dynamics. *Europhys. Lett.* **52**, 271–276 (2000).
69. H. S. Wijesinghe, N. G. Hadjiconstantinou, Discussion of hybrid atomistic–continuum methods for multiscale hydrodynamics. *Int. J. Multiscale Comput. Eng.* **2**, 189–202 (2004).
70. H. S. Wijesinghe, R. D. Hornung, A. L. Garcia, N. G. Hadjiconstantinou, Three-dimensional hybrid continuum–atomistic simulations for multiscale hydrodynamics. *J. Fluids Eng.* **126**, 768–777 (2004).
71. T. Werder, J. H. Walther, P. Koumoutsakos, Hybrid atomistic–continuum method for the simulation of dense fluid flows. *J. Comput. Phys.* **205**, 373–390 (2005).
72. L. L. Baker, N. G. Hadjiconstantinou, Variance reduction for Monte Carlo solutions of the Boltzmann equation. *Phys. Fluids* **17**, 051703.1–051703.4 (2005).
73. E. Lauga, H. A. Stone, Effective slip in pressure-driven Stokes flow. *J. Fluid Mech.* **489**, 55–77 (2003).
74. F. W. Went, The size of man. *American Scientist* **56**, 400–413 (1968).
75. W. C. Tang, T.-C. Nguyen, R. T. Howe, Laterally driven polysilicon resonant microstructures. *Sensors and Actuators* **20**, 25–32 (1989).
76. C. Mastrangelo, C. H. Hsu, A simple experimental technique for the measurement of the work of adhesion of microstructures, in *Technical Digest IEEE Solid-State Sensors and Actuators Workshop*, pp. 208–212 (1992).
77. L.-S. Fan, Y.-C. Tai, R. S. Muller, Integrated movable micromechanical structures for sensors and actuators. *IEEE Transactions on Electronic Devices* **35**, 724–730 (1988).
78. L.-S. Fan, Y.-C. Tai, R. S. Muller, IC-processed electrostatic micromotors. *Sensors and Actuators* **20**, 41–47 (1989).
79. Y.-C. Tai, R. S. Muller, IC-processed electrostatic synchronous micromotors. *Sensors and Actuators* **20**, 49–55 (1989).
80. S. Brunauer, *Physical Adsorption of Gases and Vapours*, Oxford University Press (1944).
81. A. Majumdar, I. Mezic, Stability regimes of thin liquid films. *Microscale Thermophys. Eng.* **2**, 203–213 (1998).
82. A. Majumdar, I. Mezic, Instability of ultra-thin water films and the mechanism of droplet formation on hydrophilic surfaces. *J. Heat Transfer* **121**, 964–971 (1999).
83. J. N. Israelachvili, *Intermolecular and Surface Forces*, second edition, New York: Academic Press (1991).

Chapter 2

Using the Kinetic Equations for MEMS and NEMS

Carlo Cercignani, Aldo Frezzotti and Silvia Lorenzani
Dipartimento di Matematica del Politecnico di Milano
Piazza Leonardo da Vinci 32
20133 Milano - Italy
carlo.cercignani@polimi.it

Micro and nano-devices are often operated in gaseous environments (typically air) and thus their performances are affected by the gas around them. Since the smallest characteristic length of MEMS/NEMS is comparable with (or smaller than) the mean free path of the gas molecules, the traditional computational fluid dynamics (CFD) methods, based on the Euler or the Navier-Stokes equations, fail to predict the flows related with these devices. Therefore, an accurate analysis of such micro-fluidic systems in the entire Knudsen regime requires the solution of the Boltzmann equation, which describes the behavior of the distribution function of the gas molecules. The application of kinetic theory methods is illustrated by deriving a generalized Reynolds equation from the linearized Boltzmann equation. The analysis, valid for arbitrary Knudsen number, is based on two different kinetic models of the collisional operator: the Bhatnagar, Gross and Krook (BGK) model and the ellipsoidal statistical (ES) model. The gas-wall interaction model and the resulting boundary conditions allow for bounding surfaces with different physical structure. It is further shown that MEMS flows having a complex geometry can be successfully studied by numerical solution of kinetic equations whose predictions are in very good agreement with experimental data. Finally, it is shown that kinetic theory methods can be extended to dense fluids by a simple generalization of Enskog kinetic equation which describes a fluid whose molecules interact through Sutherland's potential.

Contents

2.1 Introduction . . . 38
2.2 The Boltzmann Equation . . . 39
2.3 The Linearized Boltzmann Equation and the BGK Model . . . 42
2.4 The Macroscopic Balance Equations . . . 43
2.5 Boundary Conditions . . . 47

2.6 The Modified Reynolds Equation . . . 49
2.7 The Reynolds Equation and the Poiseuille-Couette Problem . . . 51
2.8 The Generalized Reynolds Equation for Unequal Walls . . . 55
2.9 A Kinetic Approach for the Evaluation of Damping in MEMS . . . 62
2.10 Kinetic Theory Extension to Dense Fluids . . . 67
2.10.1 The Mathematical Model . . . 69
2.10.2 Fluid-Wall Interaction and Boundary Conditions . . . 72
2.11 Numerical Results . . . 74
References . . . 77

2.1. Introduction

The presence of a fluid film is known to reduce the sliding friction between solid objects. Although one usually thinks of a liquid (typically, oil), the case of a gas lubricant (typically, air) is also very important in several applications. Sometimes, problems of gas lubrication are not so obvious, because air is so easily available that one tends to disregard its presence. As technology expands and the size of components becomes smaller and smaller, the role of rarefied gases as lubricants becomes increasingly important. We recall that a gas is called rarefied when the mean free path between collisions (of the order of 60 nanometers at room pressure and temperature) is comparable with a typical size of the region where it flows. A typical example is provided by modern computers: the read/write head must be as close as possible to a rotating disk, and the air in between has accordingly a thickness of the order of a mean free path.

In lubrication theory, the thickness of the gas layer is extremely small compared with its lateral dimensions. Properly handled, this observation can be used to eliminate from the equations the dependence upon one of the three space variables. This possibility was exploited since long time by the famous hydrodynamicist Osborne Reynolds[1] to integrate the mass balance equation across the layer and to use the linearized Navier–Stokes equation for momentum balance to evaluate the quantities appearing as integrands. Fortunately, Reynolds's argument can be extended to rarefied gases; the only difference is that the linearized Boltzmann equation (Sec. 2.3) must now be used to evaluate the averaged velocity components in the mass balance equation.

From a very superficial consideration of the matter one might expect that the main problem of lubrication theory is to predict the friction which results from a given configuration of solid objects. However, a little more reflection reveals that the real problem is quite different. Lubricating layers are usually found between two solid bodies which are acted upon by forces (such as gravity) tending to push them together. To carry this load, the gas layer must develop normal stresses, largely dominated by pressure. Thus the first task of lubrication theory is to predict

the pressure distribution and from it the load-carrying capacity. Therefore we must relate the velocity components to the pressure gradients and to the motion of the solid surfaces bounding the gas layer. Since the variations of thickness are very slow, this result is obtained by solving highly idealized problems between parallel plates, such as plane Couette and Poiseuille flows, which will be considered in Sec. 2.7. Thus these problems, far from being didactic exercises, play a very important role in applications of enormous practical importance.

The application of kinetic theory methods described below is not restricted to problems involving rarefied gas flows. As shown in last section of the chapter, it is possible to formulate kinetic equations for dense fluids using approximate (but reasonable) models for molecular correlations. In spite of their phenomenological nature, such kinetics equations provide a description of the fluid which is more general than hydrodynamics which appears as a particular case, hence they can be used to bridge hydrodynamic fluid treatment with molecular dynamics simulations.

2.2. The Boltzmann Equation

The phenomena associated with the dynamics of molecules are not so simple, especially because the number of molecules usually considered is extremely large: there are about 2.7×10^{19} in a cubic centimeter of a gas at atmospheric pressure and a temperature of $0°$C.

Given the vast number of particles to be considered, it would of course be a hopeless task to attempt to describe the state of the gas by specifying the so-called microscopic state, *i.e.*, the position and velocity of every individual sphere; we must have recourse to statistics. A description of this kind is made possible because, in practice, all that our typical observations can detect are changes in the macroscopic state of the gas, described by quantities such as density, bulk velocity, temperature, stresses, heat flow, which are related to some suitable averages of quantities depending on the microscopic state.

The exact dynamics of N particles is a useful conceptual tool, but cannot in any way be used in practical calculations because it requires a huge number of real variables (of the order of 10^{20}). This was realized by Maxwell and Boltzmann when they started to work with the distribution function $f(\mathbf{x}, \boldsymbol{\xi}, t)$. The latter is a function of seven variables, *i.e.*, the components of the two vectors $\mathbf{x}$ (the position of a molecule) and $\boldsymbol{\xi}$ (the velocity of a molecule) and time t. In particular, Boltzmann wrote an evolution equation for f by means of a heuristic argument, which we shall try to present in such a way as to show where extra assumptions are introduced.

In order to simplify the treatment, we shall for the moment assume that the molecules are hard spheres, whose center has position $\mathbf{x}$. When the molecules collide, momentum and kinetic energy must be conserved; thus the velocities after the impact, $\boldsymbol{\xi}'$ and $\boldsymbol{\xi}'_*$, are related to those before the impact, $\boldsymbol{\xi}$ and $\boldsymbol{\xi}_*$, by

$$\begin{aligned}\boldsymbol{\xi}' &= \boldsymbol{\xi} - \mathbf{n}[\mathbf{n}\cdot(\boldsymbol{\xi}-\boldsymbol{\xi}_*)] \\ \boldsymbol{\xi}'_* &= \boldsymbol{\xi}_* + \mathbf{n}[\mathbf{n}\cdot(\boldsymbol{\xi}-\boldsymbol{\xi}_*)]\end{aligned} \tag{2.1}$$

where $\mathbf{n}$ is the unit vector along $\boldsymbol{\xi}-\boldsymbol{\xi}'$.

In the absence of collisions, f would remain unchanged along the trajectory of a particle and would satisfy

$$\frac{\partial f}{\partial t} + \boldsymbol{\xi}\cdot\frac{\partial f}{\partial \mathbf{x}} + \mathbf{X}\cdot\frac{\partial f}{\partial \boldsymbol{\xi}} = 0 \tag{2.2}$$

where $\mathbf{X}$ is any external force per unit mass, such as gravity, acting on the molecule, which will be neglected in the rest of this chapter.

In order to evaluate the effects of collisions on the time evolution of f, we need to write an equation of the following form:

$$\frac{\partial f}{\partial t} + \boldsymbol{\xi}\cdot\frac{\partial f}{\partial \mathbf{x}} = G - L. \tag{2.3}$$

Here $Ld\mathbf{x}d\boldsymbol{\xi}dt$ gives the expected number of particles with position between $\mathbf{x}$ and $\mathbf{x}+d\mathbf{x}$ and velocity between $\boldsymbol{\xi}$ and $\boldsymbol{\xi}+d\boldsymbol{\xi}$ which disappears from these ranges of values because of a collision in the time interval between t and $t+dt$ and $Gd\mathbf{x}d\boldsymbol{\xi}dt$ gives the analogous number of particles entering the same range in the same time interval. The count of these numbers is not difficult, if a bit long, provided that we know the joint probability of finding two molecules at given positions with given velocities (see Refs. 2 and 3).

However, if the number of particles N is very large and the molecular diameter σ (expressed in common units, such as, *e.g.*, centimeters) is very small, we can obtain an equation which is rigorously valid only in the so called *Boltzmann-Grad limit*, when $N\to\infty, \sigma\to 0$ with $N\sigma^2$ finite.

In this situation, the collisions between two preselected particles are rather rare events. Thus two spheres that happen to collide can be thought to be two randomly chosen particles and it makes sense to assume that the probability density of finding the first molecule at $\mathbf{x}$ with velocity $\boldsymbol{\xi}$ and the second at $\mathbf{x}_*$ with velocity $\boldsymbol{\xi}_*$ is the product of the probability density of finding the first molecule at $\mathbf{x}$ with

velocity $\boldsymbol{\xi}$ times the probability density of finding the second molecule at $\mathbf{x}_*$ with velocity $\boldsymbol{\xi}_*$. If we accept this we can write (assumption of *molecular chaos*) the *Boltzmann equation* in the following form:

$$\frac{\partial f}{\partial t} + \boldsymbol{\xi} \cdot \frac{\partial f}{\partial \mathbf{x}} = \frac{1}{m} \int_{R^3} \int_{\mathcal{B}^-} [f(\mathbf{x}, \boldsymbol{\xi}', t) f(\mathbf{x}, \boldsymbol{\xi}'_*, t)$$

$$- f(\mathbf{x}, \boldsymbol{\xi}, t) f(\mathbf{x}, \boldsymbol{\xi}_*, t)] |(\boldsymbol{\xi}_* - \boldsymbol{\xi}) \cdot \mathbf{n}| d\boldsymbol{\xi}_* d\mathbf{n}. \tag{2.4}$$

So far we have assumed the molecules to be identical hard spheres. There are several possible generalizations of this molecular model, the most obvious being the case of molecules which are identical point masses interacting with a central force, a good general model for monatomic gases. If the range of the force extends to infinity, there is a complication due to the fact that two molecules are always interacting and the analysis in terms of "collisions" is no longer possible. If, however, the gas is sufficiently dilute, we can take into account that the molecular interaction is negligible for distances larger than a certain σ (the "molecular diameter") and assume that when two molecules are at a distance smaller than σ, then no other molecule is interacting with them and the binary collision analysis considered in the previous section can be applied. The only difference arises in the factor $\sigma^2 |(\boldsymbol{\xi}_* - \boldsymbol{\xi}) \cdot \mathbf{n}|$ which turns out to be replaced by a function of $V = |\boldsymbol{\xi}_* - \boldsymbol{\xi}|$ and the angle θ between $\mathbf{n}$ and $\mathbf{V}$ (see Refs. 2 and 4). Thus the Boltzmann equation for monatomic molecules takes on the following form:

$$\frac{\partial f}{\partial t} + \boldsymbol{\xi} \cdot \frac{\partial f}{\partial \mathbf{x}} = N \int_{R^3} \int_{\mathcal{B}_-} [f(\mathbf{x}, \boldsymbol{\xi}', t) f(\mathbf{x}, \boldsymbol{\xi}'_*, t)$$

$$- f(\mathbf{x}, \boldsymbol{\xi}, t) f(\mathbf{x}, \boldsymbol{\xi}_*, t)] B(\theta, |\boldsymbol{\xi}_* - \boldsymbol{\xi}|) d\boldsymbol{\xi}_* d\theta d\epsilon \tag{2.5}$$

where ϵ is the other angle which, together with θ, identifies the unit vector $\mathbf{n}$. The function $B(\theta, V)$ depends, of course, on the specific law of interaction between the molecules. In the case of hard spheres, of course

$$B(\theta, |\boldsymbol{\xi}_* - \boldsymbol{\xi}|) = \cos\theta \sin\theta |\boldsymbol{\xi}_* - \boldsymbol{\xi}|. \tag{2.6}$$

In spite of the fact that the force is cut at a finite range σ when writing the Boltzmann equation, infinite range forces are frequently used. This has the disadvantage of making the integral in Eq. (2.5) rather hard to handle; in fact, one cannot split it into the difference of two terms (the loss and the gain), because each of them would be a divergent integral. This disadvantage is compensated in the case

of power law forces, because one can separate the dependence on θ from the dependence upon $|\mathbf{V}|$. In fact, one can show[2,4] that, if the intermolecular force varies as the n-th inverse power of the distance, then

$$B(\theta, |\boldsymbol{\xi}_* - \boldsymbol{\xi}|) = \beta(\theta)|\boldsymbol{\xi}_* - \boldsymbol{\xi}|^{\frac{n-5}{n-1}} \tag{2.7}$$

where $\beta(\theta)$ is a non-elementary function of θ (in the simplest cases it can be expressed by means of elliptic functions). In particular, for $n = 5$ one has the so-called Maxwell molecules, for which the dependence on V disappears.

Sometimes the artifice of cutting the grazing collisions corresponding to small values of $|\theta - \frac{\pi}{2}|$ is used (angle cutoff). In this case one has both the advantage of being able to split the collision term and of preserving a relation of the form (2.7) for power-law potentials.

Since solving the Boltzmann equation with actual cross sections is complicated, in many numerical simulations use is made of the so-called variable hard sphere (VHS) model in which the diameter of the spheres is an inverse power law function of the relative speed $|\mathbf{V}|$.

2.3. The Linearized Boltzmann Equation and the BGK Model

The solutions describing equilibria of the Boltzmann equation are the so-called Maxwellians, *i.e.*, distributions of the form

$$M = \rho_0(2\pi R T_0)^{-3/2} \exp[-|\boldsymbol{\xi} - \mathbf{v_0}|^2/(2RT_0)] \tag{2.8}$$

where ρ_0, $\mathbf{v_0}$, T_0 are parameters having the meaning of density, bulk velocity and temperature in an equilibrium state. The vector $\mathbf{v_0}$ is usually taken to be zero.

We can look for solutions written as

$$f = M(1 + h). \tag{2.9}$$

Then the Boltzmann equation takes on the form:

$$\frac{\partial h}{\partial t} + \boldsymbol{\xi} \cdot \frac{\partial h}{\partial \mathbf{x}} = Lh + \Gamma(h, h) \tag{2.10}$$

where L is the linearized collision operator:

$$Lh = 2M^{-1}Q(Mh, M) \tag{2.11}$$

and $\Gamma(h, h)$ the nonlinear part (assumed to be small compared to the linear one):

$$\Gamma(h,h) = M^{-1}Q(Mh,Mh). \tag{2.12}$$

Here $Q(f,g)$ is the bilinear symmetric operator uniquely associated with $Q(f,f)$. The rigorous theory for solutions of the form (2.9) was given by S. Ukai (see Ref. 5 for more details).

In many applications, the collision term in the Boltzmann equation is replaced by the so-called BGK model (see Refs. 4 and 6 for more details):

$$J(f) = \nu[\Phi(\boldsymbol{\xi}) - f(\boldsymbol{\xi})] \tag{2.13}$$

where the collision frequency ν depends on the local density ρ and the local temperature T, whereas Φ is the local Maxwellian:

$$\Phi = \rho(2\pi RT)^{-3/2}\exp[-|\boldsymbol{\xi} - \mathbf{v}|^2/(2RT)] \tag{2.14}$$

having the same density, temperature and bulk velocity $\mathbf{v}$ as f. Notice that from the viewpoint of nonlinearity the BGK model is worse than the Boltzmann equation, but offers the advantage that one can derive integral equations for $\rho, \mathbf{v}, T$. The linearized form reads:

$$L_{BGK} = \nu_0\Bigg[\int \hat{M}(\boldsymbol{\xi}_*)h(\boldsymbol{\xi}_*)d\boldsymbol{\xi}_* + \frac{\boldsymbol{\xi}}{RT_0}\cdot\int \boldsymbol{\xi}_*\hat{M}(\boldsymbol{\xi}_*)h(\boldsymbol{\xi}_*)d\boldsymbol{\xi}_*$$

$$+\frac{2}{3}\left(\frac{|\boldsymbol{\xi}|^2}{2RT_0} - \frac{3}{2}\right)\int\left(\frac{|\boldsymbol{\xi}_*|^2}{2RT_0} - \frac{3}{2}\right)\hat{M}(\boldsymbol{\xi}_*)h(\boldsymbol{\xi}_*)d\boldsymbol{\xi}_* - h\Bigg] \tag{2.15}$$

where $\hat{M} = M/\rho_0$ and is extremely useful, as we shall see.

2.4. The Macroscopic Balance Equations

In this section we compare the microscopic description supplied by kinetic theory with the macroscopic description supplied by continuum gas dynamics. For definiteness, in this section f will be assumed to be an expected mass density in phase space. In order to obtain a density $\rho = \rho(x,t)$ in ordinary space, we must integrate f with respect to $\boldsymbol{\xi}$:

$$\rho = \int_{R^3} f d\boldsymbol{\xi} \tag{2.16}$$

The bulk velocity $\mathbf{v}$ of the gas (*e.g.*, the velocity of a wind), is the average of the molecular velocities $\boldsymbol{\xi}$ at a certain point $\mathbf{x}$ and time instant t; since f is proportional to the probability for a molecule to have a given velocity, $\mathbf{v}$ turns out to be

$$\mathbf{v} = \frac{\int_{R^3} \boldsymbol{\xi} f d\boldsymbol{\xi}}{\int_{R^3} f d\boldsymbol{\xi}} \tag{2.17}$$

(the denominator is required even if f is taken to be a probability density in phase space, because we are considering a conditional probability, referring to the position $\mathbf{x}$). Equation (2.17) can also be written as follows:

$$\rho \mathbf{v} = \int_{R^3} \boldsymbol{\xi} f d\boldsymbol{\xi} \tag{2.18}$$

or, using components:

$$\rho v_i = \int_{R^3} \xi_i f d\boldsymbol{\xi} \qquad (i = 1, 2, 3) \tag{2.19}$$

The bulk velocity $\mathbf{v}$ is what we can directly perceive of the molecular motion by means of macroscopic observations; it is zero for a gas in equilibrium in a box at rest. Each molecule has its own velocity $\boldsymbol{\xi}$ which can be decomposed into the sum of $\mathbf{v}$ and another velocity

$$\mathbf{c} = \boldsymbol{\xi} - \mathbf{v} \tag{2.20}$$

called the random or peculiar velocity; $\mathbf{c}$ is clearly due to the deviations of $\boldsymbol{\xi}$ from $\mathbf{v}$. It is also clear that the average of $\mathbf{c}$ is zero.

The quantity ρv_i which appears in Eq. (2.19) is the i-th component of the mass flow or, alternatively, of the momentum density of the gas. Other quantities of similar nature are: the momentum flow

$$m_{ij} = \int_{R^3} \xi_i \xi_j f d\boldsymbol{\xi} \qquad (i, j = 1, 2, 3)\,; \tag{2.21}$$

the energy density per unit volume:

$$w = \frac{1}{2} \int_{R^3} |\boldsymbol{\xi}|^2 f d\boldsymbol{\xi}\,; \tag{2.22}$$

the energy flow:

$$r_i = \frac{1}{2}\int_{R^3} \xi_i |\boldsymbol{\xi}|^2 f d\boldsymbol{\xi} \qquad (i = 1, 2, 3)\,. \tag{2.23}$$

Equation (2.21) shows that the momentum flow is described by the components of a symmetric tensor of second order, because we must describe the flow in the i-th direction of the j-th component of momentum. It is to be expected that in a macroscopic description only a part of this tensor will be identified as a bulk momentum flow, because, in general, m_{ij} will be different from zero even in the absence of a macroscopic motion ($\mathbf{v} = 0$). It is thus convenient to re-express the integral in m_{ij} in terms of $\mathbf{c}$ and $\mathbf{v}$. Then we have:

$$m_{ij} = \rho v_i v_j + p_{ij} \tag{2.24}$$

where:

$$p_{ij} = \int_{R^3} c_i c_j f d\boldsymbol{\xi} \qquad (i, j = 1, 2, 3) \tag{2.25}$$

plays the role of the stress tensor (because the microscopic momentum flow associated with it is equivalent to forces distributed on the boundary of any region of gas, according to the macroscopic description).

Similarly one has:

$$w = \frac{1}{2}\rho\,|\mathbf{v}|^2 + \rho e, \tag{2.26}$$

where e is the internal energy per unit mass (associated with random motions) defined by:

$$\rho e = \frac{1}{2}\int_{R^3} |\mathbf{c}|^2 f d\boldsymbol{\xi}\,; \tag{2.27}$$

and:

$$r_i = \rho v_i(\frac{1}{2}|\mathbf{v}|^2 + e) + \sum_{j=1}^{3} v_j p_{ij} + q_i \qquad (i = 1, 2, 3)\,, \tag{2.28}$$

where q_i are the components of the so called heat flow vector:

$$q_i = \frac{1}{2}\int_{R^3} c_i |\mathbf{c}|^2 f d\boldsymbol{\xi}\,. \tag{2.29}$$

The decomposition in Eq. (2.28) shows that the microscopic energy flow is a sum of a macroscopic flow of energy (both kinetic and internal), of the work (per unit area and unit time) done by stresses, and of the heat flow.

In order to complete the connection, as a simple mathematical consequence of the Boltzmann equation, one can derive five differential relations satisfied by the macroscopic quantities introduced above; these relations describe the balance of mass, momentum and energy and have the same form as in continuum mechanics. To this end let us consider the Boltzmann equation

$$\frac{\partial f}{\partial t} + \boldsymbol{\xi} \cdot \frac{\partial f}{\partial \mathbf{x}} = Q(f, f). \tag{2.30}$$

If we multiply both sides by one of the so-called collision invariants ψ_α ($\alpha = 0, 1, 2, 3, 4$), defined as $\psi_0 = 1$, $\psi_i = \xi_i$ ($i = 1, 2, 3$), $\psi_4 = |\boldsymbol{\xi}|^2$ and integrate with respect to $\boldsymbol{\xi}$, we have, thanks to the fact that collisions preserve mass, momentum and energy (see Refs. 2 and 3):

$$\int_{R^3} \psi_\alpha(\boldsymbol{\xi}) Q(f, f) d\boldsymbol{\xi} = 0, \tag{2.31}$$

and hence, if it is permitted to change the order by which we differentiate with respect to t and integrate with respect to $\boldsymbol{\xi}$:

$$\frac{\partial}{\partial t} \int \psi_\alpha f d\boldsymbol{\xi} + \sum_{i=1}^{3} \frac{\partial}{\partial x_i} \int \xi_i \psi_\alpha f d\boldsymbol{\xi} = 0 \qquad (\alpha = 0, 1, 2, 3, 4) \tag{2.32}$$

If we take successively $\alpha = 0, 1, 2, 3, 4$ and use the definitions introduced above, we obtain

$$\frac{\partial \rho}{\partial t} + \sum_{i=1}^{3} \frac{\partial}{\partial x_i}(\rho v_i) = 0, \tag{2.33}$$

$$\frac{\partial}{\partial t}(\rho v_j) + \sum_{i=1}^{3} \frac{\partial}{\partial x_i}(\rho v_i v_j + p_{ij}) = 0, \qquad (j = 1, 2, 3) \tag{2.34}$$

$$\frac{\partial}{\partial t}(1/2\rho|\mathbf{v}|^2 + \rho e) + \sum_{i=1}^{3} \frac{\partial}{\partial x_i} \left[\rho v_i (1/2|\mathbf{v}|^2 + e) + \sum_{j=1}^{3} v_j p_{ij} + q_i \right] = 0. \tag{2.35}$$

These equations have the so-called conservation form because they express the circumstance that a certain quantity (whose density appears differentiated with

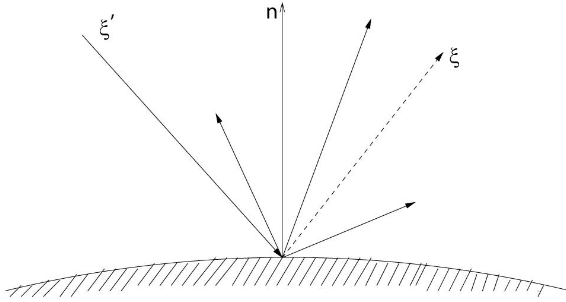

Fig. 2.1. The velocity $\boldsymbol{\xi}$ of a re-emerging molecule is not uniquely determined by the velocity possessed by the same molecule before hitting the wall, unless specular reflection applies (dashed line).

respect to time) is created or destroyed in a certain region Ω because something is flowing through the boundary $\partial\Omega$. In fact, when integrating both sides of the equations with respect to $\mathbf{x}$ over Ω, the terms differentiated with respect to the space coordinates can be replaced by surface integrals over $\partial\Omega$, thanks to the divergence theorem.

2.5. Boundary Conditions

The Boltzmann equation must be accompanied by boundary conditions, which describe the interaction of the gas molecules with solid or liquid walls. It is to this interaction that one can trace the origin of the drag and lift exerted by the gas on another body and the heat transfer between the gas and the boundaries.

The study of gas-surface interaction may be regarded as a bridge between the kinetic theory of gases and solid state physics and is an area of research by itself. The difficulties of a theoretical investigation are due, mainly, to our lack of knowledge of the structure of surface layers of solid and liquid bodies and hence of the effective interaction potential of the gas molecules with the wall. When a molecule impinges upon a surface, it is adsorbed and may form chemical bonds, dissociate, become ionized or displace surface molecules. Its interaction with the solid surface depends on the surface finish, the cleanliness of the surface, its temperature, *etc.* It may also vary with time because of outgassing from the surface. Preliminary heating of a surface also promotes purification of the surface through emission of adsorbed molecules. In general, adsorbed layers may be present; in this case, the interaction of a given molecule with the surface may also depend on the distribution of molecules impinging on a surface element. For a more detailed discussion the reader should consult Ref. 4.

In general, a molecule striking a surface with a velocity $\boldsymbol{\xi}'$ reemerges from it with a velocity $\boldsymbol{\xi}$ which is strictly determined only if the path of the molecule within the wall can be computed exactly. This computation is very hard, because it depends upon a great number of details, such as the locations and velocities of all the molecules of the wall and an accurate knowledge of the interaction potential. Hence it is more convenient to think in terms of a probability density $R(\boldsymbol{\xi}' \to \boldsymbol{\xi}; \mathbf{x}, t; \tau)$ that a molecule striking the surface with velocity between $\boldsymbol{\xi}'$ and $\boldsymbol{\xi}' + d\boldsymbol{\xi}'$ at the point $\mathbf{x}$ and time t will re-emerge at practically the same point with a velocity between $\boldsymbol{\xi}$ and $\boldsymbol{\xi} + d\boldsymbol{\xi}$ (Fig. 2.1) after a time interval τ (adsorption or sitting time). If the function (or distribution) R is known, then we can easily write down the boundary condition for the distribution function $f(\mathbf{x}, \boldsymbol{\xi}, t)$. If the surface is assumed to be at rest, then

$$f(\mathbf{x}, \boldsymbol{\xi}, t)|\boldsymbol{\xi} \cdot \mathbf{n}| = \int_0^\infty d\tau \int_{\boldsymbol{\xi}' \cdot \mathbf{n} < 0} R(\boldsymbol{\xi}' \to \boldsymbol{\xi}; \mathbf{x}, t; \tau) f(\mathbf{x}, \boldsymbol{\xi}', t - \tau)|\boldsymbol{\xi}' \cdot \mathbf{n}| d\boldsymbol{\xi}' \tag{2.36}$$

$$(\mathbf{x} \in \partial\Omega, \boldsymbol{\xi} \cdot \mathbf{n} > 0).$$

The kernel R can be assumed to be independent of f under suitable conditions which we shall not detail here.[4] If, in addition, the effective adsorption time is small compared to any characteristic time of interest in the evolution of f, we can let $\tau = 0$ in the argument of f appearing in the right hand side of Eq. (2.36); in this case the latter becomes:

$$f(\mathbf{x}, \boldsymbol{\xi}, t)|\boldsymbol{\xi} \cdot \mathbf{n}| = \int_{\boldsymbol{\xi}' \cdot \mathbf{n} < 0} R(\boldsymbol{\xi}' \to \boldsymbol{\xi}; \mathbf{x}, t) f(\mathbf{x}, \boldsymbol{\xi}', t)|\boldsymbol{\xi}' \cdot \mathbf{n}| d\boldsymbol{\xi}' \tag{2.37}$$

$$(\mathbf{x} \in \Omega, \boldsymbol{\xi} \cdot \mathbf{n} > 0).$$

where

$$R(\boldsymbol{\xi}' \to \boldsymbol{\xi}; \mathbf{x}, t) = \int_0^\infty d\tau R(\boldsymbol{\xi}' \to \boldsymbol{\xi}; \mathbf{x}, t; \tau) \tag{2.38}$$

Eq. (2.37) is, in particular, valid for steady problems.

The scattering kernel is a fundamental concept in gas-surface interaction, by means of which other quantities should be defined. Frequently its use is avoided by using the so-called accommodation coefficients, with the consequence of lack of clarity, misinterpretation of experiments, bad definitions of terms and misunderstanding of concepts. The basic information on gas-surface interaction, which should be in principle obtained from a detailed calculation based on a physical

model, is summarized in a scattering kernel. The further reduction to a small set of accommodation coefficients can be advocated for practical purposes, provided this concept is firmly related to the scattering kernel (see Refs. 3 and 4).

In view of the difficulty of computing the kernel $R(\boldsymbol{\xi}' \to \boldsymbol{\xi})$ from a physical model of the wall, a different procedure, which is less physical in nature, is usually adopted. The idea is to construct a mathematical model in the form of a kernel $R(\boldsymbol{\xi}' \to \boldsymbol{\xi})$ which satisfies certain basic physical requirements (see Refs. 2 and 3) and is not otherwise restricted except by the condition of not being too complicated.

One of the simplest kernels is

$$R(\boldsymbol{\xi}' \to \boldsymbol{\xi}) = \alpha M_w(\boldsymbol{\xi})|\boldsymbol{\xi} \cdot \mathbf{n}| + (1-\alpha)\delta(\boldsymbol{\xi} - \boldsymbol{\xi}' + 2\mathbf{n}(\boldsymbol{\xi}' \cdot \mathbf{n})) \qquad (0 \leq \alpha \leq 1) \tag{2.39}$$

This kernel corresponds to Maxwell's model, according to which a fraction $(1-\alpha)$ of molecules undergoes a specular reflection, while the remaining fraction α is diffused with the Maxwellian distribution of the wall M_w. This model contains pure diffusion according to a nondrifting Maxwellian as a limiting case (Eq. (2.39) with $\alpha = 1$). The use of this particular model is justified for low-velocity flows over technical surfaces, but is inaccurate for flows with orbital velocity.

2.6. The Modified Reynolds Equation

The starting point to obtain the rarefied version of the Reynolds equation for lubrication is the mass balance equation, Eq. (2.33), which, as we have seen, is a consequence of the Boltzmann equation. This equation is considerably simplified by the fact that the variations of density do not show up for slow motion in the steady case, which is the most important in applications and we shall consider henceforth. Thus

$$\frac{\partial u}{\partial x} + \frac{\partial v}{\partial y} + \frac{\partial w}{\partial z} = 0 \tag{2.40}$$

where the three components of the bulk velocity are denoted by u, v, w.

Let us consider a layer of gas between two walls located at $z = 0$ and $z = D(x, y)$; the lower wall moves in its own plane (see Fig. 2.2, where, for simplicity, the y-direction has been suppressed). If we integrate Eq. (2.40) across the layer, we obtain

$$\frac{\partial}{\partial x}\int_0^D u dz + \frac{\partial}{\partial y}\int_0^D v dz = 0. \tag{2.41}$$

Since the problem is linear and the pressure gradient is assumed to be constant across the layer, each component u, v is proportional to the sum of the velocities given by a Poiseuille flow with pressure gradient dp/dx, dp/dy, respectively, and a Couette flow with the lower wall moving with velocity components U and V.

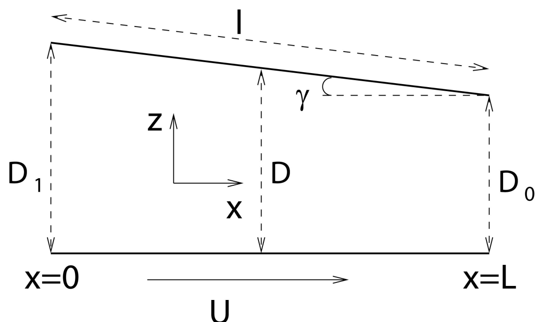

Fig. 2.2. Geometry of a slider bearing.

In the case of Couette flow the evaluation of the integral: $F_C^{(1)} = \int_0^D u_C dz$ is easy, if the walls are assumed to be identical. In fact, in this situation the profile is antisymmetric with respect to the midpoint and $F_C^{(1)} = UD/2$. Similarly $F_C^{(2)} = \int_0^D v_C dz = VD/2$. The behavior of the flow rate for plane Poiseuille flow is much more complicated and is given by

$$F_P^{(1)} = \int_0^D u_P dz = -\frac{1}{\rho_0\sqrt{2RT_0}}\frac{\partial p}{\partial x}D^2 Q(\delta);$$

$$F_P^{(2)} = \int_0^D v_P dz = -\frac{1}{\rho_0\sqrt{2RT_0}}\frac{\partial p}{\partial y}D^2 Q(\delta) \tag{2.42}$$

where δ is the ratio between the distance and the (unperturbed) mean free path:

$$\delta = \frac{pD}{\mu\sqrt{2RT}}$$

and $Q(\delta)$ is the nondimensional flow rate which can be obtained by solving the problem of plane Poiseuille flow. Thus the modified Reynolds equation reads as follows

$$\frac{\partial}{\partial x}\left[\frac{\partial p}{\partial x}D^2 Q(\delta)\right] + \frac{\partial}{\partial y}\left[\frac{\partial p}{\partial y}D^2 Q(\delta)\right] = \rho_0\sqrt{2RT_0}\left[\frac{U}{2}\frac{\partial D}{\partial x} + \frac{V}{2}\frac{\partial D}{\partial y}\right]. \tag{2.43}$$

Given $D = D(x, y)$, this is an (elliptic) partial differential equation for p which must be solved for an assigned value of p (usually constant) at the boundary.

We have assumed so far that the linearization assumption holds everywhere. It may turn out, however, that the pressure undergoes a significant change. In this case, one can still utilize the linearized Boltzmann equation to compute the local flow rate, but one should use the local pressure p throughout, rather than the unperturbed pressure p_0. The modified Reynolds equation then reads as follows

$$\frac{\partial}{\partial x}\left[\frac{D^2 Q(\delta)}{\sqrt{2RT}}\frac{\partial p}{\partial x}\right]+\frac{\partial}{\partial y}\left[\frac{D^2 Q(\delta)}{\sqrt{2RT}}\frac{\partial p}{\partial y}\right]=\frac{1}{2}\left[U\frac{\partial(\rho D)}{\partial x}+V\frac{\partial(\rho D)}{\partial y}\right]. \quad (2.44)$$

This generalized Reynolds equation was first introduced by Fukui and Kaneko.[7,8] In the continuum limit we have

$$Q(\delta)=\frac{1}{6}\frac{pD}{\mu\sqrt{2RT}}$$

and Eq. (2.44) becomes

$$\frac{\partial}{\partial x}\left[\frac{\rho D^3}{\mu}\frac{\partial p}{\partial x}\right]+\frac{\partial}{\partial y}\left[\frac{\rho D^3}{\mu}\frac{\partial p}{\partial y}\right]=6\left[U\frac{\partial(\rho D)}{\partial x}+V\frac{\partial(\rho D)}{\partial y}\right] \quad (2.45)$$

which is essentially the equation originally given by Reynolds.[1]

2.7. The Reynolds Equation and the Poiseuille-Couette Problem

The micromachinery fabrication techniques have become more and more mature in the last ten years. In particular, the micro-electro-mechanical systems (MEMS) developed rapidly and found many applications in microelectronics, medicine, biology, optics, aerospace and other high technology fields. Both experimental and computational efforts have been undertaken to understand the specific features of the microscale flows. A basic constituent of the MEMS devices is the microchannel, the region between two parallel plates that can reveal many specific features of the low speed internal flows in microdevices. Typically the first devices were integrated micro-channel/pressure sensor systems. The Knudsen number at the outlet of the channel at room conditions is 0.05 for nitrogen, and even higher for helium; hence the flow is surely beyond the slip flow regime. The pressure distribution along the channel and the flow rates across these channels are found to deviate from the linear distribution of the Poiseuille flow. Monte Carlo methods were used to simulate microchannel flows but they meet with the excessively high demands to the storage and computation time. The gradual regulation of the inlet

and outlet boundary conditions of the channel seems to be tremendously difficult for DSMC in solving the long channel flows. In fact the typical DSMC simulation of the micro channel flow is limited to high speeds. Recently, the so called information preservation (IP) method was proposed;[9,10] it uses a conservative scheme and a super-relaxation technique, which results in excellent agreement with experimental data.

However, the kinetic theory of MEMS does not require heavy computational tools. The generalized Reynolds equation can be used to calculate the gas film lubrication problem provided that the flow rate of Poiseuille flow is calculated from the linearized Boltzmann equation. The case of a microchannel with parallel plates was treated by C. Shen.[11]

Following Refs. 6 and 12, let us consider again two plates separated by a distance D and a gas flowing parallel to them, in the x direction, due to a pressure gradient. The lower boundary ($z = -D/2$) moves to the right with velocity U, while the upper boundary ($z = D/2$) is fixed. Both boundaries are held at a constant temperature T_o. However, at variance with our previous discussions, we assume the gas-surface interaction to be different at the wall.

As usual, if the pressure gradient and the velocity U are taken to be small, it can be assumed that the Boltzmann equation can be linearized about a Maxwellian. If we consider the linearized BGK model for the collision operator, the Boltzmann equation reads:

$$\frac{1}{2}k + c_z \frac{\partial Z}{\partial z} = \frac{1}{\ell}\left[\pi^{-\frac{1}{2}} \int_{-\infty}^{+\infty} e^{-c_{z_1}^2} Z(z, c_{z_1})\, dc_{z_1} - Z(z, c_z)\right] \tag{2.46}$$

where by definition

$$Z(z, c_z) = \pi^{-1} \int_{-\infty}^{+\infty} \int_{-\infty}^{+\infty} e^{-c_x^2 - c_y^2} c_x h(z, \mathbf{c})\, dc_x\, dc_y$$

$$k = \frac{1}{p}\frac{\partial p}{\partial x} = \frac{1}{\rho}\frac{\partial \rho}{\partial x}$$

with p and ρ being the gas pressure and density, respectively, and ℓ the mean free path. Consequently, the bulk velocity of the gas is given by:

$$q(z) = \pi^{-\frac{1}{2}} \int_{-\infty}^{+\infty} e^{-c_{z_1}^2} Z(z, c_{z_1})\, dc_{z_1}. \tag{2.47}$$

From Eq. (2.46) we obtain the integral relation:

$$Z(z, c_z) = \exp(-(z + \frac{D}{2}\text{sgn}c_z)/(c_z\ell))Z(-\frac{D}{2}\text{sgn}c_z, c_z) + \int_{-\frac{D}{2} sgnc_z}^{z} \exp\left(\frac{-|z-t|}{|c_z|\ell}\right)[q(t) - k\ell/2]/(c_z\ell)\,dt \quad (2.48)$$

with the values at the boundary, $Z(-\frac{D}{2}\text{sgn}c_z, c_z)$, depending on the model of boundary condition chosen. This problem was first treated by Cercignani and Daneri[6] for completely diffusing walls. In the following, we will take into account the Maxwell boundary conditions as in Ref. 12 and consider two walls having different physical properties, *i.e.*, with two accommodation coefficients (α_1, α_2). In this case, the boundary conditions can be written as:

$$Z^+(D/2, c_z) = (1 - \alpha_1)Z^-(D/2, -c_z)$$

$$Z^+(-D/2, c_z) = \alpha_2 U + (1 - \alpha_2)Z^-(-D/2, -c_z)$$

where U is expressed in units of $(2RT_o)^{1/2}$; $Z^-(-D/2, c_z)$, $Z^-(D/2, c_z)$ are the distribution functions of the molecules impinging upon the walls; similarly, $Z^+(-D/2, c_z)$, $Z^+(D/2, c_z)$ are the distribution functions of the molecules reemerging from the same walls.

Once the function at the boundary, $Z(-\frac{D}{2}\text{sgn}c_z, c_z)$, has been evaluated following the analytical procedure reported in Refs. 12 and 13, the substitution of the integral formula (2.48) in the definition (2.47) of $q(z)$ gives the following expression for the bulk velocity of the gas:

$$q(z) = \frac{1}{2}k\ell[1 - \psi_p(u)] + U\psi_c(u). \quad (2.49)$$

Equation (2.49) shows that the gas velocity is induced by the superposition of two distinct effects. The gas moves by an imposed pressure gradient (Poiseuille flow) and by the shear driven flow due to the motion of the bottom surface (Couette flow). The non-dimensional functions $\psi_p(u)$ and $\psi_c(u)$, giving the Poiseuille and Couette contributions, respectively, satisfy the following integral equations:

$$\psi_p(u) = 1 + \frac{1}{\sqrt{\pi}}\int_{-\delta/2}^{\delta/2} \mathrm{d}w\,\psi_p(w)\Big\{(1-\alpha_1)S_{-1}(\delta - u - w) + (1-\alpha_2)S_{-1}(\delta + u + w) + (1-\alpha_1)(1-\alpha_2)[S_{-1}(2\delta - u + w) + S_{-1}(2\delta + u - w)] + T_{-1}(|u - w|)\Big\} \quad (2.50)$$

$$\psi_c(u) = \frac{\alpha_2}{\sqrt{\pi}}\Big[T_o(\frac{\delta}{2}+u) + (1-\alpha_1)S_o(\frac{3}{2\delta}-u)$$
$$+ (1-\alpha_1)(1-\alpha_2)S_o(\frac{5}{2\delta}+u)\Big]$$
$$+ \frac{1}{\sqrt{\pi}}\int_{-\delta/2}^{\delta/2} \mathrm{d}w\, \psi_c(w)\Big\{(1-\alpha_1)S_{-1}(\delta-u-w)$$
$$+ (1-\alpha_2)S_{-1}(\delta+u+w) + (1-\alpha_1)(1-\alpha_2)[S_{-1}(2\delta-u+w)$$
$$+ S_{-1}(2\delta+u-w)] + T_{-1}(|u-w|)\Big\} \tag{2.51}$$

where $T_n(x)$ is the Abramowitz function defined by

$$T_n(x) = \int_0^{+\infty} t^n \exp(-t^2 - x/t)\, dt$$

$S_n(x)$ is a generalized Abramowitz function defined by

$$S_n(x,\delta,\alpha_1,\alpha_2) = \int_0^{+\infty} \frac{t^n \exp(-t^2 - x/t)}{1-(1-\alpha_1)(1-\alpha_2)\exp(-2\delta/t)}\, dt$$

and the following non-dimensional variables have been introduced:

$$\delta = D/\ell, \qquad w = t/\ell, \qquad u = z/\ell.$$

Using Eq. (2.49), the flow rate (per unit time through unit thickness) defined by:

$$F = \rho \int_{-D/2}^{D/2} q(z)dz \tag{2.52}$$

can be expressed as the sum of the Poiseuille flow (F_p) and the Couette flow (F_c) as follows:

$$F = F_p + F_c = -\frac{\partial p}{\partial x} D^2 Q_p(\delta,\alpha_1,\alpha_2) + \frac{\rho U D}{2} Q_c(\delta,\alpha_1,\alpha_2) \tag{2.53}$$

where

$$Q_p(\delta,\alpha_1,\alpha_2) = -\frac{1}{\delta} + \frac{1}{\delta^2}\int_{-\delta/2}^{\delta/2} \psi_p(u)du$$

$$Q_c(\delta,\alpha_1,\alpha_2) = \frac{2}{\delta}\int_{-\delta/2}^{\delta/2} \psi_c(u)du$$

are the non-dimensional volume flow rates.

2.8. The Generalized Reynolds Equation for Unequal Walls

One can easily extend the generalized Reynolds equation to the case of unequal walls:

$$\frac{d}{dx}\left(\frac{dp}{dx}D^2Q_p(\delta,\alpha_1,\alpha_2)-\frac{\rho UD}{2}Q_c(\delta,\alpha_1,\alpha_2)\right)=0 \tag{2.54}$$

For the purpose of a direct comparison with the classical Reynolds equation (2.45), let us introduce the Poiseuille relative flow rate:

$$\tilde{Q}_p(\delta,\alpha_1,\alpha_2)=\frac{Q_p(\delta,\alpha_1,\alpha_2)}{Q_{con}} \tag{2.55}$$

where $Q_{con}=\delta/6$. If one introduces the following dimensionless quantities

$$X=x/l,\qquad P=p/p_o,\qquad H=D/D_o,$$

the rarefaction parameter δ can be expressed as: $\delta=\delta_oPH$, where δ_o is the characteristic inverse Knudsen number defined by the minimum film thickness, D_o, and the ambient pressure p_o as:

$$\delta_o=\frac{p_oD_o}{\mu\sqrt{2RT_o}}.$$

(see Fig. 2.2). Finally, assuming that the heat generation in the gas is very small, so that an isothermal process can be considered, the non-dimensional generalized Reynolds equation reads:

$$\frac{d}{dX}\left(\tilde{Q}_p(\delta_oPH,\alpha_1,\alpha_2)PH^3\frac{dP}{dX}-Q_c(\delta_oPH,\alpha_1,\alpha_2)\Lambda PH\right)=0. \tag{2.56}$$

The bearing number Λ in Eq. (2.56) is defined as

$$\Lambda=\frac{6\mu Ul}{p_oD_o^2} \tag{2.57}$$

where μ is the viscosity coefficient. If the two walls are identical ($\alpha_1=\alpha_2=\alpha$), the Couette flow rate is independent of the Knudsen number regardless of the value of the accommodation coefficient α and Eq. (2.56) reduces to the generalized Reynolds equation introduced by Fukui and Kaneko.[7,8]

Writing the non-dimensional film thickness H in terms of the longitudinal coordinate X,

$$H=\frac{D_1}{D_o}-\frac{l}{L}\left(\frac{D_1}{D_o}-1\right)X \tag{2.58}$$

such that

$$\frac{dP}{dX} = -\frac{l}{L}\left(\frac{D_1}{D_o} - 1\right)\frac{dP}{dH}.$$

Equation (2.56) can be immediately integrated to give:

$$\frac{l}{L}\left(\frac{D_1}{D_o} - 1\right)\tilde{Q}_p(\delta_o PH, \alpha_1, \alpha_2)PH^3\frac{dP}{dH} + Q_c(\delta_o PH, \alpha_1, \alpha_2)\Lambda PH = K_1 \tag{2.59}$$

where K_1 is a constant of integration. The substitution of

$$PH = \zeta \tag{2.60}$$

in Eq. (2.59) gives:

$$\frac{d\zeta}{dH} = \frac{\zeta}{H} - \frac{[Q_c(\delta_o\zeta, \alpha_1, \alpha_2)\Lambda\zeta - K_1]}{l/L(D_1/D_o - 1)\tilde{Q}_p(\delta_o\zeta, \alpha_1, \alpha_2)H\zeta}. \tag{2.61}$$

The boundary conditions to be matched to Eq. (2.61) read

$$\zeta = D_1/D_o \qquad \text{at} \qquad \mathrm{H} = \mathrm{D_1/D_o}$$

$$\zeta = 1 \qquad \text{at} \qquad \mathrm{H} = 1.$$

Equation (2.61) can be solved numerically using relaxation methods. To apply this numerical scheme, the differential equations have to be replaced by finite-difference equations on a point mesh. The solution of the resulting set of equations is determined by starting with a guess and improving it iteratively using Newton's method. The Poiseuille and Couette flow rate coefficients, $Q_p(\delta, \alpha_1, \alpha_2)$, $Q_c(\delta, \alpha_1, \alpha_2)$, have been evaluated by means of the numerical method described in Ref. 13 and a variational technique for the integrodifferential form of the Boltzmann equation based on the BGK model.[12,14]

Once $\zeta(H)$ has been numerically evaluated on a grid that spans the domain of interest, Eqs. (2.58) and (2.60) give the pressure field in the gas film as a function of X. Furthermore, a prediction of the vertical force acting on the upper surface of the slider bearing, crucial for practical design, may be obtained from the load carrying capacity W, defined as

$$W = \frac{l}{L}\int_0^{L/l}(P-1)\,dX. \tag{2.62}$$

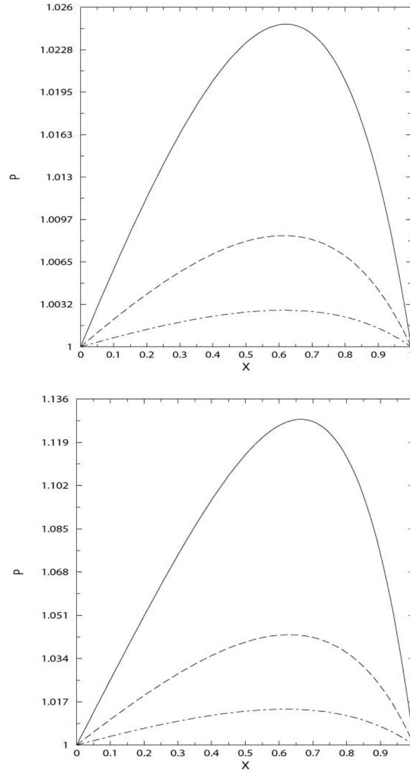

Fig. 2.3. Pressure profile for $\delta_o = 0.5$. The line styles indicate $\alpha = 0.8$ (solid), $\alpha = 0.3$ (dashed), and $\alpha = 0.1$ (dot dashed). The bearing number Λ is 10 (top) and 50 (bottom).

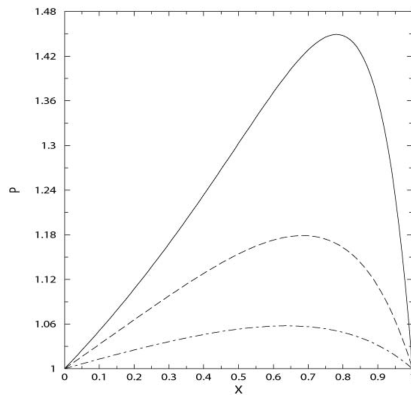

Fig. 2.4. Pressure profile for $\delta_o = 0.5$. The line styles indicate $\alpha = 0.8$ (solid), $\alpha = 0.3$ (dashed), and $\alpha = 0.1$ (dot dashed). The bearing number Λ is 200.

In order to investigate the effects of the rarefaction parameter δ_o and the bearing number Λ on the basic lubrication characteristics (pressure distribution and load carrying capacity), the parameters describing the gas film geometric configuration were fixed at the following values: $D_1/D_o = 2$, $L/D_o = 100$. Figures 2.3 and 2.4 show the pressure field as a function of the longitudinal coordinate X at three different bearing numbers: $\Lambda = 10, 50, 200$. To assess the influence of the boundary conditions, the profiles corresponding to different accommodation coefficients (for bounding walls supposed physically identical) are drawn in Figs. 2.3 and 2.4.

Looking at the pictures, one sees that the pressure distribution in the gas film increases with increasing Λ. Furthermore, at fixed bearing number, the pressure field reduces by increasing the fraction of gas molecules specularly reflected by the walls. Figures 2.5 and 2.6 report the pressure profiles for the same parameters as in Figs. 2.3 and 2.4, except that now the two bounding plates are allowed to re-emit the impinging gas molecules differently, so that two accommodation coefficients must be used. We keep the accommodation coefficient of the upper wall (α_1) fixed and vary the other one (α_2).

A comparison with Figs. 2.3 and 2.4 shows that, for every Λ, the pressure distribution significantly depends on α_2 and only weakly on α_1.

It is worth noting that, when Λ increases, the Couette contribution to the lubrication flow rate becomes dominant compared with the Poiseuille flow. Therefore, if the two walls are identical, the influence of the Knudsen number on the load carrying capacity decreases as Λ increases, since Q_c is independent of δ and α. On the contrary, if the two walls have a different physical structure the load carrying capacity shows a dependence on both the Knudsen number and the accommodation coefficients α_1, α_2.

In order to investigate more specifically the effects of the rarefaction parameter δ_o and the accommodation coefficients, Fig. 2.7 shows the pressure profiles in the near-free molecular flow and near-continuum flow limits for different values of α_1 and α_2. The picture reveals that, for small δ_o, if one keeps the accommodation coefficient of the slider (α_1) fixed and varies the other one (α_2), the pressure distribution in the gas film, at fixed bearing number, increases with increasing α_2, as it always happens in the continuum region, while at fixed α_2, the pressure distribution decreases by increasing α_1. Such kind of inverted pressure profiles, which appear in studying the slider air bearing problem in the free-molecular flow regime, are triggered by the Couette contribution to the lubrication flow rate.[14] For the validation of the code, the results obtained with the modified Reynolds equation have been compared with the numerical findings obtained from DSMC (Direct Simulation Monte Carlo) simulations (Alexander *et al.* 1994)[15] and IP

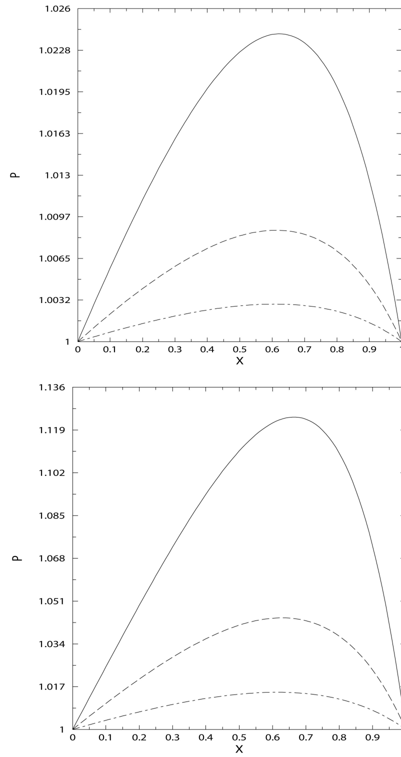

Fig. 2.5. Pressure profile for $\delta_o = 0.5$. The line styles indicate $\alpha_1 = 0.5\,\alpha_2 = 0.8$ (solid), $\alpha_1 = 0.5\,\alpha_2 = 0.3$ (dashed), and $\alpha_1 = 0.5\,\alpha_2 = 0.1$ (dot dashed). The bearing number Λ is 10 (top) and 50 (bottom).

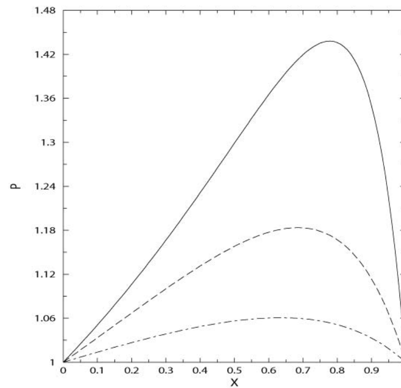

Fig. 2.6. Pressure profile for $\delta_o = 0.5$. The line styles indicate $\alpha_1 = 0.5\,\alpha_2 = 0.8$ (solid), $\alpha_1 = 0.5\,\alpha_2 = 0.3$ (dashed), and $\alpha_1 = 0.5\,\alpha_2 = 0.1$ (dot dashed). The bearing number Λ is 200.

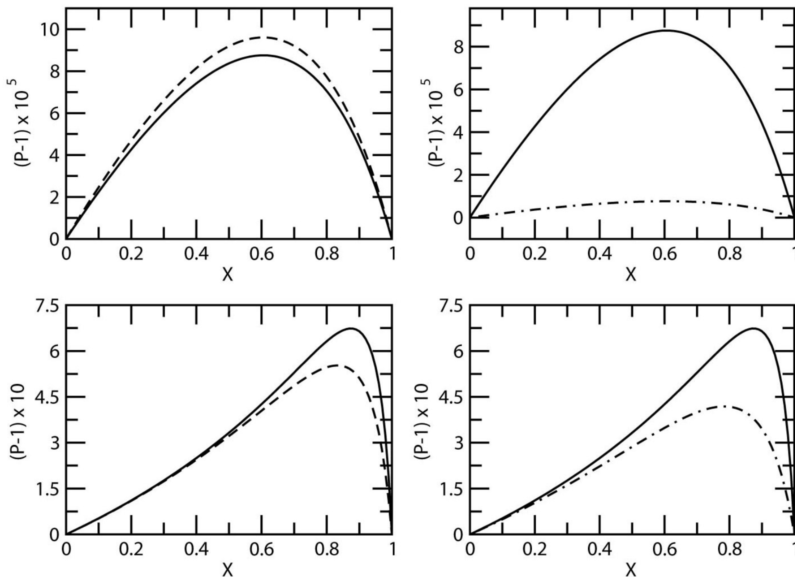

Fig. 2.7. Pressure profiles, from the Reynolds equation, versus X for $\Lambda = 50$. The line styles indicate $\alpha_1 = 0.1$ $\alpha_2 = 0.8$ (dashed), $\alpha_1 = 0.8$ $\alpha_2 = 0.8$ (solid), $\alpha_1 = 0.8$ $\alpha_2 = 0.1$ (dot dashed). The inverse Knudsen number δ_o is 10^{-3} (top panels) and 10 (bottom panels).

(Information Preservation) method (Jiang *et al.* 2005)[16] in the case of Maxwell's boundary conditions on two physically identical walls (see Figs. 2.8 and 2.9). The parameters describing the gas film geometric configuration were fixed at the following values: $D_1/D_o = 2$, $L/D_o = 100$.

In Figs. 2.8 and 2.9 two different Reynolds equation solutions have been presented, obtained using the BGK model and a more refined kinetic model of the collisional Boltzmann operator, that is the linearized ellipsoidal statistical (ES) model, which allows the Prandtl number to assume its proper value. Because of its simplicity compared to the Boltzmann equation, the BGK model is widely used in the kinetic theory of gases, although one of the best known shortcomings of this model is that the Prandtl number turns out to be unity. Since the classical value for a monoatomic gas is known to be $Pr = 2/3$, one cannot make both viscosity and thermal conductivity agree with the Chapman–Enskog values for a Maxwell gas. This circumstance is easily avoided in linearized problems since viscosity and temperature effects can be decoupled. However, even in the frame of a linearized analysis, one is induced to suspect that the incorrect Prandtl number can be influent in the transitional regime. Therefore, it appears worthwhile to investigate the slider bearing problem through the generalized Reynolds equation based

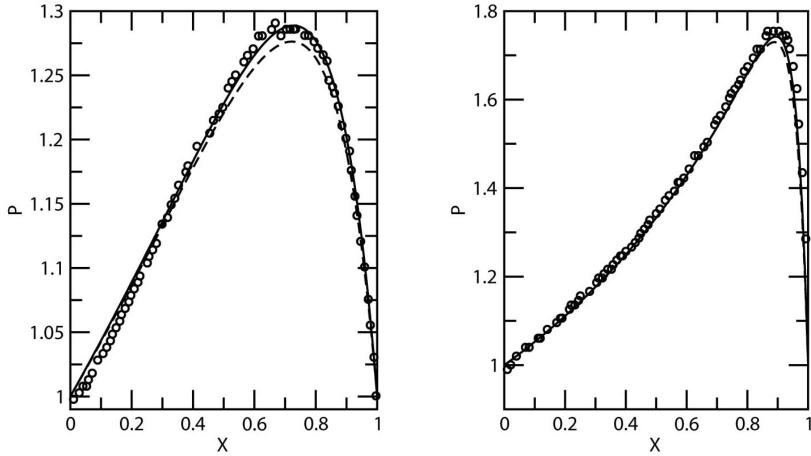

Fig. 2.8. Pressure profile versus X. Comparison between the Reynolds-BGK results (solid line), the Reynolds-ES results (dashed line) and DSMC data (Alexander *et al.* 1994) (open circles). The parameters are: $\delta_o = 0.7$, $\Lambda = 61.6$, $\alpha = 1$ (left); $\delta_o = 0.2$, $\Lambda = 1264$, $\alpha = 1$ (right).

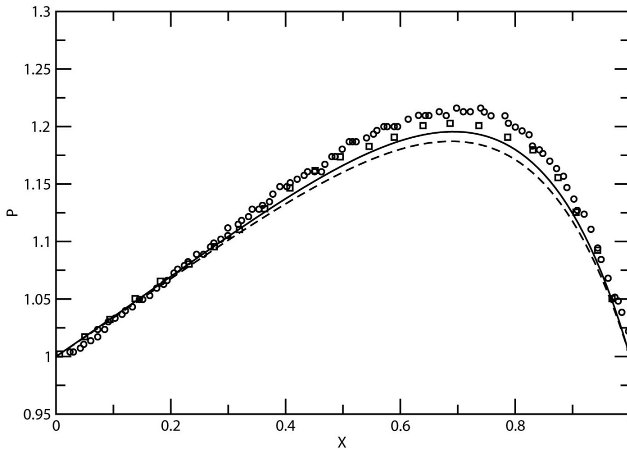

Fig. 2.9. Pressure profile versus X. Comparison between the Reynolds-BGK results (solid line), the Reynolds-ES results (dashed line), DSMC data (Alexander *et al.* 1994) (open circles) and the IP data (Jiang *et al.* 2005) (open squares). The parameters are: $\delta_o = 0.7$, $\Lambda = 61.6$, $\alpha = 0.7$.

on a model more refined than the BGK one. Figures 2.8 and 2.9 show that the present Reynolds equation solutions, obtained using the ES and BGK models, are in good agreement with the DSMC data presented by Alexander *et al.* (1994) and the IP results reported by Jiang *et al.* (2005). It is worth noting that, in Fig. 2.9,

the results of the IP method given by Jiang *et al*. (2005) are closer to the Reynolds equation numerical solutions than the DSMC data obtained previously by Alexander *et al*. (1994). Furthermore, the solution of the Reynolds equation based on the ES model slightly underestimates the pressure profiles given by the DSMC and IP simulations suggesting that in isothermal conditions and at low Mach numbers the corrections introduced by a more refined kinetic model of the collisional Boltzmann operator are extremely small. The load capacity values, corresponding to the set of parameters listed in Figs. 2.8 and 2.9, are summarized in Table 2.1. Finally, it is worth stressing that the inverted pressure profiles, showed in Fig. 2.7, arise irrespective of which of the two kinetic models (BGK or ES) have been considered to derive the Reynolds equation.

2.9. A Kinetic Approach for the Evaluation of Damping in MEMS

Beyond the lubrication problems, shear-and pressure-driven gas flows are encountered in several MEMS applications like surface-micromachined inertial sensors, resonating filter structures for signal processing and micromachined capacitive accelerometers, where the distance between the capacitor plates is minimized in order to increase the efficiency of actuation and improve the sensitivity of detection. The damping, due to the internal friction of the flowing gas, in the small gaps between these oscillating microstructures, is an important design parameter since it determines, *e.g.*, the frequency-domain behavior of the sensor or the quality factor of the vibrating filter structure. At low pressures or in ultra thin films, the

Table 2.1. Summary of load capacity values.

δ_o	0.7	0.2	0.7
Λ	61.6	1264	61.6
α_1	1.	1.	0.7
α_2	1.	1.	0.7
Load capacity			
Reynolds (BGK)	0.174	0.347	0.122
Reynolds (ES)	0.167	0.345	0.117
DSMC (Alexander *et al.*, 1994) (from pressure)	0.175	0.357	0.129
DSMC (Alexander *et al.*, 1994) (from force)	0.174	0.329	0.132

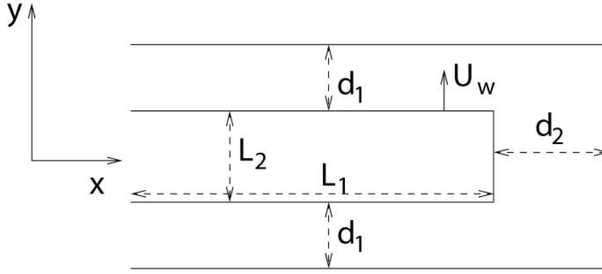

Fig. 2.10. Geometry of a two-dimensional microchannel. The fixed parameters of the apparatus are: $d_1 = 2.6\,\mu m$; $d_2 = 4.2\,\mu m$; $L_1 = 15\,\mu m$; $L_2 = 3.9\,\mu m$. The central shuttle-plate, of thickness L_2, moves with velocity U_w in the y direction while the external boundaries are fixed.

gas rarefaction effects and the molecular interaction with the surfaces effectively change the viscosity. In this flow regime, the continuum equations are no longer valid and the Boltzmann equation must be considered to understand and compute the rarefied flows related with these devices. In spite of its apparently complex structure, a real micromechanical accelerometer usually has a highly repetitive layout whose basic units consist of two or three-dimensional microchannels where different sets of bounding walls move in the direction perpendicular or parallel to their surfaces.

Let us consider the two-dimensional microchannel shown in Fig. 2.10 where the plates parallel to the x direction generate a Poiseuille-like flow, while those parallel to the y direction induce a Couette-like flux. Since the gaps between the moving elements and the fixed boundaries are only a few micrometres wide, the mean free path of the gas molecules is not negligible compared to the gap width and the gas cannot be treated as a continuous medium. Therefore, the behavior of a gas as it moves along the tube must be studied through the Boltzmann equation. Since the various types of motions experienced by the accelerometer components are typically at very low Mach number, it can be assumed that the velocity distribution of the gas flow only slightly deviates from that occurring at an equilibrium state. Moreover, if one assumes that the flow field can be described quasi-statically, it is convenient to linearize the Boltzmann equation about a Maxwellian M by setting:

$$f = M(1 + h) \tag{2.63}$$

where $h(\tilde{\mathbf{x}}, \boldsymbol{\xi})$ is the small perturbation of the basic equilibrium state, with $\tilde{\mathbf{x}}$ being the coordinate vector and $\boldsymbol{\xi}$ the molecular velocity. The above mentioned absolute

Maxwellian M is given by:

$$M(\boldsymbol{\xi}) = \frac{\rho_0}{(2\pi RT_0)^{3/2}} \exp\left\{ -\frac{(\xi_x^2+\xi_y^2+\xi_z^2)}{2RT_0} \right\} \tag{2.64}$$

where ρ_0 and T_0 are the equilibrium density and temperature, respectively, and R is the gas constant. If one assumes the linearized Bhatnagar, Gross and Krook (BGK) model for the collision operator (see Eq. (2.15)), which describes the effect of molecular interactions, the steady state Boltzmann equation reads:

$$c_x \frac{\partial h}{\partial \tilde{x}} + c_y \frac{\partial h}{\partial \tilde{y}} = \frac{\pi^{-3/2}}{\ell} \left[\int e^{-c'^2} h(\tilde{x},\tilde{y},\mathbf{c}')d\mathbf{c}' + 2c_x \int c'_x e^{-c'^2} h(\tilde{x},\tilde{y},\mathbf{c}')d\mathbf{c}' \right.$$
$$\left. + 2c_y \int c'_y e^{-c'^2} h(\tilde{x},\tilde{y},\mathbf{c}')d\mathbf{c}' \right] - h(\tilde{x},\tilde{y},\mathbf{c})/\ell \tag{2.65}$$

where ℓ is the mean free path and the following non-dimensional velocity variable has been introduced:

$$\mathbf{c} = \frac{\boldsymbol{\xi}}{\sqrt{2RT_0}} \tag{2.66}$$

In Eq. (2.65) integrations are extended to the whole velocity space. Since the microchannel walls are mantained at the same constant temperature, the thermal perturbation, which would have to appear in Eq. (2.65), has been dropped out.

Multiplying Eq. (2.65) by $(1/\sqrt{\pi})\exp(-c_z^2)$ and integrating with respect to c_z, we obtain the following equation

$$c_x \frac{\partial}{\partial x}\mathcal{G}(x,y,c_x,c_y) + c_y \frac{\partial}{\partial y}\mathcal{G}(x,y,c_x,c_y) = -\mathcal{G}(x,y,c_x,c_y)$$
$$+ \rho(x,y) + 2c_x v_x(x,y) + 2c_y v_y(x,y) \tag{2.67}$$

for the reduced distribution function $\mathcal{G}(x,y,c_x,c_y)$ defined by

$$\mathcal{G}(x,y,c_x,c_y) = \pi^{-1/2} \int_{-\infty}^{+\infty} e^{-c_z^2} h(x,y,\mathbf{c}) dc_z \tag{2.68}$$

where the spatial variables have been rescaled as follows

$$x = \tilde{x}/\ell; \qquad y = \tilde{y}/\ell.$$

In Eq. (2.67), the macroscopic fields associated to the perturbation are defined as

$$\rho(x,y) = \pi^{-1} \int_{-\infty}^{+\infty} \int_{-\infty}^{+\infty} e^{-(c_x^2+c_y^2)} \mathcal{G}(x,y,c_x,c_y)\, dc_x dc_y \tag{2.69}$$

$$v_x(x,y) = \pi^{-1} \int_{-\infty}^{+\infty} \int_{-\infty}^{+\infty} c_x e^{-(c_x^2+c_y^2)} \mathcal{G}(x,y,c_x,c_y)\, dc_x dc_y \tag{2.70}$$

$$v_y(x,y) = \pi^{-1} \int_{-\infty}^{+\infty} \int_{-\infty}^{+\infty} c_y e^{-(c_x^2+c_y^2)} \mathcal{G}(x,y,c_x,c_y)\, dc_x dc_y \tag{2.71}$$

with $\rho(x,y)$ being the perturbation part of the density of molecules, $v_x(x,y)$ and $v_y(x,y)$ the x and y components of the bulk velocity of the gas, respectively. This transformation permits to greatly simplify the numerical solution of the Boltzmann equation since it reduces the three-dimensional molecular velocity field to two-dimensional.

Appropriate boundary conditions on the plates, describing the gas-wall interactions, must be supplied for Eq. (2.67) to be solved. Assuming the diffuse-specular reflection condition of Maxwell's type, according to which the reemitted molecules are partly reflected by the wall in a specular fashion and partly diffused with a Maxwellian distribution described by the wall properties (*i.e.*, its temperature and velocity) (see Eq. (2.39)), the linearized boundary conditions to be matched to Eq. (2.67), can be derived inserting Eq. (2.63) in Eq. (2.37) where the kernel R is given by Eq. (2.39).

The solution of the problem described by Eq. (2.67) can be determined by pursuing the long-time behavior of the solution of the initial and boundary-value problem. That is, we consider Eq. (2.67) with the additional $\partial\mathcal{G}/\partial t$ term on the left-hand side and an initial condition (*e.g.*, $\mathcal{G} = 0$) beyond the boundary conditions of Maxwell's type. The time-dependent problem can then be solved numerically by a deterministic finite-difference method.

The structure of the simulated gas flow is summarized in Fig. 2.11 where the vector plot of the velocity field corresponding to a Knudsen number in the transitional flow regime ($\mathrm{Kn} \simeq 0.29$) is shown.

In order to complement this global visualization, the contour plot of the x and y components of the macroscopic gas velocity along the channel are presented in Figs. 2.12 and 2.13, respectively.

The most apparent features are the v_x parabolic profiles in the cross-stream directions of the longest branches of the channel where a Poiseuille-like flow is induced and similar parabolic profiles of the y component of the gas velocity in the stream-wise direction of the transversal section of the channel where a coupled Poiseuille-Couette flow develops.

In order to model the damping forces occurring as a result of the internal friction of the flowing gas underneath the plates, the following elements of the stress tensor have been evaluated:

$$P_{xx}(x,y) = \frac{\rho_0}{2} + \frac{\rho_0}{\pi} \int_{-\infty}^{+\infty} \int_{-\infty}^{+\infty} dc_x dc_y c_x^2 e^{-(c_x^2+c_y^2)} \mathcal{G}(x,y,c_x,c_y) \tag{2.72}$$

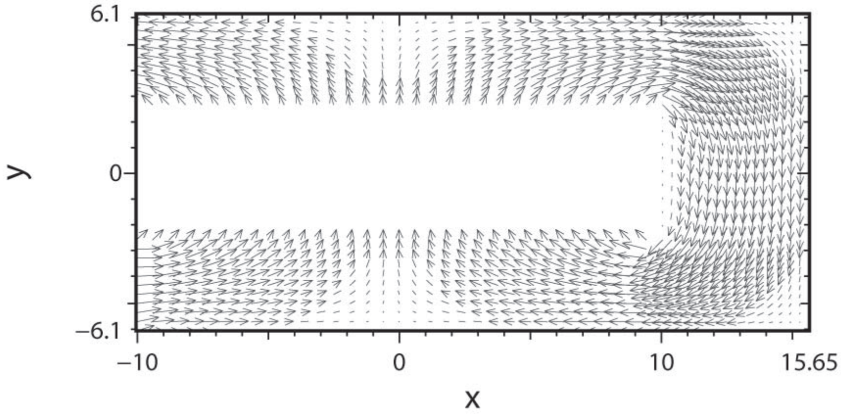

Fig. 2.11. Velocity field corresponding to $\mathrm{Kn} \simeq 0.29$.

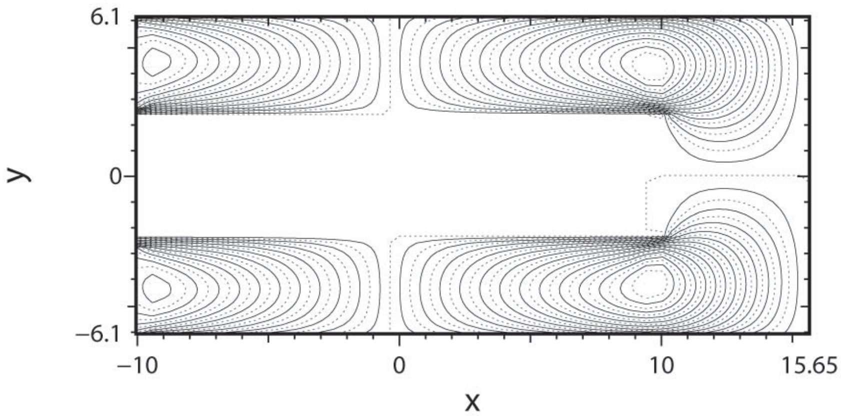

Fig. 2.12. x-component of the bulk velocity field, v_x, at $\mathrm{Kn} \simeq 0.29$.

$$P_{yy}(x,y) = \frac{\rho_0}{2} + \frac{\rho_0}{\pi} \int_{-\infty}^{+\infty} \int_{-\infty}^{+\infty} dc_x dc_y c_y^2 e^{-(c_x^2+c_y^2)} \mathcal{G}(x,y,c_x,c_y) \quad (2.73)$$

$$P_{yx}(x,y) = \frac{\rho_0}{\pi} \int_{-\infty}^{+\infty} \int_{-\infty}^{+\infty} dc_x dc_y c_x c_y e^{-(c_x^2+c_y^2)} \mathcal{G}(x,y,c_x,c_y). \quad (2.74)$$

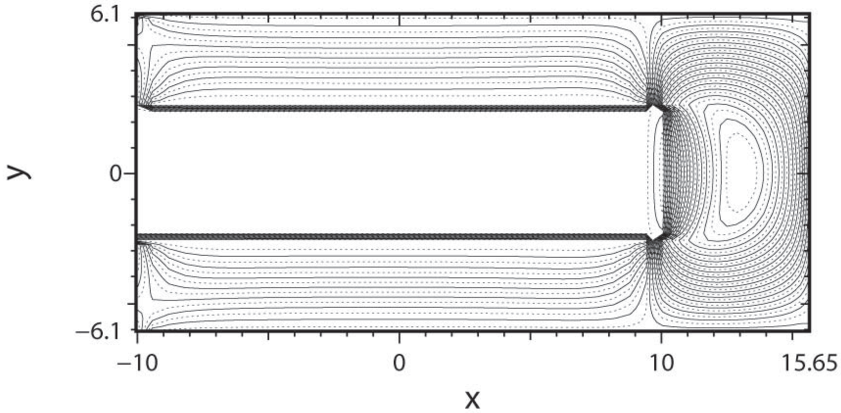

Fig. 2.13. y-component of the bulk velocity field, v_y, at $\mathrm{Kn} \simeq 0.29$.

Figure 2.14 shows a comparison between our numerical findings and the experimental data collected on a silicon biaxial accelerometer produced by STMicroelectronics,[17] where quantitatively correct outcomes can be achieved by analyzing and scaling the results obtained on a single unit like the one depicted in Fig. 2.10.

Our numerical outputs, obtained assuming two different values for the accommodation coefficient of the bounding walls, $\alpha = 1$ (circles) and $\alpha = 0.9$ (crosses), which is the current value assigned to the accommodation coefficient of silicon surfaces, compare very well with experiments in the transitional flow regime as well as in the near-free molecular flow limit.

2.10. Kinetic Theory Extension to Dense Fluids

Nanofluidics is a relatively young and interdisciplinary science whose aim is the study of fluid flows around or within nanosized structures.[18,19] The growing number of applications requires the development of theoretical tools capable of providing a general description of fluids (liquids and gases) at length scales comparable with molecular sizes. Such a description cannot be based only on hydrodynamic equations (HE), since several studies[20] have shown that HE do not always give a correct description of fluid flows in nano-channels. The reasons for HE failure can be found in the strongly non-local structure of some fundamental fluid properties (stress tensor, heat flux vector) which appears at the nanoscale and cannot be

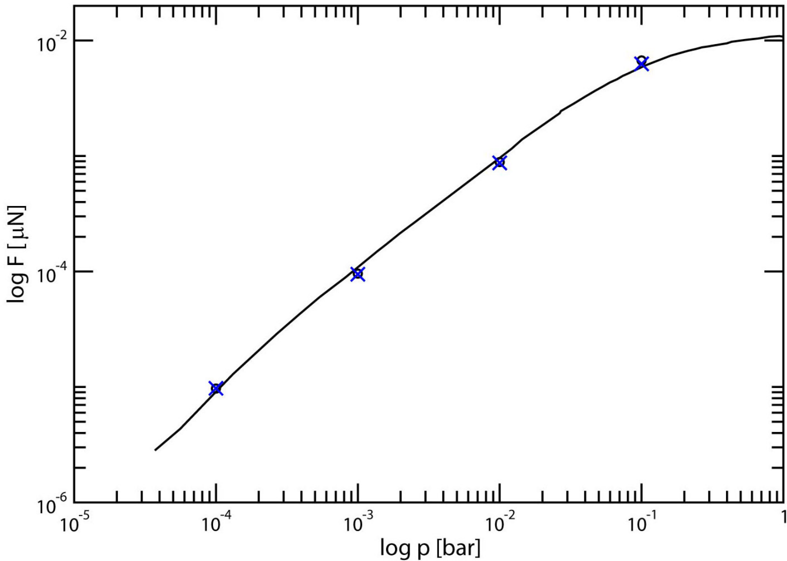

Fig. 2.14. Damping forces F (expressed in micro-Newton) exerted by the gas on the rotor versus the pressure p (expressed in bar). Comparison between the experimental data collected by STMicroelectronics (solid line) and our numerical findings for two values of the accommodation coefficient: $\alpha = 1$ (circles), $\alpha = 0.9$ (crosses).

easily approximated by local expressions.[21] In many situations, the largest deviations from hydrodynamic behavior are observed in the vicinity of solid boundaries, whereas the fluid bulk can often be accurately described by HE. Therefore, it is tempting to try extending the validity of HE by developing slip boundary conditions, following the methods of kinetic theory of dilute gases.[4] However, the task appears considerably more complex in the case of dense gases or liquids[22] and slip coefficients have been often obtained from molecular dynamics (MD) simulations.[23] Although MD techniques provide an extremely powerful tool in nanofluidics studies, it is clear that an intermediate level of fluid description is necessary to bridge the gap between pure MD numerical experiments and hydrodynamics. Kinetic theory of dense fluids[24] provides a number of theoretical methods of various sophistication and complexity which may be applied to obtain a generalized hydrodynamic approach[22] in the form of slip boundary conditions or non-local constitutive relationships.[25] The kinetic approach can also be convenient from the numerical point of view, since kinetic equations can be efficiently solved by particle schemes which are computationally less demanding that MD.[26] The formulation of kinetic equations for dense fluids in which the molecular mean

free path is of the order of the molecular size, is still an open problem, the main difficulty being the correct modeling of molecular correlations necessary to obtain the closure relationships to truncate the BBGKY hierarchy.[24] The phenomenological theory proposed by Enskog[27] to describe a dense hard sphere fluid has been later improved,[28,29] however the generalization has been obtained at the expense of tractability of the resulting equation. In this short note we describe a simple extension of Enskog kinetic equation which describes a fluid whose molecules interact through Sutherland's potential which combines hard sphere interaction with a soft attractive potential tail. As shown in Refs. 30 and 31, the adoption of simplifying assumptions on pair correlations leads to a closed kinetic equation for the one-particle distribution function. The resulting equation is often referred to as Enskog-Vlasov (EV) equation since it differs from the original Enskog equation because of an additional term which describes a self-consistent force field generated by the attractive potential tail. Kinetic equations of the EV type have been applied in several studies of equilibrium and non-equilibrium structure of non-uniform dense fluids.[32–34] In most of available studies, EV equation is used to obtain non-uniform equilibrium density profiles and/or hydrodynamic equations. However, Enskog-like kinetic equations can be solved numerically by particle schemes[26,33] without introducing additional assumptions beside those intrinsic in the equation itself. Next sections describe and discuss the results of the application of EV equation to flows in nanochannels of simple geometry. Furthermore, it is shown that the kinetic model can be extended to incorporate the interaction of the fluid with solid walls within the same formalism.

2.10.1. *The Mathematical Model*

Following Refs. 30 and 31, we consider a fluid composed by spherical and identical molecules of mass m_1, interacting by Sutherland potential

$$\phi^{(11)}(\rho) = \begin{cases} +\infty & \rho < \sigma_1 \\ -\overline{\phi}^{(11)} \left(\frac{\rho}{\sigma_1}\right)^{-\gamma^{(11)}} & \rho \geq \sigma_1 \end{cases}, \tag{2.75}$$

which results from the superposition of a hard sphere potential and a soft potential tail depending on the distance ρ between the centers of two interacting molecules. The hard sphere diameter is σ_1, whereas $\overline{\phi}^{(11)}$ and $\gamma^{(11)}$ are two positive constants which are related to the value of the right limit of $\phi^{(11)}(\rho)$ at $\rho = \sigma_1$ and to the range of the soft interaction, respectively. It is possible to obtain the following

exact kinetic equation for the one-particle distribution function

$$\frac{\partial f_1}{\partial t} + \boldsymbol{\xi} \circ \nabla_{\boldsymbol{x}} f_1 = -\nabla_{\boldsymbol{\xi}} \circ \left[\int_{\rho > \sigma_1} \hat{\boldsymbol{k}} \frac{d\phi^{(11)}}{d\rho} f_2(\boldsymbol{x}, \boldsymbol{\xi}, \boldsymbol{x}_1, \boldsymbol{\xi}_1 | t)\, d\boldsymbol{x}_1\, d\boldsymbol{\xi}_1 \right] + \sigma_1^2 \int \left[f_2(\boldsymbol{x}, \boldsymbol{\xi}^*, \boldsymbol{x} + \sigma \hat{\boldsymbol{k}}, \boldsymbol{\xi}_1^* | t) - f_2(\boldsymbol{x}, \boldsymbol{\xi}, \boldsymbol{x} - \sigma \hat{\boldsymbol{k}}, \boldsymbol{\xi}_1 | t) \right] (\boldsymbol{\xi}_r \circ \hat{\boldsymbol{k}})^+ \, d\boldsymbol{\xi}_1\, d^2\hat{\boldsymbol{k}}. \tag{2.76}$$

In Eq. (2.76) $f_1(\boldsymbol{x}, \boldsymbol{\xi}|t)$ denotes the one-particle distribution function of molecular velocity $\boldsymbol{\xi}$ at spatial location $\boldsymbol{x}$ at time t, whereas $f_2(\boldsymbol{x}, \boldsymbol{\xi}, \boldsymbol{x}_1, \boldsymbol{\xi}_1|t)$ is the pair distribution function. The first integral at $r.h.s$ of Eq. (2.76) represents the soft tail contribution to the rate of change of f_1, being $\rho = \|\boldsymbol{x}_1 - \boldsymbol{x}\|$ and $\hat{\boldsymbol{k}}$ the unit vector $\boldsymbol{x} - \boldsymbol{x}_1/\rho$. The contribution of hard collisions is given by the second integral where $\boldsymbol{\xi}^*$ and $\boldsymbol{\xi}_1^*$ are the post-collisional velocity vectors of two colliding molecules, $\boldsymbol{\xi}_r$ is the relative velocity $\boldsymbol{\xi}_1 - \boldsymbol{\xi}$. The integral over $\hat{\boldsymbol{k}}$ is limited to the hemisphere where the condition $\boldsymbol{\xi}_r \circ \hat{\boldsymbol{k}} > 0$ holds.

Equation (2.76) is exact but of little use, since it also involves the pair distribution function $f_2(\boldsymbol{x}, \boldsymbol{\xi}, \boldsymbol{x}_1, \boldsymbol{\xi}_1|t)$. A closed equation for the one-particle distribution function is obtained by the following two approximations:

(a) In the hard sphere collision integral in Eq. (2.76), it is assumed that

$$f_2(\boldsymbol{x}, \boldsymbol{\xi}, \boldsymbol{x} - \sigma_1\hat{\boldsymbol{k}}, \boldsymbol{\xi}_1|t) = \chi^{(11)}(\boldsymbol{x}, \boldsymbol{x} - \sigma_1\hat{\boldsymbol{k}}|\,\{n\}) f_1(\boldsymbol{x}, \boldsymbol{\xi}|t)\, f_1(\boldsymbol{x} - \sigma_1\hat{\boldsymbol{k}}, \boldsymbol{\xi}_1|t) \tag{2.77}$$

being $\chi^{(11)}(\boldsymbol{x}, \boldsymbol{x} - \sigma_1\hat{\boldsymbol{k}}|\,\{n\})$ the contact value of the pair correlation function in a hard sphere fluid.

(b) Pair correlations are completely neglected in the soft potential contribution in Eq. (2.76). Accordingly, it is assumed that

$$f_2(\boldsymbol{x}, \boldsymbol{\xi}, \boldsymbol{x}_1, \boldsymbol{\xi}_1|t) = f_1(\boldsymbol{x}, \boldsymbol{\xi}|t) f_1(\boldsymbol{x}_1, \boldsymbol{\xi}_1|t) \tag{2.78}$$

Taking into account Eqs. (2.77) and (2.78) and dropping the subscript, Eq. (2.76) takes the form

$$\frac{\partial f}{\partial t} + \boldsymbol{\xi} \circ \nabla_{\boldsymbol{x}} f + \frac{\boldsymbol{F}^{(11)}(\boldsymbol{x}|t)}{m} \circ \nabla_{\boldsymbol{\xi}} f = C^{(11)}(f, f) \tag{2.79}$$

$$\boldsymbol{F}^{(11)}(\boldsymbol{x}|t) = \int_{\|\boldsymbol{x}_1 - \boldsymbol{x}\| > \sigma_1} \frac{d\phi^{(11)}}{d\rho} \frac{\boldsymbol{x}_1 - \boldsymbol{x}}{\|\boldsymbol{x}_1 - \boldsymbol{x}\|} n(\boldsymbol{x}_1|t)\, d\boldsymbol{x}_1 \tag{2.80}$$

$$C^{(11)}(f,f) = \sigma_1^2 \int \Big\{ \chi^{(11)}(\boldsymbol{x}, \boldsymbol{x} + \sigma_1 \hat{\boldsymbol{k}} | \{n\}) f(\boldsymbol{x} + \sigma_1 \hat{\boldsymbol{k}}, \boldsymbol{\xi}_1^* | t) f(\boldsymbol{x}, \boldsymbol{\xi}^* | t) - \\ \chi^{(11)}(\boldsymbol{x}, \boldsymbol{x} - \sigma_1 \hat{\boldsymbol{k}} | \{n\}) f(\boldsymbol{x} - \sigma \hat{\boldsymbol{k}}, \boldsymbol{\xi}_1 | t) f(\boldsymbol{x}, \boldsymbol{\xi} | t) \Big\} (\boldsymbol{\xi}_r \circ \hat{\boldsymbol{k}})^+ d\boldsymbol{\xi}_1 d^2 \hat{\boldsymbol{k}}. \tag{2.81}$$

Equation (2.79), also named Enskog-Vlasov kinetic equation, describes a hard sphere fluid under the action of the self-consistent force field (see Eq. (2.80)) generated by the soft attractive tail. In the Standard Enskog Theory (SET) $\chi^{11}(\boldsymbol{x}, \boldsymbol{x} - \sigma_1 \hat{\boldsymbol{k}} | \{n\})$ is approximated by using the value of the pair correlation function in a fluid in *uniform equilibrium* with density $n(\frac{\boldsymbol{x}+\boldsymbol{x}_1}{2}|t)$. An approximate, but accurate expression for $\chi_{SET}(n)$ can be obtained from the equation of state of the hard sphere fluid proposed by Carnahan and Starling,[35] as

$$\chi_{SET}(n) = \frac{1}{nb}\left(\frac{p^{hs}}{n\kappa T} - 1\right) = \frac{1}{2}\frac{2-\eta}{(1-\eta)^3}, \qquad b = \frac{2\pi\sigma_1^3}{3}, \qquad \eta = \frac{\pi\sigma_1^3 n}{6} \tag{2.82}$$

SET theoretical properties have been considerably improved in Revised Enskog Theory (RET)[28] where $\chi^{(11)}$ is the contact value of the pair correlation function in a fluid in *non-uniform equilibrium*. The use of RET formulation is more difficult since $\chi^{(11)}(\boldsymbol{x}, \boldsymbol{x} - \sigma_1 \hat{\boldsymbol{k}} | \{n\})$ is a functional of the density field $n(\boldsymbol{x}|t)$. Although an expression for $\chi(\boldsymbol{x}, \boldsymbol{x} - \sigma \hat{\boldsymbol{k}} | \{n\})$ can be obtained as a formal cluster expansion in the density, in practical applications simpler approximations are recommended. Following Ref. 36, in the present work the pair correlation function at contact has been computed as

$$\chi^{(11)}(\boldsymbol{x}, \boldsymbol{x} - \sigma_1 \hat{\boldsymbol{k}} | \{n\}) = \chi_{SET}[\overline{n}(\boldsymbol{x} - \sigma \frac{\hat{\boldsymbol{k}}}{2})] \tag{2.83}$$

$$\overline{n}(\boldsymbol{x}|t) = \frac{3}{4\pi\sigma_1^3} \int n(\boldsymbol{x}_1|t) w(\boldsymbol{x}, \boldsymbol{x}_1)\, d\boldsymbol{x}_1 \tag{2.84}$$

$$w(\boldsymbol{x}, \boldsymbol{x}_1) = \begin{cases} 1 & \|\boldsymbol{x}_1 - \boldsymbol{x}\| < \sigma_1 \\ 0 & \|\boldsymbol{x}_1 - \boldsymbol{x}\| > \sigma_1 \end{cases}. \tag{2.85}$$

According to the three expressions above, a functional form for $\chi^{(11)}$ is obtained from the simpler χ_{SET} by replacing the actual value of the density at the contact point of two colliding spheres with the value of the density field *averaged* over a spherical volume of radius σ_1. Similar approximations are used in density functional theories of non-uniform fluids and considerably improve the results of SET.

2.10.2. *Fluid-Wall Interaction and Boundary Conditions*

When dealing with problems in which the fluid interacts with solid walls, it is necessary to formulate appropriate boundary conditions for Eq. (2.79). The simplest approach to fluid-wall interaction modeling is obtained by replacing the wall with a smooth and impenetrable surface which acts on $f(\boldsymbol{x}, \boldsymbol{\xi}|t)$ through the scattering kernel described in Sec. 2.5. Although the adoption of boundary conditions in the form given by Eq. (2.39) is possible in modeling dense fluid flows, it is worth stressing that their simplest time independent formulation is based on the assumption that the time scale of fluid-wall interaction is much shorter than the time scale of fluid-fluid interaction. Such an assumption is certainly justified in dilute gas dynamics, but it represents an oversimplification in studying dense fluids flows which require a more detailed modeling of fluid-wall interaction.[23] As a compromise between the completely phenomenological approach outlined above and a more realistic (but computationally expensive) approach based on MD simulations,[23] a kinetic model of fluid wall interaction can be formulated. For simplicity, we consider the one-dimensional flow of a liquid in a channel bounded by two infinite planar parallel walls. The walls separation is denoted by $2L_z$ and the motion of the fluid is observed in a Cartesian reference frame whose x and y axis are parallel to the walls, whereas the coordinate z spans the gap between the walls. The origin O of the reference frame is located at distance L_z from the walls.

It is assumed that the walls are composed by spherical molecules having a diameter σ_2, mass m_2 and number density $n_2(z)$ given by the following expression:

$$n_2(z) = \begin{cases} n_w & |z| > L_z \\ 0 & |z| \leq L_z \end{cases} \tag{2.86}$$

n_w being the constant value of the wall density. Although no explicit assumption is made about the interaction among wall molecules, it is assumed that each wall is in a state of equilibrium described by the velocity distribution functions

$$f_w(z, \boldsymbol{\xi}) = \begin{cases} \frac{n_w}{(2\pi R_2 T_L)} \exp\left[-\frac{(\boldsymbol{\xi}-\boldsymbol{u}_L)^2}{2R_2 T_L}\right] & z \leq -L_z \\ \frac{n_w}{(2\pi R_2 T_R)} \exp\left[-\frac{(\boldsymbol{\xi}+\boldsymbol{u}_R)^2}{2R_2 T_R}\right] & z \geq L_z \end{cases} . \tag{2.87}$$

In the above expressions, T_L and T_R denote the temperature of the left and right wall, respectively. The walls are allowed to have velocities $\boldsymbol{u}_L$ and $\boldsymbol{u}_R$, parallel to the wall themselves. Accordingly, it is assumed that $\boldsymbol{u}_L = -\boldsymbol{u}_R = U_w \hat{\boldsymbol{x}}$, being $\hat{\boldsymbol{x}}$ a unit vector parallel to the x axis. The gas constant R_2 is defined as k_B/m_2, where k_B is the Boltzmann constant.

In complete analogy with the treatment of fluid molecules interaction, it is assumed that wall molecules interact with fluid molecules through the following

Sutherland potential

$$\phi_{12}(\rho) = \begin{cases} +\infty & \rho < \sigma_{12} \\ -\overline{\phi}^{(12)} \left(\frac{\rho}{\sigma_{12}}\right)^{-\gamma^{(12)}} & \rho \geq \sigma_{12} \end{cases} \tag{2.88}$$

where the hard sphere radius is now defined as $\sigma_{12} = (\sigma_1 + \sigma_2)/2$. The microscopic description of the fluid motion can be strongly simplified if one assumes that the superposition of long range tails of the interaction potential $\phi^{(12)}(\rho)$ only produces an average steady force field. Fluctuations due to the random motion of wall and fluid molecules are taken into account only in the short range hard sphere potential, as described below. It can be easily shown that the force field $F_z^{(12)}(z)$ generated by the soft tails of wall molecules is given by the following expression:

$$F_z^{(12)}(z) = 2\pi\overline{\phi}^{(12)} \left[\sigma_{12}^{\gamma^{(12)}} \int_{|z-z'|>\sigma_{12}} \frac{(z'-z)n_2(z')}{|z-z'|^{\gamma^{(12)}}}\, dz' + \int_{|z-z'|\leq\sigma_{12}} (z'-z)n_2(z')\, dz' \right]. \tag{2.89}$$

The short range interaction of fluid and wall molecules can be described by a term having the same structure of the collision integral $C^{(11)}(f, f)$:

$$C^{(12)}(f_w, f) = \sigma_{12}^2 \int \Big\{ \chi^{(12)}(z, z+\sigma_{12}k_z|\{n_2\}) f_w(z+\sigma_{12}k_z, \boldsymbol{\xi}_1^*) f(z, \boldsymbol{\xi}^*|t) - \chi^{(12)}(z, z-\sigma_{12}k_z|\{n_2\}) f_w(z-\sigma_{12}k_z, \boldsymbol{\xi}_1|t) f(z, \boldsymbol{\xi}|t) \Big\} \cdot (\boldsymbol{\xi}_r \circ \hat{\boldsymbol{k}})^+ d\boldsymbol{\xi}_1 d^2\hat{\boldsymbol{k}} \tag{2.90}$$

The collision term in Eq. (2.90) is a linear functional of f since f_w is given and it is not modified by collisions. The pair correlation function $\chi^{(12)}$ can be approximated by the expression given in Eq. (2.82) in which n is set equal to the wall number density n_w.

The final form of the kinetic equation for f is obtained by adding the field $F_z^{(12)}(z)$ and the fluid-wall collision term to Eq. (2.79)

$$\frac{\partial f}{\partial t} + \xi_z \frac{\partial f}{\partial z} + \frac{F_z(z|t)}{m_1} \frac{\partial f}{\partial \xi_z} = C^{(11)}(f, f) + C^{(12)}(f_w, f) \tag{2.91}$$

$$F_z(z|t) = F_z^{(12)}(z) + F_z^{(11)}(z|t) \tag{2.92}$$

$$F_z^{(11)}(z|t) = 2\pi\overline{\phi}^{(11)} \left[\sigma_1^{\gamma^{(11)}} \int_{|z-z'|>\sigma_1} \frac{(z'-z)n_1(z'|t)}{|z-z'|^{\gamma^{(11)}}}\, dz' + \int_{|z-z'|\leq\sigma_1} (z'-z)n_1(z'|t)\, dz' \right]. \tag{2.93}$$

2.11. Numerical Results

Kinetic equations in the form described above can be efficiently solved numerically by the particles schemes described in Refs. 26 and 33. The numerical method has been applied to study a simple Couette flow as a model problem and obtain the dependence of its properties from the relevant flow parameters. In a first series of computations, the soft tail of the interaction potential $\phi^{(11)}$ has been suppressed and Maxwell model has been adopted to describe fluid-wall interactions. A number of solutions have been obtained varying the wall separation $2L_z$ and the averaged fluid density $n_0 = \frac{1}{2L_z}\int_{-L_z}^{L_z} n(z)\,dz$. The nominal shear rate $\beta = U_w/L_z$ has been fixed to a small value to obtain an almost isothermal flow. A parallel series of MD simulations have also been performed to obtain the "exact" behavior of a dense hard sphere fluid and assess the accuracy of kinetic theory predictions in the simplest situation. The same boundary conditions given in Eq. (2.39) have been used in MD simulations in which the motion of 10^4 hard spheres has been computed from the exact collision dynamics. Figure 2.15 shows normalized density profiles in a hard sphere liquid for two different values of the average reduced density $\eta_0 = \pi\sigma_1^3 n_0/6$. The channel width is $11\sigma_1$, but the region accessible to the centers of the spherical molecules is only $10\sigma_1$ wide along z.

It is interesting to observe that density is not constant since collisions push molecules toward the walls. Density oscillations indicate partial ordering of molecular layers which becomes more evident for higher values of n_0. The comparison of EV results with companion MD simulations shows that in the density range considered here, the agreement is rather good. Velocity profiles are shown in Fig. 2.16. In spite of the strong density variations in the vicinity of the walls, velocity profiles exhibit a more regular shape and show little deviation from an overall linear behavior which would be found in a hydrodynamic treatment of the problem. However, the average slope of $u_x(z)$ profiles is different from the nominal slope β since the fluid velocity at locations $\pm(L_z - \sigma_1/2)$ is not equal to the velocity of the walls.

The deviation from hydrodynamic behavior of Couette flow in nanosized channels is best appreciated by considering the behavior of the P_{xz} component of the stress tensor which, both in the hydrodynamic and kinetic treatment, is constant across the channel and depends only on external flow parameters. Figure 2.17 shows the numerical value of P_{xz} obtained by solving EV equation for different Couette flows in which the nominal shear rate β and average density n_0 were kept fixed while varying the channel width $2L_z$. The results obtained from kinetic theory have been compared with the values of P_{xz} obtained from the viscosity of a dense hard sphere gas $\mu(n_0, T_w)$ (see Ref. 24) using both the nominal

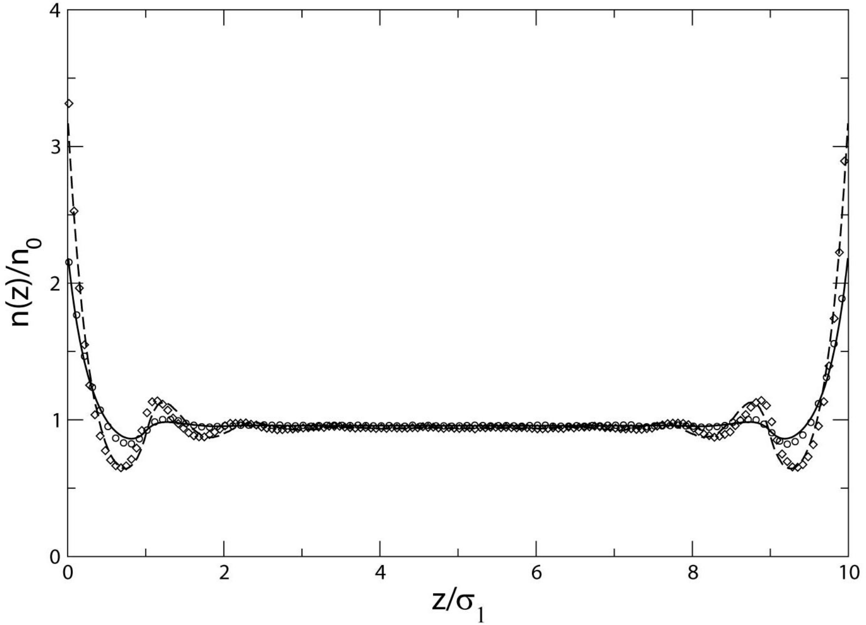

Fig. 2.15. Density profiles in the Couette flow of a dense hard sphere gas between rigid walls with full accommodation [$\alpha = 1$, in Eq. (2.39)]. Solid line: EV density profile $\eta_0 = 0.2$, $\beta = Uw/L_z = 0.0597$; dashed line: EV density profile $\eta_0 = 0.3$, $\beta = Uw/L_z = 0.1262$; circles: MD density profile $\eta_0 = 0.2$, $\beta = Uw/L_z = 0.0597$; diamonds: MD density profile $\eta_0 = 0.3$, $\beta = Uw/L_z = 0.1262$.

shear rate β and an effective value of the shear rate, $\overline{\beta}$. The latter has been obtained by fitting the EV velocity profile with a straight line, hence it takes into account velocity slip at the walls.

The results clearly show that hydrodynamic predictions based on nominal shear rate are not accurate, on the other hand including slip effects through the effective shear rate considerably reduces the distance between kinetic theory and hydrodynamic values of P_{xz}.

A more realistic description of fluid-wall interaction can be obtained by replacing the rigid wall, which scatters molecules according to Eq. (2.39), with the kinetic model which includes the collision term $C^{(12)}(f_w, f)$. Although a complete account of the model properties cannot be given here, it is worth mentioning that numerical experiments show that the scattering patterns of molecules from a "solid" surface described by Eq. (2.90) compare well with experimental data[4] which exhibit a rather marked deviation from Maxwell's model. Moreover, the

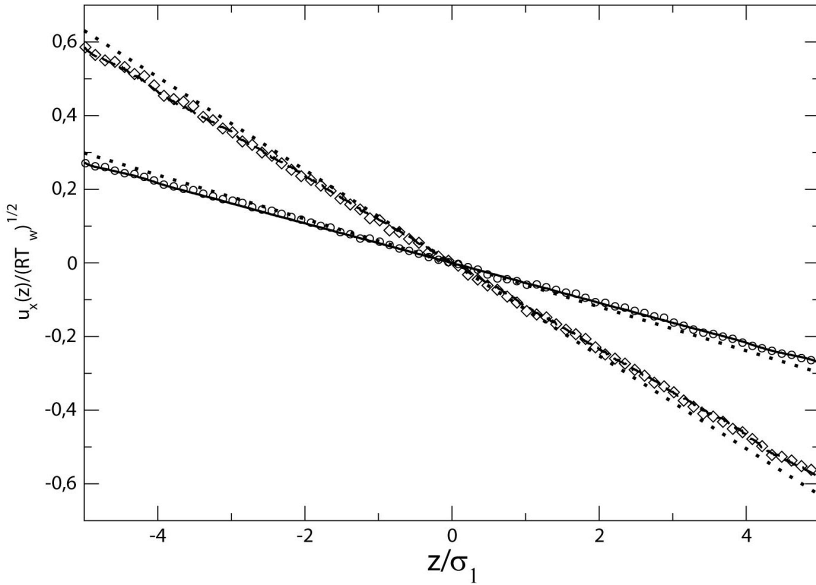

Fig. 2.16. Velocity profiles in the Couette flow of a dense hard sphere gas between rigid walls with full accommodation [$\alpha = 1$, in Eq. (2.39)]. Solid line: EV velocity profile $\eta_0 = 0.2$, $\beta = Uw/L_z = 0.0597$; dashed line: EV velocity profile $\eta_0 = 0.3$, $\beta = Uw/L_z = 0.1262$; circles: MD velocity profile $\eta_0 = 0.2$, $\beta = Uw/L_z = 0.0597$; diamonds: MD velocity profile $\eta_0 = 0.3$, $\beta = Uw/L_z = 0.1262$; dotted lines: hydrodynamic prediction with nominal shear rate.

model predicts different accommodation coefficients for energy and momentum as well as the correct behavior of the energy accommodation coefficient when the mass ratio m_2/m_1 is changed. Figure 2.18 shows the results of a Couette flow simulation in a hard sphere liquid ($\phi^{(11)} = 0$) having an average reduced density η_0 equal to 0.3 and flowing between two walls described by Eq. (2.90). The wall separation is $12\sigma_1$, the wall velocities are $\pm 0.2\sqrt{RT_w}$ and the mass ratio m_2/m_1 is set equal to 4.875. The finite extent of fluid-wall interaction causes the fluid to "feel" walls when molecule centers are at distance σ_{12} from the nominal wall "surface". However, the walls are no longer impenetrable and the liquid confinement observed in Fig. 2.18(a) is a result of the collisions with wall molecules. An adsorbed layer of liquid molecules can be clearly observed in the regions where the density falls rapidly to zero in the vicinity of the walls and the velocity profile suffers an abrupt deviation from the almost linear behavior shown in liquid bulk. The velocity slip effect is stronger than in the simulations described above, indicating that the effective tangential momentum accommodation coefficient is not unity.

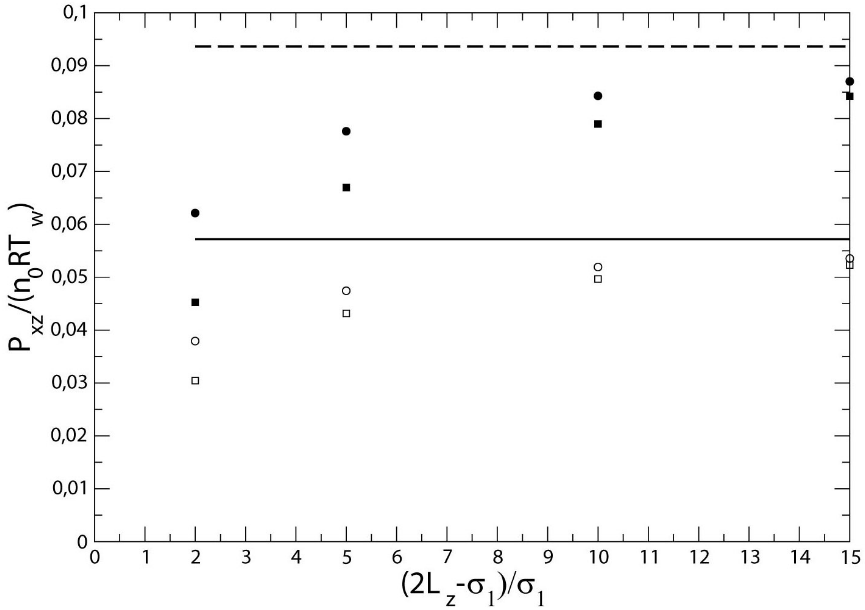

Fig. 2.17. P_{xz} versus channel width in the Couette flow of a dense hard sphere gas between rigid walls with full accommodation [$\alpha = 1$, in Eq. (2.39)]. Squares: EV prediction, $\eta_0 = 0.2$, $\beta = 0.0597$; circles: hydrodynamics predictions with effective shear rate $\overline{\beta}$, $\eta_0 = 0.2$, $\beta = 0.0597$; solid line: hydrodynamics predictions with nominal shear rate β, $\eta_0 = 0.2$, $\beta = 0.0597$; filled squares: EV prediction, $\eta_0 = 0.25$, $\beta = 0.088$; filled circles: hydrodynamics predictions with effective shear rate $\overline{\beta}$, $\eta_0 = 0.25$, $\beta = 0.088$; dashed line: hydrodynamics predictions with nominal shear rate β, $\eta_0 = 0.25$, $\beta = 0.088$.

Acknowledgment

The research described in the paper was supported by MIUR of Italy.

References

1. O. Reynolds, On the theory of lubrication and its application to Mr. Beauchamp Tower's experiments including an experimental determination of the viscosity of the olive oil, *Philos. Trans. R. Soc. London*. **A177**, 157–234, (1886).
2. C. Cercignani, *Mathematical Methods in Kinetic Theory*. (Plenum Press, New York, 1969; 1990).
3. C. Cercignani, *Slow Rarefied Flows. Theory and Application to Micro-Electro-Mechanical Systems*. (Birkhäuser, Basel, 2006).
4. C. Cercignani, *Theory and Application of the Boltzmann equation*. (Springer Verlag, New York, 1988).

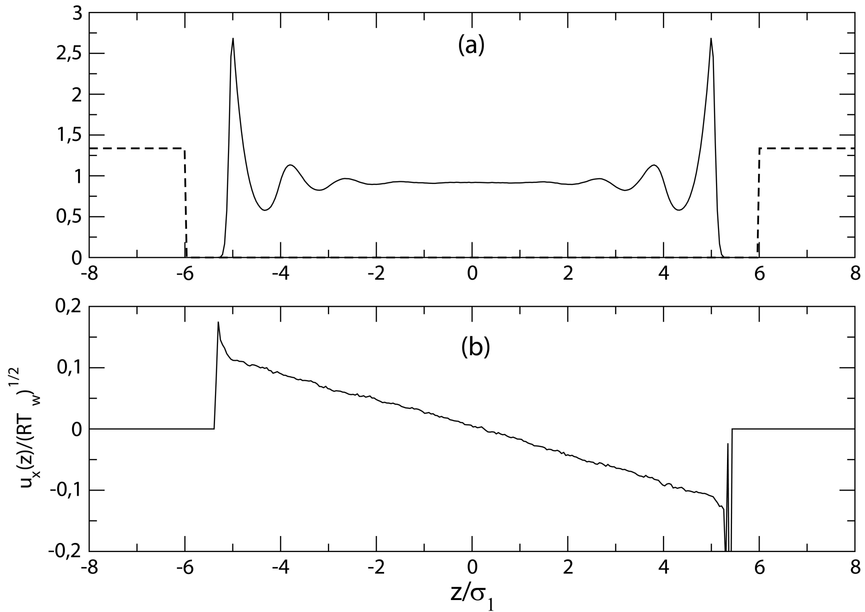

Fig. 2.18. Couette flow of a dense hard sphere fluid with fluid-wall interaction described by Eq. (2.91). $\overline{\phi}^{(11)} = \overline{\phi}^{(12)} = 0$, $\sigma_1 = \sigma_2$, $m_2/m_1 = 4.875$, $U_w = 0.2\sqrt{RT_w}$, $\eta_0 = 0.3$. Graph (a) Solid line: liquid density $n(z)/n_0$; dashed line: $n_2(z)\sigma_2^3$. Graph (b) normalized velocity profile $u_x(z)/\sqrt{RT_w}$.

5. S. Ukai, On the existence of global solutions of mixed problems for the nonlinear Boltzmann equation, *Proc. Japan Acad. Ser. A Math. Sci.* **50**, 179–184, (1974).
6. C. Cercignani and A. Daneri, Flow of a rarefied gas between two parallel plates, *Journal of Applied Physics*. **34**, 3509–3513, (1963).
7. S. Fukui and R. Kaneko, Analysis of ultra-thin gas film lubrication based on linearized Boltzmann equation, *Journal of Tribology*. **110**, 253–262, (1988).
8. S. Fukui and R. Kaneko, Analysis of ultra-thin gas film lubrication based on the linearized Boltzmann equation, *JSME International Journal*. **30**, 1660–1666, (1987).
9. J. Fan and C. Shen. Statistical simulation of low-speed unidirectional flows in transitional regime. In eds. R. Brun, R. Campargue, R. Gatignol, and J. Lengrand, *Rarefied Gas Dynamics*, vol. 2, pp. 245–252. Cepadues Editions, (1999).
10. C. Shen, J. Fan, and C. Xie, Statistical simulation of rarefied gas flows in microchannels, *J. Comp. Physics*. **189**, 512–526, (2003).
11. C. Shen, Use of the degenerated Reynolds equation in solving the microchannel flow problem, *Phys. Fluids*. **17**, 046101–6, (2005).
12. C. Cercignani, M. Lampis, and S. Lorenzani, Variational approach to gas flows in microchannels, *Phys. Fluids*. **16**, 3426–3437, (2004).

13. C. Cercignani, M. Lampis, and S. Lorenzani. Flow of a rarefied gas between parallel and almost parallel plates. In ed. M. Capitelli, *Rarefied Gas Dynamics*, vol. 762, *AIP Conf. Proc.*, pp. 719–724, New York, (2005). AIP.
14. C. Cercignani, M. Lampis, and S. Lorenzani, Plane Poiseuille-Couette problem in micro-electro-mechanical systems applications with gas-rarefaction effects, *Phys. Fluids*. **18**, 087102–14, (2006).
15. F. Alexander, A. Garcia, and B. Alder, Direct simulation Monte Carlo for thin film bearings, *Phys. Fluids*. **6**, 3854–3860, (1994).
16. J. Jiang, C. Shen, and J. Fan. Statistical simulation of thin-film bearings. In ed. M. Capitelli, *Rarefied Gas Dynamics*, vol. 762, *AIP Conf. Proc.*, pp. 180–185, New York, (2005). AIP.
17. A. Frangi, A. Frezzotti, and S. Lorenzani, On the application of the bgk kinetic model to the analysis 3 of gas-structure interactions in mems, *Comp. and Structures*. p. doi:10.1016/j.compstruc.2007.01.011, (2007).
18. G. E. Karniadakis, N. Aluru, and A. Beskok, *Microflows and nanoflows: fundamentals and simulation*. (Springer, New York, 2005).
19. J. G. T. Eijkel and A. van den Berg, Nanofluidics: what is it and what can we expect from it?, *Microfluid Nanofluid*. **1**, 249–267, (2005).
20. K. P. Travis, B. D. Todd, and D. J. Evans, Departure from Navier-Stokes hydrodynamics in confined liquids, *Phys. Rev. E*. **55**, 4288–4295, (1996).
21. J. Zhang, B. D. Todd, and K. P. Travis, Viscosity of confined inhomogeneous nonequilibrium fluids, *J. Chem. Phys.* **121**, 10778–10786, (2004).
22. L. A. Pozhar and K. E. Gubbins, Transport theory of dense, strongly inhomogeneous fluids, *J. Chem. Phys.* **99**, 8970–8996, (1993).
23. M. Cieplak, J. Koplik, and J. R. Banavar, Boundary conditions at a fluid-solid interface, *Physical Review Letters*. **86**, 803–806, (2001).
24. P. Resibois and M. DeLeener, *Classical kinetic theory of fluids*. (J. Wiley & Sons, New York, 1977).
25. D. J. Evans and G. P. Morriss, *Statistical Mechanics of Nonequilibrium Liquids*. (Academic Press, London, 1990).
26. A. Frezzotti, A particle scheme for the numerical solution of the Enskog equation, *Phys. Fluids*. **9**, 1329–1335, (1997).
27. D. Enskog, Kinetische Theorie der Wärmeleitung, Reibung und Selbstdiffusion in gewissen verdichteten Gasen und Flüssigkeiten, *Kungl. Svenska Vet.-Ak. Handl.* **63**, n. 4, (1921).
28. H. van Beijeren and M. H. Ernst, The modified Enskog equation, *Physica*. **68**, 437–456, (1973).
29. L. A. Pozhar and K. E. Gubbins, Dense inhomogeneous fluids: Functional perturbation theory, the generalized Langevin equation, and kinetic theory, *J.Chem. Phys.* **94**, 1367–1384, (1991).
30. M. Grmela, Kinetic equation approach to phase transitions, *J. Stat. Phys.* **3**, 347–364, (1971).
31. J. Karkheck and G. Stell, Kinetic mean-field theories, *J. Chem. Phys.* **75**, 1475–1487, (1981).
32. H. T. Davis, Kinetic theory of inhomogeneous fluid: Tracer diffusion, *J. Chem. Phys.* **86**, 1474–1477, (1986).

33. A. Frezzotti, L. Gibelli, and S. Lorenzani, Mean field kinetic theory description of evaporation of a fluid into vacuum, *Phys. Fluids*. **17**, 012102–12, (2005).
34. Z. Guo, T. S. Zhao, and Y. Shi, Generalized hydrodynamic model for fluid flows: From nanoscale to macroscale, *Phys. Fluids*. **18**, 067107–11, (2006).
35. N. Carnahan and K. Starling, Equation of state for nonactracting rigid spheres, *J. Chem. Phys*. **51**, 635–636, (1969).
36. J. Fischer and M. Methfessel, Born-Green-Yvon approach to the local densities of a fluid at interfaces, *Phys. Rev. A*. **22**, 2836–2843, (1980).

Chapter 3

Applying the Direct Simulation Monte Carlo (DSMC) Method to Gas-Filled MEMS Devices

M. A. Gallis

Engineering Sciences Center
Sandia National Laboratories
Albuquerque, NM 87185-0826 USA
*magalli@sandia.gov**

The Direct Simulation Monte Carlo (DSMC) method is presented as a tool to investigate gas force and heat transfer in microscale geometries. The principles, characteristics, and convergence behavior of DSMC are examined. The ability and accuracy of DSMC for near-equilibrium and strongly nonequilibrium conditions are demonstrated by comparison with analytical solutions of the Boltzmann equation from Chapman–Enskog theory and the Moment–Hierarchy method. Solutions in the noncontinuum hydrodynamic regime address the issue of continuum breakdown. Finally, real-world microsystem applications are presented where DSMC is used either to simulate the flow field directly or to provide more accurate boundary conditions for continuum solvers.

Contents

3.1 Introduction . . . 82
3.2 Basic Method . . . 84
  3.2.1 Statistical Error . . . 87
  3.2.2 Discretization Error . . . 88
  3.2.3 Number of Simulators per Cell . . . 88
  3.2.4 Cell Size . . . 88
  3.2.5 Time Step . . . 89
  3.2.6 Comprehensive Study of Discretization Error . . . 90
3.3 Comparison to Chapman–Enskog Theory . . . 91
  3.3.1 Theoretical Results . . . 91
  3.3.2 Fourier and Couette Flow . . . 93
  3.3.3 DSMC Results . . . 94
3.4 Comparison to Moment-Hierarchy Theory . . . 97

*Sandia is a multiprogram laboratory operated by Sandia Corporation, a Lockheed Martin Company, for the United States Department of Energy's National Nuclear Security Administration under contract DE-AC04-94AL85000.

3.4.1 Theoretical Results . . . 98
3.4.2 Simulation Results . . . 99
3.5 Simulations of Microscale Flows . . . 102
3.5.1 Heat Transfer at Arbitrary Knudsen Numbers . . . 102
3.5.2 Heat Transfer in a Microgap . . . 103
3.5.3 Thermal Actuation . . . 106
3.5.4 Heat Transfer from a Microbeam to the Substrate . . . 107
3.5.5 Gas Damping . . . 109
3.5.6 Gas Damping of a Cantilevered Microbeam . . . 111
3.5.7 Thermally Driven Flows . . . 112
3.6 Conclusions . . . 115
References . . . 116

3.1. Introduction

As Micro-Electro-Mechanical-System (MEMS) technology matures and advances towards further miniaturization and more sophisticated designs, the need for an accurate and reliable description of fluid mechanics and heat transfer at the microscale increases.[1–3]

It is well known that, in principle, the conservation equations of classical mechanics are valid for all flow regimes but do not form a closed set of equations: their closure depends on constitutive relations. The Navier–Stokes equations achieve closure by using Newton's and Fourier's laws[4] to relate shear stress, heat flux, and mass diffusion to velocity, temperature, and density gradients. Thus, their applicability is limited to the continuum hydrodynamic regime, where these constitutive relations are valid. The addition of velocity-slip and temperature-jump boundary conditions extends their applicability to cases where noncontinuum effects are limited to thin layers adjacent to solid boundaries. Typically, the velocity-slip and temperature-jump boundary conditions break down before the constitutive relationships become invalid.[2]

Many MEMS devices operate outside this continuum hydrodynamic regime.[1,2] Large gradients and large surface-to-volume ratios create significant departures from equilibrium even at ambient conditions. Departure from equilibrium can be achieved in two ways: through rarefaction effects (molecules colliding with solid boundaries more frequently than with each other) and through gradients in flow properties.

One way of describing the noncontinuum regime is to consider two types of Knudsen numbers: a *system* Knudsen number, defined as the ratio of the mean free path to a characteristic geometric length scale, and a *local* Knudsen number, defined as the ratio of the mean free path to a local hydrodynamic length scale determined from the heat flux or shear stress. If both types of Knudsen numbers are small, then the flow is both the system Knudsen number is not small, then

the flow is not hydrodynamic, with noncontinuum effects produced by molecule collisions with solid surfaces. On the other hand, if the system Knudsen number is small but the local Knudsen number is finite, then the flow is hydrodynamic, with noncontinuum effects produced by flow gradients.

The exact Knudsen number for which the continuum approach ceases to be reliable depends on the particular application and the desired accuracy. For a Knudsen number of 0.01, deviations become noticeable, while the error of the continuum approach becomes significant when the Knudsen number exceeds 0.1. In this case, the Navier–Stokes equations are superseded by the Boltzmann equation,[5] which is the fundamental mathematical model for gases at the molecular level.

The Boltzmann equation (see Chapter 2) describes the rate of change of the molecular velocity distribution function of a dilute gas under the assumption of molecular chaos:

$$\frac{\partial(nf)}{\partial t} + \mathbf{c} \cdot \frac{\partial(nf)}{\partial \mathbf{r}} + \mathbf{F} \cdot \frac{\partial(nf)}{\partial \mathbf{c}} = \int_{-\infty}^{\infty} \int_{0}^{4\pi} n^2 (f^* f_1^* - f f_1) c_r d\Omega d\mathbf{c}_1, \quad (3.1)$$

where t is time, $\mathbf{r}$ is the position in physical space, $\mathbf{c}$ is the molecular velocity, $\mathbf{F}$ is the external force per unit mass (here, independent of velocity), n is the number density, the distribution functions f and f^* are evaluated at the molecule's pre-collision and post-collision velocities $\mathbf{c}$ and $\mathbf{c}^*$, and the distribution functions f_1 and f_1^* are evaluated at the collision partner's pre-collision and post-collision velocities $\mathbf{c_1}$ and $\mathbf{c_1^*}$.

In physical terms, the left side of the equation describes changes to the velocity distribution function from molecular transport while the right side describes changes from molecular collisions.

Despite the physical simplicity of the Boltzmann equation, analytical closed-form solutions are extremely rare and exist only for simplified geometries and molecular interactions (see the examples treated in Chapter 2). The best known analytical solution is the Chapman–Enskog solution[6] which applies only in the hydrodynamic near-equilibrium regime, *i.e.*, only when the velocity distribution function differs from equilibrium by a small perturbation.

The Boltzmann equation is generally not tractable for continuous-variable techniques, such as finite-element or finite-volume.[7,8] The application of CFD-type methods to obtain solutions to the Boltzmann equations is constrained by the need to discretize the velocity distribution function in phase space, which, even for a single-species monatomic gas, is seven-dimensional and of infinite extent. The problem is even more acute for polyatomic molecules, for which the Boltzmann equation cannot be formulated as rigorously as for monatomic gases.[5–7]

The advent of digital computers in the 1960s led to a new type of method that provides a microscopic, rather than macroscopic, simulation of the flow. In 1963, Bird[9] proposed a method for simulating nonequilibrium gas behavior based on kinetic theory that calculates molecular collisions using stochastic procedures rather than the deterministic procedures used in Molecular Dynamics. This improved the computational efficiency greatly compared to other Monte Carlo and "particle" methods. As a result, Bird's Direct Simulation Monte Carlo (DSMC) method is used almost universally in rarefied gas dynamics and whenever mean-free-path phenomena are of interest. DSMC has been applied to an impressive array of problems ranging from hypersonic to subsonic flows and from chemical and physical vapor deposition (CVD/PVD) to plasma flows.[10,11]

In this chapter, we will review the DSMC method, examine its accuracy, and assess its convergence characteristics. Finally, we will apply DSMC to real-world MEMS problems.

3.2. Basic Method

A detailed exposition of the DSMC algorithm can be found in Bird's monographs[10,11] and in the references within. Herein, we will review some of the most important points in the DSMC algorithm.

DSMC uses a molecule-based, stochastic algorithm (see Fig. 3.1) to approximate the continuous molecular velocity distribution function with a discrete number of computational molecules, or "simulators".[11] It has been theoretically shown[12] that the DSMC algorithm provides an exact solution to the Boltzmann equation in the limit of infinite simulators and vanishing discretization errors (time step and cell size). The simplicity of the DSMC algorithm is one of its most attractive features. DSMC uses computational molecules that move, reflect from walls, and collide with each other to simulate the noncontinuum behavior of a dilute gas under the assumption of molecular chaos. Each computational molecule typically represents a large number of real molecules. The basic assumption of DSMC is that the molecular motion and collision phase can be decoupled, which is appropriate when the time step is much smaller than the mean collision time. Thus, the molecular motion and collisions that take place simultaneously are broken into two cyclically repeated parts. This separation reflects the processes described by the left and right sides of the Boltzmann equation (convective and collision part), respectively. It is noted that the Boltzmann equation, when originally proposed by Boltzmann, was based on physical arguments similar to those used to describe DSMC.

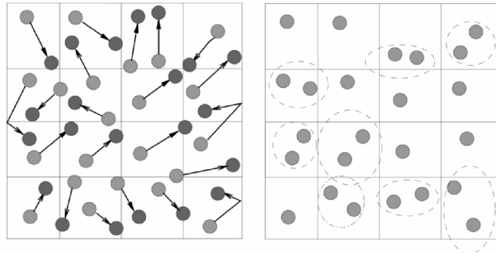

Fig. 3.1. DSMC algorithm schematic diagram: left, move phase; right, collide phase.

During a time step, each molecule moves ballistically at its velocity. The time step is selected so that it is smaller than the mean time between collisions. Molecules that cross a solid boundary during the move phase are reflected back into the computational domain. These reflections can be specular, diffuse at the wall temperature, diffuse without energy change, or a linear combination of these (in a probabilistic sense). More complicated reflection models are also available.[5,11,13]

Between moves, pairs of molecules within each cell are randomly selected to collide at the appropriate rate. The stochastic collisions of computational molecules reproduce the statistics of collisions of real molecules. In the established DSMC algorithm,[11] collision candidates are selected from anywhere within a computational cell. However, refinements of the collision algorithm have been implemented where neighboring molecules are preferentially selected for collision.[14,15] Collision dynamics are treated by molecular collision models that provide a compromise between physical realism and computational efficiency. The most popular models are the variable-soft-sphere (VSS) model of Koura and Matsumoto[11,16] and the variable-hard-sphere (VHS) model of Bird.[11] These models represent the hard-sphere interaction exactly and provide good approximations to inverse-power-law (IPL) interactions, including the Maxwell interaction. Although more complicated models can be devised, these simple models are preferred since the most important feature of the model is the variation of the cross section with relative speed. Other inputs, such as the scattering angle, have a relatively smaller effect on observable gas properties.

The computational mesh in DSMC serves two functions. First, the computational mesh enables identification of pairs of molecules as possible collision partners. Second, it provides a means for accumulating statistical information about the flow, (*e.g.*, number density, velocity, temperature, shear stress, heat flux, and other moments of the velocity distribution function). The cell size is selected

as a fraction of the local mean free path. Thus, any collision pair selected from within it satisfies the condition of geometric proximity. As in continuum methods, adaptive-grid schemes have been used in DSMC to allow the grid to adapt to changes in the local density and temperature.[17,18]

Moments of the velocity distribution function are sampled within each mesh cell over one or more time steps to provide macroscopic quantities. Sampling in the standard DSMC algorithm takes place after collisions are performed. However, sampling can be done either before collisions or both before and after collisions. If the flow is statistically steady, long-time averages can be used to reduce statistical uncertainty (the ergodic hypothesis).

As a numerical technique, DSMC is an explicit time-marching method that therefore can simulate unsteady flows.[19–23] Steady-state solutions are obtained as asymptotic limits of unsteady solutions.

Some of the advantages of DSMC, not shared by other methods that predict nonequilibrium noncontinuum flows, are its simplicity and lack of numerical instabilities. Complicated physical effects, such as chemical reactions and radiation, can be added to the molecular model without any changes to the algorithm or its stability as a numerical technique.[24]

The advantages of DSMC come at a cost: DSMC is computationally intense like most Monte Carlo methods. Therefore, its successful application to real problems depends heavily on its parallel performance. Monte Carlo methods usually have good parallel performance. This is because the workload depends mainly on the simulators within a cell: there is relatively less need to communicate information between cells. DSMC codes have demonstrated near-linear scaling up to several thousand processors. With the advent of massively parallel computers, problems considered impossible only a few years ago, such as transient three-dimensional simulations, are currently within reach.

Figure 3.2 presents the performance of the DSMC code Icarus[25] on a 3-Tflop 9000-processor platform. All physical and numerical parameters are fixed except for the number of simulators per cell, which is adjusted to keep the number of simulators per processor constant. The number of computational cells is kept the same, which increases the communication load as the number of processors is increased. Thus, this constitutes a worst-case scenario for a scaling assessment. Here, the performance is defined as the number of time steps per hour normalized by the 1000-processor result. The performance is reduced by only 15% as the number of processors is increased by 800%. This improvement is typical of what can be expected for DSMC with parallel processing.

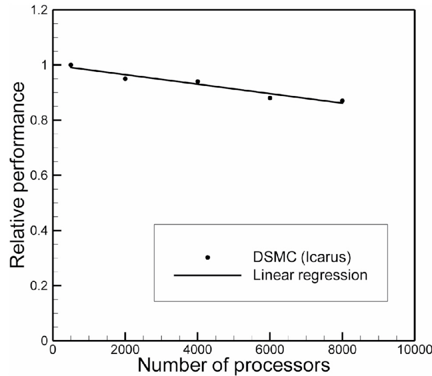

Fig. 3.2. Parallel performance of a DSMC simulation: good scaling is observed.

3.2.1. *Statistical Error*

The ability of DSMC to deal with complicated physical and chemical phenomena in gases[24] stems from using a stochastic scheme to represent the distribution function instead of solving the Boltzmann equation directly. Due to this stochastic representation, moments of the distribution, which provide macroscopic quantities, are recovered via sampling. From a numerical standpoint, this means that additional computational work must be performed to recover the desired quantities from a flow that has reached steady state (considered "converged" in some simulation methods). In fact, it is common for DSMC simulations to consume the majority of their computational time after the flow reaches steady state. The difficulty associated with distinguishing a quantity from background noise increases if its magnitude is small compared to the background, a common occurrence in MEMS flows. In these systems, mean flow speeds are often more than two orders of magnitude smaller than the thermal speeds of the molecules themselves.

Bird observes that statistical fluctuations decrease with the inverse square root of the sample size and thus can be reduced to any desired level by continuing the simulation (time averaging) or by repeating it with different initial random seeds (ensemble averaging).[11] Several authors[26–31] offer expressions that relate statistical error in DSMC to the square root of the sample size. Garcia[32] points out that DSMC fluctuations have the same characteristics as real fluctuations. This implies that the statistical noise in a flow with a one-to-one representation of simulators to real molecules is the real physical noise, which is something that is missing from the Boltzmann equation.

3.2.2. *Discretization Error*

Besides the number of samples, which controls the statistical error, three other parameters control the numerical accuracy of a DSMC simulation: the number of simulators per cell, N_c; the time step, Δt; and the cell size, Δx. This deterministic error (hereafter referred to as discretization error) has recently been the target of extensive investigation. A review of the most important findings is given herein.

To determine the convergence behavior of a numerical technique, a convergence functional is needed that is sensitive to small changes of the velocity distribution function and for which a theoretical prediction exists. Rader *et al.*[33] indicate that radically different convergence behavior is obtained if different functionals are used. In particular, they point out that temperature is a very *insensitive* convergence functional.

3.2.3. *Number of Simulators per Cell*

In the limit of vanishing time step and cell size and for infinite sample size, the remaining discretization error for any functional is inversely proportional to the number of simulators per cell, N_c.[29–33] For the ratio of the DSMC thermal conductivity, K_{DSMC}, to the actual value, K, the discretization error from approximating the velocity distribution function with a finite number of simulators has the form

$$\lim_{N_c \to \infty,\, \Delta t \to 0} \frac{K_{\text{DSMC}}}{K} = 1 + \frac{A}{N_c}, \tag{3.2}$$

Rader *et al.*[33] calculated the A parameter to be negative (-0.083), which has an important and counter-intuitive effect on convergence since it actually reduces the error for small number of simulators.

3.2.4. *Cell Size*

Alexander *et al.*[34] apply Green–Kubo theory to derive expressions for the cell-size discretization error of hard-sphere gas transport coefficients. Their expression for the thermal-conductivity ratio, in the limit of vanishing time step and infinite number of simulators per cell, is

$$\lim_{N_c \to \infty,\, \Delta t \to 0} \frac{K_{\text{DSMC}}}{K} = 1 + \frac{32}{225\pi}(\Delta\tilde{x})^2, \tag{3.3}$$

where $\Delta\tilde{x} = \Delta x/\lambda_{o,\text{HS}}$ is a dimensionless cell size, $\lambda_{o,\text{HS}} = (\sqrt{2}\pi d_{\text{ref}}^2 n_o)^{-1}$ is the hard-sphere molecular mean free path, d_{ref} is the molecular diameter, and n is the number density. This spatial discretization error arises from selecting

collision partners from anywhere within a cell of finite size Δx. To reduce this error, modifications to DSMC have been proposed that preferentially select nearby molecules as collision partners. These "nearest neighbor collision schemes" have been demonstrated to reduce this error at a small computational cost[14,15] when collision-partner selection is performed either by the use of sub-cells within a cell, from which collision partners are selected, or by sorting molecules in an one-dimensional array based on their geometrical proximity. It should be noted, however, that no formal convergence study of these "nearest neighbor" schemes has yet been performed.

3.2.5. *Time Step*

Hadjiconstantinou[35] applies Green–Kubo theory to derive expressions for the time-step discretization error of hard-sphere gas transport coefficients. His expression for the thermal-conductivity ratio, in the limit of vanishing cell size and infinite simulators per cell, is

$$\lim_{N_c \to \infty,\, \Delta t \to 0} \frac{K_{\mathrm{DSMC}}}{K} = 1 + \frac{64}{675\pi}(\Delta\tilde{t})^2, \tag{3.4}$$

where $\Delta\tilde{t} = \Delta t/t_o$ is a dimensionless time step, $t_o = \lambda_o/c_m$ is the mean collision time, $c_m = \sqrt{2k_B T_o/m}$ is the most probable molecular speed at temperature T for a molecule of mass m, and k_B is the Boltzmann constant. This error arises from the fact that DSMC performs collisions at discrete times between the move operations, whereas collisions actually occur continually throughout time. Garcia and Wagner[36] provide DSMC simulations in which, for all functionals and in all cases, both transient and steady-state DSMC calculations agree with Green–Kubo theory to within the stated computational uncertainties.

Modifications to the standard DSMC procedure have been suggested to reduce time-step discretization errors. Rebrov and Skovorodko[37] propose that sampling be performed twice per time step: before and after the collision operation, *i.e.*, move-sample-collide-sample. This minor adjustment to standard DSMC greatly improves cell-based averages for higher moments of the distribution function, (*e.g.*, heat and momentum fluxes). Ohwada[38] proposes that true second-order convergence is achieved in unbounded problems for all functionals if, for each time step Δt, advection takes place for $\Delta t/2$, collision for Δt, advection for an additional $\Delta t/2$, followed by sampling.

3.2.6. *Comprehensive Study of Discretization Error*

The apparent convergence rate for one discretization parameter can be influenced by the value of the other parameters. Thus, the theoretical convergence rate for one parameter is achieved only in the limit where contributions from the other two discretization parameters vanish.

Rader *et al.*[33] studied the convergence behavior of DSMC for the Fourier problem with a hard-sphere argon-like gas. The calculations are performed for many combinations of cell size, time step, and number of simulators per cell. Figure 3.3 shows the results of their finite-simulator-number calculations: the left plot shows the dependence of the thermal-conductivity ratio on $\Delta\tilde{t}$ for $\Delta\tilde{x} = 0.416$ at 7 values of N_c, and the right plot shows the dependence on $\Delta\tilde{x}$ for $\Delta\tilde{t} = 0.492$. A least-squares fitting procedure using a Taylor-series expansion in the error parameters is applied to obtain a best-fit expression for the thermal-conductivity ratio, shown with solid lines in Fig. 3.3.

$$\frac{K_{\text{wall}}}{K} = 1.001 + 0.0287\Delta\tilde{t}^2 + 0.0405\Delta\tilde{x}^2 + -\frac{0.083}{N_c} + F(\Delta\tilde{x}, \Delta\tilde{t}, \frac{1}{N_c}). \quad (3.5)$$

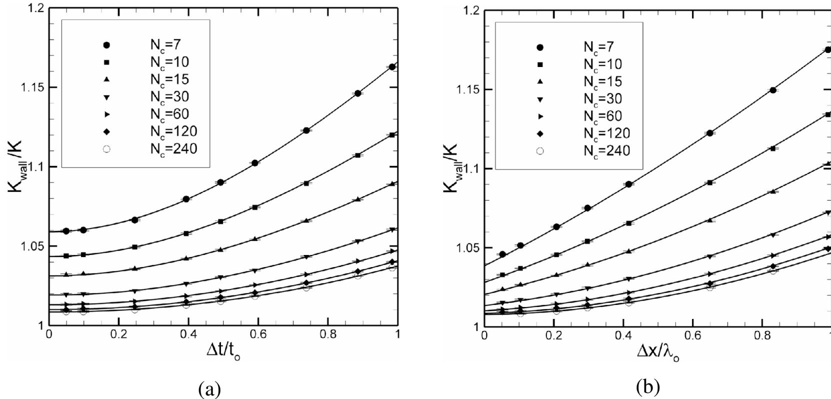

(a) (b)

Fig. 3.3. Convergence of DSMC: (a) effect of time step; (b) effect of cell size.

The first three terms in the above expression indicate the following. First, DSMC reproduces the actual value of the thermal conductivity to within 0.1%. Second, the coefficients of $\Delta\tilde{x}^2$ and $\Delta\tilde{t}^2$ are in good agreement with the Green–Kubo expressions in Eqs. (3.3) and (3.4).

According to Rader *et al.*,[33] the function F contains another 12 terms that are needed to adequately correlate the discretization error, besides the three lowest-order, "pure" terms shown above. The function F is a polynomial of higher-order terms in $\Delta\tilde{t}$, $\Delta\tilde{x}$, and $1/N_c$. The need for so many higher-order terms reveals the complexity of the convergence behavior as the discretization parameters approach $O(1)$. The form of this equation was arrived at by trial and error: no physical explanation is offered for the individual terms. Moreover, the particular form of F is expected to be problem-dependent.

When smaller numbers of simulators are used, additional terms are needed in the correlation. For example, first-order convergence in $1/N_c$ is typically obtained over the investigated time-step range only when $N_c > 30$ or with fewer simulators only when smaller time steps are used. The appearance of a term with the form $\Delta\tilde{x}/N_c$ in F indicates[33] that a first-order convergence rate in $\Delta\tilde{x}$ is observed in the limit of vanishing time step if too few simulators are used.

3.3. Comparison to Chapman–Enskog Theory

Chapman–Enskog (CE) theory[6] provides a method for obtaining the normal solution of the Boltzmann equation in terms of an expansion in the gradients of hydrodynamic flow properties or, equivalently, powers of the heat-flux and shear-stress Knudsen numbers. One of the most celebrated properties of CE theory is its ability to predict the transport properties of gases under conditions of near-equilibrium. In the following sections, we will examine the ability of DSMC to reproduce the CE solution of the Boltzmann equation in the near-equilibrium limit. This ability is not only of academic interest: many MEMS devices operate in this regime. The approach followed in this section is discussed in greater detail by Gallis *et al.*[39,40]

3.3.1. *Theoretical Results*

CE theory describes the state of a nonequilibrium gas in the hydrodynamic limit for a small heat-flux vector and a small shear-stress tensor, *i.e.*, the Navier–Stokes equations). First-order CE theory generates a closed-form expression for the distribution function in terms of macroscopic hydrodynamic fields and their gradients:

$$f = f^{(0)}(1 + \Phi^{(1)} + \Psi^{(1)}), \tag{3.6}$$

$$f^{(0)} = n \exp[-\tilde{c}^2]/(\pi^{3/2} c_m^3), \tag{3.7}$$

$$\Phi^{(1)} = -(8/5)\tilde{A}[\tilde{c}]\tilde{\mathbf{c}} \cdot \tilde{\mathbf{q}}, \tag{3.8}$$

$$\Psi^{(1)} = -2\tilde{B}[\tilde{c}](\tilde{\mathbf{c}} \circ \tilde{\mathbf{c}} : \tilde{\tau}). \tag{3.9}$$

Here, $f^{(0)}$ is the equilibrium (Maxwellian) distribution, $\Phi^{(1)}$ and $\Psi^{(1)}$ are the first-order nonequilibrium perturbations from this distribution, $c_m = \sqrt{2k_BT/m}$ is the most probable molecular thermal speed for the equilibrium distribution, m is the molecular mass, n is the number density, T is the temperature, k_B is the Boltzmann constant, $\tilde{\mathbf{c}} = \mathbf{u} - \mathbf{U}$ is the thermal velocity of a molecule, $\mathbf{u} = (u, v, w)$ is the velocity of a molecule, $\mathbf{U} = (U, V, W) = \langle \mathbf{u} \rangle$ is the average value of $\mathbf{u}$, $\tilde{\mathbf{c}} = \mathbf{c}/c_m$ is the normalized molecular thermal velocity, $\tilde{\mathbf{c}} \circ \tilde{\mathbf{c}} = \tilde{\mathbf{c}}\tilde{\mathbf{c}} - (\tilde{c}^2/3)\mathbf{I}$ is a traceless dyadic, $\tilde{\mathbf{q}} = \mathbf{q}/(mnc_m^3)$ and $\tilde{\tau} = \tau/(mnc_m^2)$ are the nondimensional heat-flux vector and shear-stress tensor, and $\tilde{A}$ and $\tilde{B}$ are expansions in the Sonine polynomials $S_j^{(k)}$:

$$\tilde{A}[\tilde{c}] = \sum_{k=1}^{\infty} (a_k/a_1) S_{3/2}^{(k)}[\tilde{c}^2],\ \tilde{B}[\tilde{c}] = \sum_{k=1}^{\infty} (b_k/b_1) S_{5/2}^{(k-1)}[\tilde{c}^2], \tag{3.10}$$

$$\tilde{S}_j^{(k)}[\xi] = \sum_{i=0}^{k} \frac{(j+k)!(-\xi)^i}{(j+i)!i!(k-i)!}. \tag{3.11}$$

The heat-flux vector $\mathbf{q}$, the shear-stress tensor τ, the thermal conductivity K, and the viscosity μ obey the following relations:

$$\mathbf{q} = -K\nabla T,\ \tau = \mu\{(\nabla \mathbf{U} + \nabla \mathbf{U}^T) - \frac{2}{3}(\nabla \cdot \mathbf{U})\mathbf{I}, \tag{3.12}$$

$$K = -(5/4)k_B c_m^2 a_1,\ \mu = (1/2)mc_m^2 b_1, \tag{3.13}$$

$$K = \left(\frac{K_\infty}{K_1}\right)\left(\frac{15}{4}\right)\left(\frac{k_B}{m}\right)\left(\frac{\mu_1}{\mu_\infty}\right)\mu. \tag{3.14}$$

Here, K_∞/K_1 and μ_∞/μ_1 are the CE infinite-to-first-approximation ratios of the thermal conductivity and the viscosity, respectively. The a_k and the b_k are the heat-flux and shear-stress Sonine-polynomial coefficients, respectively. Ratios of these coefficients can be expressed in terms of moments of the velocity distribution function, where, for convenience, the nonzero components of the heat-flux vector and the shear-stress tensor are taken to be q_x and τ_{xy}, respectively:[39]

$$\frac{a_k}{a_1} = \sum_{i=1}^{k} \left(\frac{(-1)^{i-1}k!(5/2)!}{(k-i)!i!(i+3/2)!}\right) \frac{\langle \tilde{c}^{2i}\tilde{c}_x \rangle}{\langle \tilde{c}^2 \tilde{c}_x \rangle}, \tag{3.15}$$

$$\frac{b_k}{b_1} = \sum_{i=1}^{k} \left(\frac{(-1)^{i-1}(k-1)!(5/2)!}{(k-i)!(i-1)!(i+3/2)!} \right) \frac{\left\langle \tilde{c}^{2(i-1)} \tilde{c}_x \tilde{c}_y \right\rangle}{\langle \tilde{c}_x \tilde{c}_y \rangle}. \tag{3.16}$$

CE theory provides the means[6,39] to determine the thermal conductivity, the viscosity, and the Sonine-polynomial coefficients in Eqs. (3.13)–(3.16) for a specified molecular interaction. In the theoretical analysis,[39] the IPL interaction model is used.

In the DSMC simulations, the VSS interaction is used to approximate the IPL interaction. Both the IPL and VSS molecular interactions yield thermal conductivities and viscosities with a T^ω temperature dependence. The VSS interaction, as implemented in the literature,[39,40] uses a molecular diameter that depends on the relative molecular speed c_r according to $d \propto c_r^{1/2-\omega}$, where the reference molecular diameter is given below:[11,39,40]

$$d_{\mathrm{ref}} = \left(\frac{5(a+1)(a+2)(m k_B T_{\mathrm{ref}}/\pi)^{1/2}}{4a(5-2\omega)(7-2\omega)\mu_{\mathrm{ref}}(\mu_1/\mu_\infty)} \right)^{1/2}. \tag{3.17}$$

It is emphasized that the molecular diameter calculated in this way is a function of the infinite-order-approximation gas viscosity, unlike in the original approach.[11,16] Here, α is the angular-scattering parameter. VSS uses this parameter to simulate an IPL anisotropic interaction. More details about these parameters can be found in the literature.[39,40]

The (local) heat-flux and shear-stress Knudsen numbers are defined to be the nondimensional heat flux and shear stress, respectively:

$$\mathrm{Kn}_q = |\tilde{q}_x| = |q_x|/(mnc_m^3), \quad \mathrm{Kn}_\tau = |\tilde{\tau}_{xy}| = |\tau_{xy}|/(mnc_m^2). \tag{3.18}$$

3.3.2. *Fourier and Couette Flow*

Fourier flow, shown in Fig. 3.4 is one of the simplest situations for studying gas behavior under highly nonequilibrium conditions. The gas is motionless and confined between two infinite, parallel walls separated by a distance L. The walls are motionless but have unequal temperatures $(T_1 \neq T_2)$. In steady state, a uniform heat flux and a temperature gradient exist in the domain. When the heat-flux Knudsen number is small, the heat flux is proportional to the temperature gradient in the bulk gas, *i.e.*, several mean free paths away from the walls) according to Fourier's law, where the coefficient of proportionality is the thermal conductivity:

$$q_x = -K_{\mathrm{eff}} \frac{\partial T}{\partial x} \tag{3.19}$$

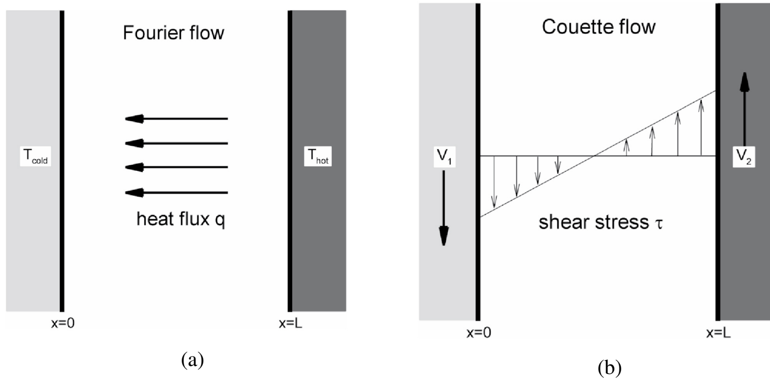

Fig. 3.4. (a) Schematic of Fourier flow. (b) Schematic of Couette flow.

Couette flow, also shown in Fig. 3.4, is another simple situation for studying gas behavior under highly nonequilibrium conditions. In this situation, the walls are isothermal (temperatures $T_1 = T_2$) but have unequal tangential velocities ($V_1 \neq V_2$). In steady state, the normal velocity component is zero, and a uniform shear stress and a tangential-velocity gradient exist in the domain. When the shear-stress Knudsen number is small, the shear stress is proportional to the tangential-velocity gradient in the bulk gas according to Newton's law, where the coefficient of proportionality is the viscosity:

$$\tau_{xy} = -\mu_{\text{eff}} \frac{\partial V}{\partial x} \tag{3.20}$$

When the walls have unequal temperatures and tangential velocities, both Fourier and Couette flow are obtained. More specifically, at small heat fluxes and shear stresses, Fourier's and Newton's laws are jointly observed in the bulk gas well away from the walls.

3.3.3. *DSMC Results*

Following Refs. 39 and 40, we consider a gas that has the molecular mass and the reference viscosity of argon. VSS ω and α values are used to represent Maxwell and hard-sphere molecular interactions. The Maxwell and hard-sphere models are two cases of the IPL model that bracket most known molecules. The molecular parameters used in the simulations are given in Table 3.1. Initially, the gas is motionless and at the reference pressure and temperature: $p_{\text{init}} = p_{\text{ref}} = 266.644$ Pa (2 torr) and $T_{\text{init}} = T_{\text{ref}} = 273.15$ K. The most probable molecular thermal speed

at these conditions is $c_m = 337.3\,\mathrm{m/s}$. The domain has a length $L = 1\,\mathrm{mm}$ and is bounded by two parallel solid walls that reflect all molecules diffusely at the wall temperature (unity accommodation). The system Knudsen number at the initial conditions is $\lambda/L = 0.0237$, so the walls are about 42 mean free paths apart. Since the Knudsen layers produced by the walls are generally about 4-10 mean free paths thick, the normal solution occupies a large fraction of the domain.

Table 3.1. Chapman–Enskog (CE) molecular parameters.

Symbol	Hard-Sphere	Maxwell
ω	1/2	1
α (VSS)	1	2.13986
μ_∞/μ_1	1.016034	1
K_∞/K_1	1.025218	1
D_∞/D_1	1.018954	1

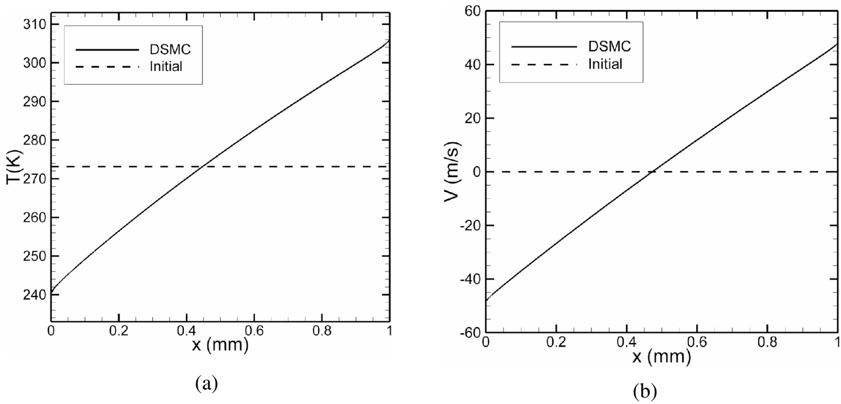

Fig. 3.5. Temperature and velocity profiles for Fourier and Couette flow: (a) Fourier flow; (b) Couette flow.

Figure 3.5 presents the temperature and velocity profiles for a simulation with Maxwell molecules for $\Delta T = 70\,\mathrm{K}$ and $\Delta V = 100\,\mathrm{m/s}$. In this simulation, the left wall is colder ($T_1 = 238.15\,\mathrm{K}$) and moving downward ($V_1 = -50\,\mathrm{m/s}$), whereas the right wall is hotter ($T_2 = 308.15\,\mathrm{K}$) and moving upward ($V_2 = 50\,\mathrm{m/s}$). The heat-flux and shear-stress Knudsen numbers corresponding to these conditions are $\mathrm{Kn}_q \approx 0.006$ and $\mathrm{Kn}_\tau \approx 0.003$, respectively, so CE theory is expected to apply in the central region of the domain.

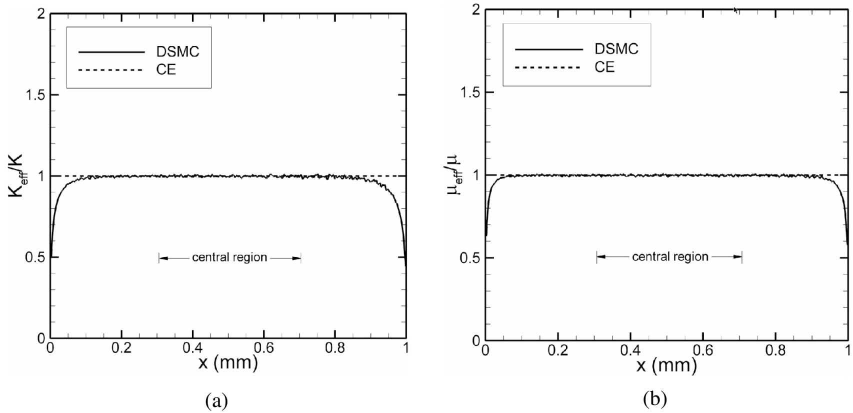

Fig. 3.6. Thermal-conductivity and viscosity profiles: (a) Fourier flow; (b) Couette flow.

Figure 3.6 shows the normalized effective thermal-conductivity and viscosity profiles for these conditions. The effective values K_{eff} and μ_{eff} are determined using Eqs. (3.19) and (3.20) and are normalized using the CE values. A value of unity indicates that the CE value is obtained, which occurs in the central region of the domain. The Knudsen layers are restricted to about 10-25% of the domain adjacent to each wall.

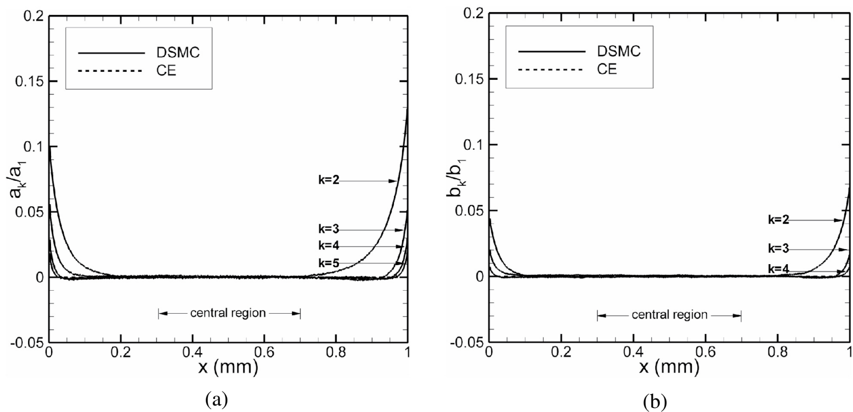

Fig. 3.7. Maxwell Sonine-polynomial-coefficient profiles at small Knudsen number: (a) a_k/a_1 for Fourier flow; (b) b_k/b_1 for Couette flow.

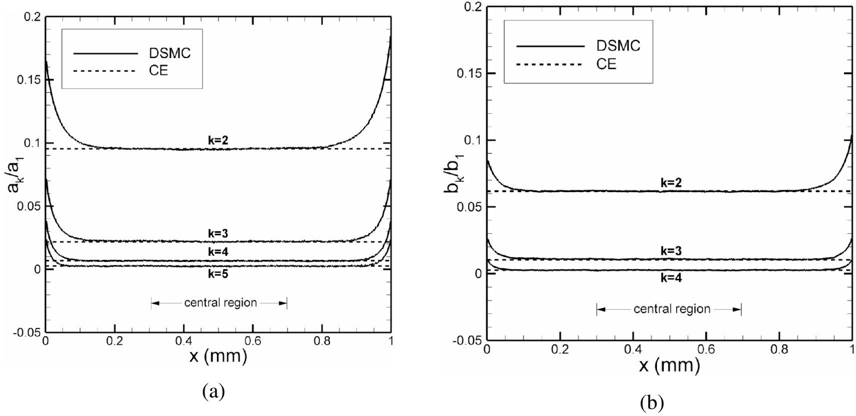

Fig. 3.8. Hard-sphere Sonine-polynomial-coefficient profiles at small Knudsen number: (a) a_k/a_1 for Fourier flow; (b) b_k/b_1 for Couette flow.

Figure 3.7 shows the profiles of the Sonine-polynomial-coefficient ratios a_k/a_1 and b_k/b_1 for these conditions. The solid curves are the DSMC values from Eqs. (3.15) and (3.16), and the dashed lines are the CE values. As observed for the thermal conductivity and the viscosity, the a_k/a_1 and the b_k/b_1 achieve the CE values in the central region of the domain and depart from the CE values only in the Knudsen layers.

Figure 3.8 shows the corresponding profiles obtained using hard-sphere molecules instead of Maxwell molecules but with all other conditions unchanged. Unlike Maxwell molecules, hard-sphere molecules have nonzero CE values for a_k/a_1 and the b_k/b_1 when $k \geq 2$. The CE values are shown with dashed lines, as in the previous figure. The profiles of temperature, velocity, thermal conductivity, and viscosity for hard-sphere molecules are almost identical to the corresponding profiles for Maxwell molecules in Figs. 3.5 and 3.6.

The heat-flux and shear-stress Knudsen numbers at these conditions are $\mathrm{Kn}_q \approx 0.006$ and $\mathrm{Kn}_\tau \approx 0.003$, respectively, so CE theory applies in the central region of the domain, and departures are observed only in the Knudsen layers adjacent to the walls.

3.4. Comparison to Moment-Hierarchy Theory

Under highly nonequilibrium conditions, the Chapman–Enskog (CE) theory discussed in the previous section is no longer applicable and is superseded by the Moment-Hierarchy (MH) method. The MH method is useful for Maxwell

molecules because the collision rate for the Maxwell interaction is independent of the molecular relative speed. This property allows the Boltzmann equation to be represented as an infinite hierarchy of moment equations, where each moment depends only on lower-order moments. By solving this system of equations, we can calculate moments of the Boltzmann equation without actually solving it.[7,41–45] Thus, for Maxwell molecules, the MH theory gives expressions for the thermal conductivity, the viscosity, and the Sonine-polynomial-coefficient ratios in terms of the heat-flux and shear-stress Knudsen numbers. For hard-sphere and other IPL molecules, where the collision rate is a function of the relative speed, the MH method cannot form a closed set of equations. More details about the MH theory and comparing it to DSMC are given in Refs. 7, 39, and 40.

3.4.1. *Theoretical Results*

The Boltzmann equation (Eq. (3.1)) in the absence of body forces has the following form:

$$\frac{\partial f}{\partial t} + \mathbf{u} \cdot \nabla f = J[\mathbf{c}|f, f] \tag{3.21}$$

where $J[\mathbf{c}|f, f]$ is the collision operator. Moments of the Boltzmann equation relate moments of f to moments of $J[\mathbf{c}|f, f]$, where their nondimensional forms are given below and $\tilde{f} = (c_m^3/n)f$:

$$M_{k_1k_2k_3} = \int \tilde{c}_x^{k_1}\tilde{c}_y^{k_2}\tilde{c}_z^{k_3}\tilde{f}[\tilde{\mathbf{c}}]d\tilde{\mathbf{c}} = \left\langle \tilde{c}_x^{k_1}\tilde{c}_y^{k_2}\tilde{c}_z^{k_3} \right\rangle \tag{3.22}$$

$$J_{k_1k_2k_3} = \int \tilde{c}_x^{k_1}\tilde{c}_y^{k_2}\tilde{c}_z^{k_3} J[\tilde{\mathbf{c}}|\tilde{f}, \tilde{f}]d\tilde{\mathbf{c}}. \tag{3.23}$$

For the special situation of Maxwell molecules, the $J_{k_1k_2k_3}$ can be expressed as bilinear combinations of the $M_{k_1k_2k_3}$, where the coefficients in these combinations are linear combinations of the eigenvalues of the linearized collision operator. This property enables an exact solution to the Boltzmann equation f to be obtained recursively for Fourier flow and Couette flow with Maxwell molecules without actually solving the Boltzmann equation.[7,41–45] Thus, in the limit of small shear stress (*i.e.*, $\mathrm{Kn}_\tau \to 0$), the Sonine-polynomial-coefficient ratios a_k/a_1 and b_k/b_1 for $k \geq 2$ are even polynomials in Kn_q of degree $2(k-1)$:

$$\frac{a_k}{a_1} = (-1)^{k-1}\sum_{j=1}^{k-1} A_{kj}\mathrm{Kn}_q^{2j}, \tag{3.24}$$

$$\frac{b_k}{b_1} = (-1)^{k-1} \sum_{j=1}^{k-1} B_{kj} \mathrm{Kn}_q^{2j}. \tag{3.25}$$

Using the approach of Sabbane and Tij,[46] the nonzero coefficients in the above can be calculated for the VSS-Maxwell interaction.

In a similar fashion, Garzó and Santos[7] apply the MH method to determine how the thermal conductivity K_{eff} and the viscosity μ_{eff} for Maxwell molecules depend on the small but finite shear-stress Knudsen number Kn_τ (K and μ are the CE values):

$$\frac{K_{\mathrm{eff}}}{K} = F_K[\mathrm{Kn}_\tau] = 1 - c_K \mathrm{Kn}_\tau^2 + O[\mathrm{Kn}_\tau^4], \tag{3.26}$$

$$\frac{\mu_{\mathrm{eff}}}{\mu} = F_\mu[\mathrm{Kn}_\tau] = 1 - c_\mu \mathrm{Kn}_\tau^2 + O[\mathrm{Kn}_\tau^4]. \tag{3.27}$$

Values of c_K and c_μ for VSS–Maxwell interactions in the literature[40] indicate that both coefficients are positive. Thus, Maxwell-molecule gases are shear-insulating and shear-thinning: the thermal conductivity and the viscosity decrease as the shear stress increases. DSMC VSS simulations indicate this is true for other IPL molecular interactions.[40]

3.4.2. *Simulation Results*

The flow domain in Fig. 3.4 is considered. The parameters used in the simulations are identical to the ones used in the previous section except that the temperature and velocity differences are increased so that noncontinuum effects are no longer small in the bulk gas. The walls have temperatures $T_1 = T_{\mathrm{ref}} - \Delta T/2$ and $T_2 = T_{\mathrm{ref}} + \Delta T/2$ and tangential velocities $V_1 = -\Delta V/2$ and $V_2 = \Delta V/2$ with temperature differences up to $\Delta T = 400\,\mathrm{K}$ and velocity differences up to $\Delta V = 800\,\mathrm{m/s}$.

Figure 3.9 shows the profiles of the Sonine-polynomial-coefficient ratios for Maxwell molecules at the same conditions as in Fig. 3.7 except that ΔT is increased from 70 K to 200 K. Under these conditions, the heat-flux Knudsen number Kn_q is increased from about 0.006 to about 0.017. The approximate nature of this statement reflects the fact that Kn_q is not constant throughout the domain but increases from hot to cold at constant pressure (*i.e.*, from right to left). The solid curves are the DSMC results, and the dashed lines are the CE results. The DSMC results differ significantly from the CE results in the central region of the

domain. More specifically, the a_k/a_1 and the b_k/b_1 differ increasingly from the corresponding CE values from right to left just as Kn_q increases from right to left.

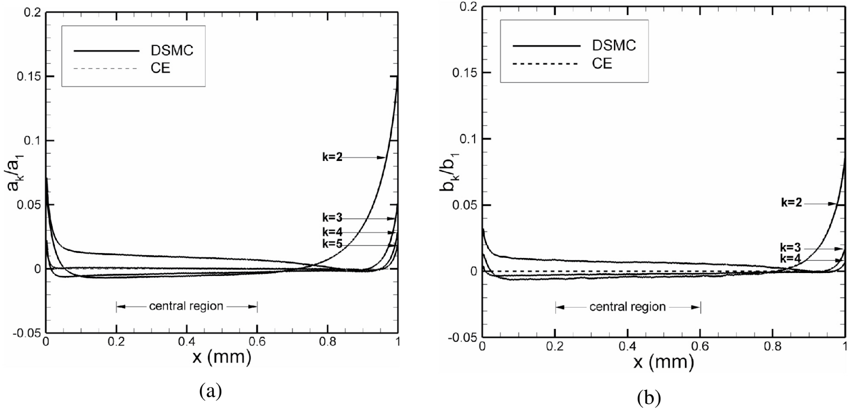

Fig. 3.9. Maxwell Sonine-polynomial-coefficient profiles at finite Knudsen number: (a) a_k/a_1 for Fourier flow; (b) b_k/b_1 for Couette flow.

Within the central region, the variation of the a_k/a_1 and the b_k/b_1 with Kn_q represents the normal solution to the Boltzmann equation. Since Kn_q varies across the domain, a single DSMC simulation provides the normal solution for the range of Kn_q values in the central region. The same approach is used subsequently to determine the variation of K_{eff}/K and μ_{eff}/μ with Kn_q.

Figure 3.10 shows the a_k/a_1 and the b_k/b_1 for Maxwell molecules as functions of Kn_q as determined above. The symbols indicate the DSMC values. Each cluster of points along a curve corresponds to values obtained from the central region of a single DSMC simulation with temperature differences of $\Delta T = 70, 200,$ $300,$ and $400\,\mathrm{K}$ and a velocity difference of $\Delta V = 100\,\mathrm{m/s}$. In all cases, Kn_τ is below 0.005, which classifies the flow in the continuum-hydrodynamic regime as far as shear stress is concerned. The solid and long-dashed curves are the corresponding MH results for VSS-Maxwell interactions, in the zero-shear-stress limit ($\mathrm{Kn}_\tau \to 0$) from Eqs. (3.24) and (3.25). The dashed lines indicate the CE values of 0.

The DSMC values agree closely with the MH VSS-Maxwell values except for a_4/a_1 and a_5/a_1 at $\Delta T = 400\,\mathrm{K}$ (the largest temperature difference. This difference is attributed[40] to discretization errors and to the small but finite Kn_τ. The DSMC and MH results for the VSS-Maxwell interaction are in good agreement, which provides strong evidence that DSMC produces the correct velocity

distribution function. It is noted that the a_k/a_1 and the b_k/b_1 differ from the CE values when $\mathrm{Kn}_q > 0.01$, a value that has been greatly debated in the literature.[1,2,8,9,11]

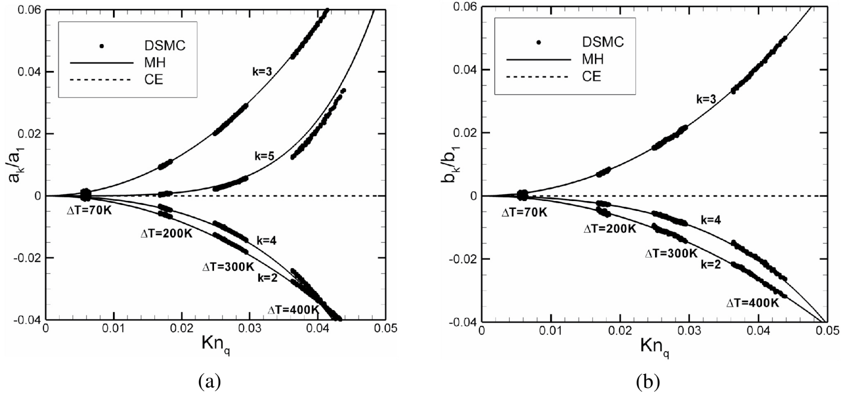

Fig. 3.10. Dependence of Maxwell Sonine-polynomial coefficients on Knudsen number: (a) a_k/a_1 for Fourier flow; (b) b_k/b_1 for Couette flow.

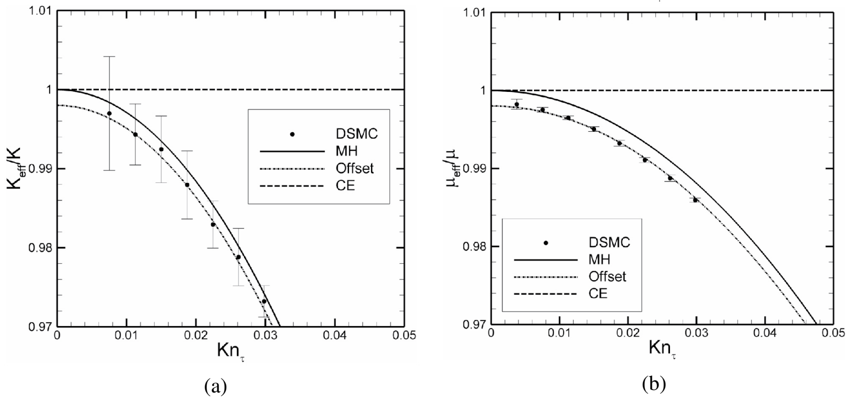

Fig. 3.11. Knudsen-number dependence of Maxwell thermal conductivity and viscosity: (a) K_{eff}/K; (b) μ_{eff}/μ.

Figure 3.11 shows K_{eff}/K and μ_{eff}/μ for Maxwell molecules as functions of Kn_τ. The symbols represent DSMC values with tangential velocity differences of $\Delta V =$ 0-800 m/s in increments of 100 m/s and a temperature difference of $\Delta T = 0\,\mathrm{K}$. The effective thermal conductivity is determined based on the

spatially nonuniform temperature and heat-flux profiles that appear because of viscous dissipation. In each plot, there are three theoretical curves. The dashed lines are the CE results, which are appropriate only for vanishing shear-stress and heat-flux Knudsen numbers, the solid curves are the MH results for Maxwell molecules (Eqs. (3.26) and (3.27)), and the long-dashed curves are the MH results offset by a small arbitrary amount. The offset MH values are in excellent agreement with the DSMC values. The small negative offsets (-0.002 for both transport coefficients) probably represent the discretization errors discussed above. Gallis *et al.*[40] point out that the decreases in these quantities with increasing Kn_τ are less than 3%. Thus, even under highly nonequilibrium conditions, the CE values are accurate enough for many engineering calculations.

3.5. Simulations of Microscale Flows

The number of references in the literature that report successful applications of DSMC to solve MEMS problems continues to increase.[47–50] The same DSMC algorithm (and in some cases the same DSMC code) can be applied to both subsonic near-continuum problems and hypersonic rarefied flow problems (although the former class of problems requires subsonic boundary conditions[8,11]).

In the following sections, we will demonstrate the way that DSMC can be used in conjunction with other techniques to study MEMS flows in an efficient manner. We will demonstrate the use of both continuum and molecular approaches and the limits of applicability of each method.

3.5.1. *Heat Transfer at Arbitrary Knudsen Numbers*

So far, we have examined flows in the hydrodynamic regime (small system Knudsen number), where nonequilibrium effects are produced by a temperature or velocity gradient. In this section, we will examine the scenario in which rarefaction produces noncontinuum effects. As the system Knudsen number progressively increases, noncontinuum effects from wall interactions become more pronounced. As outlined in the introduction, DSMC is usually the method of choice for problems when mean free path effects become significant.

The Navier–Stokes slip-jump (NSSJ) method uses continuum constitutive relations (Newton's and Fourier's laws) in the bulk gas and treats noncontinuum effects via "velocity slip" and "temperature jump" at the boundary.[51–53] These boundary conditions allow for the tangential velocity and the temperature at a gas-solid interface to be discontinuous. The velocity and temperature jumps across the interface are proportional to the normal shear stress and the heat flux,

respectively. More specifically, the temperature-jump condition is given by $q = h\Delta T$, where

$$h = \left(1 + \frac{\zeta}{4}\right)\left(\frac{\sigma}{2-\sigma}\right)\left(\frac{p\bar{c}}{T}\right) \tag{3.28}$$

Here, q is the normal heat flux at the gas-solid interface, ΔT is the temperature difference across the interface, h is the heat transfer coefficient, σ is the energy accommodation coefficient ($0 \leq \sigma \leq 1$), $\bar{c} = \sqrt{8k_BT/\pi m}$ is the mean molecular speed in an equilibrium gas, and $\lambda = 2\mu/\rho\bar{c}$ is the molecular mean free path. The velocity-slip and temperature-jump boundary conditions have been the focus of extensive research.[1,51–53]

Despite their *ad hoc* treatment of noncontinuum effects, the NSSJ equations remain a useful tool for describing gases in the near-continuum regime, even if only in a qualitative sense. In this section, we will examine the same problem using both the NSSJ equations and the DSMC method.

3.5.2. *Heat Transfer in a Microgap*

In this section, we follow the work in Ref. 54, where the NSSJ and DSMC methods are applied to study steady microscale heat transfer in a "microgap" geometry. The microgap geometry is identical to the Fourier problem of Fig. 3.4 except that the gas is contained in a 1-μm gap. The walls are at fixed temperatures T_A and T_B, and the gas-solid interfaces use the heat transfer coefficient in Eq. (3.28) to relate the heat flux to the temperature jump. The metric of comparison between the NSSJ and DSMC results is the heat flux because it is the most important quantity from an engineering point of view.

Argon and nitrogen are examined (see Table 3.2). Unlike the monatomic argon "molecule", which transports only translational energy, the diatomic nitrogen molecule transports both translational and internal energy and thus has more complicated noncontinuum effects.[11] Gas pressures of 10^1-10^7 Pa for NSSJ and 10^2-10^6 Pa for DSMC (free-molecular to continuum) are considered. Accommodation coefficients of 1.0, 0.9, 0.5, and 0.1 are investigated, which span the values encountered experimentally.[55] Boundary temperatures of $T_A = 285$ K and $T_B = 315$ K are examined, yielding a temperature gradient of 30 K/μm. Higher temperature gradients of 300 K/μm produce similar results.[54]

Figure 3.12 shows the NSSJ and DSMC gas-temperature profiles for nitrogen (argon is nearly identical) over the above pressure range with an accommodation coefficient of 1.0. At low pressures, the gas is nearly isothermal, as expected for free-molecular conditions.[11] At high pressures, the temperature variation is almost linear across the gas layer, and the temperature jumps at the gas-solid

Table 3.2. Material properties for simulations.[11]

Quantity	Symbol	Argon	Nitrogen	Unit
Molecular mass	m	66.3×10^{-27}	46.5×10^{-27}	kg
Temperature, reference	T_{ref}	273.15	273.15	K
Pressure, reference	p_{ref}	101325	101325	Pa
Mass density, reference	ρ_{ref}	1.781	1.249	kg/m^3
Molecular mean speed, reference	$\bar{c}_{\text{ref}}$	380.6	454.5	m/s
Mean free path, reference	λ_{ref}	0.0624	0.0583	μm
Viscosity, reference	μ_{ref}	2.117×10^{-5}	1.656×10^{-5}	Pa·s
Thermal conductivity, reference	K_{ref}	0.01641	0.02426	W/m·K
Specific heat at constant pressure	C_p	520.6	1039.2	J/kg·K
Specific heat ratio	γ	5/3	7/5	pure
Viscosity temperature exponent	ω	0.81	0.74	pure
Angular scattering exponent	α	1.40	1.36	pure
Internal energy mode number	ζ	0	2	pure
Internal energy collision number	Z	irrelevant	5	pure

interfaces are small, as expected for continuum conditions.[1] The NSSJ profiles agree closely with the DSMC profiles at the highest two pressures but differ noticeably at the lowest three pressures. More specifically, the slopes (proportional to the heat fluxes in the NSSJ simulations) differ increasingly in a relative sense as the pressure is decreased.

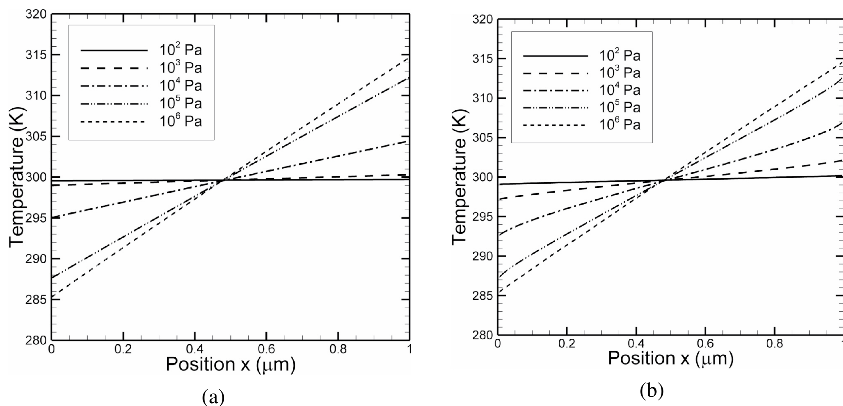

Fig. 3.12. Microgap temperature profiles for nitrogen: (a) NSSJ; (b) DSMC.

Figure 3.13 shows the heat flux as a function of gas pressure and accommodation coefficient for both gases. The argon and nitrogen results are similar

except that nitrogen transports more energy due to its internal degrees of freedom. The heat flux is independent of pressure at high pressures, as expected for continuum conditions, and is linear in pressure at low pressures, as expected for free-molecular conditions. The NSSJ values are in good agreement with the DSMC values except for order-unity accommodation coefficients and pressures in the range of 10^4-10^5 Pa, at which the molecular mean free path is comparable to the 1-μm gap height. In this situation, the NSSJ heat-flux values exceed the corresponding DSMC values by up to 8%.

Gallis *et al.*[54] point out that these observations contrast with the previous observation that the slopes of the NSSJ and DSMC temperature profiles differ by progressively greater relative amounts as the pressure is reduced. This contrast is reconciled[54] by the fact that Fourier's law of heat conduction does not apply to free-molecular heat transport (*i.e.*, at low pressure).[11] This underscores the fact that the NSSJ method cannot produce temperature profiles and heat fluxes that are both in agreement with the (more accurate) corresponding DSMC results.

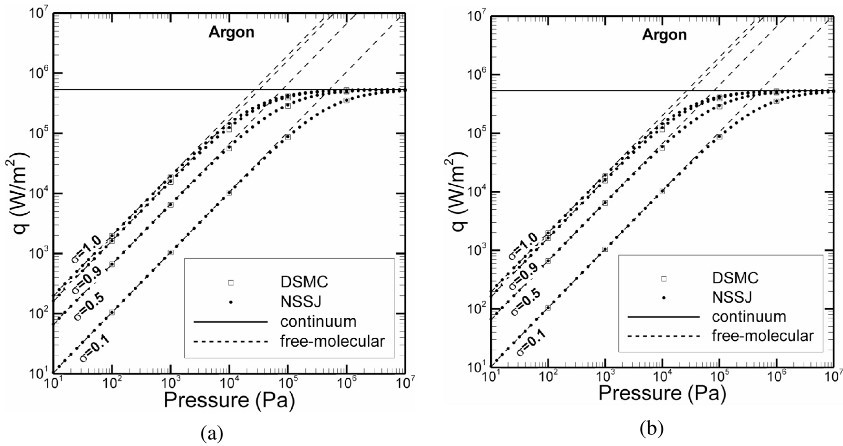

Fig. 3.13. Microgap heat flux versus pressure: (a) argon; (b) nitrogen.

The generally good agreement between the NSSJ and DSMC heat-flux values for all combinations of gases, pressures, boundary temperatures, and accommodation coefficients indicates that the NSSJ approach can be used with the indicated uncertainty to predict gas-phase heat transfer across microscale gaps between solids.

As an empirical modification to reduce the differences observed in the microgap geometry, the following expression for the heat transfer coefficient h is

suggested[54] as a replacement for Eq. (3.28):

$$h = \left(1 + \frac{\zeta}{4}\right)\left(\frac{\sigma}{2-\sigma}\right)\left(\frac{p\bar{c}}{T}\right) \Big/ \left(1 + \frac{c_1\sigma}{1 + c_2(\lambda/G)}\right) \tag{3.29}$$

Here, the numerator is from Eq. (3.28), λ is the mean free path, G is the gap height, c_1 is a constant that represents the effect of molecular collisions within the Knudsen layer,[56] and c_2 is a constant that enables the denominator to behave correctly in the free-molecular ($\lambda \gg G$) and continuum ($\lambda \ll G$) limits.

Values for c_1 and c_2 are empirically determined by adjusting them until the NSSJ heat fluxes match the corresponding DSMC heat fluxes. Based on the DSMC values in Fig. 3.13, the following values are found: $c_1 = 0.176$ and $c_2 = 0.647$ for argon, and $c_1 = 0.167$ and $c_2 = 0.599$ for nitrogen. Using Eq. (3.29) instead of Eq. (3.28) reduces the maximum difference between the NSSJ and DSMC heat fluxes from 8% to 0.4% (*i.e.*, the maximum error is reduced by a factor of 20).

Equation (3.29) is suggested instead of Eq. (3.28) for gas-filled regions bounded by parallel solid walls with a uniform gap height when the constants c_1 and c_2 are known. For a single planar wall bounding a gas-filled half-space, the limit of Eq. (3.28) as $G \to \infty$ is used.

3.5.3. *Thermal Actuation*

One way to achieve microscale motion is through thermal actuation, in which Joule-heating-induced thermal expansion of a microstructure, often a microbeam, produces motion. The length increase is proportional to the microbeam temperature rise, and the temperature rise is found by balancing the volumetric heating rate against the heat loss to the nearby substrate through the surrounding air, along the length of the microbeam to the anchor points, and via radiation (typically a small effect).

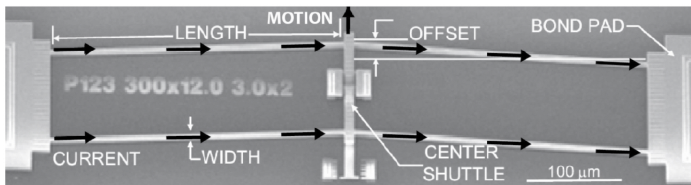

Fig. 3.14. Microscale thermal actuator.[55]

Figure 3.14 from Ref. 55 shows an example of thermal actuation. Electric current runs through the beams supporting the shuttle. Joule heating elongates these beams, which produces motion of the shuttle in the indicated direction. For this thermal actuator, noncontinuum heat-transfer effects are observed in the gas even at atmospheric pressure. As we shall see in the following section, ignoring them can lead to a significant error in the calculation of the heat flux from the beam to the substrate even at atmospheric conditions. Thus, models of noncontinuum gas-phase heat transfer are required to simulate microscale thermal actuation accurately.

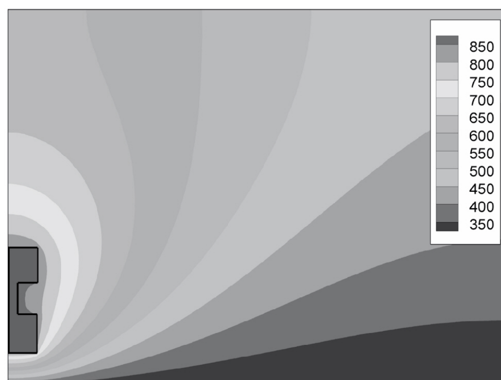

Fig. 3.15. I-beam geometry and temperature contours at 84 kPa.

3.5.4. *Heat Transfer from a Microbeam to the Substrate*

In this section, we will follow the analysis of Ref. 54 and examine the steady-state heat transfer from a heated microbeam surrounded by ambient nitrogen gas to the substrate 2 μm away.

Figure 3.15 shows the microbeam geometry and the temperature profile at 84 kPa with an accommodation coefficient of unity. The microbeam has an I-beam cross section with three layers. The top layer is 3.8 μm wide and 2.25 μm thick, the middle layer is 1.3 μm wide and 2 μm thick, and the bottom layer is 3.8 μm wide and 2.5 μm thick. A 2 μm gap separates the lower surface of the microbeam from the upper surface of the adjacent substrate. The substrate is 0.1 μm thick and extends across the entire lower surface of the computational domain.

For these simulations, the following boundary conditions are used. Insulating boundary conditions are applied on the top, side, front, and back of the domain

and on the symmetry plane in the gas. The lower substrate surface is held at a temperature of $T_A = 298\,\mathrm{K}$, and the symmetry surface of the microbeam cross section is held at a temperature of $T_B = 873\,\mathrm{K}$. This latter boundary condition replaces the volumetric Joule heating within the microbeam, which would otherwise be used to produce this temperature. The large thermal conductivity of the solid compared to the gas renders the solid nearly isothermal, so replacing the volumetric heat source with the above temperature boundary condition hardly affects the temperature distribution. The gas in these simulations is nitrogen with properties from Table 3.2. Gas pressures of 10^1-10^7 Pa for NSSJ and 10^2-10^5 Pa for DSMC are examined with accommodation coefficients of 1.0, 0.8, 0.5, and 0.2.

Ignoring noncontinuum effects in the gas causes the microbeam temperature to be significantly underpredicted for a fixed volumetric heating rate (by about 150 K for an accommodation coefficient of 0.5).[54] Since the degree of actuation is directly related to the average temperature rise along the microbeam, it is important to include noncontinuum effects when computing the gas-phase heat transfer.

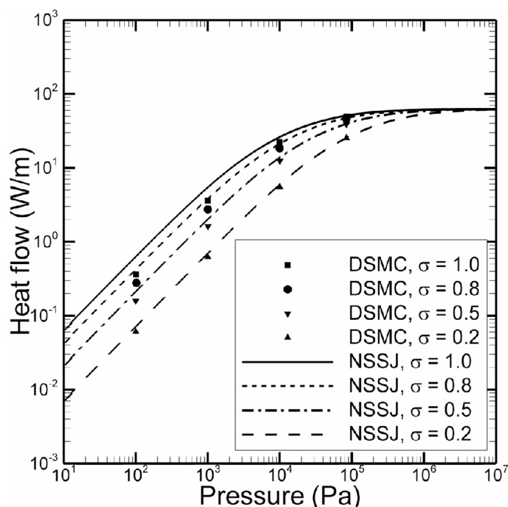

Fig. 3.16. Heat flow per unit length versus pressure for the microbeam.

Figure 3.16 shows the microbeam heat flow per unit length from NSSJ and DSMC simulations from Ref. 54. The NSSJ method systematically overpredicts the heat flow relative to the DSMC method. Although the differences are small for most conditions, the NSSJ method predicts values that are approximately double the DSMC values for low pressures and order-unity accommodation coefficients.

This discrepancy is unlike the discrepancy observed for the microgap in that it occurs at low, rather than intermediate, pressures, and that it is a factor-of-two, rather than an 8%, effect. While relatively large, these differences are small in an absolute sense, (*e.g.*, two orders of magnitude smaller than the continuum heat-flux value).

The good agreement between the NSSJ and DSMC methods at atmospheric pressure indicates that the NSSJ method can be used to predict gas-phase heat transfer for microscale devices in ambient air with reasonable accuracy. However, as noncontinuum effects become important either through flow rarefaction or through wall interactions, the NSSJ approach gradually becomes less accurate.

In a low-pressure situation, the noncontinuum region surrounding the microbeam does not consist of thin, planar regions. To the contrary, a near-free-molecular region bounded by ambient gas and the substrate, both of which are at the ambient temperature, surrounds the microbeam. When this region's size (*i.e.*, the molecular mean free path) is large compared to the microbeam, the microbeam appears as a small, finite object interacting in a free-molecular way with a large gas-filled region. This explains the factor-of-two discrepancy noted above.[54]

3.5.5. *Gas Damping*

In this section, we will focus on a common phenomenon in microfluidic devices with moving surfaces, *squeeze film damping*.[1] This phenomenon takes place when two surfaces, close to each other, execute an out-of-plane motion, causing gas to be drawn into and expelled from the region between the two surfaces. The gas pressure in the gap is increased above ambient during times of squeezing and is decreased below ambient during times of suction, whereas the gas pressure outside the gap remains essentially at ambient.

Keeping in mind that most MEMS devices are characterized by large width-to-height ratios, we can consider gas in a thin gap of large but finite lateral size. The edges of the gap communicate with an essentially unbounded region of motionless gas at uniform conditions.

Under these circumstances, the Navier–Stokes equations for the gas in the gap can be simplified and, in the limit of small Reynolds number, take the form known as the Reynolds equation (RE):[1,4]

$$\frac{\partial}{\partial t}(\rho G) = \nabla \cdot \left\{ \left(\frac{\rho G^3}{12\mu} \right) \left(1 + \chi \frac{6\Lambda}{G} \nabla p \right) \right\}, \tag{3.30}$$

$$\rho = \frac{mp}{k_B T}, \frac{\Lambda}{\lambda} = \frac{2-\sigma}{\sigma}, \lambda = \frac{2\mu}{\rho \bar{c}}, \bar{c} = \sqrt{\frac{8 k_B T}{\pi m}} \tag{3.31}$$

Here, the gas has molecular mass m, mass density ρ, temperature T, pressure p, viscosity μ, molecular mean speed $\bar{c}$, and molecular mean free path λ, the Boltzmann constant is k_B, the accommodation coefficient lies in the range $0 \leq \sigma \leq 1$, and the gap has height G, which can vary with position and time. The coefficient χ is discussed below and obtains the value of unity in the continuum (Navier–Stokes) limit. The RE applies in a two-dimensional domain that is the projection of the object onto the adjacent planar substrate (*i.e.*, the object's "footprint"). More specifically, although the pressure varies with lateral position and time, it is independent of vertical (out-of-plane) position.

To solve the RE, a boundary condition for the pressure is required on the edge of the domain. A common assumption is that the pressure at the edge equals the ambient pressure. This assumption, valid only when the lateral extent of the gap is much larger than the height of the gap, often breaks down for MEMS devices. In general, the following boundary condition represents the pressure with good accuracy:[50]

$$p_\infty - p = \eta G \left(\frac{\partial p}{\partial \eta}\right) + \zeta \left(\frac{12 \mu U}{G}\right) / \left(1 + \chi \frac{6\Lambda}{G}\right). \tag{3.32}$$

Here, p_∞ is the ambient pressure of the surrounding gas, and η is the outward normal direction. The coefficients η, ζ, and χ can be empirically calculated by comparing DSMC and NSSJ simulations.[50]

The advantages of using the RE to calculate the force on a moving microdevice are its simplicity and its computational efficiency. The disadvantage is that the RE is a simplified form of the NSSJ equations and therefore does not treat noncontinuum effects rigorously. In many cases, the gaps are small enough (or become so during operation) that noncontinuum effects are important. These effects are incorporated by appropriate selection of parameters in the boundary condition (Eq. (3.32)). DSMC and NSSJ calculations can be used to simulate the quasi-static gas flow around a moving microbeam to determine the coefficients in the modified RE boundary condition.

The force on the object is found by integrating the difference of the pressure from ambient over the object's (gap-bounding) surface and is proportional to the velocity, where is the gas-damping coefficient:

$$F = -\int_S (p_\infty - p)dS = -\beta U. \tag{3.33}$$

The gas forces on a MEMS device can significantly affect performance and reliability. For example, gas forces can protect a device from shock but can damp its motion. Thus, they must be considered when the dynamic response of these devices is calculated. However, one must not neglect the fact that, although gas forces may be significant in some instances, during normal operation these forces are often small. Thus, although incorporating gas forces into a structural-mechanics code by coupling a fluids solver to a solids solver is possible, this is typically computationally expensive and technically excessive.

With this goal and these restrictions in mind, we will incorporate noncontinuum effects into the RE equation in a way that can produce an accurate closed-form description of the gas forces on a moving MEMS device. We shall see one such application adapted from Ref. 50 in the following section.

3.5.6. *Gas Damping of a Cantilevered Microbeam*

In this section, we will see how NSSJ and DSMC can be applied to predict the gas-damping force on a moving cantilevered microbeam and how the RE can be used to provide a compact model for this force.[50]

Figure 3.17 shows an array of cantilevered microbeams. Their cross sections have a 20-μm width, a 2-μm thickness, and a 2-μm gap height. NSSJ and DSMC simulations are performed for these devices.[50] The microbeam moves upward with a velocity of 1 m/s. The surrounding gas is nitrogen at 295 K and at either 13.3 kPa or 101 kPa. The gas-damping force is found by integrating the vertical stress around the microbeam, and the gas-damping coefficient is found through Eq. (3.33). Mesh-refinement and domain-size studies[50] indicate that the NSSJ and DSMC simulations discussed below are accurate to within 1% and 5% respectively.

Figure 3.18 presents a quasi-static DSMC calculation where the microbeam moves upward, creating a low-pressure region underneath it. The plot shows the pressure distribution and the streamlines.

Figure 3.19 shows the damping coefficients from the NSSJ and DSMC simulations. In all cases, the NSSJ values lie above the DSMC values, indicating that the NSSJ method slightly overpredicts the gas-force. Also shown are RE results using three different boundary conditions: the original boundary condition, the modified boundary condition with the NSSJ coefficients, and the modified boundary condition with the DSMC coefficients. For large gap heights, the RE with the

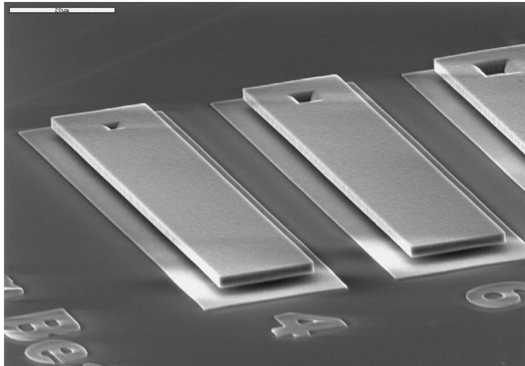

Fig. 3.17. Cantilevered microbeams.[50]

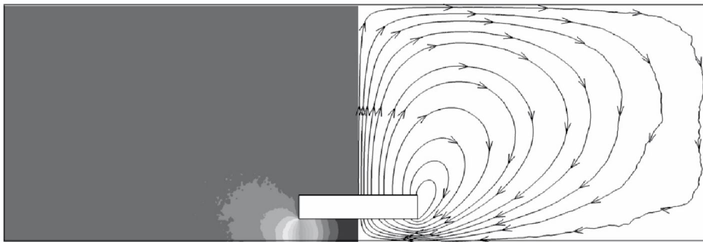

Fig. 3.18. Quasi-steady DSMC simulation of a microbeam moving upward: left side, pressure contours; right side, streamlines.

original boundary condition does a poor job in reproducing the NSSJ and DSMC results. This is caused by the boundary condition, not the RE itself: the modified boundary condition yields values that are in good agreement with the simulations. For small gap heights, the NSSJ and DSMC results differ significantly; nevertheless, the RE with the corresponding modified boundary condition is in excellent agreement with the simulations. Thus, the modified boundary condition with the appropriate coefficients significantly improves the accuracy of the RD for large gaps (relative to the beam width) and small gaps (relative to the mean free path).

3.5.7. *Thermally Driven Flows*

Flows caused by temperature gradients along channels have been known since the time of Boltzmann. However, it is not widely appreciated that a steady but nonuniform heat flow in a gas-filled geometry bounded by solids at different but

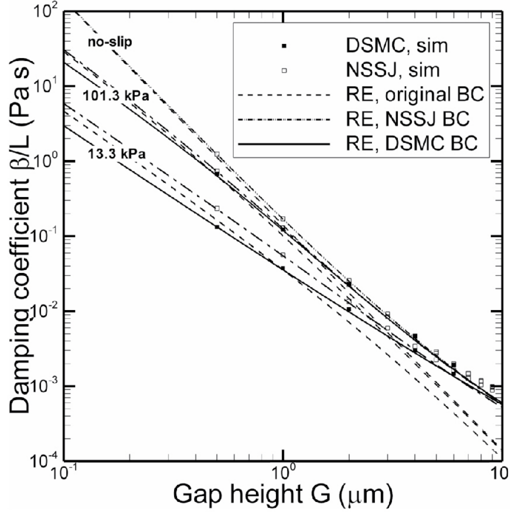

Fig. 3.19. Damping coefficient versus gap height.

uniform temperatures establishes a noncontinuum stress field that induces a steady gas motion.[1,57,58]

It is emphasized that this type of gas motion is not caused by transient effects, buoyancy, or thermal creep (gas motion driven by a temperature gradient along a solid surface[58]). This gas motion exists only when the isotherms (temperature contours) in the gas are nonparallel.[57,58] Thus, no gas motion occurs for the microgap, which has parallel isotherms, but gas motion can occur for the microbeam, which has nonparallel isotherms.

Although this phenomenon is absent even from formulations of the Navier–Stokes equations that specifically include the effects of velocity slip and temperature jump (the NSSJ equations), DSMC inherently captures this type of gas motion. Figure 3.20 shows the flow patterns and the temperature distributions from DSMC simulations of the microbeam surrounded by nitrogen at three different pressures, 84, 8.4, and 0.84 kPa, where the substrate and microbeam temperatures are $T_A = 298$ K and $T_B = 873$ K, respectively. The Knudsen numbers for these flows based on the clearance between the beam and the substrate are 0.03, 0.3, and 3 for the three pressures. The maximum flow speeds are 0.1 m/s at 84 kPa, 2 m/s at 8.4 kPa, and 1 m/s at 0.84 kPa. For the DSMC simulations, the discretization and statistical errors were kept (see Ref. 54) to approximately 1%.

The "noisiness" of the flow at 84 kPa is explained by the fact that the velocity is comparable to the DSMC stochastic uncertainty based on the number of sampled

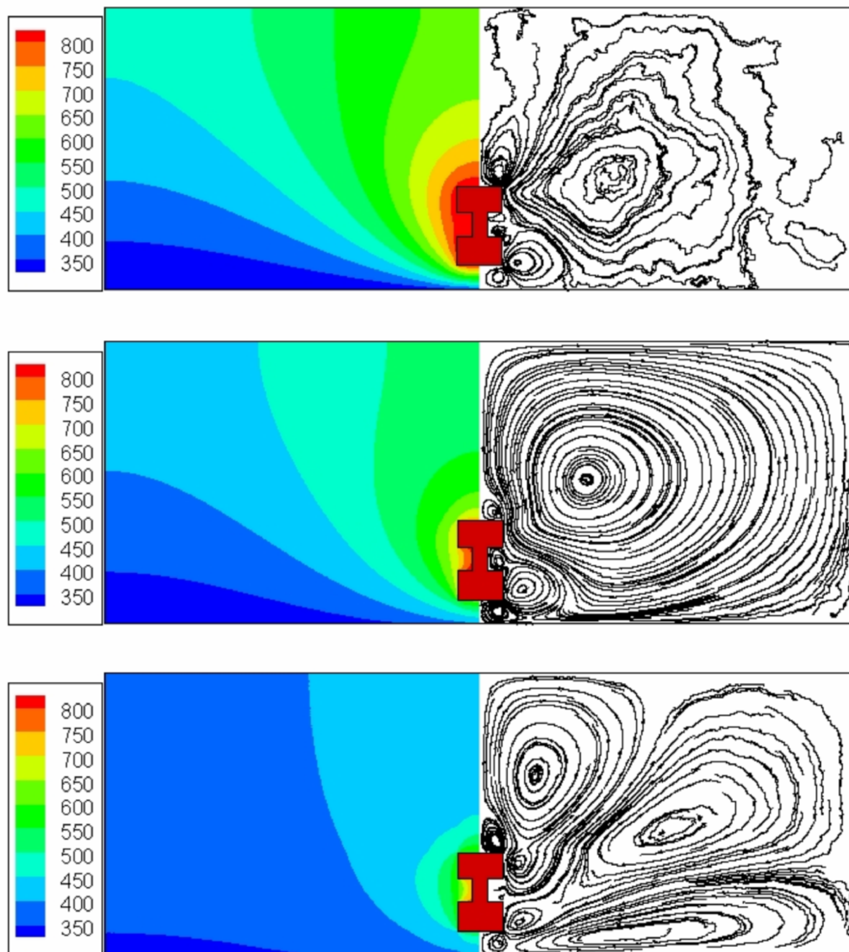

Fig. 3.20. Examples of thermally driven microscale flows.[54] Top to bottom: 84, 8.4, and 0.84 kPa. Left: temperature contours (isotherms). Right: streamlines.

molecules per cell ($\sim 10^7$) and typical molecular speeds ($\sim 500\,\mathrm{m/s}$). Although noisier, the flow at 84 kPa has the same basic pattern as the flow at 8.4 kPa.

These flows have features in common with the "thermal edge flow" observed by Sone and Aoki. In all cases, the gas moves toward the uppermost and lowermost right corners of the microbeam, where the heat flux is largest, and away from the notch in the side of the microbeam, where the heat flux is smallest. Also, the gas in the gap moves inward along the heated microbeam surface toward the

symmetry plane and outward along the colder substrate surface away from the symmetry plane. These directions are the same as those observed by Sone in his simulation of flow in a small gap between two concentric cylinders, where the inner cylinder is hotter than the outer cylinder.[57]

At this point, the question of the importance of this phenomenon is raised. The molecular energy transport in DSMC makes no distinction between conduction and convection heat transfer. However, the relative between conduction and convection heat transfer. However, the relative importance of convection and conduction for these flows is assessed in Ref. 54 by evaluating the Peclet number. The Peclet numbers are 0.01 at 84 kPa, 0.02 at 8.4 kPa, and 0.001 at 0.84 kPa. Based on these extremely small values, convection is relatively unimportant, and conduction is the dominant heat-transfer mode for the microbeam. Possible applications of this phenomenon are discussed by Sone.[58]

3.6. Conclusions

In this chapter, we have given an overview of the Direct Simulation Monte Carlo (DSMC) method as a tool to study gas-filled MEMS devices. DSMC has been shown theoretically and computationally to provide simulations that are in agreement with exact solutions of the Boltzmann equation. More specifically, the Chapman–Enskog (CE) values for the thermal conductivity, the viscosity, and the Sonine-polynomial-coefficient ratios are obtained to high accuracy, indicating that DSMC correctly reproduces the CE velocity distribution.

DSMC and Moment-Hierarchy (MH) results for the VSS-Maxwell interaction are in good agreement. This provides strong evidence that DSMC produces the correct velocity distribution even for large local Knudsen numbers and large departures from equilibrium.

As a numerical method, DSMC is an explicit time-marching technique that can simulate transient as well as steady-state flow fields. As discretization errors become small, DSMC approaches the correct limit, with error terms similar to predictions of Green–Kubo theory.

DSMC is computationally more demanding than most continuum CFD methods. This problem is partially alleviated by its superior parallel performance. Another feature of DSMC, often overlooked, is the lack of numerical instabilities even for the most physically and geometrically complicated problems. This feature, with its unmatched accuracy, makes DSMC a unique method to study physical phenomena at the mean-free-path level.

Using DSMC for subsonic-flow MEMS simulations is not without issues. The difficulty of distinguishing between statistical noise and the flow field has hindered

its widespread application. However, besides the cases for which DSMC is the only applicable method, there are other cases where DSMC can provide useful input. DSMC can be used concurrently with continuum methods and analytical approaches to develop empirical models that can be implemented in engineering codes.

Acknowledgments

Sandia is a multiprogram laboratory operated by Sandia Corporation, a Lockheed Martin Company, for the United States Department of Energy's National Nuclear Security Administration under contract DE-AC04-94AL85000. The author gratefully acknowledges many helpful technical interactions with the following individuals: D. J. Rader, J. R. Torczynski, E. S. Piekos, G. A. Bird, A. Santos, M. Tij, W. Wagner, A. L. Garcia, and N. G. Hadjiconstantinou. J. R. Torczynski and M. F. Barone are also thanked for critically commenting on the manuscript.

References

1. G. Karniadakis, A. Beskok, and N. Aluru, *Microflows and Nanoflows: Fundamentals and Simulation*. (Springer, New York, 2005).
2. M. Gad-el-Hak, *MEMS: Introduction and Fundamentals*. (Cambridge University Press, Cambridge, 2006).
3. J. A. Pelesko and D. H. Bernstein, *Modeling MEMS and NEMS*. (Chapman & Hall/CRC, Boca Raton, 2003).
4. G. K. Batchelor, *An Introduction to Fluid Dynamics*. (Cambridge University Press, Cambridge, 2000).
5. C. Cercignani, *Rarefied Gas Dynamics: From Basic Concepts to Actual Applications*. (Cambridge University Press, Cambridge, 2000).
6. S. Chapman and T. G. Cowling, *The Mathematical Theory of Non-uniform Gases. Third edition*. (Cambridge University Press, Cambridge, 1970).
7. V. Garzó and A. Santos, *Kinetic Theory of Gases in Shear Flows: Nonlinear Transport*. (Kluwer Academic Publishers, Dordrecht, 2003).
8. W. Liou and Y. Fang, *Microfluid Mechanics*. (McGraw-Hill, New York, 2006).
9. G. A. Bird, Approach to translational equilibrium in a rigid sphere gas, *Physics of Fluids*. **6**, 1518–1519, (1963).
10. G. A. Bird, *Molecular Gas Dynamics*. (Clarendon Press, Oxford, 1976).
11. G. A. Bird, *Molecular Gas Dynamics and the Direct Simulation of Gas Flows*. (Clarendon Press, Oxford, 1994).
12. W. Wagner, A convergence proof for Bird's Direct Simulation Monte Carlo method for the Boltzmann equation, *Journal of Statistical Physics*. **66**, 1011–1044, (1992).
13. R. G. Lord, Some extensions to the Cercignani-Lampis gas-surface scattering kernel, *Physics of Fluids A*. **3**, 706–710, (1991).

14. G. A. Bird, *Forty Years of DSMC, and Now?*, In eds. T. J. Bartel and M. A. Gallis, *Rarefied Gas Dynamics: 22nd International Symposium*, vol. 585, pp. 372–380. American Institute of Physics, Melville, NY, (2001).
15. G. J. LeBeau, K. A. Boyles, and F. E. L. III. Virtual subcells for the Direct Simulation Monte Carlo method. Technical Report AIAA 95-1031, American Institute of Aeronautics and Astronautics, Reston, (2003).
16. K. Koura and H. Matsumoto, Variable soft sphere molecular model for air species, *Physics of Fluids A*. **4**(5), 1083–1085, (1992).
17. C. D. Robinson and J. K. Harvey, *A Parallel DSMC Implementation on Unstructured Meshes with Adaptive Domain Decomposition*, In *Proceedings of the Twentieth International Symposium on Rarefied Gas Dynamics*, pp. 227–232. Peking University Press, Beijing, China, (1996).
18. C. K. Oh, E. S. Oran, and B. Z. Cybyk. Microchannel Flow Computed with DSMC-MLG. Technical Report AIAA 95-2090, American Institute of Aeronautics and Astronautics, Reston, (1990).
19. S. Stefanov, P. Gospodinov, and C. Cercignani, Monte Carlo simulation and Navier-Stokes finite difference calculation of unsteady-state rarefied gas flow, *Physics of Fluid*. **10**(1), 289–300, (1998).
20. J. H. Park, P. Bahukudumbi, and A. Beskok, Rarefaction effects on shear driven oscillatory gas flows: a Direct Simulation Monte Carlo study in the entire Knudsen regime, *Physics of Fluids*. **16**, 317–330, (2004).
21. Y. C. Fang, W. W. Liou, and G. A. Bird. Three-dimensional simulations of Rayleigh-Bénard convection by DSMC. Technical Report AIAA 2004-2671, American Institute of Aeronautics and Astronautics, Reston, (2004).
22. G. A. Bird, *Three-dimensional Forced Chaotic Flows*, In eds. A. D. Ketsdever and E. P. Muntz, *Rarefied Gas Dynamics: 19th International Symposium*, vol. 663, pp. 133–140. American Institute of Physics, (2003).
23. N. G. Hadjiconstantinou, Oscillatory shear-driven gas flows in the transition and free-molecular-flow regimes, *Physics of Fluids*. **17**, 100611, (2005).
24. R. A. Dressler, *Chemical Dynamics in Extreme Environments*. (World Scientific, Singapore, 2001).
25. T. J. Bartel, S. Plimpton, and M. A. Gallis. Icarus: A 2-D Direct Simulation Monte Carlo (DSMC) code for multi-processor computers, manual v10.0. Technical Report SAND-2901, Sandia National Laboratories, Albuquerque NM, (2001).
26. M. A. Fallavollita, D. Baganoff, and J. D. McDonald, Reduction of simulation cost and error for particle simulations of rarefied flows, *Journal of Computational Physics*. **109**, 30–36, (1993).
27. D. A. Fedosov, S. V. Rogasinsky, M. I. Zeifman, M. S. Ivanov, A. A. Alexeenko, and D. A. Levin, *Analysis of Numerical Errors in the DSMC Method*, In ed. M. Capitelli, *Rarefied Gas Dynamics: 24th International Symposium*, pp. 589–594. Number 762. American Institute of Physics, (2005).
28. G. Chen and I. D. Boyd, Statistical error analysis for the Direct Simulation Monte Carlo technique, *Journal of Computational Physics*. **126**, 434–448, (1996).
29. C. Graham and S. Méléard, Stochastic particle approximations for generalized Boltzmann models and convergence estimates, *Annals of Probability*. **25**, 115–132, (1997).

30. S. Caprino, M. Pulvirenti, and W. Wagner, Stationary particle systems approximating stationary solutions to the Boltzmann equation, *SIAM Journal on Mathematical Analysis*. **29**, 913–934, (1998).
31. N. G. Hadjiconstantinou, A. L. Garcia, M. Z. Bazant, and G. He, Statistical error in particle simulations of hydrodynamic phenomena, *Journal of Computational Physics*. **187**, 274–297, (2003).
32. A. L. Garcia, Nonequilibrium fluctuations studies by a rarefaction simulation, *Physical Review A*. **34**, 1454–1457, (1986).
33. D. J. Rader, M. A. Gallis, J. R. Torczynski, and W. Wagner, DSMC convergence behavior of the hard-sphere-gas thermal conductivity for Fourier heat flow, *Physics of Fluids*. **18**, 077102, (2006).
34. F. J. Alexander, A. L. Garcia, and B. J. Alder, Cell size dependence of transport coefficients in stochastic particle algorithms, *Physics of Fluids*. **12**, 1540–1542, (2000).
35. N. G. Hadjiconstantinou, Analysis of discretization in the direct simulation Monte Carlo, *Physics of Fluids*. **12**, 2634–2638, (2000).
36. A. L. Garcia and W. Wagner, Time step truncation error in direct simulation Monte Carlo, *Physics of Fluids*. **12**, 2621–2633, (2000).
37. K. Rebrov and P. A. Skovorodko, *An Improved Sampling Procedure in DSMC Method*, In ed. C. Shen, *Rarefied Gas Dynamics: Proceedings of the 20th International Symposium*, pp. 133–140. American Institute of Physics, (1997).
38. T. Ohwada, Higher order approximation methods for the Boltzmann equation, *Journal of Computational Physics*. **139**, 1–14, (1998).
39. M. A. Gallis, J. R. Torczynski, and D. J. Rader, Molecular gas dynamics observations of Chapman-Enskog behavior and departures therefrom in nonequilibrium gases, *Physical Review E*. **69**, 042201, (2004).
40. M. A. Gallis, J. R. Torczynski, D. J. Rader, M. Tij, and A. Santos, Normal solutions of the Boltzmann equation for highly nonequilibrium Fourier flow and Couette flow, *Physics of Fluids*. **18**, 017104, (2006).
41. A. Santos and V. Garzó, *Exact Non-linear Transport from the Boltzmann Equation*, In eds. J. K. Harvey and R. G. Lord, *Rarefied Gas Dynamics: 19th International Symposium*, pp. 13–22. Oxford University Press, (1995).
42. M. Tij and A. Santos, Combined heat and momentum transport in a dilute gas, *Physics of Fluids*. **7**(11), 2858–2866, (1995).
43. E. Asmolov, N. K. Makashev, and V. I. Nosik, Heat transfer between parallel plates in a gas of Maxwellian molecules, *Soviet Physics Doklady*. **24**(11), 892–894, (1979).
44. N. K. Makashev and V. I. Nosik, Steady-state Couette flow (with heat transfer) of a gas of Maxwellian molecules, *Soviet Physics Doklady*. **25**(8), 589–591, (1981).
45. E. S. Asmolov, N. K. Makashev, and V. I. Nosik, Heat transfer between plane parallel plates in a gas of Maxwellian molecules, *Soviet Physics Doklady*. **24**, 892–894, (1979).
46. M. Sabbane and M. Tij, Calculation algorithm for the collisional moments of the Boltzmann equation for Maxwell molecules, *Computer Physics Communications*. **142**, 19–29, (2002).
47. A. A. Alexeenko, D. A. Fedosov, S. F. Gimelshein, D. A. Levin, and R. J. Collins, Transient heat transfer and gas flow in a MEMS-based thruster, *Journal of MicroElectroMechanical Systems*. **15**(1), 181–194, (2006).

48. A. D. Ketsdever, M. Clarbough, S. F. Gimelshein, and A. A. Alexeenko, Experimental and numerical determination of micropropulsion device efficiencies at low Reynolds numbers, *AIAA Journal*. **4**(3), 663–641, (2005).
49. E. S. Piekos and K. Breuer. DSMC modeling of micromechanical devices. Technical Report AIAA 95-2089, American Institute of Aeronautics and Astronautics, Reston, (1995).
50. M. A. Gallis and J. R. Torczynski, An improved Reynolds-equation model for gas damping of microbeam motion, *Journal of MicroElectroMechanical Systems*. **13**(4), 653–659, (2004).
51. N. G. Hadjiconstantinou, Comment on Cercignani's second order slip coefficient, *Physics of Fluids*. **15**(8), 2352–2354, (2004).
52. M. J. McNenly, M. A. Gallis, and I. D. Boyd, Empirical slip and viscosity performance for microscale gas flow, *International Journal for Numerical Methods in Fluids*. **49**, 1169 2261191, (2005).
53. N. G. Hadjiconstantinou, The limits of navier-stokes theory and kinetic extensions for describing small-scale gaseous hydrodynamics, *Physics of Fluids*. **18**, 111301, (2006).
54. M. A. Gallis, J. R. Torczynski, and D. J. Rader, A computational investigation of noncontinuum gas-phase heat transfer between a heated microbeam and the adjacent ambient substrate, *Sensors and Actuators*. **in press**, (2007).
55. S. P. Kearney, L. M. Phinney, and M. S. Baker, Spatially resolved temperature mapping of electro-thermal actuators by surface Raman scattering, *Journal of MicroElectroMechanical Systems*. **15**(2), 314–321, (2006).
56. S. K. Loyalka, Slip and jump coefficients for rarefied gas flows: variational results for Lennard-Jones and N(r)-6 potentials, *Physica*. **163**, 813–821, (1990).
57. K. Aoki, Y. Sone, and N. Masukawa, *A Rarefied Flow Induced by a Temperature Field*, In eds. J. Harvey and G. Lord, *Rarefied Gas Dynamics*, pp. 215–220. Oxford University Press, (1995).
58. Y. Sone, *Kinetic Theory and Fluid Dynamics*. (Birkhäuser, Boston, 2002).

This page intentionally left blank

Chapter 4

New Approaches for the Simulation of Micro-Fluidics in MEMS

T. Y. Ng, Hua Li and K. Y. Lam

School of Mechanical and Aerospace Engineering
Nanyang Technological University
50 Nanyang Avenue, Singapore 639798
lihua@ntu.edu.sg

L. S. Pan and D. Xu

Institute of High Performance Computing
*Agency for Science, Technology and Research (A*STAR)*
1 Science Park Road, 01-01 The Capricorn
Singapore Science Park II, Singapore 117528

In this chapter, we examine the size effects on liquid and gas micro-flows. For micro-gas flows, the rarefied effect results in relatively high Knudsen numbers. The conventional direct simulation Monte Carlo (DSMC) method has been widely used to handle this class of micro-flow. However, the problem arises when the characteristic velocities of the micro-gas flow become very small ($< 3\,\mathrm{ms}^{-1}$), and the use of conventional DSMC in such instances often incur in large statistical errors. Unfortunately, the typical micro-gas flow velocities in most MEMS devices are in the low velocity range. In this chapter, a multiscale coarse-grain molecular block (or "big molecule") model is developed to replace the actual molecular model. These molecular blocks are then used to replace the particles in the DSMC method, and a molecular block direct simulation Monte Carlo (MB-DSMC) method is established. As the mass of the molecular block is larger, the statistical error incurred by the MB-DSMC method is smaller, and this novel method is used to examine low velocity micro-gas flows. Similarly, liquid flows in MEMS and BioMEMS devices can be very different from well established and extensively studied macro-scale liquid flows. For the latter, conventional fluid dynamics principles such as the Navier–Stokes equations can be used to predict the flow fields with very good accuracy expected. For the former however, some factors which are normally neglected in macro-scale liquid flows now have to be considered if accurate predictions are to be attained. In this chapter, a refined one-equation turbulent model is introduced to account for the size effects, and

the phenomenon of early transition (at lower Reynolds number) from laminar to turbulent flow in micro-scale liquid flows is examined in detail.

Contents

4.1 Introduction . . . 122
4.1.1 Micro-Fluidic Gas Flows — Introduction and Review . . . 122
4.1.2 Micro-Fluidic Liquid Flows — Introduction and Review . . . 124
4.2 Modeling and Simulation of Gaseous Micro-Flow . . . 126
4.2.1 The Molecular Block Direct Simulation Monte Carlo (MB-DSMC) Method . . . 126
4.2.2 MB-DSMC Simulation Results for Gaseous Flows . . . 132
4.2.3 Conclusion . . . 139
4.3 Modeling and Simulation of Liquid Micro-Flow . . . 140
4.3.1 A Modified One-Equation Model for Micro-Scale Liquid Flow . . . 140
4.3.2 Simulation Results for Liquid Flow in Micro-Tubes . . . 142
4.3.3 Conclusions . . . 148
References . . . 150

4.1. Introduction

The underlying principles that govern the flow characteristics of fluids (both liquids and gases) in MEMS and BioMEMS devices are complex, and deviate (both qualitatively and quantitatively) from conventional macro-flow characteristics. In the context of micro-flow modeling and simulation, it is necessary to identify the major differences and incorporate them into existing continuum models/theories, or develop an entirely new solution framework.

For micro-gas flows, a multiscale coarse-grain molecular block (or "big molecule") model is developed to replace the actual molecular model. These molecular blocks are then used to replace the particles in the DSMC method, and a molecular block direct simulation Monte Carlo (MB-DSMC) method is established. Next, a modified one-equation turbulent model is introduced to account for the size effects, and the phenomenon of early transition (at lower Reynolds number) from laminar to turbulent flow in micro-scale liquid flows is examined in detail.

4.1.1. *Micro-Fluidic Gas Flows — Introduction and Review*

As computational speed and memory become more readily available, the direct simulation Monte Carlo (DSMC) method has emerged as the primary method for investigating flows with high Knudsen number K_n (= λ/L), where λ is the molecular mean free path and L the characteristic length of the flow. Fundamental work on the DSMC method has been described in several well-known books, such as those by Bird[1,2] and Garcia.[3] In his review on DSMC methodologies, Bird[4]

discussed the early development of this class of method and compared it with other methods used in molecular dynamics and solutions of Boltzmann and Navier–Stokes equations. There were also further excellent reviews by Muntz,[5] Cheng,[6] Cheng and Emmanuel,[7] Oran *et al.*[8] and Bird.[9] Muntz[5] summarized works in rarefied gas dynamics with an emphasis on the computational aspects. Cheng's[6] emphasis was on hypersonic viscous flows and high-temperature gas dynamics, while Cheng and Emmanuel[7] discussed the application of the DSMC method as a predictive tool and compared DSMC computations with experimental and Navier–Stokes analyses in the low K_n regime. Oran *et al.*[8] looked into the use of the DSMC method in investigating the characteristics of gas flow in micro-devices so as to optimize the design of related MEMS devices, while Bird[9] discussed the recent advances and the current challenges of the DSMC method and examined its range of applicability and validity.

In the DSMC method, large statistical errors can be a serious problem, especially when simulating low-speed flows in micro-devices. Nance *et al.*[10] simulated a micro-channel flow similar to plane Poiseuille flow using the DSMC method, and they observed from their results that even if the characteristic velocity is around 15 m/s, the statistical errors in the velocity and shear stress fields are large compared to the corresponding physical signals even when using the analytical solution of Navier–Stokes equations as the initial conditions in the simulation. It can easily be extrapolated that if the characteristic velocity is smaller, the statistical errors will tend to inundate the real physical signals. Theoretically, the statistical error is inversely proportional to the square root of the sample size, and in other words, as the sample number increases, the statistical error should approach zero. Following this line of thought, some researchers believe that the statistical errors of the DSMC method can be sufficiently small only when the sample size is sufficiently large. However, in the actual computational analysis, there are two factors affecting the rate and trend of the decrease of the statistical error, which have not been taken into account in the derivative process of the theoretical results. Firstly, the random process described in the statistical theory is an absolute ideal process, while that generated by a computer is a quasi-random process. Secondly, the theoretical result is obtained under the condition that gas is in an equilibrium state, while the computationally simulated gas flows are usually in a non-equilibrium state. The numerical analyses of Pan *et al.*[11] have shown that the statistical error of the DSMC method does indeed decrease with the increase of sample size, but there is also limit to this reduction. Hence, it is not just the high computational cost, but it is also incorrect to assume that the statistical error in the DSMC method will become satisfactorily small by simply increasing the sample size.

Fan and Shen[12] presented a DSMC-IP method which achieved very good results for one-dimensional slow-speed flows. Cai *et al.*[13] then made some modifications to the DSMC-IP method and extended it to solve two-dimensional slow-speed flows in micro-channels. The basic ideas of this method cover three aspects. Firstly, the computational processes of the original DSMC algorithm remain unchanged. Secondly, the macroscopic physical information in each cell is assumed to move with the represented molecules used in the DSMC method. Thirdly, the change of the macroscopic physical information is calculated through the mechanical features of the cell. Obviously, this method would require additional memory and extended CPU time. Pan *et al.*[11] investigated the features of the statistical error in the DSMC method. The conclusions were that the magnitude of the statistical error depends on gas type and temperature, where lower temperatures and/or larger molecular masses results in smaller statistical errors. Based on the relationship between the statistical error and temperature, they presented a modified DSMC algorithm for simulating low-speed microflows without temperature gradient. However, in practical micro-devices, apart from the velocity and stress fields, the heat transfer is often a very important physical phenomenon. In this chapter, a molecular block model is first presented. The molecular block direct simulation Monte Carlo (MB-DSMC) method is then constructed using the molecular blocks to replace the particles in the original DSMC method. The present method imposes no restriction on the temperature field, and can therefore be used to simulate low-speed micro-flows irrespective of whether there is a temperature gradient in the flow field.

4.1.2. *Micro-Fluidic Liquid Flows — Introduction and Review*

Liquid flows in fluidic MEMS devices may be very different from the flows in common macro-scale devices. For the latter, conventional continuum fluid dynamics principles can be adopted to simulate the flow behavior, where Navier–Stokes equations are usually used to predict these flow fields, and very good accuracy can be expected. For the former however, due to the micro-scale dimensions of the flow field, some factors which are normally neglected in the continuum theory now have to be reconsidered in order to obtain an accurate prediction. It is not adequate to use Navier–Stokes equations directly without any modification to the original physical model and boundary conditions. A fundamental understanding of the flow characteristics, such as the velocity and pressure distributions, is critical in the design of fluidic micro-devices. From their experimental measurements, Wu and Little[14,15] found that for gas flow and heat transfer in fine channels, the

friction factors are very different from those predicted by the conventional theory of fluid flow. The friction factors are larger than those obtained from the traditional Moody chart, and this indicates an early transition from laminar to turbulent flow occurring at a Reynolds number of about 400 to 900 for the various the configurations tested.

Experiments on liquid flows and heat transfer in micro channels were also carried out by Tuckerman.[16] It was found that the flow rates roughly agreed with Poiseuille flow predictions. Pfahler *et al.*[17] carried out an experiment on fluid flow in micro-channels. At first, it was verified that the experimental measurements agreed well with the conventional theory. However, subsequently work showed that deviations occurred for smaller channels. In Pfahler *et al.*,[18] experimental measurements of the friction factor or apparent viscosity for an isopropyl alcohol/silicon oil mixture in larger micro-channels were in good agreement with the theoretical prediction based on the conventional theory. As the channel size is decreased, the apparent viscosity began to drift from the theoretical values. Choi *et al.*[19] also found that the flows in micro-channels are significantly different from those predicted by conventional theory. Wang and Peng,[20] from experimental studies of the forced convection of liquid in micro channels, found that the transition from laminar to turbulent flow occurs when the Reynolds number (Re) is less than 800, and a fully developed turbulent flow is initiated in the Re range of 1000 to 1500. In their later studies[21,22] on liquid flow in rectangular micro-channels, it was found that the transition occurs at a Re range of 200 to 700, and a fully developed turbulent flow occurs at the Re range of 400 to 1500. The transitional Re reduces and the transition range becomes smaller as the dimension of the micro-channel decreases.

Mala and Li[23] experimentally investigated liquid flow in circular micro-tubes of diameter range 50-254 μm. Once again, it was found that the flow characteristics significantly depart from the predictions of conventional theory for micro-tubes with relatively smaller diameters. However, for those with larger diameters, the experimental measurements were found to be in rough agreement with conventional theory. In addition, an increase in Re results in a significant increase in the pressure gradient compared to that predicted by the Poiseuille flow theory. It was further observed that an early transition from laminar to turbulent flow occurred at Re greater than $300 - 900$, and the flow becomes fully developed turbulent flow at Re $> 1000 - 1500$.

In most circumstances of liquid flow in MEMS devices, the incompressible Navier–Stokes equations are still being adopted to describe the flow behavior.[24,25] For flow in the laminar flow region described by the Navier–Stokes equation, one can employ an apparent viscosity, μ_a, instead of the fluid viscosity,

μ, together with a no-slip wall boundary condition to simulate the flow fields. The resulting numerical results are in agreement with experimental observations. To simulate the flow field in the turbulent flow region, a feasible method is to adopt the concept of turbulent viscosity, μ_t. This term is introduced into the averaged Navier–Stokes equations in order to predict the averaged turbulent flow field, where the turbulent viscosity is calculated from turbulence models. However, as most of the models are developed for macro-scale flow, there are only a few turbulence models available for turbulent liquid flows at the micro-scale.

In this chapter, based on the observations of the above-mentioned references, we assume that the flow becomes fully developed turbulent flow in micro tubes when Re is greater than 1000, and that the flow features can be predicted using turbulent flow theory. A one-equation turbulence model is introduced and modified with consideration of a micro-dimension flow feature in order to predict the low turbulent water flow in micro-tubes. Comparison studies between the present numerical calculations and experimental measurements will also be carried out. The numerical results obtained will add to our physical understanding of the liquid flow behavior in micro devices.

4.2. Modeling and Simulation of Gaseous Micro-Flow

4.2.1. *The Molecular Block Direct Simulation Monte Carlo (MB-DSMC) Method*

In a continuous medium model, the gas consists of the "fluid points" of continuous distribution. Such a "fluid point" must not only be small enough macroscopically such that it can be treated as a point without volume, but also sufficiently large microscopically so that statistical treatment can be performed within it. The velocity of the "fluid point" is the mean velocity of molecules within it. This can then be treated a large molecular block. An important advantage of this model is that it now becomes unnecessary to account for the thermal motions of molecules when describing and/or simulating the flow field, and the numerical results obtained through Navier–Stokes equations have no statistical error. Although there is no direct relationship between the continuous medium (large molecular block) model and the DSMC model, a conceptual inspiration can be drawn, and in the following, a small molecular block model will be presented.

4.2.1.1. *Basic Model and Assumptions*

Based on the theory of molecular gas dynamics, the instantaneous velocity $\mathbf{V}$ of a molecule comprises two parts:

$$\mathbf{V} = \mathbf{V}_0 + \mathbf{V}' \tag{4.1}$$

where $\mathbf{V}_0$ is the stream velocity (or statistical mean velocity) and $\mathbf{V}'$ the random thermal velocity with zero mean vector. From the Maxwellian distribution, the random thermal velocity is proportional to the most probable molecular thermal velocity

$$\mathbf{V}' \propto \sqrt{\frac{2kT}{m}} \tag{4.2}$$

where k is the Boltzmann constant, while T and m are respectively the macroscopic temperature and the mass of molecule. It is well known that the statistical error of the stream velocity is a non-zero mean value of the random thermal velocity. Thus the statistical error of the stream velocity, $\delta\mathbf{V_0}$ is also proportional to the most probable molecular thermal velocity for a given sample size

$$\delta\mathbf{V}_0 \propto \sqrt{\frac{2kT}{m}}. \tag{4.3}$$

Equation (4.3) indicates that if the molecular mass is enlarged by a factor of α the statistical error of velocity will contract by $\sqrt{\alpha}$ for the given temperature and sample size. Following this line of thought, the following molecular block model is presented:

(1) It is assumed that α real molecules in a small volumetric region are taken as one 'big molecule' or 'molecular block', and its instantaneous velocity also comprises two parts

$$\mathbf{V}_b = \mathbf{V}_0 + \mathbf{V}_b' \tag{4.4}$$

From the kinetic theory of a system of particles and Eq. (4.1), the mass of the 'big molecule' as well as the two velocity terms on the right-hand side of Eq. (4.4) can be written as

$$m_\mathrm{b} = \alpha m \tag{4.5}$$

$$\mathbf{V}_\mathrm{b}' = \frac{1}{\alpha}\sum_{\alpha}\mathbf{V}'. \tag{4.6}$$

(2) It is assumed that the random thermal velocity $\mathbf{V}_b'$ possesses a similar probability distribution function as that of $\mathbf{V}'$ except that the mass term in the distribution function is now m_b.

(3) The reference diameter and the number density of the "big molecule" are determined based on the two conditions: i) the mean free path of the 'big molecules' is equal to that of the actual gas molecules; and ii) the macroscopic viscosity of gas remains unchanged.

The first requirement in the third assumption ensures the slip velocity of gas flow on the solid wall remains unchanged after using the 'big molecules', while the second requirement is meant to keep the macro-dynamic features of flow field unchanged.

From molecular gas dynamics, the mean free path λ and dynamic viscosity μ of gas molecules are (from Eqs. (4.65) and (3.61) of Bird[2])

$$\lambda = \frac{1}{\sqrt{2}\pi d_{\mathrm{ref}}^2 n}\left(\frac{T}{T_{\mathrm{ref}}}\right)^{\omega-1/2} \tag{4.7}$$

$$\mu = \frac{15\sqrt{\pi m k}(4km)^{\omega-1/2}T^{\omega}}{\Gamma(9/2-\omega)\sigma_{\mathrm{T,ref}}C_{\mathrm{r,ref}}^{2\omega-1}} \tag{4.8}$$

where ω $(1/2 \le \omega \le 1)$, is the viscosity index, n the number density of the gas molecules, Γ the gamma function, T_{ref} the reference temperature (273 K) of the gas, and $\sigma_{\mathrm{T,ref}}$, $C_{\mathrm{r,ref}}^{2\omega-1}$ and d_{ref} respectively the total collision cross section, relative thermal velocity and diameter of the gas molecule at T_{ref}. Note that ω is $1/2$ for the hard sphere model of the molecule, and varies accordingly with the type of gas for the variable hard sphere (VHS) and the variable soft sphere (VSS) models. From Eqs. (4.60) and (4.61) of Bird,[2] it can be deduced that

$$\sigma_{\mathrm{T,ref}}C_{\mathrm{r,ref}}^{2\omega-1} = \frac{\pi d_{\mathrm{ref}}^2}{\Gamma(5/2-\omega)}\left(\frac{4kT_{\mathrm{ref}}}{\mathrm{m}}\right)^{\omega-1/2}. \tag{4.9}$$

Substituting Eq. (4.9) into Eq. (4.8), the dynamic viscosity of the gas is obtained as

$$\mu = \frac{60\sqrt{mk}\sqrt{T_{\mathrm{ref}}}}{(7-2\omega)(5-2\omega)\sqrt{\pi}d_{\mathrm{ref}}^2}\left(\frac{T}{T_{\mathrm{ref}}}\right)^{\omega}. \tag{4.10}$$

Equations (4.7) and (4.10) indicate that for a given temperature, the mean free path and the dynamic viscosity of the gas molecules are dependent on the reference diameter, the number density and the molecular mass.

The third assumption ensures that the mean free path and the dynamic viscosity of the 'big molecule' are similar to those of the actual molecules in both the value and the function relationships, which depend on the mass and reference diameter. From Eqs. (4.7) and (4.10), the reference diameter and the number density

of the 'big molecule' can be written as

$$d_{\mathrm{b,ref}} = \alpha^{1/4} d_{\mathrm{ref}} \tag{4.11}$$

$$n_{\mathrm{b}} = \frac{n}{\sqrt{\alpha}}. \tag{4.12}$$

Substituting Eqs. (4.5), (4.11) and (4.12) into Eqs. (4.7) and (4.10), we obtain

$$\lambda = \frac{1}{\sqrt{2}\pi d_{\mathrm{ref}}^2 n}\left(\frac{T}{T_{\mathrm{ref}}}\right)^{\omega-1/2} = \frac{1}{\sqrt{2}\pi d_{\mathrm{b,ref}}^2 n_{\mathrm{b}}}\left(\frac{T}{T_{\mathrm{ref}}}\right)^{\omega-1/2} = \lambda_{\mathrm{b}} \tag{4.13}$$

$$\mu = \frac{60\sqrt{mk}\sqrt{T_{\mathrm{ref}}}}{(7-2\omega)(5-2\omega)\sqrt{\pi}d_{\mathrm{ref}}^2}\left(\frac{T}{T_{\mathrm{ref}}}\right)^{\omega} = \frac{60\sqrt{m_{\mathrm{b}}k}\sqrt{T_{\mathrm{ref}}}}{(7-2\omega)(5-2\omega)\sqrt{\pi}d_{\mathrm{b,ref}}^2}\left(\frac{T}{T_{\mathrm{ref}}}\right)^{\omega} = \mu_{\mathrm{b}} \tag{4.14}$$

where λ_{b} and μ_{b} are respectively the mean free path and the dynamic viscosity of the 'big molecules'.

4.2.1.2. *A Discussion on the Macro Quantities*

Equation (4.12) indicates that the number density of the 'big molecule' is equal to that of the real molecule divided by $\sqrt{\alpha}$ rather than α even though the mass of a 'big molecule' is α times that of a real molecule. Hence, the present 'big molecule' should be regarded here as a virtual molecule by which the statistical error in numerical simulation may be decreased. It is different from a single real large molecule of the same mass. If the number density of the 'big molecule', n_b, is determined simply through the number density of the real molecules divided by α, then the mean free path and the dynamic viscosity of the 'big molecules' will be different from those of the real molecules, and the physical features of flow field described by these 'big molecules' will then be different from those described by the actual real molecules.

After obtaining the mass and number density of the 'big molecule', the macroscopic density of the gas can be calculated by

$$\rho = \frac{n_{\mathrm{b}} m_{\mathrm{b}}}{\sqrt{\alpha}}. \tag{4.15}$$

Similarly, the other physical quantities of the gas flow can also be expressed through the features of the 'big molecule', such as the stream velocity

$$\mathbf{V}_0 = \bar{\mathbf{V}}_b \tag{4.16}$$

where the overbar denotes the statistical mean. From the second assumption, the thermal velocity of a ‘big molecule’ can be written as

$$\mathbf{V}'_\mathrm{b} \propto \sqrt{\frac{2kT}{m_\mathrm{b}}} \tag{4.17}$$

and from Eq. (4.2), we have

$$\mathbf{V}'_\mathrm{b} = \frac{\mathbf{V}'}{\sqrt{\alpha}}. \tag{4.18}$$

According to the definitions of the temperature and the stress tensor in molecular gas dynamics

$$T = \frac{m}{3k}\overline{(\mathbf{V}')^2} = \frac{m_\mathrm{b}}{3k}\overline{(\mathbf{V}'_\mathrm{b})^2} \tag{4.19}$$

$$\vec{P} = nm\overline{\mathbf{V}'\mathbf{V}'} = \sqrt{\alpha}n_\mathrm{b}m_\mathrm{b}\overline{\mathbf{V}'_\mathrm{b}\mathbf{V}'_\mathrm{b}} \tag{4.20}$$

As the statistical error of stream velocity is equal to the non-zero mean thermal velocity of the samples, Eq. (4.18) thus indicates that in the case of the same sample size, the statistical error $\delta \mathrm{V}_{0,b}$ of the molecular block model will be smaller than that of the real molecular model $\delta \mathrm{V}_0$

$$\delta\mathbf{V}_{0,\mathrm{b}} = \frac{\delta\mathbf{V}_0}{\sqrt{\alpha}} \propto \frac{1}{\sqrt{\alpha}}\sqrt{\frac{2kT}{m}} \tag{4.21}$$

This implies that if 100 real molecules are taken as a molecular block, the corresponding statistical error will reduce by 90%.

4.2.1.3. *Molecular Block DSMC Algorithm*

In the original DSMC method, the particles tracked in the simulation process form the representation of the gas molecules. Each representation has the same mass and reference diameter as the real molecule. We have discussed in the previous section that the real molecules can be replaced by molecular blocks (or virtual ‘big molecules’) under certain assumed conditions. The various formulae expressed through the molecular blocks, such as Eq. (4.15) for the density, Eq. (4.16) for the stream velocity, Eq. (4.19) for the temperature, and Eq. (4.20) for the stress, remain unchanged in form except that there are now factors of $1/\sqrt{\alpha}$ and α in Eqs. (4.15) and (4.20), respectively. According to the present model, a molecular block DSMC (or MB-DSMC) method can thus be easily formulated by using these molecular blocks to replace the particles in the original DSMC method. In fact, the steps of the MB-DSMC method are similar to those of the original DSMC method with the exception of a few modifications.

In the first modification, the number of real molecules, α, in a molecular block must be determined before performing the DSMC computation. If we wish to reduce the statistical error of the original DSMC method by 90%, α can be taken as 100. After deciding on α, the molecular mass, reference diameter and number density parameters (m, d and n) in the original DSMC code must be replaced by $m_{\rm b}$, $d_{\rm b,ref}$ and n_b which have been respectively defined in Eqs. (4.5), (4.10) and (4.12). In the second modification, the original time step should also be modified. The present time step is determined by the following equation

$$\Delta t = \frac{\Delta x}{\sqrt{2kT_{\rm c}/m}} \tag{4.22}$$

where Δx denotes the cell width and T_c is the characteristic temperature of the flow field. This time step is larger than that used in the original DSMC method.

In the DSMC method, the macroscopic physical quantities in a cell are derived by taking the various statistical mean values of the samples. These samples are the instantaneous velocities of simulated particles in the cell obtained at different time steps. If the time step is too large, the particles and their velocities will change too fast in one time step, and this will result in large scattering in the distribution of the samples in velocity space, causing large statistical scatter and computational errors. If the time step is too small, both the collision pairs inside each cell and the number of particles entering and leaving the cell will be deduced in one time step leading to a higher degree of correlation among the samples. Bird[2] has suggested that the flow be sampled after every four time steps and that each time step is taken to be 25% of the cell width divided by the typical particle velocity. As the thermal velocity of the molecular block is less than the molecular thermal velocity, the present time step can thus be longer.

The choice of the collision pairs of particles in a cell has a direct effect on the results as the sample size of the DSMC method in the cell is the sum of particles in the finite number of time steps. For the present MB-DSMC method, according to the "no-time-counter" (NTC) scheme proposed by Bird,[2] the probable collision pairs in the cell in one time step is

$$S_{\rm p} = \frac{\sqrt{\alpha}}{2}\overline{N_{\rm b}}N_{\rm b}F_{\rm Nb}(\sigma_{\rm T,b}V_{\rm r,b})_{\max}\frac{\Delta t}{V_{\rm c}} \tag{4.23}$$

where $\sigma_{\rm T,b}$ and $V_{\rm r,b}$ are the collision area and relative speed between two molecular blocks. The volume of the cell is denoted by $V_{\rm c}$ and $N_{\rm b}$ denotes the number of simulated molecular blocks in the cell, and each simulated molecular block represents $F_{\rm Nb}$ molecular blocks. Finally, in the present method, in place of the original DSMC equations, Eqs. (4.15), (4.19) and (4.20) must now be used instead to calculate the density, temperature and stress of the gas.

It can be seen from this discussion that the computational source code for the present MB-DSMC method can be easily obtained by making very simple modifications to the original DSMC code. As the primary steps are similar, the CPU time required by the MB-DSMC method is almost the same as that of the original DSMC method.

4.2.2. *MB-DSMC Simulation Results for Gaseous Flows*

The preceding discussions indicate that although there is fundamentally no major difference between the present algorithm and the original one, the statistical error of the stream velocity with the present algorithm decreases significantly while the mean free path and the dynamic viscosity remain unchanged. On the other hand, the present method is also able to simulate the heat transfer characteristics. As the MB-DSMC method is based on the three assumed conditions mentioned earlier, it is important to check their correctness.

For these verifications, a micro Couette flow, a micro plane Poiseuille flow and the heat transfer between two plates (see Fig. 4.1) are simulated using both the MB-DSMC and original DSMC methods, and the results are then compared.[31] For the one-dimensional micro Couette flow and heat transfer without convection, the two plates are taken to be 1 μm apart, and the computational flow domain is divided into 100 cells. For the micro Poiseuille flow between two plates, the domain size is 1 μm $\times$ 20 μm and is divided into 25 $\times$ 500 cells. The gases used here are monatomic, such as argon, krypton and helium.

4.2.2.1. *Decrease in Statistical Error*

Figures 4.2, 4.3 and 4.4 show respectively the comparisons of the velocity distributions of the Couette flows for three different gases (xenon, argon and helium), obtained by the analytical solution, the original DSMC method and the MB-DSMC method using different numbers of molecules in the molecular block.[31] The results are obtained under the condition that the temperature of the two plates is constant at 295 K. The sample size used is taken to be 2×10^6 for both the MB-DSMC and the original DSMC methods. As the characteristic velocity is small (2 m/s), which also implies that the Mach number is very low (less than 0.006), the effects of the change of stream velocity on the temperature field is thus small and the temperature in the gas flow can therefore be assumed to be constant. In this case, the exact solutions of velocity distributions can be obtained using Navier–Stokes equations with consideration for velocity slip boundary conditions. The slip velocity condition used here is of the form presented by Pan *et al.*[32]

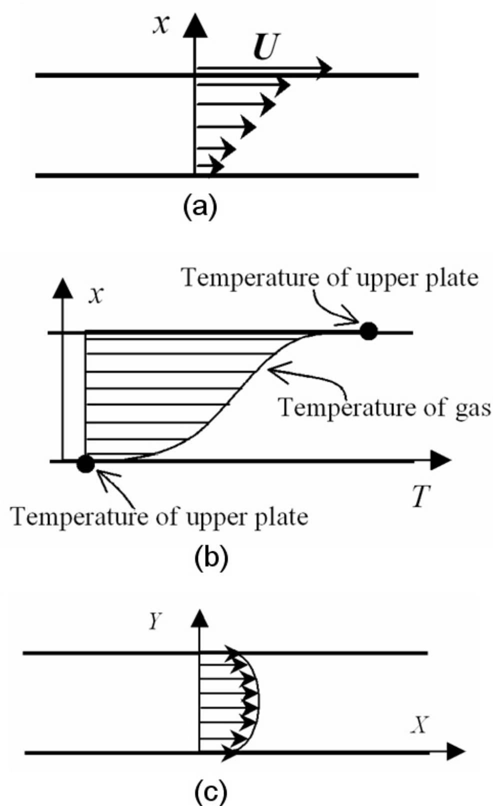

Fig. 4.1. The three cases studied: (a) micro-Couette flow; (b) temperature distribution in micro-channel; and (c) micro-Poiseuille flow.

It is clearly observed from Figs. 4.2 to 4.4 that the statistical error of the velocity from the original DSMC method is so large compared to the practical stream velocity values (from analytical solution) that the numerical signal almost loses all its physical meaning. For the present method, when α is taken as 25, the decrease in the statistical error is immediately obvious. With the increase of α to 100, the velocity distribution curves come very close to those of the exact solutions for all three the three gases considered. As α is further increased to 1000, the numerical solutions are almost coincident with the exact solutions on all the grid nodes. These results verify the error prediction of Eq. (4.21), namely that when a molecular block contains α real molecules, the statistical error of the stream velocity will be reduced by $1/\sqrt{\alpha}$.

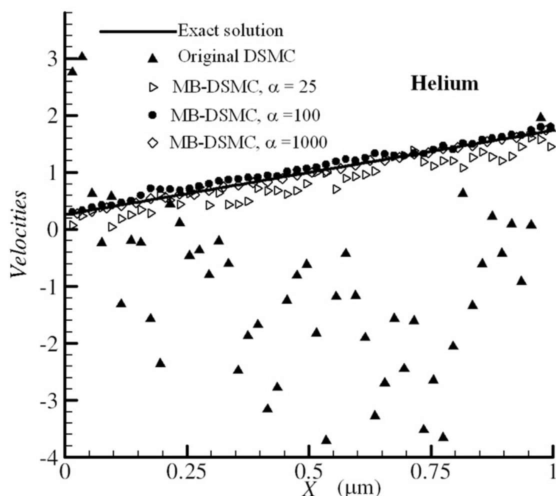

Fig. 4.2. Velocity distribution for helium – a comparison.

From the perspective of reducing the statistical error of the velocity, it would seem good to employ a very large value of α when applying the MB-DSMC method. However, we find that as α is increased to 1000 and beyond, the precision of the velocity does not improve further. It is thus not necessary to employ a very large value of α in the MB-DSMC method, and the present numerical simulations show that a good choice for α to be set at is around 100.

4.2.2.2. *Consistency of the Mean Free Path*

Equation (4.13) indicates that the mean free path of a molecular block must be equal to that of a real molecule. This is very important for ensuring that the numerical analysis is capable of correctly describing the slip feature of the real gas velocity on the wall. As Eq. (4.13) is based on the principles of molecular gas dynamics as well as the three assumptions of the molecular block model, it becomes necessary to verify the consistency or constancy of the mean free path obtained by the MB-DSMC method. Based on the theory of molecular gas dynamics, the mean free path of a molecule is defined as the mean thermal speed of the molecule divided by the mean collision frequency. If this definition is explicitly used to carry out the verification, the computational effort will be extremely large because of the need to calculate the statistical mean thermal speed and the average collision frequency of a molecule under a few scenarios. Fortunately, instead of this form of direct verification, an indirect way can be used.

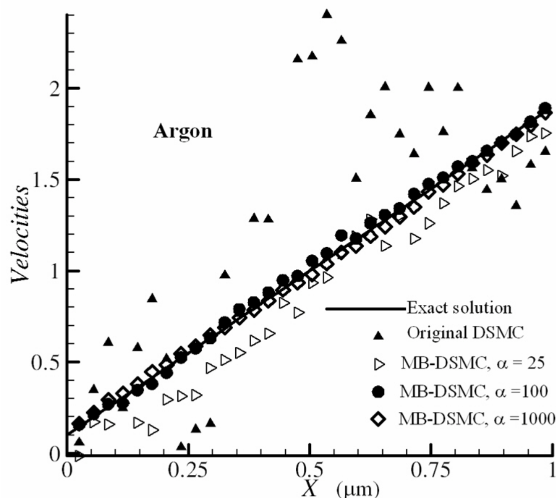

Fig. 4.3. Velocity distribution for argon – a comparison.

As the slip boundary condition of the velocity is a linear function of the mean free path of the molecules (Pan *et al.*[32]), the exact solutions obtained from solving the Navier–Stokes equations with this condition will correspondingly change with the mean free path a well. Therefore, if the mean free path of the molecular block model is not equal to that of real molecule model, the velocity distribution curves obtained by the MB-DSMC method will deviate from the lines described by the exact solutions. Figures 4.2 to 4.4 show that when α is large enough ($\alpha \geq 100$), the velocity distributions from the present method, for all the three gases considered, are very close to the exact solutions. This is a clear indication that the MB-DSMC method established here does not alter the mean free path of the real molecules.

For the discrepancy of the velocity distributions from the exact solutions in the case of low α, this can be mainly attributed to the statistical error originating from the MB-DSMC method. Close examination of the MB-DSMC method with the DSMC method will reveal that the latter is a special case of the former, with $\alpha = 1$. Hence, as α decreases, the statistical error of the velocity computed by the MB-DSMC method increases. In fact, it can be observed from Figs. 4.2 to 4.4 that the results from the original DSMC method display quite large discrepancies relative to the exact solutions. Thus, the discrepancy of the velocity distributions in the case of low α does not imply that the mean free path of a molecular block deviates from that of a real molecule.

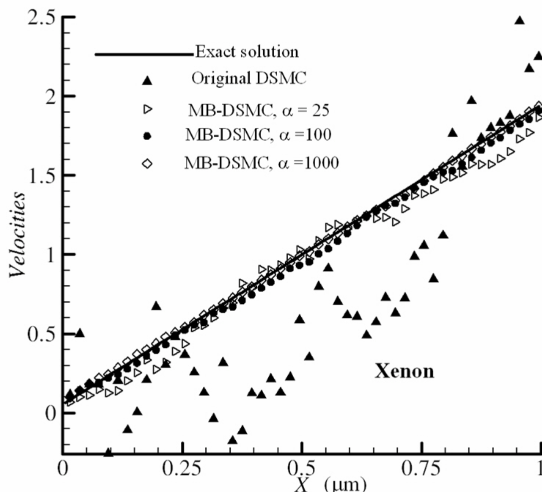

Fig. 4.4. Velocity distribution for xenon – a comparison.

4.2.2.3. *Consistency of the Dynamic Viscosity*

Analytical solutions for the pressure distribution of micro Poiseuille flow along a micro-channel have been obtained by Arkilic *et al.*[33] using the dimensional analysis and perturbation calculus methods. This pressure distribution is related to the inlet and outlet pressures and, by means of the same analysis, one can deduce the pressure distribution corresponding to a given average inlet velocity and inlet pressure as

$$\frac{p}{p_{\mathrm{i}}} = -6\sigma\frac{\lambda_{\mathrm{i}}}{H} + \sqrt{\left(1 + 6\sigma\frac{\lambda_{\mathrm{i}}}{H}\right)^2 - \frac{24\mu\overline{U_{\mathrm{i}}}}{p_{\mathrm{i}}H}\frac{x}{H}} \tag{4.24}$$

where p and p_i are the respective pressures at x and the inlet, μ is the dynamic viscosity, λ_i and $\overline{U_{\mathrm{i}}}$ the mean free path and the average velocity of the gas molecules at the inlet, H the height of the channel, and σ the coefficient equal to 1.1254 (Pan *et al.*[32]).

To verify the consistency or constancy of the dynamic viscosity of the present model and method, the micro Poiseuille flow for argon is simulated using both the MB-DSMC and the original DSMC methods, and the results are plotted in Fig. 4.5. It can be observed that though the pressure distributions obtained by the two numerical methods are different, the differences between them are very

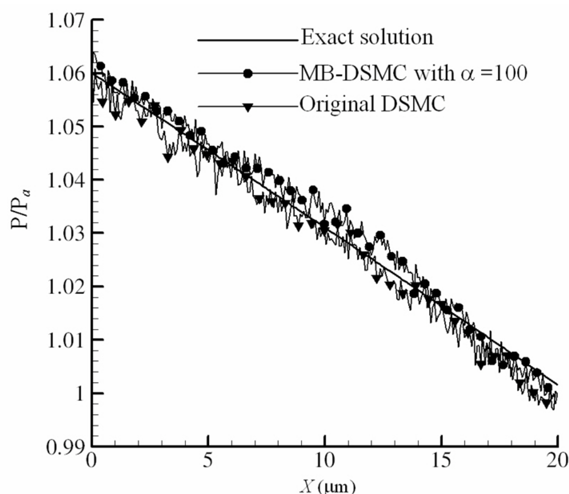

Fig. 4.5. Pressure distribution in micro-Poiseuille flow – a comparison.

small. The pressure losses obtained from the two numerical methods are slightly higher than that of the analytical solution, and this is probably due to the neglect of higher-order terms in Eq. (4.24) in the analytical dimensional analysis. The comparison of these three sets of results indicates that the present molecular block methodology does not alter the dynamic viscosity of gas.

However, Fig. 4.5 also reveals that the pressure distribution along a micro-channel is almost linear even though Eq. (4.24) describes the nonlinear relationship of the pressure with x. It indicates that in the case of very low speed, the constant pressure gradient can still serve as a good approximation for micro-channel slip flow. Physically, this may be due to the rarefaction of gas which neutralizes its compressibility. The nonlinear feature of the pressure change of slip flow through a micro-channel thus presents itself noticeably only in cases of high stream velocities.

4.2.2.4. *Validation of Temperature Field Simulation*

In many microdevices, heat transfer is a primary physical phenomenon of concern. Theoretically, the MB-DSMC method can be used to simulate this physical phenomenon because no requirement has been made for the temperature of the gas in the process of formulating this method, and the computational steps are in fact almost the same as those of the original DSMC method. However, as the 'big molecule' model is not the actual molecular model, we have to check whether

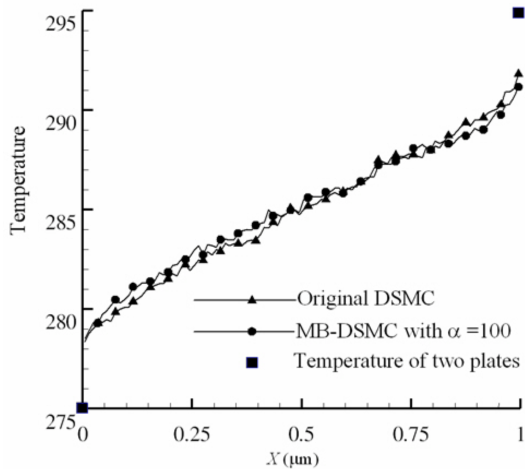

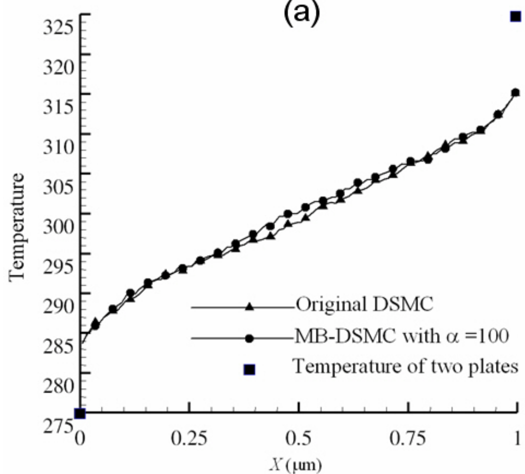

Fig. 4.6. A comparison of temperature distribution (for argon) between two plates by the MB-DSMC method and the original DSMC method, with plate temperature differences of (a) -20°C; and (b) -50°C.

any discrepancy arises between the temperature fields obtained by both these methods.

Figure 4.6 shows the temperature distributions of argon between two infinitely long plates obtained by the MB-DSMC and the original DSMC methods.[31] As the

plates are infinitely long, the convection of the gas is not considered. In Fig. 4.6(a), the temperatures of the two plates are 275°C and 295°C, while the corresponding temperatures for Fig. 4.6(b) are 275°C and 325°C. It can be clearly observed that the temperature jumps between the gas and the wall computed by the two methods are very similar, both qualitatively and quantitatively. The temperature distributions in both cases obtained by the two methods are both nonlinear, especially near the plates. Although the temperature distribution curves by the two methods do not exactly coincide with each other, the discrepancy between them is very small.

Thus, for the simulation of the temperature field, it can be inferred that the MB-DSMC method has similar accuracy as the original DSMC method.

4.2.3. *Conclusion*

Conventional DSMC methods can incur large statistical errors for low-speed gas flows. In most micro-devices, the gas flows are indeed of low velocity ($<$3 m/s) and it was thus necessary that some modifications be made to the conventional DSMC method for this range of velocities.

In this section, a molecular block, or ‘big molecule’ model, is developed to replace the actual molecular model. The mass of the ‘big molecule’ is the sum of the actual mass of molecules contained within this molecular block, while the reference diameter and the number density of the ‘big molecule’ are determined through conditions that the mean free path and the dynamic viscosity of the ‘big molecule’ are similar to those of the actual molecules. The form of the formulae used for calculating the stress and density of gas flow in this new model are similar to those in the real molecular model, and differences are only due to a constant coefficient. For temperature calculations, the formula remains unchanged.

These molecular blocks were then used to replace the particles in the DSMC method, and a MB-DSMC method, the computational process of which remains largely unchanged, was formulated. As the mass of the molecular block is larger, the statistical error of the MB-DSMC method tends to be significantly smaller. In fact, present numerical verifications have shown that when the molecular number in a molecular block is taken to be 100, the obtained velocity and pressure distributions are in excellent agreement with the exact solutions, while the statistical errors have reduced by 90%. In addition, simulations of the temperature field revealed that the MB-DSMC method has similar accuracy as the original DSMC method.

4.3. Modeling and Simulation of Liquid Micro-Flow

4.3.1. *A Modified One-Equation Model for Micro-Scale Liquid Flow*

In tensor notation, the incompressible, two-dimensional, steady, time-averaged Navier–Stokes equations of momentum and continuity of fluid flow are

$$u_{\mathrm{j}}\frac{\partial u_{\mathrm{i}}}{\partial x_{\mathrm{j}}} = -\frac{\partial}{\rho\partial x_{\mathrm{i}}}\left(p+\frac{2}{3}\rho k\right)+\frac{\partial}{\partial x_{\mathrm{j}}}\left[(\nu+\nu_{\mathrm{t}})\left(\frac{\partial u_{\mathrm{i}}}{\partial x_{\mathrm{j}}}+\frac{\partial u_{\mathrm{j}}}{\partial x_{\mathrm{i}}}\right)\right] \tag{4.25}$$

$$\frac{\partial u_{\mathrm{i}}}{\partial x_{\mathrm{i}}} = 0 \tag{4.26}$$

where u_i is the velocity component, k the turbulent kinetic energy, p the pressure, ρ the density; ν the kinematic viscosity and ν_t the turbulent kinematic viscosity, which is determined from the turbulence model.

Wolfshtein's one-equation turbulence model[26] is developed from conventional fluid mechanics and is widely used in macro-flow applications. Considering its ability to handle internal flow, this one-equation turbulence model is adopted for the present study on flows in micro-tubes. However, the model has been modified to cater for micro-flow characteristics.

The turbulent kinetic energy k is obtained from the modeled kinetic energy transport equation

$$u_{\mathrm{i}}\frac{\partial k}{\partial x_{\mathrm{i}}} = \nu_{\mathrm{t}}\frac{\partial u_{\mathrm{i}}}{\partial x_{\mathrm{j}}}\left(\frac{\partial u_{\mathrm{i}}}{\partial x_{\mathrm{j}}}+\frac{\partial u_{\mathrm{j}}}{\partial x_{\mathrm{i}}}\right)+\frac{\partial}{\partial x_{\mathrm{i}}}\left[\left(\nu+\frac{\nu_{\mathrm{t}}}{\sigma_{\mathrm{k}}}\right)\frac{\partial k}{\partial x_{\mathrm{i}}}\right]-\varepsilon \tag{4.27}$$

where ε is the dissipation rate of turbulent kinetic energy and

$$\nu_{\mathrm{t}} = C_\mu k^{1/2} l_\mu \tag{4.28}$$

$$\varepsilon = C_{\mathrm{D}} k^{3/2}/l_{\mathrm{D}} \tag{4.29}$$

$$l_\mu = C_{\mathrm{l}} y[1.0-\exp(-A_\mu R_{\mathrm{y}})] \tag{4.30}$$

$$l_{\mathrm{D}} = C_{\mathrm{l}} y[1.0-\exp(-A_{\mathrm{D}} R_{\mathrm{y}})] \tag{4.31}$$

$$R_{\mathrm{y}} = k^{1/2} y/\nu \tag{4.32}$$

where $C_\mu = 0.09$, $C_{\mathrm{l}} = \kappa C_\mu^{-3/4}$, $\kappa = 0.42$, $C_{\mathrm{D}} = 1.0$, $A_{\mathrm{D}} = 0.2$, y denotes the vertical distance to the wall.[26]

In the original Wolfshtein macro-flow model, A_μ is a constant value of 0.014. However, in micro-tubes, it is found that with the decrease of the tube diameter, A_μ departs from its macro-flow value. For micro tubes with diameters less than 100 μm, A_μ has a constant value of 0.004; while for those with diameters larger

than 130 μm, A_μ recovers its value of 0.014. For those diameters between 100 and 130 μm, A_μ can be interpolated, see Fig. 4.7. More experimental measurements in the transit region between 100 and 130 μm are required in order to obtain a more accurate formula for this region.

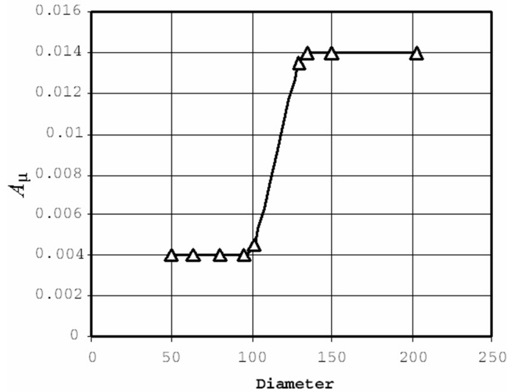

Fig. 4.7. Variation of A_μ with micro tube diameter.

From the variation of A_μ with the micro-tube diameter, it may be concluded that the micro-flow effect should be considered for micro-tubes with diameters less than 130 μm.

For a two-dimensional steady flow, the momentum equation, Eq. (4.25), the continuum equation, Eq. (4.26), and the kinetic energy transport equation, Eq. (4.27) can be written as

$$\frac{\partial}{\partial x_{\mathrm{j}}}(u_{\mathrm{j}}\varphi) = \frac{\partial}{\partial x_{\mathrm{j}}}\left(\Gamma_\varphi \frac{\partial \varphi}{\partial x_{\mathrm{j}}}\right) + S_\varphi \tag{4.33}$$

where u_j is the velocity component and φ is a general dependent variable, which stands for *u*, *v* and *k* respectively. Γ_φ is the diffusive coefficient and S_φ represents all source terms which cannot be expressed as either convection or diffusion. Using the control volume technique, Eq. (4.33) is integrated over a control volume, *V*

$$\oint\int_V \left[\frac{\partial}{\partial x}(u\varphi) - \frac{\partial}{\partial x}\left(\Gamma_\varphi \frac{\partial \varphi}{\partial x}\right) + \frac{\partial}{\partial y}(v\varphi) - \frac{\partial}{\partial y}\left(\Gamma_\varphi \frac{\partial \varphi}{\partial y}\right)\right] \mathrm{d}V = \oint\int_V S_\varphi \mathrm{d}V. \tag{4.34}$$

Applying Gauss' theorem, the volume integral on the left-hand side is expressed in terms of a surface integral and Eq. (4.34) can be rewritten as

$$F_{\rm e} - F_{\rm w} + F_{\rm n} - F_{\rm s} = \bar{S}_\varphi \cdot \Delta V \tag{4.35}$$

where the subscripts *e*, *w*, *n* and *s* indicate the eastern, western, northern and southern faces of the control volume, respectively. With the approximations for convection, diffusion and the source terms, Eq. (4.35) can now be rearranged as[27,28]

$$\sum_{\rm i} \alpha_{\rm i}^\varphi \varphi_{\rm P} = \sum_{\rm i} \alpha_{\rm i}^\varphi \varphi_{\rm i} + S_U^\varphi \tag{4.36}$$

where the α_i^φ are coefficients and

$$\alpha_{\rm P}^\varphi = \sum_{\rm i} \alpha_{\rm i}^\varphi - S_{\rm P}^\varphi \tag{4.37}$$

Equation (4.36) can be easily solved by a 'line-by-line' iterative method, and the present work adopts the SIMPLE (semi-implicit method for pressure-linked equations) algorithm[29] to calculate the pressure field.

The iterative solution is considered to have converged when the sum of the normalized absolute residuals across all nodes is less than a prescribed small value ε

$$\sum \left| \frac{\varphi_{\rm i.j}^{\rm n} - \varphi_{\rm i.j}^{\rm n-1}}{\varphi_{\rm in}} \right| < \varepsilon \tag{4.38}$$

where $\varphi_{\rm in}$ is the value of the variable at the inlet boundary. In the present computations, ε is set at 1.0×10^{-6}.

4.3.2. *Simulation Results for Liquid Flow in Micro-Tubes*

The grid independence of the results were first examined before further calculations were carried out. Fully developed laminar flows in a circular tube with diameter *d* and calculation domain of $d \times 10d$ were repeatedly calculated with different grid distributions and grid numbers. The numerical results were compared with the analytical solution of laminar flow in a circular pipe

$$u(r) = -\frac{1}{4\mu}\frac{{\rm d}p}{{\rm d}x}\left(\frac{d^2}{4} - r^2\right) \tag{4.39}$$

It was found that a 30$\times$5 grid provides very good accuracy with velocity errors of less than 0.01% for laminar liquid flow.

Following the grid independence test of laminar liquid flow, a grid independence test for turbulent liquid flow calculations was also carried out. The final grid chosen for turbulent flow calculations was 50$\times$5, as depicted in Fig. 4.8. Due

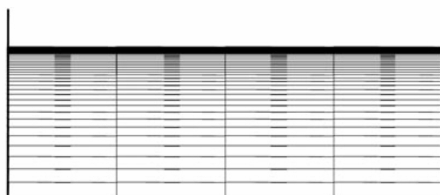

Fig. 4.8. A 50×5 grid system.

to the axisymmetric geometric feature, only half of the domain is meshed and calculated. It should be noted that more grid lines are distributed near the solid wall of the micro tube in order to capture the expected rapid change or much steeper gradient of the flow field. It should also be pointed out that the present calculation is performed for fully developed flow and periodic boundary conditions are defined on the inlet and outlet boundaries, and it is therefore more than sufficient to use five nodes along the flow direction. In this study, the Re range considered is $1000 - 2000$. In addition, a non-slip velocity boundary condition is used on the wall, and a symmetric boundary condition is applied about the axis.

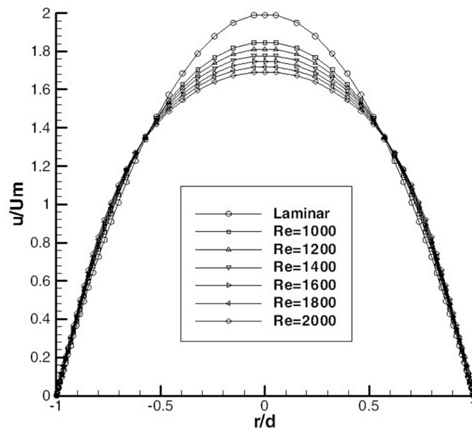

Fig. 4.9. The cross-sectional velocity profile, d=50 μm.

The cross-sectional velocity profiles, *u* (normalized by the mean velocity, u_m), of turbulent flows in micro-tubes of diameters 50, 63.5, 80, 101, 130 and 254 μm are plotted in Figs. 4.9 to 4.14 for various Re values, together with the analytical solutions of the laminar liquid flow.[30] It is clearly observed that at lower Re

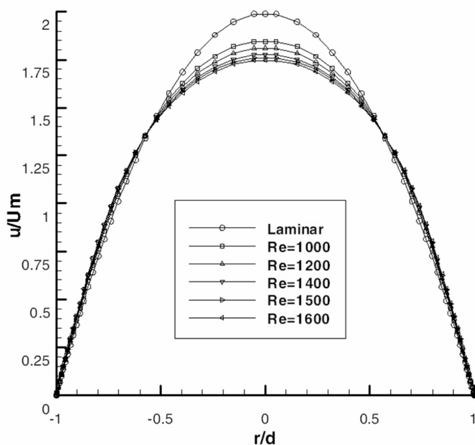

Fig. 4.10. The cross-sectional velocity profile, d=63.5 μm.

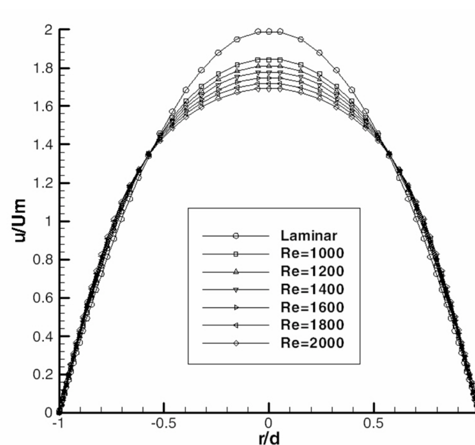

Fig. 4.11. The cross-sectional velocity profile, d=80 μm.

values, the velocity profiles of turbulent flow are very close to the laminar flow velocity profile. This is probably because the turbulence intensity is low at low Re values. However, with the increases of Re, the velocity distributions become much flatter, approaching those of typical velocity profiles of the high Re turbulent flows. This phenomenon is similar to the flow characteristics observed in macro-tube flows. Comparing these six figures, it also noted that, at the same Re value,

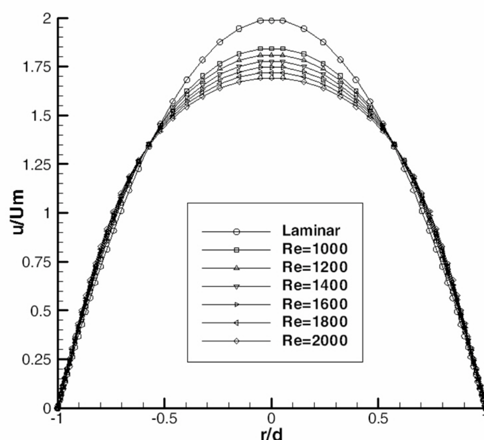

Fig. 4.12. The cross-sectional velocity profile, d=101 μm.

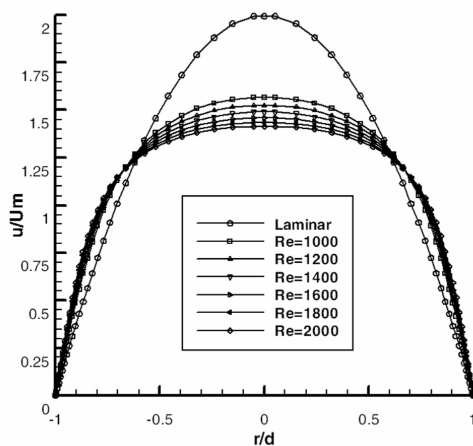

Fig. 4.13. The cross-sectional velocity profile, d=130 μm.

a flat velocity distribution is formed much earlier in the micro-tube with a larger diameter than that with a smaller one.

Figures 4.15 to 4.20 show the cross-sectional profiles of the non-dimensional turbulent kinetic energy, k/U_m^2, of the micro-tube at various Re values and diameters.[30] The values of the turbulent kinetic energy of a relatively larger micro-tube

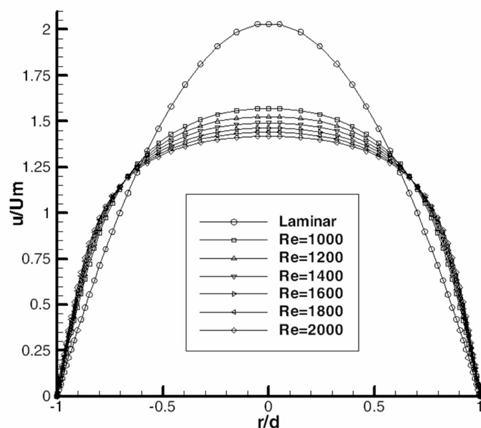

Fig. 4.14. The cross-sectional velocity profile, d=254 μm.

(d = 130 μm or d = 254 μm) are much higher than those of smaller micro-tubes at the same Re value. This implies that a smaller micro-tube has a lower turbulence value at the same Re value even though its transition from laminar to turbulent flow occurs earlier than that of a macro-scale tube. Thus, the smaller the diameter of the tube, the lower the turbulent kinetic energy, at the same Re value. Comparing these six figures, it can be observed that there are differences in the turbulent kinetic energy distribution at the near-wall region. For the smaller tubes, from the wall to the axis, the turbulent kinetic energy starts from zero but increases extremely steeply to its first maximum value at a position still very near the wall. It reaches its second maximum value at $r/d \approx 0.5$. The first maximum value is significantly higher than the second maximum value. However, for the relatively larger tubes (d = 130 μm and d = 254 μm), at high Reynolds numbers, the first maximum value near the wall is significantly lower than the second maximum value. Furthermore, the second maximum value is reached at $r/d \approx 0.8$. In the cases considered, the turbulent kinetic energy drops to its lowest value at the centre of the tube. This trend is similar to that observed in macro-tube turbulent flows.

The pressure gradient along the micro-tube can be calculated in a straightforward manner from $\mathrm{d}p/\mathrm{d}l = -(p_{\mathrm{in}} - p_{\mathrm{out}})/l$, where p_{in} is the pressure at the inlet section, p_{out} the pressure at the outlet section, and l the length of micro-tube. Figure 4.21 compares the present predictions with the experimental measurements[23] against Re for various micro-tube diameters. It can be clearly observed that as

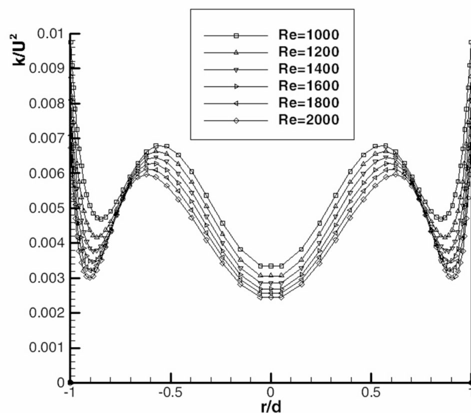

Fig. 4.15. The turbulent kinetic energy profile, d=50 μm.

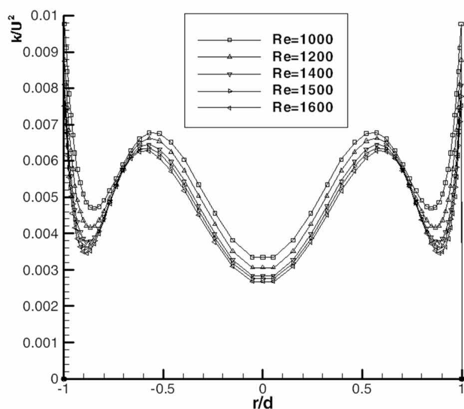

Fig. 4.16. The turbulent kinetic energy profile, d=63.5 μm.

Re increases, the pressure gradient steadily increases in an almost linear manner. It can be seen that the present predictions are in good agreement with the experimental measurements.[23] From these comparisons of the numerical results, we may deduce that the present refined one-equation turbulent model, with its modifications, is suitable for turbulent flow calculation in micro-tubes, and can provide very good predictions.

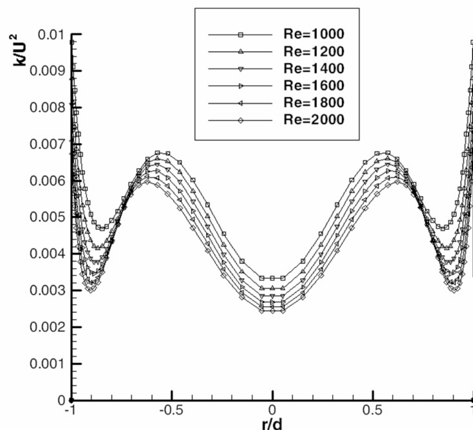

Fig. 4.17. The turbulent kinetic energy profile, d=80 μm.

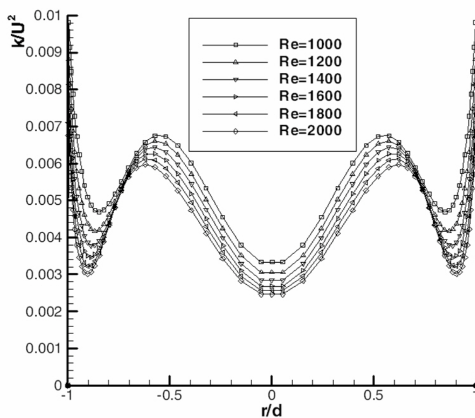

Fig. 4.18. The turbulent kinetic energy profile, d=101 μm.

4.3.3. *Conclusions*

In this section, fully developed turbulent liquid flow in micro-tubes at various Reynolds numbers and micro tube diameters are numerically simulated using the control volume method with a modified one-equation turbulence model, and it was found that this refined model can provide a good prediction for turbulent flows of water in micro-tubes.

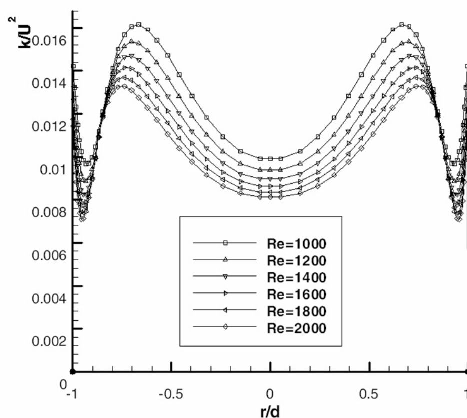

Fig. 4.19. The turbulent kinetic energy profile, d=130 μm.

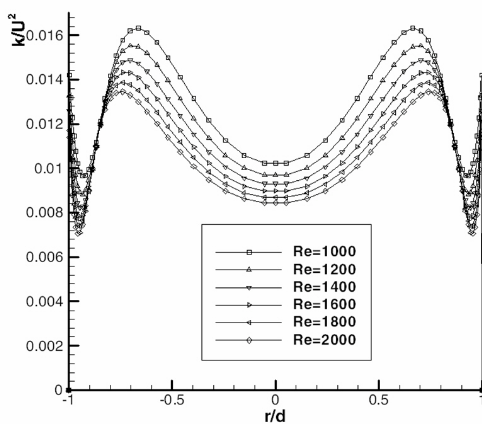

Fig. 4.20. The turbulent kinetic energy profile, d=254 μm.

At lower Re values, the cross-sectional velocity profile of turbulent liquid flow is not very different from that of laminar liquid flow. However, with an increase in Re, the velocities gradually approach typical turbulent liquid flow profiles. Micro-tubes with larger diameters have much flatter velocity profiles and higher turbulent values at the same Re value, compared with those tubes with smaller diameters, even though the transition from laminar to turbulent flow occurs earlier in micro-tubes (as compared to macro-scale tubes). In other words, micro-tubes with larger

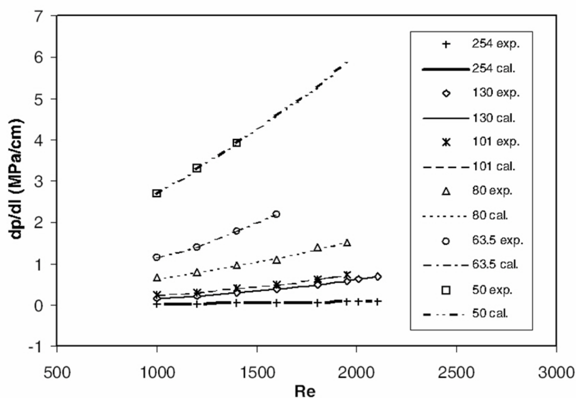

Fig. 4.21. Pressure gradient at different Re values – a comparison with experimental data.[23]

diameters will have much stronger turbulence effect than that those with smaller diameters.

The pressure gradient increases with the Re value. The tubes with smaller diameters require high pressure gradients to maintain the same average velocity. For turbulent flow in micro-tubes with diameters larger than $\sim$130 μm, the flow can be simulated using the conventional one-equation turbulence model; while for turbulent flow in micro-tubes with diameters smaller than $\sim$100 μm, the flow has to be calculated using the modified one-equation turbulence model in order to obtain a good prediction. In other words, micro-flow phenomena should be considered for micro-tubes with diameters smaller than 130 μm.

References

1. G. A. Bird, *Molecular Gas Dynamics*, Clarendon: Oxford (1976).
2. G. A. Bird, *Molecular Gas Dynamics and the Direct Simulation of Gas Flows*, Clarendon: Oxford (1994).
3. A. L. Garcia, *Numerical Methods for Physics*, Prentice-Hall: Englewood Cliffs, NJ (1994).
4. G. A. Bird, Monte Carlo simulation of gas flows. *Annu. Rev. Fluid Mech.*, **10**, 11 (1978).
5. E. P. Muntz, Rarefied gas dynamics. *Annu. Rev. Fluid Mech.*, **21**, 387 (1989).
6. H. K. Cheng, Perspectives on hypersonic viscous flow research. *Annu. Rev. Fluid Mech.*, **25**, 455 (1993).
7. H. K. Cheng and G. Emmanuel, Perspectives on hypersonic nonequilibrium flow. *AIAA J.*, **33**, 385 (1995).

8. E. S. Oran, C. K. Oh and B. Z. Cybyk, Direct simulation Monte Carlo: recent advances and applications. *Annu. Rev. Fluid Mech.*, **30**, 403 (1998).
9. G. A. Bird, Recent advances and current challenges for DSMC. *Comput. Math. Appl.*, **35**, 1 (1998).
10. R. P. Nance, D. B. Hash and H. A. Hassan, Role of boundary conditions in Monte Carlo simulation of MEMS devices. *AIAA* paper 97-0375 (1997).
11. L. S. Pan, G. R. Liu, B. C. Khoo and B. Song, A modified direct simulation Monte Carlo method for low-speed microflows. *J. Micromech. Microeng.*, **10**, 21 (2000).
12. J. Fan and C. Shen, *Statistical Simulation of Low-Speed Unidirectional Flows in Transitional Region*, 21st Int. Symp. on Rarefied Gas Dynamics, Marseille, France (1998).
13. C. P. Cai, I. D. Boyd, J. Fan and G. V. Candler, Direct simulation methods for lowspeed microchannel flows. *AIAA* paper 99-3801 (1999).
14. P. Y. Wu and W. A. Little, Measurement of friction factors for the flow of gases in very fine channels used for microminiature JouleThomson refrigerators. *Cryogenics*, **23**, 273 (1983).
15. P. Y. Wu and W. A. Little, Measurement of heat transfer characteristics of gas flow in fine channel heat exchanger used for microminiature refrigerators. *Cryogenics*, **24**, 415 (1985).
16. D. B. Tuckerman, *Heat Transfer Microstructures for Integrated Circuits*, PhD Thesis, Department of Electrical Engineering, Stanford University, CA (1984).
17. J. Pfahler, J. Harley, H. H. Bau and J. Zemel, Liquid and gas transport in small channels. *Am. Soc. Mech. Eng., Dyn. Sys. Control Div.*, **19**, 149 (1990).
18. J. Pfahler, J. Harley, H. H. Bau and J. Zemel, Gas and liquid flow in small channels. *Am. Soc. Mech. Eng., Dyn. Sys. Control Div.*, **32**, 49 (1991).
19. S. B. Choi, R. R. Baron and R. O. Warrington, Fluid flow and heat transfer in microtubes. *Am. Soc. Mech. Eng., Dyn.. Sys. Control Div.*, **40**, 89 (1991).
20. B. W. Wang and X. F. Peng, Experimental investigation on forced flow convection of liquid flow through microchannels. *Int. J. Heat Mass Transfer*, **37**, 73 (1994).
21. X. F. Peng, G. P. Peterson and B. W. Wang, Heat transfer characteristics of water flowing through microchannels. *Exp. Heat Transfer*, **7**, 265 (1994).
22. X. F. Peng, G. P. Peterson and B. W. Wang, Heat transfer characteristics of water flowing through microchannels. *Exp. Heat Transfer*, **7**, 249 (1994).
23. G. M. Mala and D. Q. Li, Flow characteristics of water in microtubes. *Int. J. Heat Fluid Flow*, **20**, 142 (1999).
24. C. Yang, D. Q. Li and J. H. Masliyah, Modeling forced liquid convection in rectangular microchannels with electrokinetic effects. *Int. J. Heat Mass Transfer*, **41**, 4229 (1998).
25. W. L. Qu, G. M. Mala and D. Q. Li, Pressure-driven water flows in trapezoidal silicon microchannels. *Int. J. Heat Mass Transfer*, **43**, 353 (1999).
26. M. Wolfshtein, The velocity and temperature distribution in one-D flow with turbulence augmentation and pressure gradient. *Int. J. Heat Mass Transfer*, **15**, 1787 (1972).
27. D. Xu, C. Shu and B. C. Khoo, Numerical simulation of flows in Czochralski crystal growth by second-order upwind QUICK scheme. *J. Cryst. Growth*, **173**, 123 (1997).
28. D. Xu, B. C. Khoo and M. A. Leschziner, Numerical simulation of turbulent flow in an axisymmetric diffuser with a curved surface centre-body. *Int. J. Numer. Methods Heat Fluid Flow*, **8**, 245 (1998).

29. S. V. Patankar, *Numerical Heat Transfer and Fluid Flow*, McGraw-Hill: New York (1980).
30. D. Xu, T. Y. Ng, L. S. Pan, K. Y. Lam and H. Li, Numerical simulation of fully developed turbulent liquid flows in micro tubes. *J. Micromech. Microeng.*, **11**, 175 (2001).
31. L. S. Pan, T. Y. Ng, D. Xu and K. Y. Lam, Molecular block model direct simulation Monte Carlo method for low velocity microgas flows. *J. Micromech. Microeng.*, **11**, 181 (2001).
32. L. S. Pan, G. R. Liu and K. Y. Lam, Determination of slip coefficient for rarefied gas flows using direct simulation Monte Carlo. *J. Micromech. Microeng.*, **9**, 89 (1999).
33. E. B. Arkilic, M. A. Schmidt and K. S. Breuer, Gaseous slip flow in long microchannels. *J. Microelectromech. Syst.*, **6**, 167 (1997).

Chapter 5

Evaluating Gas Damping in MEMS Using Fast Integral Equation Solvers

Attilio Frangi

Department of Structural Engineering
Politecnico di Milano, Italy
attilio.frangi@polimi.it

Wenjing Ye

G. W. Woodruff School of Mechanical Engineering
Georgia Institute of Technology, USA

Jacob White

Department of Electric Engineering and Computer Science
and the Research Laboratory of Electronics
Massachusetts Institute of Technology, Cambridge, Massachusetts, USA

Providing an estimate of gas damping in MEMS is a complex task since MEMS are fully three dimensional micro-structures which cannot in general be reduced to simple 1D or 2D models and since the gas cannot be treated as a continuum medium at the microscale. This issue is here addressed, focusing on high pressure applications, by means of Integral Equations and Fast Solvers implementing a linear, quasi-static, incompressible Stokes formulation with slip boundary conditions. The tools developed are applied to the analysis of two inertial sensors: a biaxial accelerometer and an academic Tang resonator. Numerical results are validated with experimental data. Extensions to high working frequencies and low pressures are discussed.

Contents

5.1 Introduction 154
5.2 Classical Quasi-Static Stokes Flow 155
  5.2.1 Governing Equations 155
  5.2.2 Integral Formulation 156
  5.2.3 Null Space Problem 157

5.2.4 Numerical Implementation 158
5.2.5 Fast Solvers 159
5.3 Extension to the Slip Flow Regime and Validation 161
5.3.1 Numerical Results and Comparison with Experiments 163
5.4 Extension to High Frequency Oscillatory Flow 170
5.5 Extension to Low Pressures by Means of the Corrected Viscosity Approach 175
5.6 Conclusions 178
References 178

5.1. Introduction

Estimating mechanical dissipation in air-packaged MEMS (micro-electro-mechanical systems) seems, for several reasons, to be an ideal application for the now maturing fast integral equation methods.[5–7,9–11,14,27,41,46] First, the micromechanical structures, typical examples of which are the the biaxial accelerometer (Fig. 5.2) and the Tang resonator (Fig. 5.8), are innately three-dimensional and too geometrically complicated to analyze analytically. Therefore, a numerical approach is needed. Second, the mechanical dissipation is primarily due to pressure and drag forces generated by the air surrounding the mechanical structure. Hence, even though the exterior domain is effectively infinite in extent, the only quantities of interest are velocities and forces on the structure surface. Surface-only integral equations, if they can be formulated, have a dimensional advantage over volume methods in such a setting. Third, the velocities and displacements for many MEMS of interest are small enough, and the surrounding air is viscous enough, that the flow can be described by a spatially invariant linearization. Therefore, surface-only integral equations can be formulated.

For the above reasons, there have been a number of experimentally-verified successes in evaluating gas damping for air-package MEMS using fast integral equation solvers, though considerable algorithmic development was required.[13,23,24,36,45] Much of the past effort was on improving the efficiency and robustness of quasi-static-Stokes based fast solvers, but now the focus has shifted to addressing more challenging physics. Newer MEMS use higher operating frequencies and finer dimensions, and therefore the effects of unsteady flow, gas compression, and rarefaction can no longer be ignored.

In the next two sections of this chapter, we review many of the issues associated with integral formulation, discretization and fast solution of the incompressible, quasi-static Stokes equations. In Sec. 5.3 the formulation is adapted to slip boundary conditions and validated with the experiments performed on two inertial resonators. Section 5.4 describes methods for including unsteady effects and presents numerical results for a classical Tang resonator. Finally, Sec. 5.5 proposes

a simplified "corrected viscosity" approach for estimating damping at low pressures which proves to be effective for the specific inertial MEMS addressed in this chapter and anticipates an issue discussed at length in Chapter 2.

5.2. Classical Quasi-Static Stokes Flow

The most mature and best validated of the fast solvers for estimating gas damping in MEMS are based on solving integral formulations of the 3D incompressible quasi-static Stokes equations.[13,24,36,45] For quasi-static Stokes to be a good model of the gas surrounding a micromachined structure, the gas should be incompressible, sufficiently viscous, moving slowly, and not be too rarified. This list of assumptions hold, at least loosely, for air-packaged MEMS like arrays of electrostatically positioned micromirrors,[45] inertial sensors like the biaxial accelerometer of Fig. 5.2, and structures like the Tang resonator of Fig. 5.8. In this background section the quasi-static Stokes model is given, and the standard integral formulation and the common numerical discretizations described. In later sections, the quasi-static Stokes assumptions will be revisited, and techniques for extending the model to include the effects of unsteady flow, compression, and rarefaction will be described.

5.2.1. *Governing Equations*

For an isotropic Newtonian fluid, if the fluid velocity, $\mathbf{u}$, is divergence-free, then the relation between $\mathbf{u}$ and the stress tensor, $\boldsymbol{\sigma}$, is given by[47]

$$\boldsymbol{\sigma}(\mathbf{x}) = -p(\mathbf{x})\mathbb{1} + \eta\left(\nabla\mathbf{u}(\mathbf{x}) + \nabla^T\mathbf{u}(\mathbf{x})\right) \tag{5.1}$$

where η is the fluid viscosity and $\nabla\mathbf{u}$ denotes a matrix of velocity partial derivatives whose elements are given by

$$(\nabla\mathbf{u})_{ij} = \frac{\partial u_i}{\partial x_j}.$$

The quasi-static Stokes equations are derived from combining incompressibility, conservation of mass, and conservation of momentum yielding the well-known quasi-static Stokes equations

$$\nabla p(\mathbf{x}) - \eta\Delta\mathbf{u}(\mathbf{x}) = \mathbf{0} \qquad \nabla\cdot\mathbf{u}(\mathbf{x}) = 0 \quad \text{in} \quad \Omega \tag{5.2}$$

where Ω denotes the volume occupied by the fluid.

The standard boundary conditions for the classical quasi-static Stokes equation are no-slip conditions. In a later section, generalizations of the no-slip boundary condition will be used to model rarefaction effects. For the case of several

interacting micromachined structures surrounded by fluid, the no-slip condition implies that for each structure surface point, the fluid velocity must match the structure's velocity. More precisely, for the MEMS problem, the domain of the fluid, Ω, is defined as the domain exterior to the micromachined structures. For each point $\mathbf{x}$ on surface S, where S is defined to be the union the structure surfaces,

$$\mathbf{u}(\mathbf{x}) = \mathbf{g}(\mathbf{x}) \tag{5.3}$$

where $\mathbf{g}(\mathbf{x})$ is the velocity of the micromachined structure at point $\mathbf{x}$. Note also that typically the velocity distant from the micromachined structures is assumed to approach zero. Nonzero background velocities can be treated by perturbation.

Given $\mathbf{u}$ which satisfies Eqs. (5.2) and (5.3), the vector force density the structure exerts on the fluid can be computed from the product of the stress tensor with the surface normal pointing out of Ω. That is, at each structure surface point $\mathbf{x}$,

$$\mathbf{t}(\mathbf{x}) = \boldsymbol{\sigma}(\mathbf{x}) \cdot \mathbf{n}(\mathbf{x})$$

where $\mathbf{n}(\mathbf{x})$ is the surface normal pointing outside the fluid domain. Note that $\mathbf{t}$ is the negative of force per unit area exerted by the fluid on the structure surface. In a modest abuse of terminology, we refer to the vector $\mathbf{t}$ as a traction force density even though it contains components which act in a direction normal to the surface.

5.2.2. *Integral Formulation*

Either Greens identities[34] or Lorentz reciprocity[42] can be used to derive an integral formulation that relates the Stokes flow generated traction forces to the surface velocities. Specifically, if $\mathbf{x}$ is a point on a smooth region of in S,

$$\frac{1}{2}\mathbf{u}(\mathbf{x}) = \int_S \{\boldsymbol{\mathcal{V}}(\mathbf{r}) \cdot \mathbf{t}(\mathbf{y}) - [\boldsymbol{\mathcal{K}}(\mathbf{r}) \cdot \mathbf{n}(\mathbf{y})] \cdot \mathbf{u}(\mathbf{y})\} \, \mathrm{d}S_y \tag{5.4}$$

where $\mathbf{r} \equiv \mathbf{x} - \mathbf{y}$, the kernels (also referred to as Greens functions) $\boldsymbol{\mathcal{V}}$ and $\boldsymbol{\mathcal{K}}$ are given by

$$V_{ik}(\mathbf{r}) = \frac{1}{8\pi\eta}\left(\frac{\delta_{ik}}{r} + \frac{r_i r_k}{r^3}\right)$$

$$K_{iqk}(\mathbf{r}) = -\frac{3}{4\pi}\frac{1}{r^5} r_i r_q r_k \,,$$

and the integrals of the strongly singular kernel, $\boldsymbol{\mathcal{K}}$, should be interpreted in the Cauchy principal value sense. The kernels $\boldsymbol{\mathcal{V}}$ and $\boldsymbol{\mathcal{K}}$ are often interpreted as generating the velocities associated with stokeslet and stresslet point sources,[34] but these kernels also coincide with the Kelvin kernels used in the displacement equation for incompressible elasticity.[17]

Combining the no-slip boundary conditions with Eq. (5.4) yields a first kind integral equation which relates the known structure velocities to the unknown fluid traction forces

$$\frac{1}{2}\mathbf{g}(\mathbf{x}) = \int_S \{\boldsymbol{\mathcal{V}}(\mathbf{r}) \cdot \mathbf{t}(\mathbf{y}) - [\boldsymbol{\mathcal{K}}(\mathbf{r}) \cdot \mathbf{n}(\mathbf{y})] \cdot \mathbf{g}(\mathbf{y})\}\, \mathrm{d}S_y. \tag{5.5}$$

In the common case where the structure velocities correspond to rigid body motion, the second integral in Eq. (5.5) vanishes, resulting in

$$\frac{1}{2}\mathbf{g}(\mathbf{x}) = \int_S \boldsymbol{\mathcal{V}}(\mathbf{r}) \cdot \mathbf{t}(\mathbf{y}) \mathrm{d}S_y. \tag{5.6}$$

The formulation in Eq. (5.6) is common in the literature on integral equations for Stokes flow, but there are alternatives that can have superior properties. For example, the above formulation is a vector integral equation with matrix kernels that are non-diagonal. In two dimensions, more efficient alternatives have appeared.[8] Of more immediate concern is the fact that Eq. (5.6) does not have a unique solution, an issue that will be addressed in the next section.

5.2.3. *Null Space Problem*

The differential form of Stokes equation (5.2) only involves the gradient of the pressure and is therefore insensitive to spatially constant shifts in pressure. Since the pressure is a component of $\mathbf{t}$, and $\mathbf{t}$ is the unknown in Eq. (5.6), Eq. (5.6) cannot have a unique solution. The matter is even more problematic when the surface S corresponds to N unconnected structures. In that case,

$$[\mathcal{V}\mathbf{t}] = \int_S \boldsymbol{\mathcal{V}}(\mathbf{r}) \cdot \mathbf{t}(\mathbf{y}) \mathrm{d}S_y$$

has null space $\mathcal{N}(\mathcal{V})$ of dimension N whose basis is given by

$$\mathbf{t}^{\alpha}(\mathbf{x}) = \begin{cases} \mathbf{n}(\mathbf{x}), & \mathbf{x} \in S^{\alpha} \\ 0 & \text{elsewhere} \end{cases}, \qquad 1 \leq \alpha \leq N. \tag{5.7}$$

Many techniques exist for dealing with the null space of Eq. (5.6).[34] Unfortunately, standard BEM approaches are ill-conditioned when applied to complex structures even if the null space is filtered out exactly.

In order to cure the issue of ill-conditioning, a new boundary element method, the Mixed Velocity Traction approach (MVT), has been recently proposed[23] and extended to large scale problems[24] using fast solvers.

The second tool required for setting up the MVT is the traction integral equation, an integral identity which can be obtained through careful differentiation of

Eq. (5.4), for a smooth $\mathbf{x} \in S$:

$$\frac{1}{2}\mathbf{t}(\mathbf{x}) = \int_S \{-[\mathbf{n}(\mathbf{x}) \cdot \boldsymbol{\mathcal{K}}(\mathbf{r})] \cdot \mathbf{t}(\mathbf{y}) - [\mathbf{n}(\mathbf{x}) \cdot \boldsymbol{\mathcal{W}}(\mathbf{r}) \cdot \mathbf{n}(\mathbf{y})] \cdot \mathbf{u}(\mathbf{y})\} \, \mathrm{d}S_y \quad (5.8)$$

where $\boldsymbol{\mathcal{W}}$ is a fourth order two-point kernel with components:

$$W_{qiks}(\mathbf{r}) = \frac{\eta}{4\pi}\frac{1}{r^3}\Big[2\delta_{sk}\delta_{iq} + \frac{3}{r^2}\big(\delta_{ik}r_q r_s + \delta_{kq}r_i r_s + \delta_{is}r_k r_q + \delta_{sq}r_i r_k\big) - 30\frac{r_i r_k r_q r_s}{r^4}\Big]$$

Equation (5.8) also contains an hypersingular integral interpreted here in the finite-part sense. Again, when the structure velocities correspond to rigid body motion the integral of $[\mathbf{n}(\mathbf{x}) \cdot \boldsymbol{\mathcal{W}}(\mathbf{r}) \cdot \mathbf{n}(\mathbf{y})] \cdot \mathbf{g}(\mathbf{y})$ over a closed surface vanishes. The MVT simply consists in enforcing a linear combination of Eqs. (5.6) and (5.8):

$$\mathbf{g}(\mathbf{x}) - \frac{\gamma}{\eta}\frac{1}{2}\mathbf{t}(\mathbf{x}) = \int_S \Big\{\boldsymbol{\mathcal{V}}(\mathbf{r}) \cdot \mathbf{t}(\mathbf{y}) + \frac{\gamma}{\eta}[\mathbf{n}(\mathbf{x}) \cdot \boldsymbol{\mathcal{K}}(\mathbf{r})] \cdot \mathbf{t}(\mathbf{y})\Big\}\mathrm{d}S_y \qquad (5.9)$$

where γ is a length scale to be calibrated. The benefits of this formulation have been pointed out in Ref. [23] where it has been shown that the mixed formulation is well posed when $\gamma > 0$ and that not only does it filter out automatically all the exact null space of the velocity equation, but also considerably improves the condition number which is crucial for the iterative solvers employed.

5.2.4. *Numerical Implementation*

The numerical solutions of Eq. (5.6) require, as usual, the discretization of S (in this case we choose a triangulation $\mathcal{T}$ with M flat triangles) and the choice of the space X_h to which the interpolation of $\mathbf{t}$ belongs. Since $\mathbf{t}$ represents tractions which are typically discontinuous along edges and corners, we choose X_h as the space of piecewise constant functions. At this stage, different alternative procedures can be employed. In the Galerkin approach Eq. (5.9) is contracted with a traction test field $\tilde{\mathbf{t}}(\mathbf{x}) \in X_h$, integrated over S and enforced for any choice of $\tilde{\mathbf{t}}(\mathbf{x}) \in X_h$.

Let τ_β and τ_γ be generic triangles of the mesh with $\mathbf{x} \in \tau_\beta$ and $\mathbf{y} \in \tau_\gamma$, and let A_β be the area of τ_β. If $\mathbf{T}_\gamma$ is the traction on τ_γ, the discretized Galerkin approach yields the linear system:

$$\int_{\tau_\beta} \mathbf{g}(\mathbf{x})\mathrm{d}S_x - A_\beta\frac{\gamma}{2\eta}\mathbf{T}_\beta \qquad \forall\beta = \{1 : M\} \qquad (5.10)$$
$$= \sum_{\gamma=1}^{M}\left[\int_{\tau_\beta}\int_{\tau_\gamma}\Big(\boldsymbol{\mathcal{V}}(\mathbf{r}) + \frac{\gamma}{\eta}\mathbf{n}(\mathbf{x}) \cdot \boldsymbol{\mathcal{K}}(\mathbf{r})\Big)\mathrm{d}S_y\mathrm{d}S_x\right] \cdot \mathbf{T}_\gamma$$

However, though accurate, this approach requires the evaluation of lengthy double surface integrals. This issue has been studied at length, but still represents a considerable obstacle when computing time becomes an issue and hence, typically, in large scale problems associated to MEMS.

The classical and faster collocation approach consists in enforcing Eq. (5.9) at the center of each triangle. It is worth stressing that the collocation approach can be recovered from Eq. (5.10) by employing a single point quadrature rule for the integration over $\mathbf{x}$, where $\mathbf{x}_\beta$ represents the center of mass of the τ_β triangle.

Recently, however, it has been shown in Ref. [23] that, in the context of this mixed velocity approach, a different approximate numerical scheme requiring only single surface integrals can be advantageously applied: qualocation.[35] In this approach, Eq. (5.10) is applied with a one point Gauss–Hammer rule for the integration over $\mathbf{y}$ (the inner integration) while a standard numerical rule or an analytical approach is applied for the outer integral. Hence qualocation is, in a sense, the dual of collocation with respect to the Galerkin approach. Numerical examples[23] show that qualocation is less sensitive to the value of the coupling parameter than collocation. For instance, it can be proved that, as $\gamma \rightarrow \infty$, the field $\mathbf{t}$ obtained from collocation vanishes, while this is not the case with qualocation.

5.2.5. *Fast Solvers*

As is clear from Eq. (5.9), the discretized integral equations generate systems of equations that are *dense*. If direct factorization is used to solve memory required to store the matrix will grow like n^2 and the matrix solve time will increase like n^3. If instead, a preconditioned Krylov-subspace method like GMRES[1] is used to solve the system, then it is possible to reduce the solve time to order n^2 but the memory requirement will not decrease.

In order to develop algorithms that use memory and time that grows more slowly with problem size, it is essential *not* to form the matrix explicitly. Instead, one can exploit the fact that Krylov-subspace methods for solving systems of equations only require matrix-vector products and not an explicit representation of the matrix and this can be accomplished in nearly order n operations.[2–4] Several researcher simultaneously observed the powerful combination of discretized integral equations, Krylov-subspace methods, and fast matrix-vector products.[5–7] Such methods are now referred to, somewhat pejoratively, as fast solvers. Among these techniques, two in particular have been applied to the analysis of gas damping in MEMS: the Fast Multipole Method and the Precorrected FFT. Acceleration is achieved by computing the far-field interactions in an approximate way, while

near-field interaction still resorts to classical technique for numerical integration of nearly-singular or singular integrals.

Fast Multipole Method. Fast Multipole Accelerators represent nowadays a well established technique applied successfully in different fields of mechanics. A recent review of BE accelerated formulations can be found in Ref. [32]. A complete explanation of FMM is however beyond the scope of this paper and reference is made to Ref. [27] for details.

The fundamental identity for our developments is the expansion for the inverse radius:

$$\frac{1}{r} = \sum_{b=0}^{\infty} \sum_{a=-b}^{a=b} \overline{S^{ab}}(\mathbf{x}-\mathbf{O}) R^{ab}(\mathbf{y}-\mathbf{O}) \tag{5.11}$$

where $\mathbf{O}$ is a properly chosen pole such that $|\mathbf{y}-\mathbf{O}| < |\mathbf{x}-\mathbf{O}|$, the bar denotes complex conjugate and S^{ab}, R^{ab} are solid harmonics which can be computed by means of simple and fast algebraic recursive formulae. As a consequence of Eq. (5.11) it is quite apparent that any expression to integrate can be expressed as the sum of terms in the form $F(\mathbf{O},\mathbf{x})G(\mathbf{O},\mathbf{y})$. Now, let us suppose to evaluate the double surface integral of $F(\mathbf{O},\mathbf{x})G(\mathbf{O},\mathbf{y})$ in the context of a Galerkin approach. The integration with respect to $\mathbf{x}$ and $\mathbf{y}$ can be decoupled:

$$\int_{\tau_\beta}\int_{\tau_\gamma} F(\mathbf{O},\mathbf{x})G(\mathbf{O},\mathbf{y})\mathrm{d}S_x\mathrm{d}S_y = \left(\int_{\tau_\beta} F(\mathbf{O},\mathbf{x})\mathrm{d}S_x\right)\left(\int_{\tau_\gamma} G(\mathbf{O},\mathbf{y})\mathrm{d}S_y\right)$$

If τ_β and τ_γ are "well separated" (according to some suitable error estimates[27]) the integral over τ_γ is invariant w.r.t. the choice of τ_β and *vice-versa*. This concept is exploited via the construction of hierarchical octree structures and complex upward and downward swap procedures. Further details concerning the application of this technique to MEMS can be found in Frangi *et al.*[24]

Precorrected FFT. Precorrected-FFT technique is another method to accelerate the matrix-vector product.[41] Unlike the FMM, the key technique employed in the precorrected FFT method is the Fast Fourier Transformation instead of multipole expansion.

To compute the far-field interaction, the first step in the precorrected-FFT technique is to enclose the meshed problem domain with a 3D uniform grid. This grid serves for two purposes. First, it distinguishes the near- and far-field interactions. Second, it forms the basis for the FFT. It should be pointed out this grid can be independent of the surface mesh of the problem domain. The grid spacing is determined based on the balance between accuracy and efficiency.

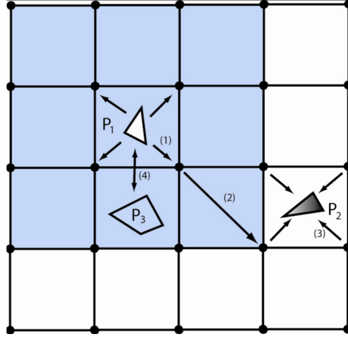

Fig. 5.1. A 2D pictorial representation of steps of the precorrected-FFT algorithm: (1) Projection; (2) FFT; (3) Interpolation; and (4) Nearby Interaction. The shaped region represents the near-field area for panel P_1.

Once the grid is established, the far-field interaction, *i.e.*, the interaction between panel P_1 and panel P_2, is computed by the following three steps as sketched in Fig. 5.1. First the density function or the source of panel P_1 is projected onto the surrounding grid points (Step 1). This can be achieved by a transposed polynomial interpolation.[43] Second, the FFT is employed to compute the matrix-vector products on the grid points by convolving the projected grid-point densities with the corresponding kernels, *e.g.*, Green's function (Step 2). Finally, the matrix-vector product on the evaluation panel, P_2, is obtained by proper extrapolation from the products on its surrounding grid points via polynomial interpolation (Step 3).

Mathematically, the procedure of computing the far-field interaction can be represented by the following expression:

$$\int_\Gamma G(\mathbf{x},\mathbf{y})f(\mathbf{y})\mathrm{d}s(\mathbf{y}) \approx \sum_m W_m \left\{ \sum_n \left[G(\mathbf{x}_m,\mathbf{y}_n) \int_\Gamma P_n(f)\mathrm{d}s(\mathbf{y}) \right] \right\} \quad (5.12)$$

In Eq. (5.12), G and f represents the kernel and density functions, W and P are the interpolation and projection operators, and m, n are the index of grid points that surround the evaluation and source panels respectively.

5.3. Extension to the Slip Flow Regime and Validation

Working pressures of MEMS are spread over a large range (1 bar – 10^{-6} bar). This issue, associated to the micro-scale at hand, promotes rarefaction effects which, at low pressures, have to be dealt with using techniques of rarefied gas-dynamics.[21,26] A measure of rarefaction is provided by the Knudsen number

$\mathrm{Kn} = \lambda/L$, where λ is the molecular mean free path and L is a typical dimension of the flux, *e.g.*, the gap between plates in Poiseuille (squeeze) flow. As a rule of thumb, when $\mathrm{Kn} < .01$ classical tools of macroscale fluid flow can be applied, (*e.g.*, Navier–Stokes solvers). In the range $.01 < \mathrm{Kn} < .1$ an accurate prediction of the flow properties can be obtained by applying a continuum approach with slip boundary conditions (slip BC). Since the dimensions typical of MEMS are of a few microns, the flow mainly develops in the slip regime even at ambient pressure. For larger values of Kn the flows enters the so called transition regime which can be analysed only by means of kinetic theories, (*e.g.*, Boltzmann equation) and will be addressed by means of simplified techniques in Sec. 5.5.

Let $\mathbf{t}^S$ denote the surface components of tractions:

$$\mathbf{t}^S(\mathbf{x}) = [\mathbb{1} - \mathbf{n}(\mathbf{x}) \otimes \mathbf{n}(\mathbf{x})] \cdot \mathbf{t}(\mathbf{x}),$$

where $\mathbb{1} - \mathbf{n}(\mathbf{x}) \otimes \mathbf{n}(\mathbf{x})$ is the surface projector tensor. As pointed out recently,[15,37] first order boundary slip conditions should be expressed in terms of $\mathbf{t}^S$:

$$\mathbf{u}(\mathbf{x}) = \mathbf{g}(\mathbf{x}) - c_t \mathbf{t}^S(\mathbf{x}) \qquad c_t := \frac{2-\sigma}{\sigma}\frac{\lambda}{\eta} \tag{5.13}$$

where σ is the tangential momentum accommodation coefficient.[29]

It is worth stressing that, for planar structures, Eq. (5.13) reduces to the more familiar boundary condition:

$$\mathbf{u}(\mathbf{x}) = \mathbf{g}(\mathbf{x}) - \frac{2-\sigma}{\sigma}\lambda\frac{\partial u_t}{\partial n}, \tag{5.14}$$

where $\partial u_t/\partial n$ is the normal derivative of the tangential velocity at the wall.

Since Eq. (5.13) operates linearly on $\mathbf{t}$, the BEM formulation Eq. (5.9) can be easily adopted, yielding:[24]

$$\begin{aligned}\mathbf{g}(\mathbf{x}) - \frac{c_t}{2}\mathbf{t}^S(\mathbf{x}) - \frac{\gamma}{\eta}\frac{1}{2}\mathbf{t}(\mathbf{x}) &= \int_S \Big\{ \boldsymbol{\mathcal{V}}(\mathbf{r}) \cdot \mathbf{t}(\mathbf{y}) + c_t \left[\boldsymbol{\mathcal{K}}(\mathbf{r}) \cdot \mathbf{n}(\mathbf{y})\right] \cdot \mathbf{t}^S(\mathbf{y}) \\ &\quad + \frac{\gamma}{\eta}\left([\mathbf{n}(\mathbf{x}) \cdot \boldsymbol{\mathcal{K}}(\mathbf{r})] \cdot \mathbf{t}(\mathbf{y}) - c_t \left[\mathbf{n}(\mathbf{x}) \cdot \boldsymbol{\mathcal{W}}(\mathbf{r}) \cdot \mathbf{n}(\mathbf{y})\right] \cdot \mathbf{t}^S(\mathbf{y})\right) \Big\} \mathrm{d}S_y.\end{aligned} \tag{5.15}$$

On the contrary, when using Eq. (5.14), the integral representation of the normal derivative of velocity[22]

$$\frac{1}{2}\frac{\partial \mathbf{u}}{\partial n}(\mathbf{x}) = \int_S \left\{ \frac{\partial \boldsymbol{\mathcal{V}}(\mathbf{r})}{\partial n(\mathbf{x})} \cdot \mathbf{t}(\mathbf{y}) - \left[\frac{\partial \boldsymbol{\mathcal{K}}(\mathbf{r})}{\partial n(\mathbf{x})} \cdot \nu(\mathbf{y})\right] \cdot (\mathbf{u}(\mathbf{y}) - \mathbf{u}(\mathbf{x})) \right\} \mathrm{d}S_y \tag{5.16}$$

is required to form a close set of integral equations. In the above equation, all integrals exist in their principal value sense. When the slip boundary condition,

Eq. (5.14), is substituted into Eq. (5.16) and into the velocity equation (5.6), the system of these two integral equations can be solved to obtain the unknow tractions and normal derivative of tangential velocity.

5.3.1. *Numerical Results and Comparison with Experiments*

5.3.1.1. *Biaxial Accelerometer*

A series of experimental tests have been performed on the silicon biaxial accelerometer of Fig. 5.2 produced by STMicroelectronics.

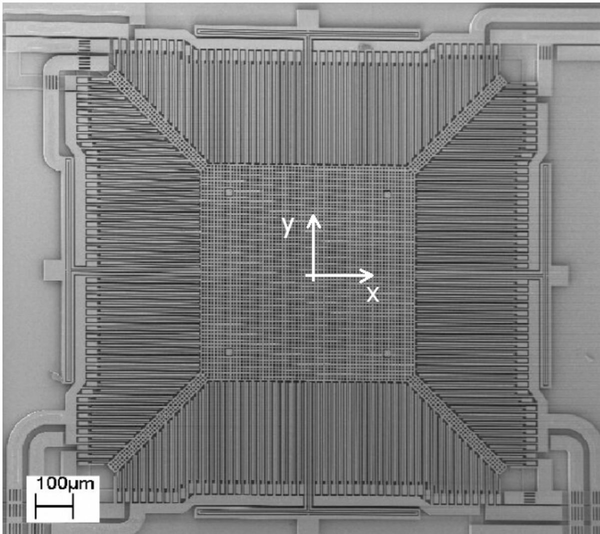

Fig. 5.2. Biaxial accelerometer.

The accelerometer consists of a central suspended *shuttle* and four series of external *stators* attached to the substrate. Both parts are endowed with a series of long and thin plates interdigited into capacitors serving both as actuators and sensors. The length of the longest plates is $277\,\mu$m, the in-plane width is $3.9\,\mu$m, the height is $15\,\mu$m and the air gaps between plates are $2.6\,\mu$m. The gap between the shuttle and the substrate is $4.2\,\mu$m. The shuttle is attached to the substrate by means of silicon springs which are stiff in the out-of-plane (z) direction and very compliant in the xy plane. Hence the shuttle is essentially free to move parallel to the xy plane and is otherwise constrained.

During the experimental tests, performed at different pressures employing a Baratron pressure transducer, the accelerometer is set in oscillation along the y direction by means of electrostatic actuation in a wide range of frequencies centered at the undamped resonating frequency $f_0 = 4400\,\mathrm{Hz}$. The actuating forces are such that the maximum amplitude of oscillation of the plates is much smaller than the air gaps. A set of plates, *i.e.*, those parallel to the x direction, mainly a Poiseuille-like flow, while those parallel to the y direction induce a Couette-like flux.

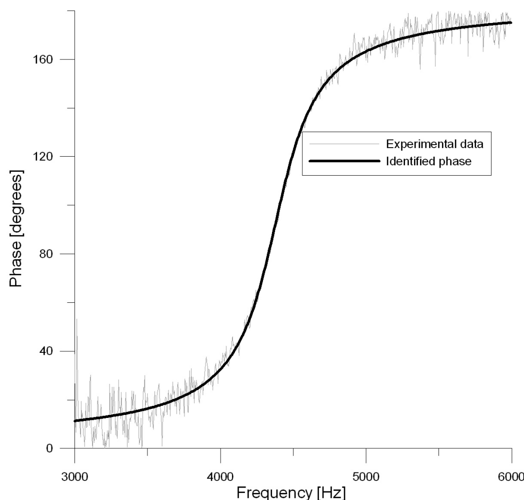

Fig. 5.3. Plot of phase lag versus frequency at a given pressure.

In these working conditions the accelerometer can be effectively represented by a linearized 1D model

$$M\ddot{y} + C\dot{y} + Ky = F\cos\omega t \qquad \text{or} \quad \ddot{y} + 2\xi\omega_0\dot{y} + \omega_0^2 y = \frac{F}{M}\cos\omega t \quad (5.17)$$

where M denotes the mass of the structure, K the equivalent stiffness due to springs and C the damping coefficient. Since the amplitude of the oscillation is small with respect to the plate gap, C, K, F can be reasonably taken as independent of y.

The typical experimental output employed is represented by the thin irregular line in Fig. 5.3 where the phase lag ϕ between the input voltage and the

measured displacement is plotted at a given pressure in a broad frequency range. Sensing is achieved by means of electrostatic capacitors embedded in the MEMS. These data are used to identify the "experimental" values of ξ in the associated 1D model. Indeed the angle ϕ can be easily related to the ξ coefficient by the classical relation:

$$\tan\phi = \frac{2\xi\omega/\omega_0}{1-(\omega/\omega_0)^2} \tag{5.18}$$

and, finally, $C = 2\xi\omega_0 M$.

The thick line in Fig. 5.3 is the plot of ϕ from Eq. (5.18) with the optimal choice of ξ (obtained via Matlab optimization procedures). The good quality of fitting seems to justify the adoption of the 1D model. A similar procedure is repeated at different pressures.

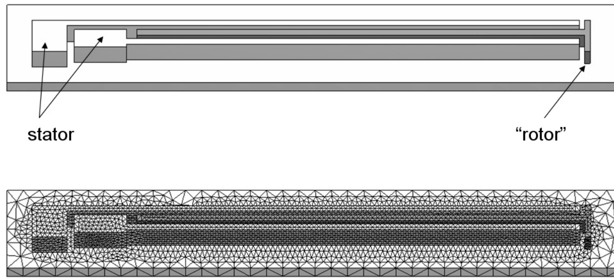

Fig. 5.4. Single unit employed for the simplified squeeze and Couette analysis: geometry and finest mesh.

It is worth stressing that the Quality Factor Q is often employed in MEMS research rather than ξ. Unfortunately, many alternative definitions of Q can be found in the literature which all coincide in the limit for high Q, but may differ substantially at low Q. Since according to one the most common definitions, $Q = 1/(2\xi)$, Q is inversely proportional to ξ, all the comparisons will be presented in terms of $C = 2\xi\omega_0 M$ which actually represents the viscous force on the shuttle (in the 1D model) at unit velocity.

This example has been analysed by means of the FFM MVT formulation (detailed in the previous Sections) in order to provide an estimate of the damping coefficient C. It is indeed worth recalling that the MVT implemented herein is based on a linear quasi-static Stokes formulation and that the damping force depends linearly on the input-velocity of the structures which can be hence taken as unitary. In this case, the force exerted by the fluid on the rotor directly yields the desired damping coefficient C.

The highly repetitive layout and the simple movement along the y direction permit to restrict the analysis to simple "units" and extrapolate the results to the overall structure. Hence focus is set, initially, on the geometry of Fig. 5.4, where a rotor plate (darker) and two stator plates (lighter) are considered. Two different situations are addressed, corresponding to Poiseuille and Couette flow, by simply imposing a unit velocity orthogonal and parallel to the plates, respectively.

Several meshes have been analysed with increasing refinement. In Table 5.1 the force on the rotor computed with the finest mesh of 25400 elements (76200 unknown parameters) is presented. As anticipated, the global force on the "rotor" is obtained by simply scaling the one obtained for the simple unit by the global length of the rotor plates in squeeze and Couette flow, respectively. An additional analysis has been performed on a sample of the central bulky mass with holes to provide an estimate of the contribution to the global force. As expected, Poiseuille flow provides the most important contribution. The values of the forces mentioned above (collected in Table 5.1) are computed at ambient pressure both for no-slip and slip boundary conditions, assuming $\sigma = .9$ and a mean free path of $\lambda = 0.064\,\mu$m. While stick BC overestimate the force on the rotor, an excellent agreement is obtained with slip BC.

Table 5.1. Comparison of experimental results with the numerically computed damping forces at ambient pressure: contribution from different parts of the rotor and global results.

	Numerical "no slip"	Numerical "slip"	Experimental
Poiseuille flow	2.32×10^{-4} N	2.10×10^{-4} N	-
Couette flow	7.37×10^{-6} N	7.03×10^{-6} N	-
Mass with holes	2.10×10^{-6} N	1.94×10^{-6} N	-
Total force	2.41×10^{-4} N	2.19×10^{-4} N	2.21×10^{-4} N

Next, the effect of decreasing pressure is analysed in Fig. 5.5, where F/F_0 is plotted against p/p_0 (F_0 denotes the experimental force evaluated at ambient pressure p_0). Different pressures can be simulated by setting the correct value of the c_t slip coefficient in Eq. (5.13).

The agreement between experiments and analysis is excellent for $p > .15p_0$ (Kn $\simeq .1$ at $p = .15p_0$) but accuracy rapidly deteriorates at lower pressures, as largely expected. Indeed, at these levels of pressure, the methods of rarefied gas dynamics should be applied either through the adoption of a modified viscosity, or by direct solution of kinetic models.

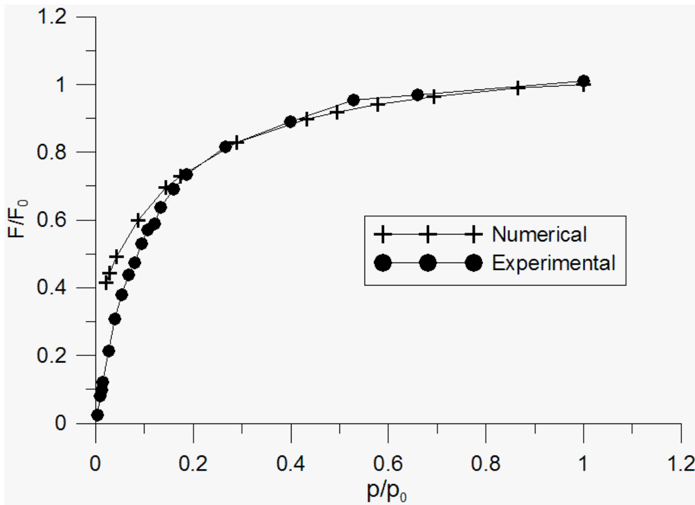

Fig. 5.5. Global force on the rotor at different pressures: comparison of numerical and experimental results.

A final set of analyses have been performed to test the robustness of the formulation with respect to the complexity of the geometry, as depicted in Fig. 5.6, where the lighter part is the stator and the darker one the shuttle portion considered. The bulky mass with holes has been omitted following the indications of the previous analyses.

Three different meshes have been considered and the results in terms of computed global force are collected in Table 5.2.

Table 5.2. Comparison between meshes of increasing refinement.

Mesh employed	mesh 1	mesh 2	mesh 3
Number of unknowns	125058	272364	548388
Global force	1.80×10^{-4} N	2.01×10^{-4} N	2.12×10^{-4} N

The iterative GMRES solver employed[25] rapidly converges, as can be appreciated in Fig. 5.7. It has been empirically remarked that: i) the rate of convergence remains virtually unchanged down to relative residuums of $10^{-8} \simeq 10^{-9}$; ii) the error on the global force, with respect to its value at convergence of the iterative procedure, is of the same order as the relative residuum. Hence a very mild stopping condition can be employed for the GMRES solver.

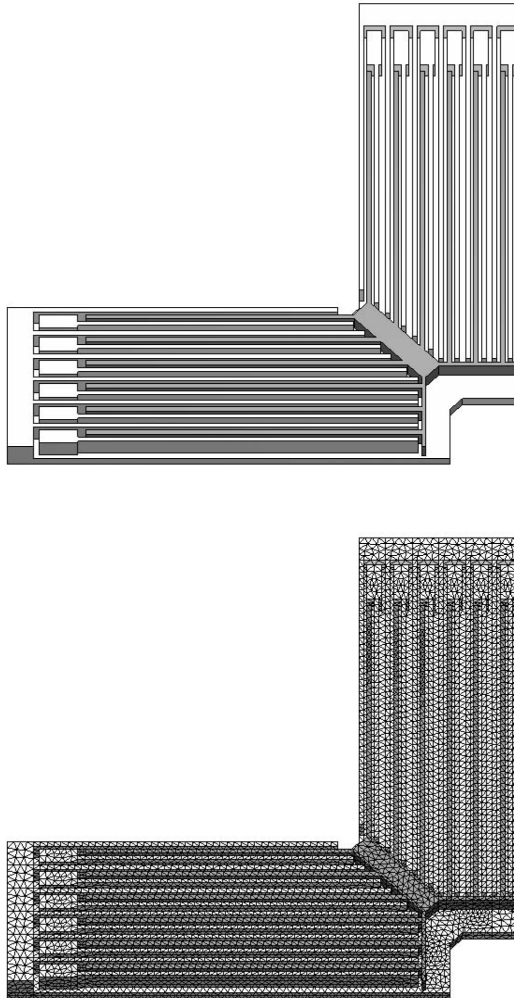

Fig. 5.6. More realistic model of one fourth of the MEMS: geometry and mesh.

5.3.1.2. *Tang Resonator*

As a further validation of the working hypotheses, let us now focus on the academic Tang resonator of Fig. 5.8.

The main components of the resonator consist of two folded beams (springs), two comb drives, each with two sets of fingers, one moving and one fixed, and a

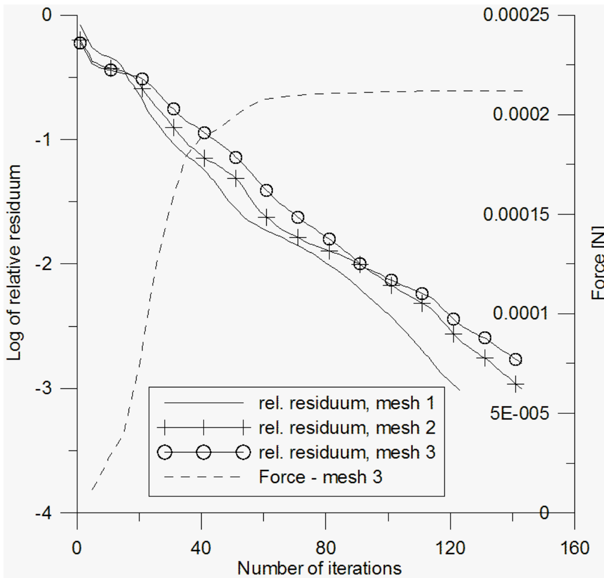

Fig. 5.7. Convergence of the GMRES solver and of the force computed.

shuttle connecting folded beams and moving fingers. When a bias AC voltage is applied to one comb drive, the electrostatic force moves the moving fingers and thus the shuttle and the folded beam towards the fixed fingers while the mechanical restoring force of the beams brings them back to their equilibrium position, resulting in an oscillating motion.

The length of each finger is $20\,\mu$m, the in-plane width is $3.2\,\mu$m and the air gaps are $2.6\,\mu$m wide; the length of each spring is $405\,\mu$m, while its width is $2.2\,\mu$m. The out-of-plane dimension of the whole structure is $15\,\mu$m. The gap between the shuttle and the substrate is $1.8\,\mu$m. Also this structure has a first resonating frequency of approximately $4400\,$Hz.

The BEM formulation described in previous sections can be suitably modified to account for the deformability of the structure which is essential to capture squeeze film effects between the springs[20] which are very close in this unusual layout. Several meshes have been tested, and the results presented in the sequel refer to the finest mesh adopted (see Fig. 5.9) containing $\simeq$ 342000 elements, which amount to $\simeq$ 1388000 unknowns.

Considering the gaps between the structure and the substrate and between fingers, the transition region starts at approximately $p = .1$ bar. At higher pressures,

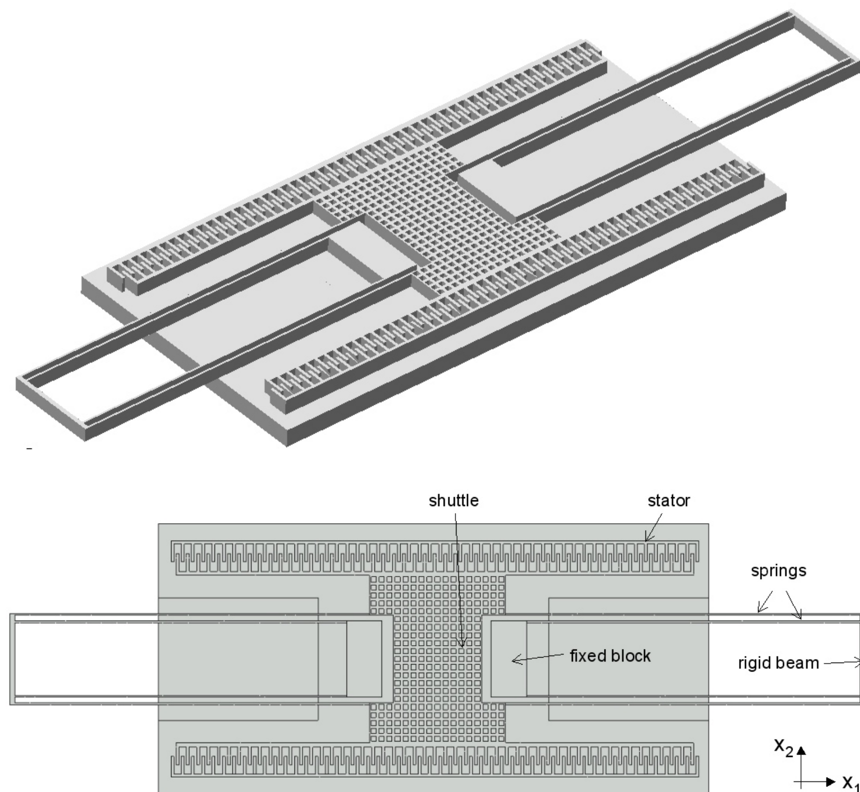

Fig. 5.8. Comb finger resonator: 3D view and 2D layout.

the code with slip-boundary conditions is thus expected to be accurate. This is confirmed by the results plotted in Fig. 5.10 where the linear scale on the left shows the good agreement at high pressures, while the log scale on the right puts in evidence the divergence at low pressures, which is largely expected since the working conditions are entering the transition regime which should be addressed by different techniques (see Sec. 5.5 and Chapters 2 and 3).

5.4. Extension to High Frequency Oscillatory Flow

The results presented in previous sections hold under specific hypotheses. Three non-dimensional parameters are generally identified as crucial: the Mach number

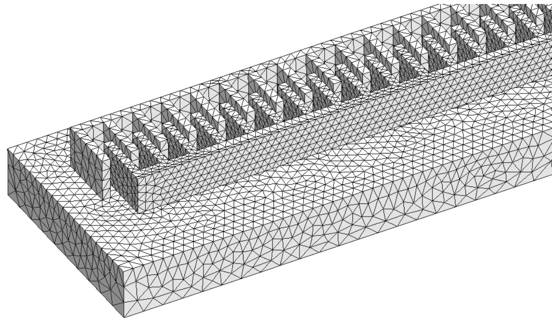

Fig. 5.9. Comb finger resonator: detail of the finest mesh adopted.

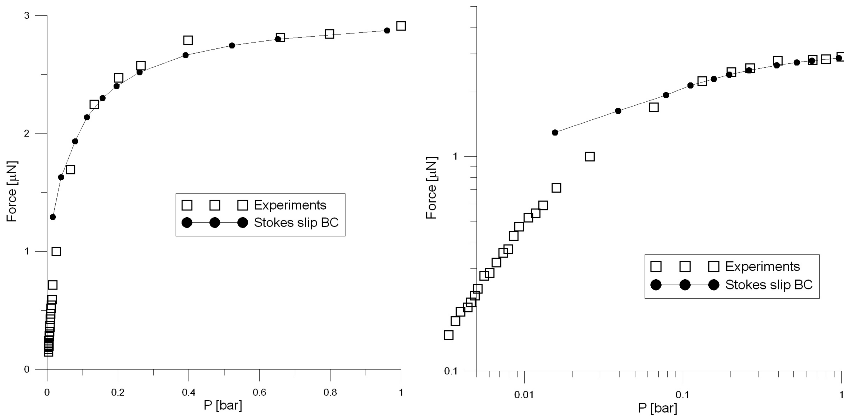

Fig. 5.10. BEM results with slip BC: comparison with experiments in liear and log-scale.

M; the Reynolds number R$e = UL/\nu$ and the Stokes number St $= fL^2/\nu$.[33] U is the flow velocity, ν is the kinematic viscosity, L is a typical flow length and f is the frequency of oscillation. If all these parameters are small compared to unity, the proposed linear quasi-static approach is deemed acceptable and compares very well with experiments. When f increases, these conditions may fail. Taking into account inertia effects, the governing equations for oscillatory flows[36,49] change to

$$\nabla P(\mathbf{x}) - \mu \Delta \mathbf{u}(\mathbf{x}) = i\omega\rho\mathbf{u} \qquad \nabla \cdot \mathbf{u}(\mathbf{x}) = 0 \quad \text{in} \quad \Omega_\infty - \Omega \tag{5.19}$$

and the corresponding integral equation is the same as Eq. (5.5) with the following kernel functions:

$$V_{ik}(\mathbf{r}) = \frac{1}{8\pi\mu} A(R)\frac{\delta_{ik}}{r} + B(R)\frac{r_i r_k}{r^3}$$

$$K_{iqk}(\mathbf{r}) = -\frac{\delta_{ij} r_k + \delta_{kj} r_i}{4\pi r^3}[e^{-R}(R+1) - B] - \frac{\delta_{ik} r_j (1-B)}{4\pi r^3}$$

$$- \frac{r_i r_j r_k}{4\pi r^5}[5B - 2e^{-R}(R+1)]$$

where $\mathbf{r} = \mathbf{y} - \mathbf{x}$, $r = \|\mathbf{y} - \mathbf{x}\|$ and

$$A = 2e^{-R}\left(1 + \frac{1}{R} + \frac{1}{R^2}\right) - \frac{2}{R^2}, \quad B = -2e^{-R}\left(1 + \frac{3}{R} + \frac{3}{R^2}\right) + \frac{6}{R^2},$$

$$R = r\sqrt{\frac{-i\omega\mu}{\rho}}.$$

The numerical implementation of this model using integral equations becomes more involved but, at least in principle, can be addressed with the same techniques described above.[36,49] In some recent contributions,[36,49] also compressibility has been addressed, with satisfactory results.

Let us now focus on a Tang micro resonator similar to that of Sec. 5.3.1.2 whose dimensions are shown in Table 5.3. The natural frequency and the quality factor of this resonator, measured using a computation vision system,[36] are 19.2 kHZ and 27 respectively.

Table 5.3. Resonator dimensions.

Finger gap	2.88μm
Finger length	40.05μm
Finger overlap	19.44μm
Spring length	151μm
Spring width	1.1μm
Center plate	$54.9 \times 19.26\mu\text{m}^2$
Side plate1 $\times$ 2	$28.26 \times 89.6\mu\text{m}^2$
Side plate2 $\times$ 4	$11.3 \times 40.5\mu\text{m}^2$
Thickness	1.96μm
Substrate gap	2μm
Truss length	78μm
Truss width	13μm

Both the spring stiffness and the mass can be predicted based on the given resonator structure. However, the spring stiffness is difficult to be estimated accurately unless material properties of the structure are known with confidence.[36] For this study, since the focus is on the modeling of air damping, the spring stiffness, 0.816 N/m, is obtained based on the measured frequency and the estimated mass of 5.61×10^{-11} kg. Due to small Reynold's number (2×10^{-3}) and small Knudsen number (0.03), the fluid behavior is expected to be reasonably accurately described by solutions of the incompressible Stokes equation with no-slip boundary condition.

A home-made 3D solver, "FastStokes", was employed to compute the drag forces on the micro resonator. Based on the integral formulation (5.6), FastStokes combines the iterative method GMRES with the precorrected-FFT technique for fast matrix-vector productes. The discretized structure is shown in Fig. 5.11. Note both the resonator and the substrate are discretized, for a total of 20148 panels.

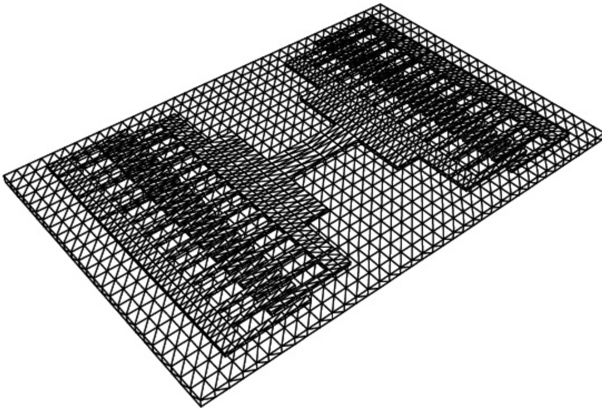

Fig. 5.11. Meshed resonator and substrate.

The viscous drag forces on the resonator oscillating at $f = 19200$ Hz were computered using progressively finer discretizations, to insure that the discretization error was sufficiently small. Results converge to within one percent with as few as 10000 panels. For these simulations, the kinematic viscosity and the density of air were assumed to be $0.157\,\text{cm}^2/\text{s}$ and $1.177\,\text{kg/m}^3$, respectively. The amplitude of the velocity was set to be 6.72 m/s based on the experimental data. It should be pointed out in FastStokes, the velocity integral formulation (5.6) for oscillatory flows is employed. The convergence is expected to be improved if the mixed velocity integral formulation Eq. (5.9) is adopted.

A detailed analysis of the distribution of the drag force, shown in Table 5.4, reveals that the contribution to the drag force from the fluid between the resonator and the substrate is 53.9% and the drag force from the side contributes 30.1%. This explains why the previous models, *i.e.*, the 1D Couette and 1D Stokes models, seriously underestimate the drag force as they can not capture correctly the side contribution due to the infinitely long-plate assumption.

Table 5.4. Distribution and comparison of drag force on Tang resonator computed by FastStokes.

Drag (pN)	Bottom	Side	Top
Couette	424.37	57.37	?
1D Stokes	437.93	57.37	52.67
FastStokes	510.72	294.50	142.8

The quality factor of the resonator can now be calculated based on the computed drag force, the mass and the spring stiffness. Results are shown in Table 5.5 together with the measurement result and those estimated from 1D models. Both 1D models overestimate the value of the quality factor by a factor of two. Result from the 3D analysis agrees well with the experimental result, with an error of 10%. This indicates that 3D effects are profound in this resonator.

Table 5.5. Quality factor of the resonator: simulation results and experimental data.

Methods	Total Drag (pN)	Q
Couette	481.70	58.9
1D Stokes	547.97	51.8
FastStokes	948.02	29.9
Measurement		27

At $f = 19200\,\text{Hz}$, it is of interest to examine the importance of the inertial force. As mentioned previously, the non-dimensional Stokes number is a good indicator of the importance of the inertial force as compared to the viscous force. However, the characteristic length L must be chosen carefully to reflect the local length scale of the flux. For flow between the moving resonator and substrate, L is simply the gap and thus the Stokes number is around 4.9×10^{-3}, which means the inertial force can be neglected. However, for flow on the top of the resonator, a suitable choice of L is the penetration depth which in this case is 37

times larger than the gap.[36] As a result, the Stokes number for the top flow is around 6.7, indicating the contribution of the inertial force on top drag would be quite significant.

Drag forces obtained from the steady Stokes solver and the unsteady Stokes solver are shown in Table 5.6. The difference in total drag is around 6%. As an examination of Table 5.6 indicates, the most significant contribution of the inertial force is to the top drag force with a nearly 33% increase in its drag, while the drag from the fluid between the resonator and the substrate remains almost the same. This fact is consistent with the above predictions based on the Stokes number.

Table 5.6. Distribution of drag force: Steady versus Unsteady.

Drag force (pN)	Steady	Unsteady
Bottom	508.75	510.72
Side	284.84	294.50
Top	102.31	142.8
Total	895.9	948.02

5.5. Extension to Low Pressures by Means of the Corrected Viscosity Approach

As clearly demonstrated in Sec. 5.3, continuum hypotheses fail when the Knudsen number increases above a certain threshold which is conventionally set as $\mathrm{Kn} = .1$. This regime is properly addressed in Chapters 1–4 of this book with the refined tools of rarefied gas dynamics.

However, in same cases simplified approaches apply, as discussed briefly in the sequel. Since the rarefaction effects and the molecular interactions with the surfaces of the micromechanical structures change the gas viscosity, one possible approach to account for the microscopic dynamics is to employ an effective viscosity η_{eff} instead of the static viscosity coefficient η.[29,38,39]

Indeed the effective viscosity approach applies rigorously in two simple but typical situations (Poiseuille and Couette flow), as discussed in Chapter 2. If two plates oscillate in a direction perpendicular to their surfaces (Poiseuille flow), the pressure distribution in the gas film can be computed from the generalized Reynolds equation employing the effective viscosity:[29,38]

$$\eta_{\mathrm{eff}}^{P} = \frac{\eta}{F(\delta)}\frac{\delta}{6} \tag{5.20}$$

where $\delta = \sqrt{\pi}/(2\,\mathrm{Kn})$ is a rarefaction parameter, Kn being the Knudsen number and $F(\delta)$ the Poiseuille flow-rate coefficient. In the continuum limit: $F(\delta) \rightarrow \delta/6$, so that $\eta_{\text{eff}}^{P} \rightarrow \eta$.

On the contrary, if the plate motion is purely in the lateral direction (Couette flow), the equivalent viscosity can be related to the shear stress τ according to:[29,38,39]

$$\eta_{\text{eff}}^{C} = \eta\, 2\delta\, \tau \tag{5.21}$$

where $\tau = \left|\mathbf{t}^{S}\right| / (\rho U)$, ρ being the gas density and U the relative velocity of laterally moving micromechanical structures. In the continuum limit: $\tau \rightarrow 1/(2\delta)$, so that $\eta_{\text{eff}}^{C} \rightarrow \eta$.

A general computation of both F and τ can be found in the cited references as a function of the Knudsen number and is based on the solution of the linearized BGK model of the Boltzmann equation with suitable boundary conditions allowing for different accommodation coefficients of the plates.

Even if theoretical explanations are still under investigation, it can be argued that a similar procedure should also prove effective with the full 3D Stokes model. For example, let us consider the resonator of Sec. 5.3.1.2. If the modified viscosity approach applies and since the formulation adopted is linear in η, the global force exerted on the shuttle can be expressed as $F = F_0 \eta_{\text{eff}}/\eta$, where F_0 is the force evaluated at $\mathrm{Kn} = 0$ employing the static viscosity η and $c_t = 0$ in the Stokes equations, *i.e.*, with stick boundary conditions. However, in the Tang resonator both "Poiseuille-like" and "Couette-like" flows provide significant contributions to the overall damping and the corrected viscosity is different in these two elementary cases so that a composite approach must be adopted. The idea basic idea is to employ the BEM code to obtain an estimate of the damping forces F_0^C and F_0^P at $\mathrm{Kn} = 0$ for the portion of the structure where Couette and Poiseuille flows dominate, respectively. The sum of F_0^C and F_0^P corresponds to the real damping force exerted on the structure at high pressure ($\mathrm{Kn} = 0$). When pressure decreases the global force corrected according to the effective viscosity approach is: $F = F_0^C \eta_{\text{eff}}^C(\mathrm{Kn})/\eta + F_0^P \eta_{\text{eff}}^P(\mathrm{Kn})/\eta$. The main obstacle is that Kn is not well defined for the overall 3D structure. However, since the Knudsen number is inversely proportional to pressure, it is a reasonable choice to assume that the correction will have the form:

$$F = F_0^C \frac{\eta_{\text{eff}}^C(\alpha/p)}{\eta} + F_0^P \frac{\eta_{\text{eff}}^P(\beta/p)}{\eta} \tag{5.22}$$

where α and β are constants to be calibrated numerically as detailed in the sequel. The starting point of the calibration procedure is the remark, confirmed in Sec. 5.3,

that the BEM code with slip boundary conditions is very accurate in the slip flow regime. Hence, the Stokes code with static viscosity and slip boundary conditions can be utilized to run a series of analysis in the slip regime, *i.e.*, with $p > .1$ bar; the viscous forces computed are afterwards employed to identify the best values of α and β in Eq. (5.22) by means of standard numerical procedures, *e.g.*, Matlab optimization routines. It is maybe worth stressing once more that this is only a numerical procedure and that no experiments are used to identify α and β.

Once this coefficients are available, Eq. (5.22) can be compared with experimental results to validate all the working hypotheses introduced, as presented in Fig. 5.12. The continuous curve is the plot of Eq. (5.22), while the squares denote experimental results. Numerical results compare accurately with experiments well into the transition region and beyond.

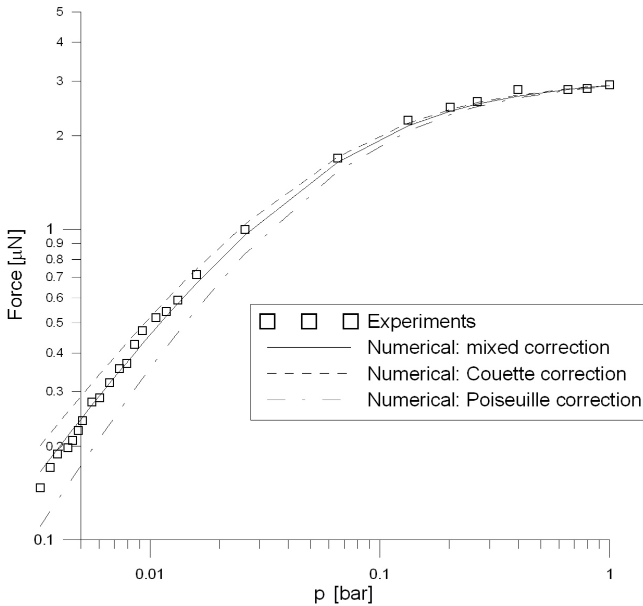

Fig. 5.12. Comparison of measured and computed forces acting on the shuttle at different pressures.

The other two curves in Fig. 5.12, showing increasing errors at low pressures, represent the numerical results obtained by applying, to the whole damping structure, the simple Couette correction and the simple Poiseuille correction, respectively. The same procedure has been also applied to the biaxial resonator of Fig. 5.2 yielding similar conclusions.

However, these technique can be applied only if the flow generating damping forces can be classified either as Poiseuille or Couette, at least as a first approximation. This might be considered as a serious limitation, even if a vast class of MEMS fall into this category.

5.6. Conclusions

We have focused here on a specific but rather diffused class of inertial sensors like accelerometers, gyroscopes and and other resonators which consist of a fixed stator and a suspended shuttle which vibrates at a certain frequency. We have shown that, for a large set of operating conditions in the high-moderate pressure range, fluid damping can be conveniently addressed by means of a linear, incompressible, quasi-static Stokes approach. Integral equations are hence an ideal and robust tool since they reduce the dimensionality of the domain to be analysed allowing for the analysis of full-scale 3D structures and since they are expressed in terms of traction unknowns yielding directly and accurately the viscous force of interest. It has been shown that this approach, coupled with slip boundary conditions, compares very well with available experiments on two different MEMS.

However, when working frequencies increase or pressures decreases, underlying hypotheses might be violated. As a consequence, the effect of inertia has been included for rapidly oscillating flows and a simple “corrected viscosity” approach for low pressures has been proposed and validated for the MEMS layouts at hand.

Acknowledgments

The first author acknowledges the contribution of EU NoE Design for Micro and Nano Manufacture (PATENT-DfMM), contract no: 507255 and of Cariplo Foundation.

References

1. Y. Saad and M. H. Schultz, GMRES: A generalized minimal residual algorithm for solving nonsymmetric linear systems. *SIAM J. Sci. Statist. Comput.*, **7**, pp. 105–126, (1986).
2. J. Barnes and P. Hut, A hierarchical $O(N \log N)$ force-calculation algorithm. *Nature*, **324**, pp. 446–449, (1986).
3. L. Greengard and V. Rokhlin, A fast algorithm for particle simulations. *J. Comput. Phys.*, **73**, pp. 325–348, (1987).
4. R. W. Hockney and J. W. Eastwood, *Computer simulation using particles*. New York: Adam Hilger, (1988).

5. V. Rokhlin, Rapid solution of integral equation of classical potential theory, *J. Comput. Phys.*, **60**, pp. 187–207, (1985).
6. W. Hackbusch and Z. P. Nowak, On the Fast Matrix Multiplication in the Boundary Element Method by Panel Clustering, *N*umer. Math., **54**, pp. 463-491, (1989).
7. D. T. Borup and O. P. Gandhi, Calculation of high-resolution SAR distributions in biological bodies using the FFT algorithm and conjugate gradient method, *IEEE Transactions on Microwave Theory and Techniques*, **33**, pp. 417–419, (1985).
8. L. Greengard and M. C. Kropinski, An Integral Equation Approach to the Incompressible Navier-Stokes Equation in Two Dimensions, *Siam J. Sci. Comput.*, **20**, 318–336, (1998).
9. K. Nabors, F. T. Korsmeyer, F. T. Leighton, and J. White. Preconditioned, adaptive, multipole-accelerated iterative methods for three-dimensional first-kind integral equations of potential theory. *SIAM J. Sci. Statist. Comput.*, **15**, pp. 713–735, (1994).
10. M. D. Altman, J. Bardhan, B. Tidor and J. White, FFTSVD: A Fast Multiscale Boundary Element Method Solver Suitable for BioMEMS and Biomolecule Simulation, *IEEE Transactions on Computer-Aided Design of Integrated Circuits and Systems*, (Special BioChips Issue) **25**, pp. 274–284 (2006).
11. M. Kamon, M. J. Tsuk, and J. White, FastHenry, A Multipole-Accelerated 3D Inductance Extraction Program, *Proceedings of the 30th Design Automation Conference*, Dallas, (1993).
12. N. R. Aluru and J. White, A fast integral equation technique for analysis of microflow sensors based on drag force calculations, *Proc. MSM, Santa Clara, CA*, pp. 283-286, (1998).
13. Xin Wang, J. Kanapka, W. Ye, N. Aluru, J. White, Algorithms in FastStokes and its application to micromachined device simulation, *IEEE Transactions on Computer-Aided Design of Integrated Circuits and Systems*, (Special BioChips Issue), **25**, pp 248–257, (2006).
14. C.C. Lu and W. C. Chew. Fast algorithms for solving hybrid integral equations. *IEEE Proceedings-H*, **140**, pp. 455–460, (1993).
15. C. L. Bailey, R.W Barber and D. R. Emerson, Is it safe to use Navier-Stokes for gas microflows?, *Proceedings of Eccomas2004*, on CDROM, (2004).
16. A. Beskok, G. E. Karniadakis and W. Trimmer, Rarefaction and compressibility effects in gas microflows, *J. Fluids Engng*, **118**, 448–456, (1996).
17. M. Bonnet, *Boundary Integral Equation Methods for Solids and Fluids*, Wiley, Chichester, 1999.
18. S. Chapman and T. G. Cowling, *The mathematical theory of non-uniform gases*, Cambridge University Press, Cambridge, 1960.
19. C. Cercignani and A. Daneri, Flow of a rarefied gas between two parallel plates, *Journal of Applied Physics*, **34**, 3509–3513, (1963).
20. C. Cercignani, A. Frangi, S. Lorenzani and B. Vigna, BEM approaches and simplified kinetic models for the analysis of damping in deformable MEMS, *Engng. Analysis with Boundary Elem.*, to appear, (2007).
21. C. Cercignani, *The Boltzmann equation and its applications*, Springer, New York, 1988.
22. J. Ding and W. Ye, A fast integral approach for drag force calculations to to oscillatory slip Stokes flows., *Int. J. Num. Meth. Engng.*, **60**, 1535–1567, (2004).

23. A. Frangi and J. Tausch, A qualocation enhanced approach for the Dirichlet problem of exterior Stokes flow, *Engng. Analysis with Boundary Elem.*, **29**, 886–893, (2005).
24. A. Frangi, G. Spinola and B. Vigna, On the evaluation of damping in MEMS in the slip-flow regime, *Int. J. Num. Meth. Engng.*, **68**, 1031–1051, (2006).
25. V. Frayss, L. Giraud, S. Gratton and J. Langou, A set of GMRES routines for real and complex arithmetics on high performance computers, *CERFACS technical report*, TR/PA/03/3, (2003).
26. M. Gad-el-Hak, The fluid mechanics of microdevices - the Freeman scholar lecture, *J. Fluids Eng.*, **121**, 5–33, (1999).
27. L. Greengard and V. Rokhlin, A new version of the fast multipole algorithm for the Laplace equation in three dimensions, *Acta Numerica*, **6**, 229–269, (1997).
28. M. Gad-el-Hak, ed. *The MEMS handbook*, CRC Press, 2002.
29. G. E. Karniadakis and A. Beskok, *Micro flows, fundamentals and simulation*, Springer, New York, 2002.
30. J. S. Milroy, S. Hinduja and K. Davey, The elastostatic three dimensional boundary element method: analytical integration for linear isoparametric triangular elements, *Appl. Math. Modelling*, **21**, 763–782, (1997).
31. S. Mukherjee, S. Telekunta, Y.X. Mukherjee, BEM modeling of damping forces on MEMS with thin plates, *Engng. Analysis with Boundary Elem.*, **29**, 1000–1007, (2005).
32. N. Nishimura, Fast multipole accelerated boundary integral equation methods, *Applied Mech. Reviews*, **55**, 299–324, (2002).
33. J. H. Park, P. Bahukudumbi and A. Beskok, Rarefaction effects on shear driven oscillatory gas flows: A direct simulation Monte Carlo study in the entire Knudsen regime, *Physics of Fluids*, **16**, 317–330, (2004).
34. H. Power and L. Wrobel, *Boundary Integral Methods in Fluid Mechanics*, Computational Mechanics Publications, Southampton, 1995.
35. J. Tausch and J. White, Second Kind Integral Formulations of the Capacitance Problem, *Adv. Comput. Math.*, **9**, 217–232, (1998).
36. W. Ye, X. Wang, W. Hemmert, D. Freeman and J. White, Air damping in lateral oscillating micro-resonators: a numerical and experimental study, *Journal of MEMS*, **12**, 557–566, (2003).
37. S. Yuhong, R. W. Barber and D. R. Emerson, Inverted velocity profiles in rarefied cylindrical Couette gas flow and the impact of the accommodation coefficient, *Physics of Fluids*, **17**, 047102–7, (2006).
38. T. Veijola, H. Kuisma, J. Lahdempera and T. Ryhanen, Equivalent circuit model of the squeezed gas film in a silicon accelerometer, *Sensors & Actuators*, **48**, 239–248, (1995).
39. T. Veijola, H. Kuisma and J. Lahdempera, The influence of gas-surface interaction on gas-film damping in a silicon accelerometer, *Sensors & Actuators*, **66**, 83–92, (1998).
40. T. Veijola and M. Turowski, Compact damping models for laterally moving microstructures with gas-rarefaction effects, *Journal of Microelectromechanical Systems*, **10**, 263–273, (2001).
41. J. R. Phillips and J. White, A precorrected-FFT method for electrostatic analysis of complicated 3D structures, *IEEE Trans. Comput. Aided Devices*, **16**, 1059–1072, (1997).

42. C. Pozrikidis, *Boundary Integral and Singularity Methods for Linearized Viscous Flows*, Cambridge Univeristy Press, Cambridge (1992).
43. W. Ye, J. Kanapka, X. Wang and J. White, Efficiency and accuracy improvements for FastStokes, a precorrected-FFT accelerated 3D Stokes solver, *Technical Proceedings of the 1999 International Conference on Modeling and Simulation of Microsystems*, 502–505, (1999).
44. G. A. Bird, *Molecular Gas Dynamics and the Direct Simulation of Gas Flows*, Oxford Sicence Publication, (1994).
45. X. Wang, M. Judy and J. White, Validating Fast Simulation of Air Damping in Micromachined Devices, Proceedings of *MEMS '02*, January, (2002).
46. L. Ying, G. Biros, and D. Zorin, A kernel-independent adaptive fast multipole algorithm in two and three dimensions *J. Comp. Physics*, **196**, 591–626, (2004).
47. G.K.Batchelor, *An Introduction to Fluid Dynamics*, Cambridge University Press, Cambridge, (2000).
48. X. Wang and J. White, Analyzing Fluid Compression Effects in Complicated Micromachined Devices, *Proceedings of Transducers 01* (2001).
49. X. Wang, *FastStokes: A Fast 3D Fluid Simulation Program for Micro-Electro-Mechanical Systems*, Ph.D. Thesis, MIT, (2002).

This page intentionally left blank

Chapter 6

Experimental Techniques for Damping Characterization of Micro and Nanostructures

Alain Bosseboeuf and Hervé Mathias

Institut d'Electronique Fondamentale, Université Paris-Sud, UMR CNRS 8622
F-91405 ORSAY Cedex, France
alain.bosseboeuf@ief.u-psud.fr

After presenting some general considerations on damping mechanisms, quality factor analysis methods and *ex-situ* excitation techniques, we first review a number of classical and recent optical techniques that are suitable for quality factor measurements of in-plane, out-of-plane and torsional vibrations of micro-resonators; then, techniques based on electrical measurement and some possible architectures for integrated Q factor measurements are examined; finally, approaches suitable for nanoresonators are discussed.

Contents

6.1 Introduction 183
6.2 General Requirements, Analysis Procedures and Techniques 184
6.2.1 Damping Mechanisms and their Parameters 184
6.2.2 Measurement System Requirements 186
6.2.3 Methods for Quality Factor Extraction 187
6.2.4 Vibration Excitation Techniques 192
6.3 Quality Factor Measurements by Optical Techniques 195
6.3.1 General Features of Optical Measurement Techniques 195
6.3.2 Damping Measurement of In-Plane Vibrations 197
6.3.3 Damping Measurements of Out-of-Plane and Torsional Vibrations 205
6.3.4 Conclusion 215
6.4 Electrical Techniques and Alternative Techniques for Quality Factor Measurement 215
6.4.1 Electrical Techniques 215
6.4.2 Measurement Techniques for Nanoresonators 223
References 226

6.1. Introduction

Micro and nanoresonators have been extensively employed in a number of applications as sensors of electrostatic[5] and magnetic[6] fields, of gases and liquids,[7]

of biological[8] and chemical processes;[9] as sensors of strain and/or force,[12] of pressure,[12,13] of inertia,[12,14,15] and of mass.[16,17] They have also been applied to communication and signal processing,[10] as reference oscillators[11] and to evaluate properties of thin film materials.[1–4]

More recently they have also been increasingly applied to the investigation of fundamental phenomena[18,116] including quantum effects[19] or to the detection of individual biological species.[20]

Damping of vibrations is a major issue for micro and nanoresonators. Despite numerous theoretical and experimental works, vibration damping remains difficult to predict, especially at low pressure where surface and material effects dominate. Often, a stronger than expected damping is observed. In a more general way, damping modelling of resonators having an intricate (and imperfect) geometry, or prone to acoustic or other coupling, is complex and measurements often remains the only way to accurately evaluate damping. In this chapter we will review the main experimental techniques available for such a characterization. In Sec. 6.2, we will first recall very briefly the main vibration energy loss mechanims in micro and nanoresonators and will present some techniques and analysis procedures that are common to all measurements techniques. Damping is often evaluated from direct measurement of the resonator motion by optical means. Optical techniques suitable for the characterization of in-plane, out-of-plane and torsional vibration damping of microresonators are reviewed in Sec. 6.3. Finally, electrical techniques and some alternative approaches developed recently for nanoresonators are discussed in Sec. 6.4.

6.2. General Requirements, Analysis Procedures and Techniques

6.2.1. *Damping Mechanisms and their Parameters*

For most sensing applications of micro and nanoresonators, achieving a high value of the quality factor Q is a key issue because the thermomechanical noise, which gives the minimum measurable force, is governed by dissipation processes. Maintaining a high Q factor reduces as well power requirements and results in an improved stability. A high Q value is also needed to achieve electromechanical filters with a narrow bandwidth or to get accurate resonant frequency measurements. For other applications, the variation of the quality factor or of the resonant frequencies with the surrounding environment is the quantity of interest. For example the pressure dependence of the Q factor of an integrated resonator is commonly used to evaluate the vacuum level inside wafer-level packages[21] and fluid density and/or viscosity can be evaluated from dynamic measurements of resonators.[7]

Consequently, numerous theoretical and experimental investigations were performed to understand the vibration energy loss mechanisms of (electro)mechanical resonators. Energy losses of a mechanical oscillator comprise external losses in which energy flows out of the oscillator and is dissipated in the ambient medium by viscous friction, by acoustic waves or through supports, and to internal losses involving various processes within the bulk and at the surfaces of the oscillator. The total quality factor Q_{tot} depends on the contribution of each of these mechanisms:

$$\frac{1}{Q_{\text{tot}}} = \sum_i \frac{1}{Q_i} = \frac{1}{Q_{\text{bulk}}} + \frac{1}{Q_{\text{surface}}} + \frac{1}{Q_{\text{support}}} + \frac{1}{Q_{\text{viscous}}} + \ldots. \tag{6.1}$$

where Q_{bulk} is related to bulk material losses such as thermoelastic damping,[22] phonon mediated dissipation,[23] defect related losses,[24,25] etc...., Q_{surface} arises from surface losses[25,26] related to surface stress, surface roughness, adsorbed layers, natural oxides and other not well identified phenomena, Q_{support} is related to irreversible losses at the anchors[22,27,28] and Q_{viscous} results from gas damping.

It is clear from Eq. (6.1) that the total Q factor is limited by the major loss mechanism. To characterize the damping of a mechanical micro or nanoresonator it is necessary to understand the parameters of the different mechanisms. In gaseous media, vibration energy loss results from gas-structure interactions and varies according to the pressure range, the gas viscosity, the vibration direction, the vibration frequency and the device geometry (see Chapters 1, 2, and 5). At atmospheric pressure, gas damping is largely the dominant loss mechanism and Q factor values of micro and nanostructures are typically in the 10 to 1000 range. In liquid media viscous damping is very large, Q values being typically lower than 10 and damping produces a significant shift of the resonant frequencies. These quantities depend on the density and viscosity of the surrounding liquid. Finally, at sufficiently low pressure (below $10^{-3} - 10^{-4}$ mbar) other mechanisms limit the quality factor which is usually large (in the order of 10^5 for single crystal resonators at room temperature[22]). Material thermal and mechanical properties, their structure, the amount of bulk and surface defects, and the device surface topography then play a significant role.

Vibration loss mechanisms are temperature dependent[29] phenomena, the highest Q factor being obtained at low pressure and low temperature. They depend as well in a complex way on the resonator size and geometry. Nevertheless there is a clear trend towards a reduction of the Q factor when the resonator is reduced from the submillimeter scale towards the nanoscale.[30] In vacuum, this partly due to a larger contribution of surface effects.

6.2.2. *Measurement System Requirements*

Measurements into vacuum are clearly required to investigate damping related to bulk and surface phenomena. They are also interesting for material fatigue assessment because high quality factors allow large vibration amplitudes and more accurate measurements of the time-dependence of the quality factor or the resonant frequencies. When external pressure can be varied, the different regimes of gas damping and their modelling can be investigated. Likewise, measurements of resonant frequencies, amplitudes and/or quality factor as function of pressure are required for the calibration of resonant pressure sensors. For resonating sensors used for vacuum packaging process evaluation, a pressure range in the 10^{-3} mbar-1000 mbar covers most of the needs as internal pressure of packages seldom exceeds this range. Finally, published works show that measurements in an ultra-high vacuum chamber allowing high temperature annealing or/and measurements at cryogenic temperatures provide valuable information on bulk material and surface related damping phenomena.

Relatively few measurements of Q factors as function of temperature have been published even if the ability to perform measurements as function of temperature is useful to find the limiting mechanisms or more generally to get data in the usual temperature range of component specifications.

Ideally, for damping characterization of microresonators, the measurement technique should have a detection limit lower than the thermomechanical noise of the resonator, a lateral resolution in the micrometer range or below and the largest possible frequency bandwidth. In practice, a detection limit of vibration amplitude around one nanometer, a lateral resolution of a few micrometers and a bandwidth of a few MHz already cover a large part of the needs. Nevertheless, a larger frequency bandwidth and a lower detection limit become necessary for damping investigation of high order vibration modes or to characterize nanoresonators, acoustic devices and electromechanical RF filters. In these latter cases, it might be necessary to measure vibration amplitudes down to the picometer range and resonant frequencies up to 1 GHz.[31]

As discussed in the next section, point-wise vibration spectra or transient response measurements are in principle sufficient for quality factor evaluation. However identification of the device resonances can sometimes be tedious because they can be mixed with parasitic resonances of the excitation system or of the sample holder and because various external coupling and vibration mode intermixing may occur. Vibration mapping must then be performed to remove the resulting ambiguities.

6.2.3. *Methods for Quality Factor Extraction*

In order to simplify the discussion, the resonator under test is assumed to be accurately modelled using the mass-spring-damper model shown in Fig. 6.1.

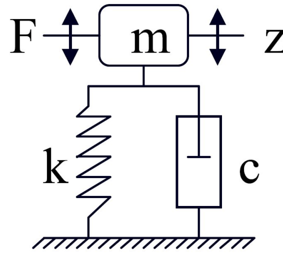

Fig. 6.1. Classical model used to represent a damped oscillator under forced vibrations.

The corresponding equation of motion under forced vibrations is given by:

$$m\frac{\mathrm{d}^2 z}{\mathrm{d}t^2} + c\frac{\mathrm{d}z}{\mathrm{d}t} + kz = F_a \cos(\omega t) \tag{6.2}$$

where m is the mass of the resonator, c the (viscous) damper constant, k the spring constant, F_a the magnitude of the applied sinusoidal force and ω its pulsation.

A similar equation can be established when the resonator is excited from its base. In both cases the micro/nanoresonator is thus equivalent to a second order low pass filter with a natural frequency given by:

$$\omega_n = 2\pi f_n = \sqrt{\frac{k}{m}} \tag{6.3}$$

and a quality factor Q, representing the filter selectivity around the resonant frequency. Q is related to damping characteristics and is given by the following equation:

$$Q = \frac{m}{c}\omega_n = \frac{\sqrt{km}}{c} \tag{6.4}$$

This quality factor is one of the main features of sensors based on vibrating MEMS since it defines their ultimate resolution in terms of frequency variation. The following subsections will focus on two families of techniques allowing for experimental quality factor extraction: frequency domain analysis and transient response analysis.

6.2.3.1. *Frequency Domain Analysis*

This first class of methods consists in extracting the quality factor Q from the resonator's transfer function monitored in the frequency domain (Fig. 6.2).

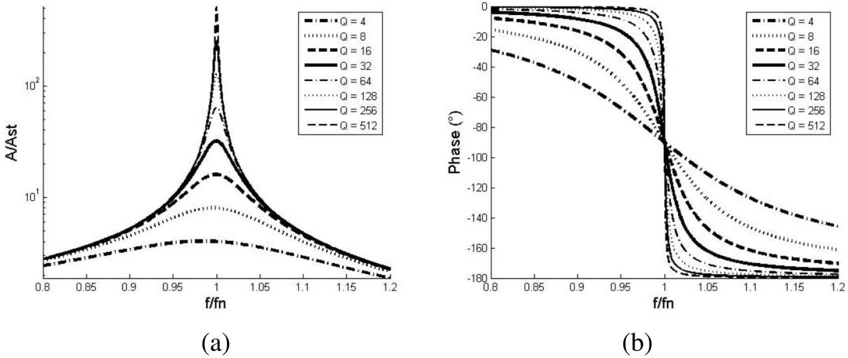

Fig. 6.2. Relative displacement amplitude (a) and phase (b) as function of the normalized frequency f/f_0 for MEMS/NEMS resonators having different Q values.

A first extraction method is based on phase computations. The phase between the resonator displacement and actuation force is indeed given by:

$$\phi(f) = \tan^{-1}\left\{\frac{\left(\frac{f}{Qf_n}\right)}{1-\left(\frac{f}{f_n}\right)^2}\right\} \tag{6.5}$$

Notice that at the natural frequency, the phase is $-90°$, which is a way to determine f_n. The slope of the phase curve around f_n is proportional to Q:

$$\frac{d\phi}{df}(f_n) = -\frac{2Q}{f_n} \tag{6.6}$$

This extraction method is interesting since large variations of the phase are observed. For example, it has been used to determine the quality factor of high frequency (>1 GHz) piezoelectrically transduced disk resonators.[32] This method is well suited for low to mid Q values (215 in the example). For higher values, its accuracy is limited by the frequency resolution of the spectral analysis and to the phase noise.

Other methods are based on the monitoring of the displacement or the vibration amplitude. Around a resonant frequency, the amplification gain varies with

frequency as follows:

$$A(f) = \frac{x}{F_a}(f) = \frac{A_{st}}{\left\{\left[1 - \left(\frac{f}{f_n}\right)^2\right]^2 + \left[\frac{f}{Qf_n}\right]^2\right\}^{1/2}} \tag{6.7}$$

which is a lorentzian function, A_{st} being the static gain.

As shown on Fig. 6.2, the maximum gain frequency or resonant frequency, $f_{\max}$, depends on Q:

$$\frac{f_{\max}}{f_n} = \sqrt{1 - \frac{1}{2Q^2}} \tag{6.8}$$

The lower the quality factor Q, the larger will be this shift of the maximum peak with respect to resonant frequency. For example, the relative frequency shift for $Q = 50$ is of only 0.01% while it is 1% for $Q = 5$. Measuring this frequency shift is adapted for low Q value, typically for resonators working in liquids.[8] The highest measurable Q value again depends on the frequency resolution. The lower limit is linked to the resolution of amplitude measurements.

In most cases, the quality factor is sufficiently high to consider that $f_{\max} = f_n$. It can then be assumed that the maximum value corresponds to the gain at natural frequency, which is proportional to Q: $A(f_n) = A_{st}Q$.

If the static gain is known, measuring the maximum displacement for a known actuation force yields Q. In practice the static gain is approximated by the gain value outside and far from any resonance with the same excitation level. The corresponding accuracy is not optimal since it depends on the ratio of a large value over a low and noisy value. To improve the accuracy, a very common technique[33,34] to get a quick but reliable estimation of the quality factor is to measure, as shown in Fig. 6.3, the frequencies f_+ and f_- defined by:

$$A(f_+) = A(f_-) = \frac{A_{\max}}{\sqrt{2}} \tag{6.9}$$

The quality factor is obtained by computing the ratio between $f_{\max}$ and the bandwidth $f_+ - f_-$:

$$\frac{f_{\max}}{f_+ - f_-} = \frac{1}{\sqrt{1 + \frac{1}{Q}\frac{\sqrt{1 - 1/(4Q^2)}}{1 - 1/(2Q^2)}} - \sqrt{1 - \frac{1}{Q}\frac{\sqrt{1 - 1/(4Q^2)}}{1 - 1/(2Q^2)}}} \approx Q. \tag{6.10}$$

The accuracy is better since the necessary amplitude measurement is performed using relative measurements and only requires a single analysis. These extraction

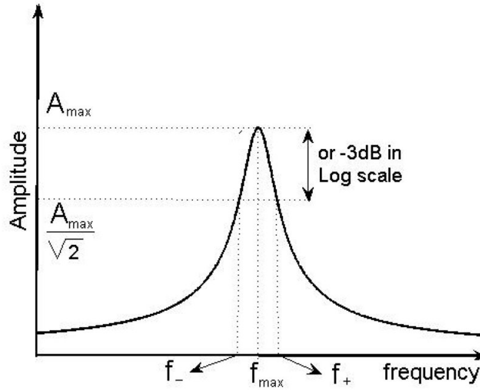

Fig. 6.3. Q computation using -3dB bandwidth.

methods are well suited for quality factors ranging from a few tens to a few thousands. For higher values, depending on the resonant frequency and the frequency resolution of the spectral analysis, an accurate value for the maximum displacement may be difficult to obtain. In these cases, a fit with a Lorentzian function with the resonant frequency, the static gain and the quality factors as parameters, gives better results.[22,35,36]

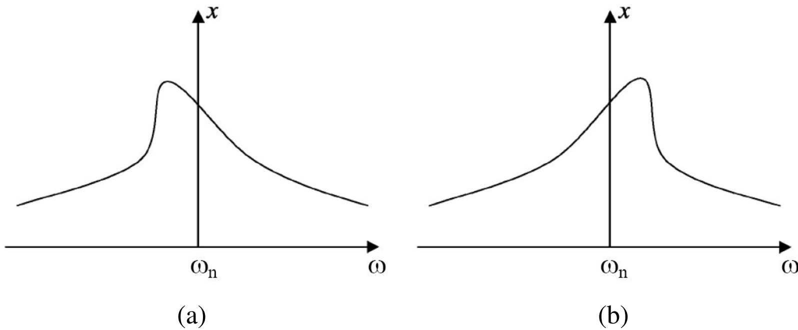

Fig. 6.4. Non-linear effects for large MEMS displacement: soft spring effect (a) and hard spring effect (b).

For these frequency domain methods, care must be taken to keep the actuation force sufficiently small to remain in the linear vibration domain. Depending on the type of actuation and on the resonator structure, different kinds of nonlinear effects may appear for large displacements. Non-linearities arise when the

(effective) spring stiffness k becomes dependent on the resonator structure displacement z. Depending on the sign of higher order terms of the spring restoring force, there is a resonant frequency shift either downward (soft-spring effect, Fig. 6.4(a)) or upward (hard spring effect, Fig. 6.4(b)) together with a modification of the resonant bandwidth and the occurrence of an hysteresis when the frequency is scanned in the reverse direction.[37,38] Hard spring effect is typically related to a non-linear mechanical behaviour while soft spring effect is usually related to a non-linear actuation, a typical case being electrostatic actuation. To give an order of magnitude, hard spring effect begins to occur for vibration amplitudes larger than a few percents of the vibrating thickness for bridge-like resonators and beyond about 10-20% of the vibrating thickness for a cantilever beam. It is clear that Q factor extraction methods described above are no longer valid when resonance curves are distorted because of non-linear effects.

6.2.3.2. *Transient Response Analysis*

Since Q is linked to the damping characteristic of the MEMS resonator, the transient response to a non periodic signal may be exploited to extract the quality factor value.[39] Figure 6.5 shows the corresponding time domain response, for different values of Q, to a pulse force variation. The response is a pseudo-periodic decaying signal whose envelope is an exponential curve with a time constant linked to Q. For an initial velocity equal to zero, it is given by:

$$x(t) = \underbrace{x(0)e^{\left(-\frac{\pi f_n}{Q}t\right)}}_{envelope}\Bigg[\cos\left(2\pi f_n t\sqrt{1-\frac{1}{4Q^2}}\right) + \frac{1}{\sqrt{4Q^2-1}}\sin\left(2\pi f_n t\sqrt{1-\frac{1}{4Q^2}}\right)\Bigg] \tag{6.11}$$

Q can then be extracted by measuring the time T_m needed for the envelope to reach a given value z_m:

$$Q = T_m \frac{\pi f_n}{\ln\left(\frac{x(0)}{x_m}\right)} \tag{6.12}$$

This method is suitable for large values of Q. In this way very large values ($Q > 10^5$) may be accurately measured, provided that the measurement duration is large enough with respect to the pseudo-period of the decaying signal.

There is however a practical problem with this method: MEMS resonators have several different resonant modes and resonant frequencies. If not correctly

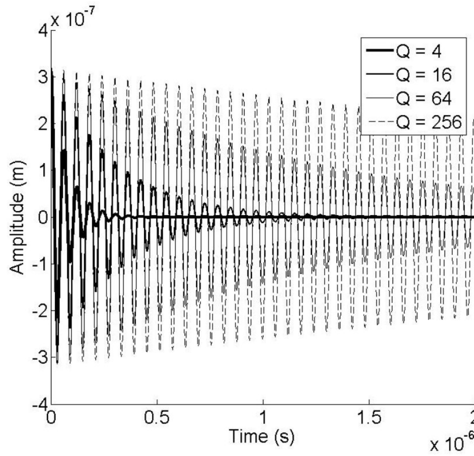

Fig. 6.5. Transient response of a MEMS resonator to a pulse force variation.

chosen, the applied pulse may put into play other modes in addition to the one desired. For example, in the theoretical case of a dirac pulse with a white spectrum, all the resonant modes of the structure would be excited in the same way. Then, specific signal processing methods might be needed to identify and characterize the different modes composing the transient signal.[40]

However, a good choice of the applied pulse could also solve this problem. Figure 6.6 shows different possible signals and their corresponding spectra. First, by adjusting the length of a pulse, one can modify the corresponding sinc-function shaped spectrum so that undesirable modes are not excited. The width of the lobes in the frequency domain is indeed equal to the inverse of the pulse duration[40] (Fig. 6.6(a)). If the considered mode is the first resonant mode, a sinc-shaped pulse may be used since its rectangular spectrum width is equal to its pseudo-pulsation[40] (Fig. 6.6(b)). Finally, the best choice, allowing to select only the desired mode, is to use a sinusoidal signal at the desired resonant frequency and to record the transient response when it is switched off. The corresponding spectrum is indeed close to a delta-shaped function at the resonant frequency (Fig. 6.6(c)).

6.2.4. *Vibration Excitation Techniques*

Modal testing[42,43] consists in identifying the natural resonant frequencies, the modal damping and the corresponding modal shapes of the structures. Once known, they can be used to predict the vibration at any point of the structure under a given excitation. Modal testing normally needs an excitation with a known force,

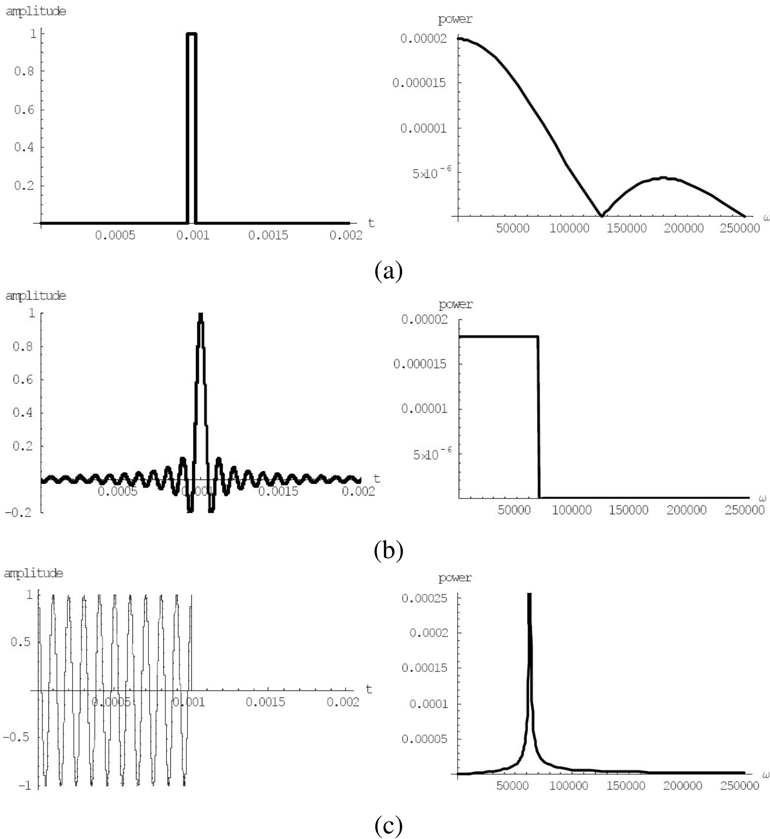

Fig. 6.6. Possible non periodical actuation signals to perform transient analysis and their corresponding spectra: (a) single pulse, (b) single sinc-function pulse, (c) sinusoid at resonant frequency multiplied by downward unit step function.

a measurement of the frequency response of the micro/nanostructures and extraction of the modal parameters from the measured data. Such a modal analysis is difficult to apply to micro and nanoresonators because the excitation level required is so low that it cannot be easily controlled. For example vacuum measurements of very high Q microresonators needs excitation amplitudes in the picometer range or less to avoid the occurrence of non-linear vibrations at resonance. Luckily enough, in comparison to macroscopic mechanical systems, MEMS and NEMS devices have simpler geometry and dynamic behaviour as well as high quality factors. So a known and pure in-plane, out-of plane or torsion excitation is often not mandatory in practice.

When the resonator under test cannot be actuated in situ, an external excitation system must be chosen. Several excitation techniques were implemented by experimenters. The main common ones are discussed in the following.

Electrothermal actuation[44,45] is based on Joule effect generated by an alternate current. This method induces a direct but inhomogeneous actuation by thermal expansion of the resonator material and can be applied only to conducting devices with two isolated access. Excitation direction is determined by device geometry and the maximum efficient excitation frequency is limited by the device thermal constant (typically a few (tens) kHz for a microresonator). In other terms, the modulated temperature becomes rapidly a small fraction of the mean temperature rise when the current modulation frequency is increased. A major drawback of this technique is thus device heating which affects both the elastic and damping behaviour. An elegant way to overcome this issue is to use magnetomotive actuation.[46,47] In this technique the device is driven at resonance by a low variable current in the presence of a high magnetic field (several Tesla). The resulting Lorentz force has an orientation given by the magnetic field and is suitable for the actuation of resonators up to very high frequencies and it has been indeed applied to nanoresonators including carbon nanowires and nanotubes.[46,47]

A very common and easy to implement excitation, is to put or glue the sample (bare die, die mounted in a package or wafer) on a piezoelectric actuator which acts as a shaker.[42,48] For frequencies up to a few hundreds of kHz, a PZT multistack actuator allows both out-of-plane and in-plane vibration excitation with a nominal amplitude ranging from a fraction of Angström to a micrometer or more. When a larger frequency range is needed, a metallised single piezoelectric disk (out-of-plane vibrations) or a shear plate (in-plane vibrations) becomes necessary. These devices are able to generate vibrations up to a few (tens) MHz but in a single direction and with a nominal amplitude limited to a few nm. Larger amplitudes can be obtained with a high voltage ultrasonic shaker. Base excitation with such systems is normally sufficient for damping measurements even for highly decoupled resonators at high pressure[22] possibly because some amplifying (levering) effect by the substrate or the support often occurs and because most common vibrometry techniques have a detection limit in the nanometer range or much below.

When a direct, local and non contact excitation of vibrations is needed, optical actuation with a focused and intensity-modulated light beam is a possible alternative.[49–55] The efficiency of this actuation is not straightforward to predict as several phenomena may be involved such as direct[49–54] and indirect[53] photothermal effect, radiation pressure,[50,51] light interferences,[52] electronic strain,[53] and eventually photoelectric effects[54] or change of material structure.[55] Consequently optical actuation depends on many parameters including light beam characteristics

(intensity, wavelength, focusing, position, modulation frequency), resonator material properties (optical, thermal and mechanical) and resonator geometry. This actuation technique is usually suitable for low level excitation of out-of-plane or torsion vibrations at moderate frequencies. Actually, in vacuum, a very low excitation is required and self excitation of simple beams can even be achieved with continuous light in some conditions.[51]

For metallic (coated) devices, the photo thermal effect, *i.e.*, the generation of thermal stress gradient by light absorption, is the dominant mechanism and the light beam power must be low to limit heating. For semiconductor resonators, electronic strain generated by the diffusion of photocarriers may produce an equivalent and even larger actuation than the photothermal effect but with an opposite sign and a faster response time.[53] A suitable choice of parameters allows measurements at higher frequency with reduced heating. Finally, for transparent devices, interference effects can be tuned to increase actuation efficiency and radiation pressure actuation can be exploited up to several hundreds of MHz even if the resulting actuation force is very low (typically around 1 pN per mW of incident light power).

Other less common ex-situ excitation techniques include excitation with an atomic force microscopy tip,[56] non-contact excitation by acoustic pressure waves generated by a loudspeaker[57] or solid acoustic waves, distant excitation by electrostatics,[58] shock base excitation with an electrical discharge or a pneumatic gun,[59] excitation of magnetic film coated devices with an electromagnetic coil and other ones.[60]

6.3. Quality Factor Measurements by Optical Techniques

6.3.1. *General Features of Optical Measurement Techniques*

In this section we will focus on optical measurement techniques suitable for quality factor measurements from vibration spectra or transient response. Information on full field optical techniques suitable for mode shape measurements of microresonators can be found in a recent book[61] and in several papers.[60,62,63]

Optical characterization techniques of the quality factor of resonators rely on the use of a sensing light beam focused or collimated on the device and the detection with a photodetector or a camera of the reflected, transmitted, diffracted or scattered light (Fig. 6.7).

The major interest of optical techniques is their ability to allow non-contact, direct, spatially resolved and quantitative measurements of out-of-plane, in-plane and torsional motions. In addition, contrary to electrical measurements, most of

them do not need specific sample preparation, nor electrodes, so that they can be applied at any stage of the device development provided than an external excitation technique is used. Finally, they have mapping capabilities, a useful feature for vibration mode analysis.

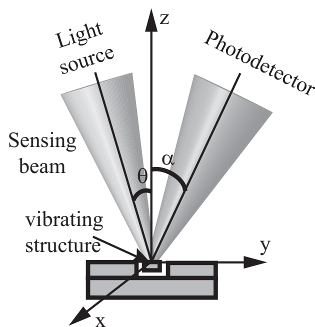

Fig. 6.7. General principle of vibration measurement of microstructures by optical techniques. θ is the incidence angle ($0 \leq \theta \leq 90°$) and α is the detection angle ($0 \leq \alpha \leq 180°$).

In a general way, the signal to noise ratio of optical detection techniques is inversely proportional to the detection bandwidth so lock-in detection or heterodyning techniques are typically used. The detection limit of optical techniques is also improved by an increase of the detected light power, and thus of the sensing beam power. In practise the sensing beam light power is actually limited by device heating caused by the photothermal effect. It may become significant and may even damage the device for a small and absorbing device and a highly focused beam.[64] The temperature rise can be computed by solving the heat diffusion equation with absorbed light power density as a volume heat source or by using heat flow as a surface boundary condition.[49–54] Experimentally, excessive heating can be detected by a variation of the resonant frequencies when the light power is changed.

Another common issue of optical vibrometry techniques is the measurement of (semi-)transparent devices. In this case, a thin metallic layer is often added on the device surface to increase the reflectivity and to avoid light interference effects within the device or between the bottom surface and the substrate. If the additional layer is sufficiently thin, resonant frequencies variation may be negligible but for intrinsic losses characterization, this must be clearly avoided because it can largely affect the vacuum quality factor. As discussed in Sec. 6.3.3.2, in some cases light interference effects between the device and the substrate can be exploited to obtain very high sensitivity measurements of out-of-plane vibrations.

In a general way, optical techniques can be applied to quality factor measurements as a function of working pressure by performing measurements through the window port of a vacuum chamber. Nevertheless this becomes difficult when a highly focused sensing beam is required because of the lack of commercially available long distance and compensated lenses with high numerical aperture. Fortunately, some techniques still work when the light beam spot size is larger than the device lateral dimensions despite the resulting degradation of signal to noise ratio. Another solution is to use a thin (micromachined) transparent membrane as a window. For measurements as function of temperature, a vacuum environment or a N_2 blowing is recommended to avoid microscope lenses heating or water vapour condensation/freezing on the sample.

Unless otherwise stated, we will henceforth assume that the top surface of the vibrating structure is horizontal (in the $x - y$ plane) and that the sensing beam is vertical ($\theta = 0$) or tilted with respect to the vertical z-axis (see Fig. 6.7). Consequently out-of-plane vibrations are along the z axis and in-plane vibrations are along a direction in the $x - y$ plane.

6.3.2. *Damping Measurement of In-Plane Vibrations*

Because lateral actuation is easier to integrate, many resonating sensors are designed for in-plane vibrations. Most micromachined resonators have optically smooth top surfaces, *i.e.*, surfaces with a roughness much lower that the optical wavelength, at least in the visible range. Consequently for low in-plane displacements, the surfaces are locally invariant by translation and the only way to detect in-plane motion is to exploit the presence of sharp edges at the periphery of the microstructure and around the openings made in the moving microstructure. We will examine below three kind of techniques based respectively on image processing, on partial obscuration (knife-edge techniques) and on diffraction. Then we will briefly mention techniques suitable for sufficiently rough surfaces.

6.3.2.1. *Image Processing Techniques*

The most common techniques for in-plane vibration measurements of microresonators are based on optical microscopy associated with image processing. For all these techniques, the detection limit depends on the ratio of the pixel size to the lens magnification and on the contrast between the moving part image area and the background image area.

The simplest technique, initially proposed by Burns and Helbig,[65] is to analyse by image processing the vibration-induced blur at the edges of the device. For

vibrations larger than a few pixels, motion direction can readily be determined by comparing images in the static and dynamic cases. This is illustrated in Fig. 6.8 for images of a laterally driven comb drive resonator (Tang resonator) taken from our institute.

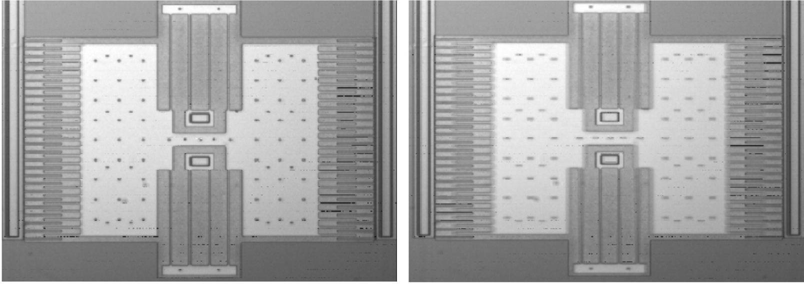

Fig. 6.8. Images of a Tang resonator fabricated in MUMPS polysilicon technology. a) Image at rest (no motion). b) Time-averaged blurred image recorded at resonance ($f = 8.2$ kHz). Vibration is along the horizontal axis.

The blurred image is the convolution of the image taken at rest and the optical point spread function related to blur. If the vibration period is much lower than the image integration time, the blur profile depends on the vibration amplitude and its direction but not on its frequency. By minimizing the difference between synthetic blurred images generated from the image at rest and the real blurred image, vibration amplitudes down to a fraction of a pixel can be measured. By applying this method on an image line, Burns *et al.*[65] demonstrated motion amplitude measurements with a reproducibility of +/-0.2 pixel (50 nm at the sample level) and quality factor values in agreement with values measured by stroboscopic microscopy. Work in progress shows that full field bi-directional measurements with a detection limit lower than 0.1 pixel can be achieved.

This method has a limited resolution and is not able to measure the vibration phase but it can be applied at any the vibration frequency higher than the video rate. Time-resolved measurements with a lower detection limit can be achieved by processing optical microscopy images recorded in the stroboscopic mode. This technique, first investigated at MIT,[66,67] is now the most widely used one for in-plane vibration measurements of MEMS. Various implementations with various names were developed by several laboratories[22,61,62,68–71] and manufacturers of optical profilometer-vibrometers. In this technique, the sample is illuminated with light pulses. If the light pulses are synchronized to the vibration and if their duration is much lower than the vibration period, the resulting “frozen” image

corresponds to a position of the moving microstructure during its sinusoidal vibration cycle. This illustrated in Fig. 6.9 for the case of two positions around the extrema at resonance of the Tang resonator of Fig. 6.8.

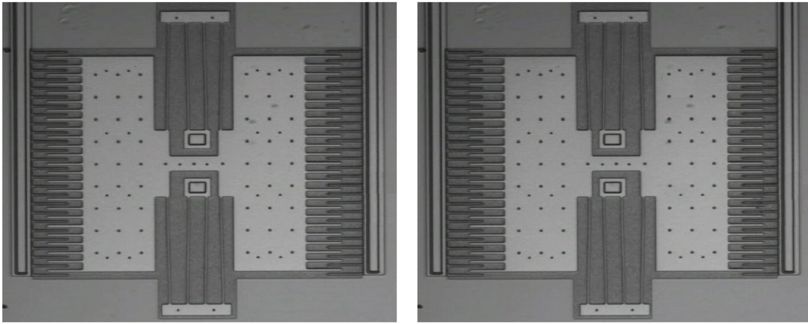

Fig. 6.9. Stroboscopic images of a Tang Resonator at resonance. a) Shuttle mass close to the maximum left position b) Shuttle mass close to the maximum right position.

The resonator motion can be quantified by image processing techniques based on intensity gradient analysis[66–70] or on correlation.[72] Finally, by varying the delay of the light pulse with respect to the vibration period, the whole sinusoidal motion can be extracted. By repeating this process for different frequencies, motion versus frequency can be measured around a resonance and the quality factor can be computed as indicated in Sec. 6.2.3.1. This technique can also be applied to repetitive transients to get the quality factor from the decreasing oscillations. In that case, the light pulse delay is changed for each transient.

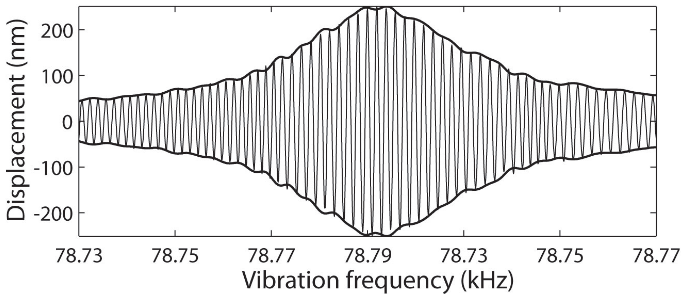

Fig. 6.10. Spatially-averaged motion around the fundamental resonance of a Si beam measured by optical stroboscopic microscopy at a pressure of 5×10^{-4} mbar.

A convenient way to modulate the phase is to adjust the light pulse repetition rate at a frequency f_2 slightly larger or lower than the vibration frequency f_1. Then the apparent motion is a slowed down version of the real motion at the frequency $\Delta f = |f_2 - f_1|$. If Δf is slower than the video rate and an optimized in-flight image processing algorithm is used, the full field bi-directional motion can be measured as function of frequency in real time.[22,62] An example of vacuum measurement on a Si cantilever beam by this method is shown in Fig. 6.10.

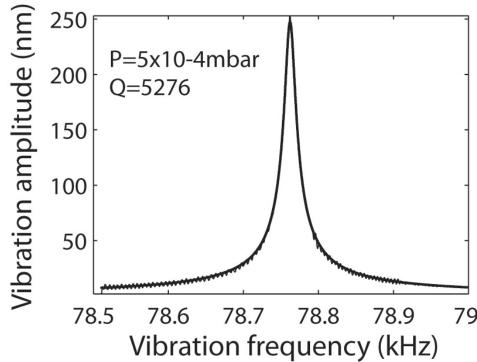

Fig. 6.11. Resonant peak of a Si cantilever beam measured by optical stroboscopic microscopy with image processing.

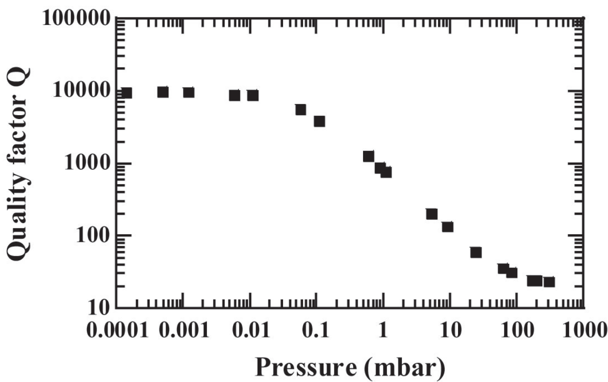

Fig. 6.12. Quality factor pressure dependence for the Tang resonator of Fig. 6.9. Measurement by stroboscopic optical microscopy with image processing.

Then the vibration amplitude and phase can be extracted by Fast Fourier Transform (FFT) demodulation which, at the same time, drastically reduces the

noise and effects of parasitic vibrations.[22] Figure 6.11 gives the result of such an amplitude demodulation for the signal of Fig. 6.10 in a larger frequency range. Finally the quality factor can be extracted from a Lorentzian fit of the resulting curves as discussed in Sec. 6.2.3.1.

Vibration amplitudes as low as 1 nm (corresponding to 5×10^{-3} pixel) can be measured at video rate by this method even in a vacuum chamber with the pumping system on.[22] Figure 6.12 shows the pressure dependence of the quality factor of the Tang resonator of Fig. 6.9 measured by this method and clearly indicate that, in this case, air damping limits the quality factor for pressures down to about 8×10^{-3} mbar.

As mentioned just above, stroboscopic microscopy measurements allow both quantitative amplitude and phase measurements of in-plane vibrations. However, since phase measurements are more sensitive to drift and need a noise-sensitive unwrapping step, published measurements of the quality factor exploiting this technique are generally based on amplitude measurements.

Most stroboscopic image processing algorithms used for motion estimation suffer from the following drawbacks: first, they usually assume image brightness conservation that is not totally true when some out-of-plane or torsion motion occurs. Secondly they assume rigid body motion (which is only locally true) and they tend to produce a systematic motion bias and to favour motion vectors perpendicular to edges. Finally they are sensitive to drifts. These drawbacks can be reduced by making use of spatial and temporal filtering techniques[69] but at the expense of lower spatial resolution and measurement rate. Likewise, if measurement duration is not an issue, a very low detection limit can be obtained by image averaging and the dynamic range can be increased by using a pyramidal approach where image processing is applied to images with increasing lateral resolution.

The frequency bandwidth limitation of this technique arises from the need of high power short light pulses with a high repetition rate. Most systems use a single Light Emitting Diodes (LED) or an array of them as the light source. Their response time being typically a few tens ns, the frequency range is typically limited to a few MHz although measurements at higher frequency can be made if the vibration amplitude is low or by applying a suitable correction.

Time-averaged and stroboscopic optical microscopy techniques described above can be applied on isolated micron-size resonators and even on device smaller than the optical resolution of the microscope lenses. However this possibility is limited by the need to average the results in an area of a few (tens) pixels wide.

6.3.2.2. *Knife-Edge Techniques*

In-plane vibrations of an opaque microstructure can be detected from the modulation of the reflected or transmitted intensity of a light beam focused on an edge of the moving part[73–75] (Fig. 6.13).

In the reflection mode (Fig. 6.13(a)), the amount of modulation of the detected beam depends on the vibration amplitude and on the ratio of the light power reflectivities of the moving structure and the substrate.[75] Even for similar reflectivities, a resolution in the nanometer range can still be achieved by using a highly focused beam because the beam modulation is also dependent on the beam defocus between the vibrating microstructure and the substrate.[75] The counterpart is a slight sensitivity to out-of-plane vibrations. When the moving structure is (semi)-transparent, light interferences occur in the structure and in the gap (see Sec. 6.3.3.2) and the signal is sensitive to both in-plane and out-of-plane vibrations in a complex way.

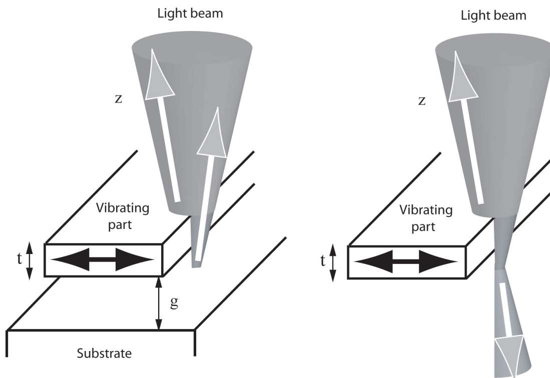

Fig. 6.13. Principle of the knife-edge techniques for in-plane vibration measurements. a) reflection mode b) transmission mode.

The best sensitivity is achieved in the transmission mode for an opaque structure but this can be used only in some specific cases.

This technique provides only a point-wise and unidirectional measurement but is able to measure both the amplitude and the phase of in-plane vibrations[75] as well as non repetitive transient responses by using a lock-in detection scheme, a spectral analyser or an oscilloscope. In addition, its frequency range is only limited by the bandwidth of the photodetector and the detection electronics so that high frequency vibration measurements can be performed by using high speed

components.[73] Finally, in-plane vibration modes can be imaged by scanning the sample and recording the signal at the edges of each etch release hole.[73]

The sensitivity is optimum for a small spot size centred on the edge but a small spot size limits the linear detection range which is about 10% of the spot diameter for a Gaussian sensing light beam.[75] For opaque vibrating structures without a substrate below, both a large dynamic range and a high sensitivity can be obtained in the reflection mode with a large spot size, by using a laser Doppler vibrometer as a measurement tool.[74] In this later case a noise floor of 10^{-11} m/$\sqrt{\text{Hz}}$ could be reached.

The knife-edge technique was tested only by few authors but it has a good complementarity with the methods based on image processing described above. Actually, both techniques are implemented on the same optical microscope at IEF-UPS. Integrated versions of this technique in the transmission mode were implemented by different authors by using optical fibers or waveguides. In this case, the optical sensing and detected beams are in the substrate plane and partial obscuration or the change of light coupling efficiency is detected.

6.3.2.3. *Grating Interferometry*

An interesting technique based on grating interferometry was proposed recently.[76] This technique needs the fabrication of a reflective diffraction grating on the moving micro structure (Fig. 6.14). When a coherent laser beam is focused on a grating at normal incidence, light is diffracted in several directions θ_m (Fig. 6.14) given by:

$$\theta_m = \arcsin(m\lambda/a) \tag{6.13}$$

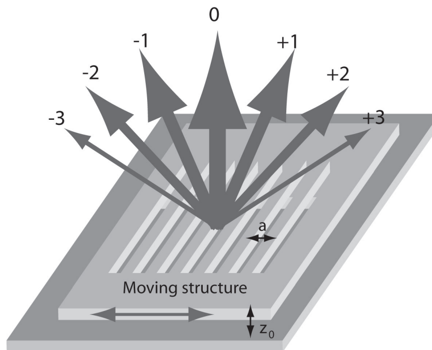

Fig. 6.14. Diffraction of light by a grating made in the resonator.

where m is the diffraction order, λ the wavelength of the illuminating beam and a the grating pitch.

In the experimental set-up proposed by Zhou and Chau[76] (Fig. 6.15) the diffracted beams of order $m = -1$ and $m = +1$ are collected with a beam splitter, collimated by lenses and combined with a mirror and beam splitters to obtain an interference pattern (Fig. 6.15). The intensity of one of these beams and of the interference pattern are monitored by photodiodes and amplified.

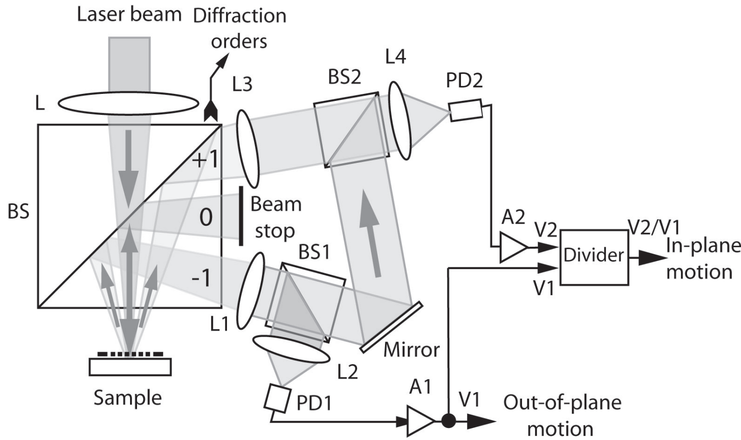

Fig. 6.15. Scheme of a grating interferometry set-up. L = lenses, BS = Beam splitters, PD = Photodiodes, A = Amplifiers.

The signal V_1 corresponding to the amplified intensity of the diffracted beam of order ± 1 varies with the out-of-plane displacement z as follows:[76]

$$V_1 = f_1 I_{in} \sin^2 \left[\frac{\pi(z_0 + z)}{\lambda} (1 + \theta_{-1}) \right] \tag{6.14}$$

where f_1 is the fraction of detected light in the diffracted beam after transmission and amplification, I_{in} is the intensity of the illuminating laser beam, z_0 is the initial offset and λ is the illuminating beam wavelength.

In addition, the ratio of the signals V_2/V_1, where V_2 is the interference signal, (Fig. 6.15) varies with the displacement in the x direction as follows:[76]

$$\frac{V_2}{V_1} = a + b \cos \left(\frac{4\pi x}{a} + \Delta\phi \right) \tag{6.15}$$

where c and d are constants related to the losses of the optical beam paths, the photodiodes efficiency and gains of the transimpedance amplifiers. $\Delta\phi$ is a phase offset and a is the grating pitch.

These equations show that out-of-plane and unidirectional in-plane motion of the moving structure can be measured simultaneously by this technique. By using a 50 μm HeNe laser spot size, a detection limit equal to $0.23\ \mathrm{nm}/\sqrt{\mathrm{Hz}}$ for in-plane vibrations and to $0.03\ \mathrm{nm}/\sqrt{\mathrm{Hz}}$ for out-of-plane vibrations has been demonstrated for a resonator having a 2 μm thick polysilicon grating with a 4 μm pitch and a 2 μm gap above the substrate.[76] This technique is thus suitable for damping measurements of relatively large structures incorporating a grating. Full 3D measurements should be possible by using a 2D grating and by duplicating the optical set-up.

6.3.2.4. *Other Optical Techniques for In-Plane Vibration Measurements*

For a moving structure having a rough or highly structured top surface, various other techniques based on the detection of the scattered light or on the formation of speckles can be applied, such as two-beam laser Doppler interferometry,[77,78] holographic techniques,[61,63] optical laser feedback interferometry[79] and speckle techniques.[61,81] A short wavelength and highly coherent illumination increases the amount of scattered light and favours the formation of speckle. So, by using a Deep UV light source, Aswendt demonstrated that Electronic Speckle Pattern Interferometry could be applied to vibration testing of MEMS having a moderate surface roughness.[81]

Finally, when the sidewall of the moving structures can be accessed or when a $45°$ mirror can be integrated near it, some of the out-of-plane vibration measurement methods described below can be employed.

6.3.3. ***Damping Measurements of Out-of-Plane and Torsional Vibrations***

A large number of techniques are available for out-of-plane displacement measurements of microstructures with (sub)nanometer resolution.[61–63] The great majority of them can be adapted for damping measurements. Generally speaking, point-wise techniques based on a single photodetector are the best methods for damping measurements. By scanning the sensing beam or the sample, vibration mode shapes can also be extracted but this is generally time-consuming. Conversely, camera based full-field techniques such as stroboscopic[61,62,67,68,70,82–84] or time-averaged[61,62,85] interference microscopy, holographic[63,80] or speckle[63,81] techniques are very performing for vibration mode mapping but slow and less sensitive for vibration spectra measurements. There is an obvious interest to build set-ups combining both types of techniques.[48] In the following, we will essentially consider the first category of techniques.

All techniques described below can equally be applied to torsional vibrations damping measurements, the most straightforward technique being optical beam deflection described just below.

6.3.3.1. *Optical Beam Deflection Techniques*

The optical beam deflection technique was historically the first vibrometry technique applied to the dynamic characterization of microstructures.[1] In this technique, the sensing beam is collimated or focused on the moving microstructure under oblique incidence and the angle of the deflected beam is detected by a position sensitive detector (PSD) which can be a partially obscured photodiode or a segmented photodiode (Fig. 6.16(a)).[3,77,87–90]

The beam deflections Δx and Δy on the photodiode are given by:[87]

$$\Delta y = 2D\left(\frac{\partial z(x,y)}{\partial y}\right)_{x_0,y_0} + 2\delta z(x_0,y_0)\sin\theta + \varepsilon \qquad (6.16)$$

$$\Delta x = 2D\left(\frac{\partial z(x,y)}{\partial x}\right)_{x_0,y_0}$$

where D is the distance from the sample and the PSD, $\delta z(x_0, y_0)$ the local vertical displacement at position x_0, y_0 with respect to the base plane and θ the angle of incidence of the sensing beam.

The first terms of these two equations give the beam deflections related to slopes variation while the second term in the first equation is the beam deflection

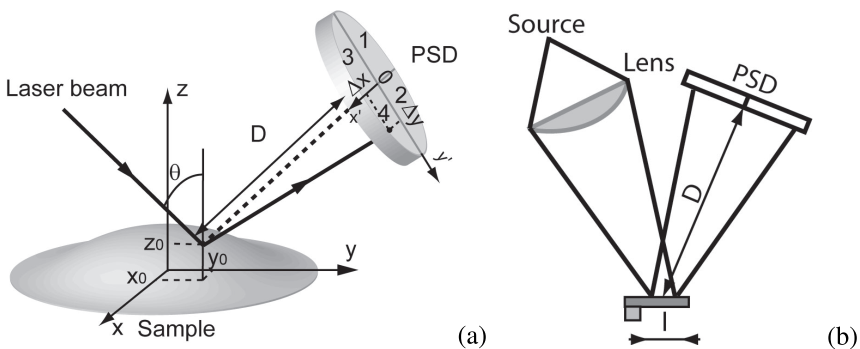

Fig. 6.16. Optical beam deflection technique. a) Principle illustrated on a circular membrane with a 4 quadrants photodiode as a Position Sensitive Detector b) Configuration for a beam focused on a cantilever beam.

related to the vertical displacement. ε represents smaller high order terms related to the shift of the beam spot on the device with respect to x_0, y_0 position.

These equations show that this technique is actually mainly sensitive to local slope variations except where there are very close to zero. Eventually they can be separated by using 2 detectors at different distances. Putman *et al.*[87] computed the sensitivity of various configurations in the case of shot noise and diffraction limited measurements on a cantilever beam with a Gaussian laser beam and a single detector. For the common case where the beam is focused close to the end of a cantilever beam and the detector is far from the beam waist region, the signal to noise ratio is given by:

$$S/N = 1.5 \left(\frac{\lambda \eta I_0}{2hc\Delta f} \right)^{1/2} 4 \left(\frac{\pi}{2} \right)^{3/2} \frac{d}{l} \frac{\delta z}{\lambda} \tag{6.17}$$

where λ and I_0 are the sensing beam wavelength and power respectively, η the quantum efficiency of the detector, h the Planck constant, c the speed of light and Δf the detection bandwidth. l is the cantilever beam length and d the spot diameter on it.

This equation shows that in this case the S/N ratio is no longer dependent on the distance D. Indeed, although the spot displacement is proportional to D, this also holds for the spot diameter on the detector. For $d/l = 1/3$, $h = 0.8$, $\lambda = 780\,\text{nm}$ and $I_0 = 1\,\text{mW}$, the theoretical S/N ratio is 7.9×10^{-15} m/(Hz)$^{1/2}$. In practice, a S/N ratio about one to two order of magnitude higher can be achieved so the sensitivity of this technique is more than sufficient for dynamic measurements of microstructures up to high frequencies. Experimental set-ups used for MEMS investigations often have much lower sensitivities in order to allow large vibration amplitude measurements.[90]

This technique is mainly suitable for sufficiently large devices because the spot size on the sample is limited by the low working distance and by the large divergence of the reflected beam when a high numerical aperture focusing lens is used. Some set-ups include a laser or sample scanning system to allow vibration mode analysis.[86]

Recent examples of application of the optical beam deflection technique to intrinsic and/or viscous damping investigations of micromechanical devices can be found in the literature.[3,88–90]

6.3.3.2. *Interferometry Techniques*

Interferometry techniques are based on the detection and processing of optical interferences between a light beam reflected on the sample surface and a light

beam reflected on a reference mirror/surface. We will successively examine the cases of homodyne interferometry, where the optical frequencies of the two beams are equal, the case of laser Doppler heterodyne interferometry, where they are different, and finally the case of Fabry–Pérot interferometry where multiple beams are interfering.

a) Two-beam homodyne interferometry. Figure 6.17 shows an optical configuration based on a monochromatic light Michelson interferometer and often used for MEMS vibration testing. Various other types of two-beam homodyne interferometers can actually be used. For example a simple, compact and convenient solution is to use Michelson, Mirau or Linnik interferometric objectives.[62] Small and eventually multipoint interferometric vibrometers can also be build by using optical fiber technology.[92,93]

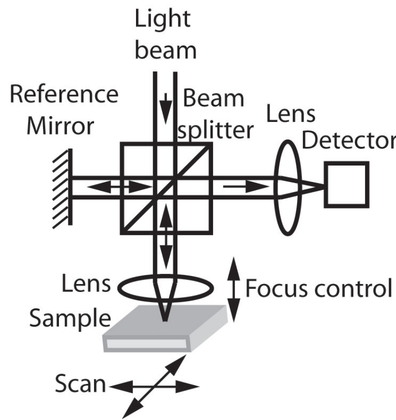

Fig. 6.17. Michelson interferometer with beam focusing on the sample.

Whatever the homodyne interferometer used, the instantaneous light intensity reaching the detector can ideally be described by the following equation:[91]

$$I_d(t) = I_R + I_S + 2\sqrt{I_R I_S}\cos(4\pi z(t)/\lambda + \phi_0) = A + B\cos(\phi) \qquad (6.18)$$

where I_R, I_S are the light intensities reflected on the reference mirror and on the sample surface respectively, $z(t)$ the time-dependent part of the out-of-plane displacement to be measured, λ the effective light source wavelength and ϕ_0 the phase offset.

All information on sample motion is contained in the phase ϕ. Various detection schemes can be implemented to demodulate this phase.

With $z(t) = a\sin(2\pi ft + \phi_1)$ and by developing the cosine term, Eq. (6.18) becomes:

$$I_d(t) = I_R + I_S + 2\sqrt{I_R I_S}\Bigg[\cos(\phi_0)\cos\left(\frac{4\pi a}{\lambda}\sin(2\pi ft+\phi_1)\right) - \sin(\phi_0)\sin\left(\frac{4\pi a}{\lambda}\sin(2\pi ft+\phi_1)\right)\Bigg]. \tag{6.19}$$

For low sinusoidal vibration amplitudes much lower than $\lambda/4\pi$ the detected intensity becomes:

$$I_d(t) = I_R + I_S + 2\sqrt{I_R I_S}\left[\cos(\phi_0) - \sin(\phi_0)\frac{4\pi a}{\lambda}\sin(2\pi ft+\phi_1)\right] \tag{6.20}$$

The detected intensity is thus sinusoidal and the vibration amplitude can be measured with a lock-in amplifier or a spectral analyser. This equation shows that, to get a constant and maximum sensitivity, a stabilisation circuit or technique must be used to adjust and maintain the mean position at $\phi_0 = \pm\pi/2$. With such stabilized interferometers, a detection limit in the 10^{-14} to 10^{-12} m/(Hz)$^{1/2}$ can be reached[31,73,93,94] allowing measurements up to the GHz range with picometer resolution.[31]

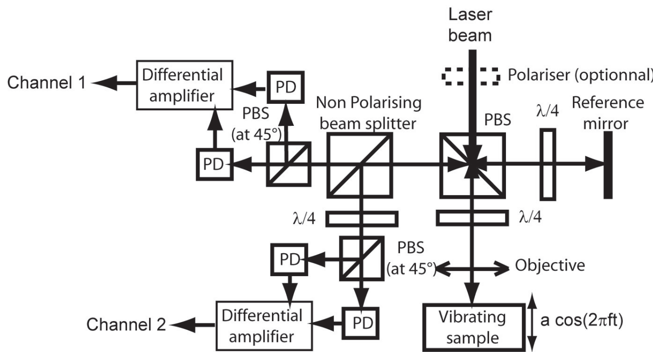

Fig. 6.18. Quadrature interferometry set-up with balanced detectors. PBS: Polarising Beam Splitter. PD: Photodiode.

Although vibration amplitude measurements versus frequency are sufficient to compute the quality factor, the vibration phase is useful in modal analysis. Phase measurements require the generation of a vibration signal in quadrature. This can be achieved electronically by using a double channel lock-in detection amplifier. Another way is to take benefit of light polarisation to generate an optical signal in

quadrature. In the set-up of Fig. 6.18[77] this is obtained by splitting the reference and sample beams with a polarising beam splitter and rotating their polarisation by 90° with quarter-wave plates. The two signals in quadrature are separated by a non polarising beam splitter with a quarterwave plate in one of the branches. Finally the quadrature signals are sent to polarising beam splitters to get in-phase and out-of-phase signals that are detected with photodiodes. This balanced detector configuration allows, by substracting the signals of the photodiodes, to increase the detected power by a factor two and to remove the DC components.[77]

Signals in quadrature can be obtained by various other interferometric schemes.[59,77] The vibration phase can then be computed by an arctangent operation on the signal ratio. The main issue of quadrature interferometry is a mutual cross-talk between the quadrature signals due to imperfection of the polarizing beam splitter, to unequal gains of the detectors, to an unbalance of the two beams, to an othogonality error between the two signals, ... This can be corrected afterward by ellipse fitting of the sine signal versus cosine signal curve (Lissajou curve).[95]

For large but linear vibrations, the average signal becomes vibration-amplitude dependent and the detected intensity contains an increasing number of harmonics with amplitudes given by Bessel functions of integer order of the vibration amplitude.[83] Then a harmonic analysis,[96] a fit of the time dependence of the signal or a fringe counting procedure[59] is required to extract the vibration amplitude.

b) Laser Doppler vibrometry. Laser Doppler vibrometry (LDV) is the most popular technique for damping measurements of out-of-plane vibrations of MEMS. This well documented[61,77] technique is based on the variation of optical frequency of a laser beam reflected or scattered by a vibrating surface (Doppler effect). For normal incidence of the sensing and detection beams (backscattering geometry) the relative frequency shift is equal to $2v/c$ where v is the out-of-plane velocity of the vibrating surface and c is the speed of light. In order to detect this very low frequency shift, a two-beam heterodyne interferometer is used.[61,77] A typical set-up based on a Mach Zehnder interferometer is shown in Fig. 6.19.[61]

In laser Doppler vibrometers, the optical frequency f_R of the reference beam, (or of the sample beam, or both) is shifted by an amount f_B with respect to the optical frequency f_S of the sample optical beam by using a Bragg cell modulated at frequency f_B. In Fig. 6.19, polarising beam splitters are used to separate orthogonal polarisation components of optical beams, and the reference and sample beams are recombined with a non polarising beam splitter to obtain interferometric signals in and out-of-phase on two photodiodes. It can be readily shown

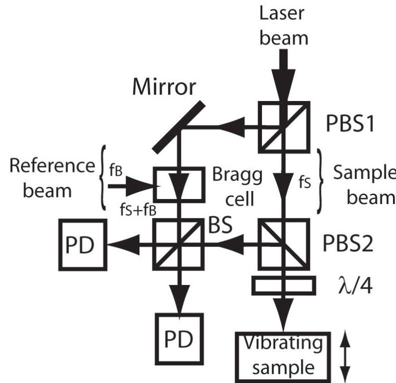

Fig. 6.19. Heterodyne Mach-Zehnder Laser vibrometer. PBS: Polarizing beam splitter, BS: Non-polarizing Beam splitter, PD: Photodiode.

that the optical signal received by each photodiode contains a term at frequency $f_R + f_S = 2f_S + f_B$ that is too fast to be detected and a beating signal at a carrier frequency $f_R - f_S = f_B$ given by:[61]

$$I_d(t) = K[I_R + I_S + 2\sqrt{I_R I_S}\cos(2\pi f_B t - \varphi(t) + \phi_0)] \qquad (6.21)$$

where K is a conversion factor, f_R and f_S the reference and object beam powers, $\varphi(t)$ the varying phase and ϕ_0 a phase offset.

A frequency or phase demodulation circuitry respectively provides the instantaneous velocity or displacement. A spectrum analyser then allows the measurement of a vibration spectrum in real time with an excellent sensitivity and a very large dynamic range. Vibration measurements of micro/nanostructures up to 100 MHz have been demonstrated. In addition differential set-ups where the reference beam is reflected on another part of the sample surface are available that allows accurate measurement even in the presence of (thermal) drifts and of external disturbances as found in clean rooms facilities and vacuum chambers. Finally, it is one of the best methods for transient response measurements.

c) Fabry–Pérot interferometry. An increasingly used technique is Fabry–Pérot (FP) interferometry. This technique takes benefits of multiple beam interferences between two reflecting parallel surfaces forming a cavity of length d (Fig. 6.20).

The amplitude reflection and transmission coefficient R and T of the Fabry–Pérot cavity can classically be computed, in the case of an arbitrary number of interfaces and for an incident plane wave, by summing the contributions of the internal reflected beams for transverse electric and transverse magnetic light

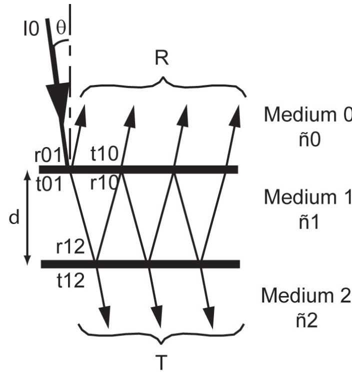

Fig. 6.20. Multiple interferences between two reflecting surfaces. rij and tij are the Fresnel reflection and transmission coefficient of interface i/j.

polarisations.[91] Then the total power reflection or transmission coefficients R_T and T_T can be computed according to the polarisation state of the sensing beam and its wavelength spectrum. For the case of an ideal (non absorbing) Fabry–Pérot interferometer at normal incidence ($\theta = 0$), $R_T = 1 - T_T$ and is given by:[91]

$$R_T = \frac{r_1 + r_2 - 2(r_1 r_2)^{1/2}\cos(4\pi d n_1/\lambda + \varphi)}{1 + r_1 r_2 - 2(r_1 r_2)^{1/2}\cos(4\pi d n_1/\lambda + \varphi')} \tag{6.22}$$

where $r_1 = |r_{01}|^2$, $r_2 = |r_{12}|^2$, are the power reflection coefficients of the two surfaces, n_1 and d are the refractive index and thickness of the Fabry–Pérot cavity and φ, φ' are related to the reflection phase shifts at the interfaces.

Variation of $R_T = 1 - T_T$ with the normalized cavity thickness dn_1/λ is plotted in Fig. 6.21 for an ideal Fabry–Pérot interferometer with two loss-less mirrors of equal reflectivity $r = r_1 = r_2$. For low values of r, high order reflections are negligible and a Fabry–Pérot interferometer behaves like a two-beam interferometer. However for large reflection coefficients a resonance occurs for $d = m\lambda/2n_1$, where m is an integer and λ is the wavelength. The half-width at half maximum of the peaks is related to the reflection coefficient r by:

$$W = \frac{2(1-r)}{r^{1/2}} = \frac{2\pi}{F} \tag{6.23}$$

where F, called the finesse, is the ratio of fringe separation to their half-width.

In a real Fabry–Pérot interferometer, the finesse is reduced by unwanted bow, surface roughness and departure from parallelism of the mirrors,[97] by the difference of reflection coefficients of the two mirrors and by the non planar profile and limited lateral extent of the incident beam.

When the distance d is close to a resonance, a large variation of reflected or transmitted intensity is produced for small variations of d. Hence, if one of the reflecting surfaces is the vibrating part of the device, vibration measurements with a very high sensitivity (but a low dynamic range) can be achieved. A noise floor of 2×10^{-16} m/$\sqrt{\text{Hz}}$ has been experimentally demonstrated.[98]

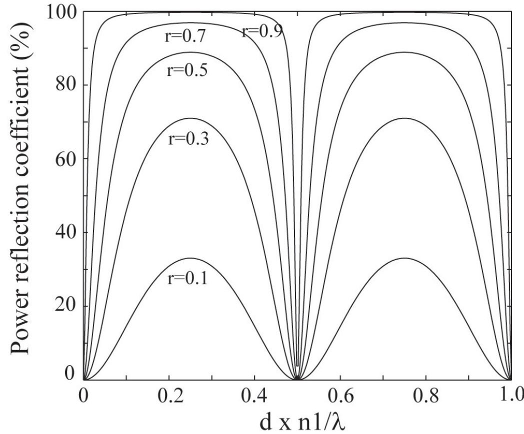

Fig. 6.21. Reflection coefficient of an ideal Fabry–Pérot cavity versus its normalized thickness for various values of the mirrors reflection coefficient. For Air/Silicon interface $r = 0.3$-0.35 in the visible-NIR range.

This measurement technique can be applied to vibration measurement of micro or nanoresonators by various ways (Fig. 6.22). The reference mirror can be the cleaved end of an optical fiber[99] (Fig. 6.22(a)), the substrate below the vibrating surface[97,100,101] (transparent devices) (Figs. 6.22(b), 6.22(d) and 6.22(e)) or an external mirror[98] (Fig. 6.22(c)). For silicon resonators thicker than $\sim 0.5 - 2\,\mu$m, a near-infrared light source is preferable for configurations 6.22(b), 6.22(d) and 6.22(e) because silicon is (slightly) absorbing in the visible range but fully transparent above $\lambda \sim 1\,\mu$m. For vacuum measurements, the preferred implementation is that of Fig. 6.22(c).

To avoid internal reflections within the device or other reflections which degrade the performances of Fabry–Pérot cavities and introduce technology-dependent intensity variations, it might be necessary to deposit anti-reflecting coatings on surfaces not acting as cavity mirrors.[97] Vibration measurements can be as well performed with a fully external Fabry–Pérot interferometer.[77] In this case, mainly used for the characterization of high frequency acoustic solid waves, curved mirrors in a confocal configuration is the typical implementation.

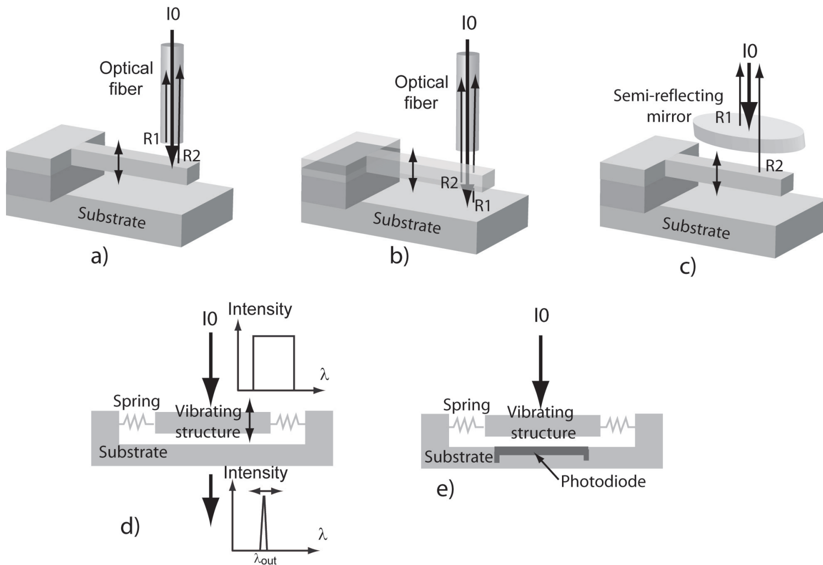

Fig. 6.22. Some configurations for the application of Fabry–Pérot interferometry to the dynamic characterization of microstructures.

In all cases, vibration-induced intensity variations can be detected with an external detector, or an integrated photodiode[97] (Fig. 6.22(e)) and analyzed as in two-beam interferometry. As a Fabry–Pérot cavity with highly reflective mirrors acts as a very narrow band filter, an alternative in this case is to use a broadband source and to measure the change of transmitted or reflected wavelength with an optical spectrum analyser (Fig. 6.22(d)).

A clear advantage of Fabry–Pérot interferometry, beside its high sensitivity, is its simple optical configuration that needs only few components. For this reason, it is increasingly used when very low vibration amplitudes and/or high vibration frequencies have to be measured. For example, Fabry–Pérot interferometry measurements up to a frequency of 640 MHz were demonstrated.[102]

6.3.3.3. *Other Techniques for Out-of-Plane Vibration Measurements*

Similarly to optical microscopy (see Sec. 6.3.2.1), interference microscopy[61,62,91] can be applied to damping measurements by in-flight processing of interferograms recorded in the time-averaged or stroboscopic mode. These techniques are slower and have a higher detection limit (0.2-5 nm) than the techniques described above, but allow parallel testing and are specially useful for vibration coupling investiga-

tions, for anchor loss investigations and for large vibration measurements. Likewise various digital holography and speckle techniques can be applied in the time-average or stroboscopic mode on MEMS with rough or mixed-type surfaces.[61]

6.3.4. *Conclusion*

As shown above, optical techniques are particularly well suited for damping measurements. They allow non-contact quality factor measurements of in-plane and out-of-plane vibrations at atmospheric pressure or in vacuum with a high sensitivity, a large frequency bandwidth and a high lateral resolution. Nevertheless some margin of progress still exists for in-plane vibration measurements. A main challenge is to increase significantly the measurement rate and to develop techniques for 3D measurements. Some of the techniques described for in-plane and out-of-plane vibrations measurement can actually be combined to perform both measurements on a single system but not simultaneously. For example, Laser Doppler Vibrometry and the knife-edge technique were used by Holmgren *et al.*[73] to perform both out-of-plane and in-plane measurements on RF microresonatores up to a few tens MHz with a high sensitivity and a high lateral resolution. This combination is probably, at present, the best one for damping measurements. Nevertheless, only very few techniques allow simultaneous and independent in-plane and out-of-plane measurements. Such a possibility was mentioned above for grating interferometry. Stroboscopic interference microscopy is also a technique allowing 3D measurements with (sub)nanometer resolution by using fringe contrast maps for in-plane measurement and phase maps for out-of-plane measurements.[67,70] For rough surfaces, Laser Doppler vibrometry with two sensing or detecting beams and speckle techniques with several light sources have also simultaneous 3D capability.[67]

6.4. Electrical Techniques and Alternative Techniques for Quality Factor Measurement

6.4.1. *Electrical Techniques*

All the optical techniques described in the previous sections permit to characterize the purely mechanical behaviour of MEMS/NEMS resonators. However, whenever the resonator is integrated in a microsystem, it is generally coupled to electro-mechanical actuation and detection transducers to be able to electrically drive the resonator and electrically read out its response. This coupling adds some extra dissipation ($1/Q_{\mathrm{elec}}$) and thus alters the mechanical quality factor Q_{mech}.

The global effective quality factor Q_{eff} can be defined as

$$Q_{\text{eff}} = \frac{Q_{\text{mech}} Q_{\text{elec}}}{Q_{\text{mech}} + Q_{\text{elec}}} \left(\text{or} \quad \frac{1}{Q_{\text{eff}}} = \frac{1}{Q_{\text{mech}}} + \frac{1}{Q_{\text{elec}}} \right) \tag{6.24}$$

The mechanical properties of the resonator in terms of damping may thus be deteriorated by the coupling at the transducers. This property has been used to tune the driving and sensing modes of a gyroscope in order to improve its global characteristics.[103]

In this part, we will first investigate the quality factor of the electronic parts and we will then present existing techniques to perform electrical measurements of quality factors.

6.4.1.1. *Damping by Electronics*

To estimate the electronic quality factor, we will consider the classical capacitive device that is driven and sensed using comb-finger designs, as in Fig. 6.23. This device is similar to the one studied in Ref. [104] but is a little more general since it allows investigating different biasing configurations. The offset voltage will also be taken into account concerning the operational amplifier.

C_D and C_S capacitors in Fig. 6.23 representing comb-finger capacitors, both the drive and sensing electrodes may create an electrostatic force on the moving mass. This force is proportional to the capacitance variation $\mathrm{d}C/\mathrm{d}x$ due to the movement of the proof mass in the x-direction and also depends on the square of the voltage difference. By construction, the capacitance variations of C_D and C_S are opposite.

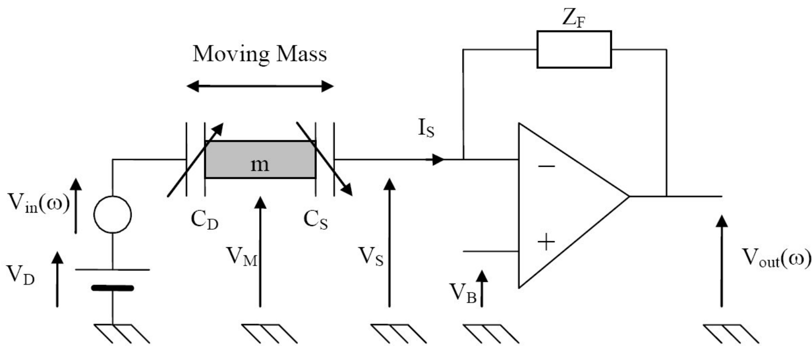

Fig. 6.23. MEMS Device and read-out circuitry.

For comb-finger designs, $\mathrm{d}C/\mathrm{d}x$ depends on the geometry, is independent of the x displacement up to first order. The global force balance is given by

$$m\frac{\mathrm{d}^2x}{\mathrm{d}t^2}+c\frac{\mathrm{d}x}{\mathrm{d}t}+kx=\frac{\left(V_D+V_{in}\left(\omega\right)-V_M\right)^2}{2}\frac{\mathrm{d}C}{\mathrm{d}x}+\frac{\left(V_S-V_M\right)^2}{2}\frac{\mathrm{d}C}{\mathrm{d}x} \quad (6.25)$$

By considering an operational amplifier with a finite gain A_V and an offset voltage V_{off}, the signal V_S is expressed by the following formula:

$$V_S=\frac{A_V\left(V_B+V_{\text{off}}\right)}{A_V+1}+\frac{Z_FI_S}{A_V+1}. \quad (6.26)$$

If A_V is chosen sufficiently large so that V_S may be considered constant ($A_v \gg Z_FI_S/(V_B+V_{\text{off}})$, the sensing current can be expressed as

$$I_S\simeq\left(V_M-\frac{A_V\left(V_B+V_{\text{off}}\right)}{A_V+1}\right)\frac{\mathrm{d}C}{\mathrm{d}x}\frac{\mathrm{d}x}{\mathrm{d}t}. \quad (6.27)$$

Using Eqs. (6.25) and (6.26) within Eq. (6.24) and considering that $A_V \gg 1$, we obtain the following expression for the electronic quality factor:

$$|Q_{\text{elec}}|=\frac{mA_V\omega_nZ_F}{\left(V_B+V_{\text{off}}-V_M\right)^2\left(\mathrm{d}C/(\mathrm{d}x)\right)^2}. \quad (6.28)$$

A compromise has thus to be found between sensing current magnitude and electronic quality factor. The gain bandwidth product of the operational amplifier has to be chosen large enough to have a sufficient read-out gain and a high quality factor at the same time.

6.4.1.2. *Standard Electrical Techniques for Quality Factor Measurements*

When an electrical signal is available, Q measurement may be directly performed using standard electronic equipment. For frequency domain analysis, three different kinds of equipment may be used: a digital oscilloscope with FFT computation, a spectrum analyzer and a network analyzer.

Performing an FFT on a digital oscilloscope is one of the quickest ways to conduct the analysis. It only requires a few milliseconds. A fixed number N of samples are acquired from a temporal signal over a given acquisition time T. This temporal signal may be the resonator response either to a sinusoid with continuously swept frequency during the acquisition time, or to a white noise. The latter technique may be useful in the case of high Q-values not to miss the resonant frequency.[106] The chosen sample rate $1/(NT)$ defines the obtained frequency resolution after the Fast Fourier transform is performed. The original spectrum is indeed also sampled N times. Increasing the acquisition time (decreasing the

sample rate) also increases the frequency resolution but reduces the obtained spectrum span. A compromise has to be found, depending on the quality factor to be measured and the characterization method used. Care must be taken that the period of the fastest signal present contains at least 2 samples (Shannon theorem) to avoid aliasing problems. The type of temporal window used to model the discrete time signal processed has also an impact on the frequency resolution. Hanning window is generally a good practical compromise between resolution and spectral leakage.[106]

In the case of a spectrum analyser, the same kind of excitation signal as with the oscilloscope has to be applied to the resonator. The principle is here to scan the input spectrum through a narrow bandpass filter, at a fixed intermediate frequency, by mixing the input signal with a varying frequency sinusoidal signal coming from a local variable oscillator. The user controls the filter resolution bandwidth and the frequency range of the local oscillator. The corresponding frequency sweep time must be large enough so that the narrow filter can settle for each frequency. The relationship between the sweep time (ST), the resolution bandwidth (RBW) and the span of the analysis is given by:

$$ST = \frac{k\,(\text{span})}{(RBW)^2} \tag{6.29}$$

where k is the constant of proportionality between resolution bandwidth and rise time of the filter. It typically ranges from 2 to 3 depending on the kind of filter employed[107] implying that a change in resolution has an important impact on the sweep time for a given span. The sweep time is generally automatically tuned to the resolution and span settings. The main advantages of the spectrum analyzer over the digital oscilloscope with FFT are a better sensitivity, a larger frequency range and also a larger dynamic range.

The vector network analyzer has several advantages over the two precedent devices: no external excitation signal is required and both phase and amplitude information is provided together with amplitude over the frequency range swept. The principle is to send a well known, internally generated variable frequency or power signal into the device under test and analyze the corresponding reflected and transmitted response. From these responses, a wealth of information may be obtained, *e.g.*, gain, phase, impedance or S-parameters.[108] The latter may be exploited to characterize resonators in terms of resonant frequency and quality factors. Seven methods using these S-parameters have been tested and compared for different characterization situations (variable Signal to Noise Ratios[36]). The optimal choice of the method depends on the SNR: non-linear least squares fit to a

Lorentzian curve is the best solution for low SNR situations while non-linear least squares fit to the phase versus frequency is preferable for higher SNR.[36]

Concerning transient analysis, the only instrument, among the ones presented, able to capture one shot events is the oscilloscope. Its memory depth and data conversion resolution are key points for time domain analysis, especially for high Q values. A data acquisition board coupled to a personal computer may even be necessary for Q values above 100000. Specific electronic circuitry may also be developed to process the transient response. Different solutions have been proposed in the past and may be adapted to the case of MEMS resonators.[99–110]

6.4.1.3. *Specific Electrical Techniques for Capacitive MEMS Devices*

Capacitive sensors represent an important and diffused example of integrated MEMS devices. For characterization purpose, they have the advantage of having built-in actuation and detection electrodes but, due to the presence of parasitic elements, feature crosstalk between actuation and detection signals. This crosstalk significantly complicates device characterization, especially with external read-out circuitry and even with precision equipment like a lock-in amplifier. Specific characterization schemes have been proposed to solve this problem.

For a device using electrostatic comb electrodes and read-out circuitry like the one shown Fig. 6.23, but where an additional parasitic capacitance C_{par} exists between driving and sensing electrodes, it is interesting to use the 2nd harmonic to characterize the resonator.[111] In this case, Z_F is a resistance R_F and $V_M = 0$. The corresponding experimental setup together with obtained results for *1f* and *2f* characterization is shown Fig. 6.24. The measured voltage at the output of the lock-in amplifier, depending on the displacement amplitudes and phases at *1f* and *2f* (respectively X_ω, φ_ω, $X_{2\omega}$ and $\varphi_{2\omega}$) and the lock-in amplifier signal characteristics (V_r, ω_r and φ_r), is given by:

$$\begin{aligned} V_{\text{out}} = {} & \underbrace{\omega R_F V_r V_B \frac{\mathrm{d}C}{\mathrm{d}x} X_\omega \left\{\sin\left[(n\omega_r+\omega)\,t+\varphi_r-\varphi_\omega\right]+\sin\left[(n\omega_r-\omega)\,t+\varphi_r+\varphi_\omega\right]\right\}}_{\text{Fundamental}} \\ & + \underbrace{2\omega R_F V_r V_B \frac{\mathrm{d}C}{\mathrm{d}x} X_{2\omega} \left\{\cos\left[(n\omega_r-2\omega)\,t+\varphi_r+\varphi_{2\omega}\right]-\cos\left[(n\omega_r+2\omega)\,t+\varphi_r-\varphi_{2\omega}\right]\right\}}_{\text{2nd Harmonic}} \\ & + \underbrace{\omega R_F V_r V_{in} \frac{1}{2} C_{\text{par}} \left\{\sin\left[(n\omega_r+\omega)\,t+\varphi_r\right]+\sin\left[(n\omega_r-\omega)\,t+\varphi_r\right]\right\}}_{\text{Parasitic}} \end{aligned} \tag{6.30}$$

Figure 6.24(b) clearly shows that the preponderant term when $n\omega_r = \omega$ is the parasitic term. The X_ω variation with V_{in} is completely lost. On the contrary, as

can be expected from Eq. (6.30), when $n\omega_r = 2\omega$, the output only depends on $X_{2\omega}$ and the resonant response can be observed and processed (Fig. 6.4(c)).

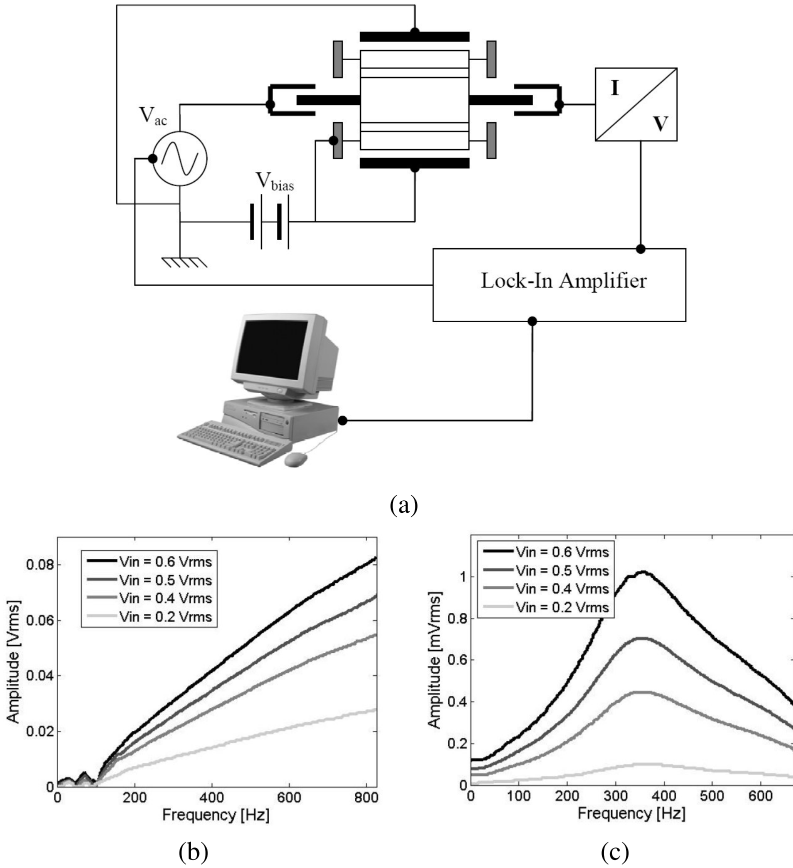

Fig. 6.24. Swept sine 2nd harmonic characterization: experimental setup (a), *1f* results (b) and *2f* results (c) for various AC voltage Vin.

This method has also been used to perform direct electrical quality factor measurement using a discrete electronics read-out circuitry associated to a lock-in amplifier.[112]

For a cantilever resonator constituting a single variable capacitor with only one electrode for actuation and detection, a similar method was proposed to characterize the resonator despite the feedthrough of the actuation voltage through the capacitance.[113] Here, the harmonic allowing characterization is the third one (*3f*).

The experimental setup is very similar to the one of Fig. 6.24(a), adapted to a single variable capacitor. The results have been compared with optical measurement and the resonant curves are very similar.[113]

6.4.1.4. *Architectures for Integrated Quality Factor Measurement*

The quality factor being one of the key parameters of an important class of MEMS devices, namely integrated sensors based on resonant frequency shift monitoring, some quality factor measurement architectures, suitable for integration, have been developed in order to reduce testing costs and to allow embedded on-line quality factor extraction for self-calibration.[114,115]

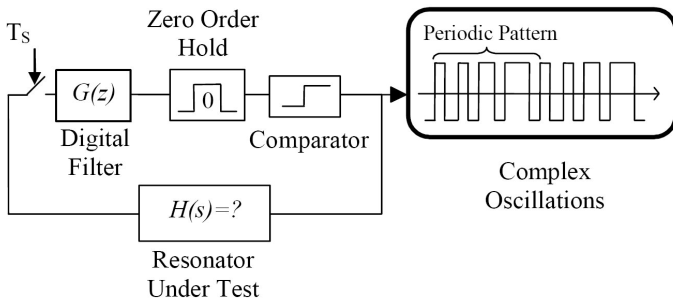

Fig. 6.25. Proposed parameter identification configuration.

A first approach aims at performing parameter identification (resonant frequency and quality factor) for the sensing resonator, whose transfer function is treated as unknown. The device has to be put in a mixed signal closed loop like the one shown in Fig. 6.25. In such a configuration, if the digital filter is well chosen, a periodic pattern composed of several successive pulses is observed. The switching instants of these pulses are characteristic of the digital filter chosen and the parameters of the unknown transfer function. By successively monitoring the complex oscillation response for different digital filters, an accurate estimation of the resonator's parameters may be obtained. This approach is particularly well suited to delta sigma integrated sensors since the testing configuration is very close to their normal working structure. The analog part of the processing is reduced, but this testing method requires intensive digital processing, which can be performed by a Digital Signal Processor (DSP). Switched-Capacitors filters, allowing a modification of the implemented coefficients, could be used as an alternative to the DSP.[114]

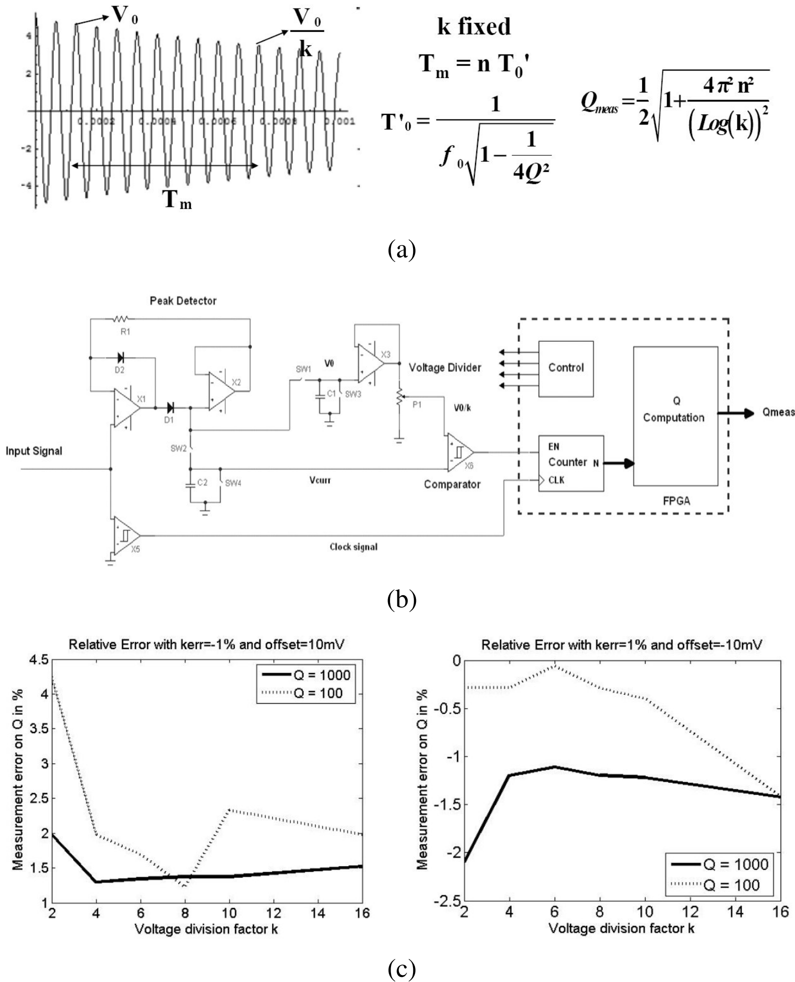

Fig. 6.26. Low Cost Integrated quality factor Measurement : (a) Measurement principle, (b) proposed architecture, (c) accuracy estimation with worst case non-idealities values.

More specifically, for the integrated measurement of the quality factor, several different architectures, based on the methods presented in previous sections, and suitable for integration, have been compared using accuracy, speed and cost as criteria.[115] Two have been found to be potentially interesting for online testing applications. The first one, where a Phase Lock Loop (PLL) is associated to the MEMS device to constitute an oscillator, uses the amplitude at resonance

measurement method. Since the static gain of the resonator transfer function is not known with a sufficient accuracy, this solution is not satisfactory. However, it is very interesting for online monitoring of the quality factor variations without disturbing the normal operation of the sensor. The second proposed architecture is based on transient response measurement.[109,110] The principle is to count the number of pseudo-periods necessary for the decaying signal to go from a starting level V_0 down to a final value determined by dividing V_0 by a fixed factor k. A peak detector allows checking at each pseudo-period if the envelope is still superior to the final threshold. As long as it is true, the pseudo-periods are counted. The counting clock is generated from the decaying signal and thus no a priori knowledge of the device's resonant frequency is necessary. Figure 6.26 shows the measurement principle (a), the proposed architecture (b) and finally an estimation of the final accuracy (c), taking into account the most critical non-idealities in the circuit. The latter curves show that an optimal value of k exists between 4 and 8. Setting $k = 4.81$ would thus be an interesting choice since the post processing would only consist in multiplying by a factor of 2 the counter output to get the quality factor value. The integrated quality factor measurement architecture would thus be very cheap with accuracy in the order of a few percent.

6.4.2. *Measurement Techniques for Nanoresonators*

Mechanical resonators having at least one lateral dimension below 1μm and a thickness in the range of a few tens to a few hundreds of nanometers are usually called nanoresonators. However this term is also often used for resonators with lateral dimensions in the low micrometer range. The ultimate case of nanoresonators is that of carbon nanotubes or nanowires which can have a width down to a few (tens) nanometers. Nanoresonators are mainly intended for RF applications and ultra-sensitive sensors.

The low stiffness and vibration amplitudes of nanoresonators make them particularly sensitive to the interaction with the measurement system. Indeed, whatever the measurement technique used, some energy is exchanged between the device and the detection system which can alter the quality factor of the resonator. Actually this is used in parametric resonators to artificially increase the quality factor through a modulation of the resonator stiffness.[116] Some work was also done to use light interaction to decrease the quantum noise limit of interferometric techniques.[117] In all cases, care must be taken to minimise and check the effect of the measurement on the damping behaviour of the device.

Other obvious issues of optical techniques are the (semi)transparency of the non metallic nanoresonators and the large spot size with respect to the lowest

lateral dimension when visible light is used. Decreasing the sensing beam wavelength down to the Deep Ultra-Violet (DUV) range is a possible way to overcome these limitations. For electrical measurements, some issues are the low signal level and the large crosstalk between actuation and detection circuits. Other issues are the high resonant frequencies (up a few GHz) and the low vibration amplitudes to be measured.

Some of the optical and electrical techniques described in Sec. 6.3 could be applied to some nanoresonators. Concerning optical techniques this was demonstrated for laser Doppler vibrometry[118] and for Fabry–Pérot interferometry,[102] which is presently one of the most common techniques for damping measurements of out-of-plane vibrations of nanoresonators. In the following, we will describe alternative techniques that are or should be suitable for damping measurements of nanoresonators.

6.4.2.1. *Electron Microscopy Techniques*

Modern scanning electron microscopes (SEM) have a lateral resolution down to a few nanometers. Some optical techniques developed for microresonators can be extended to electron microscopy such as in-plane vibration measurements based on blur analysis of time-averaged images, stroboscopic microscopy with image processing and the knife edge technique. Up to now, these techniques were only demonstrated on microresonators but they should be applicable on nanoresonators. An example of resonance curve measured by the knife-edge electron microscopy technique is shown in Fig. 6.27.

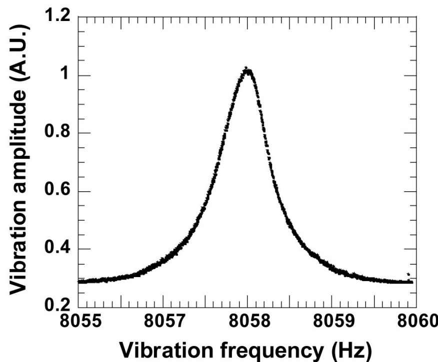

Fig. 6.27. Resonant curve of a Tang resonator measured in vacuum by the knife-edge technique in a scanning electron microscope.

These measurements were performed by Gilles *et al.* at IEF-UPS on the Tang resonator of Fig. 6.8 by focusing the electron beam on the edge of a finger of one of the comb-drives and by measuring the vibration-induced modulation of the secondary electron intensity by lock-in detection. Concerning electron stroboscopic microscopy, some vibration measurements were also demonstrated on microresonators at low frequency.[119] As stroboscopic SEM were developed in the past for contrast potential measurements on integrated circuits or other fast components with response times in the picosecond range,[120] this technique should be suitable for nanoresonators characterization.

Because a vacuum environment is needed for SEM operation, these techniques can be applied only for intrinsic damping measurements.

6.4.2.2. *Near-Field Microscopy Techniques*

Near-field microscopes have a high lateral resolution. By using the tip of an Atomic Force Microscope (AFM) as a probe, out-of-plane vibrations measurements with a high lateral resolution and high vertical resolution could be achieved.[121–125] Such measurements have been demonstrated on high frequency micro or nanoresonators up to a frequency of $\sim$50 MHz[122] as well as on carbon nanotubes.[125] For damping measurements, it must be insured that interaction with the tip has no effect on the quality factor of the resonator. This is critical for nanoresonators as tip-surface interaction might change the dynamic behaviour of an AFM cantilever beam. Indeed, this phenomenon is exploited in acoustic force microscopy, ultrasonic force microscopy and mechanical spectroscopy for mechanical measurements at nanoscale.[126,127] In addition the positioning of the tip on the nanoresonator is not an easy task. Atomic Force Microscopy is thus a viable technique for damping measurements of nanoresonators at atmospheric pressure or in vacuum if a low throughput is not a major concern.

6.4.2.3. *Electromotive Measurements*

As explained in Sec. 6.2.4, a nanoresonator can be set in vibration by magnetomotive actuation, *i.e.*, by passing an alternate current in the device under a high magnetic field. In the same way, motion of the resonator in the magnetic field generates an electromotive force V_{EMF} along the leads on the resonator (Fig. 6.28). For a beam-like resonator V_{EMF} is given by $V_{\mathrm{EMF}}(t) = \xi L B \,\mathrm{d}w/\mathrm{d}t$ where ξ is a constant close to one and related to the mode shape, L the beam length, B the magnetic field and w the displacement.

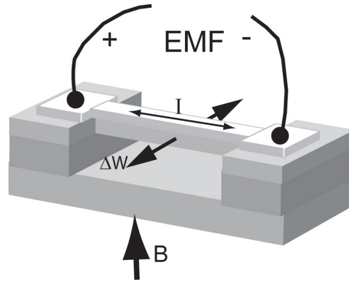

Fig. 6.28. Vibration detection by electromotive force measurement.

Measurement of V_{EMF} by an external circuit provides the nanoresonator velocity. As for capacitive measurements, the measured quality factor might be affected by the measurement circuit.[46] This measurement technique could be applied to high frequency (100MHz) and low temperature (4K) damping measurements of nanowires.[47]

Acknowledgments

Some of the results presented in this chapter were obtained with measurement systems developed in collaboration with Fogale Nanotech company and with the support of the french network of basic research technology (RTB), of the French National Agency of Research (ANR), of Ile-de-France region, of Essonne department and of the DGA. The authors also wish to thank their colleagues of the Micro Nano Systems group of Institut d'Electronique Fondamentale, and especially Fabien Parrain and Jean-Paul Gilles, for providing some unpublished measurements. Part of this chapter is based on training courses and research work performed in the frame of the European Network of Excellence PATENT DfMM.

References

1. K. E. Petersen, C.R. Guarnieri, Young's modulus measurements of thin films using micromechanics, *J. Appl. Phys.* **50**, 6761(1979)
2. M. Tabib-Azar, K. Wong and W. Ko, Aging phenomena in heavily doped (p+) micromachined silicon cantilver beams, *Sensors and Actuators* **A33**, 199 (1992)
3. A. Fabre, E. Finot, J. Demoment, S. Contreras and J.P. Goudonnet, Microscale technique for in-situ measurement of elastic parameters of materials under reactive atmosphere, *Rev. Sci. Instrum.* **72**, 3914 (2001)
4. Z. Huang, G. Leighton, R. Wright, F. Duval, H.C. Chung, P. Kirby and R.W. Whatmore, Determination of piezoelectric coefficients and elastic constant of thin films by laser scanning vibrometry techniques, *Sensors and Actuators* A, (2006) in press

5. C. Peng, X. Chen, O. Bai, L. Luo and S. Xia, A novel high performance micromechanical resonant electrostatic field sensor used in atmospheric electric field detection, *Proc. MEMS 2006*, Istanbul, Turkey, 698 (2006)
6. J. W. Kang, H. Guckel and Y. Ahn, Amplitude detecting micromechanical resonating beam magnetometer, *Proc. MEMS 98*, 372 (1998)
7. C. Harrison, S. Ryu, A. Goodwin, K. Hsu, E. Donzier, F. Marty and B. Mercier, A MEMS device for measuring the physical properties of fluids, *Proc SPIE* **6111**, 6110D (2006)
8. N. V. Lavrik, M.J. Sepaniak and P. G. Datskos, Cantilver transducers as a platform for chemical and biological sensors, *Rev. Sci. Instrum.* **75**, 2229 (2004)
9. F. Lochon, I. Dufour and D. Rebiere, A microcantilever chemical sensors optimization by taking into account losses *Sensors and Actuators* **B 118**, 292 (2006)
10. K.Wang, A.C.Wong, and C.T. Nguyen,.VHF free-free beam high-Q micromechanical resonators, *J. MEMS*, **9**, 347 (2000)
11. G.K.Ho, J.K.C. Perng and F. Ayazi, Process compensated micromechanical resonators, *Proc. MEMS 2007*, Kobe Japan, 183 (2007)
12. G. Stemme, Resonant silicon sensors, *J. Micromech. Microeng*. **1**, 113 (1991)
13. S. Bianco, M. Cocuzza, S. Ferrero, E. Giuri, G. Piacenza, C.F. Pirri, D. Bich, A. Merialdo, P. Schina and R. Correale, Silicon resonant microcantilevers for absolute pressure measurement, *J. Vac. Sci. Technol.* **B24(4)**, 1803 (2006)
14. N. Yazdi, F. Ayazi and K. Najafi, Micromachined inertial sensors, *Proc. IEEE* **86**, 1640 (1998)
15. F. Ayazi and K. Najafi,A HARPSS polysilicon vibrating ring gyroscope, *J. MEMS* **10**,169 (2001)
16. M. Villarroya, J. Verd, J. Teva, G. Abadal, E. Forsen, F.Perez-Murano, A. Uranga, E. Figueras, J. Montserrat, J. Esteve, A. Boisen and N. Barniol, System on chip mass sensor based on polysilicon cantilvers arrays for multiple detection, *Sensors and actuators* **A132**, 154 (2006)
17. D. Jin, W. Li, J.Liu, G. Zuo, Y. Wang, M. Liu and H. Yu, High-mode resonant piezoresistive cantilver sensors for tens-femtogram resoluble mass sensing in air *J. Micromech. Microeng*., **16**, 1017 (2006)
18. R.H. Blick, A. Erbe, L. Pescini, A. Kraus, D.V. Scheible, F.W. Beil, E. Hoehberger, A. Hoerner, J. Kirschbaum, H. Lorenz and J.P. Kotthaus, Nanostructured silicon for studying fundamental aspects of nanomechanics, *J. Phys. Condens. matter.* **14**, R905 (2002)
19. D. Kleckner and D. Bouwmeester, Sub-kelvin cooling of a micromechanical resonator, *Nature* **444**, 75 (2006)
20. V. Cimalla, F. Niebelschütz, K. Tonisch, Ch. Foerster, K. Bruekner, I. Cimalla, T. Friedich, J. Pezoldt, R. Stephan, M. Hein and O. Ambacher, Nanoelectromechanical devices for sensing applications, *Sensors and Actuators* B (2006) In press
21. J. Frömel, D. Billep, T. Gebner and M. Wiemer, Application of micromechanical resonant structures for measuring the sealing of bonded sensor systems, *J. Microsyst. Technol.,* **12**, 481 (2006)
22. B. Le Foulgoc, T. Bourouina, O. Le Traon, A. Bosseboeuf, F. Marty, C. Breluzeau, J.P. Grandchamp and S. Masson., Highly decoupled single-crystal silicon resonators: an approach for the intrinsic quality factor, *J. Micromech. Microeng.* **16**, S45 (2006)

23. R. Lifshitz, Phonon-mediated dissipation in micro- and nano-mechanical systems, *Physica* **B 316-317**, 397 (2002)
24. P. Mohanty, D.A. Harrington, K.L. Ekinci, Y.T. Yang, M.J. Murphy and M.L. Roukes, Intrinsic dissipation in high-frequency micromechanical resonators, *Phys. Rev*. **B 66**, 085416-1 (2002)
25. J. Yang, T. Ohno and M. Esashi, Surface effects and high quality factors in ultrathin single crystal silicon cantilevers, *Appl. Phys. Lett*., **77**, 3860 (2000)
26. R.E. Mihailovich and N.C. MacDonald, Dissipation measurements of vacuum-operated single-crystal silicon miroresonators, *Sensors and Actuators* **A50**, 199 (1995)
27. D.S. Bindel, E. Quévy, T. Koyama, S. Govindjee, J. W. Demmel and R. T. Howe, Anchor loss simulation in resonators, *Proc. MEMS 2005*
28. Z. Hao, A. Erbil and F. Ayazi, An analytical model for support loss in microachined beam resonators with in-plane flexural vibrations, *Sensors and Actuators* **A 109**, 156 (2003)
29. B. Chim, C. M. Jha, T. White, R.N. Candler, M. Hopcroft, M. Argawal, K.K. Park, R. Melamud, S. Chandorkar and T.W. Kenny, Temperature dependence of the quality factor of MEMS resonators, *Proc. IEEE MEMS 2006*, Istanbul, Turkey, 590 (2006)
30. K.L. Enicki and M.L. Roukes, Nanoelectromechanical systems, *Rev. Sci. Instrum*., **76**, 061101 (2005)
31. J.E. Graebner, B.P. Barber, P.L. Gammel, D.S. Greywall and S. Gopani. Dynamic visualization of subangstrom high-frequency surface vibrations, *Appl. Phys. Lett*. **78**, 159 (2001)
32. L. Yan, J. Wu, and W. C. Tang, A 1.14 GHz piezoelectrically transduced disk transducer, *Proc. MEMS 2005*, 203 (2005)
33. S. Y. No, A. Hashimura, S. Pourkamali and F. Ayazi, Single-Crystal Silicon HARPSS Capacitive Resonators with Submicron Gap-Spacing, *Solid-State Sensor, Actuator and Microsystems workshop*, 281 (2002).
34. G. Piazza, R. Abdolvand, G. K. Ho and F. Ayazi, Voltage-tunable piezoelectrically-transduced single-crystal silicon micromechanical resonators, *Sensors and Actuators*, **A111**, 71 (2004).
35. I. Bargatin, E. B. Myers, J. Arlett, B. Gudlewski and M. L; Roukes, Sensitive detection of nanomechanical motion using piezoresistive signal downmixing, *Appl. Phys. Lett*., **86**, 133109 (2005).
36. P. J. Petersan and S. M. Anlage, Measurement of resonant frequency and quality factor of microwave resonators: Comparison of methods, *J. Appl. Phys*., **84**, 3392 (1998).
37. V. Kaajakari, T. Mattila, A. Oja and H. Seppä, Non-linear limits for single-crystal silicon microresonators, *IEEE J. MEMS* **13**, 715 (2004).
38. M. Agarval, S. A. Chandorkar, R. N. Candler, B. Kim, M. A; Hopcroft, R. Melamud, C. M. Jha, T. W. Kenny and B. Murmann, Optimal drive condition for non-linearity reduction in electrostatic microresonators, *Appl. Phys. Lett*., **89**, 214105 (2006).
39. P. Y. Kwok, M. S. Weinberg and K. S. Breuer, Fluid Effects in Vibrating Micromachined Structures, *IEEE J. MEMS* **14**, 770 (2005).
40. K. Tittelbach-Helmrich, An integration method for the analysis of multiexponential transient signals, *Meas. Sci. Technol*., **4**, 1323 (1993).

41. Y. S. Shmaliy, A study on resonant frequency and Q factor tunings for MEMS vibratory gyroscopes, *Continuous-Time Signals*, Springer, Dordrecht, The Nederlands, (2006).
42. O. B. Ozdolongar, B.D. Hansche and T.G. Carne, Experimental Modal Analysis for Microelectromechanical Systems, *Experimental Mechanics* **45**, 498 (2005)
43. A.B. Stanbridge and D.J. Ewins, Extraction of damped and undamped natural mode shapes from area-scan ODS, *Proc. SPIE* **6345**, 63450G, (2006)
44. R.R.A. Syms, Long-travel electrothermally driven resonant cantilever actuator, *J. Micromech. Microeng.*, **12**, 211 (2002)
45. T. S. J. Lammerink, M. Elwenspoek and J. H. J. Fluitman, Frequency dependence of thermal excitation of micromechanical resonators, *Sensors and Actuators* **A27(1-3)**, 685 (1991)
46. N. Cleland and M.L. Roukes, External control of dissipation in a nanometer-scale radio frequency mechanical resonator, *Sensors and actuators* **A72**, 256 (1999)
47. A. Husain, J. Hone, H.W.ch. Postma, X.M.H. Huang, T. Drake, M. Barbic, A. Scherer and M.L. Roukes, Nanowire-based very-high-frequency electromechanical resonator, *Appl. Phys. Lett*. **83**, 1240 (2003)
48. A. Bosseboeuf, J.P. Gilles, K. Danaie, R. Yahiaoui, M. Dupeux, J.P. Puissant, A. Chabrier, F. Fort and P.Coste. A versatile microscopic profilometer-vibrometer for static and dynamic characterization of micromechanical devices, *Proc. SPIE* **3825**, 123 (1999)
49. L.M. Zhang, D. Walsh, D. Uttamchandani and B. Culshaw, Effect of optical power on the resonant frequency of optical powered silicon microresonators, *Sensors and Actuators* **A29**, 73 (1991)
50. O. Marti, A. Ruf, M. Hipp, H. Bielefeldt, J. Colchero and J. Mlynek, Mechanical and thermal effects of laser irradiation on force microscope cantilevers, *Ultramicroscopy* **42-44**, 345 (1992)
51. J. Yang, T. Ohno and M. Esashi, Surface effects and high quality factors in ultrathin single crystal silicon cantilevers, *Appl. Phys. Lett*. **77**, 3860 (2000)
52. A.V. Churenkov, Photothermal excitation and self-excitation of silicon microresonators, *Sensors and Actuators* **A39**, 141 (1993)
53. A. Prak and T.S.J. Lammerink. Effect of electronic strain on the optically induced mechanical moment in silicon microstructures, *J. Appl. Phys*. **71**, 5242 (1992)
54. R. M. A. Fatah, Mechanisms of optical activation of micromechanical resonators, *Sensors and Actuators* **A33**, 229 (1992)
55. T. Ikahara, M. Tanaka,, S. Shimada and H. Matsuda. Optically-driven actuator using photo-induced phase-transition material, *Proc. MEMS 2001*, 256 (2001)
56. M. Zalatutdinov,B. Illic, D. Czaplewski, A. Zehnder, H.G. Craighead and J.M. Parpia, Frequency-tunable micromechanical oscillator, *Appl. Phys.Lett.* **77**, 3287 (2000)
57. A. Biswas, T. Weller and L.P.B. Katehi, Stress determination of micromembranes using laser vibrometry, *Rev. Sci. Instrum.* **67**, 1965 (1996)
58. B.S. Berry, W.C. Pritchet and C.E. Uzoh, Dynamical method for the thermomechanical study of thin membranes, *J. Vac. Sci. Technol*. **B7**, 1565 (1989)
59. K. Ueda, T. Usada, T. Ishimagi and T. Kurosawa, Current status of measurement standrds for vibration and shock in NRLM, *Proc. SPIE* **4072**, 113 (2000)

60. R.M. Lin and W.J. Wang, Structural dynamic of Microsystems-current state of research and future directions, *Mechanical Systems and Signal Processing* **20**, 1015 (2006)
61. *Optical inspection of Microsystems*. W. Osten Ed. Taylor & Francis Group, Boca Raton (2007).
62. A. Bosseboeuf and S. Petitgrand, Characterisation of the static and dynamic behaviour of M(O)EMS by optical techniques: status and trends, *J. Micromech. Microeng.* **13**, S23 (2003)
63. M. Kujawinska, Modern optical measurement station for micro-materials and microelements studies, *Sensors and Actuators* **A99**, 144 (2002)
64. D. Burns and V.M. Bright., Optical power induced damage to microelectromechanical mirrors, *Sensors and Actuators* **A70**, 6 (1998)
65. J. Burns and H. F. Helbig, A system for automatic electrical and optical characterization of microelectromechanical devices, *IEEE J. MEMS* **8**, 473 (1999)
66. C.Q. Davis and D.M. Freeman, Using a light microscope to measure motions with nanometer accuracy, *Opt. Eng.* **37**, 1299 (1998)
67. W. Hemmert, M.S. Mermelstein and D.M. Freeman, Nanometer resolution of three dimensional motions using video interference microscopy, *Proc. MEMS* 99, 301 (1999)
68. C. Rembe and R.S. Muller, Measurement system for full three-dimensional motion characterization of MEMS, *J. Micromech. Microeng.* **11**, 479 (2002)
69. A. Hafiane, S. Petitgrand, O. Gigan, S. Bouchafa and A. Bosseboeuf, Study of subpixel image processing algorithms for MEMS in-plane vibration measurements by stroboscopic microscopy, *Proc. SPIE* **5145**, 169 (2003)
70. S. Petitgrand and A. Bosseboeuf, Simultanous mapping of out-of-plane and in-plane vibrations of MEMS with (sub)nanometer resolution, *J. Micromech. Microeng.* **14**, S97 (2004)
71. B. Serio, J.J. Hunsinger and B. Cretin, In-plane measurements of micromechanical systems vibrations with nanometer resolution using the correlation of synchronous images, *Rev. Sci. Instrum.* **75**, 335 (2004)
72. B. Serio, J.J. Huninger, D.D. Teyssieux and B. Cretin, Phase correlation method for subpixel in-plane vibration measurements of MEMS by stroboscopic microscopy, *Proc. SPIE* **5856**, 755 (2005)
73. O. Holmgren, K. Kokkonen, T. Mattila, V. Kaajari, A. Oja, J. Kiihamâki, J.V. Knuutila, and M.M. Salomaa. Imaging of in- and out-of-plane vibrations in micromechanical resonator, *Electron lett.* **41**, 121 (2005)
74. B. Cretin, B. Serio and P. Vairac, In-plane optical measurement of vibrations of MEMS: gradient methods using interferometry and image processing, *Proc. SPIE* **5145**, 161 (2003)
75. A. Bosseboeuf, F. Parrain, P. Coste, C. Breluzeau, J.-P. Gilles and X. Le Roux, Inplane vibration measurement of microdevices by the knife-edge technique in reflection mode *Proc. 7th Int. Conf. on Vibration measurements by laser techniques*, 19-33 Juin 2006, Ancona, Italy (2006) In press
76. G. Zhou, F.S. Chau, Grating-assisted optical microprobing of in-plane and out-of-plane displacements of microelectromechanical devices, *J. MEMS* **15**, 388 (2006)

77. C.B. Scruby and L.E. Drain. *Laser ultrasonics-techniques and application*. Adam Hilger, Bristol (1990)
78. S. Ueha, K. Shiota, T. Okada, and J. Tsujiuchi, Optical heterodyne measurement of in-plane vibrations, *Opt. Commun*. **10**, 88 (1974)
79. V. Annovazzi-Lodi, S. Merlo, M. Norgia, Comparison of capacitive and feedback interferometric measurements on MEMS, *IEEE J. MEMS* **10**, 327 (2001)
80. W. Osten, S. Seebacher and W.P.O. Jüptner, Application of digital holography for the inspection of microcomponents, *Proc. SPIE* 4400, 1 (2001)
81. P. Aswendt, Micromotion analysis by deep-UV speckle interferometry, *Proc. SPIE* **5145**, 17 (2003)
82. M. Hart, R.A. Conan, K. Lau and R.S. Muller, Stroboscopic interferometer for dynamic MEMS characterization, *IEEE J. MEMS* **9**, 409 (2000)
83. S. Petitgrand, R. Yahiaoui, K. Danaie, A. Bosseboeuf and J.P. Gilles, 3D measurement of micromechanical devices vibration mode shapes with a stroboscopic interferometric microscope, *Optics and Lasers in Engineering* **36**, 77 (2001)
84. S. Petitgrand, A. Bosseboeuf, Simultanaous mapping of phase and amplitude of MEMS vibrations by microscopic interferometry with stroboscopic illumination, *Proc. SPIE* **5145**, 33 (2003)
85. S. Petitgrand, R. Yahiaoui, A. Bosseboeuf, K. Danaie, Quantitative time-averaged microscopic interferometry for micromechanicaldevice vibration characterization, *Proc. SPIE* **4400**, 51 (2001)
86. G. Benedetto, R. Gavioso, R. Spagnolo, Measurement of microphone membrane displacement with an optical beam deflection technique, *Rev. Sci. Instrum*. **66**, 5563 (1995)
87. C.A. J. Putman, B. G. De Grooth, N. F. Van Hulst, J. Greve, A detailed analysis of the optical beam deflection technique for use in atomic force microscopy, *J. Appl. Phys*. **72**, 6 (1992)
88. C. Bergaud, L. Nicu, Viscosity measurements based on experimental investigations of composite cantilever beam eigenfrequencies in viscous media, *Rev. Sci. Instrum*. **71**, 1 (2000)
89. J. Gaspar, V. Chu, J.P. Conde, Amorphous silicon elecrostatic microresonators with high quality factors, *Appl. Phys. Lett*. **84**, 622 (2004)
90. M. Baù, M. Motterlini, V. Ferrari, D. Marioli, A. Taroni. Contactless system for dynamic characterization of microresonators, *Electron. Lett.* **42**, 525 (2006)
91. P. Hariharan, *Optical interferometry*, 2nd edition, Elsevier science (USA) (2003)
92. R. Di Sante and L. Scalise, Multipoint optical fiber vibrometer, *Rev. Sci. Instrum.* **73**, 1321 (2002)
93. A. D. Drake, D. C. Leiner, Fibe-optic interferometer for remote subangstrom vibration measurement, *Rev. Sci. Instrum*. **55**, 162 (1984)
94. J.F. Li, O. Moses and D. Viehland, Simple, high resolution interferometer for the measurement of frequency-dependent responses in ferroelectric ceramics, *Rev. Sci. Instrum.* **66(1)**, 215 (1995)
95. C.-M. Wu, C.-S. Su and G.-S. Peng, Correction of non-linearity in one-frequency optical interferometry, *Meas. Sci. Technol*. **7**, 520 (1996)

96. W. Jin, L. M. Zhang, D. Uttamchandani and B. Culshaw, Modified J1…J4 method for linear readout of dynamic phase changes in a fiber-optic, *Appl. Opt*. **30**, 4496 (1991)
97. E.J. Eklund, A. M. Shkel, Factors affecting the performance of micromachined sensors based on Fabry–Pérot interferometry, *J. Micromech. Microeng.* **15**, 1770 (2005)
98. I. Tittonen, G. Breitenbach, T. Kalkbrenner, T. Müller, R. Conradt, S. Chiller, E. Steinsland, N.Blanc and N.J. de Rooij, Interferometric measurements of the position of a macroscopic body: towards observation of quantum limits, *Phys. Rev.* **A59**, 1038 (1999)
99. T.K. Gangopadhyay, Non-contact vibration measurement based on extrinsic Fabry–Pérot interferometer implemented using arrays of single-mode fibres, *Meas. Sci. Technol*. **15**, 911 (2004)
100. R.L. Waters and M. E. Aklufi, Micromachined Fabry–Pérot interferometer for motion detection, *Appl. Phys. Lett.* **81**, 3320 (2002)
101. D.W. Carr, L. Sekaric and H.G. Craighead, Measurement of nanomechanical resonant structures in single-crystal silicon, *J. Vac. Sci. Technol*. **B16**, 3821 (1998)
102. L. Sekaric, J.M. Parpia, H.G. Craighead, T. Feygeleson, B.H. Houston and J.E. Butler, Nanomechanical resonant structures in nanocrystalline diamond, *Appl. Phys. Lett.* **81**, 4455 (2002)
103. C. Jeong, S. Seok, B. Lee, H. Kim and K. Chun, A study on resonant frequency and Q factor tunings for MEMS vibratory gyroscopes, *J. Micromech. Microeng.* **14**, 1530 (2004)
104. Duwel, J. Gorman, M. Weinstein, J. Borenstein and P. Ward, Experimental study of thermoelastic damping in MEMS gyros, *Sensors and Actuators* **A103**, 70 (2003).
105. J. S. Aldridge and A. N. Cleland, Noise-enabled precision measurements of a Duffing nanomechanical resonator, *Phys. Rev. Lett*. **94**, 156403 (2005).
106. M. Cerna and A. F. Harvey, *The Fundamentals of FFT-Based Signal Analysis and Measurement*, Application Note AN041, National Instruments (2000)
107. *Spectrum Analysis Basics*, Application Note AN150, Agilent Technologies (2006).
108. *Understanding the Fundamentals of Vector Network Analysis*, Application Note AN 1287-1, Agilent Technologies (2000).
109. L. Molyneux, A timing device for the measurement of damping capacity in vibrating samples, *J. Phys. E: Sc. Instrum.* **1**, 1214 (1968).
110. J.M. Mason and H. G. Leventhall, Rapid measurement of the decay rate of vibrations, *J. Phys. E: Sci. Instrum.* **2**, 1104 (1969)
111. V. J. Logeeswaran, F. E. H. Tay, M. L. Chan, F. S. Chau, and Y. C. Liang, *Analog Integrated Circuits and Signal Processing* **37**, 17 (2003)
112. P. Bruschi, A. Nannini and F. Pieri, Electrical measurement of the quality factor of microresonators and its dependence on the pressure, *Sensors and Actuators* **A114**, 21 (2004)
113. F. A. Ghavanini, H. Rödjegård and P. Enoksson, An easy-to-implement method for the evaluation of capacitive resonant sensors, *J. Micromech. Microeng*. **16**, S156 (2006)
114. J. Juillard, E. Colinet, L. Nicu and C. Bergaud, Digital self-calibration method for MEMS sensors, *IEEE Trans. on Instrumentation and Measurement* **54**, 1438 (2005).

115. H. Mathias, F. Parrain, J. P. Gilles, S. Megherbi and A. Dupret, Quality Factor Measurement and Reliability for MEMS Resonators, *Proc. Symposium on Design, Test, Integration and Packaging of MEMS/MOEMS (DTIP)*, 210 (2005).
116. A. N. Cleland, Foundation of nanomechanics, Springer-Verlag Berlin-Heidelberg-New York (2003)
117. V.B. Braginsky and S.P. Vyatchanin, Low quantum noise tranquilizer for Fabry–Pérot interferometer, *Phys. Lett*. **A293**, 228 (2002)
118. G.M. Kim, S. Kawai, M. Nagashio, H. Kawakatsu and J. Brugger, Nanomechanical structures with 91MHz resonance frequency fabricated by local deposition and dry etching, *J. Vac. Sci. Technol.* **B22**, 1658 (2004)
119. I. Ogo, N.C. MacDonald, Application of time-resolved scanning electron microscopy to the analysis of the motion of micromechanical structures, *J. Vac. Sci. Technol*. **B**, 1630-1633 (1996)
120. K. Ura, H. Fujioka, T. Hosokawa, Picosecond pulse stroboscopic scanning electron microscope, *J. Electron. Microscopy* **27**, 247 (1978)
121. V. Agache , B. Legrand, K. Nakamura, H. Kawakatsu, L. Buchaillot, H. Toshiyoshi, D. Collard, H. Fujita, Characterization of vertical vibration of electrostatically actuated resonators using atomic force microscopy in non contact mode, *Proc. Transducers'05*, Seoul, Korea, June 5-9 2005, 2023 (2005)
122. E. Quévy, A. San Paulo, E. Basol, R.T. Howe, T-J. King, J. Bokor, Back-end-of-line poly SiGe disk resonators, *Proc. MEMS 2006*, Istanbul, Turkey, 234(2006)
123. S. Ryder, K. B. Lee, X. Meng, L. Lin, AFM characterization of out-of-plane high frequency microresonators, *Sensors and Actuators* **A114**, 135 (2004)
124. B. Illic, S. Krylov, L.M. Bellan, H.G. Craighead, Dynamic characterization of nano oscillators by atomic force microscopy, *Proc. MEMS 2007*, Kobe, Japan, 21 (2007)
125. A. Volodin, C. Van Haesendonck, R.Tarkianinen, M. Ahlskog, A. Fonseca, J.B. Nagy, AFM detection of the mechanical resonances of coiled carbon nanotubes, *Appl. Phys*. **A720**, S75 (2001)
126. E. Dupas, G. Grenaud, A. Kulik, J.L. Loubet. High-frequency mechanical spectroscopy with an atomic force microscope, *Rev. Sci. Instrum*. **72**, 3810 (2001)
127. J.A. Turner, J. S. Wiehn, Sensitivity of flexural and torsional vibration modes of atomic force microscope cantilever to surface stiffness variations, *Nanotechnology* **12**, 322-330 (2001)

This page intentionally left blank

Chapter 7

Nonlinear Dynamics of Electrostatically Actuated MEMS

S. K. De and N. R. Aluru

Department of Mechanical Science and Engineering
Beckman Institute for Advanced Science and Technology
University of Illinois at Urbana-Champaign
Urbana, IL 61801
aluru@uiuc.edu

The multi-physical nature of microelectromechanical systems (MEMS) makes the development of CAD tools for MEMS a challenging task. Besides, the non-linear coupling between the different physical domains in MEMS can give rise to interesting non-linear dynamic properties which can be exploited for various applications like chaotic micro-fluidic mixers, secure communications, MEMS filters with shiftable resonant frequencies, *etc*. In this chapter, an efficient physical level simulation tool, namely, the full-Lagrangian Newton method is presented for the dynamic analysis of electrostatic MEMS. This new scheme has several advantages of conventional MEMS simulation tools in terms of speed and convergence rates. The simulation tool is used to explore new non-linear dynamic properties of electrostatic MEMS. Complex non-linear oscillations and the period doubling route to chaos are observed under superharmonic excitations and the presence of U-sequence in MEMS is reported. Under superharmonic excitation, the sequence is found to be a modified form of the U-sequence termed as "UM-sequence". The effect of these complex oscillations on thermoelastic damping (an inherent dissipation mechanism that limits the quality factor of these devices) in electrostatic MEMS is also studied.

Contents

7.1 Introduction 236
7.2 Theory of MEMS Dynamics 238
  7.2.1 Mechanical Analysis 239
  7.2.2 Thermal Analysis 240
  7.2.3 Fluidic Analysis 240
  7.2.4 Electrostatic Analysis 245
7.3 Dynamic Analysis in the Absence of Damping 246

7.3.1 Numerical Simulations in the Absence of Damping 248
7.4 Dynamic Analysis in the Presence of Fluid Damping 252
7.4.1 Numerical Simulations in the Presence of Fluid Damping 253
7.4.2 Nonlinear Dynamic Properties in the Presence of Fluid Damping 260
7.5 Dynamic Analysis in the Presence of Fluid and Thermal Damping 271
7.5.1 Classical Theory of Thermoelastic Damping 274
7.5.2 Modified Theory of Thermoelastic Damping 275
7.5.3 Numerical Simulations in the Presence of Fluid and Thermal Damping 278
7.6 Conclusions 283
References 284

7.1. Introduction

Microelectromechanical systems (MEMS) have several wide spread industrial applications like accelerometers,[1] inertial sensors,[2] chemical/biological sensors,[3] RF switches/filters,[4] *etc.* Advanced simulation and modeling tools are needed for the efficient design and analysis of MEMS devices. However, the multi-energy domains (for example, electrical, fluidic, thermal, mechanical, *etc.*) present in MEMS devices and the non-linear coupling that exists between them make the development of such computational tools very challenging.[5] Physical level simulation tools for the design and analysis of MEMS devices have been developed over the years.[6–9] These conventional simulation tools perform the mechanical analysis on the undeformed geometry of the device using a Lagrangian approach and the analyses of the other physical domains present are performed on the deformed geometry – such an approach is defined as a semi-Lagrangian-scheme in this work. A relaxation method is used for self-consistency between the physical domains. Consequently, there is a need to update the geometry of the structure during each relaxation iteration in each time step. This in turn requires re-meshing of the surface (when the deformation is large) and re-computation of the interpolation functions used in the numerical method during each relaxation iteration in each time step. This significantly increases the computational effort making the self-consistent analysis of MEMS an extremely complex and challenging task. Besides, the non-linear coupling between the different domains can significantly lower the convergence rate of the relaxation scheme (for example, near pull-in conditions in the electro-mechanical coupling case[10–13]) thereby indicating the need for Newton based methods for such tightly coupled cases. The accurate computation of the inter-domain coupling terms in the Jacobian matrix of the Newton method is difficult in the conventional semi-Lagrangian approaches where the mechanical analysis is performed on the undeformed geometries and the other analyses are performed on the deformed geometries.

In this chapter, a full-Lagrangian-scheme is presented for the dynamic analysis of electrostatic MEMS. Surface re-meshing and re-computation of interpolation functions is eliminated due to the Lagrangian formulation of all the physical domains thereby making the method very efficient and fast. The different physical domains have been coupled together using Newton method. A Lagrangian description of all the physical domains makes it possible to compute the inter-domain coupling terms in the Jacobian matrix of the Newton method exactly. Dynamic analysis of several types of MEMS devices (beams, comb-drives, micromirrors) is then performed using the newly developed scheme. The physical level simulation tool is next used to explore new non-linear dynamic properties of electrostatic MEMS. The inherent source of non-linearity in electrostatic MEMS is the non-linear coupling between the electrostatic force and the displacement of the microstructure. The effect of these nonlinearities on the dynamic properties of electrostatic MEMS is studied here. Complex non-linear oscillations in the form of M oscillations per period or M-cycles and the period doubling route to chaos[14] resulting in the formation of $2^n M$-cycles in the system, where n corresponds to the nth period doubling bifurcation in the sequence and M corresponds to the Mth superharmonic frequency of excitation are observed. Beyond the period doubling route to chaos, U(Universal)-sequence[14] is observed for electrostatic MEMS. A modified form of the U-sequence is found to exist in the chaotic region of the MEMS devices under superharmonic excitations. The appearance of a periodic window with K-cycles in the normal U-sequence is replaced by the appearance of a periodic window with KM-cycles in the modified sequence termed as the "UM-sequence", at the Mth superharmonic frequency of excitation. The effect of these complex non-linear oscillations on thermoelastic damping, and hence the quality factor of the microstructures, is also studied. The classical theory of thermoelastic damping developed by Zener[15,16] and later improved by Lifshitz and Roukes[17] is modified for application to microstructures under arbitrary electrostatic actuation. The simulation results from the physical level analysis are compared with the predictions of the classical theory and the modified theory.

The rest of the chapter is outlined as follows: Sec. 7.2 presents the theory of electrostatic MEMS, where the physical models for the different energy domains in MEMS and the coupling between the different domains is discussed and Sec. 7.3 presents the full-Lagrangian Newton scheme and numerical simulation results for the dynamic analysis MEMS in the absence of fluid and thermal damping based on electro-mechanical coupling. The full-Lagrangian Newton scheme and numerical simulations in the case of electro-mechanical-fluidic coupling, *i.e.*, dynamic analysis of MEMS in the presence of fluid damping is presented in

Sec. 7.4. The new non-linear dynamic properties of electrostatic MEMS observed using numerical simulations are also presented in Sec. 7.4. Section 7.5 presents the full-Lagrangian Newton scheme and numerical simulations in the case of electro-thermo-mechanical-fluidic coupling for electrostatic MEMS. The effect of the complex non-linear oscillations on thermoelastic damping in electrostatic MEMS are also studied in Sec. 7.5 and conclusions are presented in Sec. 7.6.

7.2. Theory of MEMS Dynamics

The coupling between the different energy domains is explained by considering a generic electrostatic MEMS device shown in Fig. 7.1. Figure 7.1 shows a typical electrostatic MEM device – a deformable fixed-fixed beam over a fixed ground plane/electrode. We will explain the coupling among the energy domains by considering the example shown in Fig. 7.1, but the discussion is in general applicable to other MEM devices as well. Considering Fig. 7.1, a potential difference V

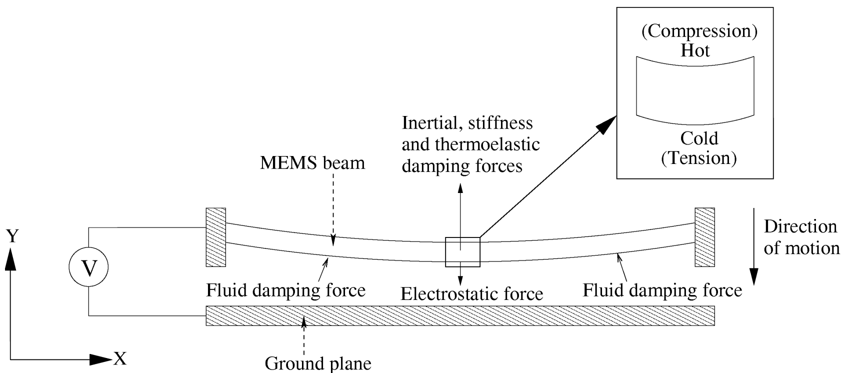

Fig. 7.1. Illustration of thermo-electro-fluidic-mechanical coupling in electrostatic MEMS through an example – a fixed-fixed MEMS beam over a ground plane: the deformed structure with the various forces acting on it when it is moving downward.

applied between the two conductors (the beam and the ground electrode) induces electrostatic charges on the surface of the conductors. The distribution of electrostatic charges on the surface of the conductors depends on the relative position of the two conductors. These electrostatic charges give rise to electrostatic force acting on the beam, as shown in Fig. 7.1. When the beam deforms due to the electrostatic force, the charge redistributes on the surface of the conductors and consequently, the electrostatic force also changes. At the same time, the displacement

of the surrounding fluid/air due to the deformation of the beam gives rise to a fluid damping force. Besides, the deformation of the beam causes stress inhomogeneities within the beam which gives rise to temperature fluctuations[18] (the side in compression gets warmer and the side in tension gets cooler as shown in Fig. 7.1) and hence a thermoelastic damping force. The electrostatic force and the fluid damping pressure acting on the beam together cause the beam to deform to a state where they are balanced by the internal stiffness, inertial and thermoelastic damping forces at that time instant (see Fig. 7.1). The stiffness force depends on the displacement of the beam at the given time instant and on the material properties of the beam. The inertial force depends on the acceleration of the beam at that time instant and on the density of the beam. The fluid damping force depends on the velocity and position of the beam at the time instant. In summary, a self-consistent final state is reached for a given time step where the sum of all the forces (the inertial force, the mechanical stiffness force, the fluid and the thermoelastic damping forces and the electrostatic force) is zero. The physical models for the different energy domains in electrostatic MEMS are presented next.

7.2.1. *Mechanical Analysis*

The mechanical deformation of the microstructure due to the various forces acting on it is obtained by performing 2D geometrically non-linear analysis of the microstructure. The transient governing equations for an elastic body using a Lagrangian description are given by[19]

$$\rho\ddot{\mathbf{u}} = \nabla \cdot (\mathbf{FS}) + \mathbf{F}_{bf} \qquad in \quad \Omega \tag{7.1}$$

$$\mathbf{u} = \mathbf{G} \qquad on \quad \Gamma_g \tag{7.2}$$

$$\mathbf{P} \cdot \mathbf{N} = \mathbf{H}_{sf} \qquad on \quad \Gamma_h \tag{7.3}$$

$$\mathbf{u}|_{t=0} = \mathbf{G_0} \qquad in \quad \Omega \tag{7.4}$$

$$\dot{\mathbf{u}}|_{t=0} = \mathbf{V_0} \qquad in \quad \Omega \tag{7.5}$$

where ρ is the material density in the undeformed (initial) configuration. $\mathbf{F}$ is the deformation gradient, $\mathbf{u}$, $\dot{\mathbf{u}}$ and $\ddot{\mathbf{u}}$ are the displacement, velocity and acceleration vectors, respectively and $\mathbf{F}_{bf}$ is the body force. $\mathbf{N}$ is the unit outward normal vector in the initial configuration, $\mathbf{S}$ is the second Piola-Kirchhoff stress, $\mathbf{G}$ is the prescribed displacement, $\mathbf{G_0}$ and $\mathbf{V_0}$ are the initial displacement and velocity, respectively, $\mathbf{H}_{sf}$ is the surface traction acting on the surface of the structures and $\mathbf{P}$ is the first Piola-Kirchhoff stress tensor. A Newmark scheme[20] with an implicit trapezoidal rule is used to solve the non-linear dynamical system posed in Eqs. (7.1)-(7.5).

7.2.2. *Thermal Analysis*

The temperature profile T in the micro-structure is obtained by solving a Lagrangian form of the heat equation[21,22]

$$\nabla \cdot \mathbf{h} = \frac{E\alpha}{1-\nu} T\dot{e} + \rho C_p \dot{T} \qquad \text{in} \quad \Omega \tag{7.6}$$

where ρ is the material density in the undeformed (initial) configuration, $\mathbf{h} = \bar{J}\mathbf{F}^{-1}\mathbf{q}$ is the referential heat flux vector[22] and $\mathbf{q}$ is the heat flux in the deformed configuration which can be computed as $\mathbf{q} = k\mathbf{F}^{-T}\nabla T$, where k is the thermal conductivity of the material. e is the sum of the diagonal components of $\mathbf{E}$, $\bar{J} = det(\mathbf{F})$ and the dots in Eq. (7.6) indicate derivative with respect to time. The second Piola-Kirchhoff stress $\mathbf{S}$ in the case of thermoelastic damping is given by[21]

$$\mathbf{S} = \mathbf{CE} - \frac{E\alpha}{1-\nu}\theta\mathbf{I} = \mathbf{S}^M + \mathbf{S}^T \tag{7.7}$$

where $\mathbf{S}^M$ and $\mathbf{S}^T$ are the mechanical and thermal components of $\mathbf{S}$, $\mathbf{C}$ is the material tensor and $\mathbf{E} = (\mathbf{F}^T\mathbf{F} - \mathbf{I})/2$ is the Green-Lagrangian strain and ν is the Poisson's ratio ($\mathbf{I}$ is the identity matrix). $\theta = T - T_0$ is the change in the temperature from the ambient temperature T_0.

7.2.3. *Fluidic Analysis*

Figure 7.2 shows a MEMS fixed-fixed beam (microstructure) moving with a peak velocity V_y towards a ground plane due to some electrostatic force (not shown in Fig. 7.2). The length of the MEMS beam is denoted by l and its height from the ground plane in the undeformed state is denoted by h in Fig. 7.2. The region exterior to the microstructure is divided into two regions, namely Regions A and B, in our discussion. Region A is located between the microstructure and the ground plane. The remaining portion exterior to the microstructure is denoted by Region B, as shown in Fig. 7.2. If (a) the length of the microstructure l is sufficiently larger than the height h, (b) the microstructure is moving perpendicular to the ground plane (as in this case) and (c) the Reynold's number is small, the fluid pressure/velocity variation in region B is minimal and can be neglected.[23,24] In that case, the fluid damping force can be computed by solving the compressible Reynold's squeeze film equation for region A. For all other cases, where l and h are comparable or when the motion of the microstructure is complicated, the compressible Navier–Stokes equations have to be solved in both regions A and B to compute the fluid damping force.

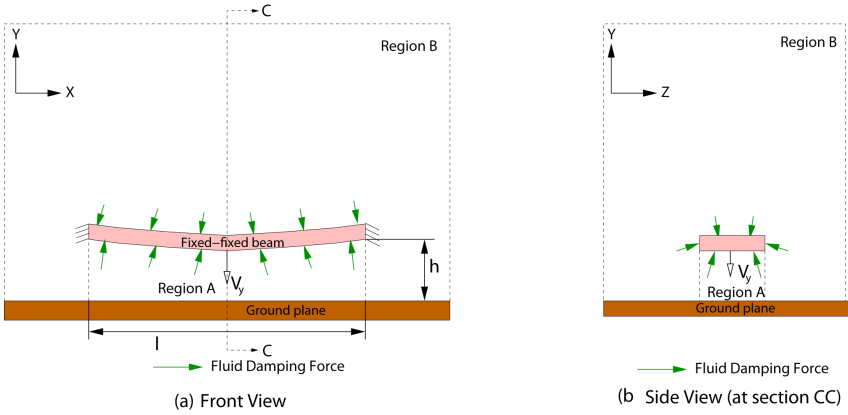

Fig. 7.2. Illustration of coupling between the mechanical and fluidic domains in electrostatic MEMS through an example - a MEMS fixed-fixed beam moving with a peak velocity V_y towards a ground plane giving rise to a fluid flow and the air/fluid damping force acting on it; (a) front view (in the X–Y plane) and (b) side view (in the Y–Z plane at section CC).

7.2.3.1. *Compressible Reynold's Squeeze Film Equation (CRSFE)*

The isothermal Reynold's squeeze film equation for a compressible slip flow is given by[8,25]

$$\frac{\partial}{\partial x}\left[(1+6K)\,h^3 P_f\frac{\partial P_f}{\partial x}\right]+\frac{\partial}{\partial z}\left[(1+6K)\,h^3 P_f\frac{\partial P_f}{\partial z}\right]=12\eta\frac{\partial(P_f h)}{\partial t} \quad (7.8)$$

where h is the gap between the movable structure and the ground electrode of the MEM device (same as the fluid film thickness), P_f is the fluid pressure under the structure (region A in Fig. 7.2) and η is the viscosity of the surrounding fluid. $K = \lambda/h$ is the Knudsen number, where λ is the mean free path of the surrounding fluid. The rarefaction/slip flow effects present in the system due to the small device dimensions and/or low ambient pressures are taken into account by the term $1 + 6K$ in Eq. (7.8). This correction term for the isothermal Reynold's squeeze film equation was derived by Schrag and Wachutka[24] by assuming first order slip flow boundary conditions and is valid up to $K = 1$. The variation of the fluid pressure, P_f, in the height direction (Y-direction in Figs. 7.2 and 7.3) is assumed to be negligible in CRSFE.[23] As a result, the fluid domain, where the Reynold's squeeze film equation is solved (for region A in Fig. 7.2) is the projection of the MEM structure on the $X - Z$ plane (ground plane)[8] as shown in Fig. 7.3. As the moving structure deforms due to the application of an external electric field, the projected fluid domain also changes. Equation (7.8) is written in the deformed configuration

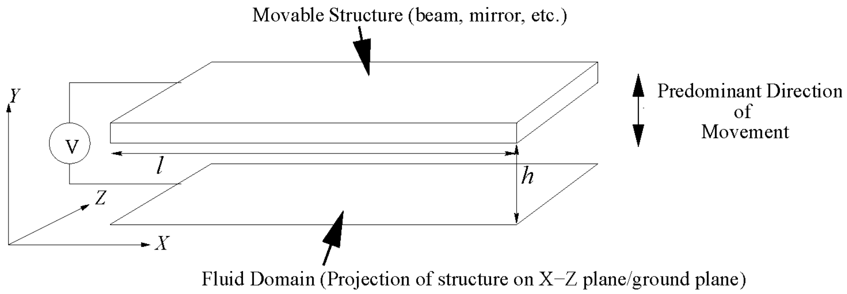

Fig. 7.3. Structural and fluidic domains for Reynold's squeeze film damping analysis.

(projected fluid domain) which varies with time (x and z are the coordinates in the deformed configuration). A Lagrangian form of Eq. (7.8) is given by[26]

$$\frac{\partial}{\partial X}\left[(1+6K)\,h^3 P_f \frac{\partial P_f}{\partial X}\left(1+\frac{\partial u}{\partial X}\right)^{-1}\right]\left(1+\frac{\partial u}{\partial X}\right)^{-1}+ \frac{\partial}{\partial Z}\left[(1+6K)\,h^3 P_f \frac{\partial P_f}{\partial Z}\right] = 12\eta\frac{\partial (P_f h)}{\partial t} \quad (7.9)$$

where X, Z are the coordinates of the fluid domain corresponding to the undeformed state of the movable structure and u is the deformation of the movable structure in the X-direction. As the 2D mechanical equations are solved in the $X-Y$ domain, mechanical deformation and its variation in the Z-direction are assumed to be zero. The fluid pressure, P_f, obtained from Eq. (7.9) is integrated along the Z-direction to compute an effective fluid pressure, P_{fe}, which is applied as a boundary condition in the 2D mechanical analysis in the $X-Y$ domain.[8]

The mean free path, λ (used for computing K in Eq. (7.9)), is related to the ambient temperature and pressure by the relation[27]

$$\lambda = \frac{k_b T}{\sqrt{2}\pi p d^2} \quad (7.10)$$

where k_b is the Boltzmann constant, T is the absolute temperature, p is the ambient pressure and d is the collision diameter of the fluid molecules (d = 3.66 Å for air[27]). The effective fluid pressure, P_{fe}, from the fluidic analysis and the electrostatic pressure, P_e, obtained from the electrostatic analysis (discussed in Sec. 7.2.4) are used to compute $\mathbf{H}_{sf}$ in Eq. (7.3) in the case of electrostatic MEMS using

$$\mathbf{H}_{sf} = \bar{J}(P_e - P_{fe})\mathbf{F}^{-T}\mathbf{N} \quad (7.11)$$

where $\bar{J} = det(\mathbf{F})$. A self-consistent solution of the coupled electro-mechanical-fluidic analysis at each time step is obtained using a Newton method which is described in Sec. 7.4.

7.2.3.2. *Compressible Navier–Stokes Equations (CNSE)*

A more general method to determine the fluid damping forces is to use the compressible Navier–Stokes equations. A Lagrangian form of the compressible Navier–Stokes equations (assuming a Newtonian viscous fluid) can be written as[28]

$$\frac{\partial \rho_f \bar{J}_f}{\partial t} = 0 \tag{7.12}$$

$$\frac{\partial \rho_f \bar{J}_f \mathbf{u_f}}{\partial t} - \nabla \cdot \left(\bar{J}_f \mathbf{T_f} \mathbf{F_f}^{-T} \right) = 0 \tag{7.13}$$

where ρ_f is the fluid density, $\mathbf{u_f}$ is the fluid velocity vector, $\mathbf{F_f} = \mathbf{I} + \nabla \mathbf{x_f}$ is the deformation gradient of the fluid ($\mathbf{x_f}$ is the displacement vector of the fluid) and $\bar{J}_f = det(\mathbf{F_f})$. $\mathbf{T_f}$ is the fluidic stress tensor in the deformed configuration given by

$$\mathbf{T_f} = -P_f \mathbf{I} + \begin{bmatrix} \sigma_{xx} & \tau_{xy} \\ \tau_{yx} & \sigma_{yy} \end{bmatrix} \tag{7.14}$$

where $\mathbf{I}$ is the 2×2 identity matrix. σ_{xx}, τ_{xy}, τ_{yx} and σ_{yy} are the viscous stress terms in the deformed configuration of the fluid. The ideal gas equation, $P_f = \rho_f RT$, is used to relate the density of the fluid with the pressure (for air) and isothermal conditions are assumed. R is the gas constant and T is the absolute temperature. σ_{xx}, τ_{xy}, τ_{yx} and σ_{yy} (viscous stress terms in the deformed configuration) can be expressed in the Lagrangian frame as

$$\sigma_{xx} = \frac{2\eta}{3} \left[\frac{2M}{\bar{J}_f} \frac{\partial u_f}{\partial X} - \frac{2B}{\bar{J}_f} \frac{\partial u_f}{\partial Y} + \frac{L}{\bar{J}_f} \frac{\partial v_f}{\partial X} - \frac{A}{\bar{J}_f} \frac{\partial v_f}{\partial Y} \right] \tag{7.15}$$

$$\tau_{xy} = \eta \left[-\frac{L}{\bar{J}_f} \frac{\partial u_f}{\partial X} + \frac{A}{\bar{J}_f} \frac{\partial u_f}{\partial Y} + \frac{M}{\bar{J}_f} \frac{\partial v_f}{\partial X} - \frac{B}{\bar{J}_f} \frac{\partial v_f}{\partial Y} \right] \tag{7.16}$$

$$\sigma_{yy} = \frac{2\eta}{3} \left[-\frac{M}{\bar{J}_f} \frac{\partial u_f}{\partial X} + \frac{B}{\bar{J}_f} \frac{\partial u_f}{\partial Y} - \frac{2L}{\bar{J}_f} \frac{\partial v_f}{\partial X} - \frac{2A}{\bar{J}_f} \frac{\partial v_f}{\partial Y} \right] \tag{7.17}$$

where η is the viscosity of the fluid, P_f is the fluid pressure and u_f and v_f are the fluid velocities in the X- and Y-directions, respectively. The geometrical terms

A, B, L, and M (the components of the deformation gradient $\mathbf{F_f}$) are obtained using the relations

$$\frac{\partial A}{\partial t}-\frac{\partial u_f}{\partial X}=0; \qquad \frac{\partial B}{\partial t}-\frac{\partial v_f}{\partial X}=0; \qquad \frac{\partial L}{\partial t}-\frac{\partial u_f}{\partial Y}=0; \qquad \frac{\partial M}{\partial t}-\frac{\partial v_f}{\partial Y}=0. \tag{7.18}$$

There are several advantages of using a Lagrangian formulation over a conventional Eulerian formulation for the compressible Navier–Stokes equations (CNSE). In the Lagrangian formulation, the fluid and the solid points/meshes at the solid-fluid interface remain fixed at all time instants, as a result of which, the transfer of boundary conditions from mechanics to fluidics and *vice versa* can be done accurately and easily.[29] This also allows the exact computation of the mechanical to fluidic and fluidic to mechanical coupling terms of the Jacobian matrix in the Newton method. Besides, once the equations are mapped back to the original undeformed fluid domain/co-ordinate system (Eqs. (7.12) and (7.13)), rediscretization of the deformed fluid domain and recomputation of the interpolation functions for the deformed fluid domain are eliminated.

The coupling between the solid (microstructure) and the fluid is realized through standard boundary conditions at the fluid-microstructure interface, namely, the kinematic conditions,[28] expressing the continuity of velocity and the continuity of stress. However, some of the MEMS devices simulated in this work are in the slip flow regime (*i.e.*, $0.01 \geq K \geq 0.1$) where the rarefaction effects are modeled through the first order slip flow boundary condition at the fluid-microstructure interface (same approximation as that used in Eq. (7.8)),

$$u_s - u_w = K\frac{\partial u_s}{\partial \mathbf{n}} = K\left(\mathbf{F_f}^{-T}\nabla u_s \cdot \frac{\mathbf{F_f}^{-T}\mathbf{N}}{|\mathbf{F_f}^{-T}\mathbf{N}|}\right) \tag{7.19}$$

where u_s is the tangential velocity of the fluid at the fluid-microstructure interface and u_w is the tangential microstructure velocity at that point and K is the Knudsen number. $\mathbf{n}$ and $\mathbf{N}$ denote the outward unit normal vector at the wall/fluid-microstructure interface in the deformed and the undeformed configurations, respectively. The fluidic stress, $\mathbf{T_f}$, obtained from the fluidic analysis and the electrostatic pressure obtained from the electrostatic analysis are used to compute $\mathbf{H}_{sf}$ in Eq. (7.3) in the case of electrostatic MEMS using the relation

$$\mathbf{H}_{sf} = \bar{J}\left[P_e\mathbf{I} + \mathbf{T_f}\right]\mathbf{F}^{-T}\mathbf{N}. \tag{7.20}$$

A self-consistent solution of the coupled electro-mechanical-fluidic analysis at each time step is obtained using a Newton method as described in Sec. 7.4.

7.2.4. *Electrostatic Analysis*

The 2D governing equation for electrostatic analysis can be written in a boundary integral form as[30]

$$\phi(p) = \int_{d\omega} \frac{1}{\epsilon} G(p, q)\sigma(q) d\gamma_q + C \tag{7.21}$$

$$\int_{d\omega} \sigma(q) d\gamma_q = C_T \tag{7.22}$$

where ϵ is the dielectric constant of the medium, p is the source point, q is the field point which moves along the boundary of the conductors and G is the Green's function. In two dimensions, $G(p, q) = -ln|p - q|/2\pi$, where $|p - q|$ is the distance between the source point p and the field point q. C_T is the total charge of the system and C is an unknown variable which can be used to compute the potential at infinity. Equations (7.21) and (7.22) are defined in the deformed configuration of the conductors, *i.e.*, the surface charge density is computed by solving the boundary integral equations on the deformed geometry of the conductors. The boundary integral equations can be written in the Lagrangian frame (see Ref. 31 for details)

$$\phi(p(P)) = \int_{d\Omega} \frac{1}{\epsilon} G(p(P), q(Q))\sigma(q(Q))\bar{\mathbf{J}}(Q) d\Gamma_Q + C \tag{7.23}$$

$$\int_{d\Omega} \sigma(q(Q))\bar{\mathbf{J}}(Q) d\Gamma_Q = C_T \tag{7.24}$$

$$\bar{\mathbf{J}}(Q) = [\mathbf{T}(Q) \cdot \mathbf{C}(Q)\mathbf{T}(Q)]^{1/2} \tag{7.25}$$

where ϵ is the dielectric constant of the medium, ϕ is the electrostatic potential, and σ is the electrostatic surface charge density. P and Q are the source and field points in the initial configuration corresponding to the source and field points p and q in the deformed configuration, and G is the Green's function. In two dimensions, $G(p(P), q(Q)) = -ln|p(P) - q(Q)|/2\pi$, where $|p(P) - q(Q)|$ is the distance between the source point $p(P)$ and the field point $q(Q)$. C_T is the total charge of the system and C is an unknown variable which can be used to compute the potential at infinity. $\mathbf{T}(Q)$ is the tangential unit vector at field point Q and $\mathbf{C}(Q)$ is the Green deformation tensor. Equations (7.23)-(7.25) are solved to obtain the distribution of surface charge density σ on the conductors. The surface traction due to the electrostatic pressure can be computed from the surface charge density by the relation

$$\mathbf{H}_{sf} = P_e \bar{J} \mathbf{F}^{-T} \mathbf{N} \tag{7.26}$$

where P_e is the electrostatic pressure normal to the surface given by $P_e = \sigma^2/2\epsilon$ and $\bar{J} = det(\mathbf{F})$. Equation (7.26) is the non-linear connectivity between the mechanical and the electrical domains. A Newton scheme can be applied to incorporate this coupling and obtain self-consistent solutions as described in Sec. 7.3.

7.3. Dynamic Analysis in the Absence of Damping

The main step in the Newton method is the computation of the Jacobian matrix, $\bar{\mathbf{J}}(\mathbf{u}, \sigma, C)$, which for the coupled domain MEM problem is

$$\bar{\mathbf{J}}(\mathbf{u}, \sigma, C) = \begin{bmatrix} \frac{\partial \mathbf{R_M}}{\partial \mathbf{u}} & \frac{\partial \mathbf{R_M}}{\partial \sigma} & \frac{\partial \mathbf{R_M}}{\partial C} \\ \frac{\partial \mathbf{R_{E1}}}{\partial \mathbf{u}} & \frac{\partial \mathbf{R_{E1}}}{\partial \sigma} & \frac{\partial \mathbf{R_{E1}}}{\partial C} \\ \frac{\partial \mathbf{R_{E2}}}{\partial \mathbf{u}} & \frac{\partial \mathbf{R_{E2}}}{\partial \sigma} & \frac{\partial \mathbf{R_{E2}}}{\partial C} \end{bmatrix} \tag{7.27}$$

and the residual (right-hand-side), $\mathbf{r}(\mathbf{u}, \sigma, C)$, is given by

$$\mathbf{r}(\mathbf{u}, \sigma, C) = - \begin{Bmatrix} \mathbf{R_M}(\mathbf{u}, \sigma, C) \\ \mathbf{R_{E1}}(\mathbf{u}, \sigma, C) \\ \mathbf{R_{E2}}(\mathbf{u}, \sigma, C) \end{Bmatrix} \tag{7.28}$$

From Eqs. (7.1)–(7.5), the non-linear mechanical residual equation $\mathbf{R_M}$ can be written as

$$\mathbf{R_M} = \nabla \cdot (\mathbf{FS}) + \mathbf{F}_{bf} - \rho \ddot{\mathbf{u}} - c\dot{\mathbf{u}} \qquad in \quad \Omega \tag{7.29}$$

$$\mathbf{R_M} = \mathbf{G} - \mathbf{u} \qquad on \quad \Gamma_g \tag{7.30}$$

$$\mathbf{R_M} = \mathbf{H}_{sf} - \mathbf{P} \cdot \mathbf{N} \qquad on \quad \Gamma_h \tag{7.31}$$

and the electrical residual equations for the full-Lagrangian-scheme are given by

$$\mathbf{R_{E1}} = \int_{d\Omega} \frac{1}{\epsilon} G(p(P), q(Q)) \sigma(q(Q)) \mathbf{J}(Q) d\Gamma_Q - \phi(p(P)) + C \tag{7.32}$$

$$\mathbf{R_{E2}} = C_T - \int_{d\Omega} \sigma(q(Q)) \mathbf{J}(Q) d\Gamma_Q. \tag{7.33}$$

From Eqs. (7.29)–(7.33), it can be seen that computing $\partial \mathbf{R_M}/\partial \mathbf{u}$, $\partial \mathbf{R_{E1}}/\partial \sigma$ and $\partial \mathbf{R_{E2}}/\partial \sigma$ is straight-forward. The terms $\partial \mathbf{R_M}/\partial C = 0$, $\partial \mathbf{R_{E1}}/\partial C = 1$ and $\partial \mathbf{R_{E2}}/\partial C = 0$. The electrical to mechanical coupling term $\partial \mathbf{R_M}/\partial \sigma$ is non-zero only for Eq. (7.31) (electrostatic pressure acting at prescribed boundary points of the domain) and can be computed directly

$$\frac{\partial \mathbf{R_M}}{\partial \sigma} = \frac{\partial \mathbf{H}_{sf}}{\partial \sigma} = \frac{\partial P_e}{\partial \sigma} \bar{J} \mathbf{F}^{-T} \mathbf{N} = \frac{\sigma}{\epsilon} \bar{J} \mathbf{F}^{-T} \mathbf{N}. \tag{7.34}$$

The terms $\partial \mathbf{R_{E1}}/\partial \mathbf{u}$ and $\partial \mathbf{R_{E2}}/\partial \mathbf{u}$ are difficult to compute directly in the case of semi-Lagrangian methods as the domain of integration (Eqs. (7.21) and (7.22)) is in the deformed configuration which is itself a function of $\mathbf{u}$. A matrix free approach[11] has been employed in the past to compute these terms. The matrix free approach can be sensitive to perturbation parameters affecting the convergence rate (see Refs. 11 and 32 for details). However, in the full-Lagrangian formulation, since the domain of integration is constant (not a function of the displacement $\mathbf{u}$ as in the semi-Lagrangian-scheme), the integration operator can be taken out of the differentiation operator and the derivatives can be computed directly (see Ref. 33 for more details).

$$\frac{\partial \mathbf{R_{E1}}}{\partial \mathbf{u}} = \int_{d\Omega} \frac{1}{\epsilon}\sigma(q(Q))\frac{\partial}{\partial \mathbf{u}}[G(p(P), q(Q))\mathbf{J}(Q)]d\Gamma_Q \tag{7.35}$$

$$\frac{\partial \mathbf{R_{E2}}}{\partial \mathbf{u}} = -\int_{d\Omega} \sigma(q(Q))\frac{\partial}{\partial \mathbf{u}}[\mathbf{J}(Q)]d\Gamma_Q \tag{7.36}$$

$G(p(P), q(Q))$ and $\mathbf{J}(Q)$ are simple functions of $\mathbf{u}$ and their derivatives can be computed in a straight-forward manner. The potential $\phi(p(P))$ is a constant and hence vanishes in Eq. (7.35) while C and $\sigma(q(Q))$ are independent variables.

The complete algorithm for the dynamic analysis using this Newton scheme is given in Algorithm 7.1. Algorithm 7.1 will be explained in this section using Fig. 7.4 which shows a two conductor electrostatic MEMS device. Ω_1 and Ω_2 denote the original geometry of conductor 1 and conductor 2, respectively, $d\Omega_1$ and $d\Omega_2$ denote the surface or boundary of conductor 1 and conductor 2, respectively, ω_1 denotes the deformed shape of conductor 1, ω_2 denotes the deformed shape

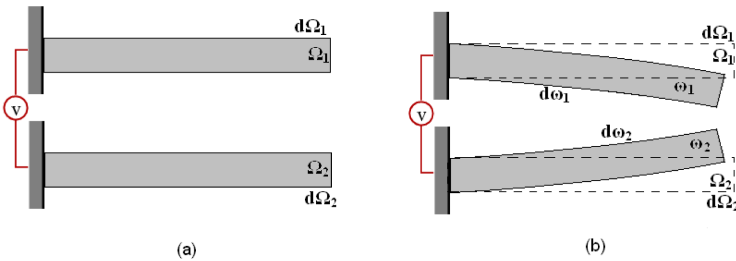

Fig. 7.4. A two conductor electrostatic system.

of conductor 2, $d\omega_1$ and $d\omega_2$ denote the deformed surfaces of conductor 1 and conductor 2, respectively. A potential difference V is applied between conductors 1 and 2. The applied potential does not change as the conductors undergo deformation or shape changes. In Algorithm 7.1, the index n stands for time instant

Algorithm 7.1. Newton algorithm for self-consistent dynamic analysis of MEM devices using the full-Lagrangian-scheme.

1: Define Ω_1, $d\Omega_1$, Ω_2, $d\Omega_2$
2: Discretize Ω_1, Ω_2 for mechanical analysis
3: Discretize $d\Omega_1$, $d\Omega_2$ for electrical analysis
4: Set $n = 0$, $t^n = t^0 = 0$
5: Initialize $\mathbf{u}(t^n) = \dot{\mathbf{u}}(t^n) = \sigma(t^n) = C(t^n) = 0$
6: Compute $\ddot{\mathbf{u}}(t_n)$ from Eq. (7.1)
7: **for** $n = 0$ to N **do**
8: Set $i = 0$ and $\mathbf{u}(t_i^{n+1}) = \mathbf{u}(t^n)$, $\sigma(t_i^{n+1}) = \sigma(t^n)$, $C(t_i^{n+1}) = C(t^n)$
9: **repeat**
10: Compute $\mathbf{T}$, $\mathbf{C}$ and $\mathbf{J}$ from $\mathbf{u}(t_i^{n+1})$
11: Compute $\bar{\mathbf{J}}(\mathbf{u}(t_i^{n+1}), \sigma(t_i^{n+1}), C(t_i^{n+1}))$
12: Compute $\mathbf{r}(\mathbf{u}(t_i^{n+1}), \sigma(t_i^{n+1}), C(t_i^{n+1}))$
13: Solve: $\bar{\mathbf{J}}(t_i^{n+1})[\Delta\mathbf{u}(t_i^{n+1})\ \Delta\sigma(t_i^{n+1})\ \Delta C(t_i^{n+1})]^T = \mathbf{r}(t_i^{n+1})$
14: Update $\mathbf{u}(t_{i+1}^{n+1}) = \mathbf{u}(t_i^{n+1}) + \Delta\mathbf{u}(t_i^{n+1})$, $\sigma(t_{i+1}^{n+1}) = \sigma(t_i^{n+1}) + \Delta\sigma(t_i^{n+1})$ and $C(t_{i+1}^{n+1}) = C(t_i^{n+1}) + \Delta C(t_i^{n+1})$
15: Update $i = i + 1$
16: **until** a self-consistent final stage is reached (*i.e.*, $|\Delta\mathbf{u}(t_{i-1}^{n+1})| < tol$ and $|\Delta\sigma(t_{i-1}^{n+1})| < tol$ and $|\Delta C(t_{i-1}^{n+1})| < tol$)
17: Update $\mathbf{u}(t^{n+1}) = \mathbf{u}(t_i^{n+1})$, $\sigma(t^{n+1}) = \sigma(t_i^{n+1})$, $C(t^{n+1}) = C(t_i^{n+1})$
18: Compute $\dot{\mathbf{u}}(t^{n+1})$ and $\ddot{\mathbf{u}}(t^{n+1})$ from $\mathbf{u}(t^{n+1})$
19: **end for**

whereas the index i denotes the ith relaxation iteration within the time step n. tol is some specified tolerance for checking convergence of the relaxation scheme. In each Newton iteration step, the Jacobian matrix and the residuals are computed and solved to get the increments $\Delta\mathbf{u}$, $\Delta\sigma$ and ΔC and the process is repeated until convergence.

7.3.1. *Numerical Simulations in the Absence of Damping*

Comb drives belong to an important class of MEMS structures which have numerous applications from micro-accelerometers, position controllers to hard disk drive actuators.[34,35] Consequently, static and dynamic characterization of these devices is very important for efficient design and development. In this section, we simulate two different comb drives (a transverse and a lateral comb drive) and look at their dynamic responses. The first comb microactuator,[35] shown in Fig. 7.5, is a transverse comb drive. The system consists of a movable center stage, 24 pairs

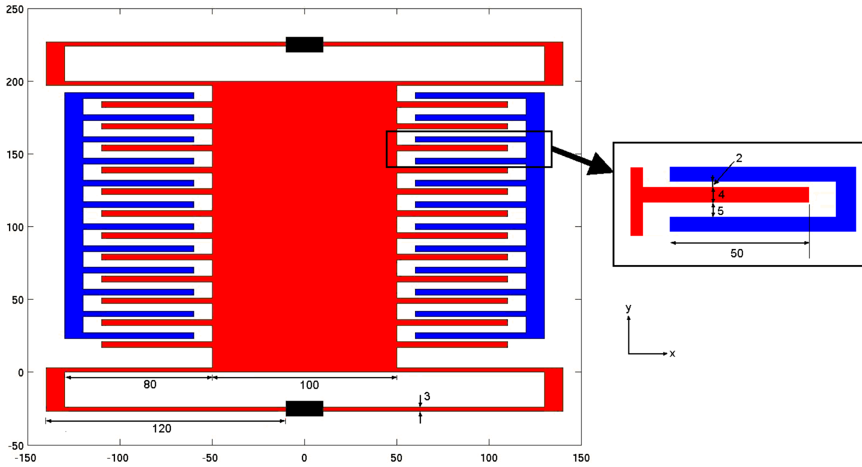

Fig. 7.5. Transverse Comb Drive: Displacement changes dominant electrostatic gap.

of interdigitated teeth and 4 spring beams. The center stage is supported by four folded spring beams anchored at the ends. Electrostatic forces are generated when a voltage is applied between the fixed and movable structures. The movable center stage is 100 μm long, 200 μm wide and 3.7 μm thick. The small and the large gaps between the electrodes are $g_1 = 2$ μm and $g_2 = 5$ μm. The overlap length $l_t = 50$ μm and finger width $t_1 = 4$ μm. The beam width is $b = 3$ μm, the lengths of the short and long parts of the folded beam are $l_1 = 80$ μm and $l_2 = 120$ μm, respectively. The Young's modulus (E) of the comb structure (nickel) is 200 GPa, the Poisson's ratio is 0.31 and the density 8908 kg/m^3. No material damping has been considered ($c = 0$). Due to symmetry, it is sufficient to consider just the lower right quadrant of the device for coupled electromechanical simulation. Figure 7.6 shows the variation of the resonant frequency of the comb drive with the applied DC bias. The resonant frequency was obtained from the time-displacement curve of the device for various applied voltages. The device exhibits spring-softening phenomena due to the electrical forces and it also indicates that mechanical non-linearity which gives rise to spring-hardening is absent. The experimentally measured resonant frequency of the structure was found to be 34 KHz while simulations indicate 33.4 KHz. It was observed experimentally that at about half of the stroke length ($x = 0.3$ μm) which occurs at 40 V, the resonant frequency decreased to 28.2 KHz. Our simulations indicate a resonant frequency of 27.5 KHz at that point, which is very close to the experimental observation.

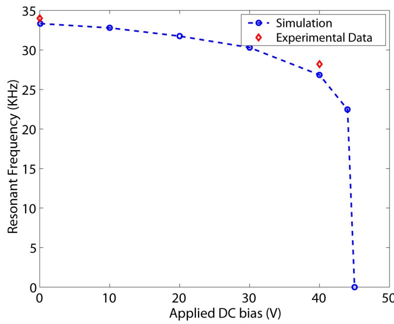

Fig. 7.6. Variation of resonant frequency with applied DC bias.

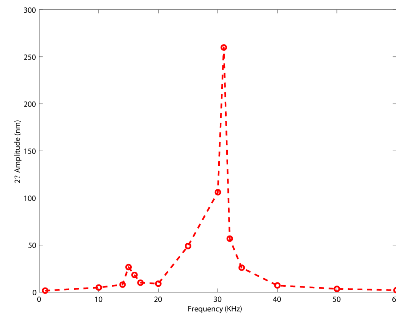

Fig. 7.7. Frequency response of the transverse comb drive.

Figure 7.7 shows the frequency response curve of the device for a 2.0 V DC bias and a 5 V p-p AC bias at various frequencies. Interestingly, two resonant peaks are observed instead of the conventional single peak at the resonant frequency. The second peak, observed at half of the natural frequency is due to the V^2 nature of the electrostatic force. Experimentally, only a single peak was observed. This is due to the fact that the second peak can be totally suppressed at low AC voltage (5 V p-p in this case) in the presence of damping (the simulations have no damping terms). The second resonant peak or the second super harmonic resonance is an interesting phenomena and has been observed experimentally in Ref. 36.

A lateral comb drive[34] actuator is also simulated with the Newton method. As shown in Fig. 7.8 the comb drive has 9 interdigited fingers on either side of a center plate. Two fixed electrodes are present – one of them is the drive port, where a voltage is applied to move the comb structure, and the other is the sense port, where the change in capacitance of the device can be sensed. However, another mode of operation applies voltages at both electrodes to drive the comb which has been simulated here. The electrostatic gap between the finger sides and the electrodes is $g = 3\ \mu$m. The entire structure is 2 μm thick (t_h). The overlap length is $l_t = 20\ \mu$m and the finger length and width are $l_f = 40\ \mu$m and $w_f = 4\ \mu$m, respectively. There are 2 pairs of folded beams each of width $b = 2\ \mu$m, the length of the folded beams is $l_b = 80\ \mu$m. The Young's modulus of the comb structure is 140 GPa, the Poisson's ratio is 0.30 and the density is 2231 kg/m^3. No material damping has been considered ($c = 0$). Due to symmetry, it is sufficient to consider just the left half of the device for coupled electromechanical simulation. Figure 7.9 shows that the resonant frequency of the comb drive remains constant with the applied DC bias. The constant resonant frequency obtained from simulation is

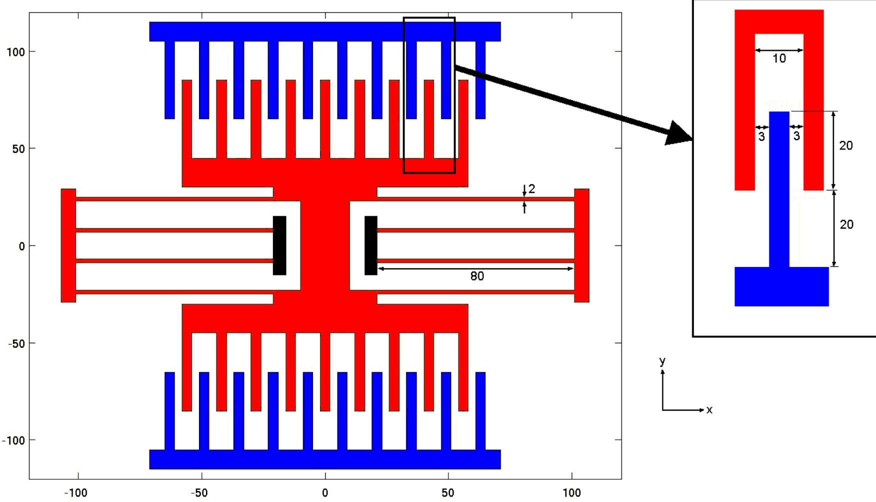

Fig. 7.8. Lateral Comb Drive: Displacement does not affect dominant electrostatic gap.

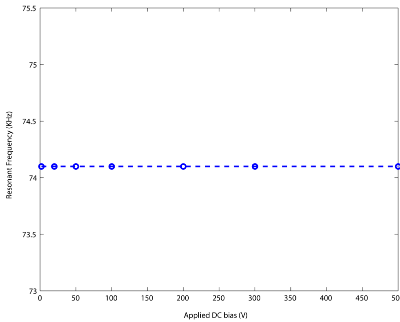

Fig. 7.9. Variation of resonant frequency with applied DC bias.

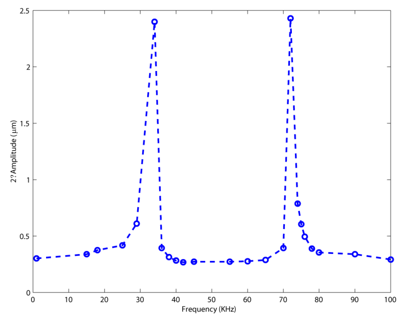

Fig. 7.10. Frequency response of the lateral comb drive.

74 KHz which is very close to the experimentally measured value of 75 KHz.[34] The constant resonant frequency (independent of applied voltage) is due to the fact that the electrostatic force is not a function of the displacement x and hence there is no spring-softening effect. Besides, as the structure is linear, there is no spring hardening as well due to the deformation. Constant resonant frequency is desirable for applications like micro-resonators and micro-filters. Figure 7.10 shows the frequency response curve of the device for a 200 V DC bias and a 200 V

p-p AC bias at various frequencies. Two resonant peaks are observed again, one at the resonant frequency of 74 KHz and the other at 34 KHz, which is approximately half of the first resonant frequency.

7.4. Dynamic Analysis in the Presence of Fluid Damping

The two hierarchical models for fluid damping are coupled with the electro-mechanical solver using a full-Lagrangian formulation and a Newton scheme, as discussed in this section. The basic step in the Newton method for the coupled electro-mechanical-fluidic analysis involves solving the equation

$$\bar{\mathbf{J}}(\mathbf{x})\Delta\mathbf{x} = -\mathbf{r}(\mathbf{x}), \quad i.e., \qquad \begin{bmatrix} \mathbf{R_{MM}} & \mathbf{R_{ME}} & \mathbf{R_{MF}} \\ \mathbf{R_{EM}} & \mathbf{R_{EE}} & \mathbf{R_{EF}} \\ \mathbf{R_{FM}} & \mathbf{R_{FE}} & \mathbf{R_{FF}} \end{bmatrix} \begin{Bmatrix} \Delta\mathbf{x_M} \\ \Delta\mathbf{x_E} \\ \Delta\mathbf{x_F} \end{Bmatrix} = - \begin{Bmatrix} \mathbf{R_M} \\ \mathbf{R_E} \\ \mathbf{R_F} \end{Bmatrix} \tag{7.37}$$

in each time step of the dynamic analysis. $\bar{\mathbf{J}}$ is the Jacobian matrix and the subscripts $\mathbf{M}, \mathbf{E}, \mathbf{F}$ denote mechanical, electrical and fluidic domains, respectively. In Eq. (7.37), $\mathbf{R_{ME}}$ denotes the electrical ($\mathbf{E}$) to mechanical ($\mathbf{M}$) coupling term in the Jacobian matrix. The other terms in $\bar{\mathbf{J}}$ are defined similarly. $\mathbf{x}$ is the vector of unknown variables where $\mathbf{x_M}$, $\mathbf{x_E}$ and $\mathbf{x_F}$ are the mechanical, electrical and fluidic variables, respectively. For the 2D mechanical and electrical analyses implemented in this work, $\mathbf{x_M} = \{u, v\}^T$, where u and v are the displacements of the microstructure in the X- and Y-directions, respectively, and $\mathbf{x_E} = \{\sigma, C\}^T$. The fluidic variables $\mathbf{x_F} = \{P_f\}$ for the 2D CRSFE and for the 2D CNSE, $\mathbf{x_F} = \{\rho_f, u_f, v_f, A, B, L, M\}^T$. The mechanical, electrical and the fluidic residual equations are denoted by $\mathbf{R_M}$, $\mathbf{R_E}$ and $\mathbf{R_F}$, respectively, in Eq. (7.37).

The full-Lagrangian Newton scheme (for both the fluid damping cases) is presented in detail in Algorithm 7.2. Algorithm 7.2 is discussed with reference to the two conductor system shown in Fig. 7.11. In Fig. 7.11, Ω_1 and Ω_2 denote the original/undeformed geometries and $d\Omega_1$ and $d\Omega_2$ denote the original/undeformed surfaces/boundaries of conductor 1 and conductor 2, respectively, where the mechanical analysis is done. Ω_f denotes the original/undeformed geometry and $d\Omega_f$ denotes the original/undeformed boundaries of the fluid domain (for fluidic analysis). The electrostatic analysis is done on the original/undeformed surfaces/boundaries of conductor 1 and conductor 2, namely, $d\Omega_1$ and $d\Omega_2$, respectively. A potential difference V is applied between conductors 1 and 2 which deforms the conductors. ω_1 denotes the deformed shape of conductor 1, ω_2 denotes the deformed shape of conductor 2, and ω_f denotes the deformed shape

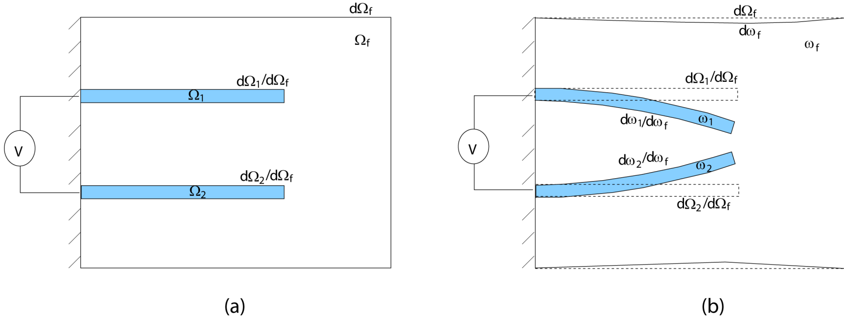

Fig. 7.11. (a) Undeformed and (b) deformed configurations of the mechanical (two cantilever beams), electrical (cantilever beam surfaces) and fluidic (surrounding air) domains in a two-conductor MEM system.

of the fluid domain. $d\omega_1$, $d\omega_2$ and $d\omega_f$ denote the deformed surfaces/boundaries of conductor 1, conductor 2 and the fluid domain, respectively. The applied potential does not change as the conductors undergo deformation or shape changes. In Algorithm 7.2, the index n stands for the time instant whereas the index i denotes the ith Newton iteration within the time step n. tol is some specified tolerance for checking convergence of the Newton scheme. Once the domains are discretized, the mechanical, electrical and the fluidic unknowns are initialized (set to zero for our case). In each time step, a Newton scheme is implemented to obtain a self-consistent solution for that time step. The initial guesses for the Newton method are generally taken to be the final solutions of the previous time step. The computation of the terms $\mathbf{R_{MM}}$, $\mathbf{R_{ME}}$, $\mathbf{R_{EM}}$ and $\mathbf{R_{EE}}$, the mechanical and electrical variables ($\mathbf{x_M}$, $\mathbf{x_E}$) and residual equations ($\mathbf{R_M}$, $\mathbf{R_E}$) in Eq. (7.37) have already been described in Sec. 7.3 (also see Ref. 33 for details). Further, note that $\mathbf{R_{EF}} = \mathbf{R_{FE}} = 0$, *i.e.*, there exists no coupling between the electrical and fluidic domains. The computation of the terms $\mathbf{R_{MF}}$, $\mathbf{R_{FM}}$ and $\mathbf{R_{FF}}$, the fluidic residual equation $\mathbf{R_F}$ and the fluidic variables $\mathbf{x_F}$ becomes straightforward due to the Lagrangian description of the equations and are given in Ref. 26 in detail.

7.4.1. *Numerical Simulations in the Presence of Fluid Damping*

The first device considered is a MEMS torsion mirror[37] shown in Fig. 7.12. The mirror plate is 1500 μm long, 1400 μm wide, and 3 μm thick. Four 150 μm long electrodes (of negligible thickness) are attached to the mirror plate and the ground plane. The distance from the center of the electrodes on the mirror to the center of the mirror is 505 μm. The gap between the mirror and the ground plane is

Algorithm 7.2. Full-Lagrangian Newton scheme for the self-consistent electro-mechanical-fluidic analysis of MEMS dynamics.

1: Define Ω_1, $d\Omega_1$, Ω_2, $d\Omega_2$, Ω_f, $d\Omega_f$
2: Discretize Ω_1, Ω_2, Ω_f for mechanical and fluidic analysis
3: Discretize $d\Omega_1$, $d\Omega_2$ for electrostatic analysis
4: Set $n = 0$, $t^n = t^0 = 0$
5: Initialize $\mathbf{x_M}(t^n)$, $\mathbf{x_E}(t^n)$, $\mathbf{x_F}(t^n)$
6: **for** $n = 0$ to N **do**
7: Set $i = 0$
8: Set $\mathbf{x_M}(t_i^{n+1}) = \mathbf{x_M}(t^n)$, $\mathbf{x_E}(t_i^{n+1}) = \mathbf{x_E}(t^n)$, $\mathbf{x_F}(t_i^{n+1}) = \mathbf{x_F}(t^n)$
9: **repeat**
10: Compute $\bar{\mathbf{J}}(t_i^{n+1}) = \bar{\mathbf{J}}(\mathbf{x_M}(t_i^{n+1}), \mathbf{x_E}(t_i^{n+1}), \mathbf{x_F}(t_i^{n+1}))$
11: Compute $\mathbf{r}(t_i^{n+1}) = \mathbf{r}(\mathbf{x_M}(t_i^{n+1}), \mathbf{x_E}(t_i^{n+1}), \mathbf{x_F}(t_i^{n+1}))$
12: Solve: $\bar{\mathbf{J}}(t_i^{n+1})[\Delta\mathbf{x_M}(t_i^{n+1})\, \Delta\mathbf{x_E}(t_i^{n+1})\, \Delta\mathbf{x_F}(t_i^{n+1})] = -\mathbf{r}(t_i^{n+1})$ (Eq. (7.37))
13: Update $\mathbf{x_M}(t_{i+1}^{n+1}) = \mathbf{x_M}(t_i^{n+1}) + \Delta\mathbf{x_M}(t_i^{n+1})$, $\mathbf{x_E}(t_{i+1}^{n+1}) = \mathbf{x_E}(t_i^{n+1}) + \Delta\mathbf{x_E}(t_i^{n+1})$, $\mathbf{x_F}(t_{i+1}^{n+1}) = \mathbf{x_F}(t_i^{n+1}) + \Delta\mathbf{x_F}(t_i^{n+1})$
14: Update $i = i + 1$
15: **until** $|\Delta\mathbf{x_M}(t_{i-1}^{n+1})| < tol$ and $|\Delta\mathbf{x_E}(t_{i-1}^{n+1})| < tol$ and $|\Delta\mathbf{x_F}(t_{i-1}^{n+1})| < tol$
16: Update: $\mathbf{x_M}(t^{n+1}) = \mathbf{x_M}(t_i^{n+1})$, $\mathbf{x_E}(t^{n+1}) = \mathbf{x_E}(t_i^{n+1})$, and $\mathbf{x_F}(t^{n+1}) = \mathbf{x_F}(t_i^{n+1})$
17: **end for**

42 μm. $I_\theta = 5.51 \times 10^{-15}$ kgm^2 is the moment of inertia of the mirror and K_θ = 4.49$\times$10^{-7} Nm/rad is the torsional stiffness of the mirror. Squeeze film damping between the mirror and the ground electrode is the dominant dissipative mechanism for this device and has been solved using the coupled electro-mechanical-fluidic solver based on 2D CRSFE in the $X - Z$ plane for the fluidic analysis. An external torque T_e = 4.84$\times$10^{-9}sin(2πft) Nm where f is the frequency in Hz is applied in the absence of any electrode voltages to the torsion mirror at 1 atm (1.013$\times$10^5 Pa). The viscosity is η = 1.82$\times$10^{-5} kg/ms and the mean free path λ for air is computed from Eq. (7.10) at 1 atm and 293 K. The frequency response curve of the torsion mirror under the external torque T_e is shown in Fig. 7.13. The transient response of the mirror under a constant external torque T_e = 4.84$\times$10^{-9} Nm is shown in Fig. 7.14. The simulated resonant frequency and the damping ratio $\zeta = 1/2Q$ (Q is the quality factor) of the mirror are 1.41 kHz and 0.20, respectively. The corresponding experimental values are 1.59 kHz and

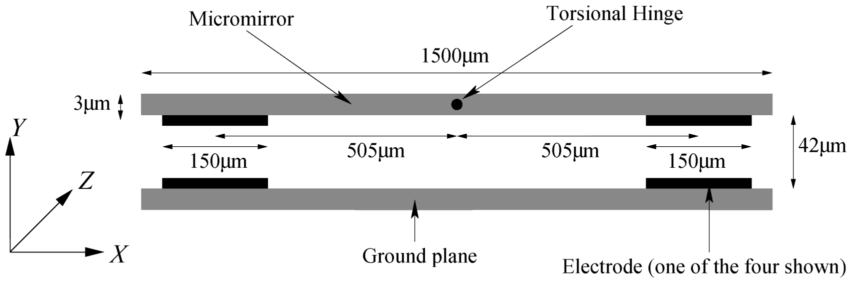

Fig. 7.12. MEMS torsion mirror.[37]

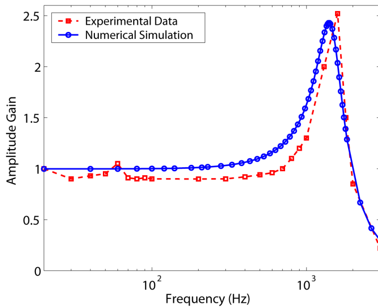

Fig. 7.13. Frequency response of the MEMS torsion mirror under an external torque T_e = $4.84 \times 10^{-9} \sin(2\pi f t)$ Nm.

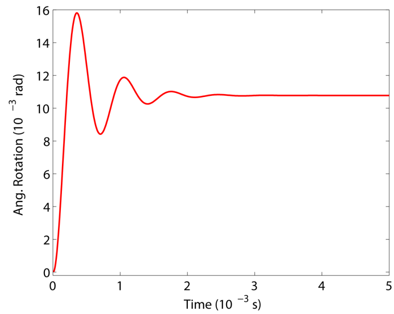

Fig. 7.14. Transient response of the MEMS torsion mirror for a constant external torque T_e = 4.84×10^{-9} Nm.

0.19. The simulated and experimental damping ratio (which primarily depends on the geometry and the ambient pressure) match well. However, there is some difference between the simulated and experimental resonant frequency. This can be attributed to the fact that the mirror surface is assumed to be rigid in the simulations thereby neglecting any elastic deformation effect of the surface.[37] Besides, experimental measurements can also have errors.

Figure 7.15 shows a MEMS piggyback actuator for hard-disk drive applications.[38] The actuator consists of a movable mass suspended by two restoring springs. The restoring springs are 500 μm long and 18 μm wide. The movable mass has 11 electrodes (movable electrodes) on it. Each movable electrode has two fixed electrodes – one on either side. One of the fixed electrode is grounded and a potential is applied on the other electrode as shown in Fig. 7.15. The movable electrodes are 500 μm long and 50 μm wide and the overlap length between

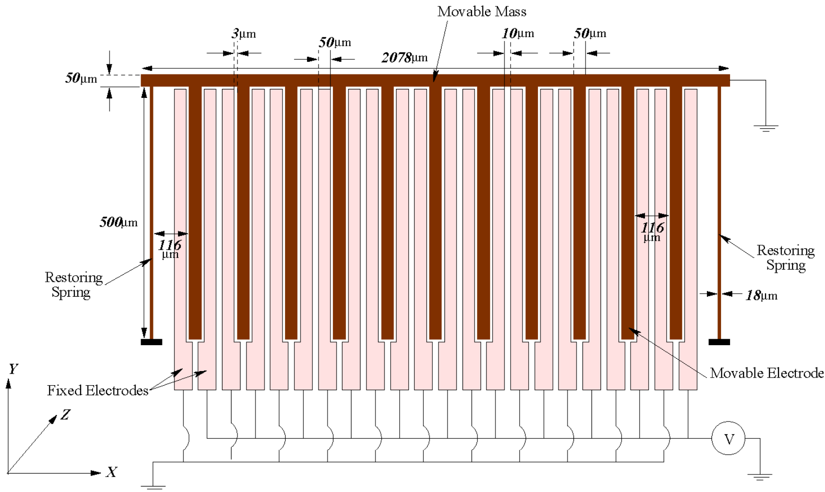

Fig. 7.15. A MEMS piggyback actuator.[38] The actuator moves in the X-direction.

the fixed and the movable electrodes is 498 μm. The gap between the movable and the fixed electrodes on either side is 3 μm. The length of the movable mass is 2078 μm. The height (normal to the plane of the paper) of the structure is 50 μm. The whole structure is made from silicon and has a Young's modulus E = 140 GPa, density ρ = 2330 kg/m^3 and Poisson's ratio ν = 0.3.[38] Squeeze film damping in the narrow air gaps between the movable electrodes and the fixed electrodes is the dominant dissipative mechanism for this device. The device is simulated using the coupled electro-mechanical-fluidic solver based on 2D CRSFE for the fluidic analysis. The viscosity of air is taken to be $\eta = 1.82 \times 10^{-5}$ kg/ms and the mean free path λ for air is computed from Eq. (7.10) at 1 atm and 293 K. The 2D CRSFE simulation is done for the narrow air gaps between the movable electrodes and the fixed electrodes in the $Y - Z$ plane (498 μm in the Y-direction and 50 μm in the Z-direction). Figure 7.16(a) shows the pressure profile in the air gap between the electrodes at a given time instant (t = 20 μs) obtained using the 2D CRSFE solver. As the overlap length of the fingers along the Y-direction (498 μm) is much larger than the width of the fingers in the Z-direction (50 μm) the pressure variation along the Y-direction is negligible compared to the pressure variation along the Z-direction. As a result, the 2D CNSE based solver simulated in the $X - Z$ plane is expected to give similar results as the 2D CRSFE solver in the $Y - Z$ plane. While the 2D CNSE solver in the $X - Z$ plane is equivalent to the 3D CNSE in this case due to negligible variations in

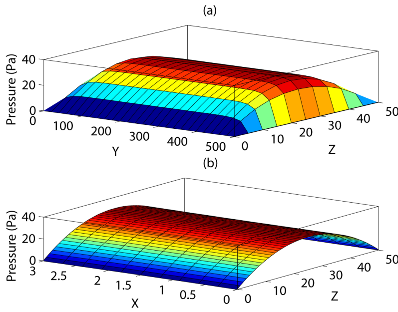

Fig. 7.16. Pressure profile in the air gaps between the electrodes of the piggyback actuator at a given time instant ($t = 20\ \mu$s) obtained using (a) the 2D CRSFE solver in the $Y - Z$ domain and (b) the 2D CNSE solver in the $X - Z$ domain.

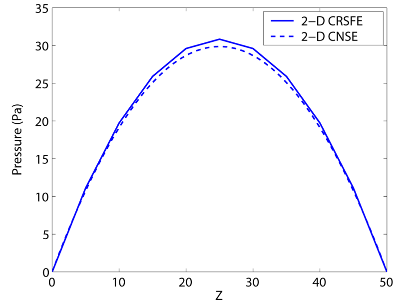

Fig. 7.17. Pressure variation in the Z-direction in the air gaps between the electrodes of the piggyback actuator at the given time instant ($t = 20\ \mu$s) using the 2D CRSFE solver (plotted at the center line $Y = 249\ \mu$m) and the 2D CNSE solver (plotted at the center line $X = 1.5\ \mu$m).

the Y-direction, the 2D CRSFE in the $Y - Z$ plane is also equivalent to the 3D CNSE in this case due to the narrow air gap between the electrodes. The pressure profile in the air gap between the electrodes at the given time instant ($t = 20\ \mu$s) obtained using the 2D CNSE solver in the $X - Z$ plane is shown in Fig. 7.16(b). Figure 7.16(b) shows that the pressure variation in the X-direction (in the height direction of the electrodes) is negligible. This is an important assumption in the derivation of the 2D CRSFE from 3D CNSE and is found to be true. Figure 7.17 compares the pressure profile in the Z-direction in the air gaps between the electrodes of the piggyback actuator at the given time instant ($t = 20\ \mu$s) obtained using the 2D CRSFE solver (plotted at the center line $Y = 249\ \mu$m) and the 2D CNSE solver (plotted at the center line $X = 1.5\ \mu$m). The pressure profiles given by the two solvers are in good agreement. Figure 7.18 shows the damped transient response of the rigid movable mass of the MEMS piggyback actuator under a 25 V DC bias. Both the solvers (the 2D CRSFE and the 2D CNSE) are found to give very similar results (as expected from the discussion above). The frequency response of the piggyback actuator at 20 V DC and 5 V AC (AC voltage of the form $V_{AC}\sin(2\pi ft)$) is simulated using the coupled electro-mechanical-fluidic solver based on 2D CRSFE for the fluidic analysis and is shown in Fig. 7.19. The resonant frequency and the quality factor of the piggyback actuator are found to be 16.8 kHz and 7.52, respectively, from the frequency response plot. The corresponding experimental values are 16 kHz for the resonant frequency and 7.73 for the quality factor. The experimental data are close to the simulated results.

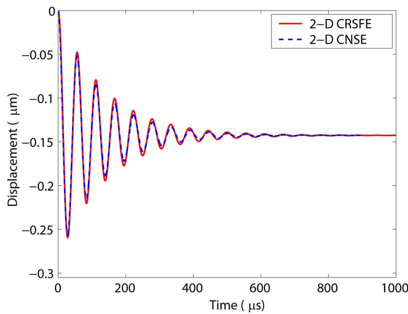

Fig. 7.18. Damped transient response of the rigid movable mass of the MEMS piggyback actuator at 25 V DC.

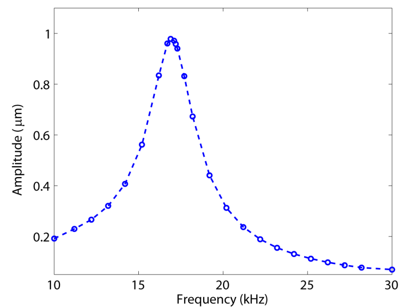

Fig. 7.19. Frequency response of the MEMS piggyback actuator at 20 V DC and 5 V AC using 2D CRSFE for fluid damping.

Figure 7.20 shows a laterally driven comb drive in air.[39] The system consists of a movable center stage, four pairs of interdigitated teeth (combs) and two spring beams. The center stage is supported by the two folded spring beams anchored at the ends. The four combs consist of a driving comb, a sensing comb and two secondary combs. Electrostatic forces are generated when a voltage is applied between the fixed and movable electrodes/fingers of the drive comb and the displacement of the movable stage is obtained by measuring the change in capacitance between the fixed and movable electrodes/fingers of the sensing comb. The fluid damping due to the fingers in the secondary combs is simulated and compared with experimental results. The spring beams are 200 μm long and 2 μm wide and the center stage is 230 μm long and 30 μm wide. All the four combs are identical with 20 pairs of movable and fixed fingers/electrodes in each. The fingers are 40 μm long and 2 μm wide and the overlap length between the fixed and the movable fingers is 14 μm. The comb gap (gap between fixed and movable fingers) is 2 μm on either side. The central truss on which the secondary combs are mounted is 220 μm long and 10 μm wide. The thickness of the whole structure is 2.1 μm. The movable structure is made from silicon and has an Young's modulus E = 140 GPa, density $\rho = 2330$ kg/m^3 and Poisson's ratio ν = 0.3.[39] Figure 7.21 shows the damped transient response of the rigid center stage of the comb-drive for a 25 V DC driving voltage. The damping from the secondary comb fingers (inter-comb damping due to the presence of the fixed and movable fingers) is only considered and the coupled electro-mechanical-fluidic solver based on 2D CNSE is used. The 2D CNSE simulation is done in the $X - Y$ plane for the fluidic analysis. The ambient conditions and the viscosity of air are taken to be the same as in the case of the micro-mirror and the piggyback actuator. The frequency response

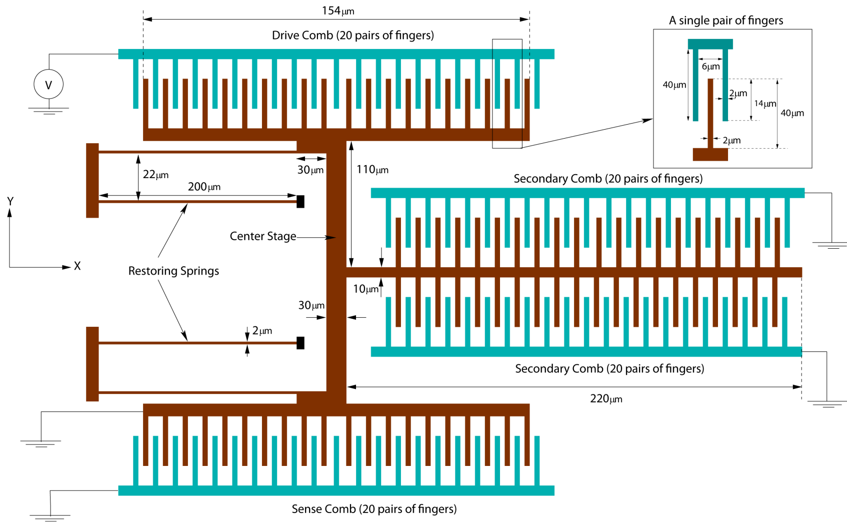

Fig. 7.20. MEMS lateral comb drive.[39] The comb drive moves in the Y-direction.

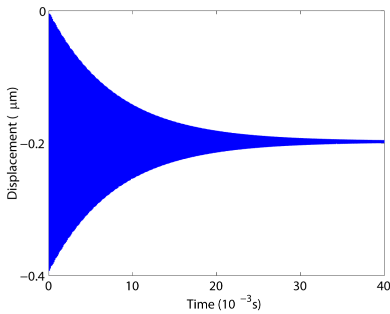

Fig. 7.21. Damped transient response of the rigid center stage of the lateral comb drive at 25 V DC.

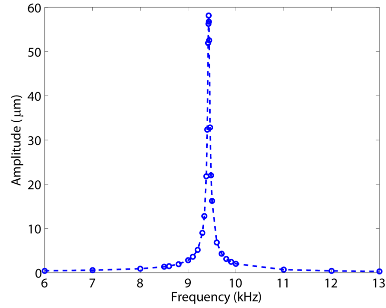

Fig. 7.22. Frequency response of the lateral comb drive at 20 V DC and 10 V AC.

curve of the lateral comb drive is plotted in Fig. 7.22. The simulations are done for a 20 V DC bias and a 10 V AC signal whose frequency is varied from 6 kHz to 13 kHz. From both Figs. 7.21 and 7.22, the resonant frequency and the quality factor (due to inter-comb damping) are found to be 9.45 kHz and 235, respectively. The experimentally measured resonant frequency is 9.6 kHz and the quality factor due to inter-comb damping is found to be 246,[39] indicating that the simulation results are close to the experimental data.

7.4.2. *Nonlinear Dynamic Properties in the Presence of Fluid Damping*

In this section, new non-linear dynamic properties of electrostatic MEMS under superharmonic excitations are presented using numerical simulations. On increasing the DC voltage, a characteristic change in the phase plot of the system, termed as "DC-symmetry breaking" is presented. Beyond "DC-symmetry breaking", applying an AC voltage with an amplitude slightly greater than the "AC-symmetry breaking" (another characteristic change in the phase plot) voltage and at the Mth superharmonic frequency of excitation results in the formation of M oscillations per period or M-cycles. On further increasing the AC voltage, a period doubling sequence takes place resulting in the formation of $2^n M$-cycles in the system, where n corresponds to the nth period doubling bifurcation in the sequence. The system goes to chaos on further increasing the AC voltage and ultimately dynamic pull-in takes place. On gradually increasing the AC voltage in the chaotic region at resonant excitation, the U(Universal)-sequence[14] is observed. A modified form of the U-sequence termed as the "UM-sequence" is found to exist in the chaotic region of the MEM system under superharmonic excitations. The appearance of the periodic windows (*i.e.*, the transition from chaos to the periodic states) in the U- and UM-sequences is found to take place through intermittent chaos.[14] The disappearance of the periodic windows (*i.e.*, the transition from the periodic states to chaos) on the other hand take place through a sequence of period doubling bifurcations. These observations are made in two different MEM devices in this chapter, namely, a MEMS fixed-fixed beam and a MEMS torsion micro-mirror, using numerical simulations. The fixed-fixed beam is made of silicon and has dimensions: $l = 80$ μm, $w = 10$ μm, and $t = 1$ μm, 1 μm over a ground plane. An Young's modulus of E = 169 GPa, density $\rho = 2330$ kg/m^3 and Poisson's ratio $\nu = 0.3$ are used for simulating the beam. The second example is the MEMS torsion mirror presented earlier.

7.4.2.1. *DC and AC Symmetry Breakings*

DC and AC symmetry breakings[40] are geometrical changes that take place in the phase-plots of the device with the variation in the DC and the AC voltages, respectively. When a DC bias is applied between a MEM structure (*e.g.*, a beam or a mirror) and the ground electrode, in the absence of any AC signal, the structure oscillates and finally comes to a steady deformed state due to the presence of fluid damping. As a result, symmetry breaking in this case takes place if the phase plot does not spiral inward in a symmetric fashion with respect to the two axes. Figures 7.23 and 7.24 show the displacement-velocity ($x - \dot{x}$) and the

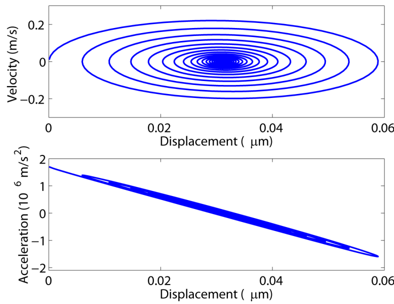

Fig. 7.23. Phase plots for the fixed-fixed beam at a small DC bias (30 V): No DC symmetry breaking.

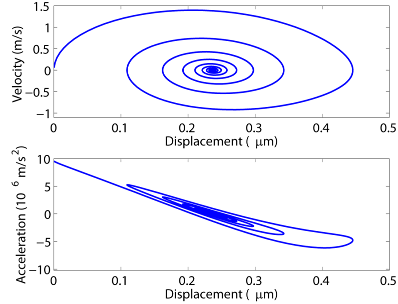

Fig. 7.24. Phase plots for the fixed-fixed beam at a large DC bias close to pull-in (71 V): DC symmetry breaking.

displacement-acceleration ($x - \ddot{x}$) phase plots for the fixed-fixed beam for a small DC bias of 30 V (dynamic pull-in occurs at 73 V DC) and a large DC bias of 71 V (close to dynamic pull-in), respectively. 30 V DC does not exhibit any symmetry breaking (spirals inward in a symmetric fashion) in the $x - \dot{x}$ plot or bending (spirals inward following a straight line) in the $x - \ddot{x}$ plot indicating it to be a linear state. For a large DC bias (71 V), symmetry breaking in the $x - \dot{x}$ plot and bending in the $x - \ddot{x}$ plot are observed. This symmetry breaking is termed as the "DC symmetry breaking" in this work. The nonlinearity in the system in the deformed state due to the DC bias can be determined by examining if DC symmetry breaking has taken place or not. The fixed-fixed beam MEM device exhibits DC symmetry breaking from around 69 V to dynamic pull-in at 73 V. The system is in a non-linear state once the DC symmetry breaking occurs. Spring softening (a decrease in the natural frequency of the structure) also indicates this nonlinearity. Similar observations are made for the MEMS torsion mirror. DC symmetry breaking in the mirror is observed between 133 V to dynamic pull-in at 142 V DC.

Once the microstructure reaches a stable non-linear state exhibiting DC symmetry breaking, it is excited with an AC voltage $V_{AC} \sin(2\pi ft)$ with frequency $f = f_0/M$, where f_0 is the resonant frequency of the microstructure at the applied DC bias and M is a natural number. The phase plots for steady-state periodic response of the structure under the AC signal and the DC bias are studied. As V_{AC} is increased, a second symmetry breaking in the $x - \dot{x}$ plot and a corresponding bending in the $x - \ddot{x}$ plot are observed. This symmetry breaking is termed as the "AC-symmetry breaking" in this work. Figures 7.25 and 7.26 show the $x - \dot{x}$ and the $x - \ddot{x}$ phase plots of the steady period response of the fixed-fixed beam for two different AC voltages under the large (71 V) DC bias at M = 1. The resonant

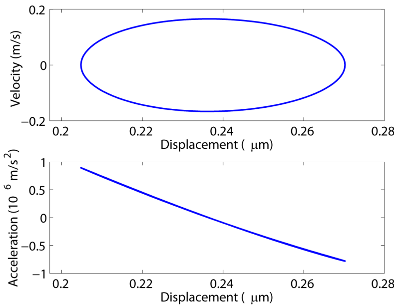

Fig. 7.25. Phase plots of the steady period response of the fixed-fixed beam at a small AC voltage (1 V): No AC symmetry breaking.

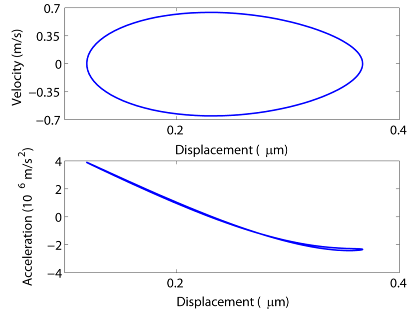

Fig. 7.26. Phase plots of the steady period response of the fixed-fixed beam at a large AC voltage (3 V): AC symmetry breaking.

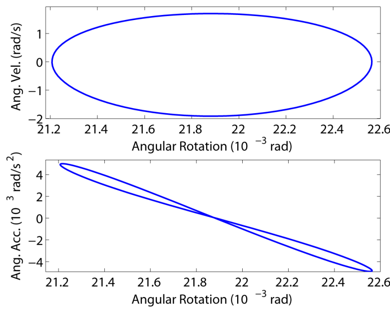

Fig. 7.27. Phase plots of steady period response of the mirror at a small AC voltage (0.5 V): No AC symmetry breaking.

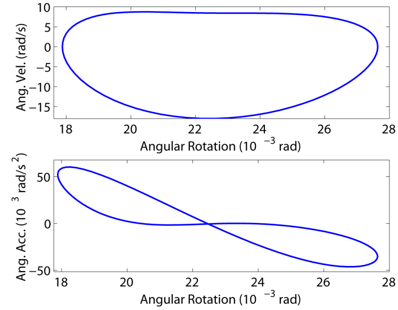

Fig. 7.28. Phase plots of steady period response of the mirror at a large AC voltage (3 V): AC symmetry breaking.

frequency is f_0 = 885 KHz at 71 V DC. No AC symmetry breaking and bending is observed for a small AC signal of 1 V in Fig. 7.25, whereas AC symmetry breaking and bending is observed for an AC signal of 3 V in Fig. 7.26. The geometrical symmetry of the orbit is broken along the y-axis in Fig. 7.26. The AC pull-in voltage at the 71 V DC bias is 4.27 V. Figures 7.27 and 7.28 show the similar phase plots of the mirror for two different AC voltages under a large (141 V) DC bias at $M = 1$. The resonant frequency is $f_0 = 425$ Hz at 141 V DC for the mirror. 0.5 V AC does not exhibit any AC symmetry breaking, whereas a large 3 V AC (AC pull-in takes place at 3.85 V AC) exhibits AC symmetry breaking.

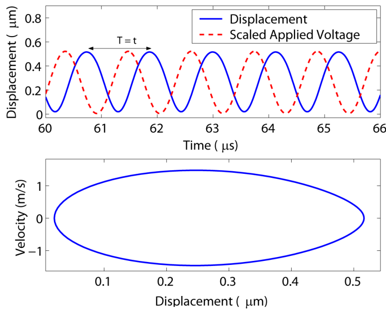

Fig. 7.29. A 1-cycle oscillation for $M = 1$ in the fixed-fixed beam at 4 V AC. Time period $\mathrm{T} = t = 1.13\ \mu$s.

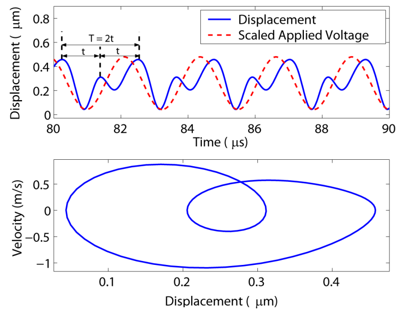

Fig. 7.30. A 2-cycle oscillation for $M = 2$ in the fixed-fixed beam at 5.9 V AC. Time period $\mathrm{T} = 2t = 2.26\ \mu$s.

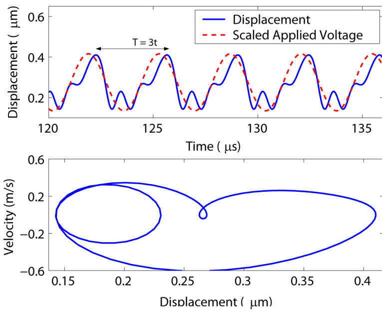

Fig. 7.31. A 3-cycle oscillation for $M = 3$ in the fixed-fixed beam at 5.9 V AC. Time period $\mathrm{T} = 3t = 3.39\ \mu$s.

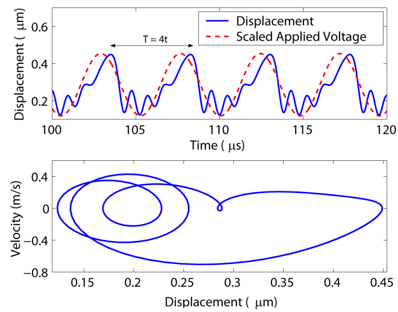

Fig. 7.32. A 4-cycle oscillation for $M = 4$ in the fixed-fixed beam at 6.2 V AC. Time period $\mathrm{T} = 4t = 4.52\ \mu$s.

7.4.2.2. *Complex Oscillations: M-cycles*

On further increasing the AC voltage beyond the AC symmetry breaking point, M oscillations per period or M-cycles are observed for an excitation frequency of f_0/M. Numerical simulations for the fixed-fixed beam are done for different values of M. A 71 V DC bias is first applied to bring the device to a non-linear steady-state exhibiting DC symmetry breaking (Fig. 7.24). An AC voltage at an excitation frequency of f_0/M is next applied for different values of M. Figures 7.29–7.32 show the M-cycles formed for M = 1, 2, 3 and 4 in the fixed-fixed beam as the AC voltage is gradually increased from the AC symmetry breaking value in each case. Up to 8-cycle oscillations are observed in the fixed-fixed beam

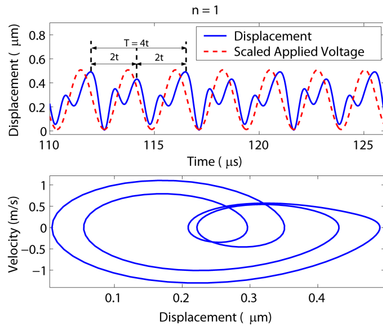

Fig. 7.33. Time series and phase plot for the n = 1 (6.2 V AC) period doubling bifurcation of the fixed-fixed beam MEM device at M = 2. Time period T = $2^n Mt$ = $4t$ = 4.52 μs.

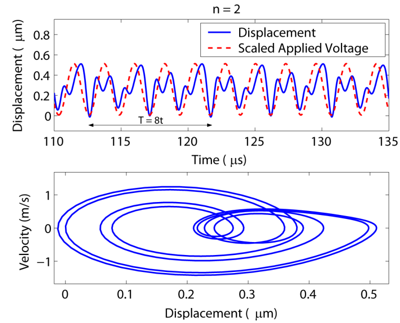

Fig. 7.34. Time series and phase plot for the n = 2 (6.32 V AC) period doubling bifurcation of the fixed-fixed beam MEM device at M = 2. Time period T = $2^n Mt$ = $8t$ = 9.04 μs.

MEM device. M-cycle oscillations are also observed in the MEMS torsion mirror for a DC voltage in the DC symmetry breaking region and for an AC voltage in the AC symmetry breaking region when the frequency of excitation is $1/M^{th}$ of the resonant frequency. The electrostatic force is primarily responsible for the formation of the M-cycles (see Refs. 40 and 41 for more details).

7.4.2.3. *Period Doubling and Chaos:* $2^n M$*-cycles*

On further increasing the AC voltage at which M-cycles are formed in the MEM device, a period doubling sequence is observed ultimately leading to chaos. The period doubling bifurcations result in the formation of $2^n M$-cycle oscillations for an original M-cycle oscillation. n corresponds to the nth period doubling bifurcation in the sequence. The phase plots for the period doubling sequence for the 2-cycle oscillation formed at M = 2 (see Fig. 7.30 for n = 0) for the fixed-fixed beam are shown in Figs. 7.33–7.35 for n = 1, 2, 3 and ∞ at 6.2 V, 6.32 V, 6.34 V and 6.35 V AC, respectively. The existence of chaos at 6.35 V AC is validated by the computation of the largest Lyapunov exponent λ of the system using the software package TISEAN.[42] A positive value of λ = 0.017 is obtained at 6.35 V AC. The time series data from the numerical simulation at 6.35 V AC is used in TISEAN for the computation of λ. The sequence of period doubling bifurcations leading to chaos through the formation of $2^n M$-cycles is also observed for other values of M in the fixed-fixed beam MEM device. The M-cycle formed at the Mth superharmonic frequency of excitation is responsible for the formation of the $2^n M$-cycles (through period doubling bifurcations) and is

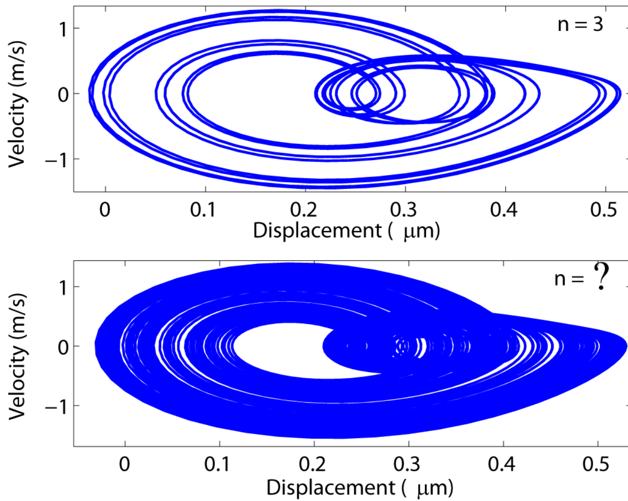

Fig. 7.35. The n = 3 (6.34 V AC) and $n = \infty$ (6.35 V AC) (chaos) period doubling bifurcations of the fixed-fixed beam MEM device at M = 2.

explained here considering the 2-cycle oscillation shown in Fig. 7.30. The 2-cycle oscillation consists of 2 peaks (separated by time t) in the time-displacement plot for a single voltage cycle of time period T = $2t$ as shown in Fig. 7.30. t is the time-period corresponding to resonant excitation (M = 1) of both the displacement and the voltage as shown in Fig. 7.29. When the first period doubling bifurcation takes place ($n = 1$), the displacement repeats itself after every 2 voltage cycles thereby giving rise to period doubling. However, each voltage cycle still consists of a 2-cycle oscillation as shown in Fig. 7.33. As a result, the total number of cycles/peaks per period in the time-displacement plot is $2 \times M$ after the first period doubling bifurcation. Consequently it can be seen that at the n-th period doubling bifurcation, the total number of cycles/peaks per period is $2^n M$.

The period doubling route to chaos at M = 1 for the MEMS torsion mirror is shown in Figs. 7.36 and 7.37 at 141 V DC bias (in the DC symmetry breaking region). AC symmetry breaking at 141 V DC for the mirror takes place at around 3 V AC (see Fig. 7.28). The period doubling bifurcations corresponding to n = 3 and ∞ take place at 3.7973 V and 3.7999 V AC, respectively. From the results presented in this section, we can observe that when DC and AC symmetry breakings are present chaos sets in through the period doubling route in electrostatic MEMS (see Refs. 40 and 41 for more details).

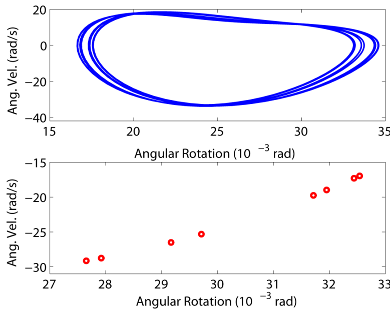

Fig. 7.36. Phase plot and Poincaré map for the n = 3 (141 V DC, 3.7973 V AC) period doubling bifurcation of the MEMS torsion mirror at $M = 1$.

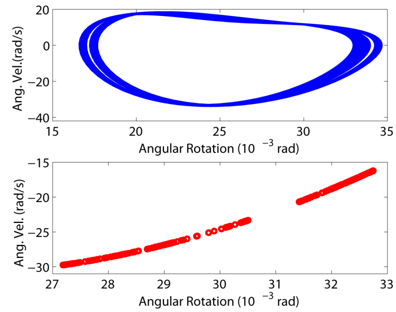

Fig. 7.37. Phase plot and Poincaré map for the $n = \infty$ (141 V DC, 3.7999 V AC) period doubling bifurcation of the MEMS torsion mirror at $M = 1$.

7.4.2.4. *U(Universal)-Sequence: K-cycles*

The region beyond the period doubling route to chaos is next investigated in this work by gradually increasing the AC voltage from the chaotic state at 3.7999 V AC for the MEMS torsion mirror. U-sequence (a sequence of periodic windows that appear beyond the period doubling route to chaos[14]) is observed in this region for the MEM device. As the AC voltage is increased from 3.7999 V, stable periodic windows are observed for certain values/regions of the AC voltage. For all other values of the AC voltage, the MEM device is found to exhibit chaos. The order in which the periodic windows appear in the U-sequence of a dynamical system can be obtained using symbolic dynamics[43] and is given as (considering up to 6-cycles):

$$6 \rightarrow 5 \rightarrow 3 \rightarrow 5 \rightarrow 6 \rightarrow 4 \rightarrow 6 \rightarrow 5 \rightarrow 6 \tag{7.38}$$

Table 7.1 shows the U-sequence and the corresponding AC voltages at which the periodic states/cycles are observed for the mirror at 141 V DC and $M = 1$. Figure 7.38 shows the phase plot and the Poincarè map for the K = 6-cycle oscillation (the first periodic window) formed at 3.8005 V AC in the MEMS torsion mirror. The phase plot and the Poincarè map for the subsequent K = 5-cycle oscillation (the second periodic window) at 3.8036 V AC are shown in Fig. 7.39. Figure 7.40 shows the phase plot and the Poincarè map and Fig. 7.41 shows the time-series plot for the K = 3-cycle oscillation at 3.8085 V AC. From Figs. 7.40 and 7.41, it can be seen that the 3-cycle is characterized by 3 loops per period in the phase plot or 3 peaks per period in the time-series plot, *i.e.*, the 3-cycle has 3 oscillations per period (which is the definition of a 3-cycle[14]). The time period

Table 7.1. U-sequence in the MEMS torsion mirror at 141 V DC and $M = 1$.

Ac Voltage V	Periodic Cycles (K)	Ac Voltage V	Periodic Cycles (K)
3.80050	6	3.82590	4
3.80360	5	3.83170	6
3.80850	3	3.83171	5
3.81620	5	3.83173	6
3.82000	6		

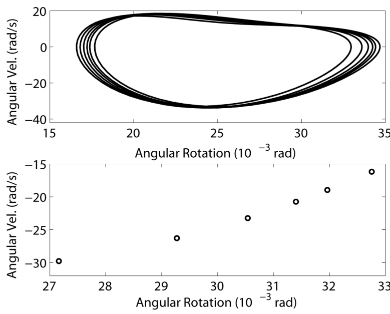

Fig. 7.38. Phase plot and Poincarè map of the K = 6-cycle oscillation at 141 V DC, 3.8005 V AC and $M = 1$.

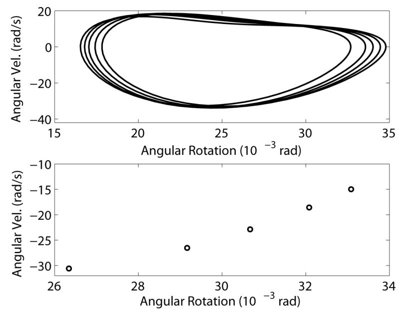

Fig. 7.39. Phase plot and Poincarè map of the K = 5-cycle oscillation at 141 V DC, 3.8036 V AC and $M = 1$.

T of the 3-cycle is 3τ, where τ is the time period of the applied voltage (also shown in Fig. 7.41). In short, a K-cycle in the U-Sequence has K oscillations per period and has a time period of $K\tau$ (indicated by K points in the Poincarè map). Figures 7.42 and 7.43 show the phase plots and the Poincarè maps for the $K = 6$ and $K = 4$-cycle oscillations following the K = 3-cycle window at 3.8085 V AC, as shown in Table 7.1. For AC voltages beyond the final K = 6-cycle window at 3.83173 V AC the MEMS mirror exhibits chaos and finally dynamic pull-in takes place at 3.85 V AC. Similar observation of U-sequence at resonant excitation is also made in the MEM fixed-fixed beam device.

7.4.2.5. *UM-Sequence: KM-cycles*

A modified form of the U-sequence is found to exist in electrostatic MEMS under superharmonic excitations and is presented here. The appearance of a periodic window with K-cycles in the normal U-sequence is replaced by the appearance of

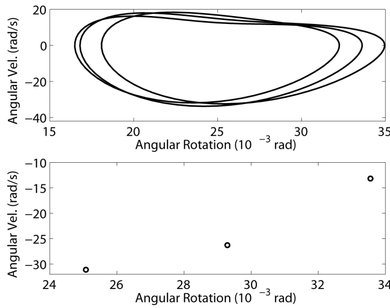

Fig. 7.40. Phase plot and Poincarè map of the K = 3-cycle oscillation at 141 V DC, 3.8085 V AC and $M = 1$.

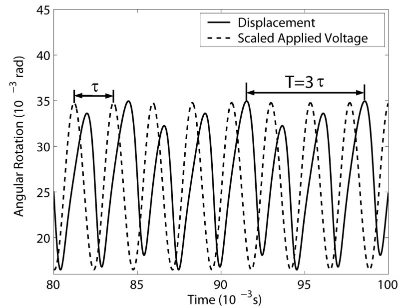

Fig. 7.41. Time series of the K = 3-cycle oscillation at 141 V DC, 3.8085 V AC and $M = 1$. τ = 2.35×10^{-3}s.

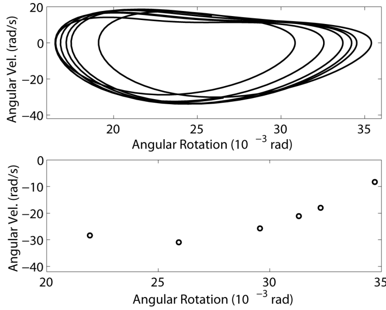

Fig. 7.42. Phase plot and Poincarè map of the K = 6-cycle oscillation at 141 V DC, 3.8200 V AC and $M = 1$.

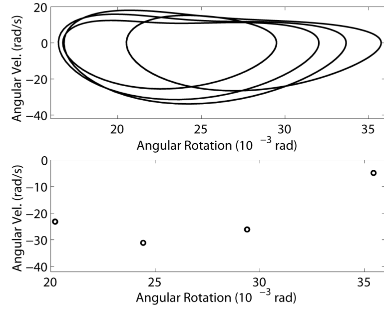

Fig. 7.43. Phase plot and Poincarè map of the K = 4-cycle oscillation at 141 V DC, 3.8259 V AC and $M = 1$.

a periodic window with KM-cycles in the modified sequence termed as the "UM-sequence", for an exciting frequency of f_0/M (M^{th} superharmonic frequency). Hence, in the UM-sequence, the order given in Eq. (7.38) is replaced by the following order at the Mth superharmonic frequency as the exciting frequency:

$$6M \rightarrow 5M \rightarrow 3M \rightarrow 5M \rightarrow 6M \rightarrow 4M \rightarrow 6M \rightarrow 5M \rightarrow 6M \qquad (7.39)$$

An M-cycle formed at the Mth superharmonic frequency of excitation (before the $2^n M$-cycle period doubling sequence) is by definition characterized by M loops per period in the phase plot or M peaks per period in the time-series plot, as shown in Figs. 7.44 and 7.45 for $M = 1$ and $M = 3$, respectively. However, the essential difference between a K-cycle in the U-sequence and an M-cycle at the Mth superharmonic excitation is that the time periods of these cycles are $K\tau$ and

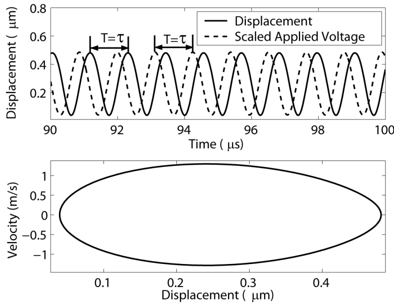

Fig. 7.44. Time series and phase plot for the $M = 1$ cycle in the MEMS fixed-fixed beam at 71 V DC and 3 V AC. τ = 1.13 μs.

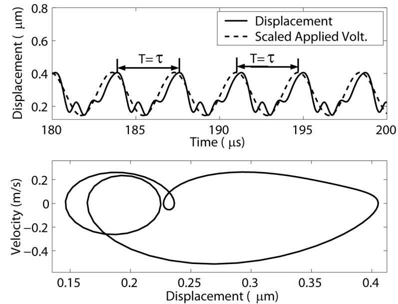

Fig. 7.45. Time series and phase plot for the $M = 3$ cycle in the MEMS fixed-fixed beam at 71 V DC and 5.93 V AC. τ = 3.39 μs.

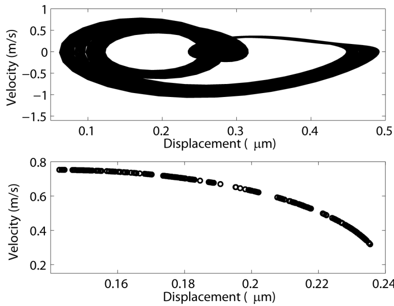

Fig. 7.46. Phase plot and Poincarè map of the chaotic state at 6.01 V AC, 71 V DC and $M = 3$ in the MEMS fixed-fixed beam.

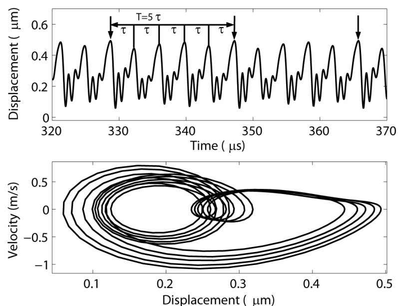

Fig. 7.47. Time series and phase plot of the 15-cycle window (K = 5, M = 3) at 6.0137 V AC, 71 V DC in the MEMS fixed-fixed beam. The time period of the applied voltage is τ = 3.39 μs.

τ respectively, where τ is the time period of the applied voltage in each case. As a result, the Poincarè map of a K-cycle in the U-sequence has K points whereas the Poincarè map of an M-cycle at the Mth superharmonic excitation has just one point, as the reference frequency used in the Poincarè map is the frequency of the applied voltage.

For the fixed-fixed beam an AC voltage around 5.9 V gives rise to 3-cycle oscillations in the MEMS fixed-fixed beam for $M = 3$ and 71 V DC bias. On further increasing the AC voltage, a sequence of period doubling bifurcations take place giving rise to $2^n M$-cycles and ultimately chaos at 6.01 V AC as shown in Fig. 7.46. The AC voltage is gradually increased beyond 6.01 V, and the UM-sequence (the $U3$-sequence in this case) is observed. Table 7.2 shows

Table 7.2. $U3$-sequence in the MEMS fixed-fixed beam at 71 V DC and $M = 3$.

Ac Voltage V	Periodic Cycles ($K \times M$)	Ac Voltage V	Periodic Cycles ($K \times M$)
6.0112	$6 \times 3 = 18$	6.0329	$4 \times 3 = 12$
6.0137	$5 \times 3 = 15$	6.0418	$6 \times 3 = 18$
6.0192	$3 \times 3 = 9$	6.0427	$5 \times 3 = 15$
6.0287	$5 \times 3 = 15$	6.0431	$6 \times 3 = 18$
6.0311	$6 \times 3 = 18$		

the $U3$-sequence and the corresponding AC voltages at which the periodic states/cycles are observed at 71 V DC and $M = 3$ for the fixed-fixed beam. The time series and phase plot for the 15-cycle window (K = 5, M = 3) at 6.0137 V AC and 71 V DC are shown in Fig. 7.47. The vertical arrows above the time series are separated by one time period T of the response and τ is the time period of the applied voltage in Fig. 7.47. Within each time period τ of the applied voltage, a M = 3-cycle oscillation is observed while the response repeats itself after K = 5 voltage time periods, giving $T = 5\tau$ and a 5×3 = 15-cycle response. Figures 7.48 and 7.49 show the time series and the phase plots for the 9-cycle window (K = 3, M = 3) at 6.0192 V AC and the 12-cycle window (K = 4, M = 3) at 6.0329 V AC, respectively, for the fixed-fixed beam at 71 V DC (refer to Table 7.2).

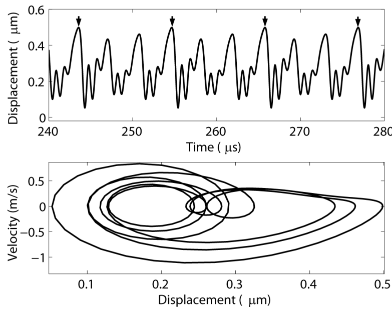

Fig. 7.48. Time series and phase plot of the 9-cycle window (K = 3, M = 3) at 6.0192 V AC, 71 V DC in the MEMS fixed-fixed beam.

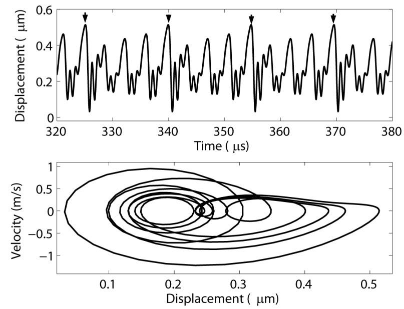

Fig. 7.49. Time series and phase plot of the 12-cycle window (K = 4, M = 3) at 6.0329 V AC, 71 V DC in the MEMS fixed-fixed beam.

In general, when a K-cycle in the U-sequence given by Eq. (7.38) is formed, the displacement repeats itself after every K voltage cycles (time period is K times the time period of the applied voltage). However, each voltage cycle consists of M loops/peaks/oscillations at the Mth superharmonic frequency of excitation.

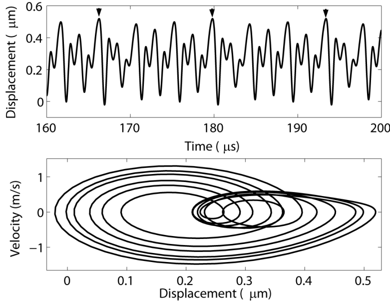

Fig. 7.50. Time series and phase plot of the first $(K = 6) \times (M = 2) = 12$-cycle window at 6.3606 V AC, 71 V DC in the MEMS fixed-fixed beam.

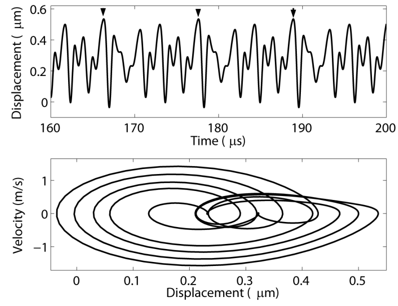

Fig. 7.51. Time series and phase plot of the first $(K = 5) \times (M = 2) = 10$-cycle window at 6.414 V AC, 71 V DC in the MEMS fixed-fixed beam.

As a result, the total number of oscillations per period of the response becomes $K \times M$ as given in Eq. (7.39) for an exciting frequency of f_0/M (as described through Fig. 7.47). However, the time period of the KM-cycle remains $K\tau$, where τ is the time period of the applied voltage. The characteristic M = 3 loops per period of the base orbit is found to be preserved in Figs. 7.47–7.49. The UM-sequence is also observed for other values of M. Figures 7.50 and 7.51 show the first $(K = 6) \times (M = 2) = 12$-cycle state for an AC voltage of 6.3606 V and the first $(K = 5) \times (M = 2) = 10$-cycle state for an AC voltage of 6.414 V in the MEMS fixed-fixed beam at 71 V DC for $M = 2$. See Ref. 44 for more details on U- and UM-sequences in electrostatic MEMS.

7.5. Dynamic Analysis in the Presence of Fluid and Thermal Damping

The heat/thermal equation is next coupled with the electro-mechanical-fluidic analysis using a full-Lagrangian formulation and a Newton scheme, as discussed in this section, for the coupled electro-thermo-mechanical-fluidic analysis of MEMS. The basic step in the Newton method for the coupled analysis in this case involves solving the equation

$$\bar{\mathbf{J}}(\mathbf{x})\Delta\mathbf{x} = -\mathbf{r}(\mathbf{x}), \quad i.e.,$$

$$\begin{bmatrix} \mathbf{R_{MM}} & \mathbf{R_{MT}} & \mathbf{R_{ME}} & \mathbf{R_{MF}} \\ \mathbf{R_{TM}} & \mathbf{R_{TT}} & \mathbf{R_{TE}} & \mathbf{R_{TF}} \\ \mathbf{R_{EM}} & \mathbf{R_{ET}} & \mathbf{R_{EE}} & \mathbf{R_{EF}} \\ \mathbf{R_{FM}} & \mathbf{R_{FT}} & \mathbf{R_{FE}} & \mathbf{R_{FF}} \end{bmatrix} \begin{Bmatrix} \Delta\mathbf{x_M} \\ \Delta\mathbf{x_T} \\ \Delta\mathbf{x_E} \\ \Delta\mathbf{x_F} \end{Bmatrix} = - \begin{Bmatrix} \mathbf{R_M} \\ \mathbf{R_T} \\ \mathbf{R_E} \\ \mathbf{R_F} \end{Bmatrix} \tag{7.40}$$

Algorithm 7.3. Full-Lagrangian Newton scheme for the self-consistent electro-thermo-mechanical-fluidic analysis of MEMS dynamics.

1: Define Ω_1, $d\Omega_1$, Ω_2, $d\Omega_2$, Ω_f, $d\Omega_f$
2: Discretize Ω_1, Ω_2, Ω_f for mechanical/thermal and fluidic analysis
3: Discretize $d\Omega_1$, $d\Omega_2$ for electrostatic analysis
4: Set $n = 0$, $t^n = t^0 = 0$
5: Initialize $\mathbf{x_M}(t^n)$, $\mathbf{x_T}(t^n)$, $\mathbf{x_E}(t^n)$, $\mathbf{x_F}(t^n)$
6: **for** $n = 0$ to N **do**
7: Set $i = 0$
8: Set $\mathbf{x_M}(t_i^{n+1}) = \mathbf{x_M}(t^n)$, $\mathbf{x_T}(t_i^{n+1}) = \mathbf{x_T}(t^n)$, $\mathbf{x_E}(t_i^{n+1}) = \mathbf{x_E}(t^n)$, $\mathbf{x_F}(t_i^{n+1}) = \mathbf{x_F}(t^n)$
9: **repeat**
10: Compute $\bar{\mathbf{J}}(t_i^{n+1}) = \bar{\mathbf{J}}(\mathbf{x_M}(t_i^{n+1}), \mathbf{x_T}(t_i^{n+1}), \mathbf{x_E}(t_i^{n+1}), \mathbf{x_F}(t_i^{n+1}))$
11: Compute $\mathbf{r}(t_i^{n+1}) = \mathbf{r}(\mathbf{x_M}(t_i^{n+1}), \mathbf{x_T}(t_i^{n+1}), \mathbf{x_E}(t_i^{n+1}), \mathbf{x_F}(t_i^{n+1}))$
12: Solve: $\bar{\mathbf{J}}(t_i^{n+1})[\Delta\mathbf{x_M}(t_i^{n+1})\, \Delta\mathbf{x_T}(t_i^{n+1})\, \Delta\mathbf{x_E}(t_i^{n+1})\, \Delta\mathbf{x_F}(t_i^{n+1})] = -\mathbf{r}(t_i^{n+1})$ (Eq. (7.40))
13: Update $\mathbf{x_M}(t_{i+1}^{n+1}) = \mathbf{x_M}(t_i^{n+1}) + \Delta\mathbf{x_M}(t_i^{n+1})$, $\mathbf{x_T}(t_{i+1}^{n+1}) = \mathbf{x_T}(t_i^{n+1}) + \Delta\mathbf{x_T}(t_i^{n+1})$, $\mathbf{x_E}(t_{i+1}^{n+1}) = \mathbf{x_E}(t_i^{n+1}) + \Delta\mathbf{x_E}(t_i^{n+1})$, $\mathbf{x_F}(t_{i+1}^{n+1}) = \mathbf{x_F}(t_i^{n+1}) + \Delta\mathbf{x_F}(t_i^{n+1})$
14: Update $i = i + 1$
15: **until** $|\Delta\mathbf{x_M}(t_{i-1}^{n+1})| < tol$ and $|\Delta\mathbf{x_T}(t_{i-1}^{n+1})| < tol$ and $|\Delta\mathbf{x_E}(t_{i-1}^{n+1})| < tol$ and $|\Delta\mathbf{x_F}(t_{i-1}^{n+1})| < tol$
16: Update: $\mathbf{x_M}(t^{n+1}) = \mathbf{x_M}(t_i^{n+1})$, $\mathbf{x_T}(t^{n+1}) = \mathbf{x_T}(t_i^{n+1})$, $\mathbf{x_E}(t^{n+1}) = \mathbf{x_E}(t_i^{n+1})$, and $\mathbf{x_F}(t^{n+1}) = \mathbf{x_F}(t_i^{n+1})$
17: **end for**

in each time step of the dynamic analysis. $\bar{\mathbf{J}}$ is the Jacobian matrix and the subscripts $\mathbf{M}, \mathbf{T}, \mathbf{E}, \mathbf{F}$ denote mechanical, thermal, electrical and fluidic domains, respectively. In Eq. (7.40), $\mathbf{R_{MT}}$ denotes the thermal ($\mathbf{T}$) to mechanical ($\mathbf{M}$) coupling term in the Jacobian matrix. The other terms in $\bar{\mathbf{J}}$ are defined similarly. $\mathbf{x}$ is the vector of unknown variables where $\mathbf{x_M}$, $\mathbf{x_T}$, $\mathbf{x_E}$ and $\mathbf{x_F}$ are the mechanical, thermal, electrical and fluidic variables, respectively. The thermal variable $\mathbf{x_T}$ in our case is the absolute temperature T and the other variables $\mathbf{x_M}$, $\mathbf{x_E}$ and $\mathbf{x_F}$ have already been defined earlier. $\mathbf{R_T}$ is used to denote the thermal residual equation and the mechanical, electrical and the fluidic residual equations are denoted by $\mathbf{R_M}$, $\mathbf{R_E}$ and $\mathbf{R_F}$, respectively, in Eq. (7.40).

The full-Lagrangian Newton scheme for the coupled electro-thermo-mechanical-fluidic analysis is presented in detail in Algorithm 7.3. Algorithm 7.3

is discussed with reference to the two conductor system shown in Fig. 7.11. In Fig. 7.11, the thermal analysis is performed in the same domain where the mechanical analysis is performed, *i.e.*, in the domains Ω_1 and Ω_2. In Algorithm 7.2, the index n stands for the time instant whereas the index i denotes the ith Newton iteration within the time step n. tol is some specified tolerance for checking convergence of the Newton scheme. Once the domains are discretized, the mechanical, thermal, electrical and the fluidic unknowns are initialized (set to zero for our case). In each time step, a Newton scheme is implemented to obtain a self-consistent solution for that time step. The initial guesses for the Newton method are generally taken to be the final solutions of the previous time step. Note that $\mathbf{R_{ET}} = \mathbf{R_{TE}} = \mathbf{R_{FT}} = \mathbf{R_{TF}} = 0$, i.e., there exists no coupling between the thermal and the electrical and fluidic domains and the other terms can be computed in a straightforward manner in the full-Lagrangian formulation.

The quality factor due to thermoelastic damping, Q_{TED}, of the MEMS beam can then be computed as[16]

$$Q_{\text{TED}}^{-1} = \frac{1}{2\pi}\frac{\Delta E_{\text{TED}}}{PE_{max}} \tag{7.41}$$

where PE_{max} is the maximum elastic potential energy stored in the MEMS beam during one complete time period of vibration. In the physical level analysis, the potential energy stored in the system is given by[20]

$$PE = w\int_A \left[\sum_{i,j=1}^{2} \frac{1}{2} s_{ij}^M e_{ij}\right] dA \tag{7.42}$$

where s_{ij}^M are the components of $\mathbf{S}^M$. The relatively insignificant thermal stress $\mathbf{S}^T$ compared to the mechanical stress $\mathbf{S}^M$ is neglected in the computation of the potential energy. e_{ij} are the components of $\mathbf{E}$, w is the width of the microstructure and A is the area of microstructure (2D domain where the mechanical analysis is done). The energy dissipated by thermoelastic damping ΔE_{TED} is given by[45]

$$\Delta E_{\text{TED}} = w\int_A \oint \left[\sum_{i,j=1}^{2} s_{ij}^T de_{ij}\right] dA \tag{7.43}$$

where $\oint$ signifies integration over a complete time period of vibration and s_{ij}^T are the components of the thermal stress $\mathbf{S}^T$. Equations (7.41), (7.42) and (7.43) are used to compute the quality factor due to thermoelastic damping from the numerical simulations.

7.5.1. *Classical Theory of Thermoelastic Damping*

The classical theory of thermoelastic damping (developed by Zener[15,16] and later improved by Lifshitz and Roukes[17]) has been used extensively to predict the quality factor due to thermoelastic damping, Q_{TED}, of MEMS beams and is found to give good agreement with experimental results for simple harmonic oscillations in the flexural mode.[46,47] Zener's theory is valid for thin rectangular beams undergoing simple harmonic vibrations in the flexural mode. According to this theory, the quality factor Q_{TED} due to thermoelastic damping is given by[15,16]

$$Q_{\text{TED}}^{-1} = \frac{E\alpha^2 T_0}{\rho C_p} \frac{\omega\tau_z}{1+(\omega\tau_z)^2} = \Delta_E \frac{\omega\tau_z}{1+(\omega\tau_z)^2}; \qquad \Delta_E = \frac{E\alpha^2 T_0}{\rho C_p} \tag{7.44}$$

where ρ is the density, E is the Young's modulus, α is the coefficient of thermal expansion and C_p is the specific heat under constant pressure of the beam material. T_0 is the ambient temperature (beam is unstrained and unstressed at this temperature) and ω is the angular frequency of excitation. τ_z is the relaxation time (the time necessary for a temperature gradient to relax) of the first mode of vibration of the beam and is given by $\tau_z = b^2/(\pi^2\kappa)$, where κ is the thermal diffusivity of the beam material and b is the beam thickness. Zener's theory works quite well for simple beams and is not suitable for microstructures with complex geometries. Besides, it is also based on the assumption that the motion of the microstructure is simple harmonic. The Zener's theory was improved in Ref. 17 by using the beam theory.[48] The equation of motion for a beam under thermoelastic damping is given by[17]

$$\rho A \frac{\partial^2 U}{\partial t^2} + \frac{\partial^2}{\partial x^2}\left(EI\frac{\partial^2 U}{\partial x^2} + E\alpha I_T\right) = 0 \tag{7.45}$$

where ρ is the density of the beam, A and I are the cross-sectional area and the mechanical contribution to the moment of inertia of the beam, respectively, and U is the displacement of the beam in the y-direction. The x-axis is defined along the length of the beam and y- and z-axes are along the thickness and the width direction of the beam, respectively. The term I_T is the thermal contribution to the beam's moment of inertia (measure of the thermal stress in the beam) and is given by $I_T = \int_A y\theta dydz$ where $\theta = T - T_0$ is the change in the temperature from the ambient temperature T_0. The linearized heat equation (assuming $\theta \ll T_0$) along the y-direction (temperature gradients along the other directions are assumed to be negligible) is given by[17]

$$\frac{\partial\theta}{\partial t} = \kappa\frac{\partial^2\theta}{\partial y^2} + y\frac{\Delta_E}{\alpha}\frac{\partial}{\partial t}\left[\frac{\partial^2 U}{\partial x^2}\right]. \tag{7.46}$$

The coupled thermoelastic equations (7.45) and (7.46) are solved assuming simple harmonic vibrations in Ref. 17 by setting

$$U(x,t) = U_1(x)e^{i\omega t}; \qquad \theta(x,y,t) = \theta_1(x,y)e^{i\omega t} \tag{7.47}$$

The temperature profile along the beam's cross-section is calculated by using the heat equation (7.46) and the computed temperature is substituted into the equation of motion (7.45) to obtain a frequency dependent elastic modulus E_ω.[17] The real part and the imaginary part of the frequency dependent elastic modulus E_ω were used in Ref. 17 to compute the quality factor due to thermoelastic damping Q_{TED} as

$$Q_{\text{TED}}^{-1} = \Delta_E \left(\frac{6}{\xi^2} - \frac{6}{\xi^3} \frac{\sinh \xi + \sin \xi}{\cosh \xi + \cos \xi} \right) \tag{7.48}$$

where $\xi = b\sqrt{\omega/(2\kappa)}$. In deriving the expression for the quality factor Q_{TED}^{-1} in the Zener's theory (Eq. (7.44)) the temperature profile in the beam was expressed in terms of the transverse thermal eigen modes (see Refs. 15 and 16 for details). On the other hand, in the Lifshitz and Roukes's theory (Eq. (7.48)) the temperature profile in the beam was computed explicitly (without expanding it in terms of the thermal eigen modes). As a result, the Lifshitz and Roukes's theory is found to be more accurate than the Zener's theory for predicting the quality factor due to thermoelastic damping in rectangular beams undergoing simple harmonic vibrations in the flexural mode.[17]

7.5.2. *Modified Theory of Thermoelastic Damping*

The theory of thermoelastic damping presented in Sec. 7.5.1 is modified to predict the value of Q_{TED} in electrostatic MEMS under complex non-linear oscillations. Under electrostatic actuation, in the presence of fluid and thermoelastic damping, the equation of motion for a MEMS beam is given by

$$\rho A \frac{\partial^2 U}{\partial t^2} + c\frac{\partial U}{\partial t} + \frac{\partial^2}{\partial x^2}\left(EI \frac{\partial^2 U}{\partial x^2} + E\alpha I_T \right) = F_e = \frac{\epsilon w V^2}{2(g-U)^2} \tag{7.49}$$

where c is the fluid damping coefficient, ϵ is the dielectric constant of the surrounding medium, V is the applied voltage, g is the gap in the undeformed state between the beam and the ground electrode, F_e is the electrostatic force per unit length and w is the width of the beam. A voltage of the form $V = V_{DC} + V_{AC}e^{i\omega t}$ is considered, where the real and the imaginary parts of $e^{i\omega t}$ correspond to a cosine and sinusoidal AC excitation, respectively. In the modified theory, we first solve the coupled thermoelastic equations (Eqs. (7.49) and (7.46)) by assuming

$$U(x,t) = \sum_{N=0}^{NT} U_N(x)e^{iN\omega t}; \qquad \theta(x,y,t) = \sum_{N=0}^{NT} \theta_N(x,y)e^{iN\omega t} \tag{7.50}$$

where NT is the number of harmonics considered. Substituting Eq. (7.50) into Eq. (7.46) and equating the coefficients of $e^{iN\omega t}$ for $N = 0, 1, 2, ..., NT$ to zero gives

$$\theta_N(x,y) = \frac{\Delta_E}{\alpha}\frac{\partial^2 U_N(x)}{\partial x^2}\left[y - \frac{\sin(y\zeta_N)}{\zeta_N \cos(b\zeta_N/2)}\right] \text{ for } N > 0; \quad \theta_0(x,y) = 0; \tag{7.51}$$

where ζ_N is given by $\zeta_N = i\sqrt{iN\omega/\kappa}$. The thermal contribution to the beam's moment of inertia, I_T, can be computed from Eq. (7.51) (noting $\theta_0(x,y) = 0$) as

$$I_T = \int_A y\theta dydz = \sum_{N=1}^{NT}\frac{\Delta_E I}{\alpha}\left[1 + f(N\omega)\right]\frac{\partial^2 U_N(x)}{\partial x^2}e^{iN\omega t} \tag{7.52}$$

where $I = wb^3/12$ is the mechanical moment of inertia of the beam (of width w and thickness b) and $f(N\omega)$ is given by

$$f(N\omega) = \frac{24}{b^3\zeta_N^3}\left[\frac{b\zeta_N}{2} - \tan\left(\frac{b\zeta_N}{2}\right)\right] \tag{7.53}$$

Substituting the expression for the displacement $U(x,t)$ from Eq. (7.50) and the expression for I_T (Eq. (7.52)) into Eq. (7.49) gives

$$\begin{aligned} -\rho A\omega^2 \sum_{N=0}^{NT} N^2 U_N(x)e^{iN\omega t} + ic\omega \sum_{N=0}^{NT} NU_N(x)e^{iN\omega t} + EI\sum_{N=0}^{NT}\frac{\partial^4 U_N(x)}{\partial x^4}e^{iN\omega t} \\ +EI\Delta_E \sum_{N=1}^{NT}\{1 + f(N\omega)\}\frac{\partial^4 U_N(x)}{\partial x^4}e^{iN\omega t} = \frac{\epsilon w(V_{DC} + V_{AC}e^{i\omega t})^2}{2\left[g - \sum_{N=0}^{NT} U_N(x)e^{iN\omega t}\right]^2}. \end{aligned} \tag{7.54}$$

From Eqs. (7.49) and (7.54) the bending moment[48] of the MEMS beam, M is given by

$$\begin{aligned} M = EI\frac{\partial^2 U}{\partial x^2} + E\alpha I_T = EI\sum_{N=0}^{NT}\frac{\partial^2 U_N(x)}{\partial x^2}e^{iN\omega t} \\ + EI\Delta_E \sum_{N=1}^{NT}\{1 + f(N\omega)\}\frac{\partial^2 U_N(x)}{\partial x^2}e^{iN\omega t} = M^M + M^T \end{aligned} \tag{7.55}$$

where M^M and M^T are the mechanical and the thermal contributions to the bending moment, respectively. The third term and the fourth terms on the left hand

side of Eq. (7.54) corresponds to $\partial^2 M^M/\partial x^2$ and $\partial^2 M^T/\partial x^2$, respectively. The stress σ in the MEMS beam is given by[48]

$$\sigma = \frac{My}{I} = \frac{M^M y}{I} + \frac{M^T y}{I} = \sigma^M + \sigma^T \tag{7.56}$$

where σ^M and σ^T are the mechanical and the thermal stresses, respectively, with σ^T significantly smaller than σ^M.[15] The strain ε in the MEMS beam is given by[48]

$$\varepsilon = y\frac{\partial^2 U}{\partial x^2} = \frac{\sigma^M}{E} \tag{7.57}$$

Using the expressions for the stress and strain in the MEMS beam, the elastic potential energy stored in the system, PE, is given by[45]

$$PE = \int_V dV \int_0^{\varepsilon} \sigma d\varepsilon \approx \int_V dV \int_0^{\varepsilon} \sigma^M d\varepsilon \tag{7.58}$$

as σ^T is negligibly small compared to σ^M and V is the volume of beam. The energy dissipated by thermoelastic damping per period of the vibration, ΔE_{TED}, is given by[16,45]

$$\Delta E_{\text{TED}} = \int_V dV \oint \sigma^T d\varepsilon \tag{7.59}$$

where $\oint$ signifies integration over a complete time period of vibration. The quality factor due to thermoelastic damping, Q_{TED}, of the MEMS beam can then be computed using Eq. (7.41). Expressing $U_N(x)$ as[49]

$$U_N(x) = \beta_N \phi(x); \qquad i.e., \qquad U(x,t) = \phi(x)\sum_{N=0}^{NT} \beta_N e^{iN\omega t}; \tag{7.60}$$

where $\phi(x)$ is the most dominant mode of vibration of the beam at the given frequency of excitation and β_N denotes the vibration amplitude, a closed form expression for the quality factor Q_{TED} for the MEMS beam can be obtained as (see Ref. 50 for details)

$$Q_{\text{TED}}^{-1} = \left[\sum_{N=1}^{NT} \Delta_E \left(\frac{6}{\xi_N^2} - \frac{6}{\xi_N^3}\frac{\sinh\xi_N + \sin\xi_N}{\cosh\xi_N + \cos\xi_N}\right) N\bar{\beta}_N^2\right]\left[\bar{\beta}_{max}^2\right]^{-1} \tag{7.61}$$

where $\bar{\beta}_N$ is the magnitude of β_N (β_N is in general complex and can be written in terms of its magnitude $\bar{\beta}_N$ and phase ϕ_N as $\beta_N = \bar{\beta}_N e^{i\phi_N}$). $\bar{\beta}_{max}$ is the maximum value of the expression $\sum_{N=0}^{NT} \beta_N e^{iN\omega t}$ evaluated over a time period $2\pi/\omega$ and $\xi_N = b\sqrt{N\omega/(2\kappa)}$. When only one harmonic ($NT = 1$) is considered in Eq. (7.61), *i.e.*, for simple harmonic motions of the beam, $\bar{\beta}_{max} = \bar{\beta}_1$ and the expression for Q_{TED} given by the modified theory (Eq. (7.61)) reduces to the expression for Q_{TED} given by the Lifshitz and Roukes's theory (Eq. (7.48)).

7.5.3. *Numerical Simulations in the Presence of Fluid and Thermal Damping*

Figure 7.52 shows the comparison between the measured and computed (both the numerical simulations and the modified theory) quality factor Q_{TED} for a set of silicon fixed-fixed[51] beams in vacuum at $T_0 = 300$ K. The length of the fixed-fixed beam was changed to obtain different resonant frequencies and the thickness was kept constant at 5 μm. The five experimental data points in Fig. 7.52 were obtained from 5 μm thick fixed-fixed beams of lengths 700 μm (at its first and third resonant frequency, 80.3 kHz and 490 kHz, respectively), 500 μm (at its third resonant frequency, 720 kHz) and 200 μm (at its first and third resonant frequency, 911 kHz and 5.05 MHz, respectively). The beams have the following materials properties:[51] $\alpha = 2.6\times10^{-6}$ K^{-1}, $E = 130$ GPa, $\nu = .28$, $\rho = 2330$ kg m^{-3}, $C_p = 712$ J kg^{-1} K^{-1}, $k = \kappa\rho C_p = 148$ W m^{-1} K^{-1}. A DC bias of 0.1 V along with an AC bias of 0.01 V is used in the numerical simulations and the modified theory to generate an electrostatic actuation force in the linear regime. The numerically simulated values of Q_{TED} and those obtained from the modified theory are close to the experimental data for both the cantilever beams and the fixed-fixed beams as shown in Fig. 7.52.

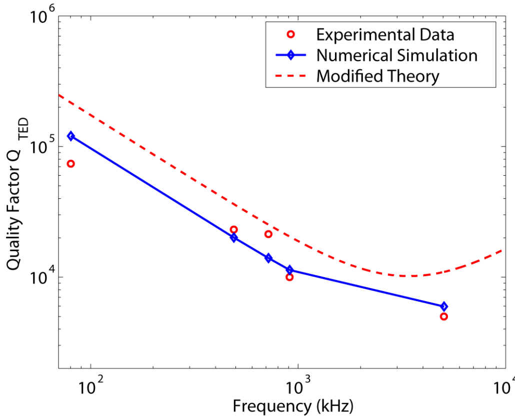

Fig. 7.52. Comparisons between the measured and the computed (numerical simulations and modified theory) quality factor Q_{TED} for a set of silicon fixed-fixed beams[51] in vacuum.

Two different sources of nonlinearity in the electrostatic force per unit length F_e can be identified from the beam equation for electrostatic MEMS (Eq. (7.49)) and they are (i) $F_e \propto V^2$ and (ii) $F_e \propto 1/(g - U)^2$. These nonlinearities in F_e can give rise to complex non-linear vibrations in the MEMS beam (discussed

earlier). The effect of these non-linear vibrations on Q_{TED} is studied in this section using the modified theory and the physical level analysis, for a MEMS fixed-fixed beam. The results obtained from the classical theory of thermoelastic damping are also discussed. When the applied voltage V is small (compared to the pull-in voltage of the MEMS beam), the displacement $U \ll g$ and the nonlinearity due to $F_e \propto 1/(g-U)^2$ is negligible (see Eq. (7.49)). However, the nonlinearity due to $F_e \propto V^2$ can still be present at such small voltages and give rise to different values of Q_{TED} than that predicted by the classical theory of thermoelastic damping.[15,17] Considering an applied voltage of the form $V = V_{DC} + V_{AC}\sin(\omega t)$, where V_{DC} is the applied DC bias and $V_{AC}\sin(\omega t)$ is the sinusoidal AC voltage, the electrostatic force per unit length F_e will have both the first and the second harmonic of the exciting angular frequency ω due to the V^2 nature, *i.e.*,

$$F_e \approx \frac{\epsilon w}{2g^2}\left[V_{DC}^2 + \frac{V_{AC}^2}{2} + 2V_{DC}V_{AC}\sin(\omega t) - \frac{V_{AC}^2}{2}\cos(2\omega t)\right] \qquad (7.62)$$

Defining $r = V_{AC}/(V_{DC}+V_{AC})$, $r = 1$ (when $V_{DC} = 0$) implies AC operation (when the second harmonic of the exciting angular frequency ω is dominant) and $r \to 0$ (when $V_{AC} \ll V_{DC}$) implies DC operation (when the first harmonic is dominant). For intermediate values of r between 0 and 1 (mixed-mode operation) both the first and the second harmonic components of the applied voltage are dominant. The effect of the different modes of operation (AC, DC and mixed-mode) on thermoelastic damping in MEMS is studied for a fixed-fixed MEMS beam (denoted as beam A) at $T_0 = 300$ K. The fixed-fixed MEMS beam (beam A) considered is made from silicon and has dimensions: $200\ \mu\text{m} \times 5\ \mu\text{m} \times 10\ \mu\text{m}$ (length $\times$ thickness $\times$ width), placed $1\ \mu$m over a ground plane. The material properties used are same as those used for the fixed-fixed beams as presented in the previous paragraph, and the beam's resonant frequency is f_0 = 1.08 MHz. The relaxation time of the beam is $\tau_z = 0.0284\ \mu$s, giving a characteristic damping frequency $f_d = 1/(2\pi\tau_z)$ (the frequency where TED is maximum, *i.e.*, Q_{TED} is minimum) of 5.6 MHz. The beam is simulated in air at 1 atms (η = 1.82×10^{-5} kg/ms and the mean free path $\lambda = 0.064\ \mu$m). Figure 7.53 shows the variation in Q_{TED} with the excitation frequency $f = \omega/(2\pi)$ for the fixed-fixed beam A, under DC operations ($V_{DC} = 1$ V and $V_{AC} = 0.0001$ V, $r \to 0$) obtained using the Zener's theory, the modified theory and the numerical simulations. The fluid damping coefficient (needed in the modified theory), $c = 0.0205$ Ns/m^2, is obtained from the linearized Reynold's squeeze film theory for beam A. The value of Q_{TED} obtained from the Zener's theory, the modified theory and the numerical simulation are very close as shown in Fig. 7.53 (the numerical simulation results are typically more accurate due to its 2D analysis as compared to the theories

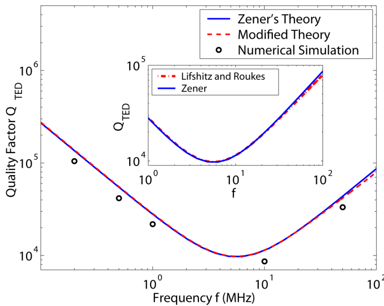

Fig. 7.53. Variation of Q_{TED} with the excitation frequency f for the MEMS fixed-fixed beam A (resonant frequency is f_0 = 1.08 MHz) under DC operations ($r \rightarrow 0$) obtained from the different theories and numerical simulation. Characteristic damping frequency is, f_d = 5.6 MHz, where Q_{TED} is minimum.

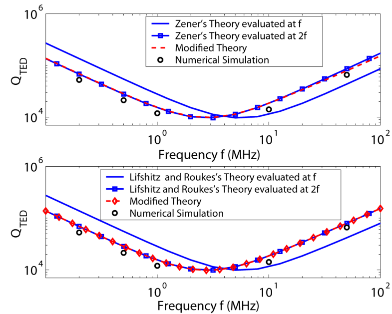

Fig. 7.54. Variation of Q_{TED} with the excitation frequency f for the MEMS fixed-fixed beam A under AC operations ($r = 1$) obtained from the different theories and numerical simulation. Characteristic damping frequency is, f_d = 2.8 MHz, where Q_{TED} is minimum.

which are based on 1D analysis of the system[51]). Under DC operations at small voltages where the nonlinearity due to $F_e \propto 1/(g-U)^2$ is negligible, the motion of the beam is simple harmonic at the excitation frequency f. In this case, the Zener's theory and the Lifshitz and Roukes's theory (compared with the Zener's theory in the inset of Fig. 7.53) match with the modified theory and are very close to the numerical simulations. The pull-in voltage of the fixed-fixed beam is found to be 120 V, thereby indicating that the applied voltages are very small. The inset of Fig. 7.53 shows some minor variations between the Zener's theory and the Lifshitz and Roukes's theory at higher frequencies which is consistent with the observations made in Ref. 17. Note that the modified theory is identical to the Lifshitz and Roukes's theory when only one harmonic ($NT = 1$) is considered in Eq. (7.61), *i.e.*, for simple harmonic motions of the beam.

For AC operations ($V_{DC} = 0$ V and $V_{AC} = 1$ V, $r = 1$), the value of Q_{TED} obtained from the Zener's theory and the Lifshitz and Roukes's theory evaluated at $\omega = 2\pi f$ does not match with the predictions of the modified theory or the numerical simulations as shown in Fig. 7.54. However, the classical theories evaluated at $2\omega = 2\pi(2f)$ agree well with the modified theory (and the results are close to the numerical simulations) as the oscillations are still simple harmonic but at twice the excitation frequency due to the V^2 nature of F_e under AC operations from Eq. (7.62). In this case, the characteristic damping frequency is found to be half of that in the DC operation, *i.e.*, $f_d = 2.8$ MHz as shown in Fig. 7.54. While minor variations can be observed between the Zener's model evaluated at

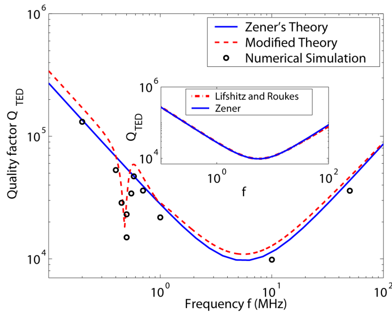

Fig. 7.55. Variation in Q_{TED} with the excitation frequency f for the MEMS fixed-fixed beam (resonant frequency is f_0 = 1.08 MHz) under mixed-mode operation at $r = .5$ ($V_{DC} = 0.5$ V, $V_{AC} = 0.5$ V), obtained from the different theories and numerical simulation.

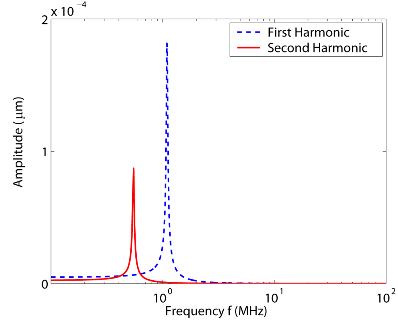

Fig. 7.56. Amplitude variation of the first and the second harmonics, β_1 and β_2, respectively, with the excitation frequency f for the MEMS fixed-fixed beam at $r = .5$ ($V_{DC} = 0.5$ V, $V_{AC} = 0.5$ V).

$2\omega = 2\pi(2f)$ and the modified theory at higher frequencies in Fig. 7.54, the value of Q_{TED} given by Lifshitz and Roukes's theory evaluated at $2\omega = 2\pi(2f)$ is found to be exactly same as the modified theory at all the frequencies. For mixed-mode operations (intermediate values of r between 0 and 1), the electrostatic force per unit length F_e contains both the first and the second harmonic components of the exciting frequency (see Eq. (7.62)). As a result, the oscillations also have both these two frequency components in them giving rise to non simple harmonic oscillations. The value of the quality factor due to thermoelastic damping, Q_{TED}, for such cases cannot be predicted correctly by the classical theories as shown in Fig. 7.55. Figure 7.55 shows the variation in Q_{TED} with the excitation frequency f for a mixed-mode operation at $V_{DC} = 0.5$ V and $V_{AC} = 0.5$ V, $r = .5$ in the fixed-fixed beam A. While the modified theory and the numerical simulations indicate the formation of a spike in the downward direction in Q_{TED} around $f_0/2$ ($f_0 = 1.08$ MHz is the resonant frequency of the beam), no such predictions are made by the Zener's or the Lifshitz and Roukes's theories. The formation of the spike in Q_{TED} around $f_0/2$ can be explained from the variation in the magnitude of the first and the second harmonics, β_1 and β_2, respectively, with the excitation frequency f for the fixed-fixed beam at $V_{DC} = 0.5$ V and $V_{AC} = 0.5$ V ($r = .5$). While the magnitude of the first harmonic β_1 peaks at the resonant frequency of the system as expected, the second harmonic β_2 becomes dominant (larger than β_1) at $f_0/2$ as shown in Fig. 7.56. Since the quality factor Q_{TED} depends on the relative strengths of the different harmonics present (Eq. (7.61)), maximum deviation between the classical theories (based on the first harmonic) and the

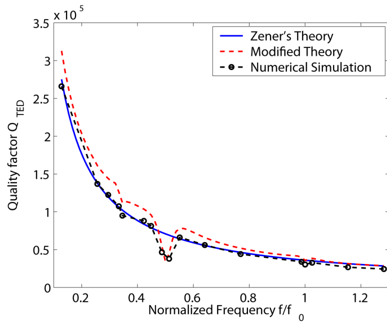

Fig. 7.57. Variation in Q_{TED} with the normalized frequency f/f_0 for the fixed-fixed beam at 100 V DC (close to the pull-in voltage) and 5 V AC. The resonant frequency at 100 V DC is $f_0 = 893$ KHz.

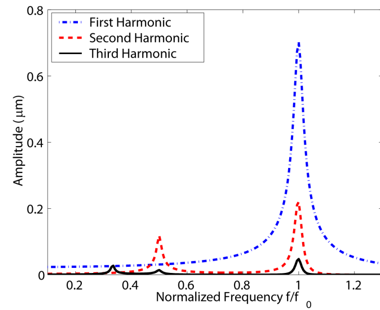

Fig. 7.58. Amplitude variation of the first three harmonics β_1, β_2 and β_3 with the normalized frequency f/f_0 for the fixed-fixed beam at 100 V DC (close to the pull-in voltage) and 5 V AC.

modified theory and numerical simulations are observed at $f_0/2$ where the second harmonic is most dominant.

When the applied voltages are large, the displacement U is comparable with the gap g and the nonlinearity due to $F_e \propto 1/(g-U)^2$ in Eq. (7.49) becomes important. Figure 7.57 shows the variation in Q_{TED} with the normalized frequency f/f_0 for the fixed-fixed beam at 100 V DC (close to the pull-in voltage) and 5 V AC. The resonant frequency of the beam at 100 V DC is $f_0 = 893$ KHz. The quality factor Q_{TED} (computed by the modified theory and also by the numerical simulations) has several spikes in its variation with respect to the normalized frequency f/f_0 as shown in Fig. 7.57. The spikes occur at the superharmonics of the resonant frequency f_0, *i.e.*, at $f = f_0/N$ for $N = 1, 2, 3, ...$, and are not predicted by the Zener's theory or the Lifshitz and Roukes's theory (not shown here as it gives very similar result as the Zener's theory).

The formation of the spikes in Fig. 7.57 can be explained by the presence of higher-order harmonics in the oscillations introduced by the $F_e \propto 1/(g-U)^2$ nonlinearity at higher voltages (close to pull-in). Harmonic balance analysis of the beam equation (Eq. (7.49)) shows the presence of several higher order harmonics in the oscillations of beam at 100 V DC and 5 V AC as shown in Fig. 7.58. The magnitude of the Mth harmonic, β_M, is found to peak/spike at the first M superharmonic frequencies of f_0, *i.e.*, at $f = f_0/N$ for $N = 1, 2, 3, ..., M$. This in turn affects the quality factor Q_{TED} at a given frequency as shown in Fig. 7.57 as the quality factor Q_{TED} at a given frequency depends on the relative strengths of the different harmonics β_N present (from Eq. (7.61)).

7.6. Conclusions

Full-Lagrangian Newton schemes have been presented for the dynamic analysis of electrostatic MEMS. The full-Lagrangian-scheme greatly improves the performance of the dynamic analysis by eliminating time consuming steps like recomputing the interpolation functions and re-discretization of the surfaces. For tightly coupled cases, relaxation gives very slow convergence and often fails to converge. Newton method becomes important for such cases. The Lagrangian description of all the physical domains enables the efficient and accurate computation of the Jacobian matrix and thereby gives excellent convergence rates. Both these features makes this method far more efficient than existing coupled solvers for the dynamic analysis of MEMS. Two hierarchical fluid models, namely, the compressible Reynold's squeeze film equation and the compressible Navier–Stokes equations are coupled with electrostatic, thermal and mechanical models using a full-Lagrangian formulation and a Newton method. The coupling of the two hierarchical fluid models (the 2D CRSFE and the 2D CNSE) with the coupled electro-mechanical solver makes it possible to simulate the dynamics of a large class of MEMS devices. While the faster 2D CRSFE based solver can be used to accurately simulate certain classes of MEMS devices (having large aspect ratios and small gaps like the micromirror and the piggyback actuator), the more accurate and comparatively slower 2D CNSE based solver can be used for MEMS devices where 2D CRSFE is not valid, for example, the cantilever beam in air.

New non-linear dynamic properties of electrostatic MEMS have also been presented in this work through the numerical simulation of detailed physical level models for the coupled electrical, mechanical and the fluidic energy domains. The formation of M-cycle oscillations at the Mth superharmonic frequency of excitation and its period doubling leading to the formation of $2^n M$-cycles is shown through numerical simulations in different MEM devices. The presence of U-sequence in electrostatic MEMS and a modified form of the U-sequence, termed as the UM-sequence is shown to be present in electrostatic MEMS under superharmonic excitation. The electrostatic force is found to be primarily responsible for the non-linear dynamic properties presented in this work. The non-linear nature of the electrostatic actuation force is also found to change the nature of thermoelastic damping in electrostatic MEMS significantly from that predicted by the classical theory of thermoelastic damping developed by Zener and later improved by Lifshitz and Roukes. The nonlinearity due to the V^2 nature of the electrostatic force is found to affect the thermoelastic quality factor Q_{TED} even at small voltages (far off from pull-in). At larger voltages (closer to pull-in), the nonlinearity due to the $1/(g - U)^2$ nature of the electrostatic force is found to affect Q_{TED}.

A modified theory is proposed for predicting thermoelastic damping in MEMS under arbitrary electrostatic actuation. The modified theory takes into account the higher-order harmonics present in the oscillations, which arise due to non-linear electrostatic force, to compute the overall thermoelastic damping coefficient and the quality factor. Although the quality factor Q_{TED} predicted by the modified theory is close to the numerical simulation predictions, typically the physical level or numerical simulations based on the coupled 2D non-linear electro-thermo-mechanical-fluidic analysis are more accurate as they involve fewer assumptions compared to the modified theory.

References

1. H. Luo, G. Zhang, L. R. Carley, and G. K. Fedder, A 1 mg lateral CMOS-MEMS accelerometer, *J. Microelectromechanical Systems*. **11(3)**, 188–195, (2002).
2. N. Yazdi, F. Ayazi, and K. Najafi, Micromachined inertial sensors, *Proc. of the IEEE*. **86(8)**, 1640–1659, (1998).
3. M. S. Weinberg, B. T. Cunningham, and C. W. Clapp, Modeling flexural plate wave devices, *J. Microelectromechanical Systems*. **9(3)**, 370–379, (2000).
4. C. T. Nguyen, Micromechanical resonators for oscillators and filters, *Proceedings of the Ultrasonics Symposium*. **489–499**, (1995).
5. S. D. Senturia, CAD challenges for microsensors, microactuators, and microsystems, *Proceedings of the IEEE*. **86(8)**, 1611–1626, (1998).
6. S. D. Senturia, R. M. Harris, B. P. Johnson, K. Songmin, K. Nabors, M. A. Shulman, and J. White, A computer-aided design system for microelectromechanical systems (MEMCAD), *J. Microelectromechanical Systems*. **1(1)**, 3–13, (1992).
7. F. Shi, P. Ramesh, and S. Mukherjee, Dynamic analysis of micro-electro-mechanical systems, *Intl. J. for Numer. Meth. in Engrg*. **39**, 4119–4139, (1996).
8. E. S. Hung and S. D. Senturia, Generating efficient dynamical models for microelectromechanical systems from a few finite-element simulation runs, *J. of Microelectromechanical Systems*. **8(3)**, 280–289, (1999).
9. W. Ye, X. Wang, W. Hemmert, D. Freeman, and J. White, Air damping in laterally oscillating microresonators: a numerical and experimental study, *J. of Microelectromechanical Systems*. **12(5)**, 557–566, (2003).
10. S. D. Senturia, N. R. Aluru, and J. White, Simulating the behavior of MEMS devices: Computational methods and needs, *IEEE Computational Science and Engineering*. **4(1)**, 30–43, (1997).
11. N. R. Aluru and J. White, An efficient numerical technique for electromechanical simulation of complicated microelectromechanical structures, *Sensors and Actuators A*. **58**, 1–11, (1997).
12. N. R. Aluru and J. White, A multi-level Newton method for mixed-energy domain simulation of MEMS, *J. Mircoelectromechanical Systems*. **8(3)**, 299–308, (1999).
13. S. K. De and N. R. Aluru, Full-Lagrangian schemes for dynamic analysis of electrostatic MEMS, *J. Mircoelectromechanical Systems*. **13(5)**, 737–758, (2004).

14. J. M. T. Thompson and H. B. Stewart, *Nonlinear dynamics and chaos*. (John Wiley & Sons, 1986).
15. C. Zener, Internal friction in solids I: Theory of internal friction in reeds, *Physical Review*. **52**, 230–235, (1937).
16. C. Zener, Internal friction in solids II: General theory of thermoelastic internal friction, *Physical Review*. **53**, 90–99, (1938).
17. R. Lifshitz and M. L. Roukes, Thermoelastic damping in micro- and nanomechanical systems, *Physical Review B*. **61(8)**, 5600–5609, (2000).
18. W. Nowacki, *Thermoelasticity*. (Pergamon Press, 1986).
19. D. S. Chandrasekharaiah and L. Debnath, *Continuum Mechanics*. (Academic Press, 1994).
20. K. J. Bathe, *Finite Element Procedures*. (Prentice-Hall, 1995).
21. H. Parkus, *Thermoelasticity*. (Blaisdell Publishing Company, 1968).
22. P. Yarrington and D. E. Carlson, Successive approximations in nonlinear thermoelasticity, *Int. J. Engng. Sci.* **14**, 113–125, (1976).
23. J. B. Starr, Squeezed-film damping in solid-state accelerometers, *Proc. of the Tech. Digest Solid-State Sensor and Actuator Workshop*. **44–47**, (1990).
24. G. Schrag and G. Wachutka, Physically based modeling of squeeze film damping by mixed-level system simulation, *Sensors and Actuators A*. **97–98**, 193–200, (2002).
25. A. Burgdorfer, The influence of the molecular mean free path on the performance of hydrodynamic gas lubricated bearings, *Trans. of the ASME: Journal of Basic Engr.* **81**, 94–100, (1959).
26. S. K. De and N. R. Aluru, Coupling of hierarchical fluid models with electrostatic and mechanical models for the dynamic analysis of MEMS, *J. of Micromech. Microeng.* **16(8)**, 1705–1719, (2006).
27. W. G. Vincenti and C. H. Kruger, *Introduction to Physical Gas Dynamics*. (John Wiley & Sons, 1967).
28. C. W. Hirt, A. A. Amsden, and J. L. Cook, An arbitrary Lagrangian-Eulerian computing method for all flow speeds, *J. Comput. Phys.* **14(3)**, 227–317, (1974).
29. W. H. Hui, A unified coordinates approach to computational fluid dynamics, *J. of Comp. Appl. Maths.* **163**, 15–28, (2004).
30. F. Shi, P. Ramesh, and S. Mukherjee, On the application of 2D potential theory to electrostatic simulation, *Comm. in Numerical Methods in Engr.* **11**, 691–701, (1995).
31. G. Li and N. R. Aluru, A Lagrangian approach for electrostatic analysis of deformable conductors, *J. Microelectromechanical Systems*. **11(3)**, 245–254, (2002).
32. H. Yie, X. Chai, and J. White, Convergence properties of relaxation versus the surface-Newton generalized-conjugate residual algorithm for self-consistent electromechanical analysis of 3D mircoelectromechanical systems, *Proc. Numerical Process and Device Modeling (NUPAD)*. **137–140**, (1994).
33. S. K. De and N. R. Aluru, Full-Lagrangian schemes for dynamic analysis of electrostatic MEMS, *J. of Microelectromechanical Systems*. **13(5)**, 737–758, (2004).
34. W. C. Tang, C. T.-Nguyen, and R. T. Howe, Laterally driven polysilicon resonant microstructures, *Sensors and Actuators*. **20**, 25–32, (1989).
35. T. Imamura, M. Katayama, Y. Ikegawa, T. Ohwe, R. Koishi, and T. Koshikawa, MEMS-based integrated head/actuator/slider for hard disk drives, *IEEE/ASME Trans. on Mechantronics*. **3(3)**, 166–174, (1998).

36. Z. Jin and Y. Wang, Electrostatic resonator with second superharmonic resonance, *Sensors and Actuators A*. **64**, 273–279, (1998).
37. F. Pan, J. Kubby, E. Peeters, A. T. Tran, and S. Mukherjee, Squeeze film damping effects on the dynamic response of a MEMS torsion mirror, *J. Micromech. Microeng.* **8**, 200–208, (1998).
38. H. Toshiyoshi, M. Mita, and H. Fujita, A MEMS piggyback actuator for hard-disk drives, *J. Microelectromechanical Systems*. **11(6)**, 648–654, (2002).
39. Z. Hang and W. C. Tang, Viscous air damping in laterally driven microresonators, *IEEE Proceedings MEMS'94*. **199–204**, (1994).
40. S. K. De and N. R. Aluru, Complex oscillations and chaos in electrostatic MEMS under superharmonic excitations, *Physical Review Letters*. **94**, 200401, (2005).
41. S. K. De and N. R. Aluru, Complex nonlinear oscillations in electrostatically actuated microstructures, *J. of Microelectromechanical Systems*. **15(2)**, 355–369, (2006).
42. R. Hegger, H. Knatz, and T. Schreiber, Practical implementation of nonlinear time series methods: The TISEAN package, *CHAOS*. **9**, 413–435, (1999).
43. C. Robinson, *Dynamical systems: stability, symbolic dynamics, and chaos*. (CRC Press Inc, 1994).
44. S. K. De and N. R. Aluru, U-sequence in electrostatic microelectromechanical systems (MEMS), *Proc. R. Soc. A*. (2006). in Press.
45. A. S. Nowick and B. S. Berry, *Anelastic Relaxation in Crystalline Materials*. (Academic Press, 1972).
46. T. V. Roszhart, The effect of thermoelastic internal friction on the Q of micromachined silicon resonators, *IEEE Proc. Solid-State Sensor and Actuator Workshop*. **13–16**, (1990).
47. K. Y. Yasumura, T. D. Stowe, E. M. Chow, T. Pfafman, T. W. Kenny, B. C. Stipe, and D. Rugar, Quality factor in micron- and submicron-thick cantilevers, *J. of Microelectromechanical Systems*. **9(1)**, 117–125, (2000).
48. E. G. Popov, *Engineering Mechanics of Solids*. (Prentice-Hall, 1997).
49. A. T. Nayfeh and D. T. Mook, *Nonlinear Oscillations*. (John Wiley & Sons, 1979).
50. S. K. De and N. R. Aluru, Theory of thermoelastic damping in electrostatically actuated microstructures, *Phys. Rev. B*. (2006). accepted for publication.
51. S. Pourkamali, A. Hashimura, R. Abdolvand, G. K. Ho, A. Erbil, and F. Ayazi, High-Q single crystal silicon HARPASS capacitive beam resonator with self-aligned sub-100-nm transduction gaps, *J. of Microelectromechanical Systems*. **12(4)**, 487–496, (2003).

Chapter 8

Coupled Deformation Analysis of Thin MEMS Plates

S. Mukherjee

Department of Theoretical and Applied Mechanics
Cornell University, Ithaca, NY 14853, USA
sm85@cornell.edu

S. Telukunta*

Siimpel Corp., Arcadia, CA, USA

The field of Micro-Electro-Mechanical Systems (MEMS) is a very broad one that includes fixed or moving microstructures. MEMS devices and systems that consist of arrays of beams and plates are of concern here. MEMS often use beam or plate shaped conductors that can be very thin — with $h/L \approx \mathcal{O}(10^{-2}-10^{-3})$ (in terms of the thickness h and length L of the side of a square pate). Such MEMS devices find applications in microsensors, microactuators, microjets, microspeakers and other systems where the conducting plates or beams oscillate at very high frequencies. Conventional Boundary Element Method (BEM) analysis of the electric field in a region exterior to such thin conductors can become difficult to carry out accurately and efficiently — especially since MEMS analysis requires computation of charge densities (and then surface tractions) separately on the top and bottom surfaces of such plates. A new Boundary Integral Equation (BIE) is proposed to handle the computation of charge densities for such high aspect ratio geometries. In the current work, this has been coupled with Finite Element Method (FEM) to obtain the response behavior of devices made of such high aspect ratio structural members. This coupling of the electrical and mechanical problems is carried out using a Newton scheme based on a Lagrangian description of both the mechanical and electrical domains. Numerical results are presented in this chapter for quasi static deformation of coupled MEMS. The effect of gap between a plate and the ground, on mechanical response of a plate subjected to increasing electric potential, and effect of geometry and boundary conditions on pull in voltage, are studied here.

*Formerly graduate student, Sibley School of Mechanical and Aerospace Engineering, Cornell University, Ithaca, NY 14853, USA

Contents

8.1 Introduction 288
8.2 Electrical Problem in the Exterior Domain 292
8.2.1 Electric Field BIEs in a Simply-Connected Body 292
8.2.2 BIEs in Infinite Region Containing Two Thin Conducting Plates 293
8.2.3 Boundary Integral Equations in the Lagrangian Formulation 296
8.3 Mechanical Problem in the Elastic Plate 302
8.3.1 The Model 302
8.3.2 FEM Model for Plates with Immovable Edges 303
8.4 Schemes for Solving the Coupled Problem 305
8.4.1 Lagrangian Relaxation Scheme for the Coupled Problem 305
8.4.2 Newton Scheme for Solving the Coupled Problem 307
8.5 Numerical Implementation 312
8.5.1 Boundary Integral Equations for Two Plates Very Close Together 312
8.5.2 Non-Linear Finite Element Analysis 313
8.5.3 BEM/FEM Coupling 314
8.5.4 Discretization 315
8.6 Numerical Results 315
8.6.1 Code Verification 315
8.6.2 MEMS Plates 318
8.7 Pull-In Analysis 323
8.8 Discussion 324
References 326

8.1. Introduction

The field of Micro-Electro-Mechanical Systems (MEMS) is a very broad one that includes fixed or moving microstructures; encompassing micro-electro-mechanical, microfluidic, micro-electro-fluidic-mechanical, micro-opto-electro-mechanical and micro-thermal-mechanical devices and systems. MEMS usually consists of released microstructures that are suspended and anchored, or captured by a hub-cap structure and set into motion by mechanical, electrical, thermal, acoustical or photonic energy source(s).

Typical MEMS structures consist of arrays of thin beams with cross-sections in the order of microns (μm) and lengths in the order of tens to hundreds of microns (see Fig. 8.1). Sometimes, MEMS structural elements are plates. An example is a small rectangular silicon plate with sides in the order of mm and thickness of the order of microns, that deforms when subjected to electric fields. Owing to its small size, significant forces and/or deformations can be obtained with the application of low voltages ($\approx$ 10 volts). Examples of devices that utilize vibrations of such plates are comb drives (see Fig. 8.1), synthetic microjets[2,3] for chemical mixing, cooling of electronic components, micropropulsion, turbulence control and other macro flow properties), microspeakers,[4] optical systems for portable

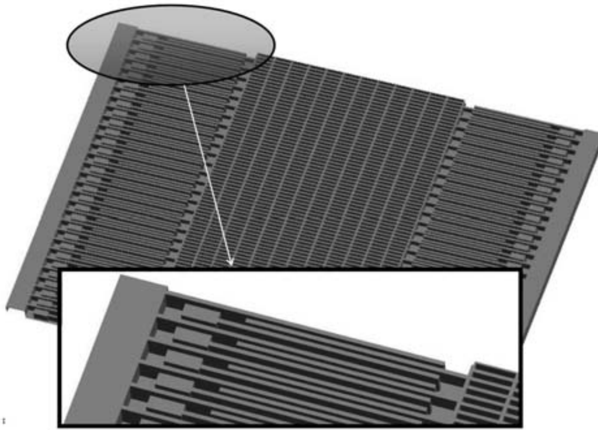

Fig. 8.1. Parallel plate resonator: Geometry and detail of the parallel plate fingers (from Ref. 1).

electronics like display devices and MEMS cameras *etc.* Schematic of such a microjet, based on micro-electro-fluidic-mechanical systems, is shown in Fig. 8.2.

Numerical simulation of electrically actuated MEMS devices have been carried out for around a decade or so by using the Boundary Element Method (BEM — see, *e.g.*, Refs. 5–9) to model the exterior electric field and the Finite Element Method (FEM — see, *e.g.*, Refs. 10–12) to model deformation of the structure. The commercial software package MEMCAD,[13] for example, uses the commercial FEM software package ABAQUS for mechanical analysis, together with a BEM code FastCap[14] for the electric field analysis. Other examples of such work are illustrated in Refs. 15–17; as well as Refs. 13 and 18 for dynamic analysis of MEMS.

The focus of this chapter is the study of quasi static response behavior of MEMS devices made up of very thin conducting plates. This requires BEM analysis of the electric field exterior to these thin conducting plates. A convenient way to model such a problem is to assume plates with vanishing thickness and solve for sum of the charges on the upper and lower surfaces of each plate.[19] The standard Boundary Integral Equation (BIE) with a weakly singular kernel is used here and this approach works well for determining, for example, the capacitance of a parallel plate capacitor. For MEMS calculations, however, one must obtain the charge densities separately on the upper and lower surfaces of a plate since the traction at a surface point on a plate depends on the square of the charge density at that point. The gradient BIE is employed in Ref. 20 to obtain these charge densities

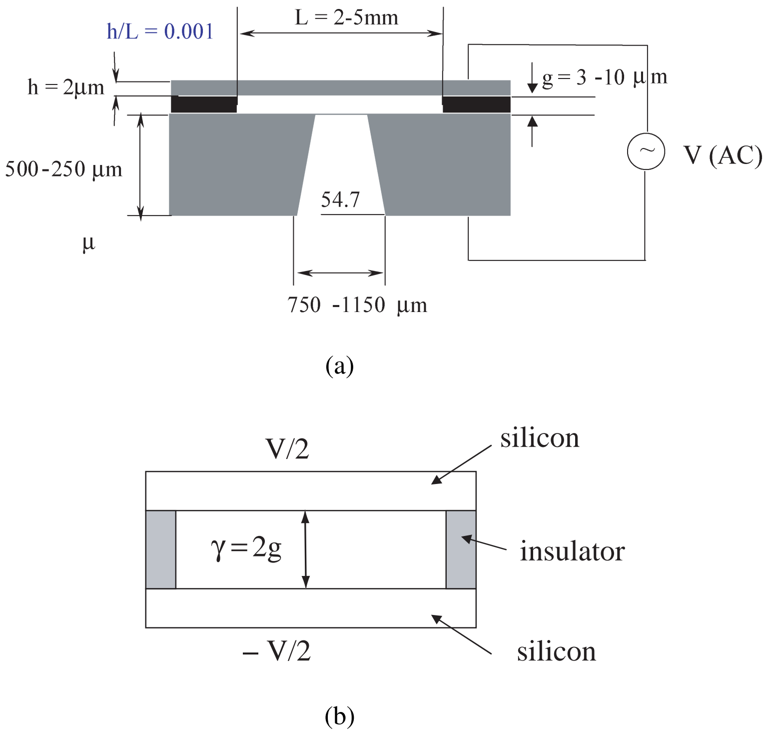

Fig. 8.2. (a) Schematic of a synthetic microjet. (b) Simulation model of a synthetic microjet (from Ref. 28).

separately. The formulation given in Ref. 20 is a BEM scheme that is particularly well-suited for MEMS analysis of very thin plates — for $h/L \leq .001$ — in terms of the length L (of a side of a square plate) and its thickness h. A similar approach can also be developed for MEMS and Nano-Electro-Mechanical Systems (NEMS) with very thin beams.[21] Similar work has also been reported recently by Chen *et al.*[22] in the context of determining fringing fields and levitating forces for 2D beam shaped conductors in MEMS combdrives.

The coupled BEM/FEM methods employed in the references cited above perform a mechanical analysis on the undeformed configuration of a structure (Lagrangian approach) and an electrical analysis on the deformed configuration (Eulerian approach). A relaxation method is then used for self-consistency between the two domains. Therefore, the geometry of the structure must be updated before an electrical analysis is performed during each relaxation iteration. This procedure increases computational effort and introduces additional numerical

errors since the deformed geometry must be computed at every stage. Li and Aluru[23] first proposed a Lagrangian approach for the electrical analysis as well, thus obviating the need to carry out calculations based on the deformed shapes of a structure. Two- and three-dimensional (2D and 3D) quasi-static Lagrangian exterior BEM analysis was addressed in Refs. 23 and 24; while a fully coupled 2D quasi-static MEMS analysis has been carried out in Ref. 25. A fully-coupled 2D dynamic Lagrangian MEMS analysis has been recently carried out by De and Aluru.[26] Additional advantages of the fully Lagrangian approach, for dynamic analysis of MEMS, are described in Ref. 26, in which a Newton method has been developed and compared with the relaxation scheme. A fully coupled Lagrangian (quasi-static) BEM/FEM analysis, but with the standard (not thin plate) BEM, is presented in Ref. 27. A similar coupled analysis with the thin plate BEM is presented in Ref. 28 and is the primary focus of the present chapter.

The topics addressed in this chapter are as follows. First, a coupled BEM-FEM analysis is presented in which the MEMS plate elements are thin and packed relatively close together. The exterior BEM analysis is three-dimensional while the FEM analysis allows for moderately large non-linear deformation of the elastic plates. A fully Lagrangian formulation is presented for both the mechanical and electrical analyses. This includes a Lagrangian formulation (new) for the gradient Boundary Integral Equation (BIE) that is needed to obtain the separate charges on the top and bottom faces of a thin conducting plate. Finally, a Newton scheme, analogous to that in Ref. 26, is developed for the present problem. Results from the Newton scheme are compared with those from an iterative relaxation scheme.

This chapter is organized as follows. The usual and gradient BIEs for potential theory, in an infinite region exterior to a structure composed of thin conducting plates, are first presented and regularized. This is then formulated in a total Lagrangian scheme. Next, a finite element scheme for deformation analysis of a plate is presented. This is followed by a description of a relaxation and a Newton scheme for coupling the electrical and mechanical problems. Finally, numerical results are presented and discussed for the model problem of a parallel plate capacitor (to simulate a microjet response behavior). These results include the effect of initial gap on plate deformation, and the effects of plate geometry and boundary conditions on pull-in voltage. A discussion section completes the chapter. Finally, it is important to realize that the actual problem of simulating a microjet involves dynamics, as well as coupling the electro-mechanical problem with microfluidics. The present chapter, however, is only a step in that direction and the effect of fluid forces is ignored in this work. A start has been made in modeling of damping forces in MEMS with thin plates (Ref. 29). Future research calls for fully coupling fluids forces in BEM/FEM MEMS modeling and analysis.

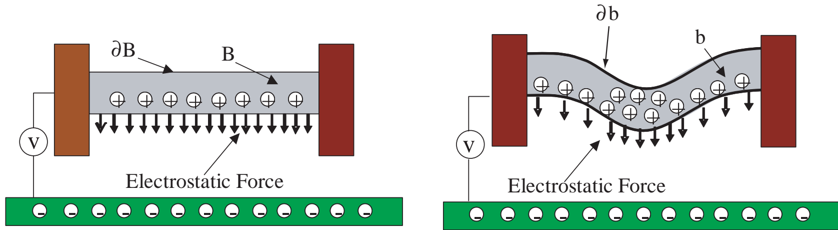

Fig. 8.3. A deformable clamped plate over a fixed ground plane (from Ref. 28).

8.2. Electrical Problem in the Exterior Domain

Figure 8.3 shows (as an example of a MEMS device) a deformable, clamped plate over a fixed ground plane. The undeformed configuration is B with boundary ∂B. The plate deforms when a potential V is applied between the two conductors, and the deformed configuration is called b with boundary ∂b. The charge redistributes on the surface of the deformed plate, thereby changing the electrical force on it and this causes the plate to deform further. A self-consistent final state is reached, and this state is computed in the present work by both the relaxation and Newton schemes.

8.2.1. *Electric Field BIEs in a Simply-Connected Body*

First consider the solution of Laplace's equation in a three-dimensional (3D) simply connected body.

8.2.1.1. *Usual BIE — Indirect Formulation*

Referring to Fig. 8.4, for a source point $\boldsymbol{\xi} \in B$ (with bounding surface ∂B), one has the usual indirect BIE:

$$\phi(\boldsymbol{\xi}) = \int_{\partial B} \frac{\nu(\mathbf{y})}{4\pi r(\boldsymbol{\xi}, \mathbf{y})\epsilon} ds(\mathbf{y}) \tag{8.1}$$

where $\mathbf{y}$ is a field point, ϕ is the potential, $\mathbf{r}(\boldsymbol{\xi}, \mathbf{y}) = \mathbf{y} - \boldsymbol{\xi}$, $r = |\mathbf{r}|$, ϵ is the dielectric constant of the medium, ds is the area of an infinitesimal surface element on ∂B and ν is the (unknown) surface density function on ∂B.

8.2.1.2. *Gradient BIE — Indirect Formulation*

Taking the gradient of ϕ at the source point $\boldsymbol{\xi}$ results in:

$$\boldsymbol{\nabla}_{\boldsymbol{\xi}}\phi(\boldsymbol{\xi}) = \int_{\partial B} \frac{\nu(\mathbf{y})}{4\pi\epsilon}\boldsymbol{\nabla}_{\boldsymbol{\xi}}\left(\frac{1}{r(\boldsymbol{\xi},\mathbf{y})}\right) ds(\mathbf{y}) = \int_{\partial B} \frac{\nu(\mathbf{y})\mathbf{r}(\boldsymbol{\xi},\mathbf{y})}{4\pi r^3(\boldsymbol{\xi},\mathbf{y})\epsilon} ds(\mathbf{y}). \quad (8.2)$$

Alternatively, one can write Eq. (8.2) as:

$$\frac{\partial\phi}{\partial\xi_k}(\boldsymbol{\xi}) = \int_{\partial B} \frac{\nu(\mathbf{y})(y_k - \xi_k)}{4\pi r^3(\boldsymbol{\xi},\mathbf{y})\epsilon} ds(\mathbf{y}) \quad (8.3)$$

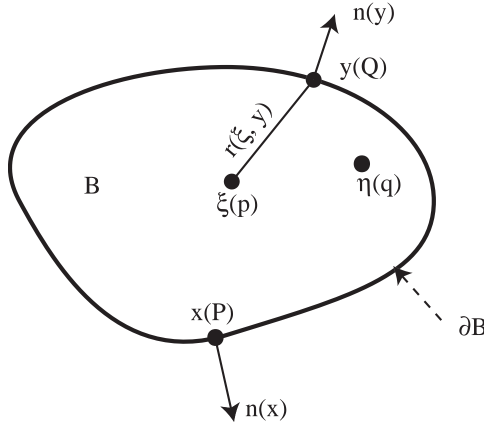

Fig. 8.4. Notation used in boundary integral equations (from Ref. 28).

Note that, in general, the function $\nu(\mathbf{y})$ is not the charge density. It becomes equal to the charge density when B is the infinite region exterior to the conductors. This is discussed in Sec. 8.2.2.

8.2.2. *BIEs in Infinite Region Containing Two Thin Conducting Plates*

Now consider the situation shown in Fig. 8.5. Of interest is the solution of the following Dirichlet problem for Laplace's equation:

$$\nabla^2\phi(\mathbf{x}) = 0, \quad \mathbf{x} \in B, \quad \phi(\mathbf{x}) \text{ prescribed for } \mathbf{x} \in \partial B \quad (8.4)$$

where B is now the region *exterior* to the two plates. The unit normal $\mathbf{n}$ to ∂B is defined to point away from B (*i.e.*, into a plate).

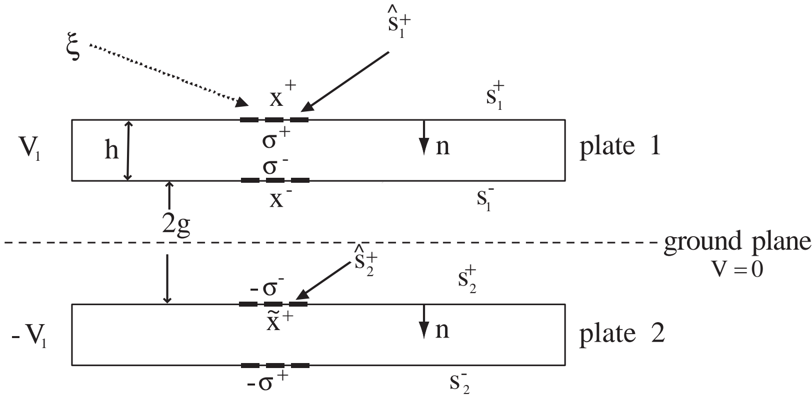

Fig. 8.5. Parallel plate capacitor with two plates (from Ref. 28).

8.2.2.1. *Regular BIE — Source Point Approaching a Plate Surface* s_1^+

As $\boldsymbol{\xi} \to \mathbf{x}^+ \in \hat{s_1}^+ \in s_1^+$ (see Fig. 8.5), one has:

$$\phi(\mathbf{x}^+) = \int_{s_1^+ - \hat{s_1}^+} \frac{\beta(\mathbf{y})}{4\pi r(\mathbf{x}^+, \mathbf{y})\epsilon} ds(\mathbf{y}) + \int_{\hat{s_1}^+} \frac{\beta(\mathbf{y})}{4\pi r(\mathbf{x}^+, \mathbf{y})\epsilon} ds(\mathbf{y}) + \int_{s_2^+} \frac{\beta(\mathbf{y})}{4\pi r(\mathbf{x}^+, \mathbf{y})\epsilon} ds(\mathbf{y}). \quad (8.5)$$

Here $\beta(\mathbf{y}) = \sigma(\mathbf{y}^+) + \sigma(\mathbf{y}^-)$, where σ is now the charge density at a point on a plate surface. The second integral above is weakly singular, while the rest are usually regular. It should be noted, however, that the last integral above becomes nearly weakly singular when both h and g are small.

A similar equation can be written for $\mathbf{x}^+ \in s_2^+$. For the case shown in Fig. 8.5, however, this is not necessary since $\beta(\mathbf{y})$ is equal and opposite on the two plates. Therefore, for this case, Eq. (8.5) is sufficient to solve for β on both the plates!

8.2.2.2. *Gradient BIE — Source Point Approaching a Plate Surface* s_1^+

It is first noted that for $\mathbf{x}^+ \in s_k^+ \cup s_k^-, \ k = 1, 2$:

$$\sigma(\mathbf{x}) = \epsilon \frac{\partial \phi}{\partial n}(\mathbf{x}) = \epsilon \mathbf{n}(\mathbf{x}) \cdot [\boldsymbol{\nabla}_{\boldsymbol{\xi}} \phi(\boldsymbol{\xi})]_{\boldsymbol{\xi}=\mathbf{x}}. \quad (8.6)$$

Consider the limit $\boldsymbol{\xi} \rightarrow \mathbf{x}^+ \in \hat{s_1}^+ \in s_1^+$. It is important to realize that this limit is meaningless for a point $\mathbf{x}$ on the edge of a plate, since the charge density is singular on its edges. One has:

$$\sigma(\mathbf{x}^+) = \int_{s_1^+ - \hat{s_1}^+} \frac{\beta(\mathbf{y})\mathbf{r}(\mathbf{x}^+, \mathbf{y}) \cdot \mathbf{n}(\mathbf{x}^+)}{4\pi r^3(\mathbf{x}^+, \mathbf{y})} ds(\mathbf{y})$$

$$+ \int_{\hat{s_1}^+} \frac{\mathbf{r}(\mathbf{x}^+, \mathbf{y}) \cdot [\beta(\mathbf{y})\mathbf{n}(\mathbf{x}^+) - \beta(\mathbf{x}^+)\mathbf{n}(\mathbf{y})]}{4\pi r^3(\mathbf{x}^+, \mathbf{y})} ds(\mathbf{y})$$

$$+ \frac{\beta(\mathbf{x}^+)}{4\pi} \Omega(\hat{s_1}^+, \mathbf{x}^+) + \int_{s_2^+} \frac{\beta(\mathbf{y})\mathbf{r}(\mathbf{x}^+, \mathbf{y}) \cdot \mathbf{n}(\mathbf{x}^+)}{4\pi r^3(\mathbf{x}^+, \mathbf{y})} ds(\mathbf{y}). \quad (8.7)$$

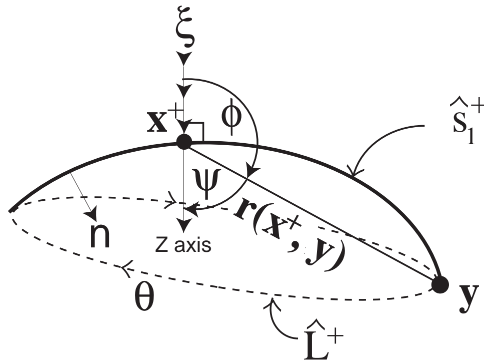

Fig. 8.6. Line integral for evaluation of solid angle (from Ref. 28).

In the above, the solid angle subtended by the surface element $\hat{s_1}^+$ at the point $\mathbf{x}^+$ is (see Ref. 30 and Fig. 8.6):

$$\Omega(\hat{s_1}^+, \mathbf{x}^+) = ⨎_{\hat{s_1}^+} \frac{\mathbf{r}(\mathbf{x}^+, \mathbf{y}) \cdot \mathbf{n}(\mathbf{y})}{r^3(\mathbf{x}^+, \mathbf{y})} ds(\mathbf{y}) = \int_0^{2\pi} [1 - \cos(\psi(\theta))] d\theta \quad (8.8)$$

where the symbol ⨎ denotes the Finite Part (FP) of the integral in the sense of Mukherjee Refs. 31 and 32.

Equations (8.7) and (8.8) give the final equation:

$$\frac{1}{2}[\sigma(\mathbf{x}^+) - \sigma(\mathbf{x}^-)] = \int_{s_1^+ - \hat{s_1}^+} \frac{\beta(\mathbf{y})\mathbf{r}(\mathbf{x}^+, \mathbf{y}) \cdot \mathbf{n}(\mathbf{x}^+)}{4\pi r^3(\mathbf{x}^+, \mathbf{y})} ds(\mathbf{y}) \tag{8.9}$$

$$+ \int_{\hat{s_1}^+} \frac{\mathbf{r}(\mathbf{x}^+, \mathbf{y}) \cdot [\beta(\mathbf{y})\mathbf{n}(\mathbf{x}^+) - \beta(\mathbf{x}^+)\mathbf{n}(\mathbf{y})]}{4\pi r^3(\mathbf{x}^+, \mathbf{y})} ds(\mathbf{y})$$

$$- \frac{\beta(\mathbf{x}^+)}{4\pi} \int_0^{2\pi} \cos(\psi(\theta)) d\theta + \int_{s_2^+} \frac{\beta(\mathbf{y})\mathbf{r}(\mathbf{x}^+, \mathbf{y}) \cdot \mathbf{n}(\mathbf{x}^+)}{4\pi r^3(\mathbf{x}^+, \mathbf{y})} ds(\mathbf{y}).$$

Here (see Fig. 8.6), a local coordinate system (x, y, z) is set up with the origin at $\mathbf{x}^+$ such that the positive z axis intersects the surface $\hat{s_1}^+$. Now, ψ is the angle between the positive z axis and $\mathbf{r}(\mathbf{x}^+, \mathbf{y})$ with $\mathbf{y} \in \hat{L}^+$, and θ the angle between the positive x axis and the projection of $\mathbf{r}(\mathbf{x}^+, \mathbf{y})$ in the xy plane.

In the above, the second integral on the right hand side is weakly singular, while the rest are usually regular. The last integral above, however, becomes nearly strongly singular if both the thickness h and the gap g are small. Once β is known on both plates, Eq. (8.9) can be used, *as a post-processing step*, to obtain σ^+ and σ^- on both plates.

8.2.3. *Boundary Integral Equations in the Lagrangian Formulation*

The Boundary Integral Equations (8.5) and (8.9), in a Lagrangian framework, are presented next.

From Nanson's,[33] one has:

$$\mathbf{n} ds = J\mathbf{N} \cdot \mathbf{F}^{-1} dS. \tag{8.10}$$

where $\mathbf{n}$ and $\mathbf{N}$ are unit normal vectors to ∂b and ∂B, at generic points $\mathbf{x}$ and $\mathbf{X}$, respectively, $\mathbf{F} = \partial \mathbf{x}/\partial \mathbf{X}$ is the deformation gradient, $J = det(\mathbf{F})$ and dS is an area element on ∂B. Here, $\mathbf{X}$ and $\mathbf{x}$ denote coordinates in the undeformed and deformed configurations, respectively.

From Eq. (8.10):

$$ds = J|\mathbf{N} \cdot \mathbf{F}^{-1}| dS \tag{8.11}$$

Next, define Σ, the charge density per unit undeformed surface area. Since $\Sigma dS = \sigma ds$, one has:

$$\Sigma = J\sigma|\mathbf{N} \cdot \mathbf{F}^{-1}| \tag{8.12}$$

Also, define:

$$B = \Sigma^+ + \Sigma^- \tag{8.13}$$

8.2.3.1. *Lagrangian Version of the Regular BIE*

Using the above, the Lagrangian version of Eq. (8.5) becomes:

$$\phi(\mathbf{x}^+(\mathbf{X}^+)) = \int_{S_1^+ - \hat{S_1}^+} \frac{B(\mathbf{Y})dS(\mathbf{Y})}{4\pi R(\mathbf{X}^+, \mathbf{Y})\epsilon} + \int_{\hat{S_1}^+} \frac{B(\mathbf{Y})dS(\mathbf{Y})}{4\pi R(\mathbf{X}^+, \mathbf{Y})\epsilon} + \int_{S_2^+} \frac{B(\mathbf{Y})dS(\mathbf{Y})}{4\pi R(\mathbf{X}^+, \mathbf{Y})\epsilon} \tag{8.14}$$

where:

$$\mathbf{r}(\mathbf{x}(\mathbf{X}), \mathbf{y}(\mathbf{Y})) \equiv \mathbf{R}(\mathbf{X}, \mathbf{Y}) = \mathbf{y}(\mathbf{Y}) - \mathbf{x}(\mathbf{X}) = \mathbf{Y} + \mathbf{u}(\mathbf{Y}) - \mathbf{X} - \mathbf{u}(\mathbf{X}) \tag{8.15}$$

$$r(\mathbf{x}(\mathbf{X}), \mathbf{y}(\mathbf{Y})) \equiv R(\mathbf{X}, \mathbf{Y}) = |\mathbf{R}(\mathbf{X}, \mathbf{Y})| \tag{8.16}$$

with $\mathbf{u}$ denoting the displacement at a point in B.

Also:

$$\mathbf{h}(\mathbf{y}) = -\frac{\sigma^2(\mathbf{y})}{2\epsilon}\mathbf{n} \tag{8.17}$$

$$\int_{\partial B} \mathbf{H} dS = \int_{\partial b} \mathbf{h} ds \tag{8.18}$$

where $\mathbf{h}$ and $\mathbf{H}$ are the tractions per unit deformed and undeformed surface areas, respectively. Using Eqs. (8.17), (8.18), (8.10) and (8.12), one gets:

$$\mathbf{H} = -\frac{J\sigma^2 \mathbf{N} \cdot \mathbf{F}^{-1}}{2\epsilon} = -\frac{\Sigma^2}{2J\epsilon} \frac{\mathbf{N} \cdot \mathbf{F}^{-1}}{|\mathbf{N} \cdot \mathbf{F}^{-1}|^2}. \tag{8.19}$$

8.2.3.2. *Lagrangian Version of the Gradient BIE*

The Lagrangian version of Eq. (8.9) is derived next.

The first, second and third terms on the right hand side of Eq. (8.9) are written as:

$$\text{First term} = \int_{S_1^+ - \hat{S_1}^+} \frac{B(\mathbf{Y})\mathbf{R}(\mathbf{X}^+,\mathbf{Y}) \bullet J(\mathbf{X}^+)(\mathbf{N}\cdot\mathbf{F}^{-1})(\mathbf{X}^+)}{4\pi R^3(\mathbf{X}^+,\mathbf{Y})J(\mathbf{X}^+)|\mathbf{N}\cdot\mathbf{F}^{-1}|(\mathbf{X}^+)} dS(\mathbf{Y}) \tag{8.20}$$

$$\begin{aligned}\text{Second term} = &\int_{\hat{S_1}^+} \frac{\mathbf{R}(\mathbf{X}^+,\mathbf{Y}) \bullet [B(\mathbf{Y})J(\mathbf{X}^+)(\mathbf{N}\cdot\mathbf{F}^{-1})(\mathbf{X}^+)]}{4\pi R^3(\mathbf{X}^+,\mathbf{Y})J(\mathbf{X}^+)|\mathbf{N}\cdot\mathbf{F}^{-1}|(\mathbf{X}^+)} dS(\mathbf{Y})\\ &- \int_{\hat{S_1}^+} \frac{\mathbf{R}(\mathbf{X}^+,\mathbf{Y}) \bullet [B(\mathbf{X}^+)J(\mathbf{Y})(\mathbf{N}\cdot\mathbf{F}^{-1})(\mathbf{Y})]}{4\pi R^3(\mathbf{X}^+,\mathbf{Y})J(\mathbf{X}^+)|\mathbf{N}\cdot\mathbf{F}^{-1}|(\mathbf{X}^+)} dS(\mathbf{Y})\end{aligned} \tag{8.21}$$

$$\text{Third term} = -\frac{B(\mathbf{X}^+)}{4\pi J(\mathbf{X}^+)|\mathbf{N}\cdot\mathbf{F}^{-1}|(\mathbf{X}^+)} \int_0^{2\pi} \cos(\psi(\theta))d\theta. \tag{8.22}$$

The fourth term is treated in the same way as the first.

One can now multiply the entire equation by $J(\mathbf{X}^+)|\mathbf{N}\cdot\mathbf{F}^{-1}|(\mathbf{X}^+)$, use the mid-plane values for (membrane assumption) $\mathbf{F}(\mathbf{X}^+) = \mathbf{F}(\mathbf{X}^-)$, and use the fact that $\mathbf{N}(\mathbf{X}^+) = -\mathbf{N}(\mathbf{X}^-)$. The resulting equation has the form:

$$\begin{aligned}&\frac{1}{2}[\Sigma(\mathbf{X}^+) - \Sigma(\mathbf{X}^-)] =\\ &\int_{S_1^+ - \hat{S_1}^+} \frac{B(\mathbf{Y})\mathbf{R}(\mathbf{X}^+,\mathbf{Y}) \bullet J(\mathbf{X}^+)(\mathbf{N}\cdot\mathbf{F}^{-1})(\mathbf{X}^+)}{4\pi R^3(\mathbf{X}^+,\mathbf{Y})} dS(\mathbf{Y})\\ &+ \int_{\hat{S_1}^+} \frac{\mathbf{R}(\mathbf{X}^+,\mathbf{Y}) \bullet [B(\mathbf{Y})J(\mathbf{X}^+)(\mathbf{N}\cdot\mathbf{F}^{-1})(\mathbf{X}^+)]}{4\pi R^3(\mathbf{X}^+,\mathbf{Y})}\\ &- \int_{\hat{S_1}^+} \frac{\mathbf{R}(\mathbf{X}^+,\mathbf{Y}) \bullet [B(\mathbf{X}^+)J(\mathbf{Y})(\mathbf{N}\cdot\mathbf{F}^{-1})(\mathbf{Y})]}{4\pi R^3(\mathbf{X}^+,\mathbf{Y})} dS(\mathbf{Y})\\ &- \frac{B(\mathbf{X}^+)}{4\pi} \int_0^{2\pi} \cos(\psi(\theta))d\theta\\ &+ \int_{S_2^+} \frac{B(\mathbf{Y})\mathbf{R}(\mathbf{X}^+,\mathbf{Y}) \bullet J(\mathbf{X}^+)(\mathbf{N}\cdot\mathbf{F}^{-1})(\mathbf{X}^+)}{4\pi R^3(\mathbf{X}^+,\mathbf{Y})} dS(\mathbf{Y}).\end{aligned} \tag{8.23}$$

Please note that the second and third terms above must be evaluated together in a numerical implementation.

The integral $I = \int_0^{2\pi} \cos(\psi(\theta))d\theta$ can be evaluated from a Lagrangian approach as follows. Referring to Fig. 8.7, and Eq. (8.15), one has:

$$\xi = r\sin(\psi)\cos(\theta), \quad \eta = r\sin(\psi)\sin(\theta), \quad \zeta = r\cos(\psi) \tag{8.24}$$

$$\mathbf{R}(\mathbf{X}^+, \mathbf{Y}) = \mathbf{r}(\mathbf{x}^+, \mathbf{y}) = \xi\mathbf{i} + \eta\mathbf{j} + \zeta\mathbf{k} \tag{8.25}$$

Now, for any point $\mathbf{y}$ on the boundary of $\hat{s}_1{}^+$ (and, therefore, $\mathbf{Y}$ on the boundary of $\hat{S}_1{}^+$) one has:

$$\mathbf{R}(\mathbf{X}^+, \mathbf{Y}) = \mathbf{Y} + \mathbf{u}(\mathbf{Y}) - \mathbf{X}^+ - \mathbf{u}(\mathbf{X}^+) \tag{8.26}$$

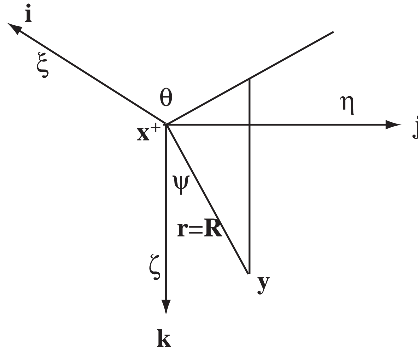

Fig. 8.7. Spherical polar coordinates for evaluation of the solid angle (from Ref. 28).

The algorithm for evaluating the integral I is described below.

(1) Given $X_1^+, X_2^+, X_3^+, \Theta, Y_2 = f(Y_1)$, find Y_1, Y_2, Y_3 from the equations:

$$Y_2 = f(Y_1), \quad Y_2 = (Y_1 - X_1^+)\tan(\Theta) + X_2^+, \quad Y_3 = X_3^+ \tag{8.27}$$

Here $Y_2 = f(Y_1)$ is the equation of the boundary of $\hat{S}_1{}^+$ and the angle Θ at $\mathbf{X}^+$ corresponds to θ at $\mathbf{x}^+$.

(2) Find $\mathbf{R}(\mathbf{X}^+, \mathbf{Y})$ from Eq. (8.26).

(3) Now obtain the corresponding values of the angles ψ and θ from:

$$\cos(\psi) = \frac{\mathbf{R}\cdot\mathbf{k}}{R}, \quad \cos(\theta) = \frac{\mathbf{R}\cdot\mathbf{i}}{R\sin(\psi)}, \quad \sin(\theta) = \frac{\mathbf{R}\cdot\mathbf{j}}{R\sin(\psi)} \tag{8.28}$$

(4) Finally:

$$I = \int_0^{2\pi} \cos(\psi(\Theta))\frac{d\theta}{d\Theta}d\Theta \tag{8.29}$$

The quantity $d\theta/d\Theta$ is determined as follows.

(5) First, the quantities $\partial Y_k/\partial\Theta,\ k = 1, 2, 3$, are obtained from the differentiated versions of Eq. (8.27) with respect to Θ; *i.e.*, from the equations:

$$\frac{\partial Y_2}{\partial\Theta} = f^{'}(Y_1)\frac{\partial Y_1}{\partial\Theta}, \quad \frac{\partial Y_2}{\partial\Theta} = \frac{\partial Y_1}{\partial\Theta}\tan(\Theta) + (Y_1 - X_1^+)\sec^2(\Theta),$$
$$\frac{\partial Y_3}{\partial\Theta} = 0. \tag{8.30}$$

Next, it is noted that $\partial y_i/\partial\Theta$ and $\partial x_i/\partial\Theta$ are:

$$\frac{\partial y_i}{\partial\Theta} = F_{ik}(Y)\frac{\partial Y_k}{\partial\Theta}, \quad \frac{\partial x_i}{\partial\Theta} = F_{ik}(X)\frac{\partial X_k}{\partial\Theta} = 0. \tag{8.31}$$

Finally, differentiate the equation:

$$\tan(\theta) = \frac{y_2 - x_2^+}{y_1 - x_1^+} \tag{8.32}$$

to get:

$$\frac{d\theta}{d\Theta} = \frac{(y_1 - x_1^+)\frac{\partial y_2}{\partial\Theta} - (y_2 - x_2^+)\frac{\partial y_1}{\partial\Theta}}{\sec^2(\theta)(y_1 - x_1^+)^2}. \tag{8.33}$$

8.2.3.3. *Two Plates Close Together*

For cases in which the gap $2g$ between the plates in Fig. 8.5 is also small, the last integral on the right hand side of Eq. (8.5) must be treated as nearly weakly singular. In this case, this integral should be written as:

$$\int_{s_2^+} \frac{\beta(\mathbf{y})}{4\pi r(\mathbf{x}^+,\mathbf{y})\epsilon}ds(\mathbf{y}) = \int_{s_2^+ - \hat{s_2}^+} \frac{\beta(\mathbf{y})}{4\pi r(\mathbf{x}^+,\mathbf{y})\epsilon}ds(\mathbf{y})$$
$$+ \int_{\hat{s_2}^+} \frac{\beta(\mathbf{y}) - \beta(\tilde{\mathbf{x}}^+)}{4\pi r(\mathbf{x}^+,\mathbf{y})\epsilon}ds(\mathbf{y}) + \frac{\beta(\tilde{\mathbf{x}}^+)}{4\pi\epsilon}\int_{s_2^+}\frac{1}{r(\mathbf{x}^+,\mathbf{y})}ds(\mathbf{y}) \tag{8.34}$$

where $\tilde{\mathbf{x}}^+ \in \hat{s_2}^+$. The first and second integrals on the right hand side of Eq. (8.34) are regular. (The second integral is $\mathcal{O}(\tilde{r}/r)$ where $\tilde{r} = |\mathbf{y} - \tilde{\mathbf{x}}^+|$. As $\tilde{r} \to 0$, $r \to 2g + h$, so that this integrand $\to 0$.) The last integral is nearly singular. A procedure for accurate evaluation of nearly singular integrals is presented in Ref. 20 and also in Sec. 8.5 of the present chapter.

Also, the last integral on the right hand side of Eq. (8.9) now becomes nearly strongly singular. This integral, called J, can be evaluated as follows. One can write:

$$
\begin{aligned}
J = & \int_{s_2^+ - \hat{s_2}^+} \frac{\beta(\mathbf{y})\mathbf{r}(\mathbf{x}^+, \mathbf{y}) \cdot \mathbf{n}(\mathbf{x}^+)}{4\pi r^3(\mathbf{x}^+, \mathbf{y})} ds(\mathbf{y}) \\
& + \int_{\hat{s_2}^+} \frac{\mathbf{r}(\mathbf{x}^+, \mathbf{y}) \cdot [\beta(\mathbf{y})\mathbf{n}(\mathbf{x}^+) - \beta(\tilde{\mathbf{x}}^+)\mathbf{n}(\mathbf{y})]}{4\pi r^3(\mathbf{x}^+, \mathbf{y})} ds(\mathbf{y}) \\
& + \frac{\beta(\tilde{\mathbf{x}}^+)}{4\pi} \Omega(\hat{s_2}^+, \mathbf{x}^+)
\end{aligned} \tag{8.35}
$$

where (see Fig. 8.6):

$$
\Omega(\hat{s_2}^+, \mathbf{x}^+) = \int_{\hat{s_2}^+} \frac{\mathbf{r}(\mathbf{x}^+, \mathbf{y}) \cdot \mathbf{n}(\mathbf{y})}{r^3(\mathbf{x}^+, \mathbf{y})} ds(\mathbf{y}) = \int_0^{2\pi} [1 - \cos(\psi(\theta))] d\theta \tag{8.36}
$$

It is noted that, in this case, the point $\mathbf{x}^+$ is slightly above $\hat{s_2}^+$ and that the second term in Eq. (8.36) denotes a "nearly FP" integral.

The idea of regularizing Eq. (8.35) with $\beta(\tilde{\mathbf{x}}^+)$ has been inspired by earlier work on evaluation of nearly singular integrals Ref. 34.

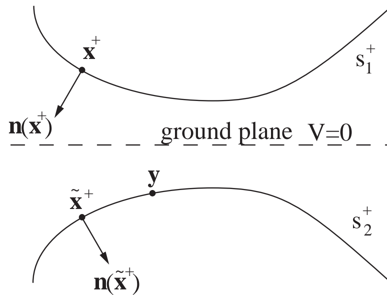

Fig. 8.8. Symmetric deformation of two plates (from Ref. 28).

Let the integrals on the right hand side of Eq. (8.35) be called J_1, J_2, J_3. Each of the three integrals is regular. The fact that the second integral J_2 is regular can be proved as follows.

It is assumed that the two plates always remain symmetric with respect to the ground plane, even after deformation (see Fig. 8.8). Their equations, therefore, are of the form $x_3 = \pm f(x_1, x_2)$. One now has:

$$\mathbf{n}(\mathbf{x}^+) \propto -\mathbf{k} + \mathbf{i}f_{,1} + \mathbf{j}f_{,2}, \qquad \mathbf{n}(\tilde{\mathbf{x}}^+) \propto -\mathbf{k} - \mathbf{i}f_{,1} - \mathbf{j}f_{,2} \tag{8.37}$$

As $\mathbf{y} \to \tilde{\mathbf{x}}^+$,

$$[\beta(\mathbf{y})\mathbf{n}(\mathbf{x}^+) - \beta(\tilde{\mathbf{x}}^+)\mathbf{n}(\mathbf{y})] \propto \mathbf{k}[\beta(\tilde{\mathbf{x}}^+) - \beta(\mathbf{y})] + [\mathbf{i}a + \mathbf{j}b][\beta(\tilde{\mathbf{x}}^+) + \beta(\mathbf{y})] \tag{8.38}$$

where $\mathbf{i}, \mathbf{j}, \mathbf{k}$ are Cartesian unit vectors and a and b are some numbers.

As $\mathbf{y} \to \tilde{\mathbf{x}}^+$, $\mathbf{r}(\mathbf{x}^+, \mathbf{y}) \propto -\mathbf{k}$, so that the integrand of J_2 is $\mathcal{O}(\tilde{r}/r^2)$ where $\tilde{r} = |\mathbf{y} - \tilde{\mathbf{x}}^+|$. In this limit, $\tilde{r} \to 0,\ \ r \to 2g + h$, so that the integrand of $J_2 \to 0$.

The Lagrangian version of the above equations are not repeated here in the interest of brevity. They are straightforward and very similar to those given in Secs. 2.3.1 and 2.3.2.

8.3. Mechanical Problem in the Elastic Plate

Non-linear deformation of plates, without initial in-plane forces, are discussed in this section. The plates are square (side = L), linearly elastic, and are of uniform rectangular cross-section (thickness h). The boundary condition considered here is a plate with all edges clamped. Also, the edges are immovable, *i.e.*, $u = v = 0$ on all edges of the plate. Here $u(x, y)$ and $v(x, y)$ are the in-plane and $w(x, y)$ the transverse displacement of the mid-plane of the plate. The force distribution (per unit area) $\mathbf{H}(x, y)$ is applied to the plate.

8.3.1. *The Model*

The kinematic equations adopted here are those for a von Karman plate (Refs. 35 and 36):

$$\begin{bmatrix} \epsilon_{xx} \\ \epsilon_{yy} \\ \gamma_{xy} \end{bmatrix} = \begin{bmatrix} u_{,x} + \frac{1}{2}(w_{,x})^2 \\ v_{,y} + \frac{1}{2}(w_{,y})^2 \\ u_{,y} + v_{,x} + w_{,x}w_{,y} \end{bmatrix}, \qquad \begin{bmatrix} \kappa_{xx} \\ \kappa_{yy} \\ \kappa_{xy} \end{bmatrix} = \begin{bmatrix} -w_{,xx} \\ -w_{,yy} \\ -2w_{,xy} \end{bmatrix} \tag{8.39}$$

where $[\epsilon] = [\epsilon_{xx},\ \epsilon_{yy}\ \gamma_{xy}]^T$ are the in-plane strains (measured at the mid-plane), and $[\kappa] = [\kappa_{xx}, \kappa_{yy}, \kappa_{xy}]^T$ are the curvatures and the twist.

The constitutive equations are:

$$[N] = H^{(I)}[C][\epsilon], \quad [M] = H^{(O)}[C][\kappa] \tag{8.40}$$

where $[N] = [N_{xx}, N_{yy}, N_{xy}]^T = h[\sigma_{xx}, \sigma_{yy}, \sigma_{xy}]^T$ are the in-plane forces per unit length, σ_{ij} are the components of stress and $[M] = [M_{xx}, M_{yy}, M_{xy}]^T$ are the bending and twisting moments. Also:

$$C = \begin{bmatrix} 1 & \nu & 0 \\ \nu & 1 & 0 \\ 0 & 0 & \frac{1}{2}(1-\nu) \end{bmatrix}, \quad H^{(I)} = \frac{Eh}{1-\nu^2}, \quad H^{(O)} = \frac{Eh^3}{12(1-\nu^2)} \tag{8.41}$$

with ν the Poisson's ratio of the plate material.

The membrane strain energy $\mathcal{E}^{(I)}$, the bending strain energy $\mathcal{E}^{(O)}$, and the work done W are (From Ref. 37):

$$\mathcal{E}^{(I)} = \frac{1}{2}\int_{\Delta} [N_x\epsilon_{xx} + N_y\epsilon_{yy} + N_{xy}\gamma_{xy}]dxdy \tag{8.42}$$

$$\mathcal{E}^{(O)} = \frac{1}{2}\int_{\Delta} [M_x\kappa_{xx} + M_y\kappa_{yy} + M_{xy}\kappa_{xy}]dxdy \tag{8.43}$$

$$W = \int_{\Delta} [H_x u + H_y v + H_z w]dxdy \tag{8.44}$$

where Δ is the area of the plate surface.

Using Eqs. (8.39)–(8.41), the energy expressions Eqs. (8.42)–(8.43) can be written in terms of the plate parameters E, ν, h and the displacement derivatives. These expressions are available in Ref. 37 on pages 313 and 95, respectively.

8.3.2. *FEM Model for Plates with Immovable Edges*

FEM discretization. Each plate element has four corner nodes with 6 degrees of freedom at each node. These are $u, v, w, w_{,x}, w_{,y}, w_{,xy}$. For each element, one has:

$$\begin{bmatrix} u \\ v \\ w \end{bmatrix} = \begin{bmatrix} N^{(I)} & 0 \\ 0 & N^{(O)} \end{bmatrix} \begin{bmatrix} q^{(I)} \\ q^{(O)} \end{bmatrix} \tag{8.45}$$

with:

$$[N^{(I)}(x,y)] = \begin{bmatrix} N_1 & 0 & N_2 & 0 & N_3 & 0 & N_4 & 0 \\ 0 & N_1 & 0 & N_2 & 0 & N_3 & 0 & N_4 \end{bmatrix},$$

$$[N^{(O)}(x,y)] = [P_1, P_2, ..., P_{16}] \tag{8.46}$$

$$[q^{(I)}] = [u_1, v_1, ..., u_4, v_4]^T,$$

$$[q^{(O)}] = [w_1, (w_{,x})_1, (w_{,y})_1, (w_{,xy})_1, ..., w_4, (w_{,x})_4, (w_{,y})_4, (w_{,xy})_4]^T \tag{8.47}$$

Here N_k and P_k are bilinear interpolation functions (Ref. 10) and $[q^{(I)}]$ and $[q^{(O)}]$ contain the appropriate nodal degrees of freedom.

Define:

$$[D] = \begin{bmatrix} w_{,x} & 0 \\ 0 & w_{,y} \\ w_{,y} & w_{,x} \end{bmatrix}, \quad [G] = \begin{bmatrix} N^{(O)}_{,x} \\ N^{(O)}_{,y} \end{bmatrix} \tag{8.48}$$

$$[B^{(I)}] = \begin{bmatrix} N_{1,x} & 0 & N_{2,x} & 0 & N_{3,x} & 0 & N_{4,x} & 0 \\ 0 & N_{1,y} & 0 & N_{2,y} & 0 & N_{3,y} & 0 & N_{4,y} \\ N_{1,y} & N_{1,x} & N_{2,y} & N_{2,x} & N_{3,y} & N_{3,x} & N_{4,y} & N_{4,x} \end{bmatrix},$$

$$[B^{(O)}] = -\begin{bmatrix} N^{(O)}_{,xx} \\ N^{(O)}_{,yy} \\ 2N^{(O)}_{,xy} \end{bmatrix} \tag{8.49}$$

Substituting the interpolations Eq. (8.45) into the expressions Eqs. (8.42)–(8.44), and minimizing the potential energy, results in the element level equations:

$$\begin{bmatrix} K^{(I)} & 0 \\ 0 & K^{(O)} \end{bmatrix} \begin{bmatrix} q^{(I)} \\ q^{(O)} \end{bmatrix} + \begin{bmatrix} 0 & K^{(IO)} \\ 2K^{(IO)T} & K^{(NI)} \end{bmatrix} \begin{bmatrix} q^{(I)} \\ q^{(O)} \end{bmatrix} = \begin{bmatrix} P \end{bmatrix} \tag{8.50}$$

The various submatrices and vector in Eq. (8.50) are:

$$[K^{(I)}] = H^{(I)} \int_{\Delta^{(e)}} [B^{(I)}]^T [C][B^{(I)}] dxdy,$$

$$[K^{(O)}] = H^{(O)} \int_{\Delta^{(e)}} [B^{(O)}]^T [C][B^{(O)}] dxdy \tag{8.51}$$

$$[K^{(IO)}] = \frac{H^{(I)}}{2} \int_{\Delta^{(e)}} [B^{(I)}]^T [C][D][G] dxdy,$$

$$[K^{(NI)}] = \frac{H^{(I)}}{2} \int_{\Delta^{(e)}} ([D][G])^T [C][D][G] dxdy \tag{8.52}$$

$$[P] = \int_{\Delta^{(e)}} \begin{bmatrix} N^{(I)} & 0 \\ 0 & N^{(O)} \end{bmatrix}^T \begin{bmatrix} \overline{H}_x \\ \overline{H}_y \\ \overline{H}_z \end{bmatrix} dxdy \tag{8.53}$$

where $\Delta^{(e)}$ is the area of a finite element. In Eq. (8.53), $[\overline{H}]$ is the resultant traction on the mid-surface of the plate.

The global version of Eq. (8.50) is now obtained in the usual way.

Note that the in-plane and out-of-plane (bending) matrices $[K^{(I)}]$ and $[K^{(O)}]$ are $\propto h$ and h^3, respectively, the matrix $[K^{(IO)}] \propto Ah$ represents coupling between the in-plane and out-of-plane displacements, and the matrix $[K^{(NI)}] \propto A^2 h$ arises purely from the non-linear in-plane strains.

It is well known that for the linear theory $[K^{(O)}] << [K^{(I)}]$ as $h \to 0$. It is very interesting, however, to note that if A/h remains $\mathcal{O}(1)$, the bending matrix $[K^{(O)}]$, which arises from the linear theory, and the matrix $[K^{(NI)}]$ from the non-linear theory, remain of the same order as $h \to 0$. This fact has important consequences for the modeling of very thin plates (Ref. 3).

8.4. Schemes for Solving the Coupled Problem

A relaxation scheme and a Newton scheme to solve the coupled problem are next presented in a total Lagrangian framework.

8.4.1. *Lagrangian Relaxation Scheme for the Coupled Problem*

Consider, for simplicity, a thin conducting plate with a ground plane with $V = 0$. Figure 8.9 shows a schematic of the applied voltage history on this plate. The deformation history $\mathbf{u}(\mathbf{x}, t)$ of this plate is obtained by a combined BEM/FEM approach as described below.

The voltage history $V(t)$ is first decomposed into a series of steps — $V_1, V_2 = V_1 + \Delta V_1, ..., V_{n+1} = V_n + \Delta V_n$. Consider the first step with applied voltage V_1. The BEM problem is first solved in the region exterior to the plate, and the charge density $\Sigma_1^{(0)}$ and resultant traction $\overline{\mathbf{H}}_1^{(0)}$ are obtained on the plate surface. The FEM problem with applied traction $\overline{\mathbf{H}}_1^{(0)}$ is next solved for the plate, resulting in the calculation of the displacement field $\mathbf{u}_1^{(0)}$ in the plate. The BEM problem is next solved in the region exterior to the deformed plate by the Lagrangian approach (*i.e.*, using the undeformed plate surface). This calculation yields the next iterate of the charge density and traction, $\Sigma_1^{(1)}$ and $\overline{\mathbf{H}}_1^{(1)}$, respectively, on the plate surface. The next iterate of the displacement field in the plate, $\mathbf{u}_1^{(1)}$, is obtained

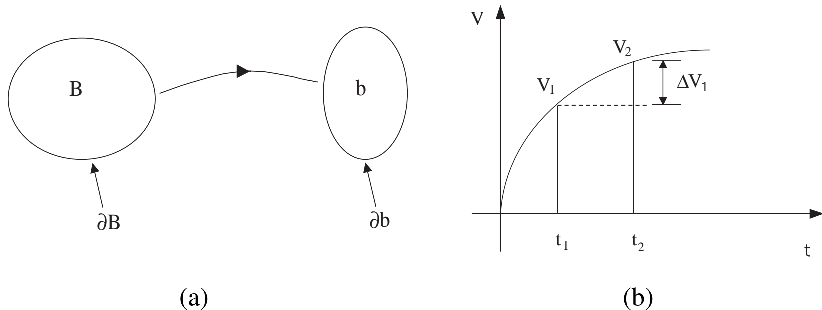

Fig. 8.9. (a) Deformation of body. (b) Voltage history (from Ref. 28).

next by solving the FEM problem in the plate with applied traction $\overline{\mathbf{H}}_1^{(1)}$. This iterative process is repeated until convergence. The converged values of the traction on the plate, and displacement field in the plate, at time t_1, are called $\overline{\mathbf{H}}_1$ and $\mathbf{u}_1$, respectively.

The next task is to proceed from time t_1 to t_2. To this end, the voltage increment ΔV_1 is first applied to the deformed configuration of the plate at time t_1. Solution of the corresponding BEM problem (using, again, the Lagrangian approach), yields the incremental charge density $\Delta\Sigma_1^{(0)}$ and incremental traction $\Delta\overline{\mathbf{H}}_1^{(0)}$. The displacement field $\mathbf{u}_2^{(0)}$ is obtained next by solving the FEM problem in the (undeformed) plate with the traction $\overline{\mathbf{H}}_2^{(0)} = \overline{\mathbf{H}}_1 + \Delta\overline{\mathbf{H}}_1^{(0)}$. The BEM problem is next solved with $V_2 = V_1 + \Delta V_1$. The result is the charge density $\Sigma_2^{(1)}$ and the traction $\overline{\mathbf{H}}_2^{(1)}$; followed by the FEM solution for $\mathbf{u}_2^{(1)}$. Again, this iterative process is continued until the converged values $\mathbf{u}_2$ and $\overline{\mathbf{H}}_2$ are obtained at time t_2.

The time step $t_2 - t_3$ is considered next, and so on, until the final time t_{n+1} is reached.

The algorithm employed for solving the coupled problem is outlined below.

(1) Apply V_1 to B.
Solve BEM problem on ∂B
Get charge density $\Sigma_1^{(0)}$ and traction $\overline{\mathbf{H}}_1^{(0)}$

(2) Solve FEM problem in B with traction $\overline{\mathbf{H}}_1^{(0)}$
Get displacement $\mathbf{u}_1^{(0)}$ on ∂B

(3) Set $k = 0$
Repeat

(4) Update ∂B, $\partial b_1^{(k)} = \partial B + \mathbf{u}_1^{(k)}$
Solve BEM problem on ∂B for $\partial b_1^{(k)}$ with V_1
Get charge density $\Sigma_1^{(k+1)}$ and traction $\overline{\mathbf{H}}_1^{(k+1)}$
(5) Solve FEM problem in B with traction $\overline{\mathbf{H}}_1^{(k+1)}$
Get displacement $\mathbf{u}_1^{(k+1)}$ on ∂B
(6) Update $k = k + 1$
Until convergence *i.e.*, $\frac{|w_1^{(k+1)} - w_1^{(k)}|}{|w_1^{(k)}|} \times 100 < tol$ and $\frac{|\Sigma_1^{(k+1)} - \Sigma_1^{(k)}|}{|\Sigma_1^{(k)}|} \times 100 < tol$

Now $t = t_1$. Get converged values $\mathbf{u}_1,\ \partial b_1 = \partial B + \mathbf{u}_1,\ \ \overline{\mathbf{H}}_1$
(7) Apply ΔV_1 to b_1
Solve BEM problem on ∂B for ∂b_1
Get charge density $\Delta\Sigma_1^{(0)}$, traction $\Delta\overline{\mathbf{H}}_1^{(0)}$
(8) Solve FEM problem in B with traction $\overline{\mathbf{H}}_2^{(0)} = \overline{\mathbf{H}}_1 + \Delta\overline{\mathbf{H}}_1^{(0)}$
Get displacement $\mathbf{u}_2^{(0)}$ on ∂B

(9) Set $k = 0$
Repeat
(10) Update ∂B, $\partial b_2^{(k)} = \partial B + \mathbf{u}_2^{(k)}$
Solve BEM problem on ∂B for $\partial b_2^{(k)}$ with $V_2 = V_1 + \Delta V_1$
Get charge density $\Sigma_2^{(k+1)}$ and traction $\overline{\mathbf{H}}_2^{(k+1)}$
(11) Solve FEM problem in B with traction $\overline{\mathbf{H}}_2^{(k+1)}$
Get displacement $\mathbf{u}_2^{(k+1)}$ on ∂B
(12) Update $k = k + 1$
Until convergence *i.e.*, $\frac{|w_2^{(k+1)} - w_2^{(k)}|}{|w_2^{(k)}|} \times 100 < tol$ and $\frac{|\Sigma_2^{(k+1)} - \Sigma_2^{(k)}|}{|\Sigma_2^{(k)}|} \times 100 < tol$

(13) Now $t = t_2$. Get converged values $\mathbf{u}_2,\ \partial b_2 = \partial B + \mathbf{u}_2,\ \overline{\mathbf{H}}_2$
(14) Proceed until t_{n+1}

8.4.2. *Newton Scheme for Solving the Coupled Problem*

The idea in this scheme is to solve the entire system of non-linear governing equations by using the Newton Method. The equations to be solved by the Newton method are the electrical domain BIE (8.14) and the mechanical domain FEM Eq. (8.50), with Eq. (8.23) as an auxiliary equation. The coupling equation (8.19) must also be used.

8.4.2.1. *Residuals and Their Gradients*

The appropriate residuals, as functions of **u** and B, as well as their gradients with respect to these variables, are given below.

The electrical residual R_E and its derivatives. The electrical residual R_E, and its derivatives with respect to B and **u** are:

$$R_E(\mathbf{u}, B) = \phi(\mathbf{X}^+) - \int_{S_1^+ - \hat{S_1}^+} \frac{B(\mathbf{Y})dS(\mathbf{Y})}{4\pi R(\mathbf{X}^+, \mathbf{Y})\epsilon} - \int_{\hat{S_1}^+} \frac{B(\mathbf{Y})dS(\mathbf{Y})}{4\pi R(\mathbf{X}^+, \mathbf{Y})\epsilon} - \int_{S_2^+} \frac{B(\mathbf{Y})dS(\mathbf{Y})}{4\pi R(\mathbf{X}^+, \mathbf{Y})\epsilon} \tag{8.54}$$

$$\frac{\partial R_E}{\partial B(\mathbf{X}^+)}(\mathbf{u}, B) = -\int_{\hat{S_1}^+} \frac{dS(\mathbf{Y})}{4\pi R(\mathbf{X}^+, \mathbf{Y})\epsilon}. \tag{8.55}$$

An alternative to Eq. (8.55) is to start from the discretized version of Eq. (8.54) and differentiate this equation with respect to the nodal value of B at the point $\mathbf{X}^+$.

Next, using:

$$\frac{\partial}{\partial \mathbf{u}(\mathbf{X})}\left(\frac{1}{R}\right) = \frac{\mathbf{R}}{R^3}, \quad \frac{\partial}{\partial \mathbf{u}(\mathbf{Y})}\left(\frac{1}{R}\right) = -\frac{\mathbf{R}}{R^3} \tag{8.56}$$

one has:

$$\begin{aligned}\frac{\partial R_E}{\partial \mathbf{u}(\mathbf{X}^+)}(\mathbf{u}, B) = &- \int_{S_1^+ - \hat{S_1}^+} \frac{B(\mathbf{Y})\mathbf{R}(\mathbf{X}^+, \mathbf{Y})dS(\mathbf{Y})}{4\pi R^3(\mathbf{X}^+, \mathbf{Y})\epsilon} \\ &- ⨍_{\hat{S_1}^+} \frac{B(\mathbf{Y})\mathbf{R}(\mathbf{X}^+, \mathbf{Y})dS(\mathbf{Y})}{4\pi R^3(\mathbf{X}^+, \mathbf{Y})\epsilon} \\ &- \int_{S_2^+} \frac{B(\mathbf{Y})\mathbf{R}(\mathbf{X}^+, \mathbf{Y})dS(\mathbf{Y})}{4\pi R^3(\mathbf{X}^+, \mathbf{Y})\epsilon} \\ &+ B(\mathbf{X}^+) ⨍_{\hat{S_1}^+} \frac{\mathbf{R}(\mathbf{X}^+, \mathbf{Y})dS(\mathbf{Y})}{4\pi R^3(\mathbf{X}^+, \mathbf{Y})\epsilon}.\end{aligned} \tag{8.57}$$

The first three terms on the right hand side of Eq. (8.57) are obtained by applying Eq. $(8.56)_1$ to Eq. (8.54), while the last one is obtained by applying Eq. $(8.56)_2$

and using $\partial R_E/\partial \mathbf{u}(\mathbf{Y})|_{\mathbf{Y}=\mathbf{X}^+}$. The second and fourth terms on the right hand side of Eq. (8.57) can be combined to a single term:

$$\int_{\hat{S_1}^+} \frac{(B(\mathbf{X}^+) - B(\mathbf{Y}))\mathbf{R}(\mathbf{X}^+, \mathbf{Y})dS(\mathbf{Y})}{4\pi R^3(\mathbf{X}^+, \mathbf{Y})\epsilon} \tag{8.58}$$

which is only weakly singular!

The mechanical residual $\mathbf{R}_M$ and its derivatives. The mechanical residual $\mathbf{R}_M$ is:

$$\mathbf{R}_M(\mathbf{u}, \mathbf{B}) = \begin{bmatrix} K^{(I)} & 0 \\ 0 & K^{(O)} \end{bmatrix} \begin{bmatrix} q^{(I)} \\ q^{(O)} \end{bmatrix} + \begin{bmatrix} 0 & K^{(IO)} \\ 2K^{(IO)T} & K^{(NI)} \end{bmatrix} \begin{bmatrix} q^{(I)} \\ q^{(O)} \end{bmatrix} - \begin{bmatrix} P. \end{bmatrix} \tag{8.59}$$

The load vector $[P]$ in Eq. (8.59) involves the resultant traction $\overline{\mathbf{H}}$ (see Eq. (8.53)). Using Eq. (8.19), as well as the relations:

$$\overline{\mathbf{H}} = \mathbf{H}^+ + \mathbf{H}^-, \;\; \mathbf{N} = \mathbf{N}^+ = -\mathbf{N}^-, \;\; \mathbf{F} = \mathbf{F}^+ = \mathbf{F}^- \tag{8.60}$$

one gets:

$$\overline{\mathbf{H}} = -\frac{AB}{2J\epsilon} \frac{\mathbf{N} \cdot \mathbf{F}^{-1}}{|\mathbf{N} \cdot \mathbf{F}^{-1}|^2} \tag{8.61}$$

where $A = \Sigma^+ - \Sigma^-$.

It is very easy to evaluate $\partial \mathbf{R}_M/\partial B = -\partial [P]/\partial B$.

The gradient $\partial \mathbf{R}_M/\partial \mathbf{u}$ has two parts. The first part comes from the first two terms on the right hand side of Eq. (8.59). (Note from Eq. (8.47) that $[q^{(I)}$ and $[q^{(O)}]$ involve the displacement components u_k as well as the slopes $w_{,x}$, $w_{,y}$ and twist $w_{,xy}$; and the stiffness matrices $K^{(IO)}$ and $K^{(NI)}$ (see Eqs. (8.52) and (8.48)) involve slopes). For the Newton scheme employed in this work, the displacement components $[u_k] = [u, v, w]$ of $\mathbf{u}$ are independent. One therefore needs to evaluate derivatives such as $\partial w_{,x_m}/\partial w$, $m = 1, 2$ as well as similar derivatives for the twist $w_{,xy}$. These derivatives, as well as those required for the components of the deformation gradient $\mathbf{F}$ (see Eq. (8.74)), are discussed below.

The second part comes from $\partial \overline{\mathbf{H}}/\partial \mathbf{u}$ and this requires evaluation of $\partial \mathbf{F}/\partial \mathbf{u}$ and $\partial J/\partial \mathbf{u}$, together with application of the chain rule. For these calculations, it is useful, in general, to use the formulae:

$$\frac{\partial F_{ij}}{\partial u_k} = \frac{\partial F_{ij}}{\partial X_m} F^{-1}_{mk}\,, \quad \frac{\partial J}{\partial u_k} = J \frac{\partial F_{ij}}{\partial u_k} F^{-1}_{ji}\,, \quad \frac{\partial \mathbf{F}^{-1}}{\partial \mathbf{u}} = -\mathbf{F}^{-1} \cdot \frac{\partial \mathbf{F}}{\partial \mathbf{u}} \cdot \mathbf{F}^{-1} \quad (8.62)$$

Please note that derivatives of the components of **F** in this work (see Eq. (8.74)) are discussed below.

Finally, the auxiliary equation (8.23) (the gradient BIE) is viewed as:

$$(1/2)A = f(\mathbf{u}, B) \quad (8.63)$$

and is used within each Newton iteration.

Derivatives of displacement gradients. First consider , for example, $\partial w_{,x}/\partial w$. One first writes $w_{,x}(x, y)$. This can be interpreted in two ways:[38]

(1) $w_{,x}(x, y(w, x))$; where $w_{,x},\ y$ are dependent variables and w, x are independent variables. Now:

$$\left.\frac{\partial w_{,x}}{\partial w}\right|_x = \frac{\partial w_{,x}}{\partial y}\frac{\partial y}{\partial w} = \frac{w_{,xy}}{w_{,y}} \quad (8.64)$$

(2) $w_{,x}(x(w, y), y)$; where $w_{,x},\ x$ are dependent variables and w, y are independent variables. This time:

$$\left.\frac{\partial w_{,x}}{\partial w}\right|_y = \frac{\partial w_{,x}}{\partial x}\frac{\partial x}{\partial w} = \frac{w_{,xx}}{w_{,x}} \quad (8.65)$$

The average value is chosen in this work. Thus:

$$\frac{\partial w_{,x}}{\partial w} = \frac{1}{2}\left(\frac{w_{,xy}}{w_{,y}} + \frac{w_{,xx}}{w_{,x}}\right), \quad \frac{\partial w_{,y}}{\partial w} = \frac{1}{2}\left(\frac{w_{,yy}}{w_{,y}} + \frac{w_{,xy}}{w_{,x}}\right). \quad (8.66)$$

The derivative of the twist $w_{,xy}$ with respect to w is evaluated in similar fashion.

The derivatives of the components of **F** in Eq. (8.74) are derived somewhat differently. First consider the derivatives of $u_{,x}$ and $u_{,y}$ with respect to u. Start with $u_{,x}(x, y) = u_{,x}(x(u, v), y(u, v))$; and similarly for $u_{,y}$. Using the chain rule:

$$\frac{\partial}{\partial u}(u_{,x}) = u_{,xx}x_{,u} + u_{,xy}y_{,u}, \quad \frac{\partial}{\partial u}(u_{,y}) = u_{,xy}x_{,u} + u_{,yy}y_{,u} \quad (8.67)$$

Similar equations are obtained for the derivatives of $v_{,x}$ and $v_{,y}$ with respect to v by replacing u with v in Eq. (8.67). Finally:

$$\begin{bmatrix} x_{,u} & x_{,v} \\ y_{,u} & y_{,v} \end{bmatrix} = \begin{bmatrix} u_{,x} & u_{,y} \\ v_{,x} & v_{,y} \end{bmatrix}^{-1} \tag{8.68}$$

Any singularities, (*e.g.*, $w_{,x} = 0$ in Eq. (8.66)), must be handled carefully. An average value of such a quantity, from neighboring nodes, is used in this work.

8.4.2.2. *The Newton Algorithm*

First, define:

$$\mathbf{R}(\mathbf{u}, B) = \begin{bmatrix} R_E(\mathbf{u}, B) \\ \mathbf{R}_M(\mathbf{u}, B) \end{bmatrix}. \tag{8.69}$$

One has the Newton iterative scheme:

$$\begin{bmatrix} \dfrac{\partial \mathbf{R}}{\partial \mathbf{u}} & \dfrac{\partial \mathbf{R}}{\partial B} \end{bmatrix}_n \begin{bmatrix} \Delta \mathbf{u} \\ \Delta B \end{bmatrix}_n = -\mathbf{R}_n, \tag{8.70}$$

$$\mathbf{u}_{n+1} = \mathbf{u}_n + \Delta \mathbf{u}_n \ , \quad B_{n+1} = B_n + \Delta B_n. \tag{8.71}$$

Starting with $n = 0$, Eq. (8.70) is iterated until convergence. At convergence, $\mathbf{R}_n \equiv \mathbf{R}(\mathbf{u}_n, B_n) \to 0$.

The voltage is applied in steps. The algorithm for a typical step *V* for the coupled scheme is described below.

(1) Solve BEM on ∂B for applied voltage *V*.
(2) Solve for $B^{(0)}$, substitute $B^{(0)}$ in Eq. (8.63) and solve for $A^{(0)}$. Use $B^{(0)}$ and $A^{(0)}$ in Eq. (8.61) to evaluate $\overline{\mathbf{H}}^{(0)}$.
(3) Solve FEM problem in B with traction $\overline{\mathbf{H}}^{(0)}$, find displacement $\mathbf{u}^{(0)}$ on ∂B.
(4) Set $k = 0$.
(5) Do
(6) Use Eqs. (8.55) and (8.57) to solve for $\partial R_E/\partial B$ and $\partial R_E/\partial \mathbf{u}$, where $B = B^{(k)}$.
(7) Next find $\partial \mathbf{R}_M/\partial B$ and $\partial \mathbf{R}_M/\partial \mathbf{u}$.
(8) Use the above computed values to evaluate $\mathbf{R}_k$ in Eq. (8.69).
(9) Use $\mathbf{R}_k$ in Eq. (8.70) to solve for $\Delta \mathbf{u}^{(k)}$ and $\Delta B^{(k)}$.

(10) Update $\mathbf{u}^{(k+1)} = \mathbf{u}^{(k)} + \Delta\mathbf{u}^{(k)}$.
(11) Update $B^{(k+1)} = B^{(k)} + \Delta B^{(k)}$.
(12) Update $k = k + 1$
(13) Compute $displacement\, residual = \frac{|w^{(k+1)} - w^k|}{|w^k|} \times 100$.
(14) While (displacement residual is high)
(15) $\mathbf{u} = \mathbf{u}^{(k+1)}$
(16) $\Sigma = \Sigma^{(k+1)}$

8.5. Numerical Implementation

8.5.1. *Boundary Integral Equations for Two Plates Very Close Together*

As mentioned before, the last integral on the right hand side of Eq. (8.34) is nearly weakly singular. Similar integrals arise when a 3D region outside a thin plate is analyzed *by the conventional BEM*. A procedure for accurate evaluation of such integrals is outlined below.

Proposed method for the accurate evaluation of nearly weakly singular integrals. Consider a source point $\mathbf{x}$ on the top face of a plate and its image point $\hat{\mathbf{x}}$ on the bottom face in Fig. 8.10. Two kinds of singular ($\mathcal{O}(1/r)$) integrals arise — a weakly singular integral on the boundary element Δ on the top face of the plate that contains $\mathbf{x}$, and, since h is small, a nearly weakly singular integral on the boundary element $\hat{\Delta}$ (the image of Δ) on the bottom face of the plate that contains $\hat{\mathbf{x}}$.[20] The weakly singular integral is evaluated by employing the mapping method outlined in Refs. 39 and 40. This method transforms such integrals over rectangular (curved or flat) domains into regular two-dimensional triangles (4 triangles). Integrals over curved quadratic or flat linear triangles are further reduced to regular line integrals that can be easily evaluated to desired accuracy by standard Gaussian quadrature.

A simple method[20] is presented below for the accurate and efficient evaluation of nearly weakly singular integrals. This approach transforms a nearly weakly singular integral into a weakly singular one; which is then evaluated by the method described in Refs. 39 and 40. A nearly weakly singular integral of interest here has the form:

$$I(\mathbf{x}) = \int_{\hat{\Delta}} \frac{ds(\mathbf{y})}{r(\mathbf{x},\mathbf{y})} \tag{8.72}$$

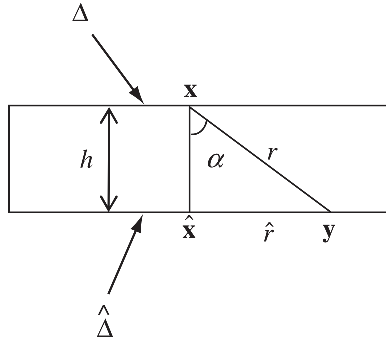

Fig. 8.10. Singular integrals (from Ref. 28).

The integrand above is multiplied by $\hat{r}/\hat{r}$ with the result:

$$I(\mathbf{x}) = \int_{\hat{\Delta}} \frac{[(\hat{r}/r)]ds(\mathbf{y})}{\hat{r}(\hat{\mathbf{x}}, \mathbf{y})} \tag{8.73}$$

Since $\hat{r}/r$ is $\mathcal{O}(1)$ and $\rightarrow 0$ as $\mathbf{y} \rightarrow \hat{\mathbf{x}}$ (*i.e.*, as $\hat{r} \rightarrow 0$), the integrand in Eq. (8.73) is weakly singular, of $\mathcal{O}(1/\hat{r})$ as $\hat{r} \rightarrow 0$. Therefore, the integral (8.73) can be evaluated by employing the methods described in Refs. 39 and 40.

Performance of new method. The performance of the new method is compared with that of standard Gauss integration.

Figure 8.11(a) shows the source point $\mathbf{x}(0, 0, h)$ and region of integration $\hat{\Delta}$ (a square of side L). Numerical results appear in Fig. 8.11(b). It is seen that for $h/L < 1/100$, standard Gauss integration, even with 36 Gauss points, cannot reduce the error below around 10%. By increasing the number of gauss points to 64, the errors dramatically increases to 42%. This is due to numerical instabilities. The new method is seen to take care of these nearly weakly singular integrals very well, even for very small values of h/L.

8.5.2. *Non-Linear Finite Element Analysis*

It is important to point out that Eq. (8.50) is non-linear due to the fact that the matrices $[K^{(IO)}]$ and $[K^{(NI)}]$ contain the gradient of w (see Eqs. (8.48) and (8.52)). Newton iterations are used to solve Eq. (8.50) once the transverse displacement w becomes significant.

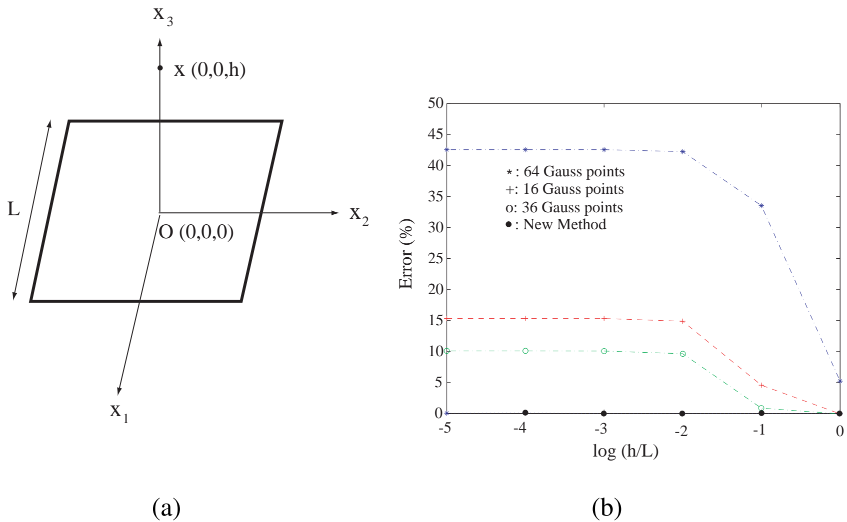

Fig. 8.11. (a) Numerical integration over a square element. (b) Errors in numerical integration over a square (from Ref. 28).

8.5.3. *BEM/FEM Coupling*

Both the relaxation scheme and Newton schemes are used for the coupling of BEM and FEM solutions. In the relaxation scheme, the BEM problem is solved for charge densities. Tractions are obtained and the resultant tractions are transferred to the FEM domain to obtain the deformed configuration. The FEM solves for the displacements and displacement gradients on a thin plate mid-surface and returns them back to the BEM. The BEM problem is solved again for the deformed configuration, and new charge densities are obtained. This process is implemented iteratively until convergence. The deformation gradient is obtained with a membrane assumption as shown below:

$$F = \begin{bmatrix} 1+u_{,x} & u_{,y} & 0 \\ v_{,x} & 1+v_{,y} & 0 \\ w_{,x} & w_{,y} & 1 \end{bmatrix}. \tag{8.74}$$

Here, u, v and w represent the nodal displacements. For the Newton scheme, the non-linear equations are solved together using Newton iterations. This procedure has been described before in Sec. 4.2.

8.5.4. *Discretization*

The BEM models only the top surface (s_k^+, see Fig. 8.5) and the FEM the mid-surface of each plate. No distinction need to be made between the top and mid surfaces since the plates are very thin. The mesh used here is as follows. The BEM and FEM domains each use 64 Q4 elements. Of course, the BEM has one degree of freedom per node and the FEM has 6 degrees of freedom at each node.

8.6. Numerical Results

8.6.1. *Code Verification*

The computer code with the thin BEM Lagrangian formulation has been carefully verified at several stages. Details are given below.

8.6.1.1. *BEM for Region Exterior to a Thin Flat Plate*

Total charge. Results from the thin BEM formulation have been compared to those from Harrington's[19] model (Fig. 8.12). For this verification, the gap ratio $(2g/L)$ has been varied from 0.1 to 0.6 in steps of 0.1, and the resulting capacitance of the MEMS plates has been compared to the values predicted by Harrington's model. The thickness ratio h/L for this problem is chosen to be 10^{-3}, $L = 2$ mm, $A = L^2$ and $C = Q/2V$, where Q is the total charge on the top plate and V and $-V$ are the potentials on the upper and lower plates, respectively. As is evident, results form the two models agree very well. It is noted here that the two models are very similar except that Harrington used constant boundary elements.

An empirical formula for the capacitance, based on Fig. 8.12, can be written as:

$$C = \frac{\epsilon L^2}{\gamma} + \epsilon \alpha L \tag{8.75}$$

where $\gamma = 2g$ is the total gap between the plates and α is he slope of the curve in Fig. 8.12. The dimensionless factor $\alpha \approx 2$.

Charge separation. For the two-plate capacitor shown in Fig. 8.5, the charge on the upper plate, neglecting the effects of the fringing fields, can be written as:

$$\sigma \approx \frac{\epsilon \Delta}{\gamma} \tag{8.76}$$

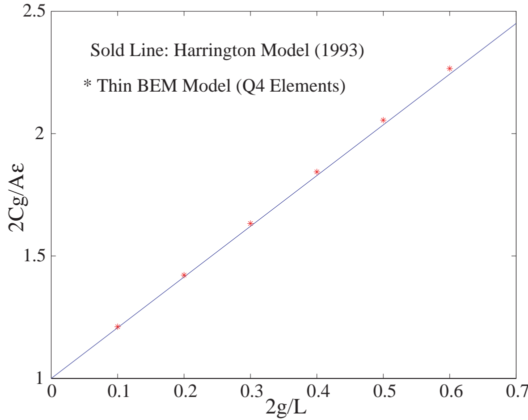

Fig. 8.12. Capacitance check of BEM model (from Ref. 28).

where Δ is the potential difference between the plates. With $\Delta = 2$ volts and $\gamma = 0.2L$, Eq. (8.76) gives $\sigma \approx 10\epsilon/L$. Table 3 of Ref. 20 (a thin plate BEM formulation), with $L = 1$, $\epsilon = 1$, has $\sigma^- = 9.907$ (at the center of the the top plate with the finest mesh). (The same numerical result is obtained with the code developed for the present chapter).

Force for small voltage. From Senturia:[43]

$$F = -\frac{\partial}{\partial\gamma}\left[\frac{C\Delta^2}{2}\right] = -\frac{1}{2}\frac{\partial C}{\partial\gamma}\Delta^2 \tag{8.77}$$

where F is the force between the plates in a two-plate capacitor.

From Eqs. (8.75) and (8.77), one gets the traction magnitude H as:

$$H = \frac{F}{L^2} = \frac{\Delta^2\epsilon}{2\gamma^2} \tag{8.78}$$

For the case in Table 3 of Ref. 20 (with $\Delta = 2$, $\gamma = 0.2L$), one has $H = 50\epsilon/L^2$.

It is noted that the traction, for small voltages, is linear in Δ^2. For larger voltages, one must use $\gamma(\mathbf{x}) = \gamma_0 - w(\mathbf{x})$,[43] with γ_0 the initial constant gap between the plates) and H becomes a function of w.

Now Eq. (8.17) is used to determine the traction. Using the values of $\sigma^- = 9.907$ and $\sigma^+ = 1.47$ from the Table 3 of Ref. 20, one gets:

$$\overline{H} = H^- - H^+ = 47.99\epsilon/L^2 \tag{8.79}$$

with $\overline{H}$ acting downwards on the top plate. The difference between the two results is 4%

8.6.1.2. *Lagrangian BEM for Region Exterior to a Curved Plate*

"Fat" plate. The proposed Lagrangian BEM algorithm has been verified before. Section 5.3 of Ref. 24, for example, considers a (3D) bent cantilever beam with dimensions $20 \times 1 \times 1$. The standard (not thin plate) BEM is used here. The differences between the numerical results from an Eulerian and a Lagrangian BEM formulation are shown to be of the order of 0.1% at various points on the surface of the bent beam. The maximum difference is only 0.09% when each conductor is discretized with 738 constant boundary elements.

Thin plate/beam. A new example is presented below.

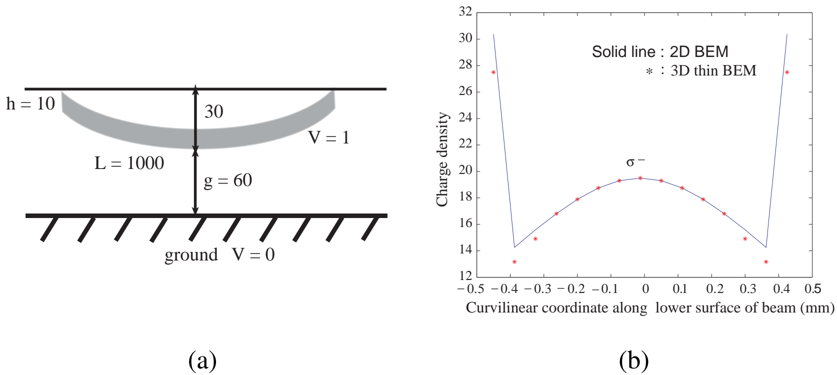

Fig. 8.13. (a) Schematic of curved beam with lengths in μm. (b) Charge distribution σ^- along the lower surface of the curved beam (from Ref. 28).

The geometry of the problem, a curved beam, is shown in Fig. 8.13(a). The length of the curved beam (top or bottom surface) is 1000 μm, its thickness is 10 μm, the deflection of the center of the bottom surface is 30 μm and the gap between the center of its bottom surface and the ground plane is 60 μm.

The charge distribution σ^- on the bottom surface of the beam, with $V = 1$, $\epsilon = 1$, is shown in Fig. 8.13(b). The solid line is the result from a standard 2D BEM code. The $*$ symbols depict the results from the (Lagrangian) 3D thin

plate BEM code for a plate with dimensions $4000 \times 1000 \times 10$ μm. For this case, σ^- is shown along a line through the center of the lower surface of the plate, parallel to its shorter edge. The results are seen to agree quite well. Of course, perfect agreement between the two models is not expected (see Tables 1 and 2 in Ref. 20).

It should be stated here that the computer programs used to generate the results shown in Fig. 8.13(b) use a length scale of mm (*i.e.*, $L = 1$ mm, $g = .06$ mm *etc.*) with $\epsilon = 1$ F/mm. Therefore, the output σ^- is in $C/(\mathrm{mm})^2$.

Finally, it is noted that for a straight beam (in Fig. 8.13(a)) with $g = .06$ mm, Eq. (8.76) in the form $\sigma = \epsilon\Delta/g$ yields a uniform $\sigma = 1/.06 = 16.67\,C/(\mathrm{mm})^2$. Clearly, this result is not satisfactory and a detailed calculation is needed to obtain the correct variation of charge density on a curved beam, as shown in Fig. 8.13(b).

8.6.1.3. *FEM for Deformation of a Thin von Karman Plate*

The FEM formulation for deformation of von Karman plates, presented in Sec. 8.3 of this chapter, has been carefully verified earlier in Ref. 3. The usual checks (*e.g.*, bending deformation of a clamped square plate under uniform applied pressure) have been successfully carried out for the current rendition of the FEM code.

8.6.1.4. *Coupling of BEM and FEM*

This coupling has been carried out with two different approaches: the relaxation scheme and the Newton scheme. As seen in Sec. 8.6.2, results from these two formulations show excellent agreement. In addition, results shown in Fig. 8.15(b) have been compared with those from earlier work (Ref. 27). This matter is discussed in Sec. 8.6.2.

8.6.2. *MEMS Plates*

Material properties. Material properties used for silicon conductors in free space are:[41,42]

$$E = 169\ \text{GPa}, \quad \nu = 0.22, \quad \epsilon = 8.85 \times 10^{-6}\ \text{F/m} \tag{8.80}$$

It is assumed that the anisotropy is negligible and the plate is made up of polysilicon material for this system.

The problem. Deformation of a silicon MEMS plate (the silicon is doped so that it is a conductor), subjected to a progressively increasing electrostatic field, is

simulated here by the coupled BEM/FEM. Each plate is clamped around its edges and two plates are used in order to have a zero voltage ground plane (the plane of symmetry) midway between them (Fig. 8.14).

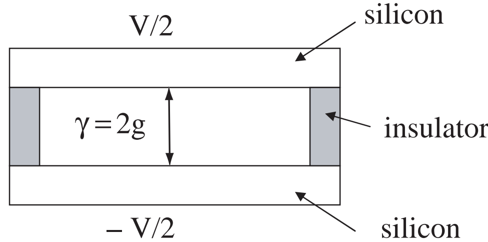

Fig. 8.14. Model Problem for microjet (from Ref. 28).

Two problems of interest have been studied in this analysis. For the first problem, each plate is square of side $L = 2$ mm, thickness $h = 6$ μm, and the gap g (distance between ground and the nearest plate surface) is 36 μm. Both plates are allowed to deform. The next problem studies the effect of gap on the deformation response of the MEMS plates. For this problem, the plates have a side of $L = 2$ mm and thickness $h = 2$ μm.

Results. Figure 8.15(a) shows the normalized central deflection of the top plate as a function of the square of the applied voltage, for relatively small values of the applied voltage. This curve is linear as expected (see Eq. (8.78)) since H linear in V^2 gives w_0 linear in V^2.

A comparison of relaxation scheme and Newton scheme is done next. The normalized plate center deflection with applied voltage is shown in Fig. 8.15(b). For the relaxation scheme, the voltage is applied in a series of 0.2 volt steps (max 2.4 volts). This time, the initial part is linear, but the response becomes non-linear for larger values of V (see Fig. 8 in Ref. 16). There are two reasons for this non-linear response. The first is that the electrical force is non-linear since $g(\mathbf{x}) = g_0 - w(\mathbf{x})$ in Eq. (8.78); and the impact of w becomes more and more pronounced as its value becomes larger and larger. The second is that the elastic response of the plate becomes non-linear as w becomes larger (see Sec. 8.3). This effect is often referred to as membrane stiffening. As can be seen, for an applied voltage of 1.5 volts the deflection of the plate center is of the order of its thickness.

It is noted that the results from the relaxation scheme agree with those from the Newton scheme (within plotting accuracy) in Fig. 8.15.

Table 8.1. Comparison of results from the present code with those from Ref. 27. $L = 3$ mm, $h = 0.03$ mm, $\gamma = 1$ mm.

$\hat{V}^2 \times 10^6$	$\hat{w}$ (present)	$\hat{w}$ (Ref. 27)
2	1.46	1.44
4	1.948	1.92
6	2.246	2.35
8	2.451	2.44

A similar problem has been solved before[27] in which the Lagrangian formulation was applied but the standard (not thin plate) BEM was used. Hence, the gradient BIE (8.9) and its Lagrangian counterpart Eq. (8.23) are absent in Ref. 27. Also, the relaxation scheme was used in that paper to couple the BEM with the FEM. Figure 8 in Ref. 27 presents the nondimensional central deflection $\hat{w} = w_0/h$ as a function of nondimensionalized voltage:

$$\hat{V}^2 = \frac{\epsilon L^5 V^2}{2\gamma^3 EI} \tag{8.81}$$

where the moment of inertia of the plate cross-section $I = Lh^3/12$. The two-plate configuration shown in Fig. 8.14 was also used in Ref. 27 with the following values of geometrical parameters: $L = 3$ mm, $h/L = 0.01$ and $\gamma = 1$ mm; the physical parameters being those given in Eq. (8.80). A comparison of results from Fig. 8 in Ref. 27 and those from the computer code developed in the present chapter, appear in Table 8.1. The results are seen to agree quite well. An L_2 norm of the difference between the two results is defined as:

$$e = \frac{\left[\sum_{i=1}^{N} (\hat{w}_i^{(1)} - \hat{w}_i^{(2)})^2\right]^{1/2}}{\sqrt{N}|\hat{w}_{max}^{(1)}|} \times 100 \tag{8.82}$$

where N is the number of points, $\hat{w}^{(1)}$ denotes the present results and $\hat{w}^{(2)}$ those from Ref. 27. From the results in Table 8.1, one gets $e = 2.246\%$.

The effect of the initial gap between the MEMS plates is shown in Fig. 8.16. These results are obtained from the Newton scheme. It can be seen that when the plates are moderately densely packed, even a few volts of applied voltage induces large deformations in the conducting plate. It is also observed that the deformations are highly non-linear when the voltage is high. The results for the smallest initial gap $(5h)$ are considered to be reliable up to about 60 mV. Beyond

that, the gap (between the center of the plate and the ground plane) is $O(h)$ and the numerical results start becoming unreliable — each iteration takes a long time to converge. It is conjectured that the plate, at this stage, is experiencing the onset of pull-in, but this requires further investigation. The issue of very densely packed plates is discussed in Sec. 8.8.

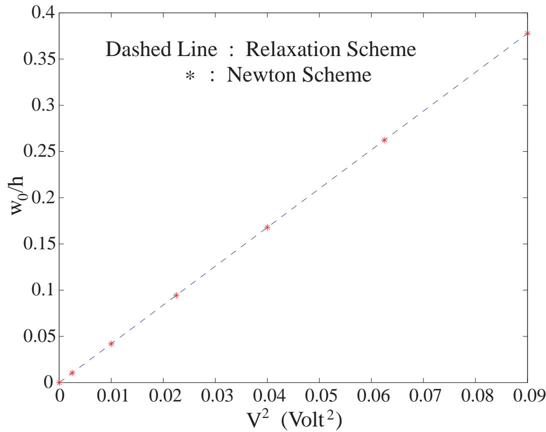

(a)

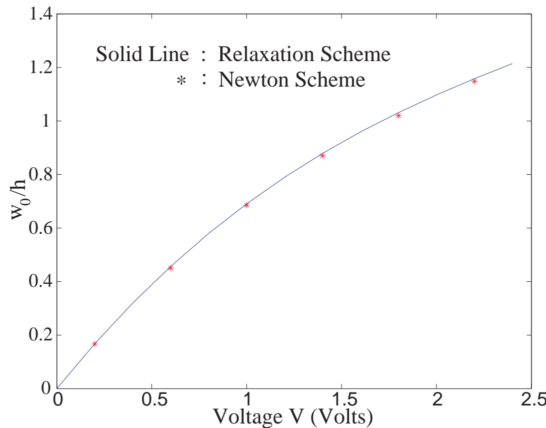

(b)

Fig. 8.15. Response behavior of microjet device (a) for low voltages and (b) for higher voltages. $L = 2$ mm, $h = 6$ μm, $g = 36$ μm (from Ref. 28).

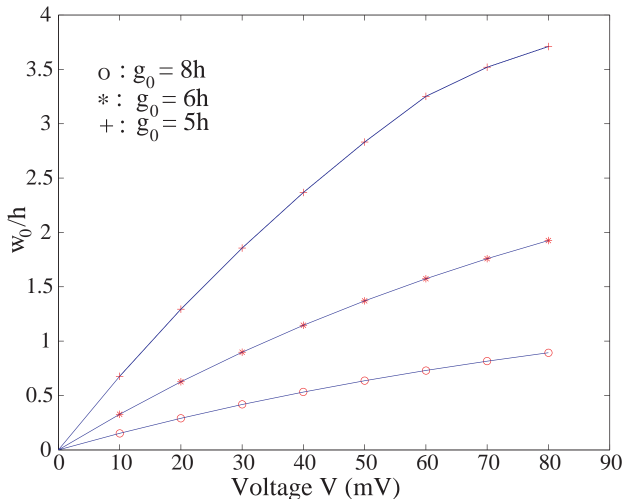

Fig. 8.16. Effect of initial gap on MEMS response behavior. $L = 2$ mm, $h = 2$ μm (from Ref. 28).

It is interesting to comment on the competing non-linearities in Figs. 8.15 and 8.16. As stated earlier in this section, the electrical non-linearity arises from the reducing gap $g(\mathbf{x}) = g_0 - w(\mathbf{x})$ due to plate deformation. This causes progressive increase of the electrostatic force between the plates, leading to larger deformation at a given voltage (compared to the case $g = g_0$) — a softening effect. The mechanical non-linearity, on the other hand, has a stiffening effect.

The gap g at the plate center only reduces from 36 μm to around 29 μm at around 2 V in Fig. 8.15(b). The non-linearity exhibited in this figure, therefore, is primarily mechanical in origin. The same is largely true for the cases $g_0 = 8h = 16$ μm and $g_0 = 6h = 12$ μm in Fig. 8.16. Here the gap at the plate center reduces to, approximately, 14.5 μm and 8.5 μm, respectively, at 80 mV (a reduction of $\approx 10\%$ and 30%), so that the non-linearity is still largely mechanical (although the electrical effect is starting to kick-in for $g_0 = 6h$).

The situation, however, is quite different for the case $g_0 = 5h$ in Fig. 8.16. In this case, the gap at the plate center reduces from 10 μm to around 4 μm at 56 mV (a 60% reduction), so that the softening due to the electrical non-linearity plays an important role. It is seen in Fig. 8.16, however, that the membrane effect does dominate the electrical effect, so that the resulting curve has decreasing slope. In fact, the plate is close to pull-in at around 80 mV. A short discussion of pull-in is presented in Sec. 8.7.

8.7. Pull-In Analysis

An important practical matter in MEMS is the pull-in voltage. Stable equilibrium of a deformed plate demands that the applied electrical force on it must be in stable equilibrium with the restoring elastic (spring) force. A well-known calculation considers the simpler problem of a *rigid spring loaded plate subjected to increasing voltage* V that is attracted towards a fixed parallel plate (ground) at zero voltage, with g_0 the initial gap between the plate and the ground.[43] The moving plate always moves down parallel to its original position. It is proved in Ref. 43 that stable equilibrium is lost and pull-in occurs when the current gap, that decreases with increasing V, reaches:

$$g_{PI} = (2/3)g_0 \tag{8.83}$$

The problem considered in this chapter is that of a deformable plate that is clamped on all its edges. It is seen in Fig. 8.16 that, with $g_0 = 5h$, the gap at the center of the plate $\approx 2h$ at $V \approx 56$ mV, *i.e.*, $\approx (2/5)g_0$. This does not contradict Eq. (8.83) since the plate in the present work is deformable and the gap between its clamped edges and the ground, for example, always remains g_0; while g between the moving rigid plate in Ref. 43 and the ground progressively decreases but always remains uniform. Also, the stiffness k in the rigid plate problem remains constant while it increases in the deformable plate problem due to membrane stiffening. An electrostatic deformation analysis of a (deformable) clamped-clamped beam[44] obtained the deflection at pull-in to be $\approx .57g_0$ which compares favorably with the present result of the plate approaching pull-in at a central deflection of around $0.6g_0$.

The results for the pull-in instability, for various geometric shapes of the actuating conductor can be seen in Fig. 8.17.

The details of the various conductor dimensions and their geometries are given below. The initial gap (g_0) in these problems is 10 μm.

Square Plate. A square shaped conducing plate is very common in MEMS due to the ease of arraying. The dimensions of the plate chosen for the analysis here are $2000 \times 2000 \times 2$ μm. For this problem several different boundary conditions are chosen and analyzed as illustrated later.

Circular Plate. Sometimes MEMS use circular shaped conductors. The dimensions chosen for this plate are such that the area of circular plate is the same as that

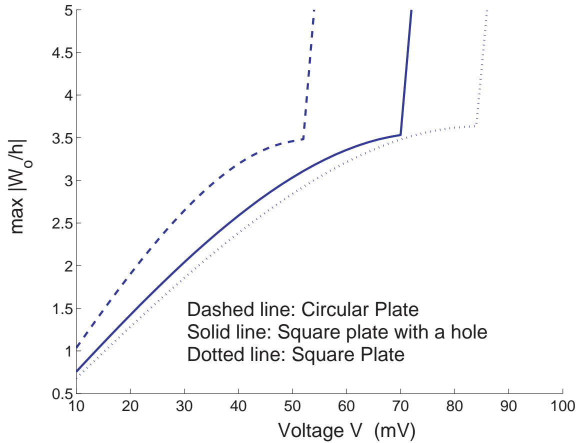

Fig. 8.17. Pull-in instability for conducting plates of different shapes.

of square plate analyzed earlier. The radius of the plate is chosen to be 1128 μm, with a thickness of 2 μm.

Square Plate with a hole. Some applications in MOEMS such as display technologies require MEMS plates to have fast switching ability. For such problems, having a tiny orifice will help reduce the damping forces or mechanical stiffness and decrease the response time (In addition to etch release time in some cases). Here, we consider a geometry which is fully clamped. The dimensions of the square plate are $2000 \times 2000 \times 2$ μm, and the central orifice has a radius of 50 μm.

Boundary Conditions. The effect of boundary conditions on the pull-in instability has been studied with a square plate of dimensions $2000 \times 2000 \times 2$ μm. 3 different boundary conditions (BCs) have been considered. These are a fully clamped BC, 2 opposite sides clamped and 4 corners clamped. The effect of boundary conditions on the pull-in is seen in Fig. 8.18.

8.8. Discussion

An accurate design analysis is essential for the successful implementation of many new MEMS-based applications. Electrostatic actuation is one of the most favoured means of actuation due to its ability to generate very high forces with small voltages at micro scale invloving high aspect ratio structures. This work

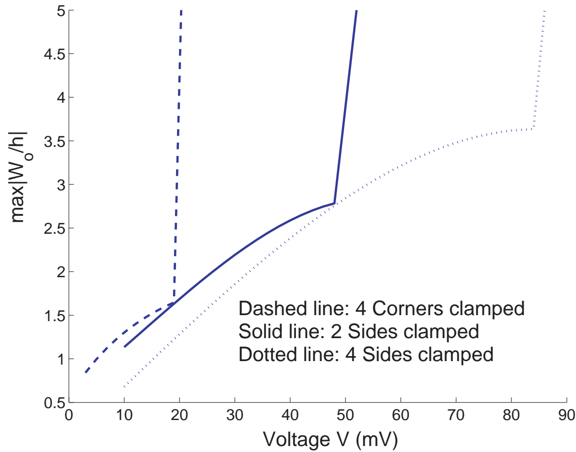

Fig. 8.18. Pull-in instability for different BC's of a square conductor.

presents a first attempt at a fully Lagrangian approach for the analysis of coupled 3D MEMS systems made up of thin structural elements that are relatively closely packed. The Lagrangian approach uses only the undeformed configuration (usually simple) of a plate for both the electrical and mechanical analyses — thus obviating the need to discretize any deformed configuration.

The hybrid BEM/FEM approach is able to handle thin plates (with $h/L = 1/1000$) efficiently. Convergence is achieved for relatively large voltage steps with only a few iterations. The proposed simple new approach for accurate evaluation of nearly weakly singular integrals works well. (It is noted that although the idea is illustrated in Sec. 8.5.1 for flat plates, it is also successfully employed when the plates become curved due to deformation). It is seen from Figs. 8.15(b)–8.18 that the non-linear effects can be very significant. Therefore, the non-linear FEM model, employed in this work, is of crucial importance. Eventually dynamical analysis and the motion of fluid between the plates must be modeled in the problem discussed in Ref. 2. This motion would cause the voltages to be increased substantially, especially at higher frequencies, due to the damping and compressibility effects of the fluid between the plates. A preliminary BEM analysis of Stoke's flow around slowly moving rigid thin plates appears in Ref. 29.

Successful modeling of MEM structures with plates that are packed very densely together (*e.g.*, with gaps that are of the order of a plate thickness) is still an open problem. One possible idea for solving this problem is to extrapolate BEM solutions for traction distributions as a function of gap size for $g \geq 10h$, down to gaps $\approx O$(h). For electrostatic problems of interest in this work here,

this extrapolation should be guided by Eq. (8.78), noting that the impact of w on $\overline{\mathbf{H}}$ quickly becomes significant when deformation of a plate starts with small γ_0. This problem is a topic of continuing research.

References

1. A. Frangi and A. di Gioia, "Multipole BEM for the evaluation of damping forces on MEMS," *Comput. Mech.,* vol. 37, pp. 24–31, 2005.
2. M. Roman and N. Aubry, "Design and fabrication of electrostatically actuated synthetic microjets," *ASME Paper No. IMECE2003-41579*, New York: American Society of Mechanical Engineers, 2003.
3. Z. Bao, S. Mukherjee, M. Roman and N. Aubry, "Non-linear vibrations of beams strings plates and membranes without initial tension," *ASME J. Appl. Mech.,* vol. 71, pp. 551–559, 2004.
4. S.C. Ko, Y.C. Kim, S.S. Lee, S.H. Choi and S.R. Kim, "Micromachined piezoelectric membrane acoustic device," *Sens. Actuators A,* vol. 103, pp. 130–134, 2003.
5. S. Mukherjee, *Boundary Element Methods in Creep and Fracture*. London: Applied Science Publishers, 1982.
6. P.K. Banerjee, *The Boundary Element Methods in Engineering.* Maidenhead, Berkshire, England: McGraw Hill Europe, 1994.
7. A. Chandra and S. Mukherjee, *Boundary Element Methods in Manufacturing.* New York: Oxford University Press, 1997.
8. M. Bonnet, *Boundary Integral Equation Methods for Solids and Fluids.* Chichester, UK: Wiley, 1999.
9. S. Mukherjee and Y.X. Mukherjee, *Boundary Methods: Elements, Contours and Nodes.* Boca Raton FL: Taylor and Francis, CRC Press, 2005.
10. T.Y. Yang, *Finite Element Structural Analysis*. New Jersey: Prentice-Hall, 1986
11. O.C. Zienkiewicz and R.L. Taylor, *The Finite Element Method, Vols. 1,2, 4th. ed.*. Maidenhead, Berkshire, UK: McGraw Hill, 1994.
12. T.J.R. Hughes, *The Finite Element Method: Linear Static and Dynamic Finite Element Analysis.* Mineola, NY: Dover, 2000.
13. S.D. Senturia, R.M. Harris, B.P. Johnson, S. Kim, K. Nabors, M.A. Shulman and J.K. White, "A computer-aided design system for microelectromechanical systems (MEMCAD)," *J. Microelectromech. Syst.,* vol. 1, pp. 3–13, 1992.
14. K. Nabors and J. White, "FastCap: a multi-pole accelerated 3D capacitance extraction program," *IEEE Trans. Comput.-Aided Design,* vol. 10, pp. 1447–1459, 1991.
15. J.R. Gilbert, R. Legtenberg and S.D. Senturia, "3D coupled electromechanics for MEMS: applications of CoSolve-EM," *Proceedings IEEE MEMS,* pp. 122–127, 1995.
16. F. Shi, P. Ramesh and S. Mukherjee, "Simulation methods for micro-electromechanical structures (MEMS) with application to a microtweezer," *Comp. Struct.,* vol. 56, pp. 769–783, 1995.
17. N.R. Aluru and J. White, "An efficient numerical technique for electromechanical simulation of complicated microelectromechanical structures," *Sens. Actuators A,* vol. 58, pp. 1–11, 1997.

18. F. Shi, P. Ramesh and S. Mukherjee, “Dynamic analysis of micro-electro-mechanical systems,” *Int. J. Num. Meth. Engng.,* vol. 39, pp. 4119–4139, 1996.
19. R. F. Harrington, *Field Computation by Moment Methods.* Piscataway, NJ: IEEE Press, 1993.
20. Z. Bao and S. Mukherjee, “Electrostatic BEM for MEMS with thin conducting plates and shells,” *Eng. Anal. Bound. Elem.,* vol. 28, pp. 1427–1435, 2004.
21. Z. Bao and S. Mukherjee, “Electrostatic BEM for MEMS with thin beams,” *Comm. Numer. Meth. Engng,* vol. 21, pp. 297–312, 2005.
22. S.W. Chuyan, Y.S. Liao and J.T. Chen, “Computational study of the effect of finger width and aspect ratios for the electrostatic levitating force of MEMS combdrive,” *J. Microelectromech. Syst.,* vol. 14, pp. 305–312, 2005.
23. G. Li and N.R. Aluru, “A Lagrangian approach for electrostatic analysis of deformable conductors,” *J. Microelectromech. Syst.,* vol. 11, pp. 245–254, 2002.
24. V. Shrivastava, N.R. Aluru and S. Mukherjee, “Numerical analysis of 3D electrostatics of deformable conductors using a Lagrangian approach,” *Eng. Anal. Bound. Elem.,* vol. 28, pp. 583–591, 2004.
25. G. Li and N.R. Aluru, “Efficient mixed-domain analysis of electrostatic MEMS,” *IEEE Trans. Comput.-Aided Design,* vol. 22, pp. 1228–1242, 2003.
26. S.K. De and N.R. Aluru, “Full-Lagrangian schemes for dynamic analysis of electrostatic MEMS,” *J. Microelectromech. Syst.,* vol. 13, pp. 737–758, 2004.
27. S. Mukherjee, Z. Bao, M. Roman and N. Aubry, “Non-linear mechanics of MEMS plates with a total Lagrangian approach,” *Comp. Struc.,* vol. 83, pp. 758–768, 2005.
28. S. Telukunta and S. Mukherjee, “Fully Lagrangian modeling of MEMS with thin plates,” *J. Microelectromech. Syst.,* vol. 15, pp. 795–810, 2006.
29. S. Mukherjee, S. Telukunta and Y.X. Mukherjee, “BEM modeling of damping forces on MEMS with thin plates,” *Eng. Anal. Bound. Elem.,* vol. 29, pp. 1000–1007, 2005.
30. S. Mukherjee, “On boundary integral equations for cracked and for thin bodies,” *Math. Mech. Solids,* vol. 6, pp. 47–64, 2001.
31. S. Mukherjee, “Finite parts of singular and hypersingular integrals with irregular boundary source points,” *Eng. Anal. Bound. Elem.,* vol. 24, pp. 767–776, 2000.
32. S. Mukherjee, “CPV and HFP integrals and their applications in the boundary element method,” *Int. J. Solids Structures,* vol. 37, pp. 6623–6634, 2000.
33. E. J. Nanson, “Note on hydrodynamics,” *The Messenger of Mathematics,* vol. 7, pp. 182-183, 1877–1878.
34. S. Mukherjee, M.K. Chati and X. Shi, “Evaluation of nearly singular integrals in boundary element contour and node methods for three-dimensional linear elasticity,” *Int. J. Solids Structures,* vol. 37, pp. 7633–7654, 2000.
35. A.H. Nayfeh and D.T. Mook, *Non-linear Oscillations*. New York: Wiley, 1979.
36. W. Han and M. Petyt, “Geometrically non-linear vibration analysis of thin rectangular plates using the hierarchical finite element method — I: The fundamental mode of isotropic plates,” *Comp. Struc.,* vol. 63, pp. 295–308, 1997.
37. A.C. Ugural, *Stresses in Plates and Shells, 2nd. ed.* US: McGraw Hill, 1999.
38. G.B. Thomas and R.L. Finney, *Calculus and Analytic Geometry Alternate ed.* US: Addison Wesley, Pearson Ed., 2003.
39. A. Nagarajan and S. Mukherjee, “A mapping method for numerical evaluation of two-dimensional integrals with 1/r singularity,” *Comp. Mech.,* vol. 12, pp. 19-26, 1993.

40. M.K. Chati and S. Mukherjee, “The boundary node method for three-dimensional problems in potential theory,” *Int. J. Num. Meth. Engng.,* vol. 47, pp. 1523-1547, 2000.
41. K.E. Petersen, “Silicon as a Mechanical Material,” *Proc. IEEE,* vol. 70, pp. 420-455, 1982.
42. W.N. Sharpe Jr., “Mechanical Properties of MEMS Materials.,” Chapter 3 in *The MEMS Handbook*, CRC Press, pp. 3-33, 2001.
43. S.D. Senturia, *Microsystem Design.* Boston: Kluwer Academic Publishers, 2001.
44. M.I. Younis, E.M. Abdel-Rahman and A. Nayfeh, “A reduced order model for electrically actuated microbeam based MEMS,” *J. Microelectromech. Syst.,* vol. 12, pp. 672-680, 2003.

Chapter 9

Pull-In Instability in Electrostatically Actuated MEMS due to Coulomb and Casimir Forces

Romesh C. Batra and Davide Spinello

Department of Engineering Science and Mechanics
Virginia Polytechnic Institute and State University
Blacksburg, VA 24061, USA
rbatra@vt.edu

Maurizio Porfiri

Department of Mechanical, Aerospace and Manufacturing Engineering
Polytechnic University
Brooklyn, NY 11201, USA

We investigate pull-in instabilities in microelectromechanical (MEM) membranes due to the Coulomb and the Casimir forces. This non-linear multiphysics problem is analyzed by the meshless local Petrov–Galerkin (MLPG) method. The moving least squares (MLS) approximation is used to generate basis functions for the trial solution, and the basis for test functions is taken to be the weight functions used in the MLS approximation. Essential boundary conditions are enforced by the method of Lagrange multipliers. The pull-in voltage and the corresponding deflection are extracted by combining the MLPG method with the pseudo-arc-length continuation algorithm, which allows for the analysis of the post-instability unstable equilibrium states of the system. For every problem studied, computed results are found to compare well with those obtained either with other numerical methods, or with those available in the literature. It is shown that beyond a critical size, the geometric effect modeled by the Casimir force becomes dominant over the Coulomb force, and the device collapses with zero applied voltage. One degree-of-freedom models to find the pull-in parameters are also proposed.

Contents

9.1 Introduction 330
9.2 Formulation of the Three-Dimensional Problem 334
9.2.1 Coupling in Electromechanical Systems 334

9.2.2 Mechanical Deformations . . . 334
9.2.3 Electrostatic Force . . . 336
9.3 The Casimir Effect . . . 338
9.4 Electrostatically Actuated Micromembranes . . . 342
9.4.1 Mathematical Model of a Micromembrane . . . 342
9.4.2 Local Weak Formulation of the Problem . . . 345
9.4.3 Discrete Non-Linear Formulation . . . 345
9.4.4 Pseudo-Arc-Length Continuation Method . . . 348
9.4.5 One Degree-of-Freedom Model . . . 350
9.4.6 Pull-In Instability . . . 352
9.4.7 Pull-In Instability and Symmetry Breaking in an Annular Circular Disk . . . 362
9.4.8 From Micro to Nano: Effect of the Scale on Pull-In and Symmetry Breaking Parameters of Micromembranes . . . 364
9.5 Summary . . . 368
References . . . 369

9.1. Introduction

Recent technological developments have opened promising research opportunities and engineering priorities in micromechanics. It is now possible to manufacture mechanical parts such as resonators, sensors, gears, and levers on a micron length scale, and to produce tiny needles to inject fluid into a living organism without stimulating nerve cells. The use of existing integrated circuit technology in the design and production of microelectromechanical systems (MEMS) allows these devices to be batch-manufactured thereby reducing the production cost. The thorough understanding, prediction, and control of MEMS behavior at the micro scale are critical issues. Multiphysics modeling is required, since coupling among different fields such as solid and fluid mechanics, thermomechanics, and electromagnetism is involved. MEMS devices find wide applications as sensors and actuators. The analysis of methods of actuation and sensing has been a topic of interest over the past several years. Different actuation and sensing properties such as piezoresistive, piezoelectric, electrostatic, thermal, electromagnetic, and optical have been used (see, *e.g.*, Ref. 1 for details). Comparisons among the aforementioned techniques in relation to the fabrication methods can be found in Refs. 1 and 2. There is no one optimal sensing and actuating method, and the choice mainly depends on the particular application. Electrostatics is often the preferred sensing and actuating technique.[1] An electrostatically actuated MEMS is generally an elastic perfect conductor suspended above a stationary rigid perfect conductor (see, *e.g.*, Ref. 3). A dielectric medium, usually air, fills the gap between them. The overall system behaves as a variable gap capacitor. An applied DC voltage is used to induce displacements of the deformable body, and a consequent change in the system capacitance. Typical applications are transistors,

switches, micro-mirrors, pressure sensors, micro-pumps, moving valves and micro-grippers, see, *e.g.*, Refs. 4–10. When an AC component is superimposed on the steady voltage to excite harmonic motions of the system, resonant devices are obtained. These devices are used in signal filtering, and chemical and mass sensing, see, *e.g.*, Refs. 11–18. The applied electrostatic voltage has an upper limit, beyond which electrostatic force is not balanced by the elastic restoring force in the deformable conductor that eventually snaps and touches the lower rigid plate, and the MEMS collapses. This phenomenon, called pull-in instability, has been observed experimentally.[19,20] The critical displacement, and the critical voltage associated with this instability are called pull-in displacement and pull-in voltage respectively. Their accurate evaluation is crucial in the design of electrostatically actuated MEMS. In particular, in micro-mirrors[7] and micro-resonators[21] the designer avoids this instability in order to achieve stable motions; however, in switching applications[5] the designer exploits this effect to optimize the performance of the device. A simple lumped spring-mass system for estimating pull-in parameters is proposed in Ref. 20 (see Fig. 9.1). The elasticity of the deformable body is lumped into the spring stiffness κ, F_{S} is the spring restoring force, V is the applied voltage, F_{E} is the electrostatic force, m is the mass of the movable electrode, g_0 is the initial gap between the two conductors, $\bar{u}$ is the displacement of the movable electrode, and $g = g_0 + \bar{u}$ is the actual gap. The pull-in instability occurs when F_{E} just exceeds F_{S}. The pull-in voltage so obtained usually exceeds that observed experimentally for many applications.[22] Moreover, the aforestated description does not incorporate inherent non-linearities of the electrostatic and the restoring forces.[10,23]

Several researchers have focused on accurately predicting the pull-in parameters. In Ref. 24 the non-linear coupling between electrical and mechanical effects

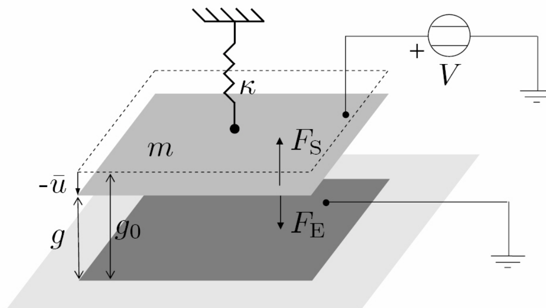

Fig. 9.1. Sketch of the lumped spring-mass system.

has been modeled by using a three-dimensional (3D) non-linear field theory. The governing equations for the deformable body and the dielectric medium are written in Lagrangian description of motion, and are solved numerically.[24,25] Numerous computer algorithms based on 3D finite element (FE) formulation of the problem have been developed (see, *e.g.*, Refs. 26–29) and used to simulate MEMS (see, *e.g.*, Refs. 22 and 30). Different computational techniques have been exploited to optimize the 3D algorithms, see, *e.g.*, Ref. 31. In order to alleviate the computational expense associated with the 3D analyses, considerable efforts have been devoted to the development of reliable reduced-order models for MEMS. Theories of rods and strings (non-linear), and plates, shells and membranes (2D) can be derived intrinsically (see, *e.g.*, Refs. 32 and 33), or can be deduced from the 3D theory (see, *e.g.*, Refs. 32 and 34). For a wide class of electrostatic MEMS, the deformable electrode is initially a flat body whose thickness h is much smaller than the characteristic length L.[35] Such electrodes can be regarded as 2D plate-like bodies. Since $h \ll L$, an approximate distributed model can be employed, where the kinematics is described only through the transverse displacement field u of points on its mid-surface (see, *e.g.*, Ref. 36). The actual gap g is therefore given by $g_0 + u$. Microplates have been studied in Refs. 37–39. When the bending stiffness of the deformable electrode is negligible as compared to its in-plane stretching, and $g_0 \ll L$, it is possible to approximate the electrode as a linear elastic membrane. The membrane approximation is valid for $L/h \geq 400$, see, *e.g.*, Ref. 40. As discussed in Ref. 41, the membrane approximation is accurate and reliable for many MEMS devices such as micro-pumps made of thin glassy polymers, and grating light valves comprised of stretched thin ribbons. For another class of electrostatic MEMS, the deformable electrode is a slender body with the length much larger than the others two dimensions.[1] These MEMS can be modeled by a beam theory. When the deformable electrode is very slender, the transverse displacement u of a point of its mid-surface is sufficient to describe the kinematics within a good approximation; see, *e.g.*, Ref. 36. This non-linear distributed model may also be adopted for thin rectangular electrodes that undergo cylindrical bending. In Ref. 14 deformations of a wide clamped-clamped microbeam have been studied with the Euler–Bernoulli beam theory, which is justified for small deflections. In Ref. 42 an effective Young's modulus has been employed to account for the plane strain deformations appropriate for wide beams or plates undergoing cylindrical bending deformations. In Ref. 11 large deflections are studied by accounting for the mid-plane stretching, allowing for the analysis of systems with initial gaps comparable to the thickness of the beam. In the large deflection theory the governing equations are non-linear, and the problem of numerically extracting the pull-in parameters is more challenging. The shooting method used in Ref. 11

produces stiff differential equations whose solutions are sensitive to initial estimates of unknown parameters and may eventually diverge. In Ref. 43 two variants of the Galerkin method are employed by using the beam mode shapes as basis functions, and in Ref. 17 the differential quadrature method is used. From an electrical point of view, the variable gap capacitor equivalent to the 2D and the non-linear structures described above is modeled by assuming that the actual gap g is differentially uniform, that is, the two conductors are locally parallel to each other. This assumption is consistent with the approximation introduced above in the mechanical models, see, *e.g.*, Ref. 3. This implies that the capacitance of the system (and therefore the applied electrostatic force) does not depend on the spatial derivatives of g. Recently, considerable research in computational mechanics has been devoted to the development of meshless methods, that provide smooth and accurate approximate solutions with a few number of nodes. Meshless methods for seeking approximate solutions of initial-boundary-value problems governed by partial differential equations include the element-free Galerkin,[44] hp-clouds,[45] the reproducing kernel particle,[46] the diffuse element,[47] the partition of unity finite element,[48] the natural element,[49] meshless Galerkin using radial basis functions (RBFs),[50] the meshless local Petrov–Galerkin (MLPG),[51,52] the smoothed particles hydrodynamics,[53] the modified smoothed particle hydrodynamics,[54] the meshless local boundary integral equation,[55] and the collocation method using RBFs.[56] All of these methods (except for the last five) use either shadow elements or a background mesh for evaluating integrals appearing in the governing weak formulation of a problem. The MLPG method has been successfully applied to several problems in mechanics: static linear plane elasticity;[51] vibrations of elastic planar bodies;[57] static analysis of beams;[58] static and dynamic analysis of functionally graded materials;[59] transient heat conduction in a bimaterial body;[60] wave propagation in bars with material interfaces[61] and in cracked beams;[62] and static analysis of non-linear electromechanical problems.[63] The MLPG method is based on a local weak formulation of the governing equations. Basis for the trial functions are usually constructed with the Moving Least Squares (MLS) approximation.[64] In the Petrov–Galerkin formulation, the test functions may be chosen from a different space than the space of trial functions. Thus several variations of the method may be obtained (see, *e.g.*, Ref. 51 for discussion). The key ingredients of the MLPG method are: local weak formulation, MLS interpolation, Petrov–Galerkin projection, numerical evaluation of domain integrals, solution of a system of equations, and computation of desired quantities at critical points. The rest of the Chapter is organized as follows. In Sec. 9.2 we formulate the initial-boundary-value problem for an electromechanical system where the deformable electrode is modeled as 3D perfect conductor undergoing

finite elastic deformations. The coupling phenomenon in a two-conductor system is illustrated. Expressions for the electrostatic potential in the form of boundary integrals are given both in the Eulerian and the Lagrangian descriptions of motion. In Sec. 9.3 we briefly explain the Casimir effect for semi-infinite parallel conductors. In Sec. 9.4 the MLPG method and a reduced order one degree-of-freedom model are used to investigate the behavior of electrostatically actuated MEMS modeled as elastic membranes. In order to find the MEMS deformations beyond the pull-in instability the pseudo-arc-length continuation method (see, *e.g.*, Refs. 65 and 66) is employed for solving the system of non-linear equations resulting from the MLPG formulation. The method is applied to four distinct geometries: a rectangle, a circular disk, an annular disk, and an elliptic disk. For the rectangular geometry the effect of partial electrodes is studied. For the annular disk, symmetry breaking after pull-in instability is investigated. For the rectangular, circular, and annular nanomembranes the effect of the Casimir force on the pull-in parameters is analyzed in Sec. 9.4.8. It is shown that beyond a certain size, the pull-in instability occurs at zero voltage. Symmetry breaking in annular nanomembranes due to the combined effects of the Coulomb and the Casimir forces is also analyzed. Conclusions are summarized in Sec. 9.5.

9.2. Formulation of the Three-Dimensional Problem

9.2.1. *Coupling in Electromechanical Systems*

The following illustrative example to explain the coupling phenomenon in electromechanical systems is taken from Ref. 24. Consider the electrostatically actuated cantilever microbeam exhibited in Fig. 9.2. When potential difference V is applied between the top deformable electrode and the bottom ground plane, electrostatic charges are induced on surfaces of the two conductors (Fig. 9.2(a)). These charges generate an electrostatic force acting along the normal to the bounding surface in the present configuration. Consequently the elastic body deforms, the charges redistribute on surfaces of the conductors, and the electrostatic force changes (Fig. 9.2(b)). The process continues until a new equilibrium configuration is reached in which the electrostatic force is balanced by the internal forces in the deformed system.

9.2.2. *Mechanical Deformations*

An electrostatically actuated MEMS can undergo large deformations depending on its geometry and the applied voltage. Here we briefly outline governing equations for large deformations of an electromechanical system where the deformable

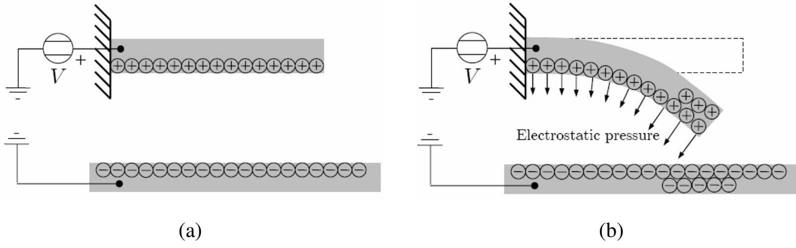

Fig. 9.2. Simple example to illustrate electromechanical coupling in electrostatic MEMS.

electrode is modeled as a 3D continuum (see Refs. 24 and 25). Let Ω be the 3D region occupied by the deformable electrode in the reference configuration, and $\mathbf{x}$, $\mathbf{x}^\star$ position vectors of a material point in the reference configuration and in the present configuration $\Omega^\star$, respectively. Equilibrium equations in Lagrangian description of motion are[67]

$$\varrho_0(\ddot{\mathbf{u}} - \mathbf{b}) = \mathrm{Div}\mathbf{FS}, \tag{9.1a}$$

$$\mathbf{S} = \mathbf{S}^{\mathrm{T}}. \tag{9.1b}$$

Equations (9.1a) and (9.1b) are the balance of linear momentum, and the balance of moment of momentum respectively. $\mathbf{S}$ is the second Piola-Kirchhoff stress tensor, $\mathbf{u} = \mathbf{x}^\star - \mathbf{x}$ the displacement field, and $\mathbf{F} = \mathbf{1} + \mathrm{Grad}\mathbf{u}$ the deformation gradient. $\mathbf{1}$ is the second-order identity tensor, ϱ_0 the mass density in the reference configuration, and $\mathbf{b}$ the external body force per unit mass. A superimposed dot means material time derivative, and Div and Grad are, respectively, the divergence and the gradient operators with respect to coordinates in the reference configuration.

Assuming that the body is made of an elastic material, the constitutive equation for $\mathbf{S}$ is[67]

$$\mathbf{S} = \hat{\mathbf{S}}(\mathbf{F}) \tag{9.2}$$

where $\hat{\mathbf{S}}$ represents the response of the material. The set of Eqs. (9.1) and (9.2) is completed with the following boundary conditions

$$\mathbf{u} = \bar{\mathbf{u}} \quad \text{on } \Gamma_{\mathbf{u}}, \qquad \mathbf{Pn} = \bar{\mathbf{t}} \quad \text{on } \Gamma_{\mathbf{n}}, \tag{9.3}$$

and initial conditions

$$\mathbf{u}(\mathbf{x}, 0) = \mathbf{u}_0(\mathbf{x}), \qquad \dot{\mathbf{u}}(\mathbf{x}, 0) = \mathbf{v}_0(\mathbf{x}), \tag{9.4}$$

where $\mathbf{n}$ is the outward unit normal to $\Gamma_{\mathbf{n}}$ in the reference configuration, $\mathbf{P} = \mathbf{FS}$ is the first Piola-Kirchhoff stress tensor, $\bar{\mathbf{t}}$ the surface traction per unit undeformed area, and $\Gamma_{\mathbf{u}}$ and $\Gamma_{\mathbf{n}}$ are parts of the boundary of Ω where displacements and

tractions are prescribed respectively. Furthermore, $\mathbf{u}_0$ and $\mathbf{v}_0$ give, respectively, the initial displacement and the initial velocity fields.

The total force on the boundary $\Gamma_{\mathbf{n}}$ equals the total force on the part $\Gamma_{\mathbf{n}^\star}$ of the present boundary into which $\Gamma_{\mathbf{n}}$ is deformed[67]

$$\int_{\Gamma_{\mathbf{n}}} \bar{\mathbf{t}} \mathrm{d}\Gamma = \int_{\Gamma_{\mathbf{n}^\star}} f_{\mathrm{e}}^\star \mathbf{n}^\star \mathrm{d}\Gamma^\star, \tag{9.5}$$

where $\mathbf{n}^\star$ is the outward unit normal to present boundary $\Gamma_{\mathbf{n}^\star}$, and $f_{\mathrm{e}}^\star$ is the electrostatic force acting along the normal to $\Gamma_{\mathbf{n}^\star}$. Equation (9.5) embodies the constraint that the electrostatic pressure acts along the normal to the boundary, a consequence of the assumptions that the bodies are perfect conductors. Therefore, the traction $\bar{\mathbf{t}}$ is given by

$$\bar{\mathbf{t}} = f_{\mathrm{e}} (\det \mathbf{F}) \mathbf{F}^{-\mathrm{T}} \mathbf{n}. \tag{9.6}$$

Here, $f_{\mathrm{e}}(\mathbf{x}) = f_{\mathrm{e}}^\star(\mathbf{x}^\star(\mathbf{x}))$, where the same symbol has been used to denote the function $\mathbf{x}^\star$ and its value $\mathbf{x}^\star(\mathbf{x})$.

In order to solve the initial-boundary-value problem defined by Eqs. (9.1)-(9.4), we need an explicit form of the function $\hat{\mathbf{S}}$ in Eq. (9.2) and of f_{e} in Eq. (9.6). In the remainder of this Chapter we will not consider the effect of body forces, and thus set $\mathbf{b} = \mathbf{0}$ in Eq. (9.1a). Furthermore, we will model deformable bodies as linear elastic membranes. Surface tractions $\bar{\mathbf{t}}$ on the top and the bottom surfaces of membranes usually appear as body forces in equations governing their deformations. We discuss below the evaluation of the electrostatic force $f_{\mathrm{e}}^\star$ exerted on the boundary of a two-conductor system.

9.2.3. *Electrostatic Force*

Consider the two-conductor system depicted in Fig. 9.3, where Ω_1 and Ω_2 are the 3D regions of space occupied by the two conductors in their reference configurations, and $\Omega_1^\star$ and $\Omega_2^\star$ in their corresponding present configurations. The region exterior to $\Omega_1^\star \cup \Omega_2^\star$ is denoted by $\bar{\Omega}$. Boundaries of $\Omega_1^\star$ and $\Omega_2^\star$ are denoted by $\Gamma_1^\star$ and $\Gamma_2^\star$ respectively, and Γ_1 and Γ_2 are the corresponding ones in the reference configurations.

The boundary-value problem for the electrostatic potential ϕ formulated in the present configuration is (see, *e.g.*, Ref. 35)

$$\triangle \phi = 0 \quad \text{in } \bar{\Omega}, \tag{9.7a}$$

$$\phi = \bar{\phi}_1 \quad \text{on } \Gamma_1^\star, \tag{9.7b}$$

$$\phi = \bar{\phi}_2 \quad \text{on } \Gamma_2^\star, \tag{9.7c}$$

$$\phi \to 0 \quad \text{as } |\mathbf{x}| \to \infty. \tag{9.7d}$$

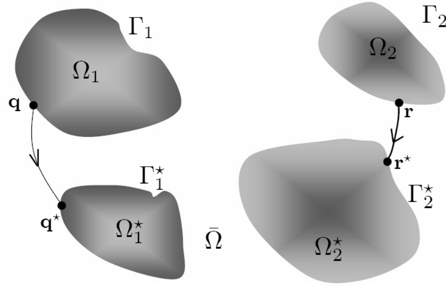

Fig. 9.3. Two-conductor system.

Here we have neglected inertia effects associated with the electric field because the speed of electric waves is considerably more than that of the mechanical waves. Thus ϕ is a harmonic function, and the boundary-value problem defined by Eq. (9.7) is studied in the potential theory. It is likely that its solution will depend upon the decay rate of ϕ in Eq. (9.7d).

The solution of the boundary-value problem (9.7) can be written as a boundary integral:[68]

$$\phi(\mathbf{q}^\star) = \int_{\Gamma^\star} G^\star(\mathbf{q}^\star, \mathbf{r}^\star)\sigma^\star(\mathbf{r}^\star)\mathrm{d}\Gamma^\star + c_\mathrm{T}, \tag{9.8}$$

where $\Gamma^\star = \Gamma_1^\star \cup \Gamma_2^\star$ is the overall surface of the conductors, $\mathbf{q}^\star$ and $\mathbf{r}^\star$ are the observation and the source points on $\Gamma^\star$, $\sigma^\star$ is the surface charge density and $G^\star$ is the Green function. The constant c_T is determined from the potential at infinity. Equation (9.8) gives the electrostatic potential in the present configuration of the system.

The area element $\mathrm{d}\Gamma^\star$ is expressed in terms of the corresponding area element $\mathrm{d}\Gamma$ by (see Ref. 67)

$$\mathrm{d}\Gamma^{\star\,2} = (\det \mathbf{F})^2(\mathbf{n} \cdot (\mathbf{F}^\mathrm{T}\mathbf{F})^{-1}\mathbf{n})\mathrm{d}\Gamma^2. \tag{9.9}$$

Therefore, Eq. (9.8) can be written in the Lagrangian description of motion as

$$\Phi(\mathbf{q}) = \int_\Gamma G(\mathbf{q}, \mathbf{r})\sigma(\mathbf{r})(\det \mathbf{F})\sqrt{\mathbf{n} \cdot (\mathbf{F}^\mathrm{T}\mathbf{F})^{-1}\mathbf{n}}\,\mathrm{d}\Gamma + c_\mathrm{T} \tag{9.10}$$

where $\sigma(\mathbf{r}) = \sigma^\star(\mathbf{r}^\star(\mathbf{r}))$, and $G(\mathbf{q}, \mathbf{r}) = G^\star(\mathbf{q}^\star(\mathbf{q}), \mathbf{r}^\star(\mathbf{r}))$.

The electrostatic potential energy stored in $\bar{\Omega}$ for the two-conductor system is given by

$$U_\mathrm{e} = \frac{\epsilon}{2}\int_{\bar{\Omega}} \mathrm{grad}\phi \cdot \mathrm{grad}\phi\,\mathrm{d}\bar{\Omega}, \tag{9.11}$$

where grad is the gradient operator with respect to coordinates in the present configuration, and ϵ is the dielectric constant of the medium comprising $\bar{\Omega}$. The electrostatic traction at the observation point $\mathbf{q}^\star$ in the present configuration is given by

$$f_{\mathrm{e}}^\star(\mathbf{q}^\star) = -\frac{\epsilon}{2}\left[\mathrm{grad}\phi \cdot \mathrm{grad}\phi\right](\mathbf{q}^\star). \quad (9.12)$$

Using the relation

$$\mathrm{Grad}\Phi = \mathbf{F}^{\mathrm{T}}\mathrm{grad}\phi, \quad (9.13)$$

imposing the condition (9.5), and substituting in it from Eqs. (9.12) and (9.9) we obtain the electrostatic traction $\bar{\mathbf{t}}$ at the observation point $\mathbf{q}$ in the reference configuration:

$$\bar{\mathbf{t}}(\mathbf{q}) = -\frac{\epsilon}{2}\left[(\det \mathbf{F})\left(\mathrm{Grad}\Phi \cdot \left(\mathbf{F}^{\mathrm{T}}\mathbf{F}\right)^{-1}\mathrm{Grad}\Phi\right)\mathbf{F}^{-\mathrm{T}}\mathbf{n}\right](\mathbf{q}). \quad (9.14)$$

Thus the solution of the 3D problem for MEMS requires solving the initial-boundary-value problem defined by Eqs. (9.1)-(9.4), (9.7) with the surface traction per unit undeformed area given by Eq. (9.14). If the surface charge distribution σ in the reference configuration is considered as the unknown instead of the electrostatic potential ϕ, the solution of the boundary-value problem in terms of σ is given by Eq. (9.10). In this case σ will appear in the expression (9.14) for $\bar{\mathbf{t}}$.

Note that the initial-boundary-value problem (9.1)-(9.4) is defined on the known region Ω_1 but the boundary-value problem (9.7) is defined in $\bar{\Omega}$ which is exterior to $\Omega_1^\star \cup \Omega_2^\star$. Assuming that the body 2 is rigid as is often the case in MEMS, then $\Omega_2^\star = \Omega_2$. The electrical and the mechanical problems are strongly coupled since $\Omega_1^\star$ is unknown a priori, and the boundary-value problem (9.7) requires that $\Omega_1^\star$ be known. A possibility is to use an iterative technique to solve the coupled electromechanical problem.

We also emphasize that mechanical deformations of the material occupying the region $\bar{\Omega}$ have been neglected. However, when $\bar{\Omega}$ is occupied by a fluid then deformations of this fluid should also be considered. This requires reformulation of the above problem.

9.3. The Casimir Effect

With the decrease in device dimensions from the micro to the nanoscale an additional force on nanoelectromechanical systems (NEMS), such as the Casimir force[69] (also see, *e.g.*, Refs. 70 and 71), should be considered.

The Casimir force represents the attraction between two uncharged material bodies due to modification of the zero-point energy associated with the electromagnetic modes in the space between them. An important feature of the Casimir effect is that even though its nature is quantistic, it predicts a force between macroscopic bodies.

van der Waals forces are related to electrostatic interaction among dipoles at the atomic scale.[72] Whereas the Casimir force between semi-infinite parallel plates depends only on the geometry, van der Waals forces depend on material properties of the media. The Casimir force is effective at longer distance than van der Waals forces;[72] the latter occur at the atomic scale, as for example in carbon nanotubes,[73] and are not considered here.

The analysis presented here is valid for semi-infinite parallel plate-like conductors. The expression for the Casimir force derived below is applicable to MEMS undergoing small deformations and of geometry consistent with the one considered here.

Consider a hollow box with perfectly conducting uncharged walls and a system of rectangular Cartesian coordinates $\{x^1, x^2, x^3\}$ aligned with the box's sides. Maxwell's equations for vanishing sources lead to the following wave equation for the electric field $\mathbf{E}$ inside the box:

$$\triangle \mathbf{E}(\mathbf{x}, t) = \frac{\partial^2 \mathbf{E}}{\partial t^2}(\mathbf{x}, t). \tag{9.15}$$

Note that components of the electric field parallel to the walls vanish at the walls. That is

$$\mathbf{E} - (\mathbf{E} \cdot \mathbf{n})\, \mathbf{n} = \mathbf{0} \quad \text{on the walls.} \tag{9.16}$$

The eigenvalue problem defined by Eqs. (9.15) and (9.16) can be solved without using initial conditions, and by separating the variables as

$$\mathbf{E}(\mathbf{x}, t) = \boldsymbol{\Xi}(\mathbf{x})\tau(t). \tag{9.17}$$

The spatial part of the solution is given by

$$\Xi^1(\mathbf{x}) = \cos\left(k_1 x^1\right) \sin\left(k_2 x^2\right) \sin\left(k_3 x^3\right), \tag{9.18a}$$

$$\Xi^2(\mathbf{x}) = \sin\left(k_1 x^1\right) \cos\left(k_2 x^2\right) \sin\left(k_3 x^3\right), \tag{9.18b}$$

$$\Xi^3(\mathbf{x}) = \sin\left(k_1 x^1\right) \sin\left(k_2 x^2\right) \cos\left(k_3 x^3\right), \tag{9.18c}$$

where $\mathbf{k} = (k_1, k_2, k_3)$ is the wave vector. Imposing boundary conditions (9.16) at the walls leads to the following relation

$$k_i = \frac{\pi \nu_i}{g}, \tag{9.19}$$

with ν_i being an integer.

Equations (9.17) and (9.18) imply that the time dependent part of the solution satisfies the harmonic oscillator equation

$$\frac{\partial^2 \tau}{\partial t^2} + \omega_{\mathbf{k}}^2 \tau = 0, \tag{9.20}$$

where $\omega_{\mathbf{k}} = c|\mathbf{k}|$ is the angular frequency of a normal mode, and c is the speed of light.

In quantum mechanics, each mode is treated as a quantum harmonic oscillator with associated energies (see, *e.g.*, Ref. 71)

$$\mathcal{E}_n^{\mathbf{k}} = \hbar \omega_{\mathbf{k}} \left(\frac{1}{2} + n \right), \tag{9.21}$$

where the integer n represents the number of photons in the mode and $\hbar$ is the Plank constant. The energy corresponding to $n = 0$ (vacuum) is the zero point energy

$$\mathcal{E}_0^{\mathbf{k}} = \frac{1}{2} \hbar \omega_{\mathbf{k}}. \tag{9.22}$$

The sum over all modes gives the zero point energy inside the box as

$$\mathcal{E}_0 = 2 \sum_{k_1, k_2, k_3} \mathcal{E}_0^{\mathbf{k}} = \sum_{k_1, k_2, k_3} \hbar c \sqrt{(k_1^2 + k_2^2 + k_3^2)}, \tag{9.23}$$

where the factor 2 is due to the two possible polarizations for $\mathbf{k}$ (see Ref. 70). Since there are an infinite number of normal modes with increasingly high frequencies, the energy $\mathcal{E}_0$ is infinite.

Consider the capacitor with perfectly conducting plates of area L^2 at a distance g in vacuum (Fig. 9.4). If $L \gg g$, the sum over k_1 and k_2 in Eq. (9.23) is replaced by an integral, $\sum_{k_i} \to (L/\pi) \int_0^\infty \mathrm{d}k_i$, $i = 1, 2$ (see Ref. 70). If g is made arbitrarily large, then the sum over k_3 can be replaced by the corresponding integral.

The Casimir force is determined by the change in the zero point energy between the state corresponding to the two plates at a finite distance g, and the state

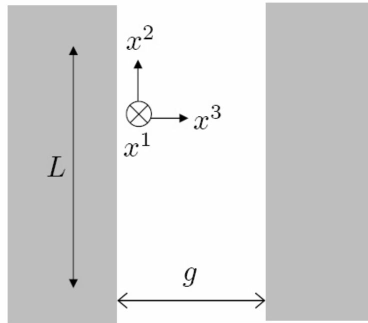

Fig. 9.4. Coordinate system for calculating the Casimir force.

corresponding to $g \to \infty$. This determines the potential energy

$$\mathcal{U}(g) = \mathcal{E}_0(g) - \mathcal{E}_0(\infty) = \hbar c \frac{L^2}{\pi^2} \int_0^\infty \int_0^\infty \left(\sum_{\nu_3} \sqrt{k_1^2 + k_2^2 + \frac{\nu_3^2 \pi^2}{g^2}} - \frac{g}{\pi} \int_0^\infty \sqrt{k_1^2 + k_2^2 + k_3^2}\, \mathrm{d}k_3 \right) \mathrm{d}k_1 \mathrm{d}k_2. \quad (9.24)$$

The resulting Casimir pressure is given by

$$f_{\mathrm{c}}(g) = -\frac{1}{L^2} \nabla \mathcal{U}(g) = -\frac{\pi^2 \hbar c}{240 g^4} \quad (9.25)$$

The detailed calculation is done in Ref. 70 employing the Euler–Maclaurin summation formula.[74] In order to truncate the infinite summation and integration at a certain wave vector $\mathbf{k}_{\mathrm{max}}$, a cutoff function is introduced.

The existence of the Casimir force poses a severe constraint on the miniaturization of electrostatically actuated devices. At the nanoscale, the Casimir force may overcome elastic restoring actions in the device and lead to the plates' sticking together during the fabrication process.

An important characteristic of the Casimir force is its strong dependence on the shape, and switching from attractive to repulsive depending on the geometry. In Ref. 75, the zero point energy of a conducting spherical shell has been computed. While parallel plates are attracted to each other because of the zero point energy, a conducting sphere tends to expand.

Typical experimental measurements of Casimir forces involve gold-coated surfaces that are modeled by a Drude-type dielectric function.[76–78]

9.4. Electrostatically Actuated Micromembranes

In this section we study pull-instability in micromembranes due to the electrostatic or the Coulomb force. Recall that the membrane approximation is valid for $L/h \geq 400$ (see, *e.g.*, Ref. 40), where L is a typical in-plane dimension and h is the membrane thickness. We also analyze the effect of the Casimir force on the pull-in parameters. We show that beyond a certain size, the pull-in instability occurs at zero voltage. This means that the system collapses during the manufacturing process. We also analyze symmetry breaking in annular membranes due to the combined effects of the Coulomb and the Casimir forces. In Ref. 79 the effect of the Casimir force is considered for non-linear membranes but that of the Coulomb force is discarded. In Ref. 80 a one degree-of-freedom model for analyzing the effect of both the Casimir and the Coulomb forces on beam-like bodies is presented, while in Ref. 81 the pull-in instability under the action of the Casimir force using a one degree-of-freedom model is studied.

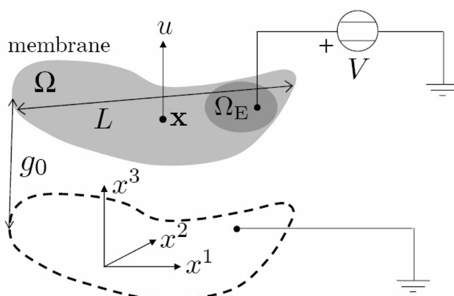

Fig. 9.5. Geometry of the microelectromechanical system.

9.4.1. *Mathematical Model of a Micromembrane*

A schematic sketch of the problem studied is shown in Fig. 9.5. We assume that (i) both bodies are perfect conductors, and are separated by a dielectric layer of permittivity ϵ, (ii) the bottom body is rigid, and the top one is deformable, and can be modeled as an elastic membrane, (iii) the membrane is either clamped or free on the boundary, (iv) the membrane undergoes static infinitesimal deformations, (v) a potential difference V exists between the two bodies, (vi) electric fringing fields are negligible (see, *e.g.*, Ref. 3), (vii) the uniform initial gap, g_0,

between the two bodies is much smaller than a typical linear dimension of the membrane, (viii) electric flux lines between the conductors are uniformly distributed over the surface of the membrane, and (ix) the effect of the change in the direction of the Casimir and the Coulomb forces as the membrane deforms is negligible. Under these assumptions the governing equation for the deflection u of the membrane is:[3]

$$\sigma_0 h \triangle u\,(\mathbf{x}) + f_{\mathrm{e}}(u(\mathbf{x}), \mathbf{x}) + f_{\mathrm{c}}(u(\mathbf{x})) = 0, \quad \mathbf{x} \in \Omega. \tag{9.26}$$

Here, Ω is the membrane domain, $\mathbf{x}$ a generic point, $\triangle$ the Laplacian operator, σ_0 the tensile stress in the membrane, h the thickness, f_{e} the electrostatic pressure on the bottom surface of the membrane, and f_{c} the Casimir pressure.

We nondimensionalize the vertical coordinate x^3 with respect to the initial gap g_0, and the in-plane coordinates x^1 and x^2 with respect to the characteristic length L (see Fig. 9.5). Equation (9.7a) for the potential ϕ becomes

$$\frac{g_0^2}{L^2}\left(\frac{\partial^2\phi}{(\partial\hat{x}^1)^2} + \frac{\partial^2\phi}{(\partial\hat{x}^2)^2}\right) + \frac{\partial^2\phi}{(\partial\hat{x}^3)^2} = 0, \tag{9.27}$$

where a superimposed hat refers to nondimensional coordinates. The assumption (vii) reduces Eq. (9.27) to

$$\frac{\partial^2\phi}{(\partial\hat{x}^3)^2} = 0. \tag{9.28}$$

Imposing the boundary conditions $\phi(0) = 0$, and $\phi(g_0 + u) = V\delta\,(\mathbf{x})$ on the bottom and the top bodies respectively, the solution is

$$\phi = \frac{V}{g_0}\frac{\delta(\mathbf{x})}{(1 + u/g_0)}x^3, \tag{9.29}$$

where

$$\delta\,(\mathbf{x}) = \begin{cases} 1, & \mathbf{x} \in \Omega_{\mathrm{E}} \\ 0, & \mathbf{x} \notin \Omega_{\mathrm{E}} \end{cases}, \tag{9.30}$$

and Ω_{E} is the part of the membrane that is electroded and where the electric potential is effective. Substitution of Eq. (9.29) into Eq. (9.12) gives the following expression for the electrostatic pressure

$$f_{\mathrm{e}}(u(\mathbf{x}), \mathbf{x}) = -\frac{\epsilon V^2}{2g_0^2}\frac{\delta(\mathbf{x})}{(1 + u(\mathbf{x})/g_0)^2}, \tag{9.31}$$

where terms depending on the spatial derivatives of u have been discarded consistent with assumption (ix).

We use the proximity force approximation (PFA) for the Casimir force f_{c} consistent with assumptions made in the mechanical and the electrostatic models,

and adopt the expression given in Eq. (9.25). In the PFA curved surfaces are viewed as superposition of infinitesimal parallel plates; see, *e.g.*, Refs. 82 and 83 and references therein. Gies and Klingmüller[83] have shown that for a sphere of radius R separated from a flat plate by a distance g, the PFA gives results within 1% accuracy for $g/R < 0.1$

The reduction of the right-hand side of Eq. (9.1a) to the left-hand side of Eq. (9.26) for small deflections u of an elastic membrane is given in Ref. 32.

We nondimensionalize the deflection by the initial gap g_0, and obtain

$$\triangle u(\mathbf{x}) = \lambda \frac{\delta(\mathbf{x})}{(1+u(\mathbf{x}))^2} + \frac{\mu}{(1+u(\mathbf{x}))^4}, \tag{9.32}$$

where we have used u to indicate the nondimensional deflection. Parameters λ and μ are defined by

$$\lambda = \frac{\epsilon_0 V^2 L^2}{2\sigma_0 h g_0^3}, \qquad \mu = \frac{\pi^2 \hbar c L^2}{240 \sigma_0 h g_0^5}. \tag{9.33}$$

As the voltage V increases, the parameter λ increases while μ stays constant. Scaling down the device dimensions (h, g_0 and L) by a factor F

$$h \to h/F, \quad g_0 \to g_0/F, \quad L \to L/F \tag{9.34}$$

increases λ by a factor of F^2 and μ by a factor of F^4, that is

$$\lambda \to F^2\lambda, \quad \mu \to F^4\mu. \tag{9.35}$$

Thus, for $F > 1$, μ increases much faster than λ with a decrease in the device dimensions.

The boundary of the domain Ω is partitioned into two disjoint parts:

$$\partial\Omega = \Gamma_u \cup \Gamma_{\mathbf{n}}, \qquad \mathring{\Gamma}_u \cap \mathring{\Gamma}_{\mathbf{n}} = \varnothing, \tag{9.36}$$

where $\mathring{\Gamma}_u$ is comprised of the interior points of Γ_u. On Γ_u essential homogeneous boundary conditions are prescribed, that is

$$u(\mathbf{x}) = 0, \qquad \mathbf{x} \in \Gamma_u, \tag{9.37}$$

while on $\Gamma_{\mathbf{n}}$ natural homogeneous boundary conditions are imposed, that is

$$\nabla u(\mathbf{x}) \cdot \mathbf{n}(\mathbf{x}) = 0, \qquad \mathbf{x} \in \Gamma_{\mathbf{n}}. \tag{9.38}$$

9.4.2. *Local Weak Formulation of the Problem*

We rewrite the non-linear Poisson Eq. (9.32) as

$$\triangle u\left(\mathbf{x}\right)=G\left(\lambda,\mu,u,\mathbf{x}\right) \tag{9.39}$$

where

$$G\left(\lambda,\mu,u,\mathbf{x}\right)=\lambda\frac{\delta\left(\mathbf{x}\right)}{\left(1+u\right)^{2}}+\frac{\mu}{\left(1+u\right)^{4}}. \tag{9.40}$$

We partition the boundary Γ_u into n_{L} connected parts, say $\Gamma_u^{(1)},\dots,\Gamma_u^{(n_{\mathrm{L}})}$. In order to enforce the essential boundary conditions we introduce n_{L} Lagrange multipliers $\gamma^{(1)},\dots,\gamma^{(n_{\mathrm{L}})}$, each of them being defined on the corresponding part of Γ_u.

We introduce a local symmetric augmented weak formulation (LSAWF) of the boundary-value problem defined by Eqs. (9.39), (9.37) and (9.38) on a subdomain Ω_{S} of the domain Ω:

$$-\int_{\Omega_{\mathrm{S}}}\nabla u\cdot\nabla\tilde{u}\,\mathrm{d}\Omega-\int_{\Omega_{\mathrm{S}}}G(\lambda,\mu,u,\mathbf{x})\,\tilde{u}\,\mathrm{d}\Omega$$
$$+\sum_{\alpha=1}^{n_{\mathrm{L}}}\left(\int_{\Gamma_{\mathrm{S}u}^{(\alpha)}}u\,\tilde{\gamma}^{(\alpha)}\mathrm{d}\Gamma+\int_{\Gamma_{\mathrm{S}u}^{(\alpha)}}\tilde{u}\,\gamma^{(\alpha)}\mathrm{d}\Gamma\right)=0. \tag{9.41}$$

As illustrated in Fig. 9.6, $\Gamma_{\mathrm{S}u}^{(\alpha)}$ is the intersection of $\partial\Omega_{\mathrm{S}}$ with $\Gamma_u^{(\alpha)}$, L_{S} is the part of $\partial\Omega_{\mathrm{S}}$ enclosed in the domain Ω, $\tilde{u}$ and $\tilde{\gamma}^{(\alpha)}$ are smooth test functions defined, respectively, in Ω_{S} and $\Gamma_{\mathrm{S}u}^{(\alpha)}$. The homogeneous natural boundary conditions (9.38) have been embedded in the weak formulation of the problem. Also, we have selected test functions $\tilde{u}$ that vanish on the inner boundary L_{S}.

9.4.3. *Discrete Non-Linear Formulation*

In order to seek an approximate solution of the non-linear problem, we use 2D MLS basis functions[a] (see, *e.g.*, Ref. 52). We use N nodes scattered on the domain and construct the set of basis functions $\varphi_1,\dots,\varphi_N$. The trial solution is consequently expressed in terms of nodal unknowns, $\hat{u}_1,\dots,\hat{u}_N$. Note that the MLS basis functions do not have the Kronecker delta property. Therefore nodal

---

[a]The boundary $\partial\Omega$ of the 2D domain Ω is approximated by piecewise straight lines connecting adjacent nodes on it.

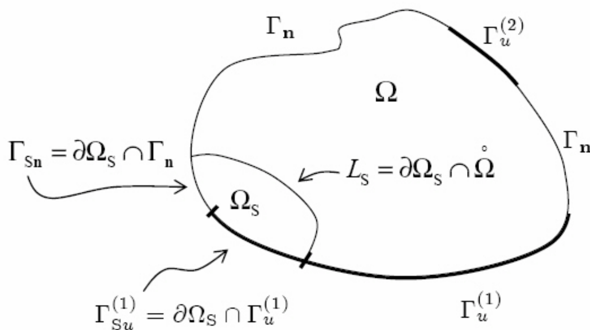

Fig. 9.6. Subdomain of the global domain.

unknowns, $\hat{u}_1, \ldots, \hat{u}_N$, do not equal values of the trial solution at the nodes. The Lagrange multiplier field $\gamma^{(\alpha)}$ is approximated by non-linear MLS basis functions constructed from nodes lying only on the curve $\Gamma_u^{(\alpha)}$. Therefore

$$\left(\gamma^{(\alpha)}\right)^h = \sum_{\beta=1}^{\nu^{(\alpha)}} \hat{\gamma}_\beta^{(\alpha)} \chi_\beta^{(\alpha)}, \tag{9.42}$$

where $\nu^{(\alpha)}$ is the number of nodes belonging to $\Gamma_u^{(\alpha)}$, $\chi_\beta^{(\alpha)}$'s are non-linear MLS basis functions, and $\hat{\gamma}_\beta^{(\alpha)}$'s are fictitious nodal values. We collect $\hat{\gamma}_\beta^{(\alpha)}$'s into n_{L} distinct vectors $\hat{\boldsymbol{\gamma}}^{(1)}, \ldots, \hat{\boldsymbol{\gamma}}^{(n_{\mathrm{L}})}$, and denote the total number of Lagrange multiplier nodes by $N_{\mathrm{L}} := \sum_{\alpha=1}^{n_{\mathrm{L}}} \nu^{(\alpha)}$.

In order to derive $N + N_{\mathrm{L}}$ equations for nodal unknowns $\hat{\mathbf{u}}$ and $\hat{\boldsymbol{\gamma}}^{(1)}, \ldots, \hat{\boldsymbol{\gamma}}^{(n_{\mathrm{L}})}$, we consider in Eq. (9.41) N subdomains $\Omega_{\mathrm{S}1}, \ldots, \Omega_{\mathrm{S}N}$, and $N + N_{\mathrm{L}}$ independent test functions:

$$\tilde{u}_1, \ldots, \tilde{u}_N, \qquad \tilde{\gamma}_1^{(\alpha)}, \ldots, \tilde{\gamma}_{\nu^{(\alpha)}}^{(\alpha)}, \quad \alpha = 1, \ldots, n_{\mathrm{L}}. \tag{9.43}$$

The discrete non-linear equations obtained from Eq. (9.41) are

$$\mathbf{K}\,\hat{\mathbf{u}} + \mathbf{G}\,(\lambda, \mu, \hat{\mathbf{u}}) + \sum_{\alpha=1}^{n_{\mathrm{L}}} \mathbf{R}^{(\alpha)} \hat{\boldsymbol{\gamma}}^{(\alpha)} = \mathbf{0}, \tag{9.44}$$

$$\mathbf{V}^{(\alpha)}\,\hat{\mathbf{u}} = \mathbf{0}, \qquad \alpha = 1, \ldots, n_{\mathrm{L}}, \tag{9.45}$$

where

$$[\mathbf{K}]_{ij} = -\int_{\Omega_\mathrm{S}^i} \nabla\varphi_j \cdot \nabla\tilde{u}_i \,\mathrm{d}\Omega, \qquad i,j = 1,\ldots,N; \tag{9.46a}$$

$$[\mathbf{G}(\lambda,\mu,\hat{\mathbf{u}})]_i = -\int_{\Omega_\mathrm{S}^i} G\left(\lambda,\mu,u^h\right) \tilde{u}_i \,\mathrm{d}\Omega, \qquad i = 1,\ldots,N; \tag{9.46b}$$

$$\left[\mathbf{R}^{(\alpha)}\right]_{i\beta} = \int_{\Gamma_{\mathrm{S}u}^{i\,(\alpha)}} \chi_\beta^{(\alpha)}\,\tilde{u}_i \mathrm{d}\Gamma, \qquad i = 1,\ldots,N, \quad \beta = 1,\ldots,\nu^{(\alpha)}; \tag{9.46c}$$

$$\left[\mathbf{V}^{(\alpha)}\right]_{\beta j} = \int_{\Gamma_{\mathrm{S}u}^{\beta\,(\alpha)}} \varphi_j\,\tilde{\gamma}_\beta^{(\alpha)} \mathrm{d}\Gamma, \quad \beta = 1,\ldots,\nu^{(\alpha)}, \quad j = 1,\ldots,N. \tag{9.46d}$$

For subdomains having the shape of a sector of a circle, integrals in Eq. (9.46) are computed by the Gauss quadrature rule.

In the MLPG1 method the test function $\tilde{u}_i$ for the i-th node is chosen to be the weight function W_i used in the MLS approximation, but with a scaled support. Test functions for a Lagrange multiplier are chosen to be the test functions $\tilde{u}_i$'s restricted to the boundary $\Gamma_{\mathrm{S}u}^{(\alpha)}$ of the domain.

Let rows of the $(N - N_\mathrm{L}) \times N$ matrix $\mathbf{Y}$ be comprised of $(N - N_\mathrm{L})$ linearly independent null vectors of the $N_\mathrm{L} \times N$ matrix $\mathbf{V}$ obtained by appending rows of matrices $\mathbf{V}^{(\alpha)}$'s, and set

$$\hat{\mathbf{u}} = \mathbf{Y}^\mathrm{T}\mathbf{u}. \tag{9.47}$$

Substituting for $\hat{\mathbf{u}}$ from Eq. (9.47) into Eq. (9.45) gives

$$\mathbf{V}^{(\alpha)}\,\mathbf{Y}^\mathrm{T}\mathbf{u} = 0, \qquad \alpha = 1,\ldots,n_\mathrm{L}, \tag{9.48}$$

which are identically satisfied for every $(N - N_\mathrm{L})$-vector $\mathbf{u}$. Similarly, let rows of the $(N - N_\mathrm{L}) \times N$ matrix $\mathbf{X}$ equal $(N - N_\mathrm{L})$ linearly independent null vectors of the $N_\mathrm{L} \times N$ matrix $\mathbf{R}^\mathrm{T}$ obtained by appending columns of matrices $\mathbf{R}^{(\alpha)}$'s, and transposing the entire matrix. Then

$$\mathbf{X}\mathbf{R}^{(\alpha)} = \mathbf{0}, \qquad \alpha = 1,...,n_\mathrm{L}. \tag{9.49}$$

Premultiplying both sides of Eq. (9.44) by $\mathbf{X}$ and substituting for $\hat{\mathbf{u}}$ from Eq. (9.47) we obtain the following reduced system of $(N - N_\mathrm{L})$ non-linear equations for $\mathbf{u}$:

$$\bar{\mathbf{K}}\,\mathbf{u} + \bar{\mathbf{G}}(\lambda,\mu,\mathbf{u}) = \mathbf{0}, \tag{9.50}$$

where

$$\bar{\mathbf{K}} = \mathbf{X}\mathbf{K}\mathbf{Y}^\mathrm{T}, \qquad \bar{\mathbf{G}}(\lambda,\mu,\mathbf{u}) = \mathbf{X}\,\mathbf{G}\left(\lambda,\mu,\mathbf{Y}^\mathrm{T}\mathbf{u}\right). \tag{9.51}$$

Having found $\mathbf{u}$ from Eq. (9.50), $\hat{\mathbf{u}}$ is computed from Eq. (9.47).

9.4.4. *Pseudo-Arc-Length Continuation Method*

The system of non-linear Eq. (9.50) may not admit a unique solution $\mathbf{u}$ for an arbitrary value of the parameter λ and a given value of μ. We use the pseudo-arc-length continuation method (see, *e.g.*, Refs. 65 and 66) to solve Eq. (9.50). It enables us to find the complete bifurcation path and the symmetry breaking bifurcation. The method is explained for the case of variable λ and fixed μ. When studying the behavior of the system under the effect of the Casimir force only, *i.e.*, for $\lambda = 0$ with varying μ, exactly the same procedure applies except that the roles of λ and μ are exchanged.

A new parameter s is added so that λ and $\mathbf{u}$ are considered functions of s. If the solution $(\mathbf{u}_{k-1}, \lambda_{k-1})$ of Eq. (9.50) is known at $s = s_{k-1}$, the solution

$$(\mathbf{u}_k, \lambda_k) = (\mathbf{u}_{k-1} + \Delta\mathbf{u}_k, \lambda_{k-1} + \Delta\lambda_k) \tag{9.52}$$

at the abscissa $s_k = s_{k-1} + \Delta s_k$ is found by solving the system of equations:

$$\bar{\mathbf{K}}\,\mathbf{u}_k + \bar{\mathbf{G}}\left(\lambda_k, \mu, \mathbf{u}_k\right) = \mathbf{0}, \tag{9.53a}$$

$$\left(\mathbf{u}_k - \mathbf{u}_{k-1}\right)^{\mathrm{T}} \mathbf{U}\,\dot{\mathbf{u}}_{k-1} + \left(\lambda_k - \lambda_{k-1}\right)\dot{\lambda}_{k-1} - \Delta s_k = 0, \tag{9.53b}$$

where $\mathbf{U}$ is a symmetric positive definite matrix, and a superimposed dot indicates derivative with respect to s. In many cases (see, *e.g.*, Ref. 65), $\mathbf{U}$ is chosen to be the identity matrix, but for the present problem, numerical experiments showed that more stable solutions are obtained by choosing $\mathbf{U} = \mathbf{\Phi}^{\mathrm{T}}\mathbf{\Phi}$, with $[\mathbf{\Phi}]_{ij} = \varphi_j\left(\mathbf{x}_i\right)$. This implies that the arc length is computed by using the actual nodal values, rather than the fictitious ones.

Geometrically interpreted, within this method we find a solution $(\mathbf{u}_k, \lambda_k)$ to the system (9.50) in an hyperplane that is at a distance Δs_k from $(\mathbf{u}_k, \lambda_k)$ and that is perpendicular to the direction vector $(\dot{\mathbf{u}}_{k-1}, \dot{\lambda}_{k-1})$.[65]

The solution of the set (9.53) of non-linear equations, for the unknowns $\Delta\mathbf{u}_k$ and $\Delta\lambda_k$, is found by using Newton's iterations. Hence the generic ν-th iteration is

$$\begin{bmatrix} \bar{\mathbf{T}}_k^{(\nu)}\left(\lambda_k^{(\nu)}, \mathbf{u}_k^{(\nu)}\right) & \bar{\mathbf{H}}_k^{(\nu)}\left(\lambda_k^{(\nu)}, \mathbf{u}_k^{(\nu)}\right) \\ \dot{\mathbf{u}}_{k-1}^{\mathrm{T}}\mathbf{U} & \dot{\lambda}_{k-1} \end{bmatrix} \begin{bmatrix} \Delta\mathbf{u}_k^{(\nu)} \\ \Delta\lambda_k^{(\nu)} \end{bmatrix} = \tag{9.54}$$

$$-\begin{bmatrix} \bar{\mathbf{K}}\,\mathbf{u}_k^{(\nu)} + \bar{\mathbf{G}}\left(\lambda_k^{(\nu)}, \mu, \mathbf{u}_k^{(\nu)}\right) \\ \left(\mathbf{u}_k^{(\nu)} - \mathbf{u}_{k-1}\right)^{\mathrm{T}} \mathbf{U}\,\dot{\mathbf{u}}_{k-1} + \left(\lambda_k^{(\nu)} - \lambda_{k-1}\right)\dot{\lambda}_{k-1} - \Delta s_k \end{bmatrix},$$

where $\left(\Delta\mathbf{u}_k^{(\nu)}, \Delta\lambda_k^{(\nu)}\right)$ indicates the ν-th solution increment; $\left(\mathbf{u}_k^{(\nu)}, \lambda_k^{(\nu)}\right)$ is the updated solution at the $(\nu-1)$-th iteration, *i.e.*

$$\mathbf{u}_k^{(\nu)} = \mathbf{u}_{k-1} + \sum_{h=1}^{\nu-1} \Delta\mathbf{u}_k^{(h)}, \qquad \lambda_k^{(\nu)} = \lambda_{k-1} + \sum_{h=1}^{\nu-1} \Delta\lambda_k^{(h)}; \tag{9.55}$$

$\bar{\mathbf{T}}_k^{(\nu)}\left(\lambda_k^{(\nu)}, \mathbf{u}_k^{(\nu)}\right)$ is the tangent stiffness at the $(\nu-1)$-th iteration, *i.e.*

$$\bar{\mathbf{T}}_k^{(\nu)}\left(\lambda_k^{(\nu)}, \mathbf{u}_k^{(\nu)}\right) = \bar{\mathbf{K}} + \mathbf{X}\left[\mathbf{D}_k^{(\nu)}\left(\lambda_k^{(\nu)}, \mathbf{u}_k^{(\nu)}\right)\right]\mathbf{Y}^{\mathrm{T}}, \tag{9.56}$$

with

$$\left[\mathbf{D}_k^{(\nu)}\left(\lambda_k^{(\nu)}, \mathbf{u}_k^{(\nu)}\right)\right]_{ij} = -\int_{\Omega_{\mathrm{S}}^i} \frac{\partial G}{\partial u^h}\left(\lambda_k^{(\nu)}, \mu, \boldsymbol{\varphi}^{\mathrm{T}}\mathbf{Y}^{\mathrm{T}}\mathbf{u}_k^{(\nu)}\right)\tilde{u}_i\varphi_j \mathrm{d}\Omega, \tag{9.57}$$

and

$$\left[\bar{\mathbf{H}}_k^{(\nu)}\left(\lambda_k^{(\nu)}, \mathbf{u}_k^{(\nu)}\right)\right]_{i} = -\int_{\Omega_{\mathrm{S}}^i} \frac{\partial G}{\partial \lambda}\left(\lambda_k^{(\nu)}, \mu, \boldsymbol{\varphi}^{\mathrm{T}}\mathbf{Y}^{\mathrm{T}}\mathbf{u}_k^{(\nu)}\right)\tilde{u}_i \mathrm{d}\Omega. \tag{9.58}$$

Iterations are performed till

$$\max\left\{\sup_{\mathbf{x}\in\Omega}\left[\boldsymbol{\varphi}(\mathbf{x})^{\mathrm{T}}\mathbf{Y}^{\mathrm{T}}\Delta\mathbf{u}_k^{(\nu)}\right], \Delta\lambda_k^{(\nu)}\right\} < \varepsilon_{\mathrm{T}}, \tag{9.59}$$

where ε_{T} is a prescribed tolerance.

Once the solution $(\mathbf{u}_k, \lambda_k)$ has been found, the direction vector $\left(\dot{\mathbf{u}}_k, \dot{\lambda}_k\right)$, for the next iteration is determined by solving

$$\begin{bmatrix} \bar{\mathbf{T}}_k^{(\bar{\nu}_k)}(\lambda_k, \mathbf{u}_k) & \bar{\mathbf{H}}_k^{(\bar{\nu}_k)}(\lambda_k, \mathbf{u}_k) \\ (\dot{\mathbf{u}}_{k-1})^{\mathrm{T}}\mathbf{U} & \dot{\lambda}_{k-1} \end{bmatrix}\begin{bmatrix}\dot{\mathbf{u}}_k \\ \dot{\lambda}_k\end{bmatrix} = \begin{bmatrix}\mathbf{0} \\ 1\end{bmatrix}, \tag{9.60}$$

where $\bar{\nu}_k$ is the number of iterations required for the solution to converge. The direction vector is then rescaled according to

$$\dot{\mathbf{u}}_k^{\mathrm{T}}\mathbf{U}\,\dot{\mathbf{u}}_k + \dot{\lambda}_k^2 = 1. \tag{9.61}$$

The length Δs_{k+1} for the next step is determined from the knowledge of the length Δs_k and the iteration number $\bar{\nu}_k$ using the following simple adaptive scheme

$$\Delta s_{k+1} = \Delta s_k\sqrt{\frac{\tau}{\bar{\nu}_k}}, \tag{9.62}$$

where τ represents the desired number of iterations for the convergence of Newton's method. The parameter τ is chosen so that if Newton's method converges rapidly the step size is increased, while if Newton's method converges slowly the step size is decreased.[65]

The pseudo-arc-length algorithm is started by assuming that for $s_0 = 0$ the solution is the pair $(\mathbf{u}_0, \lambda_0) = (\mathbf{0}, 0)$, and computing the solution $\mathbf{u}_1$ for a given small λ_1 with the standard Euler method resulting from linearizing Eq. (9.50) about $(\mathbf{u}_0, \lambda_0)$. Once the solution corresponding to this small electrostatic force is computed, the direction vector $\left(\dot{\mathbf{u}}_1, \dot{\lambda}_1\right)$ is estimated by the linear approximation

$$\dot{\mathbf{u}}_1 = \frac{1}{\Delta s_1}\left(\mathbf{u}_1 - \mathbf{u}_0\right), \qquad \dot{\lambda}_1 = \frac{1}{\Delta s_1}\left(\lambda_1 - \lambda_0\right), \tag{9.63}$$

where the initial arc length is

$$\Delta s_1 = \sqrt{\mathbf{u}_1^{\mathrm{T}}\mathbf{U}\mathbf{u}_1 + \lambda_1^2}. \tag{9.64}$$

When the tangent stiffness matrix, $\bar{\mathbf{T}}_k$ in Eq. (9.54), becomes singular the entire matrix on the left-hand side of Eq. (9.54) is generally nonsingular unless a bifurcation occurs.[65] This means that the pull-in instability may be detected, and the MEMS behavior analyzed after reaching the instability.

When a bifurcation occurs the entire matrix on the left-hand side of Eq. (9.54) becomes singular, and crossing the bifurcation point implies a change in the sign of the determinant of this matrix. In this case, the bifurcation point is determined by using the secant method, and the bifurcation path is followed by using the normal vector to the original path as an initial estimate of the direction vector.[65]

9.4.5. *One Degree-of-Freedom Model*

A closed-form solution of the boundary-value problem defined by Eq. (9.32) and boundary conditions in Eqs. (9.37) and (9.38) cannot be found. Here we give an approximate solution based on a one degree-of-freedom (d.o.f.) model of the MEMS. The approximate solution is constructed by expressing the deflection field $u(\mathbf{x})$ as the product of an unknown non-dimensional deflection parameter $\bar{u}$, and a trial function $\zeta(\mathbf{x})$ satisfying the kinematic boundary conditions in Eq. (9.37):

$$u(\mathbf{x}) = \bar{u}\zeta(\mathbf{x}). \tag{9.65}$$

The governing equation for $\bar{u}$ is derived by multiplying both sides of Eq. (9.32) with $\zeta(\mathbf{x})$, integrating the resulting equation over the domain, and substituting into it the approximate solution given by Eq. (9.65). After using the divergence theorem and recalling that $\zeta(\mathbf{x})$ satisfies the kinematic boundary conditions in Eq. (9.37), the governing equation for $\bar{u}$ becomes

$$\kappa\bar{u} = \lambda F_{\mathrm{e}}(\bar{u}) + \mu F_{\mathrm{c}}(\bar{u}), \tag{9.66}$$

where

$$\kappa = -\int_\Omega \nabla\zeta(\mathbf{x}) \cdot \nabla\zeta(\mathbf{x})\mathrm{d}\Omega, \tag{9.67a}$$

$$F_\mathrm{e}(\bar{u}) = \int_\Omega \frac{\zeta(\mathbf{x})}{(1+\bar{u}\zeta(\mathbf{x}))^2}\mathrm{d}\Omega, \tag{9.67b}$$

$$F_\mathrm{c}(\bar{u}) = \int_\Omega \frac{\zeta(\mathbf{x})}{(1+\bar{u}\zeta(\mathbf{x}))^4}\mathrm{d}\Omega. \tag{9.67c}$$

The left-hand side of Eq. (9.66) represents the virtual work done by the spring force on the virtual displacement ζ, and the sum of the two terms on the right-hand side represent the virtual work done by the external forces.

We define

$$\mathcal{F}(\bar{u},\lambda) = \kappa\bar{u} - \lambda F_\mathrm{e}(\bar{u}) - \mu F_\mathrm{c}(\bar{u}), \tag{9.68}$$

and note that the equilibrium configuration of the system is stable for $\mathcal{F} \geq 0$ and unstable for $\mathcal{F} \leq 0$. At the onset of instability the system's stiffness given by $\partial\mathcal{F}/\partial\bar{u}$ vanishes. That is

$$\kappa = \lambda\frac{\mathrm{d}F_\mathrm{e}}{\mathrm{d}\bar{u}}(\bar{u}_\mathrm{PI}) + \mu\frac{\mathrm{d}F_\mathrm{c}}{\mathrm{d}\bar{u}}(\bar{u}_\mathrm{PI}). \tag{9.69}$$

The pull-in deflection parameter $\bar{u}_\mathrm{PI}$ is obtained by eliminating λ from Eqs. (9.66) and (9.69), and by numerically solving the following resulting non-linear algebraic equation in $\bar{u}_\mathrm{PI}$:

$$(\kappa\bar{u}_\mathrm{PI} - \mu F_\mathrm{c}(\bar{u}_\mathrm{PI}))\frac{\mathrm{d}F_\mathrm{e}}{d\bar{u}}(\bar{u}_\mathrm{PI}) = \left(\kappa - \mu\frac{\mathrm{d}F_\mathrm{c}}{\mathrm{d}\bar{u}}(\bar{u}_\mathrm{PI})\right)F_\mathrm{e}(\bar{u}_\mathrm{PI}). \tag{9.70}$$

By substituting the so deduced value $\bar{u}_\mathrm{PI}$ into either Eq. (9.66) or Eq. (9.69), the pull-in voltage λ_PI is determined. Note that when $\mu = 0$, $\bar{u}_\mathrm{PI}$ is independent of κ. This one d.o.f. model has been proposed in Ref. 63 to study pull-in instability in narrow microbeams with von Kármán non-linearity and fringing fields incorporated in the electromechanical system, with $\zeta(\mathbf{x})$ equal to the microbeam's static deflection under a uniformly distributed load.

The present one d.o.f. model differs from the classical spring-mass system of Ref. 20 (see Fig. 9.1), since the essential features of the distributed mechanical system are retained through the function $\zeta(\mathbf{x})$. It also differs from that of Ref. 43 since the complete non-linear behavior of the electrostatic force is retained, and it differs from that of Ref. 22 since the pull-in voltage and the pull-in deflection are simultaneously treated as unknowns, *i.e.*, the pull-in deflection is not empirically chosen as was done in Ref. 22.

9.4.6. *Pull-In Instability*

We first study the pull-in instability due to the Coulomb force only by solving the nondimensional non-linear Poisson Eq. (9.39) with $\mu = 0$. The pseudo-arc-length algorithm explained in Sec. 9.4.4, and the one d.o.f. model explained in Sec. 9.4.5 are employed. The combined effects of the Coulomb and the Casimir forces on the pull-in instability are studied in Sec. 9.4.8. Some results presented in this subsection are from Ref. 84.

We compare results for a rectangular, and a circular MEMS from the MLPG and the one d.o.f. methods with those obtained by using the shooting method. Parameters compared are λ_{PI} and $\|u_{\mathrm{PI}}\|_{\infty}$ that equal, respectively, the value of the parameter λ for which the pull-in instability occurs, and the corresponding infinity norm of the deflection field. For a specific MEMS, the dimensional value of the pull-in voltage is obtained by substituting for λ_{PI} into Eq. (9.33), while the dimensional value of the membrane maximum deflection at the pull-in instability is obtained by multiplying $\|u_{\mathrm{PI}}\|_{\infty}$ with the initial gap g_0.

The MLS approximation uses linear monomial basis and Gaussian weight functions with circular support.[52] The radius r_i of the support of a weight function varies with the problem, and other constants defining weight functions are $k = 1$, $c_i = r_i/4$ (see Ref. 52). The integration is performed by using 9 quadrature points for each line integral, and 9×9 quadrature points for each 2D subdomain. The pseudo-arc-length continuation is started with $\lambda_1 = 0.1$, $\tau = 3$, and the tolerance ε_{T} is set equal to 10^{-6}. If the convergence is not achieved in 10 Newton's iterations the incremental arc length Δs is reduced by a factor of 2, and the algorithm is restarted from that point. In the neighborhood of the pull-in instability, more steps are needed to accurately estimate the pull-in parameters.

9.4.6.1. *Rectangular MEMS*

We consider a rectangular MEMS of unit length, width equal to $1/8$, clamped on edges $x^1 = 0, 1$, and free on edges $x^2 = 0, 1/8$. We assume that the electrostatic pressure is uniformly exerted only for $x^1 \in (\varepsilon, 1-\varepsilon)$ (see Fig. 9.7). That is, the central portion of length 2ε is electroded.

Reduction of the boundary-value problem to an initial-value problem Because of the boundary conditions and the load distribution, we assume that the solution is a function of x^1 only, and is symmetric with respect to the line $x^1 = 1/2$,[41] yielding the following non-linear non-linear boundary-value

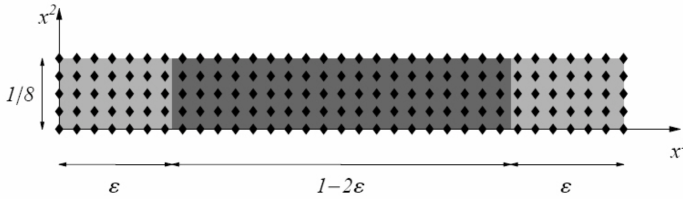

Fig. 9.7. Geometry of the rectangular MEMS with the uniform grid of 33×5 nodes used to solve the 2D boundary-value problem with the MLPG method. The electrostatic force is effective in the shaded region.

problem:

$$u_1''\left(x^1\right) = 0, \qquad x^1 \in (0, \varepsilon), \tag{9.71}$$

$$u_2''\left(x^1\right) = \frac{\lambda}{\left(1 + u_2\left(x^1\right)\right)^2}, \qquad x^1 \in (\varepsilon, 1/2), \tag{9.72}$$

$$u_1(0) = 0, \qquad u_2'(1/2) = 0, \tag{9.73}$$

$$u_1(\varepsilon) = u_2(\varepsilon), \qquad u_1'(\varepsilon) = u_2'(\varepsilon), \tag{9.74}$$

where a superimposed prime indicates derivative with respect to x^1, and u_1 and u_2 equal u in $(0, \varepsilon)$ and $(\varepsilon, 1/2)$ respectively.

The solution of the homogeneous Eq. (9.71) for $x^1 \in (0, \varepsilon)$ is

$$u_1\left(x^1\right) = c_1 x^1 + c_2, \qquad c_1, c_2 \in \mathbb{R}. \tag{9.75}$$

By imposing the first boundary condition in Eq. (9.73), we obtain

$$c_2 = 0. \tag{9.76}$$

The interface conditions (9.74) give

$$u_2(\varepsilon) = c_1 \varepsilon, \quad u_2'(\varepsilon) = c_1. \tag{9.77}$$

Hence the constant c_1 may be eliminated. The deflection field for $x^1 \in (\varepsilon, 1/2)$ is determined by solving the boundary-value problem

$$u_2''\left(x^1\right) = \frac{\lambda}{\left(1 + u_2\left(x^1\right)\right)^2}, \quad u_2(\varepsilon) = u_2'(\varepsilon)\,\varepsilon, \quad u_2'(1/2) = 0. \tag{9.78}$$

The constant c_1 is subsequently determined by either one of two conditions in Eq. (9.77).

By generalizing the approach of Ref. 41 to partially electroded plates we change variables as follows:

$$\eta = b\left(\left(\frac{1}{2}-\varepsilon\right)-x^1\right), \tag{9.79a}$$

$$u^2\left(x^1\right) = aw\left(\eta\right)-1, \tag{9.79b}$$

$$a = \frac{1}{w\left(b\left(\frac{1}{2}-\varepsilon\right)\right)+\varepsilon bw'\left(b\left(\frac{1}{2}-\varepsilon\right)\right)}, \tag{9.79c}$$

$$\lambda = \frac{b^2}{\left(w\left(b\left(\frac{1}{2}-\varepsilon\right)\right)+\varepsilon bw'\left(b\left(\frac{1}{2}-\varepsilon\right)\right)\right)^3}. \tag{9.79d}$$

We thus transform the boundary-value problem (9.78) to the following initial-value problem

$$\frac{\mathrm{d}^2 w}{\mathrm{d}\eta^2} = \frac{1}{w^2}, \qquad \frac{\mathrm{d}w}{\mathrm{d}\eta}(0)=0, \qquad w(0)=1. \tag{9.80}$$

We numerically solve the initial-value problem (9.80) with Mathematica using the built-in function NDSolve, obtain $w(\eta)$, and for every pair (w, b) we determine the corresponding pair $\left(u^2\left(x^1\right), \lambda\right)$, and the constant c_1. Once the deflection field is known on the entire strip we compute its infinity norm, which equals the mid-span deflection.

Numerical results and comparisons For the solution of the 2D boundary-value problem defined by Eqs. (9.32), (9.37) and (9.38) with $\mu = 0$ by the MLPG method, we do not assume any symmetry in the deflection u, and use a uniform grid of 33×5 nodes on the MEMS domain as shown in Fig. 9.7. The radius r_i of the support of each weight function equals $1/8$. The subdomains of integration are determined by supports of test functions, and their radii are chosen equal to $1/32$.

For the solution with the one d.o.f. method, we use two different test functions ζ in Eq. (9.65), namely

$$\zeta_{\mathrm{s}}(\mathbf{x}) = \begin{cases} -\dfrac{4x^1}{2\varepsilon+1}, & \mathbf{x}\in(0,\varepsilon)\times\left(0,\dfrac{1}{8}\right) \\ -\dfrac{4\left((x^1)^2-x^1+\varepsilon^2\right)}{4\varepsilon^2-1}, & \mathbf{x}\in(\varepsilon,1-\varepsilon)\times\left(0,\dfrac{1}{8}\right) \\ \dfrac{4(x^1-1)}{2\varepsilon+1}, & \mathbf{x}\in(1-\varepsilon,1)\times\left(0,\dfrac{1}{8}\right) \end{cases} \tag{9.81a}$$

$$\zeta_{\mathrm{m}}(\mathbf{x}) = -\sin(x^1). \tag{9.81b}$$

ζ_s is the static deflection under a uniformly distributed load in the electroded region $(\varepsilon, 1-\varepsilon) \times (0, 1/8)$ chosen in such a way that $\zeta_s(1/2, x^2) = -1$, and ζ_m is the first eigenfunction of a pinned-pinned linear bar with the normalization $\zeta_m(1/2, x^2) = -1$.

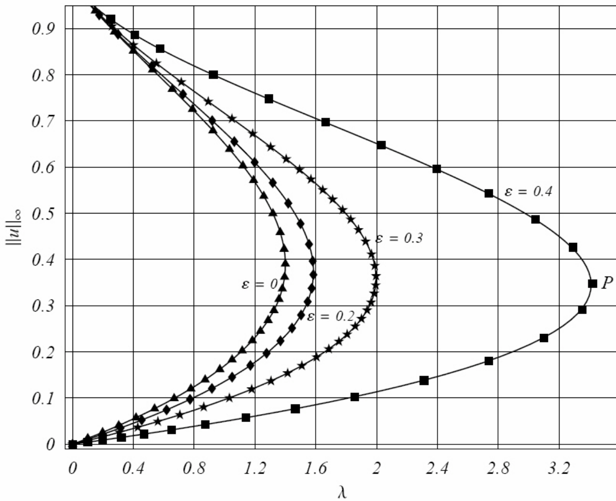

Fig. 9.8. For different values of ε, comparison of the bifurcation diagrams obtained by solving the initial-value problem (solid line) and the MLPG method (polygons) for the rectangular MEMS.

Figure 9.8 exhibits the bifurcation diagram showing the infinity norm of the deflection versus the load parameter λ. We note that plots of $\|u\|_\infty$ versus λ are qualitatively similar for all four values of ε, and the pull-in voltage decreases rapidly with a decrease of ε from 0.4 to 0. This is reasonable because the surface area on which the Coulomb force acts increases with a decrease in ε. For each value of ε the maximum deflection of the MEMS increases with an increase in λ and hence an increase in the applied voltage. This branch of the curve prior to the fold at P corresponds to stable equilibrium states, while the upper branch to unstable equilibrium states. If a given rectangular MEMS is pushed by forces other than the Coulomb force into a configuration corresponding to a point on the upper branch of a curve, equilibrium Eq. (9.32) and boundary conditions in Eqs. (9.37) and (9.38) are satisfied. The MEMS can theoretically stay in the unstable equilibrium configuration indefinitely if the external force is removed, the system is not perturbed, and the appropriate voltage is applied to the MEMS.[79]

For different values of the parameter ε, we compare in Table 9.1 the MLPG and the one d.o.f. solutions with that obtained by solving the initial-value problem

Table 9.1. For the rectangular MEMS, comparison of the MLPG and the one d.o.f. results with those obtained with the shooting method.

	Shooting Method		MLPG		One d.o.f.			
					$\zeta_{\mathrm{s}}(\mathbf{x})$		$\zeta_{\mathrm{m}}(\mathbf{x})$	
ε	λ_{PI}	$\|u_{\mathrm{PI}}\|_\infty$	λ_{PI}	$\|u_{\mathrm{PI}}\|_\infty$	λ_{PI}	$\|u_{\mathrm{PI}}\|_\infty$	λ_{PI}	$\|u_{\mathrm{PI}}\|_\infty$
0	1.400	0.3927	1.400	0.3885	1.422	0.3877	1.397	0.3916
0.2	1.584	0.3671	1.584	0.3671	1.590	0.3714	1.600	0.3716
0.3	1.996	0.3662	1.997	0.3615	1.998	0.3582	2.075	0.3532
0.4	3.412	0.3470	3.421	0.3475	3.412	0.3452	3.777	0.3387

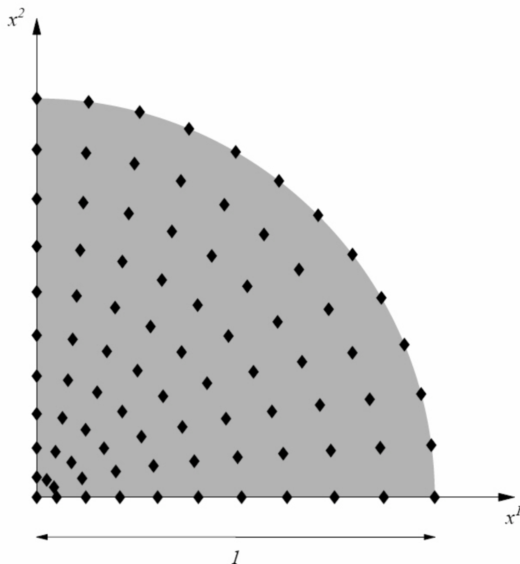

Fig. 9.9. Grid of 86 nodes on the quarter of disk.

(9.80); the latter is often referred to as the shooting method.[41] It is clear that values of λ_{PI} predicted by the MLPG and the one d.o.f. methods are very close to those obtained from the shooting method. Whereas the shooting method exploits the symmetry of the problem about $x^1 = 1/2$ and assumes the deflection to be a function of x^1 only, the MLPG method is more general and is applicable to 2D membranes with cut-out regions and irregular shaped electroded portions of the rectangular MEMS. For such problems one will need to use non-uniform distribution of nodes.

We thus note that the use of ζ_{s} and ζ_{m} in Eq. (9.65) gives nearly the same values of $\|u_{\mathrm{PI}}\|_\infty$ and λ_{PI}.

9.4.6.2. *Circular Disk*

We consider a disk of unit radius clamped along its periphery.

Reduction of the boundary-value problem to an initial-value problem Following Ref. 85 we assume that the solution is a function of the radial coordinate r only, and deformations of the disk are axisymmetric. Thus the problem defined by Eq. (9.32) reduces to the following non-linear non-linear boundary-value problem:

$$u''(r) + \frac{1}{r}u'(r) = \frac{\lambda}{(1+u(r))^2}, \quad u(1) = 0, \quad u'(0) = 0, \tag{9.82}$$

where a superimposed prime indicates derivative with respect to r.

We reduce the boundary-value problem (9.82) to the initial-value problem

$$\frac{\mathrm{d}^2 w}{\mathrm{d}\eta^2} + \frac{1}{\eta}\frac{\mathrm{d}w}{\mathrm{d}\eta} = \frac{1}{w^2}, \quad \frac{\mathrm{d}w}{\mathrm{d}\eta}(0) = 0, \quad w(0) = 1, \tag{9.83}$$

by applying the following change of variables:

$$\eta = br, \quad u(r) = aw(\eta) - 1, \quad a = \frac{1}{w(b)}, \quad \lambda = \frac{b^2}{w(b)^3}. \tag{9.84}$$

As for the rectangular MEMS, we numerically solve the initial-value problem (9.83) with Mathematica using the built-in function NDSolve, and for every pair (w, b) determine the corresponding pair $(u(r), \lambda)$. Once the deflection field is known on the entire disk we compute its infinity norm, which equals the deflection of the disk center.

Numerical results and comparisons Instead of considering the entire disk we analyze deformations of a quarter of the disk with the MLPG method by using the grid of 86 nodes shown in Fig. 9.9 but do not assume that the deflection is independent of the angular position θ. On straight boundaries we impose homogeneous natural boundary conditions arising from the symmetry of the problem. The size r_i of the support of each weight function is taken to be $2/3$. Subdomains of integration are determined by supports of test functions, and their radii are set equal to the distance between the chosen node and the one closest to it.

For the analysis with the one d.o.f. model we use the following functions for $\zeta(\mathbf{x})$ in Eq. (9.65):

$$\zeta_{\mathrm{s}}(r) = r^2 - 1, \qquad \zeta_{\mathrm{m}}(r) = -\mathrm{J}_0(\omega_0 r), \tag{9.85}$$

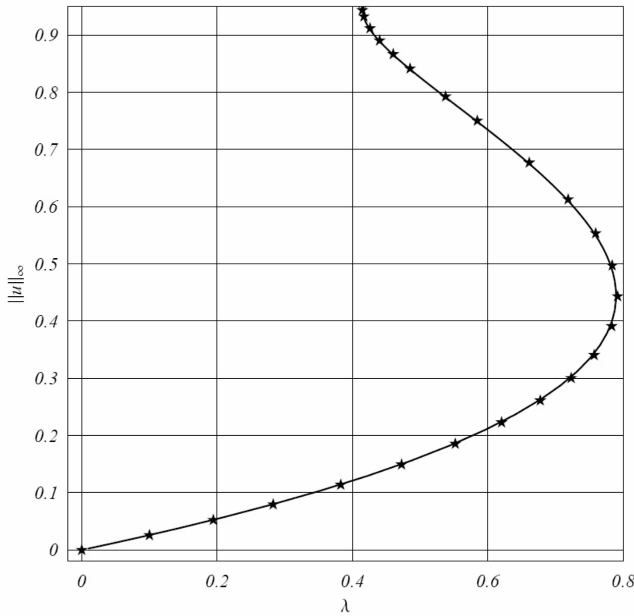

Fig. 9.10. Comparison of the bifurcation diagrams obtained with the shooting method (solid line) and the MLPG method (polygons) for the circular MEMS.

where and J_0 is the Bessel function of first kind corresponding to the fundamental frequency $\omega_0 = 2.405\,\text{rad/s}$, or the smallest root of the characteristic equation $J_0(\omega) = 0$ (see Ref. 86). Both functions in Eq. (9.85) have been normalized to equal -1 at $r = 0$. The static solution ζ_s is for axisymmetric deformations of a clamped circular membrane under a uniformly distributed load.

Figure 9.10 shows the infinity norm of the deflection, which corresponds to the deflection of the disk center, versus the load parameter λ. Results from the MLPG and the one d.o.f. methods and those from the shooting method are compared in Table 9.2. For the one d.o.f. problem, the function ζ_s gives better approximations of the pull-in parameters than the first eigenfunction ζ_m. However, both sets of results are close to those obtained by the MLPG and the shooting methods.

Table 9.2. For the circular MEMS, comparison of the MLPG and the one d.o.f. results with those from the shooting method.

	Shooting method	MLPG	One d.o.f.	
			$\zeta_s(r)$	$\zeta_m(r)$
λ_{PI}	0.7890	0.7915	0.8274	0.7834
$\|u_{PI}\|_\infty$	0.4365	0.4433	0.4404	0.4562

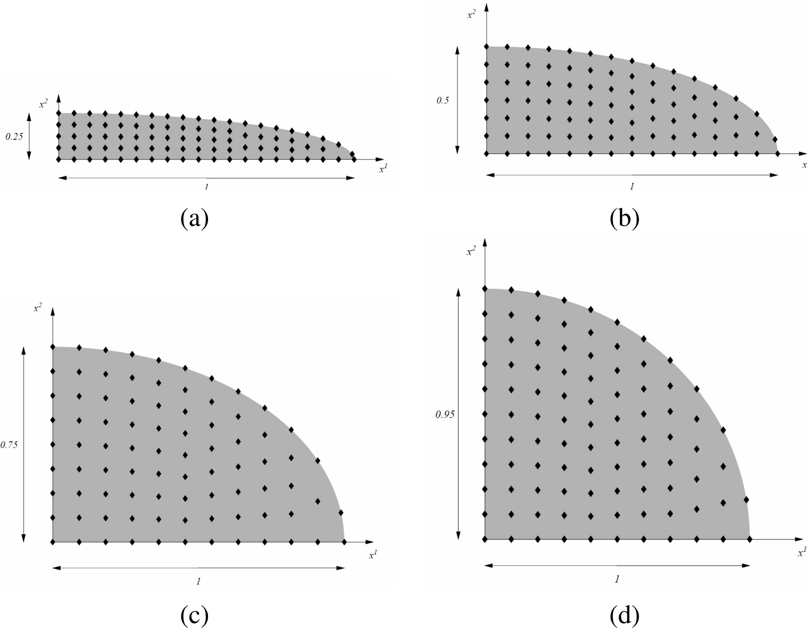

Fig. 9.11. Locations of (a) 86, (b) 87, (c) 85, and (d) 94 nodes on the quarter of an elliptic disk with (a) $b/a = 0.25$, (b) $b/a = 0.5$, (c) $b/a = 0.75$, and (d) $b/a = 0.95$.

9.4.6.3. *Elliptic Disk*

We consider an ellipse of semi-major axis $a = 1$, semi-minor axis b, and clamped along its periphery. We analyze deformation of a quarter of the ellipse, impose homogeneous natural boundary conditions on the straight edges, and investigate the effect of the aspect ratio b/a on the pull-in instability of the system.

We study four aspect ratios, namely 0.25, 0.5, 0.75, and 0.95, and adopt, respectively, grids of 86, 87, 85, and 94 nodes shown in Figs. 9.11(a)-9.11(d) when solving the boundary-value problem with the MLPG method. For a uniformly loaded elliptic membrane clamped on its edges, these nodal placements give an error of less than 0.7% in the maximum deflection with respect to the analytical solution

$$\zeta_{\mathrm{s}}\left(\mathbf{x}\right) = k_{\mathrm{s}}\left(\left(\frac{x^1}{a}\right)^2 + \left(\frac{x^2}{b}\right)^2 - 1\right), \qquad k_{\mathrm{s}} = \left(\frac{2}{a^2} + \frac{2}{b^2}\right)^{-1}. \tag{9.86}$$

Here, rectangular Cartesian coordinate axes x^1 and x^2 are aligned with the major and the minor axes of the ellipse. Values of weight function parameters in the MLPG method are the same as those for the circular disk problem.

For the solution with the one d.o.f. method we adopt the expression in Eq. (9.86) with $k_{\rm s} = 1$ for the static solution $\zeta_{\rm s}(\mathbf{x})$, and

$$\zeta_{\rm m}(\xi^1, \xi^2) = k_{\rm m}{\rm Ce}_0(\xi^1, q_0)\,{\rm ce}_0(\xi^2, q_0), \tag{9.87}$$

where (ξ^1, ξ^2) are confocal elliptic coordinates.[87] In confocal elliptic coordinates, the ellipse is mapped into the strip $[0, \operatorname{arctanh}(b/a)] \times [0, 2\pi)$. In Eq. (9.87), ${\rm ce}_0$ and ${\rm Ce}_0$ are the zero-th order Mathieu cosines of the first and the second kind, respectively, corresponding to the fundamental frequency $\omega_0 = 2\sqrt{q_0}/c$ obtained as the lowest positive root of the characteristic equation ${\rm Ce}_0(\operatorname{arctanh}(b/a), q) = 0$,[88] where $c^2 = a^2 - b^2$. We set $k_{\rm m} = -1/\max_{\xi^2 \in (0,\pi)} \zeta_{\rm m}(0, \xi^2)$.

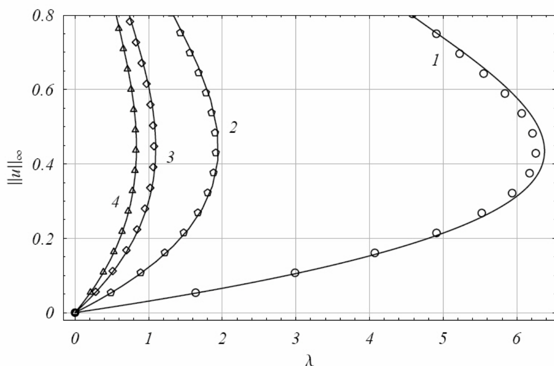

Fig. 9.12. Bifurcation diagram for four elliptic MEMS with $b/a = 0.25$ (curve 1), $b/a = 0.5$ (curve 2), $b/a = 0.75$ (curve 3), and $b/a = 0.95$ (curve 4). Solid lines: MLPG solutions with $\sim$ 90 nodes; empty polygons: finite difference solutions with 3500 points.

Figure 9.12 shows pull-in bifurcation diagrams for the four elliptic MEMS obtained with the MLPG method. Due to an increase in the stiffness of the system with a decrease in the aspect ratio, the nondimensional pull-in voltage increases significantly with a decrease in b/a. Results are compared with finite difference solutions obtained by mapping the elliptic domain into a strip via the change into confocal elliptic coordinates, homogeneous essential boundary conditions are imposed on the edge $\xi^1 = \operatorname{arctanh}(b/a)$, and homogeneous natural boundary conditions are imposed on the remaining edges. A grid of 50×70 points located, respectively, along the ξ^1 and the ξ^2 directions is used. With only $\sim$ 90 nodes, the MLPG method reproduces the finite difference results within 2% error for the nondimensional pull-in voltage, and less that 4% error for the nondimensional pull-in displacement.

Table 9.3. For the elliptic MEMS, comparison of the MLPG and the one d.o.f. results with those obtained by the finite difference method.

	Finite Difference		MLPG		One d.o.f.			
					$\zeta_s(\mathbf{x})$		$\zeta_m(\xi^1, \xi^2)$	
b/a	λ_{PI}	$\|u_{PI}\|_\infty$	λ_{PI}	$\|u_{PI}\|_\infty$	λ_{PI}	$\|u_{PI}\|_\infty$	λ_{PI}	$\|u_{PI}\|_\infty$
0.25	6.257	0.4287	6.376	0.4367	7.033	0.4404	6.581	0.5049
0.50	1.912	0.4302	1.940	0.4102	2.069	0.4404	1.936	0.4665
0.75	1.073	0.4475	1.097	0.4525	1.149	0.4404	1.085	0.4575
0.95	0.8254	0.4368	0.8347	0.4627	0.8721	0.4404	0.8256	0.4562

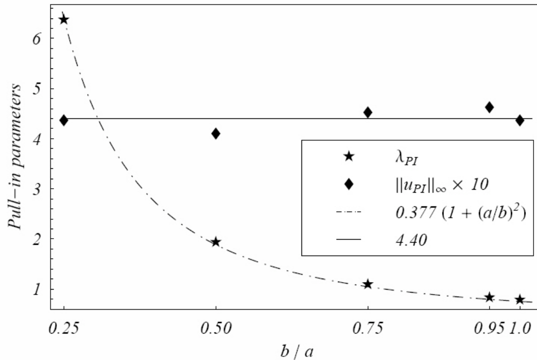

Fig. 9.13. Variation of pull-in parameters, λ_{PI} and $\|u_{PI}\|_\infty$, with the aspect ratio b/a for the elliptic MEMS.

For different values of the aspect ratio b/a, we compare in Table 9.3 the pull-in parameters from the MLPG and the one d.o.f. solutions with those obtained with the finite difference method. The one d.o.f. results approximate well the finite difference solutions obtained with 3500 grid points.

Figure 9.13 depicts the variation of the pull-in parameters, λ_{PI} and $\|u_{PI}\|_\infty$, from the MLPG solutions with the aspect ratio b/a. The nondimensional pull-in voltage data are fitted with a quadratic polynomial in a/b (dashed line), and the corresponding nondimensional pull-in maximum deflection data with a straight line (solid line). Expressions for the aforementioned polynomials are

$$\lambda_{PI} = 0.377 \left(1 + \left(\frac{a}{b}\right)^2\right) \tag{9.88a}$$

$$\|u_{PI}\|_\infty = 0.440. \tag{9.88b}$$

Note that $\|u_{PI}\|_\infty$ for all four elliptic membranes is the same as that for the circular membrane studied above, cf. Table 9.2. As the aspect ratio approaches 1, λ_{PI} for the elliptical geometry approaches that for the circular MEMS. For $a = b$,

Eq. (9.88a) gives $\lambda_{\mathrm{PI}} = 0.754$ as opposed to 0.79 in Table 9.2. It shows that λ_{PI} found from Eq. (9.88a) may be 5% off.

9.4.7. *Pull-In Instability and Symmetry Breaking in an Annular Circular Disk*

We consider an annular circular disk of inner radius 0.1, and outer radius 1 clamped along its inner and outer boundaries. Parameters compared are λ_{PI} and $\|u_{\mathrm{PI}}\|_\infty$, and, when a symmetry breaking bifurcation occurs, λ_{SB} and $\|u_{\mathrm{SB}}\|_\infty$. λ_{SB} and $\|u_{\mathrm{SB}}\|_\infty$ represent, respectively, the highest λ for which both symmetric and asymmetric deformed shapes of the annular disk can exist simultaneously, and the corresponding infinity norm of the deflection field.

Following Ref. 89 we study only one-half of the annular domain. The symmetry in the deformed membrane breaks after the pull-in instability. We impose homogeneous natural boundary conditions on the straight edges. This condition is restrictive since there may be nonaxially symmetric solutions that do not satisfy it.[89] We compare our results with those obtained in Ref. 89 by the finite-difference method with 1600 points.

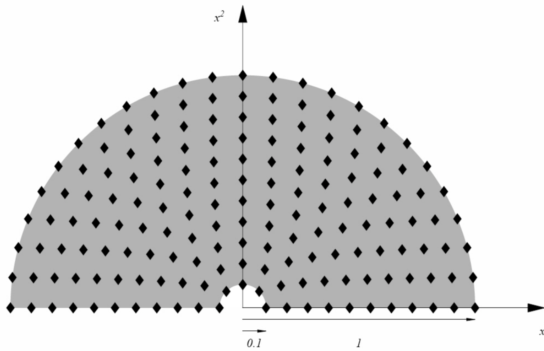

Fig. 9.14. Grid of 165 nodes on one-half of an annular disk.

In the MLPG implementation, we use the grid of 165 nodes shown in Fig. 9.14. Values of weight function parameters are the same as those for the circular disk problem studied in Sec. 9.4.6.2.

For the one d.o.f. solution we use the following expressions for the function $\zeta(\mathbf{x})$:

$$\zeta_{\mathrm{s}}(r) = k_{\mathrm{s}} \frac{r^2 \ln(R_{\mathrm{o}}/R_{\mathrm{i}}) + R_{\mathrm{o}}^2 \ln(R_{\mathrm{i}}/r) + R_{\mathrm{i}}^2 \ln(r/R_{\mathrm{o}})}{4 \ln(R_{\mathrm{o}}/R_{\mathrm{i}})}, \qquad (9.89a)$$

$$\zeta_{\mathrm{m}}(r) = k_{\mathrm{m}} \left(\mathrm{Y}_0(\omega_0 r) - \frac{\mathrm{Y}_0(\omega_0 R_{\mathrm{i}})}{\mathrm{J}_0(\omega_0 R_{\mathrm{i}})} \mathrm{J}_0(\omega_0 r) \right), \tag{9.89b}$$

where R_{i} and R_{o} are the inner and the outer radii of the annular domain. J_0 and Y_0 are the zero-th order Bessel functions of the first and the second kind, corresponding to the fundamental frequency $\omega_0 = 3.314\,\mathrm{rad/s}$ obtained as the lowest positive root of the characteristic equation $\mathrm{Y}_0(\omega R_{\mathrm{i}})/\mathrm{J}_0(\omega R_{\mathrm{i}}) - \mathrm{Y}_0(\omega R_{\mathrm{o}})/\mathrm{J}_0(\omega R_{\mathrm{o}}) = 0$. The normalization constants k_{s} and k_{m} are determined by requiring that $\min_{r \in (R_{\mathrm{o}}, R_{\mathrm{i}})} \zeta_{\mathrm{s}}(r) = -1$, and the same for $\zeta_{\mathrm{m}}(r)$. The static solution $\zeta_{\mathrm{s}}(r)$ has been derived by assuming that the deflection of the annular membrane under a uniformly distributed load is axisymmetric.

Table 9.4. Comparison of the MLPG and the one d.o.f. results with the finite-difference solution for the annular MEMS with inner radius equal to one-tenth of the outer radius.

	Finite-difference	MLPG	One d.o.f.	
			$\zeta_{\mathrm{s}}(r)$	$\zeta_{\mathrm{m}}(r)$
λ_{PI}	1.544	1.548	1.587	1.546
$\Vert u_{\mathrm{PI}} \Vert_\infty$	0.393	0.399	0.392	0.397
λ_{SB}	1.486	1.485	-	-

Figure 9.15 exhibits the infinity norm of the deflection versus the load parameter λ from the MLPG and the finite difference solutions.[89] Numerical solutions from the MLPG, the one d.o.f. and the finite-difference methods are compared in Table 9.4. The one d.o.f. model does not allow for the symmetry breaking. Pull-in parameters from the one d.o.f. model are in good agreement with those obtained

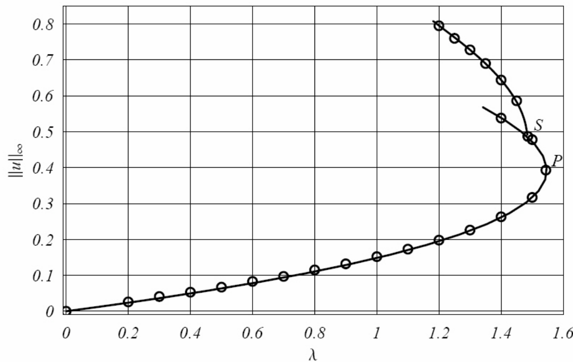

Fig. 9.15. Bifurcation diagram for the annular disk MEMS: the finite difference-solution (empty circles) and the MLPG solution (solid line).

with the MLPG and the finite difference methods. Since the symmetry breaking point, indicated by S in Fig. 9.15, is on the upper portion of the curve, *i.e.*, $\|u_{\mathrm{SB}}\|_\infty > \|u_{\mathrm{PI}}\|_\infty$, the axisymmetric and the non-axisymmetric configurations are unstable.

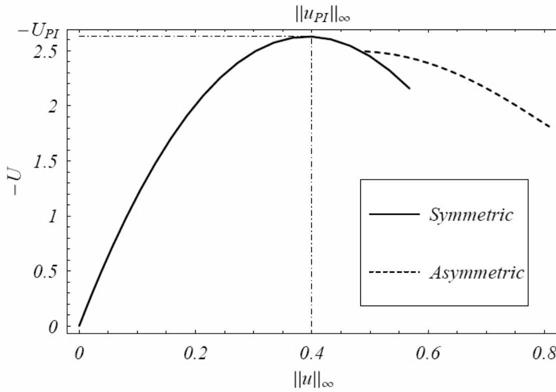

Fig. 9.16. The negative of the total potential energy U of the annular disk MEMS versus the infinity norm, $\|u\|_\infty$, of the deflection.

Figure 9.16 exhibits the plot of the negative of the total potential energy

$$U = \frac{1}{2}\int_\Omega \left(\nabla u \cdot \nabla u - \frac{2\lambda}{1+u}\right) \mathrm{d}\Omega, \tag{9.90}$$

versus the infinity norm of the deflection of the annular disk. As mentioned before, after pull-in instability both the symmetric, and the asymmetric paths are unstable. However, the energy corresponding to the asymmetric states is lower than that corresponding to the symmetric ones.

Figures 9.17(a) and 9.17(b) depict the symmetric, and the asymmetric deformed shapes of the annular disk after the pull-in, for $\lambda = 1.34$, and $\lambda = 1.18$ respectively.

9.4.8. *From Micro to Nano: Effect of the Scale on Pull-In and Symmetry Breaking Parameters of Micromembranes*

9.4.8.1. *Effect on Pull-In Parameters*

We consider the fully electroded rectangular strip, the circular disk, and the annular disk. For each of these geometries, we adopt the same distribution of nodes as considered in Sec. 9.4.6.

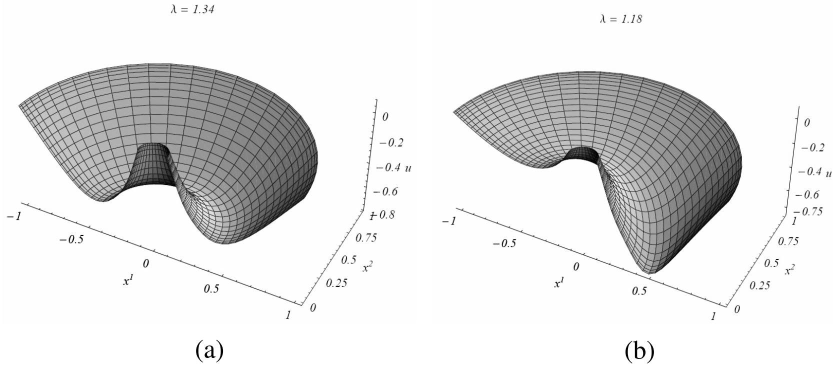

Fig. 9.17. (a) Symmetric, and (b) asymmetric solutions for the annular disk MEMS with $\lambda = 1.34$ and $\lambda = 1.18$, respectively.

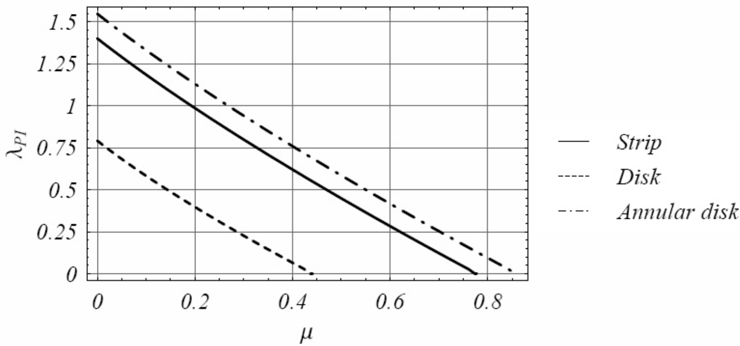

Fig. 9.18. Pull-in parameter λ_{PI} versus Casimir force parameter μ.

The non-linear Poisson Eq. (9.39) is solved by using the MLPG method in conjunction with the pseudo-arc-length continuation algorithm described in Sec. 9.4.4. The problem is first solved for $\lambda = 0$ in order to determine the critical value, μ_{cr}, of the Casimir force parameter. When $\mu = \mu_{\mathrm{cr}}$ the system collapses spontaneously with zero applied voltage. For different values of μ in the range $[0, \mu_{\mathrm{cr}}]$, the effect of the scale on pull-in parameters λ_{PI} and $\|u_{\mathrm{PI}}\|_\infty$ is investigated by solving Eq. (9.39) with variable λ. Results in this subsection are taken from Ref. 90.

Figure 9.18 exhibits the pull-in parameter λ_{PI} versus μ for the three geometries. As μ increases the pull-in parameter λ_{PI} decreases monotonically from its maximum value $\lambda_{\mathrm{PI}}^{\max}$ corresponding to $\mu = 0$. $\mu = \mu_{\mathrm{cr}}$ represents intersection of

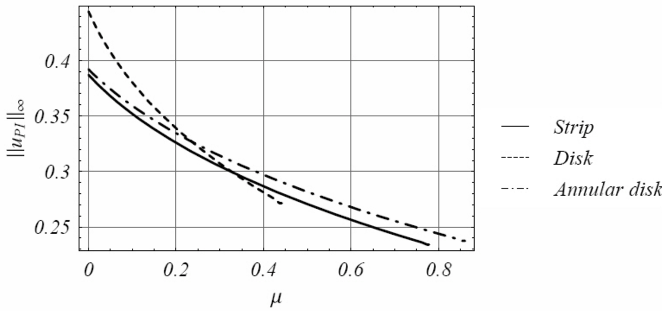

Fig. 9.19. Pull-in parameter $\|u_{\mathrm{PI}}\|_\infty$ versus Casimir force parameter μ.

Table 9.5. Characteristic parameters describing the influence of the Casimir force on pull-in instability.

Geometry	$\lambda_{\mathrm{PI}}^{\max}$	$\|u_{\mathrm{PI}}\|_\infty^{\max}$	μ_{cr}	$\|u_{\mathrm{PI}}\|_\infty^{\min}$
Strip	1.40	0.387	0.778	0.234
Disk	0.791	0.444	0.442	0.271
Annular disk	1.55	0.392	0.860	0.238

the curves with the horizontal axis. The curves may be reasonably approximated by straight lines. Using this approximation, the knowledge of the pull-in parameter $\lambda_{\mathrm{PI}}^{\max}$ and of the critical Casimir parameter μ_{cr} are sufficient to completely characterize the Casimir effect on the pull-in parameter λ_{PI}. The slopes of the three fitting straight lines are strikingly similar and approximately equal -1.8.

Figure 9.19 shows the nondimensional pull-in deflection versus μ. We notice that as μ increases, the pull-in deflection decreases from its maximum value $\|u_{\mathrm{PI}}\|_\infty^{\max}$. This means that reduced deflection ranges are allowable for large values of μ. The minimum pull-in deflection $\|u_{\mathrm{PI}}\|_\infty^{\min}$ is attained when $\mu = \mu_{\mathrm{cr}}$ and refers to the spontaneous collapse of the system without applied voltage. When L, h and g_0 are scaled down simultaneously by a factor F, then Eq. (9.35) implies that $\mu_{\mathrm{cr}} \to F^4\mu_{\mathrm{cr}}$. Thus μ_{cr} drops rapidly with a reduction in the device size.

Numerical values of $\lambda_{\mathrm{PI}}^{\max}$, $\|u_{\mathrm{PI}}\|_\infty^{\max}$, μ_{cr}, and $\|u_{\mathrm{PI}}\|_\infty^{\min}$ are summarized in Table 9.5. These reveal that the disk experiences the largest nondimensional pull-in maximum displacement as the device size changes. However, the maximum pull-in voltage is for the annular disk.

9.4.8.2. *Effect on Symmetry Breaking*

The post-instability behavior of the annular disk under effects of the Coulomb and the Casimir forces has been analyzed by solving the non-linear Eq. (9.39) for

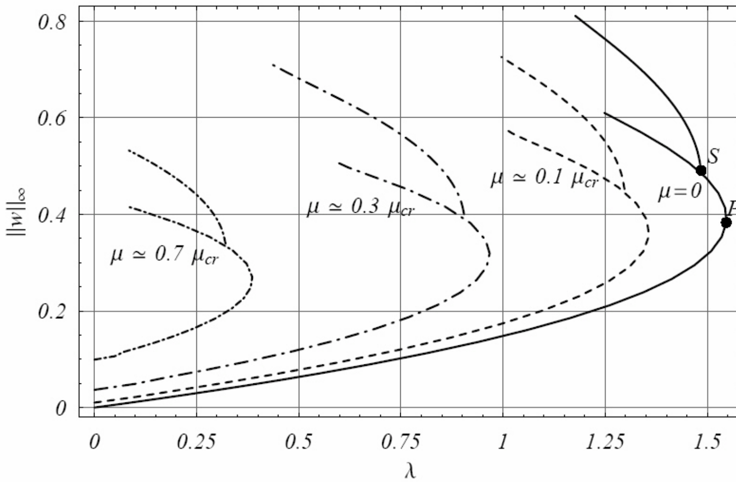

Fig. 9.20. Bifurcation diagrams of the annular membrane for four different values of μ.

different values of μ in the range $[0, \mu_{\rm cr}]$. We numerically study deformations of one-half of the annular membrane with inner radius equal to 0.1, and imposed symmetry conditions on sides contiguous to the removed domain.

Figure 9.20 shows the maximum deflection $\|u\|_\infty$ versus the voltage parameter λ for four different values of μ. As the Casimir parameter μ varies, the symmetry breaking point $(\lambda_{\rm SB}, \|u_{\rm SB}\|_\infty)$ moves. Values of $\lambda_{\rm SB}$ and $\|u_{\rm SB}\|_\infty$ are listed in Table 9.6. As μ increases the ratio $\lambda_{\rm SB}/\lambda_{\rm PI}$ decreases, meaning that the difference in the nondimensional voltage corresponding to symmetry breaking and the pull-in instability points increases; the relationship between $\mu/\mu_{\rm cr}$ and $\lambda_{\rm SB}/\lambda_{\rm PI}$ is non-linear and most likely varies with the ratio (inner radius)/(outer radius) even though that has not been investigated. In addition, as μ increases the travel range of the device from the pull-in instability to the symmetry breaking point decreases eventually approaching a constant value.

Table 9.6. Characteristic parameters describing symmetry breaking of the annular disk after pull-in instability.

$\mu/\mu_{\rm cr}$	$\lambda_{\rm SB}/\lambda_{\rm PI}$	$\|u_{\rm SB}\|_\infty/\|u_{\rm PI}\|_\infty - 1$
0	0.960	0.282
0.101	0.956	0.270
0.332	0.935	0.254
0.718	0.831	0.255

9.4.8.3. *Remarks*

We comment below on the importance of the Casimir force in the miniaturization of electrostatically actuated micromembranes, and on the validity of the present analysis.

As the device size is reduced, the effect of the Casimir force becomes more important. In the miniaturization process there is a minimum size for the device below which the system spontaneously collapses with zero applied voltage. For example, consider a circular membrane with parameters $L = 100\,\mu\mathrm{m}$, $g_0 = 1\,\mu\mathrm{m}$, $h = 0.1\,\mu\mathrm{m}$, $\sigma_0 = 10\,\mathrm{MPa}$. Substituting these values into Eq. (9.33) gives $\mu = 8.17 \times 10^{-5}$ and the effect of the Casimir force is negligible, see Fig. 9.18. Scaling down the device size by a factor $F = 10$, we have $\mu = 0.817$, which is larger than the critical Casimir parameter μ_{cr} in Table 9.5. This means that the miniaturized device spontaneously collapses under zero applied voltage. The validity of the present work is limited to MEMS for which electrostatic fringing fields, surface roughness and surface curvature,[91,92] temperature and finite conductivity[93] on the Casimir force, bending stiffness and non-linear stretching are negligible, and the two bodies are perfect conductors. Also when a nanodevice collapses, the distance between the two conductors may become small enough for the van der Waals forces to play a noticeable role.

9.5. Summary

The pseudo-arc-length continuation method coupled with the MLPG formulation of electrostatically actuated micromembranes can be used to analyze the pull-in instability and the symmetry breaking deformations of MEMS. A local symmetric augmented weak formulation of the problem is given wherein essential boundary conditions are enforced by the method of Lagrange multipliers. The MLS approximation is used to generate basis functions for the trial solution, and the test functions are taken to be the weight functions of the MLS approximation. The resulting set of non-linear equations is solved by the Newton iteration method. The accuracy and the reliability of the proposed technique have been established through comparisons of computed results with those obtained from other numerical methods.

160 nodes and nearly 100 steps in the pseudo-arc-length continuation method are sufficient to estimate the pull-in parameters and the symmetry-breaking bifurcations with an error of at most 1.53%. The convergence rate of the pseudo-arc-length continuation method does not vanish when the pull-in state is approached. With the applied voltage treated as an unknown, the number of iterations remains bounded.

The effect of the length scale on micromembranes has been studied by including the Casimir force in the mathematical model. The effect of the Casimir force on pull-in and symmetry breaking parameters has been investigated. It has been shown that there is a minimum size for the device below which it spontaneously collapses at zero applied voltage, and thus can not be fabricated.

References

1. A. Fargas Marquès, R. Costa Castelló, and A. M. Shkel. Modelling the electrostatic actuation of MEMS: state of the art 2005. Technical report, (2005). URL http://bibliotecnica.upc.es/reports/ioc/IOC-DT-P-2005-18.pdf.
2. D. Burns, J. Zook, R. Horning, W. Herb, and H. Guckel, Sealed-cavity resonant microbeam pressure sensor, *Sensors and Actuators A*. **48**(3), 179–186, (1995).
3. J. A. Pelesko and D. H. Bernstein, *Modeling MEMS and NEMS*. (Chapman & Hall, November 2002). Chapter 7.
4. W. Newell, Miniaturization of tuning forks, *Science*. **161**(3848), 1320–1326, (1968).
5. C. T. C. Nguyen, L. P. B. Katehi, and G. M. Rebeiz. Micromachined devices for wireless communications. In *Proceedings of the IEEE*, vol. 86, pp. 1756–1768, (1998).
6. T. Juneau, K. Unterkofler, T. Seliverstov, S. Zhang, and M. Judy. Dual-axis optical mirror positioning using a nonlinear closed-loop controller. In *TRANSDUCERS, 12th International Conference on Solid-State Sensors, Actuators and Microsystems*, vol. 1, pp. 560–563, (2003).
7. E. S. Hung and S. D. Senturia, Extending the travel range of analog-tuned electrostatic actuators, *Journal of Microelectromechanical Systems*. **8**(4), 497–505, (1999).
8. R. K. Gupta and S. D. Senturia. Pull-in time dynamics as a measure of absolute pressure. In *Proc. IEEE Int. Workshop on Microelectromechanical Systems (MEMS'97)*, pp. 290–294, Nagoya, Japan (Jan., 1997).
9. M. Teymoory and E. Abbaspour-Sany. A novel electrostatic micromachined pump for drug delivery systems. In *Semiconductor Electronics 2002. Proceedings. ICSE 2002. IEEE International Conference on*, (2002).
10. P. B. Chu, P. R. Nelson, M. L. Tachiki, and K. S. Pister, Dynamics of polysilicon parallel-plate electrostatic actuators, *Sensors and Actuators A*. **52**, 216–220, (1996).
11. E. M. Abdel-Rahman, M. I. Younis, and A. H. Nayfeh, Characterization of the mechanical behavior of an electrically actuated microbeam, *Journal of Micromechanics and Microengineering*. **12**(6), 759–766, (2002).
12. A. H. Nayfeh and M. I. Younis, Dynamics of MEMS resonators under superharmonic and subharmonic excitations, *Journal of Micromechanics and Microengineering*. **15**, 1840–1847, (2005).
13. J. F. Rhoads, S. W. Shaw, and K. L. Turner, The nonlinear response of resonant microbeam systems with purely-parametric electrostatic actuation, *Journal of Micromechanics and Microengineering*. **16**, 890–899, (2006).
14. H. A. Tilmans and R. Legtenberg, Electrostatically driven vacuum-encapsulated polysilicon resonators: Part II. Theory and performance, *Sensors and Actuators A*. **45**(1), 67–84, (1994).

15. M. I. Younis and A. H. Nayfeh, A study of the nonlinear response of a resonant microbeam to an electric actuation, *Nonlinear Dynamics*. **31**, 91–117, (2003).
16. S. Krylov and R. Maimon, Pull-in dynamics of an elastic beam actuated by continuously distributed electrostatic force, *Journal of Vibration and Acoustics*. **126**, 332–342, (2004).
17. J.-H. Kuang and C.-J. Chen, Dynamic characteristics of shaped micro-actuators solved using the differential quadrature method, *Journal of Micromechanics and Microengineering*. **14**(4), 647–655, (2004).
18. W. C. Xie, H. P. Lee, and S. P. Lim, Nonlinear dynamic analysis of MEMS switches by nonlinear modal analysis, *Nonlinear Dynamics*. **31**, 243–256, (2003).
19. G. I. Taylor, The coalescence of closely spaced drops when they are at different electric potentials, *Proceedings of the Royal Society A*. **306**, 423–434, (1968).
20. H. C. Nathanson, W. E. Newell, R. A. Wickstrom, and J. R. Davis, The resonant gate transistor, *IEEE Transactions on Electron Devices*. **14**(3), 117–133, (1967).
21. H. A. Tilmans and R. Legtenberg, Electrostatically driven vacuum-encapsulated polysilicon resonators: Part I. Design and fabrication, *Sensors and Actuators A*. **45**, 57–66, (1994).
22. S. Pamidighantam, R. Puers, K. Baert, and H. A. C. Tilmans, Pull-in voltage analysis of electrostatically actuated beam structures with fixed-fixed and fixed-free end conditions, *Journal of Micromechanics and Microengineering*. **12**(4), 458–464, (2002).
23. L. M. Castañer and S. D. Senturia, Speed-energy optimization of electrostatic actuators based on pull-in, *Journal of Microelectromechanical Systems*. **8**(3), 290–298, (1999).
24. G. Li and N. R. Aluru, Efficient mixed-domain analysis of electrostatic MEMS, *IEEE Transactions on Computer-Aided Design of Integrated Circuits and Systems*. **22**(9), 1228–1242, (2003).
25. S. K. De and N. R. Aluru, Full-Lagrangian schemes for dynamic analysis of electrostatic MEMS, *Journal of Microelectromechanical Systems*. **13**(5), 737–758, (2004).
26. Microcosm Technologies. URL http://www.memcad.com/.
27. S. D. Senturia, R. M. Harris, B. P. Johnson, S. Kim, K. Nabors, M. A. Shulman, and J. K. White, A computer-aided design system for microelectromechanical systems (MEMCAD), *Journal of Microelectromechanical Systems*. **1**(1), 3–13, (1992).
28. Coventor Inc. URL http://www.coventor.com/.
29. F. Shi, P. Ramesh, and S. Mukherjee, Dynamic analysis of microelectromechanical systems, *International Journal for Numerical Methods in Engineering*. **39**, 4119–4139, (1996).
30. L. D. Gabbay, J. E. Mehner, and S. D. Senturia, Computer-aided generation of nonlinear reduced-order dynamic macromodels II: Non-stress-stiffened case, *Journal of Microelectromechanical Systems*. **9**(2), 262–269, (2000).
31. S. D. Senturia, N. R. Aluru, and J. White, Simulating the behavior of MEMS devices: Computational methods and needs, *IEEE Computational Science and Engineering*. **4** (1), 30–43, (1997).
32. S. S. Antman, *Nonlinear Problems of Elasticity*. Applied Mathematical Sciences, (Springer–Verlag, New York, 2004), 2nd edition.
33. P. M. Naghdi, *The Theory of Shells and Plates*, vol. VIa/2, *Handbuch der Physik*, pp. 425–640. Springer–Verlag, Berlin-New York, (1972).

34. P. M. Naghdi. Finite deformations of rods and shells. In eds. D. E. Carlson and R. T. Shield, *Proceedings of the IUTAM Symposium on Finite Elasticity*, pp. 47–103, The Hague/Boston/London (August, 1980). Martinus Nijhoff Publishers.
35. J. Pelesko and A. Triolo, Nonlocal problems in MEMS device control, *Journal of Engineering Mathematics*. **41**(4), 345–366, (2001).
36. S. Timoshenko, *Theory of Elasticity*. (McGraw-Hill Companies, June 1970), 3rd edition.
37. O. Francais and I. Dufour, Normalized abacus for the global behavior of diaphragms: pneumatic, electrostatic, piezoelectric or electromagnetic actuation, *Journal of Modeling and Simulation of Microsystems*. **2**, 149–160, (1999).
38. T. Y. Ng, T. Y. Jiang, K. Y. Lam, and J. N. Reddy, A coupled field study on the non-linear dynamic characteristics of an electrostatic micropump, *Journal of Sound and Vibration*. **273**, 989–1006, (2004).
39. X. Zhao, E. M. Abdel-Rahman, and A. H. Nayfeh, A reduced-order model for electrically actuated microplates, *Journal of Micromechanics and Microengineering*. **14**(7), 900–906, (2004).
40. E. H. Mansfield, *The bending & stretching of plates*. (Cambridge University Press, Cambridge; New York, 1989), 2nd edition. Chapter 9.
41. J. A. Pelesko, Mathematical modeling of electrostatics MEMS with tailored dielectric properties, *SIAM Journal of Applied Mathematics*. **62**(3), 888–908, (2002).
42. P. M. Osterberg and S. D. Senturia, M-TEST: A test chip for MEMS material property measurement using electrostatically actuated test structures, *Journal of Microelectromechanical Systems*. **6**(2), 107–118, (1997).
43. M. I. Younis, E. M. Abdel-Rahman, and A. H. Nayfeh, A reduced-order model for electrically actuated microbeam-based MEMS, *Journal of Microelectromechanical Systems*. **12**(5), 672–680, (2003).
44. T. Belytschko, Y. Y. Lu, and L. Gu, Element-free Galerkin methods, *International Journal for Numerical Methods in Engineering*. **37**, 229–256, (1994).
45. C. A. M. Duarte and J. T. Oden, Hp clouds-an hp meshless method, *Numerical Methods for Partial Differential Equations*. **12**, 673–05, (1996).
46. W. Liu, S. Jun, and Y. Zhang, Reproducing kernel particle method, *International Journal for Numerical Methods in Fluids*. **20**, 1081–1106, (1995).
47. B. Nayroles, G. Touzot, and P. Villon, Generalizing the finite element method: diffuse approximation and diffuse elements, *Computational Mechanics*. **10**, 307–318, (1992).
48. J. M. Melenk and I. Babuska, The partition of unity finite element method: Basic theory and applications, *Computer Methods in Applied Mechanics and Engineering*. **139**, 289–314, (1996).
49. N. Sukumar, B. Moran, and T. Belytschko, The natural element method in solid mechanics, *International Journal for Numerical Methods in Engineering*. **43**, 839–887, (1998).
50. H. Wendland, Piecewise polynomial, positive definite and compactly supported radial basis functions of minimal degree, *Advances in Computational Mathematics*. **4**, 389–396, (1995).
51. S. N. Atluri and T. Zhu, A new meshless local Petrov-Galerkin (MLPG) approach in computational mechanics, *Computational Mechanics*. **22**, 117–127, (1998).

52. S. N. Atluri and S. Shen, The meshless local Petrov-Galerkin (MLPG) method: A simple and less-costly alternative to the finite element and boundary element methods, *CMES: Computer Modeling in Engineering and Sciences*. **3**(1), 11–51, (2002).
53. L. B. Lucy, A numerical approach to the testing of the fission hypothesis, *The Astronomical Journal*. **82**, 1013–1024, (1977).
54. G. M. Zhang and R. C. Batra, Modified smoothed particle hydrodynamics method and its application to transient problems, *Computational Mechanics*. **34**, 137–146, (2004).
55. T. Zhu, J. D. Zhang, and S. N. Atluri, A local boundary integral equation (LBIE) method in computational mechanics, and a meshless discretization approach, *Computational Mechanics*. **21**, 223–235, (1998).
56. E. J. Kansa, Multiquadrics-a scattered data approximation scheme with applications to computational fluid dynamics, ii: Solutions to parabolic, hyperbolic and elliptic partial differential equations, *Computer and Mathematics with Applications*. **19**, 147–161, (1990).
57. Y. T. Gu and G. R. Liu, A meshless local Petrov-Galerkin (MLPG) formulation for static and free vibration analysis of thin plates, *CMES: Computer Modeling in Engineering and Sciences*. **2**, 463–476, (2001).
58. S. N. Atluri, J. Y. Cho, and H.-G. Kim, Analysis of thin beams, using the meshless local Petrov-Galerkin method, with generalized moving least squares interpolations, *Computational Mechanics*. **24**, 334–347, (1999).
59. L. F. Qian, R. C. Batra, and L. M. Chen, Analysis of cylindrical bending thermoelastic deformations of functionally graded plates by a meshless local Petrov-Galerkin method, *Computational Mechanics*. **33**, 263–273, (2004).
60. R. C. Batra, M. Porfiri, and D. Spinello, Treatment of material discontinuity in two meshless local Petrov-Galerkin (MLPG) formulations of axisymmetric transient heat conduction, *International Journal for Numerical Methods in Engineering*. **61**, 2461–2479, (2004).
61. R. C. Batra, M. Porfiri, and D. Spinello, Free and forced vibrations of a segmented bar by a meshless local Petrov-Galerkin (MLPG) formulation, *Computational Mechanics*. (2006). doi: 10.1007/s00466-006-0049-6. In press.
62. U. Andreaus, R. C. Batra, and M. Porfiri, Vibrations of cracked Euler-Bernoulli beams using Meshless Local Petrov-Galerkin (MLPG) method, *CMES: Computer Modeling in Engineering and Sciences*. **9**, 111–132, (2005).
63. R. C. Batra, M. Porfiri, and D. Spinello, Electromechanical model of electrically actuated narrow microbeams, *Journal of Microelectromechanical Systems*. **15**(5), 1175–1189, (2006).
64. P. Lancaster and K. Salkauskas, Surfaces generated by moving least squares methods, *Mathematics of Computation*. **37**, 141–158, (1981).
65. E. Doedel, H. B. Keller, and J. P. Kernevez, Numerical analysis and control of bifurcation problems (I) Bifurcation in finite dimensions, *International Journal of Bifurcation and Chaos*. **1**, 493–520, (1991).
66. E. Doedel, H. B. Keller, and J. P. Kernevez, Numerical analysis and control of bifurcation problems (II) Bifurcation in infinite dimensions, *International Journal of Bifurcation and Chaos*. **1**, 745–772, (1991).
67. R. C. Batra, *Elements of Continuum Mechanics*. (AIAA: American Institute of Aeronautics and Astronautics, 2005).

68. F. Shi, P. Ramesh, and S. Mukherjee, On the application of 2D potential theory to electrostatic simulation, *Communications in Numerical Methods in Engineering*. **11**, 691–701, (1995).
69. H. B. G. Casimir, On the attraction between two perfectly conducting plates, *Proceedings of the Koninklijke Nederlandse Akademie Van Wetenschappen*. **51**, 793, (1948).
70. S. K. Lamoreaux, The Casimir force: background, experiments, and applications, *Reports on progress in Physics*. **68**, 201–236, (2005).
71. M. Borgag, U. Mohideen, and V. M. Mostepanenko, New developments in the Casimir effect, *Physics reports*. **353**, 1–205, (2001).
72. E. M. Lifshitz, The theory of molecular attractive forces between solids, *Soviet Physics JETP*. **2**, 73–83 (January, 1956).
73. Y.-P. Zhao, L. S. Wang, and T. X. Yu, Mechanics of adhesion in MEMS-a review, *Journal of Adhesion Science & Technology*. **17**(4), 519–546, (2003).
74. E. T. Whittaker and G. N. Watson, *A Course of Modern Analysis*. (Cambridge University Press, London, 1963), 4th edition.
75. T. H. Boyer, Quantum Electromagnetic Zero-Point Energy of a Conducting Spherical Shell and the Casimir Model for a Charged Particle, *Physical Review*. **174**(5), 1764–1776, (1968).
76. S. K. Lamoreaux, Demonstration of the Casimir force in the 0.6 to $6\mu m$ range, *Physical Review Letters*. **78**(1), 5–8 (Jan, 1997). doi: 10.1103/PhysRevLett.78.5.
77. C. I. Sukenik, M. G. Boshier, D. Cho, V. Sandoghdar, and E. A. Hinds, Measurement of the Casimir-Polder force, *Physical Review Letters*. **70**(5), 560–563 (Feb, 1993). doi: 10.1103/PhysRevLett.70.560.
78. B. W. Harris, F. Chen, and U. Mohideen, Precision measurement of the Casimir force using gold surfaces, *Physical Review A*. **62**(5), 052109 (Oct, 2000). doi: 10.1103/PhysRevA.62.052109.
79. F. M. Serry, D. Walliser, and G. J. Maclay, The role of the Casimir effect in the static deflection and stiction of membrane strips in microelectromechanical systems (MEMS), *Journal of Applied Physics*. **84**(5), 2501–2506 (September, 1998).
80. W.-H. Lin and Y.-P. Zhao, Casimir effect on the pull-in parameters of nanometer switches, *Microsystem Technologies*. **11**(2), 8085, (2005).
81. J. Bárcenas, L. Reyes, and R. Esquivel-Sirvent, Scaling of micro- and nanodevices actuated by Casimir forces, *Applied Physics Letters*. **87**, 263106, (2005).
82. M. Borgag, Casimir effect for a sphere and a cylinder in front of a plane and corrections to the proximity force theorem, *Physical Review D*. **73**, 125018, (2006).
83. H. Gies and K. Klingmüller, Casimir effect for curved geometries: Proximity-Force-Approximation validity limits, *Physical Review Letters*. **96**, 220401, (2006).
84. R. C. Batra, M. Porfiri, and D. Spinello, Analysis of electrostatic MEMS using meshless local Petrov-Galerkin (MLPG) method, *Engineering Analysis with Boundary Elements*. **30**(11), 949–962, (2006).
85. J. A. Pelesko and X. Y. Chen, Electrostatic deflections of circular elastic membranes, *Journal of Electrostatics*. **57**, 1–12, (2003).
86. L. Meirovitch, *Fundamentals of Vibrations*. (McGraw Hill, New York, 2001).
87. R. M. Bowen and C.-C. Wang, *Introduction to vectors and tensors*. vol. 2, (Plenum Press, 1976).

88. McLachlan, *Theory and application of Mathieu functions*. (Oxford University Press, London, 1947).
89. J. A. Pelesko, D. H. Bernstein, and J. McCuan. Symmetry and symmetry breaking in electrostatic MEMS. In *Proceedings of Modeling and Simulation of Microsystems*, pp. 304–307, (2003).
90. R. C. Batra, M. Porfiri, and D. Spinello, Effects of Casimir force on pull-in instability in micromembranes, *Europhysics Letters*. (2007). In press.
91. J.-N. Ding, S.-Z. Wen, and Y.-G. Meng, Theoretical study of the sticking of a membrane strip in MEMS under the Casimir effect, *Journal of Micromechanics and Microengineering*. **11**, 202–208, (2001).
92. G. Palasantzas and J. T. M. De Hosson, Pull-in characteristics of electromechanical switches in the presence of Casimir forces: Influence of self-affine surface roughness, *Physical Review B*. **72**, 115426, (2005).
93. V. B. Bezerra, G. L. Klimchitskaya, and V. M. Mostepanenko, Higher-order conductivity corrections to the Casimir force, *Physical Review A*. **62**, 014012, (2000).

Chapter 10

Numerical Simulation of BioMEMS with Dielectrophoresis

G. R. Liu* and C. X. Song

Center for Advanced Computations in Engineering Science (ACES)
Department of Mechanical Engineering
National University of Singapore, 9
Engineering Drive 1, Singapore 117576
mpeliugr@nus.edu.sg

Dielectrophoresis (DEP) as an effective tool for particle separation and manipulation is increasingly used in various BioMEMS applications. Numerical simulation plays an important role in DEP analyses and design. One of the most commonly used numerical techniques is the Finite Element Method (FEM) that provides weak solutions of field variables, which can have problems in obtaining the second derivatives, that are essential for computing the DEP forces. A novel meshfree method named the linearly conforming point interpolation method (LC-PIM) that provides an effective way to compute the second derivatives of the field variables, is first introduced in this chapter. The LC-PIM is then used to simulate the electric field and DEP forces for an interdigitated electrode array with either a two-phase or a four-phase signal. Solutions are compared with analytical results with excellent agreement. The method is thus validated for solving the problems with high accuracy of high order derivatives even in the high gradient regions which are common in BioMEMS. Several discussions are made to provide useful information for the design of DEP devices.

Contents

10.1 Introduction 376
10.2 The Theoretical Background of BioMEMS with DEP 377
10.3 Linearly Conforming Point Interpolation Method (LC-PIM) 379
  10.3.1 Interpolation Formulations 379
  10.3.2 Gradient Smoothing 381
  10.3.3 Variational Form 383
10.4 Results and Discussion 384
  10.4.1 Simulation of the DEP Array 385

*Fellow, Singapore-MIT alliance

10.4.2 Simulation of the Traveling Wave DEP Array 391
10.5 Conclusion 397
References 397

10.1. Introduction

The term alternating current (AC) electrokinetics refers to the particle movement arising from the interaction of non-uniform AC electric field with polarizable particles. The techniques based on AC electricnetics are increasingly used for the analysis and separation of biological particles, such as cells, bacteria, viruses and DNA.[1–3] One of these techniques is the dielectrophoresis (DEP), which arises from the interaction of AC electric field and the induced dipole in a particle.[4]

One of the DEP techniques is the field flow fractionation (FFF) method, in which DEP force levitates different particles to different vertical heights above the surface, and hydrodynamic force drives the particles traveling at different speed according to their heights to the surface to achieve the separation.[5–7] Another well known DEP technique is the traveling wave dielectrophoresis (twDEP), in which the particle motion is induced by traveling electric field.[8–10] Traveling wave DEP systems have received a great deal of attention from researchers due to the fact that there is no need for a pumping system since the forces can be exerted in the horizontal direction. Furthermore, the cell-cell interference is minimized in twDEP since the cells repel from each other rather than forming the pearl chains. Both of these techniques use an interdigitated parallel electrode array. An analytical approximation of the potential and forces for this array has been derived using both Green's function[11] and Fourier series.[12] In order to obtain the analytical expression for the forces, the potential between the electrodes is assumed to be a linear function, thus the analytical expression does not represent the exact solution. Numerical methods have also been used to determine the electric field and DEP forces from this electrode array, including point charge, charge density, finite element method, finite difference and integral equation methods.[13–16]

In this chapter, we present a novel meshless method, the linearly conforming point interpolation method (LC-PIM), for computing the numerical solution of the electric potential, electric field and DEP forces from both the DEP arrays used in FFF and twDEP arrays. LC-PIM is originally proposed by Liu and has been successfully used for solving various engineering problems with highly accurate solution for derivatives of field variables.[17–19] The LC-PIM ensures the conformability by using the gradient smoothing technique that was first used to stabilize the nodal integration in a Galerkin meshfree method.[20,21] LC-PIM is an effective technique for DEP simulation since it can capture the high gradient field

feature which is very commonly required in BioMEMS devices with DEP. Compared with conventional FEM technique, LC-PIM can successfully calculate the second derivatives of primary field variable with good accuracy, which is crucial for accurate computation of the DEP forces.

The outline of this chapter is as follows. The theoretical background of BioMEMS with dielectrophoresis is first reviewed in Sec. 10.2. The formulation procedure of LC-PIM is presented in Sec. 10.3. In Sec. 10.4, numerical results of DEP and twDEP arrays are presented and discussed. Finally conclusions are drawn in Sec. 10.5.

10.2. The Theoretical Background of BioMEMS with DEP

Dielectrophoresis (DEP) is defined as the lateral motion imparted on uncharged particles as a result of polarization induced by non-uniform electric fields. When a dielectric particle is placed in a spatially non-uniform electric field, a dipole is induced in the particle. Due to the inhomogeneous nature of the electric field, the two halves of the induced dipole experience a different force magnitude and thus a net force is produced.

Figure 10.1 shows a dielectric particle suspended in a point-plane electrode system. The induced dipole experiences a net force in the non-uniform field and the particle is driven towards the point electrode. If the particle is more polarizable than the surrounding medium, the induced net force is aligned with the increasing direction of the electric field intensity and the particle is attracted to electric field intensity maxima, such as that in Fig. 10.1. This effect is called positive dielectrophoresis. If the particle is less polarizable than the surrounding medium, the induced net force is aligned with the decreasing direction of the electric field intensity and then the particle is attracted to electric field intensity minima. This effect is called negative dielectrophoresis.

The expression of time-averaged DEP forces in an AC electric field of angular frequency ω has been derived using both effective moment method[4] and the Maxwell stress tensor method.[22]

For a homogeneous medium, the electric field can be determined by the Laplace equation of the electric potential, which is derived from the quasi-electrostatic form of Maxwell's equations,[13]

$$\nabla^2 \tilde{\phi} = 0 \tag{10.1}$$

where $\tilde{\phi}$ is the electric potential phasor and can be written as

$$\tilde{\phi} = \phi_R + i\phi_I. \tag{10.2}$$

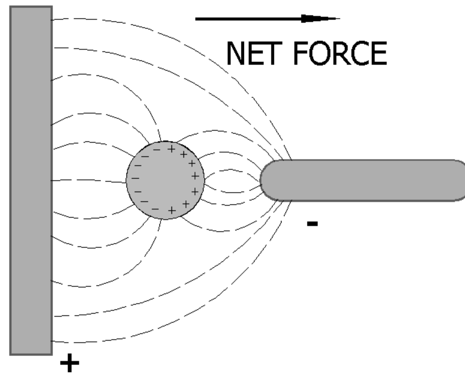

Fig. 10.1. Illustration of dielectrophoresis in a point-plane electrode system. If particle is more polarizable than surrounding medium, it moves towards highest electric field region due to positive dielectrophoresis; If particle is less polarizable than surrounding medium, it is repelled from highest electric field region due to negative dielectrophoresis.

The dipole moment for a linear isotropic dielectric spherical particle under an applied potential of a single frequency is

$$\tilde{\mathbf{p}}\left(\omega\right) = \upsilon\alpha\left(\omega\right)\tilde{\mathbf{E}} \tag{10.3}$$

where υ is the volume of the particle, α is the effective polarisability of the particle and $\tilde{\mathbf{E}}$ is the electric field phasor. The electric field is given by

$$E(x,t) = \mathrm{Re}[\tilde{\mathbf{E}}(x)e^{i\omega t}] \tag{10.4}$$

where $\mathrm{Re}[\cdot]$ denotes the real part. The DEP force arises from the interaction between the induced dipole moment and the non-uniform electric field. It is reasonably assumed that the particle diameter is much smaller than the characteristic length of the non-uniformity. All higher order moments can thus be ignored. The time-averaged DEP force can then be written as[4]

$$\langle\mathbf{F}\rangle = \frac{1}{2}\mathrm{Re}[(\tilde{\mathbf{p}}\cdot\nabla)\tilde{\mathbf{E}}^{*}] \tag{10.5}$$

where $*$ refers to complex conjugate. By substituting the phasor expressions,

Eq. (10.5) can be finally simplified to

$$\begin{aligned}\langle \mathbf{F} \rangle &= \frac{1}{4}\mathrm{Re}[\alpha\nabla(\tilde{\mathbf{E}}\cdot\tilde{\mathbf{E}}^*)] - \frac{1}{2}\upsilon\mathrm{Re}[\alpha\nabla\times(\tilde{\mathbf{E}}\times\tilde{\mathbf{E}}^*)] \\ &= \frac{1}{4}\upsilon\mathrm{Re}[\alpha]\nabla(|\mathrm{Re}[\tilde{\mathbf{E}}]|^2 + |\mathrm{Im}[\tilde{\mathbf{E}}]|^2) \\ &\quad - \frac{1}{2}\upsilon\mathrm{Im}[\alpha](\nabla\times(\mathrm{Re}[\tilde{\mathbf{E}}]\times\mathrm{Im}[\tilde{\mathbf{E}}])]\end{aligned} \tag{10.6}$$

where $\mathrm{Re}[\tilde{\mathbf{E}}] = -\nabla\phi_R$, $\mathrm{Im}[\tilde{\mathbf{E}}] = -\nabla\phi_I$.

The first term on the right hand side of Eq. (10.6) results from the spatial variation in the magnitude of the applied electric field, and the second term from the spatial variation in phase of the applied electric field. In the case of the DEP field flow fractionation, $\mathrm{Im}[\tilde{\mathbf{E}}] = 0$. In the case of twDEP, both terms are non-zero. The DEP forces are obtained first by solving the real part of the electric potential phasor ϕ_R and then the imaginary part of the electric potential phasor ϕ_I using the Laplace equation (10.1).

10.3. Linearly Conforming Point Interpolation Method (LC-PIM)

10.3.1. *Interpolation Formulations*

Formulation of the point interpolation method (PIM) is based on the Galerkin week form, and the shape functions are created using polynomial basis functions through the interpolation within local support domain.[23] The constructing procedure for PIM shape functions is presented here briefly. Consider a continuous function $u(\mathbf{x})$ at the point of interest $\mathbf{x}$ is approximated in the form,

$$u(\mathbf{x}) = \sum_{i=1}^{m} p_i(\mathbf{x})a_i = \mathbf{P}^T(\mathbf{x})\mathbf{a} \tag{10.7}$$

where $p_i(\mathbf{x})$ is a given monomial in the space coordinates $\mathbf{x}^T = [x, y]$, m is the number of monomial terms, and a_i is the coefficient for $p_i(\mathbf{x})$ which is yet to be determined. The $p_i(\mathbf{x})$ is usually built utilizing the Pascal's triangles and a complete basis is usually preferred. Polynomial basis functions for two-dimentional (2D) space are given by

$$\mathbf{p}^T(\mathbf{x}) = [1 \quad x \quad y] \qquad \text{Basis of complete first order} \tag{10.8}$$

$$\mathbf{p}^T(\mathbf{x}) = [1 \quad x \quad y \quad x^2 \quad xy \quad y^2] \qquad \text{Basis of complete 2nd order} \tag{10.9}$$

In order to determine the coefficients a_i, a support domain is formed for the point of interest at $\mathbf{x}$, with a total of n field nodes included in the support domain. In conventional PIM, the number of nodes in local support domain is always equal

to the number of basis, *i.e.*, $n = m$. The coefficients a_i in Eq. (10.7) are determined by enforcing Eq. (10.7) to pass through all n nodes in the local support domain. This leads to n linear equations

$$\left.\begin{array}{c} u_1 = a_1 + a_2 x_1 + a_3 y_1 + \cdots + a_m p_m(\mathbf{x}_1) \\ u_2 = a_1 + a_2 x_2 + a_3 y_2 + \cdots + a_m p_m(\mathbf{x}_2) \\ \vdots \\ u_n = a_1 + a_2 x_n + a_3 y_n + \cdots + a_m p_m(\mathbf{x}_n) \end{array}\right\} \tag{10.10}$$

which can be written in matrix form as

$$\mathbf{U}_s = \mathbf{P}_m \mathbf{a} \tag{10.11}$$

where $\mathbf{U_s}$ is the vector that contains all the field nodal variables in the support domain, and is in the form of

$$\mathbf{U_s} = \{\mathbf{u_1} \quad \mathbf{u_2} \cdots \mathbf{u_n}\}^{\mathbf{T}} \tag{10.12}$$

the polynomial matrix is

$$\mathbf{P}_m^T = \begin{bmatrix} ;;;1 & ;;;1 & ;;\cdots & ;1 \\ ;;x_1 & ;;;x_2 & ;;;\cdots & x_n \\ ;;y_1 & ;;y_2 & ;;\cdots & y_n \\ \vdots & ;\vdots & ;\ddots & ;\vdots \\ p_m(\mathbf{x}_1) & p_m(\mathbf{x}_2);; & \cdots & p_m(\mathbf{x}_n) \end{bmatrix} \tag{10.13}$$

the vector of coefficients is

$$\mathbf{a}^T = \{a_1 \quad a_2 \quad a_3 \quad \cdots \quad a_n\}. \tag{10.14}$$

Since $n = m$, $\mathbf{P}_m$ is a square matrix with the dimension of ($n \times m$ or $m \times m$). Assuming $\mathbf{P}_m^{-1}$ exists, a unique solution for $\mathbf{a}$ can be obtained as

$$\mathbf{a} = \mathbf{P}_m^{-1} \mathbf{U}_s \tag{10.15}$$

Substituting Eq. (10.15) back into Eq. (10.7) yields

$$\mathbf{u}(\mathbf{x}) = \mathbf{p}^{\mathbf{T}}(\mathbf{x}) \mathbf{P}_m^{-1} \mathbf{U}_s = \sum_{i=1}^{n} N_i(\mathbf{x}) u_i = \mathbf{N}(\mathbf{x}) \mathbf{U}_s \tag{10.16}$$

where $\mathbf{N}(\mathbf{x})$ are the shape functions, and can be expressed as

$$\mathbf{N}(\mathbf{x}) = \mathbf{p}^{\mathbf{T}}(\mathbf{x}) \mathbf{P}_m^{-1} = \{N_1(\mathbf{x}) \quad N_2(\mathbf{x}) \quad \cdots \quad N_n(\mathbf{x})\}. \tag{10.17}$$

The derivatives of the shape functions can be easily obtained because the PIM shape function is of polynomial form, but they are not required in LC-PIM formulation due to the use of gradient smoothing technique described below.

Note that we assume matrix $\mathbf{P}_m$ is invertible in the formulation above. However, this is not always the case. It depends on the location of the point of interest in the local support domain, and the terms of the monomials used in the basis functions.[23] Methods for creating a non-singular $\mathbf{P}_m$ can be found in Ref. 18. The node selection technique introduced in the following can easily prevent the singularity problem.

10.3.2. *Gradient Smoothing*

The strain smoothing technique has been used for overcoming the instability in nodal integration.[20,21] A similar smoothing operation is performed here on the gradient of shape functions, namely

$$\nabla^h \phi(\mathbf{x}_i) = \int_{\Omega_i} \nabla \phi(\mathbf{x}) W(\mathbf{x} - \mathbf{x}_i) d\Omega \tag{10.18}$$

where $\nabla \phi(\mathbf{x}) = [\partial \phi / \partial x_1, \partial \phi / \partial x_2]$ in two-dimensional space, W is a smoothing function, Ω_i is the representative domain of the ith field node, which can be obtained by making use of the background triangles. The representative domain is formed by sequentially connecting the centroids with the mid-edge-points of the surrounding triangles of a field node as illustrated in Fig. 10.2.

Using integration by parts, Eq. (10.18) can be rewritten as

$$\nabla^h \phi(\mathbf{x}_i) = \oint_{\Gamma_i} \phi(\mathbf{x}) W(\mathbf{x} - \mathbf{x}_i) - \int_{\Omega_i} \phi(\mathbf{x}) \nabla W(\mathbf{x} - \mathbf{x}_i) d\Omega \tag{10.19}$$

where Γ_i is the boundary of representative domain of the ith field node.

Using a piecewise constant function as the smooth function, we have

$$W(\mathbf{x} - \mathbf{x}_i) = \begin{cases} \dfrac{1}{A_i}, & \mathbf{x} \in \Omega_L \\ 0, & \mathbf{x} \notin \Omega_L \end{cases} \tag{10.20}$$

in which $A_i = \int_{\Omega_i} d\Omega$ is the area of the representative domain of ith field node. Substituting Eq. (10.20) into Eq. (10.19), we get

$$\nabla^h \phi(\mathbf{x}_i) = \frac{1}{A_i} \int_{\Gamma_i} \phi(\mathbf{x}) \mathbf{n} d\Gamma \tag{10.21}$$

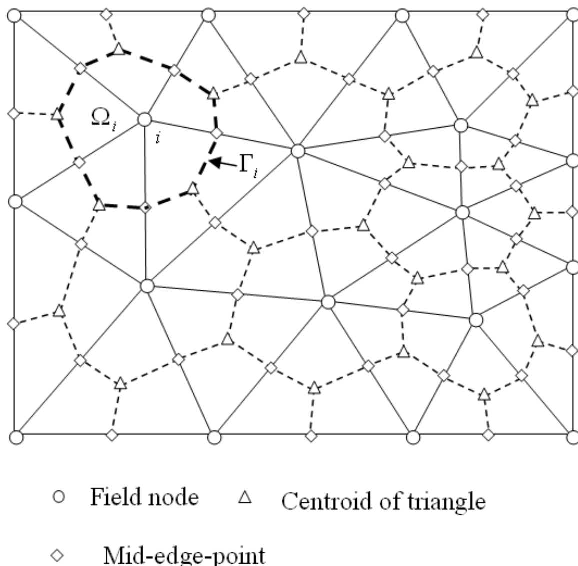

Fig. 10.2. Illustration of background triangular cells and formation of nodal representative domain.

By introducing PIM shape function into Eq. (10.21), we obtain

$$\nabla^h \phi(\mathbf{x}_i) = \sum_{I \in G_i} \tilde{\mathbf{B}}_I(\mathbf{x}_i)\phi_I \tag{10.22}$$

where

$$\tilde{\mathbf{B}}_I(\mathbf{x}_i) = \begin{bmatrix} \tilde{b}_{I1}(\mathbf{x}_i) \\ \tilde{b}_{I2}(\mathbf{x}_i) \end{bmatrix} \tag{10.23}$$

and

$$\tilde{b}_{Ij}(\mathbf{x}_i) = \frac{1}{A_i} \int_{\Gamma_i} N_I(\mathbf{x}) n_j(\mathbf{x}) d\Gamma. \tag{10.24}$$

G_i is a group of nodes that are related to i while forming the shape functions along the boundary of the representative domain of ith node. $N_I(x)$ is the PIM shape function for node I. The numerical integration of Eq. (10.24) can be performed using Trapezoidal rule or Gauss quadrature on the boundaries of representative nodal domain. In either case, we always use the vertices of the background triangle as the local support nodes such that the singularity problem in Eq. (10.15) can be always avoided. Detailed discussion of support nodes selection can be found in Ref. 18.

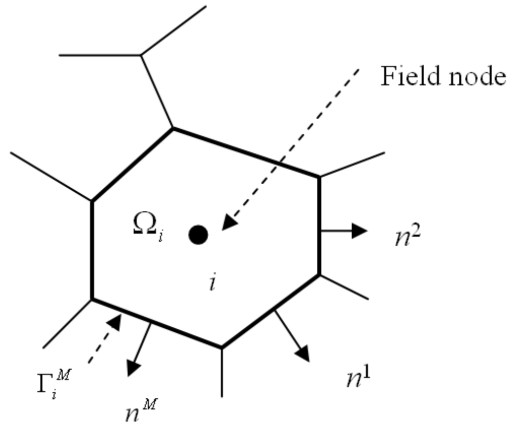

Fig. 10.3. Example of a representative domain in 2D space. Integration is performed along the boundary of the representative domain.

10.3.3. *Variational Form*

Considering a two-dimensional boundary value problem governed by a Laplace equation

$$\nabla^2 \phi = 0 \tag{10.25}$$

with the following boundary conditions

$$\phi = \Phi(x, y) \qquad \text{on } S_1 \tag{10.26}$$

$$\frac{\partial \phi}{\partial x} n_x + \frac{\partial \phi}{\partial y} n_y + g(x, y) = 0 \qquad \text{on } S_2 \tag{10.27}$$

where g is known a priori and n_x, n_y are the direction cosines of the outward normal to the surface, the union of S_1 and S_2 forms the complete boundary Γ, it can be shown that the function $\phi(x, y)$ satisfies Eqs. (10.25)–(10.27) also minimizes the functional[24]

$$I(\phi) = \frac{1}{2} \int_\Omega \left[\left(\frac{\partial \phi}{\partial x} \right)^2 + \left(\frac{\partial \phi}{\partial y} \right)^2 \right] d\Omega + \int_{S_2} g \phi dS_2 \tag{10.28}$$

The variational principle gives the equation

$$\delta I(\phi) = 0 \tag{10.29}$$

or

$$\delta I(\phi) = \int_\Omega \left[\frac{\partial \delta\phi}{\partial x} \frac{\partial \phi}{\partial x} + \frac{\partial \delta\phi}{\partial y} \frac{\partial \phi}{\partial y} \right] d\Omega + \int_{S_2} g \delta\phi dS_2 = 0 \tag{10.30}$$

The primary variable and its first derivatives can be approximated by

$$\phi^h = \sum_{I=1}^{\mathrm{NP}} \mathrm{N_I}\phi_{\mathrm{I}} \equiv \mathbf{N\Phi} \tag{10.31}$$

$$\nabla^h\phi = \sum_{I=1}^{NP} \tilde{\mathbf{B}}_{\mathbf{I}}\phi_{\mathbf{I}} \equiv \tilde{\mathbf{B}}\mathbf{\Phi} \tag{10.32}$$

Substituting Eqs. (31) and (32) into Eq. (30) and performing nodal integration, we can obtain the discretized equation

$$\mathbf{K\Phi} = \mathbf{f} \tag{10.33}$$

where $\mathbf{K}$ and $\mathbf{f}$ is obtained respectively by assembly of the following submatrices

$$\mathbf{K_{IJ}} = \sum_{\mathbf{i=1}}^{\mathbf{NP}} \tilde{\mathbf{B}}_{\mathbf{I}}^{\mathbf{T}}(\mathbf{x_i})\tilde{\mathbf{B}}_{\mathbf{J}}(\mathbf{x_i})\mathbf{A_i} \tag{10.34}$$

and

$$\mathbf{f_I} = \sum_{\mathbf{i=1}}^{\mathbf{NPb}} \mathbf{N_I}(\mathbf{x_i})\mathbf{g}(\mathbf{x_i})\mathbf{s_i} \tag{10.35}$$

where NPb is the number of points on the natural boundaries, s_i are the weights corresponding to the boundary points.

The primary variables can be obtained by Eq. (33). The first order derivatives can be obtained by substituting the results from Eq. (10.33) into Eq. (10.32). Similarly, the second derivatives can be obtained by replacing ϕ in Eq. (32) by $\partial\phi/\partial x_k$, where $k = 1, 2$.

10.4. Results and Discussion

In this section, the simulation for both the dielectrophoretic array and the traveling wave dielectrophoretic array are presented. Figure 10.4 shows the geometry of the interdigitated electrode array. For the DEP array, 180 degree voltage phase difference is applied on the adjacent electrodes. For the twDEP array, 90 degree phase difference is applied on the adjacent electrodes. The width of the electrode is d_1 and the spacing is d_2. It is assumed that the length of the electrode is much longer than the width. As a result, the problem can be simplified to two dimensions. For mathematical simplicity and computational efficiency, non-dimensional formulation is introduced. Electric potential ϕ is scaled by the applied voltage V_0 resulting a non-dimensional potential $\phi' = \phi/V_0$. The coordinates are also scaled by d, which is half of the unit cell width $d_1 + d_2$, resulting new non-dimensional

coordinates as $x' = x/d$, and $y' = y/d$. For the results presented in this chapter, $V_0 = 1\,\text{V}$, $d = 10\,\mu\text{m}$ and $d_1 = d_2 = d$.

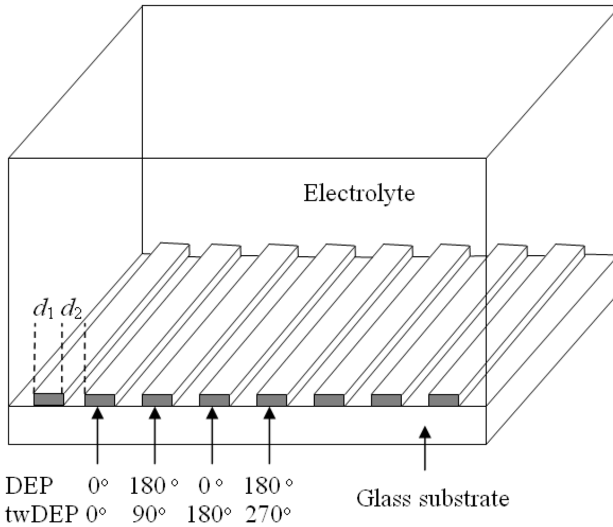

Fig. 10.4. Interdigitated electrode array used for dielectrophoretic separation and traveling wave dielectrophoresis.

10.4.1. *Simulation of the DEP Array*

The electrode array is assumed to be infinite long so that the problem can be reduced into a unit cell. The boundary condition for one unit cell of the DEP array is demonstrated in Fig. 10.5. The potential on the top boundary goes to zero as y goes to infinity. Using the symmetry nature of the electrode array, the potential on the vertical boundary is zero. The potential on the electrodes is the applied voltage V_0 (rms). In real devices, the electrode is much thinner than its width so that the thickness is ignored and the potential is applied at $y = 0$. The exact boundary condition in the gap, which arise from the requirement that the total current across the interface is continuous, is that the normal gradient of the potential equal to zero. This leads to the difficulty of obtaining analytical expression for the dielectrophoretic forces, as a result, the analytical solution is derived with the assumption that potential between the electrodes vary linearly.[12] In order to verify the reasonableness of this assumption, both of the two types of boundary conditions are used in this chapter, and the corresponding results were compared. For the case of dielectrophoretic array, the DEP force in Eq. (10.6) can be further

simplified as

$$\langle \mathbf{F}_{DEP} \rangle = \frac{1}{4} \upsilon \text{Re}[\alpha] \nabla |\nabla \phi_R|^2 = \frac{1}{4} \upsilon \text{Re}[\alpha] \frac{V_0^2}{d^3} \nabla' |\nabla' \phi_R|^2 \tag{10.36}$$

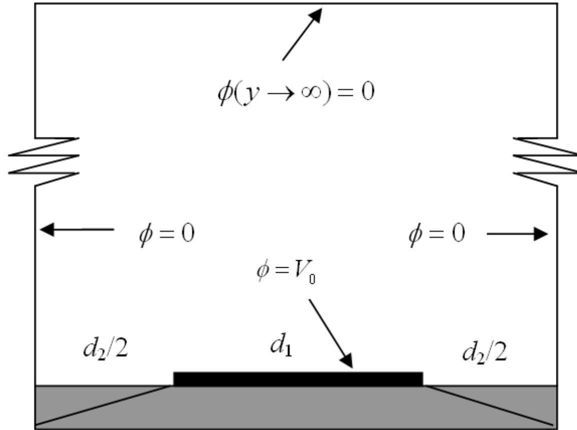

Fig. 10.5. Boundary conditions of a unit cell in dielectrophoresis array.

10.4.1.1. *Case 1: Linear Potential Change in the Gap*

The results for the case that assumes linear change of electric potential in the electrode gap are first computed. The electric potential is shown in Fig. 10.6(a), and the magnitude of electric field is shown in Fig. 10.6(b). Both the direction and the magnitude of the vector $\nabla' |\nabla' \phi_R|^2$ are demonstrated in Figs. 10.6(c) and 10.6(d). Observations of these figures are consistent with the previously reported results.[13] Away from the electrode, electric potential decrease rapidly as y increases. The magnitude of the electric field maximizes at the edge of the electrodes at $x' = 0.5$ and $x' = 1.5$, which are the high gradient regions. Above $y' = 1$, the vectors $\nabla' |\nabla' \phi_R|^2$ point downwards to the electrodes straightly. While below $y' = 1$, the vectors point towards the edges of the electrodes. Figure 10.6(d) shows that above the height $y' = 1$, the magnitude of vectors $\nabla' |\nabla' \phi_R|^2$ is constant in x direction, which agrees with the experiment results that different particles levitate at different heights, where the gravity forces balance the DEP forces. This phenomenon is used for separation and manipulation of bio-particles in the bio-medical research area.

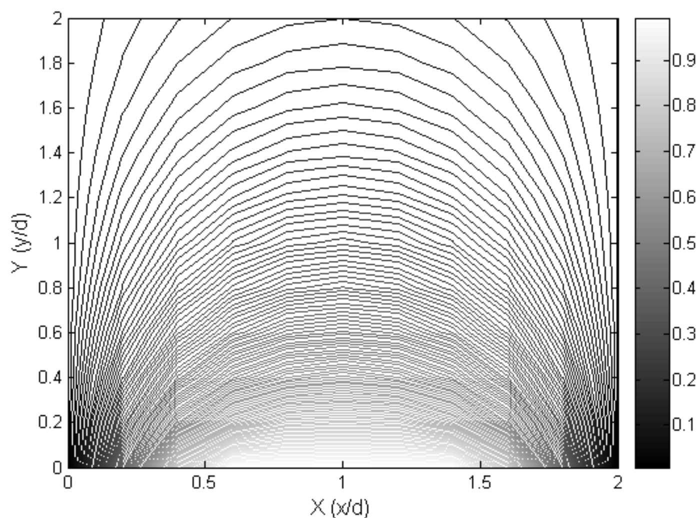

(a)

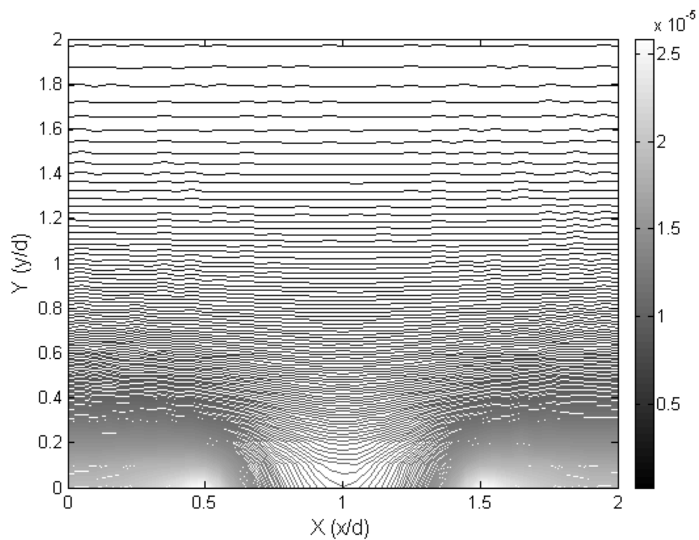

(b)

Fig. 10.6. Solution of the problem near the electrode. (a) The electric potential ϕ'. (b) The magnitude of electric field $|\nabla'\phi_R|$. (c) The magnitude of vector $\nabla'|\nabla'\phi_R|^2$. (d) The direction of vector $\nabla'|\nabla'\phi_R|^2$.

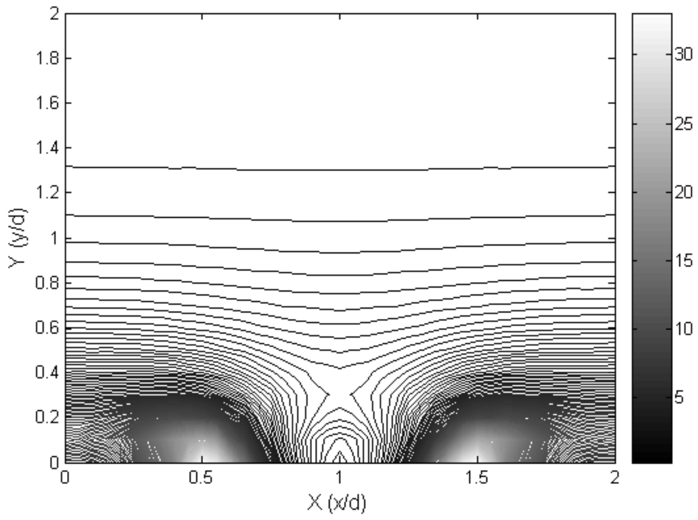

(c)

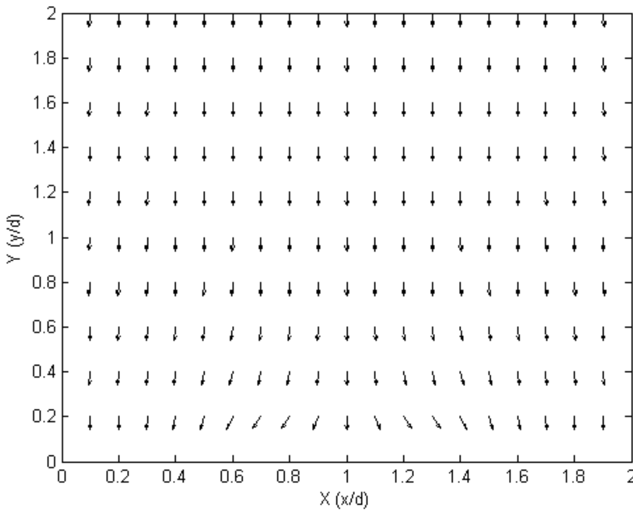

(d)

Fig. 10.6. (*Continued*)

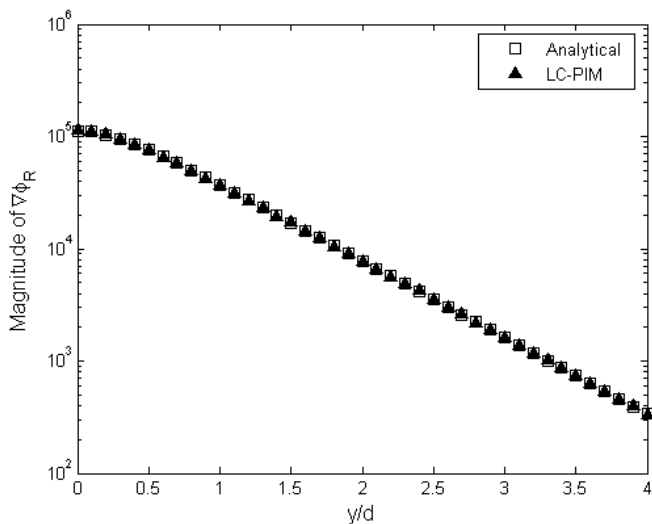

(a)

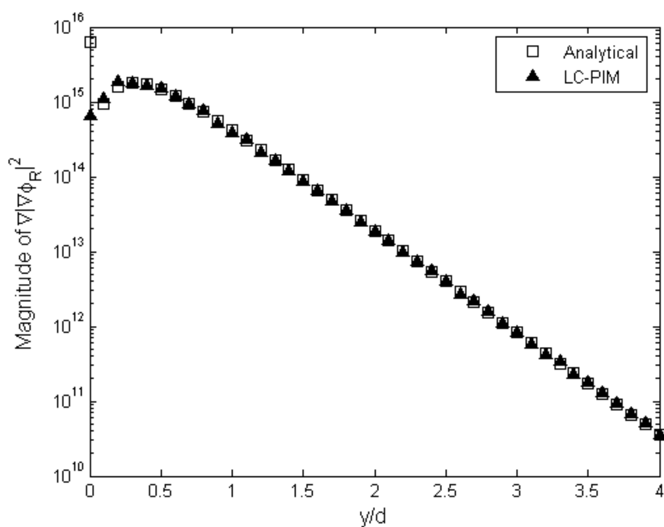

(b)

Fig. 10.7. Comparison of numerical and analytical solution on middle vertical line $x' = 1$ (a) comparison of electric field magnitude $|\nabla\phi_R|$; (b) comparison of magnitude of vector $\nabla|\nabla\phi_R|^2$.

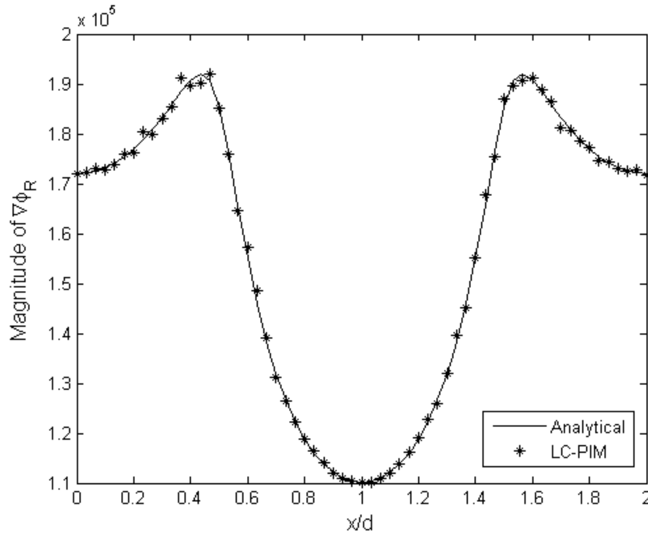

(a)

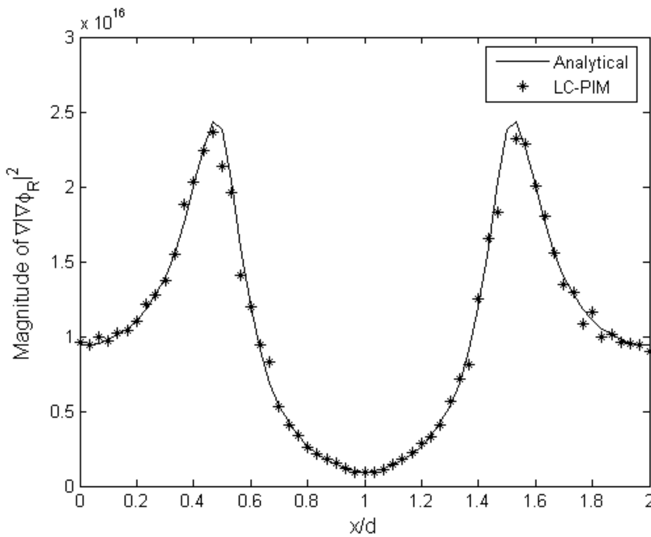

(b)

Fig. 10.8. Comparison of numerical and analytical solution on horizontal line $y' = 0.1$ (a) comparison of electric field magnitude $|\nabla\phi_R|$; (b) comparison of magnitude of vector $\nabla|\nabla\phi_R|^2$.

In order to validate the LC-PIM method used in this work, the numerical results are compared with the analytical solution derived from Fourier series analysis.[12] The magnitude of electric field and DEP force decreases exponentially along vertical direction above the height $y' = 1$. By comparing the magnitudes of vectors $\nabla\phi_R$ and vectors $\nabla|\nabla\phi_R|^2$ along the vertical line = 1, which is the symmetry line of the unit cell, Figs. 10.7(a) and 10.7(b) show very good agreement between the LC-PIM solution and the Fourier series solution. We also compared the results on a horizontal line near the electrodes, where the gradient of electric potential is very high. The magnitudes of vectors $\nabla\phi_R$ and vectors $\nabla|\nabla\phi_R|^2$ are shown in Figs. 10.8(a) and 10.8(b).

While obtaining the magnitude of $\nabla|\nabla\phi_R|^2$, the second derivatives of electric potential have to be determined first. This can not be done by the conventional Finite Element Method. LC-PIM is able to calculate the second derivatives with reasonable accuracy, and this is one of the advantages that make it a good method for simulation of DEP devices.

10.4.1.2. *Case 2: Exact Boundary Condition in the Gap*

The exact boundary condition in the gap is that the normal gradient of the electric potential equals to zero, *i.e.*, $\partial\phi/\partial y = 0$. In order to investigate the error arising from the approximate linear boundary condition, the solution with the exact boundary condition is computed. Figure 10.9 shows the difference in magnitude of vector $\nabla|\nabla\phi_R|^2$ on a horizontal line near the electrode $y' = 0.2$.

It is very obvious that the difference is considerably big, especially in the area above the gap on which the different boundary conditions are applied.

This implies that the analytical solution obtained using Fourier series can be used only to roughly predict the DEP force field. The results obtained from applying the exact boundary condition are closer to the true values of the DEP forces. It is more reliable than the analytical solutions.

10.4.2. ***Simulation of the Traveling Wave DEP Array***

10.4.2.1. *Case 3: Study of the Traveling Wave DEP Array*

Case 3 studies the traveling wave DEP array. In this case, both the two terms of the DEP forces in Eq. (10.6) are non-zero, and they are usually referred as DEP

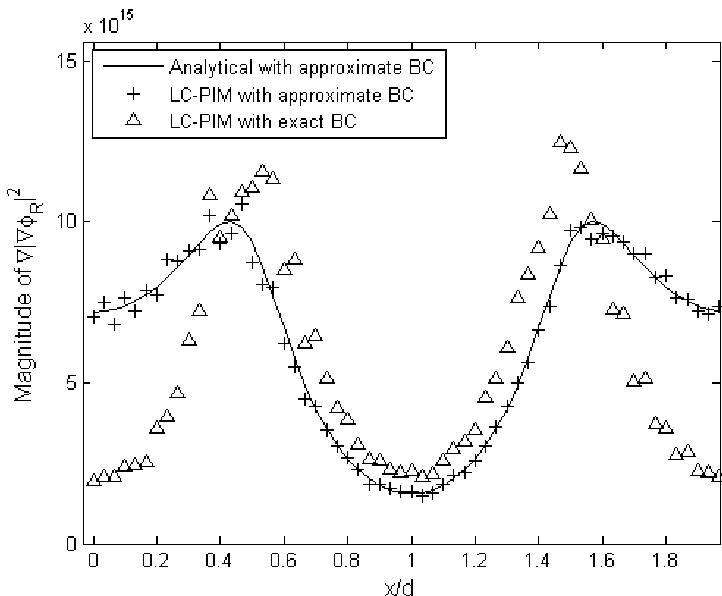

Fig. 10.9. Comparing magnitude of $\nabla|\nabla\phi_R|^2$.

and twDEP components respectively.

$$\langle \mathbf{F}_{DEP} \rangle = \frac{1}{4}\upsilon \mathrm{Re}[\alpha]\nabla(|\nabla\phi_R|^2 + |\nabla\phi_I|^2) \tag{10.37}$$

$$\langle \mathbf{F}_{twDEP} \rangle = -\frac{1}{2}\upsilon \mathrm{Im}[\alpha](\nabla \times (\nabla\phi_R \times \nabla\phi_I)) \tag{10.38}$$

Equations (10.37) and (10.38) show both force components are related to the real and imaginary part of the potential phasor, which and be computed separately by applying approperiate boundary conditions. The problem domain is simplified to a unit cell covering the center of two adjacent electrodes and the gap. The boundary conditions for both real and imaginary parts of the potential phasor are shown in Fig. 10.10. It is obvious that the boundary condition of ϕ_I is the mirror image of ϕ_R about the center line of the gap, therefore only ϕ_R needs to be solved. The solution of ϕ_I is obtained by mirroring the solution of ϕ_R about the vertical line through the center of the gap. The contour plots of the real and imaginary parts of the potential phasor are shown in Figs. 10.11(a) and 10.11(b).

The vectors $\nabla'(|\nabla'\phi'_R|^2 + |\nabla'\phi'_I|^2)$ in the DEP force component and vectors $\nabla' \times (\nabla'\phi'_R \times \nabla'\phi'_I)$ in twDEP force component are obtained. The results shown

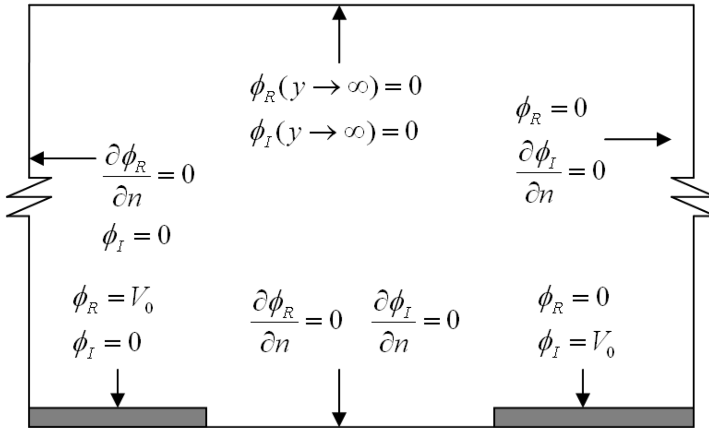

Fig. 10.10. Boundary conditions for a unit cell of traveling wave array.

are all dimensionless, to obtain the exact values, all one has to do is to multiply appropriate constant factors composed of V_0 and d. The magnitudes and directions of vectors $\nabla'(|\nabla'\phi'_R|^2 + |\nabla'\phi'_I|^2)$ are shown in Figs. 10.12(a) and 10.12(b). The results are consistent with the previous observation[13] that above $y' = 1$ the vectors point straight downwards, and the magnitude of the vectors are constant with x' across the electrode array. It is also observed that below $y' = 1$, the vectors point towards the electrode edges and the maximum magnitude of the vectors occurs at the electrode edges. All these observations are similar to those of the DEP array. The magnitudes and directions of vectors $\nabla' \times (\nabla'\phi'_R \times \nabla'\phi'_I)$ are shown in Figs. 10.13(a) and 10.13(b). Above $y' = 1$, the magnitudes of the vectors are also constant with x' across the electrode array, but the vectors are pointing in the horizontal negative x direction. Below $y' = 1$, the magnitudes reach to a maximum value at the electrode edges, and the vectors move in a circular matter near the electrode edges.

In practical applications, the DEP force component is responsible for levitating the particles at certain heights, and twDEP force component for producing the horizontal movements of the particles.

It should be noted again that, while solving the DEP and twDEP force components, the second derivatives of electric potential have to be obtained. This is not achievable using the conventional finite element method, but it is successfully solved using the LC-PIM.

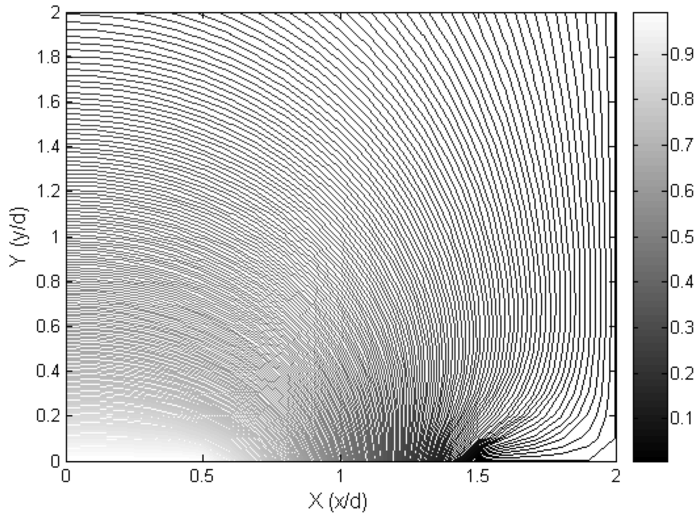

(a)

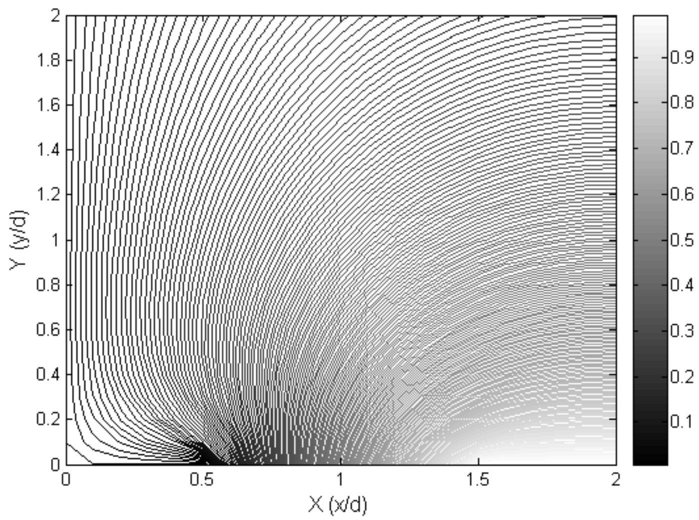

(b)

Fig. 10.11. Solution of electric potential for traveling wave array. (a) Real part of potential phasor ϕ'_R. (b) Imaginary part of potential phasor ϕ'_I.

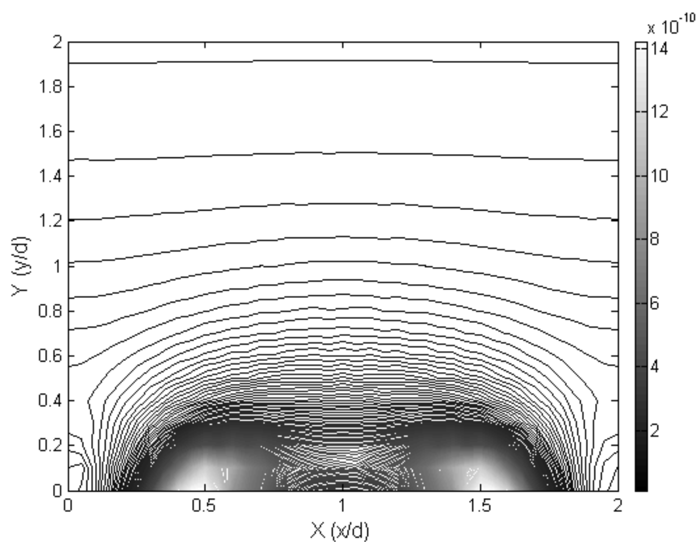

(a)

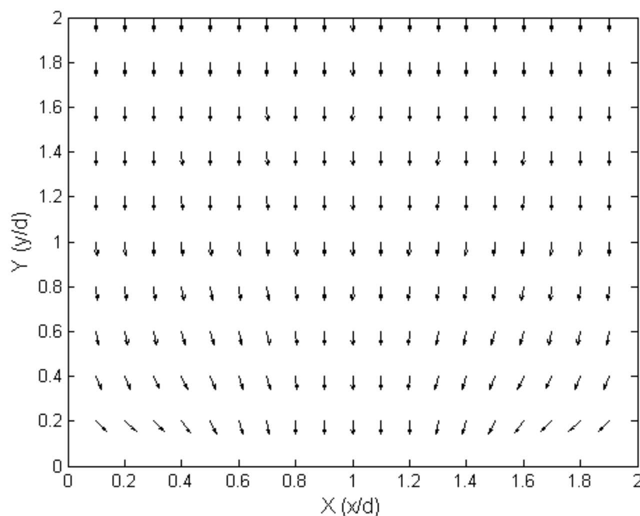

(b)

Fig. 10.12. Solution of the cDEP force component. (a) Magnitude of the vector $\nabla'(|\nabla'\phi'_R|^2 + |\nabla'\phi'_I|^2)$. (b) Direction of the vector $\nabla'(|\nabla'\phi'_R|^2 + |\nabla'\phi'_I|^2)$.

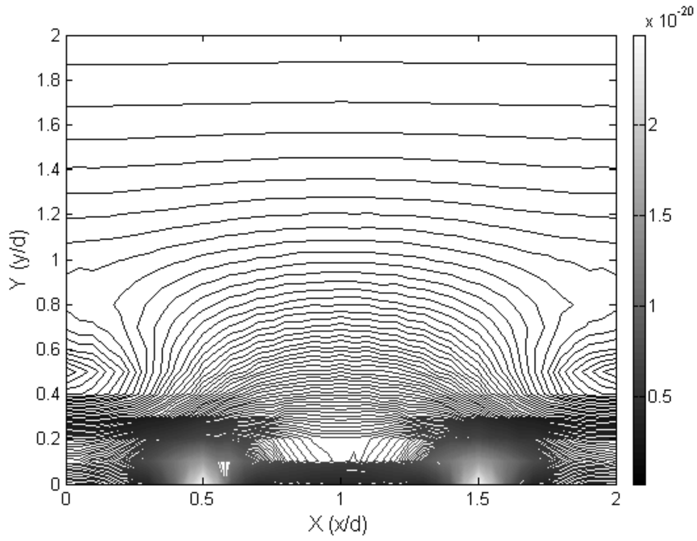

(a)

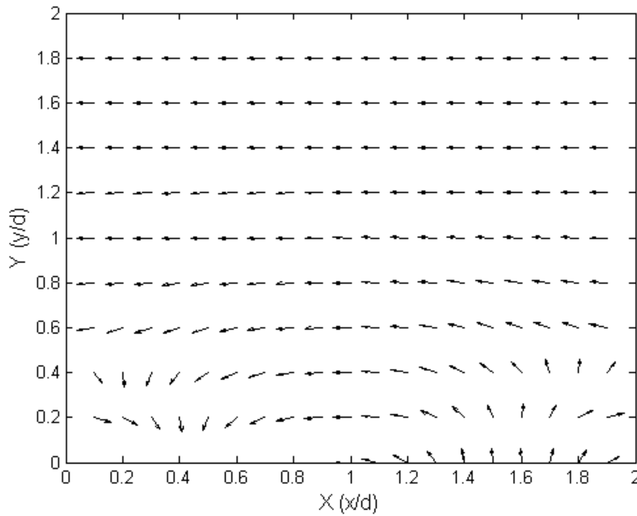

(b)

Fig. 10.13. Solution of the twDEP force component. (a)Magnitude of the vector $\nabla' \times (\nabla'\phi'_R \times \nabla'\phi'_I)$. (b) Direction of the vector $\nabla' \times (\nabla'\phi'_R \times \nabla'\phi'_I)$.

10.5. Conclusion

A novel meshfree method, LC-PIM is used for simulation of the dielectrophoretic array as well as the traveling wave dielectrphoretic array. The results have been compared with the analytical solution obtained using Fourier Series analysis, good accuracy has been demonstrated. Error that arises from the approximate boundary conditions has been analyzed. LC-PIM shows superior advantage over the conventional finite element method in solving DEP problems, due to its capability of computing the second derivatives with good accuracy. Therefore LC-PIM can be potentially used in various DEP design and modeling as a robust numerical tool.

Acknowledgment

The partial support of the Singapore-MIT Alliance is gratefully acknowledged.

References

1. R. Pethig, Using inhomogeneous ac electrical fields to separate and manipulate cells *Crit. Rev. Biotechnol.*, **16**, 331–48 (1996).
2. M. Washizu, O. Kurosawa, I. Arai, S. Suzuki, and N. Shimamoto, Applications of electrostatic stretch-and-positioning of DNA, *IEEE Trans. Indust. Appl.*, **31**, 447–56 (1995).
3. H. Morgan, M. P. Hughes, and N. G. Green, Separation of submicron bioparticles by dielectrophoresis, *Biophys. J.*, **77**, 516–525 (1999).
4. T. B. Jones, *Electromechanics of particles*, Cambridge University Press, Cambridge, (1995).
5. G. H. Markx, R. Pethig, and J. Rousselet, The dielectrophoretic levitation of Latex beads with reference to field-flow fractionation, *J. Phys. D: Appl. Phys.*, **30**, 2470–77 (1997).
6. J. Yang, Y. Huang, X.-B. Wang, F. F. Becker, and P. R. C. Gascoyne, Differential analysis of human leukocytes by dielectrophoretic field-flow-fractionation, *Biophys. J.*, **78**, 2680–89 (2000).
7. X. B. Wang, J. Vykoukal, F. F. Becker, and P. R. C. Gascoyne, Separation of polystyrene microbeads using dielectrophoretic/gravitational field-flow-fractionation, *Biophys. J.*, **74**, 2689–701 (1998).
8. R. Hagedorn, G. Fuhr, T. Muller, and J. Gimsa, Traveling-wave dielectrophoresis of microparticles, *Electrophoresis*, **13**, 49–54 (1992).
9. M. P. Hughes, R. Pethig, and X. B. Wang, Dielectrophoretic forces on particles in traveling electric fields, *J. Phys. D: Appl. Phys.*, **26**, 312–22 (1996).
10. M. S. Talary, J. P. H. Burt, J. A.Tame, and R. Rethig, Electromanipulation and separation of cells using traveling electric fields, *J. Phys. D: Appl. Phys.*, **29**, 2198–2203 (1996).

11. X. J. Wang, X. B.Wang, F. F. Becker, and P. R. C. Gascoyne, A theoretical method of electrical field analysis for dielectrophoretic electrode arrays using Green's theorem, *J. Phys. D: Appl. Phys.*, **29**, 1649–60 (1996).
12. H. Morgan, A. G. Izquierdo, D. Bakewell, N. G. Green, and A. Ramos, The dielectrophoretic and traveling wave forces generated by interdigitated electrode arrays: analytical solution using Fourier series, *J. Phys. D: Appl. Phys.*, **34**, 1553–61(2001).
13. N. G. Green, A. Ramos, and H. Morgan, Numerical solution of the dielectrophoretic and traveling wave forces for interdigitated electrode arrays using the finite element method, *J. Electrost.*, **56**, 235–54 (2002).
14. T. Schnelle, R. Hagedorn, G. Fuhr, S. Fiedler, and T. Muller, Three-dimensional electric field traps for manipulation of cells-calculation and experimental verification, *Biochim. Biophys. Acta. Gen. Subjects*, **1157**, 127–40 (1993).
15. X. B. Wang, Y. Huang, J. P. H. Burt, G. H. Markx, and R. Pethig, Selective dielectrophoretic confinement of bioparticles in potential energy wells, *J. Phys. D: Appl. Phys.*, **26**, 1278 (1993).
16. R. Pethig, Y. Huang, X. B. Wang, and J. P. H. Burt, Positive and negative dielectrophoretic collection of colloidal particles using interdigitated castellated microelectrodes, *J. Phys. D: Appl. Phys.*, **25**, 881–8 (1992).
17. Y. Li, G. R. Liu, M. T. Luan, K. Y. Dai, Z. H. Zhong, G. Y. Li, and X. Han, Contact analysis for solids based on linearly conforming RPIM, *Comput. Mech.* (in press) (2006).
18. G. R. Liu, G. Y. Zhang, K. Y. Dai, Y. Y. Wang, Z. H. Zhong, G. Y. Li, and X. Han, A linearly conforming point interpolation method (LC-PIM) for 2D solid mechanics problems, *Int. J. Comput. Methods*, **2**, 645 (2005).
19. G. Y. Zhang, G. R. Liu, Y. Y. Wang, H. T. Huang, Z. H. Zhong, G. Y. Li, and X. Han, A linearly conforming point interpolation method (LC-PIM) for three-dimensional elasticity problems, *Int. J. Numer. Methods Eng.* (revised) (2006).
20. J. S. Chen, C. T. Wu, S. Yoon, and Y. You, A stabilized conforming nodal integration for Galerkin mesh-free methods, *Int. J. Numer. Methods Eng.*, **50**, 435–466 (2001).
21. J. S. Chen, S. Yoon, and C. T. Wu, Non-linear version of stabilized conforming nodal integration for Galerkin mesh-free methods, *Int. J. Numer. Methods Eng.*, **53**, 2587–2615 (2002).
22. X. J. Wang, X. B. Wang, and P. R. C. Gascoyne, General expression for dielectrophoretic force and electrorotational torque derived using the Maxwell stress tensor method, *J. Electrostat.*, **39**, 277–95 (1997).
23. G. R. Liu, *Mesh free methods: moving beyond the finite element method*, CRC Press, Boca Raton, (2002).
24. H. H. Kenneth, L. D. Donald, E. S. Douglas, and G. B. Ted, *The Finite Element Method for engineers*, Wiley-Interscience, New York, (2001).

Chapter 11

Continuous Modeling of Multi-Physics Problems of Microsystems for Topology Optimization

G. K. Ananthasuresh

Department of Mechanical Engineering, Indian Institute of Science
Bangalore, 560012, India
suresh@mecheng.iisc.ernet.in

The multidisciplinary nature of micro and nano systems makes it difficult to use intuition in conceiving new designs. Topology optimization techniques, which can systematically generate novel designs, alleviate this problem to a large extent. Topology optimization entails optimal distribution of material(s) within a given design domain. It often appears as a discrete problem wherein we need to decide whether to place material(s) or not at each point in the domain. Several techniques have been developed to convert this discrete design parameterization into a continuous form so that computationally efficient gradient-based optimization methods could be used. The continuous parameterization often requires an interpretation for a mixture of materials or material and void, and a notion of continuous modeling in the physics of the problem. In this chapter, such continuous modeling techniques are reviewed for different problems encountered in the design of micro and some nano scale systems. The focus here is on elastic structures actuated with mechanical, electrostatic, thermal, piezoelectric, and other forces. A continuous modeling approach to protein design is also discussed. Furthermore, incorporating manufacturing constraints in the framework of topology optimization is included because the notion of continuous modeling of lithographic mask layouts used in microfabrication is relevant in that problem. The importance of the physics of the problem in continuous modeling is emphasized in all cases.

Contents

11.1 Introduction 400
11.2 Continuous Interpolation of Material Under Mechanical Loads 403
11.3 Electro-Thermal Microactuation 406
11.4 Electrostatic Microactuation 409
11.5 Miscellaneous Microsystems Problems and Emerging Techniques 413
    11.5.1 Emerging Techniques 414
11.6 Continuous Modeling of a Microfabrication Process 415

11.7 Continuous Modeling of Protein Sequences 418
11.8 Conclusions 421
References 422

11.1. Introduction

Materials play an important role in the design of micro and nano scale systems just as they do in the case of macro systems. However, the limited capabilities, the requirement of batch production, and some unique features of micro and nano fabrication techniques make the appropriate use of materials at the small scales more challenging than it is at the macro scale. Devices and systems of small sizes usually consist of heterogeneous material distribution. Microsystems (or micro-electro-mechanical systems (MEMS), as they are popularly known) are essentially layered structures made of different materials. Each material layer most often has anisotropic properties. The relevant properties are not simply mechanical or electrical but encompass multiple energy domains. For example, in a typical microsystems device, mechanical, electrical and thermal properties are relevant to a significant extent in almost all cases. When embedded or integrated actuation is used, many other properties are important. Biological entities of interest at micro (*e.g.*, cells) and nano (bio-molecules such as proteins) are also inherently heterogeneous. The distribution of different materials is also often inhomogeneous in biological systems. These features of micro and nano scale regimes are distinctly different from the engineered systems at the macro scale. Thus, the design of small scale systems is also significantly different from that practiced in conventional engineering design of systems of large size. Therefore, conventional design intuition one uses is not always useful in micro and nano system design due to the aforementioned reasons as well as the need to work with multiple energy domains and the scaling effects. This points to a need to develop systematic or even automated design methodologies that are tailored to the emerging and fast-growing technologies of nano and micro systems. Many efforts are underway to achieve this goal using a technique called *topology optimization*.[1–3]

In topology optimization, the structural topology is optimized such that an objective function is minimized while satisfying one or more constraints. The term *topology* here refers to either the notion of connectivity among different parts of the structure and/or the number of holes in the available design region. Within this design region, which is generally referred to as the *design domain*, we seek to find the optimal distribution of a given amount of material. Thus, topology optimization is equivalent to the problem of material distribution. To understand this, consider the simplest problem of structural topology optimization: obtain the

stiffest structure for a given amount of material whose volume is less than that of the design domain. The design specifications for such a problem are shown in Fig. 11.1. The figure shows the design region, Ω, a fixed portion of the boundary Γ_0 of Ω, and boundary forces $\mathbf{t}$. When the volume of the available material V^* is less than the volume of Ω, we need to decide where to place V^* amount of material within Ω so that we get the stiffest structure. From the viewpoint of connectivity, here we need to decide how the portions of the boundary where it is fixed and where the forces are applied are connected to each other. This is one interpretation of topology. The other is that how many holes need to be introduced into Ω. This decision is left to the optimization problem. This feature distinguishes topology optimization from shape or parametric optimization wherein the topology needs to be assumed a priori.

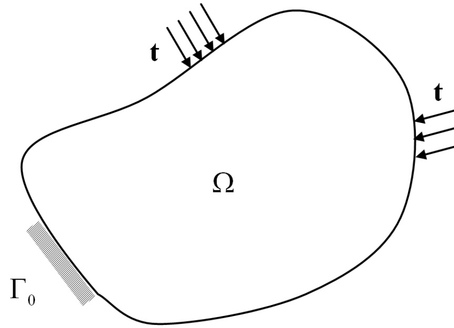

Fig. 11.1. Schematic illustration of the specifications for the structural topology optimization problem. How does one distribute V^* amount of material within Ω to make the structure the stiffest under loads **t** while it is anchored at Γ_0?

Choosing a suitable topology for the structural form is hard but is crucial for true optimality of the structure. We rely upon prior experience and/or design intuition in conceiving the suitable topology. As stated above, these two — prior experience and design intuition — are hard to come by in multi-disciplinary fields of micro and nano systems. Consequently, we need to identity suitable design variables to create a topology design space that can be searched to obtain the optimal topology. This is referred to as the *design parameterization* for topology optimization.

The simplest design parameterization for a structural problem shown in Fig. 11.1 is that of considering a binary variable $\rho(\mathbf{x})$ which can either be 1 or

0; a value of 1 implies that material is present at point $\mathbf{x}$ while 0 implies that material is absent and thus that point contributes to a hole. When we discretize Ω, and therefore $\rho(\mathbf{x})$ too, to numerically solve the topology optimization, the 1-0 parameterization leads to a discrete combinatorial problem. Combinatorial explosion is inevitable in such problems. There are techniques to solve such a problem but they are not computationally efficient and do not favorably scale with the size of the problem. Furthermore, the 1-0 problem is ill-posed in the sense that finer topological features continue to appear in the solutions as finer mesh is used. Therefore, topology optimization researchers have sought an alternative to relax this problem by making Ω continuous between 1 and 0. It leads to a simple parametric continuous optimization problem that effectively solves for the optimal topology. This raises the questions: what does it mean to have a material in an intermediate state between 1 and 0? Should there be a physical meaning to this? Can a solution with intermediate material state be manufactured? If not, how does one prevent intermediate material state and get a pure 1-0 design as the optimal solution? More importantly, how does one use this continuous interpolation of material in the equations that govern the behavior of the system? We answer these questions in this chapter in a few different settings that one encounters in microsystem design.

The remainder of the chapter is organized as per the applications considered. We begin with stiff and compliant continua under mechanical loads in Sec. 11.2. The cases of single and multiple materials are discussed. The physical meaning of the interpolation of the material state between 1 and 0 is explained. In Sec. 11.3, we consider a multi-energy domain problem of electro-thermal microactuators. Here, not only mechanical properties but also electrical and thermal properties are of relevance. Modeling of convection within the context of topology optimization is discussed. This is followed by another multi-energy domain problem of electrostatic microactuators in Sec. 11.4. Unlike other problems, physical interpretation of intermediate material state is crucial in this problem. A number of other problems where continuous material interpolation is useful for topology optimization, including piezoelectric, band-gap materials, fluid mechanics, *etc.*, are presented in Sec. 11.5. Some emerging design parameterization schemes for topology optimization are also noted in Sec. 11.5. In Sec. 11.6, inclusion of manufacturing constraints in topology optimization is considered by continuous interpolation of lithographic mask layouts in surface micromachining processes. To illustrate the generality of the state interpolation, the problem of amino acid sequence design problem in proteins is considered in Sec. 11.7. The chapter ends with concluding remarks in Sec. 11.8.

11.2. Continuous Interpolation of Material Under Mechanical Loads

The stiffness optimization problem for the specifications shown in Fig. 11.1 can be written as follows:

$$\begin{aligned}
&\underset{\rho}{\text{Minimize}} \int_{\Omega} (\mathbf{b}\cdot\mathbf{u})\, d\Omega + \int_{\Gamma} (\mathbf{t}\cdot\mathbf{u})\, d\Gamma \\
&\text{Subject to} \\
&\qquad \nabla\cdot\boldsymbol{\sigma}+\mathbf{b}=\mathbf{0} \\
&\qquad \int_{\Omega} \rho\, d\Omega - V^* \leq 0
\end{aligned} \tag{11.1}$$

where $\boldsymbol{\sigma}$ is the stress tensor, $\mathbf{t}$ the traction, and $\mathbf{b}$ the body force, if any, per unit volume. The displacement $\mathbf{u}$ is related to the stress through the strain tensor $\mathbf{E}$ and the constitutive linear elasticity tensor as follows: $\boldsymbol{\sigma} = \mathbf{E} : \varepsilon = \mathbf{E} : \left(\nabla\mathbf{u} + \nabla^T\mathbf{u}\right)/2$. The easiest way to bring in the design variable ρ into the problem statement of Eq. (11.1) as per the design parameterization discussed above is to have $\boldsymbol{\sigma} = \mathbf{E} : \varepsilon = \mathbf{E} : \left(\nabla\mathbf{u} + \nabla^T\mathbf{u}\right)/2$ where $\mathbf{E}_m$ refers to the elasticity tensor of the material that needs to be distributed within the domain and $\mathbf{E}_0$ to that of the void regions. When we consider the binary nature of ρ, it is easy to see that $\rho = 1$ implies the presence of the material and $\rho = 0$ implies the absence. This makes sense even when we interpret ρ as a continuous variable, which takes on the extreme values in the interval $[0, 1]$. This is a mathematically convenient way to deal with the topology optimization problem transformed to a parametric optimization problem in a single variable ρ that varies across the domain. Because there is no guarantee that the optimized ρ^* will have only 1 or 0 values throughout the domain, one would want to know the physical significance when ρ^* has an intermediate value between 1 and 0. In fact, historically, this idea was developed with a rigorous argument based on the *homogenization theory*.[4]

Homogenization here refers to the method of estimating the effective or average properties at the macro scale for a composite material with a microstructure. This is relevant here because the design domain parameterized with continuous ρ can be interpreted as a *composite material with a microstructure* formed by the material and the void. Bendse and Kikuchi[4] proposed and implemented this idea and called it the homogenization-based topology optimization method. Instead of using ρ, they used three variables that characterize the microstructure at every point in the design domain for the case of plane elasticity problems. The three variables define a volume fraction for an orthotropic material and help align the holes in the microstructure along the principal stress/strain directions. In this interpretation, at every point in the design a microstructure is imagined and optimization is expected to decide the optimal microstructure. A numerical update

formula for the design variables was proposed to ensure that the intermediate values are under check in the final solution. In subsequent works, some modifications to this basic technique were proposed by others. Currently, an interpolation technique called *Simple Isotropic Material with Penalty* (SIMP)[5,6] is widely used. It is given as

$$\mathbf{E} = \rho^{\eta}\mathbf{E}_0 \tag{11.2}$$

where a penalty parameter η is introduced. Numerical experiments have indicated that $\eta \geq 3$ helps push ρ to either of its limits. This can be intuitively understood from the fact that in the problem statement of Eq. (11.1), the volume constraint does not involve the penalty parameter. Therefore, a point that is occupied by a fraction (say, $\rho = 0.5$) of material takes up half of the material resource that it can take but contributes only a much smaller fraction (*i.e.*, $\rho^{\eta=3} = 0.125$) towards the objective function because of the penalty parameter. Another — a more rigorous — argument was put forth by Bendse and Sigmund[7] who used the bounds on the effective properties of microstructured materials. According to Hashin-Shtrikman bounds, a 2D isotropic material with a microstructure with a volume fraction ρ of material has its Young's modulus bounded as follows.

$$0 \leq E \leq \frac{\rho E_0}{3 - 2\rho} \tag{11.3}$$

By using the argument that the interpolated Young's modulus must obey the above bounds, Bendse and Sigmund[7] showed that ρ should be greater than or equal to three. That is, they tried to justify the physical meaningfulness of the artificial material interpolation implied by Eq. (11.2). Therefore, the mechanics of the material in the intermediate state is correct, and a suitable microstructure with that volume fraction of the material and the corresponding effective modulus exist. In fact, if one wants, by solving inverse homogenization problem, such a microstructure can also be found using another topology optimization problem.[8] If there is material in the intermediate state in the optimized solution, attention should be paid to its economical manufacturability. In the microscale, fortunately, it is indeed possible to have a desired microstructure. This is because lithography techniques do not limit the complexity of the in-plane geometry as long as it is within its minimum feature size limits.

As noted earlier, microfrabrication processes result in heterogeneous layered structures. Therefore, it is sometimes necessary to work with two materials in addition to void "material" counting as the third material. Then, the interpolation law in Eq. (11.2) can be extended as shown below by introducing two variables,

ρ_1 and ρ_2, at each point in the design domain.

$$\mathbf{E} = \rho_1^{\eta} \left\{ \rho_2^{\eta} \mathbf{E}_1 + (1 - \rho_2^{\eta}) \, \mathbf{E}_2 \right\} \tag{11.4}$$

where $\mathbf{E}_1$ and $\mathbf{E}_2$ are the elasticity tensors for the two materials that need to be optimally distributed within the design domain. This follows a mixture law for two materials and its physical meaningfulness can also be interpreted when an intermediate state between two materials exists.[7] Several other material interpolation schemes are used in the literature. Some of these are physically based (*e.g.*, Ref. 9) and others are not. A multi-material interpolation that uses a single variable was proposed.[10,11] It is given by a linear combination of normalized Gaussian distribution functions as shown below for M materials.

$$E = \sum_{i=1}^{M} E_i \exp\left(-\frac{(\rho - \mu_i)^2}{2\sigma^2} \right) \tag{11.5}$$

where μ_i can be chosen arbitrarily for each material and σ needs to be chosen sufficiently small towards the end of the iterative optimization procedure. When σ is not very small, the effective E is a mixture of different materials if ρ is different from any of the μ. Another favorable feature of this interpolation technique is that ρ is not bounded between 0 and 1 unlike other methods. It also has a disadvantage of the derivative of the interpolated material property with respect to ρ being zero at the transition points between different materials. Furthermore, the use of the Gaussian (normal) distribution function also implies that it indicates the probability of a particular material being present at a point in the deign domain. This interpretation becomes useful in protein sequence design, as discussed in Sec. 11.7, where the number of states is 20.

The interpolations noted above apply to not only the stiff structure problems but also to compliant mechanism problems that involve linear[12,13] or nonlinear displacements.[14,15] When material non-linearity is considered, the physical interpretation of material interpolation becomes hard. However, continuous interpolation in boundary condition non-linearity is possible and has a physical explanation. In the context of contact-aided compliant mechanisms (CCMs),[16–18] topology optimization problem is solved by including contact mechanics. They are used in microsystems such as mechanical signal modifiers (*e.g.*, frequency doubler[14,18]) and micromanipulation tools. In the design of CCMs, we do not know a priori know which part of the design domain would contact a rigid surface because the topology continues to change during optimization. Continuous modeling helps in the smoothening (or regularizing) of the contact by imagining that there is a “variable contact spring” whose stiffness depends on the gap between two potential contacting surfaces. Both small and large displacement models are

considered in this problem.[16,17] In a similar way, support optimization (*i.e.*, determining where the structure should be supported) can be combined with topology optimization.[19] Here, springs of parameterized stiffness are added at all finite element nodes in portions of the design domain identified as potential support regions. The physical validity of this is justifiable because springs are assumed to be connected to the structure. A similar method was also used in multi-component topology optimization[20] and optimal embedding of an object of known stiffness into a design region with optimized connections.[21] We next consider the interpolation schemes used in multi-physics problems.

11.3. Electro-Thermal Microactuation

In mechanical problems described above, we needed to continuously interpolate the elasticity tensor between that of a real material and a void. When vibration and transient problems are considered, mass density and loss coefficient (for damping) also need to be included. But all these mechanical properties remain in the same governing equation. The situation changes in many microsystems devices, which invariably act in multiple energy domains. The first problem that we will consider in this regard is concerned with electro-thermal microactuators. In electro-thermal actuation, an electrically conducting material is used to make the mechanical structure. The same material conducts electricity and heat and can support the loads. The actuation is achieved by applying an electrical potential difference between two points on the structure. See Fig. 11.2, which shows a simple electro-thermal microactuator.[22,23] The electrical potential causes current to flow. The current density inside the structure will be non-uniform because of the geometry. Consequently, the Joule heating term is also non-uniform. The ensuing steady-state temperature distribution will also be non-uniform. This causes the elastic structure to deform under the thermal loads. This is indicated in Fig. 11.2. Many variations of this exist and a general continuum can be considered for optimizing it for different objectives of micromechanisms with embedded actuation.[24–26]

In the context of topology optimization, we ought to consider which properties need to be interpolated. For this, we begin with the equations that govern the distribution of electric current.

$$\begin{aligned} &\nabla \cdot (k_e \nabla V) = 0 \qquad \text{in} \quad \Omega \\ &V = V_{\text{specified}} \quad \text{on} \qquad \Gamma_e \end{aligned} \tag{11.6}$$

where k_e is the electrical conductivity, V is the electric potential (*i.e.*, voltage) and Γ_e is the part of the boundary of the design domain, Ω, on which voltage is specified. The Joule heat generated within Ω is then given by $k_e\left(\nabla V \cdot \nabla V\right)$. This

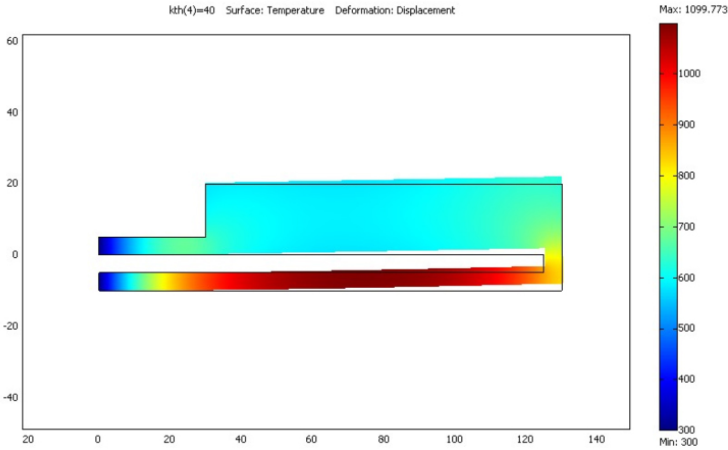

Fig. 11.2. A simple example of an electro-thermal microactuator. When the electric potential is applied between two points, the current flows non-uniformly and leads to non-uniform temperature distribution. This leads to a deformation to achieve elastic equilibrium under the thermal loads. The temperature is shown in the deformed configuration.

enters the thermal equilibrium equations as follows.

$$\begin{aligned} &\nabla \cdot (k_t \nabla T) + k_e (\nabla V \cdot \nabla V) = 0 \qquad \text{in } \Omega \\ &T = T_{\text{specified}} \qquad \text{on } \Gamma_{tT} \\ &\mathbf{n} \cdot (k_t \nabla T) = f_{tC} \qquad \text{on } \Gamma_{tC} \end{aligned} \tag{11.7}$$

where k_e is the thermal conductivity, T the temperature, $\mathbf{n}$ the unit normal to the boundary of Ω, f_{tC} the temperature-dependent boundary term that accounts for convection and radiation, and Γ_{tT} and Γ_{tC} are portions on which temperature and heat flux are specified respectively. The Joule heating term appears as the source term in the thermal problem. The temperature computed by solving Eq. (11.7) needs to be used in the elastic equilibrium equation shown below.

$$\begin{aligned} &\nabla \cdot \boldsymbol{\sigma} = 0 \text{ in } \Omega \\ &\boldsymbol{\sigma} = \mathbf{E} \{\boldsymbol{\varepsilon} - \alpha (T - T_{\text{ambient}}) \mathbf{I}\} \\ &\boldsymbol{\varepsilon} = \left(\nabla \mathbf{u} + \nabla^T \mathbf{u}\right)/2 \\ &\mathbf{u} = \mathbf{u}_{\text{specified}} \text{ on } \Gamma_m \end{aligned} \tag{11.8}$$

where $\boldsymbol{\sigma}$ and ε are the stress and strain tensors, $\mathbf{E}$ the elasticity tensor, $\mathbf{u}$ the displacement vector, Γ_m the part of the boundary on which displacement is specified, and α the thermal coefficient of expansion. We note that this problem involves sequential solution of three governing equation involving four material properties:

k_e, k_t, $\mathbf{E}$, and α. Just as we have a physical interpretation for the intermediate state of $\mathbf{E}$, as discussed in the previous section, the other three can also be interpreted using microstructure-based composite material. So, topology optimization can be carried out by taking a design variable ρ and using it to interpolate all these properties continuously as shown below (say, for two materials and void-representing silicon and silicon dioxide and the empty space).

$$\begin{Bmatrix} k_e \\ k_t \\ \mathbf{E} \\ \alpha \end{Bmatrix} = \sum_{m=1,2} \exp\left(-\frac{(\rho-\mu_m)^2}{2\sigma^2}\right) \begin{Bmatrix} k_e \\ k_t \\ \mathbf{E} \\ \alpha \end{Bmatrix}_m + \begin{Bmatrix} k_e \\ k_t \\ \mathbf{E} \\ \alpha \end{Bmatrix}_{void} \tag{11.9}$$

where the method used in Eq. (11.4) is adopted for material interpolation. Although this is quite straightforward, a complication arises in this problem when convection and radiation are considered. In micromechanical structures convection plays an important role and needs to be properly accounted for.[27] At high temperatures, radiation is also important. Modeling convention is tricky in topology optimization because we do not know where new boundaries would appear. If we consider 2D problems (which is not unreasonable for micromachined structures that have very low aspect ratios), we can include convection through top and bottom surfaces easily. For this, we will need to continuously interpolate the heat transfer coefficient h as follows.

$$h = \sum_{m=1,2} \exp\left(-\frac{(\rho-\mu_m)^2}{2\sigma^2}\right) h_m \tag{11.10}$$

Then, convection can be included for top and bottom surfaces at all points in the design domain, Ω. As can be seen in Eq. (11.10), full convention would occur at a point only if that point is fully occupied by material, *i.e.*, when $\rho = \mu_1$ or μ_2. When the point has an intermediate state of material, then convection will occur only partially. This can be physically interpreted based on the microstructure of a composite material. If the microstructure has several small holes, the effective area available is less than that for a full structure. So, reduced heat transfer coefficient is justifiable. This may not exactly correspond to it but it will model it approximately for design purposes. Besides, having a correct estimate for the convection heat transfer coefficients for micromechanical structures is quite difficult. Design calculations use conventional empirical formulae from the macro regime.[25–27] A second difficulty arises when the side-wall convection is considered. When a new hole is generated during topology optimization, additional vertical side-walls will be generated. To model convection for these, we should look at the neighboring points and see if they are absent when the material is present at

the point. This also can be modeled and physically interpreted as above. To show this mathematically, we will consider the weak variational form of the governing equation of the thermal problem (Eq. (11.7)) because we can then show all the boundary conditions as part of the governing equation. It is given below.

$$\begin{aligned}&\int_{\Omega} k_t\,(\nabla T\cdot\nabla T)\,\delta T\ t\,d\Omega-\int_{\Omega} k_e\,(\nabla V\cdot\nabla V)\,\delta T\ t\,d\Omega\\&+\int_{\Omega} 2hT\,\delta T\ d\Omega+\sum_{i=1\cdots N}\left\{\sum_{j=1}^{N_n}\frac{1}{2}\int_{l_j} h(1-\rho_j)\rho_i T\delta T\ t\,dl_k\right\}=0\end{aligned}\tag{11.11}$$

In Eq. (11.11), δT is the variation of T. The first two terms are essentially the variational form of the first two terms of the differential equation in Eq. (11.7). The third term corresponds to the convection through top and bottom surfaces of the predominantly flat structure, as discussed above. A factor of two appears in this term based on the assumption that the convection heat transfer coefficient is the same for top and bottom surfaces. The fourth term models the convection though vertical side-walls. It has a strange mixed dicrete-continuous form because we used a discretized finite element interpretation for it. Here, the terms inside the integral sign show the contribution of the side-wall convection of each finite element. Let us say that each finite element has N_n neighbors and an equal number of common boundaries, ls, with its neighboring elements. When there is material present for the ith element and its jth neighboring element is not present, then the corresponding common boundary contributes to side-wall convection. This is captured by incorporating the interpolated states of both the elements and its neighbors. A factor of half is included because each boundary will be counted twice. Although the above continuous modeling may look complicated, its implementation in each iteration of the topology optimization is not any more difficult than solving the three governing equations sequentially.[11] Physical interpretation based on microstructured material is simple here but it is not so in the problem we consider next.

11.4. Electrostatic Microactuation

Even though electrostatic actuation is the most popular actuation technique in microsystems, topology optimization for this problem has not received much attention until very recently[28,29] even though its shape optimization is well studied.[30,31] While one can speculate on some reasons for this, an important reason may be the lack of a technique to continuously interpolate the type of material between conductors, dielectrics and voids. To appreciate the need for such a continuous material interpolation, consider the fact that the electrostatic and elastic fields are

strongly coupled to each other in problems concerning electrostatically actuated micromechanical structures. For the system shown in Fig. 11.3, which shows a fully mechanically grounded conductor and another partially supported conductor, two types of analyses are needed to determine the deformed geometry of the latter conductor due to the electrostatic force between them.

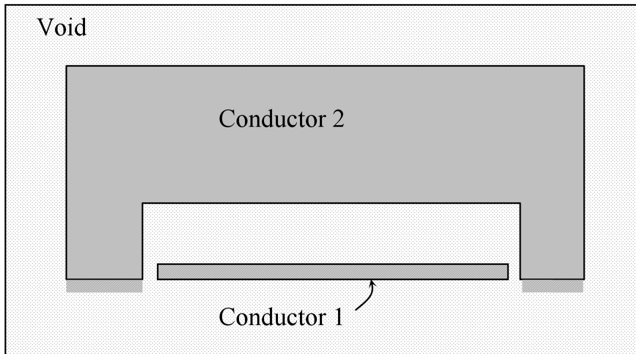

Fig. 11.3. A simple two-conductor electrostatically actuated micromachined structure problem. Conductor 1 is fully anchored while conductor 2 is partially anchored and hence it can elastically deform under the electrostatic force between them when an electric potential difference is applied. The void region in between the two conductors is indicated as the bounding box minus the areas occupied by the two conductors.

The first analysis solves for the electric potential in the void space between the two conductors given the potential on each conductor. This is done by solving the Laplace equation in the void region.

$$\nabla^2\phi = 0 \text{ in } \Omega_{void} \tag{11.12}$$

where ϕ is the potential at any point in the void region, Ω_{void}. After obtaining ϕ, we can determine the charge density, ψ, that exists only the boundaries of the two conductors. This is used, in turn, to compute the electrostatic force between the two conductors as follows.

$$\psi = \mathbf{n} \cdot \nabla\phi \qquad \text{on } \Gamma \tag{11.13}$$

$$\mathbf{f}_{es} = \left(\psi^2/2\varepsilon_0\right)\mathbf{n} \tag{11.14}$$

where $\mathbf{n}$ is the normal to the boundary Γ of the two conductors; ε_0 the permittivity of the void region, and $\mathbf{f}_{es}$ the electrostatic force. It can be seen that the electrostatic force is a boundary force. This force goes as a boundary condition (called

traction in mechanics) for the elastostatic field equations shown below.

$$\begin{aligned} &\nabla \cdot \boldsymbol{\sigma} = 0 \text{ on } \Omega \\ &\boldsymbol{\sigma} \cdot \mathbf{n} = \mathbf{f}_{es} \textbf{ on } \Gamma \\ &\boldsymbol{\sigma} = \mathbf{E} : \frac{1}{2}\left(\nabla \mathbf{u} + \nabla \mathbf{u}^{T}\right) \end{aligned} \tag{11.15}$$

where σ is the stress tensor, $\mathbf{u}$ the displacement vector, and $\mathbf{E}$ the elasticity tensor. The coupling between the governing equations of electrostatic and elastic equations (*i.e.*, Eqs. (11.12) and (11.15)) is two-way because when the deformed geometry of the conductors changes (and hence the geometry of the void region) due to the electrostatic force, the electrostatic equation needs to be solved again followed by elastic equation; and this cycle continues until a self-consistent solution between the two is achieved. In the context of topology optimization, an additional problem arises. This is because the conductor-void demarcation is not assumed a apriori. That is, we do not know which portion of the design domain becomes a conductor and which portion becomes void. Therefore, the interfaces between them are not known. This implies that we do not know where to apply the electrostatic forces, which act only on the boundaries. Recently, by tracking the interfaces, a topology optimization technique for the electrostatically actuated microstructures is proposed.[28] Instead, we can tackle this problem directly as discussed below. This has an additional advantage of being able to include dielectric materials anywhere in the design domain as part of the optimization. In micromachined structures, four types of materials can exist from the viewpoint of electrostatic equations. These are pure conductors (*e.g.*, metals used in interconnections), conductors with a dielectric constant that is significantly larger than unity (*e.g.*, polysilicon), dielectrics (*e.g.*, silicon dioxide or silicon nitride) and voids. Their properties are summarized in Table 11.1. The table shows the electrical conductivity σ, permittivity ε, and the elasticity tensor $\mathbf{E}$. Additionally, it also shows two binary variables ρ_1 and ρ_2. When they take a value of 0 or 1, four combinations arise each of which gives the four different types of materials required for the topology optimization problem of electrostatically actuated micromachined structures. Notice that in the governing equations of Eq. (11.12), there is no mention of electrical conductivity. So, before discussing how we can continuously interpolate among the four types of materials, we should discuss the need for σ.

Consider that the design domain is occupied by inhomogeneous distribution of a mixture of the above four types of materials. Then, considering the continuity of the free electric charge in conjunction with the microscope form of the Ohm's law, for the steady-state conditions, we get

$$\nabla \cdot (\sigma \mathbf{E}_e) = 0 \tag{11.16}$$

Table 11.1. Materials and their properties relevant to electrostatic-elastic analyses.

Property or variable	Conductor: c	Conductor with permittivity: cd	Insulating dielectric: d	Air or void
ρ_1	1	1	0	0
ρ_2	0	1	1	0
σ	σ_c	σ_{cd}	$\sigma_0 \approx 0$	$\sigma_0 \approx 0$
ε	$\sim\varepsilon_0$	ε_{cd}	ε_d	ε_0
$\mathbf{E}$	$\mathbf{E}_c$	$\mathbf{E}_{cd}$	$\mathbf{E}_d$	$\mathbf{E}_0 \approx \mathbf{0}$

where $\mathbf{E}_e$ is the electric field. In this condition, the design region stores some electrostatic energy in addition to partially conducting some current. This, in lumped modeling, is known as a leaky capacitor model with a resistor in parallel with a capacitor.[32] Therefore, we need to consider the continuous distribution of permittivity too. A question now arises as to how to compute the electrostatic force for this. An answer is provided by what is known as Maxwell's electrostatic stress tensor. This, with a slight modification,[33] gives the electrostatic force as a body force, $\mathbf{F}_{es}$.

$$\mathbf{F}_{es} = (\nabla \cdot \varepsilon \mathbf{E}_e)\, \mathbf{E}_e - \frac{1}{2} E_e^2 \nabla \varepsilon + \frac{1}{2} \nabla \left(E_e^2 \frac{\partial \varepsilon}{\partial \rho_m} \rho_m \right) \tag{11.17}$$

where E_e is the magnitude of $\mathbf{E}_e$ and ρ_m is the mass density. In practical situations, the last term in the expression in Eq. (11.17) can be neglected because we are interested in the forces rather than the effects of forces on re-distribution of permittivity.

The main point about Eq. (11.17) is that we are able to cast the electrostatic force as body force that acts everywhere in the design domain rather than only at the interfaces. So, we do not need to track the interfaces between conductors, dielectrics and voids as they appear and disappear in topology optimization. A simplified form of Eq. (11.17) without the negligible last term can be written as follows.

$$\mathbf{F}_{es} = \left\{ \left(\frac{\nabla \varepsilon}{\varepsilon} - \frac{\nabla \sigma}{\sigma} \right) \cdot (\varepsilon \mathbf{E}_e) \right\} \mathbf{E}_e - \frac{1}{2} E_e^2 \nabla \varepsilon. \tag{11.18}$$

This leads to a slight modification of the elastostatic equations given by Eq. (11.15) as indicated below.

$$\begin{aligned} \nabla \cdot \boldsymbol{\sigma} + \mathbf{F}_{es} &= 0 \text{ on } \Omega \\ \boldsymbol{\sigma} &= \mathbf{E} : \frac{1}{2} \left(\nabla \mathbf{u} + \nabla \mathbf{u}^T \right). \end{aligned} \tag{11.19}$$

It is worth noticing that the electrostatic force, even in its body-force disguise, still gives the force only at the regions where there is a change in either permittivity or conductivity or both. This is because all terms in Eq. (11.19) depend on the spatial gradients of the two properties-permittivity and conductivity. Nevertheless, it is a body force. When the design approaches strict demarcation between four different types of materials, we approach the purely electrostatic situation.

Using the two variables ρ_1 and ρ_2 in Table 11.1, we can now continuously interpolate all the relevant properties in the coupled electrostatic-elastostatic problem as indicated below.[34]

$$\begin{aligned}
\sigma &= \sigma_0 (1-\rho_1) + \rho_1 \{\sigma_{cd}\rho_2 + \sigma_c (1-\rho_2)\} \\
\varepsilon &= \varepsilon_0 (1-\rho_2) + \rho_2 \{\varepsilon_{cd}\rho_1 + \varepsilon_d (1-\rho_1)\} \\
\mathbf{E} &= \mathbf{E}_0 (1-\rho_1)(1-\rho_2) + \mathbf{E}_d (1-\rho_1)\rho_2 + \mathbf{E}_c \rho_1 (1-\rho_2) + \mathbf{E}_{cd}\rho_1\rho_2
\end{aligned} \tag{11.20}$$

where the continuous version of the binary nature of ρ_1 and ρ_2 is clearly visible in the interpolated elasticity tensor. The continuous modeling of the electrostatic situation for the general case of four different materials with two design variables ρ_1 and ρ_2 makes it convenient to pose and solve topology optimization problems without having to track the ensuing boundaries.[29] We will consider some other multi-physics problems where continuous modeling has been achieved.

11.5. Miscellaneous Microsystems Problems and Emerging Techniques

Continuous interpolation schemes such as the ones described in the last three sections have been used in many other domains for which topology optimization techniques have been applied.[1–3] One of the notable ones is piezoelectric actuation. Homogenization theory for micro-structure based piezoelectric materials exists and hence it can be readily used for continuous parameterization of the design domain. Then, one needs to interpolate between normal material and piezoelectric material, in addition to void, in designing the so-called flextensional micro or meso scale actuators.[3,35] It presents no additional difficulties. A second problem concerning the piezoelectric materials is the design of piezo-composites. Here, the microstructure of a piezoelectric material itself can be determined using topology optimization so that desired homogenized properties can be realized.[36] This technique for pioneered by Sigmund,[8] who first did it for desired mechanical properties by solving the inverse homogenization problem. Using this method, material microstructure for extreme properties such as negative Poisson's ratio, negative thermal expansion coefficient, *etc.*, can be realized.[37,38] For all these problems, material(s) and void need to smoothly interpolated. Here, physical significance is imperative because the resulting periodic micro structures or

mechanisms[3] ought to be physically possible equivalent materials. Phononic and photonic bandgap materials and planar waveguides[39,40] have also been designed using this technique. An interesting recent development is the application of the continuous material or state interpolation technique to the fluids problems. In a pioneering work on topology optimization involving fluids, Borrvall and Petersson[41] used Stokes equation to model low Reynolds number flows and Darcy equation for the porous flows. The porosity was varied between two extreme limits so that the limiting cases correspond to a pure solid and pure flow region. Extensions to Navier–Stokes' equation is also reported.[42,43] In another recent work, by circumventing the interpolation between solid and fluid in the above manner, lattice Boltzmann method was used to directly tackle the changing topology of the solid-fluid mixture within the design domain.[44] Fluid-structure interaction problems found in acoustics problems also permit continuous interpolation of material and switching between Helmholtz and elasticity equations as the material distribution changes.[45] Application of similar techniques for problems involving the distribution of a phase-change material and a normal material using a continuous interpolation has also been recently reported.[46] Physical interpretation for all of these interpolation schemes can be found in the cited works.

11.5.1. *Emerging Techniques*

Continuous modeling of the discrete combinatorial problem of material distribution over a fixed finite element reference mesh is not the only method available for design parameterization for topology optimization problems. In fact, changing topologies occur in many analysis problems too. A technique that is quite useful in handling variable topologies is known as the level set method. Here, the domain's topology is represented by the zero-level set curve of a function, $\Phi(\mathbf{x})$ defined at different spatial locations, $\mathbf{x}$. When Φ, the point $\mathbf{x}$ belongs to Ω and $\Phi < 0$, it does not. The curve corresponding to $\Phi = 0$ gives the boundary of Ω. The optimization problem now uses the function Φ to vary the topology. Clearly, this function is continuous. Furthermore, many options exist to define this function for any given topology. When this approach is used in topology optimization, the iterative process is seen as the time-axis and the function is taken as $\Phi(\mathbf{x}, t)$. As Φ evolves with time (*i.e.*, as iterations continue), the boundary will continue to change. The equation for the evolution of Φ is obtained by differentiating Φ with respect to time. This gives:[47,48]

$$\frac{\partial \Phi}{\partial t} + \nabla \Phi \cdot \frac{d\mathbf{x}}{dt} = \frac{\partial \Phi}{\partial t} + \nabla \Phi \cdot \mathbf{v} = 0 \tag{11.21}$$

where $\mathbf{v} = d\mathbf{x}/dt$ is the velocity of the material point at the boundary. In fact, only the component of $\mathbf{v}$ that is normal to the boundary is of interest because of the dot product in Eq. (11.21). This normal velocity of the boundary is chosen appropriately to iteratively minimize an objective function subject to some constraints. Because the boundary is well defined in this method throughout the optimization procedure, an interpretation of the physical meaning of the design variable is a moot point. It is also interesting to note that color level sets can be used deal with more than two material states.[49] It is argued that level-set based topology optimization methods cannot nucleate new holes in 2D implementation[50] although it can coalesce two holes into one. The concept of topological gradient is used to remedy this situation. The topological gradient quantifies the change in the objective function when an infinitesimally small hole is introduced at a point in the design domain. One more emerging approach to circumvent the microstructure based physical interpretation of material interpolation is to use extended finite element method (X-FEM) wherein discontinuous shape functions are appended, as necessary, to include changes within a finite element.[51] Current literature in topology optimization indicates that the use of genetic algorithms is increasing. Although the computational cost is prohibitive, possible to tackle the 0-1 design parameterization rather directly in genetic algorithm based approaches.[52] Other emerging approaches are focusing on making topology solutions readily manufacturable. The methods described in the next section approach this problem from the viewpoint of design parameterization rather than imposing additional constraints as done in some of the recent works.[53,54]

11.6. Continuous Modeling of a Microfabrication Process

Continuous modeling of a single or multiple materials in a variety of problems together with topology optimization generates good designs that are usually beyond the intuition and prior experience of the designers. However, the optimal topology solutions are not always manufacturable in their original form. This is due to two reasons. First, the manufacturing cost may be prohibitively high. For example, if a design has complicated internal structure (not microstructure) with many holes, conventional material-removal machining techniques such as milling, drilling, casting, *etc.*, result in increased computational time and hence high cost. Material-addition techniques such as stereolithography, although capable of giving just about any topology or shape, are still expensive. They do not yet give a structure that has the same structural integrity as the removal techniques. Second, topology solutions may have some features that will cause problems (*e.g.*, very high local stresses) if they are manufactured in the exact form. This is seen as

point-flexures in compliant mechanisms,[55] extremely narrow connections, unacceptably high curvatures, *etc.* So, it is almost imperative to include manufacturing constraints into topology optimization. Some efforts are under development in this regard for macro-manufacturing processes. They include explicit constraint formulation to prevent non-manufacturable features.[53,54] While the difficulties with macro-manufacturing processes can be dealt with additional constraints or post-processing of the solutions, in the case of micro-manufacturing processes, such remedies may not be sufficient. Consider, for example, an arch-like design that stands upright on a silicon substrate and is made of polysilicon. Such structures are usually made with surface-micromachining. It uses photolithography masks to pattern alternative layers of structural (*e.g.*, polysilicon) and sacrificial (*e.g.*, silicon dioxide) materials. In a chosen surface-micromachining process, the thicknesses of the layers are fixed. So, any shape in the direction perpendicular to the substrate is not possible. This difficulty cannot be resolved using simple constraints or post-processing because even a simple deviation from the stepped (with a slight roundedness) layered construction is not tolerated. For this problem, a convenient way is to tackle the topology optimization problem by continuous modeling of the lithography masks. After all, it is a lithography mask that determines the structural form in the actual manufacturing process. So, we can use a continuous variable to indicate the mask-opacity. If this variable takes a value of 1 at a point, the mask is blocked at that point; if it is 0, the mask is open; and if it is between 0 and 1, the mask is porous. Based on this idea, one can simulate the intermediate structures that have physical significance. By pushing the variable to either of its limits through penalty formulation as in SIMP, truly opaque and clear masks can be obtained. An example is shown in Fig. 11.4. Figure 11.4(a) shows the problem specifications, and Fig. 11.4(b) shows the solution obtained along with the mask openings in Fig. 11.4(c) when surface-micromachining constraints are enforced through continuous modeling of the mask layouts. In this example, the chosen process was Multi-User-MEMS Processes (MUMPs).[56] Figure 11.4(c) shows different layers of polysilicon and silicon dioxide for a vertical slice of a 3D structure. The details of this can be found in recent works.[57,58]

An alternative method that does not use continuous mask-opacity value has also been developed.[7] In this, different possible combinations of resulting layered patterns are smoothly interpolated. Consider the situation shown in Fig. 11.5 for a simple three-layer process with two structural layers with a sacrificial layer sandwiched between them. At every point in the 2D design domain that is parallel to the silicon substrate, we can have three binary variables corresponding to each layer, β_i $(i = 1, 2, 3)$, that decide the closing ($\beta_i = 1$) and opening ($\beta_i = 0$) of

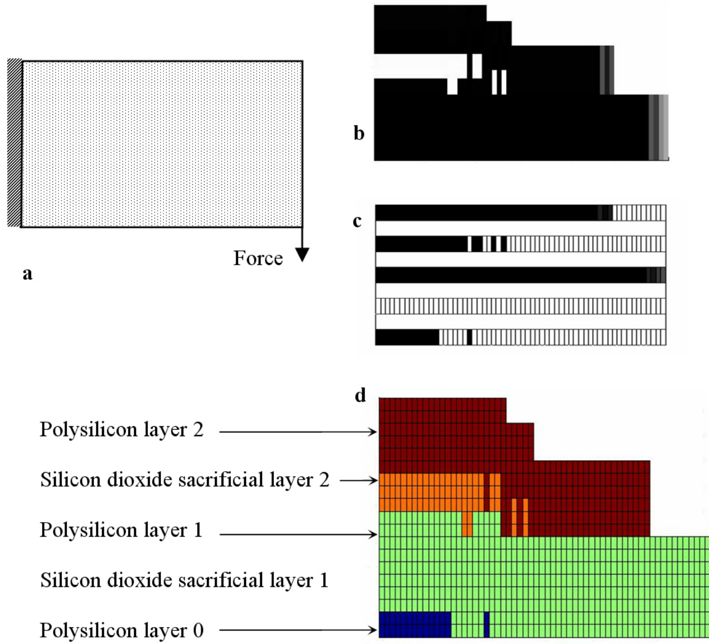

Fig. 11.4. An example of a MUMPs surface-micromachined structure designed by obeying the manufacturing constraints by maximizing the stiffness for a given volume. (a) Specifications, (b) optimal topology, (c) masks opacities corresponding to the optimal solution, (d) layered structure showing structural and sacrificial layers. The conformal effect can be observed in this figure. Notice that first silicon dioxide layer is completely absent because its mask is fully transparent everywhere.

the mask at that point. As shown in Fig. 11.5, there will be eight possible outcomes for different combinations of $\beta_1, \beta_2, \beta_3$: (0,0,0), (0,0,1), (0,1,0), (0,1,1), (1,0,0), (1,0,1), (1,1,0) and (1,1,1) and their associated physical structures. When the binary variables are made continuous between $[0, 1]$, we need to appropriately interpolate the material distribution of the eight combinations.

By denoting the material state in the vertical column at a point in the ith combination by γ_i $(i = 1, 2, 3)$, we can write the continuous interpolated state of material in the vertical column at that point as follows.

$$\begin{aligned} \rho &= \sum_{\{ijk)=1}^{8} \gamma_{\{ijk\}} \cdot c_{\{ijk\}}(\beta) \\ c_{\{ijk\}} &= f(\beta_i) \times f(\beta_j) \times f(\beta_k) \\ f(\beta_l) &= \begin{cases} \beta_l & \text{if the } l^{th} \text{ layer is present} \\ 1-\beta_l & \text{if the } l^{th} \text{ layer is absent} \end{cases} \end{aligned} \tag{11.22}$$

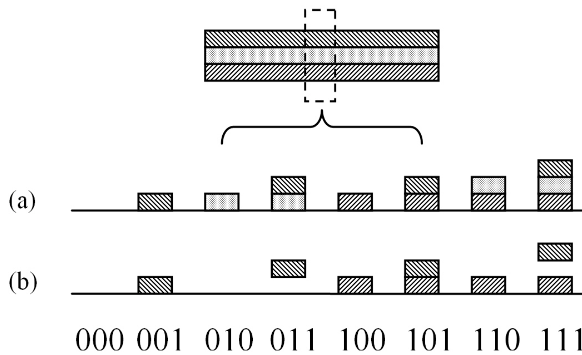

Fig. 11.5. Eight binary combinations (binary numbers "abc") corresponding to a three layer micromachining process with oxide sandwiched between polysilicon layers (a) before sacrificial layer etch (b) after etching. Polysilicon layers are shaded differently only for clarity.

This method, along with the penalty formulation to push the final result towards one of the eight combinations, gives manufacturable designs for a surface-micromachining process. The method extends to N layers wherein 2^N combinations exist but the number of variables remains equal to N for each vertical column at every point in the design domain.

11.7. Continuous Modeling of Protein Sequences

We will now consider an entirely different problem of designing the sequence of the amino acid monomers in the hetero-polymer linear chain of proteins. The design of a protein entails the determination of its sequence of amino acids for all its residue sites from among the possible 20 types. A folded protein chain is not a continuum but it too presents the problem of deciding which amino acid ought to be placed at its every residue site. It is thus a problem similar to topology optimization[59] that is converted into a parametric multi-state distribution problem.

In order to see the connection between topology optimization and protein sequence design, consider a folded protein chain shown in Fig. 11.6. For simplicity, first consider only two types of amino acids-hydrophobic (H) and polar (P)-instead of the 20 types that exist. Such models are called HP models.[60] They give useful insights into the problem without making it computationally expensive. When each residue in the chain shown in Fig. 11.6 can be H or P, it leads to a combinatorial problem. As in Secs. 11.1 and 11.2, instead of solving this binary problem, here too we can define a continuous variable that decides the state of the residue sites in the protein chain.[59,61]

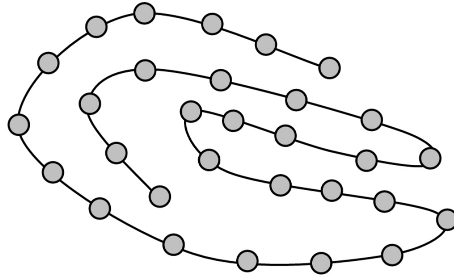

Fig. 11.6. A sample protein chain using the HP modeling. The design of this sequence entails the determination of the type of residue at each residue site. This is similar to the problem of deciding whether to place the material at a point or not, in the design.

Two methods of interpolating the state of the amino acids are proposed in the recent literature. In one case, the Gaussian distribution function-based interpolation can be used (see Eq. (11.4)). This has an added advantage that it implies the probability of a certain amino acid being present at a residue site and thus mimicking the modeling used in some Monte Carlo methods for protein design.[62] In this case, there will be as many design variables as the number of residue sites in the protein chain. In the second, 20 (or less if one in interested in reduced amino acid alphabet) variables will be defined for each site. Then, constraints need to be imposed to ensure the probability of all the amino acid occupying a site does not exceed 1. In either case, energy can be written out explicitly for the intermediate amino acid states. The state interpolation in the first case is non-linear while it is linear in the second. Mathematical form of both the schemes are discussed below. For the first case, the interpolated state of the ith residue state S_i is given by

$$S_i = \sum_{j=1}^{M} V_j \exp\left\{ \frac{(\rho_i - \mu_j)^2}{2\sigma^2} \right\} \tag{11.23}$$

where there are M types of amino acids. The values of V_j are the numerical indicators associated with each amino acid type, j. The μ_j and σ need to be chosen to evenly space the peaks of each Gaussian distribution function along the ρ_i-axis so that S_i will assume a value of V_j when $\rho_i = \mu_j$. It works best when $M = 2$ and needs a slight modification and introduction of a second variable for $M \geq 2$. For the case of $M = 2$, which applies to the HP models, we can take $V_1 = 1$ and $V_2 = 0$ to indicate H and P types respectively.

The above interpolation does not restrict ρ_i with any bounds but the second one (shown below) does. Here, a separate variable is used to indicate the state

of each of the M amino acid types at each of the N residues. Thus, there will be NM variables each of which must lie within $[0, 1]$. A linear constraint is needed to ensure that only one amino acid type exists at each residue site or their combined presence does not exceed a value of 1. This gives the following equations for interpolation, which works for any number of amino acid types.

$$S_i^{(k)} = x_{M(i-1)+k} \tag{11.24}$$

$$\sum_{k=1}^{M} x_{(i-1)M+k} = 1 \tag{11.25}$$

Energy, usually free energy, plays an important role in computational protein studies. Accurate calculation of energy for a given protein chain of a known sequence is very time-consuming. Hence, reduced and normalized energy between inter-residue pairs is needed. Such methods exist; one such method known as Miyazawa-Jernigan (MJ)[63] potentials are widely used. Using this, the total energy can be written by taking all possible inter-residue pairings and their corresponding energy levels multiplied by a number that quantifies the extent to which that pairing occurs. For the first interpolation scheme, for $M = 2$, the energy U can be written as follows.

$$U = \sum_{i=1}^{N} \sum_{j=1}^{N} \left[e_{\mathrm{HH}} S_i S_j + e_{\mathrm{HP}} \left\{ S_j (1 - S_j) + (1 - S_j) S_j \right\} + e_{\mathrm{PP}} (1 - S_j)(1 - S_j) \right] \tag{11.26}$$

where e_{HH}, e_{HP} and e_{PP} are known energy values between H and P type amino acid residues.[63] The same energy can be computed in terms of NM variables using the second scheme as follows.

$$U = \sum_{i=1}^{N} \sum_{j=1}^{N} \Big[e_{\mathrm{HH}} x_{2(i-1)+1} x_{2(j-1)+1} + e_{\mathrm{HP}} \Big\{ x_{2(i-1)+1} x_{2j} + x_{2i} x_{2(j-1)+1} \Big\} + e_{\mathrm{PP}} x_{2i+1} x_{2j} \Big] \tag{11.27}$$

where the odd entries in the $\mathbf{x}$ vector interpolate the H state and the even entries the P state. The second formulation works with any number of amino acid types. By noting that the energy expression given in Eq. (11.27) is quadratic while the constraints (see Eq. (11.25)) are linear, we see that the energy minimization problem becomes a problem of quadratic programming. This can be solved for a global minimum and its solution provides a lower bound on the energy of a conformation.[65] This method has shown promising results for HP models as well as real protein models involving all 20 amino acid monomers. Biologically useful

insights are yet to come from this approach but its computational efficiency is adequately demonstrated.

11.8. Conclusions

In this chapter, various methods of interpolating material for the purpose of convenient design parameterization for topology optimization are described. Keeping the reference domain fixed while varying the state of the material(s) and void is the hallmark of topology optimization. In microsystems, several energy domains are coupled to each other in a single problem. Hence, several different material properties need to be simultaneously interpolated. To illustrate this, electro-thermal and electrostatic microactuators were considered. Physical interpretation of the interpolated properties is often useful to ensure that the physics of the problem is not seriously violated. After all, iterative optimization progresses with the help of gradients and they, in turn, depend on the physical governing equations. Hence, physical interpretation of the intermediate materials is useful although most topology optimization methods use techniques to get pure material(s)-void designs in the optimized solution. Several new topology optimization problems are emerging, fluids problems in particular with relevance to micro-fluidics. Some of these are briefly noted in this chapter. Two other problems, one related to manufacturing constraints in surface-micromachined structures and another in protein sequence design are discussed. These problems also use interpolated states (not materials) to solve the topology optimization problems. A few topology optimization techniques, which do not warrant material interpolation, are also noted. These include level set methods and genetic algorithms. Designing microstructures of materials, often with extreme properties, is another unique capability of the topology optimization method. This versatile technique will continue to play a significant role in the micro and nano technologies as well as the conventional macro technology.

Acknowledgments

The author gratefully acknowledges his present and past students, research assistants and post-docs with whom the parts of the work reported here was done during the last decade. They include: Professor Anupam Saxena (Indian Institute of Technology — Kanpur, India), Dr. Luzhong Yin (Intellisense Inc.), Dr. Nilesh Mankame (General Motors Research Lab., Warren, MI, USA), Dr. Sung Koh (Post-Doc, Korea), Aravind Alwan (University of Illinois at Urbana Champaign, USA), and Girish Krishnan, Manish Agrawal and V.S.S. Srinivas (Indian Institute of Science, Bangalore, India).

References

1. M. P. Bendse and O. Sigmund, *Topology optimization: theory, methods and applications*, Springer, (2003).
2. G. K. Ananthasuresh, *Optimal synthesis methods for MEMS*, Kluwer Academic Publishers (2003).
3. M. P. Bendse, N. Olhoff, and O. Sigmund, *Topological design optimization of structures, machines and materials*, Springer, (2006).
4. M. P. Bendse and N. Kikuchi, Generating optimal topologies in structural design using a homogenization method, *Comp. Meth. Appl. Mech. Engng.*, **71**, (1988).
5. G. I. N. Rozvany and M. Zhou, The COC algorithm, part I: cross-section optimization or sizing, *Comp. Meth. Appl. Mech. Engng.*, **89**, 281–308, (1991)
6. G. I. N. Rozvany, M. Zhou, and O. Sigmund, Topology optimization in structural design, *Advances in Design Optimization*, Chapter 10, pp. 340-399, (1994).
7. M. P. Bendse and O. Sigmund, Material interpolation schemes in topology optimization, *Archives of Applied Mechanics*, **89**, pp. 635–654, (1999).
8. O. Sigmund, Materials with prescribed constitutive parameters: an inverse homogenization problem, *International Journal of Solids and Structures*, **31**, pp. 2313–2329, (1994).
9. H. C. Gea, Topology optimization: a new micro-structural based design domain method, *Computers and Structures*, **61**, pp. 781–788, (1996).
10. L. Yin and G. K. Ananthasuresh, Topology optimization of compliant mechanisms with multiple materials using a peak function material interpolation scheme, *Struc. Multi. Disc. Optn.*, **23**, pp. 49–62, (2001).
11. L. Yin and G. K. Ananthasuresh, Novel design technique for electro-thermally actuated compliant micromechanisms, *Sensors and Actuators, A Phy.*, **97-98**, pp. 599–609, (2002).
12. M. Frecker, G. K. Ananthasuresh, S. Nishiwaki, N. Kikuchi, and S. Kota, Topological synthesis of compliant mechanisms using multicriteria optimization, *J. Mech. Des.*, **199**, pp. 238–245, (1997).
13. A. Saxena and G. K. Ananthasuresh, On an optimal property of compliant mechanisms, *Struc. And Mult. Disci. Optn.*, **19**, pp. 36–49, (2000).
14. A. Saxena and G. K. Ananthasuresh, Topology synthesis of compliant mechanisms for non-linear force-deflection and curved path specifications, *J. Mech. Des.*, **123**, pp. 33–42, (2001).
15. C. B. W. Pedersen, T. Buhl, and O. Sigmund, Topology synthesis of large displacement compliant mechanisms, *Int. J. Num. Meth. Engng.*, **50**, pp. 2683–2705, (2001).
16. N. Mankame and G. K. Ananthasuresh, Topology synthesis of contact-aided-compliant mechanisms with small deformations, *Comp. Struc.*, **82**, pp. 1267–1290, (2004).
17. N. Mankame and G. K. Ananthasuresh, *Int. J. Num. Meth. Engng.*, online since 2006, DOI: 10.1002/nme.1861, in press.
18. N. Mankame and G. K. Ananthasuresh, A novel compliant mechanism for converting reciprocating translation into enclosing curved paths, *J. Mech. Des.*, **126**, pp. 667–672, (2004).

19. T. Buhl, Simultaneous topology optimization of structure and supports, *Struc. Multi. Disc. Optim.*, **23**, pp. 336–346, (2002).
20. H. Chickermane and H. C. Gea, Design of multi-component structural systems for optimal layout topology and joint locations, *Eng. Comput.*, **13**, pp. 235–243, (1997)
21. Z. Qian and G. K. Ananthasuresh, An optimal embedding problem in topology optimization, *Mech. Based Des. Mach. Struc.*, **32**, pp. 165–193, (2004).
22. H. Guckel, K. Klein, T. Christenson, K. Skrobis, M. Laudon, and E. G. Lovell, Thermomagnetic metal flexure actuators, *Technical Digest of Solid State Sensors and Actuators Workshop*, Hilton-Head Island, p. 73, (1992)
23. J. Comtois and V, Bright, Surface micromachined polysilicon thermal actuator arrays and applications, *Technical Digest of Solid State Sensors and Actuators Workshop, Hilton-Head Island* pp. 174–177, (1996).
24. T. Moulton and G. K. Ananthasuresh, Design and manufacture of electro-thermal-compliant micro devices, *Sens. Actuators A*, **90**, pp. 38–48, (2001).
25. O. Sigmund, Design of multiphysics actuators using topology optimization – Part IL one-material structures, *Comp. Meth. Appl. Mech. Engng.*, **190**, pp. 6577–6604, (2001).
26. N. Mankame and G. K. Ananthasuresh, Topology synthesis of electro-thermal-compliant mechanisms using line elements, *Struc. Multi. Disc. Optmn.*, **26**, pp. 209–218, (2004).
27. N. Mankame and G. K. Ananthasuresh, Comprehensive thermal modeling and characterization of an electro-thermal-compliant microactuator, *J. Micro. Mech. Micro. Engng.*, **11**, pp. 452–462, (2001).
28. M. Raulli and K. Maute, Topology optimization of electrostatically actuated microsystems, *Struc. Mult. Disc. Optmn.*, **30**, pp. 342–359.
29. A. Alwan and G. K. Ananthasuresh, Topology optimization of electrostatically actuated micromechanical structures with accurate electrostatic modeling of the interpolated material model, *ASME Design Engineering Technical Conferences*, paper no. DETC2006-99684.
30. W. Ye, S. Mukherjee, and N. C. MacDonald, Optimal shape design of an electrostatic comb drive in microelectromechanical systems, *J. MEMS*, **7**, pp. 16–26, (1998).
31. W. Ye and S. Mukherjee, Optimal design of three-dimensional MEMS with applications to electrostatic comb-drives, *Int. J. Num. Meth. Engng.*, **45**, pp. 175–194, (1999).
32. H. A. Haus and J. R. Melcher, *Electromagnetic fields and energy*, web.mit.edu/6.013_book/www/ (2006).
33. I. E. Tamm, *Fundamentals of the theory of electricity*, Mir Publishers, Moscow, (1976).
34. A. Alwan and G. K. Ananthasuresh, Topology optimization of micromechanical structures that are compatible with surface micromachining, *J. of Phys. Conf. Ser. 34*, pp. 264–271, (2006).
35. E. C. N. Silva, S. Nishiwaki, and N. Kikuchi, Topology optimization in design of flextensional actuators, *IEEE Trans. Ultrasonics, Ferroelectrics and Frequency Control*, **47**, pp. 657–671, (2000).
36. E. C. N. Silva, J. S. O. Fonseca, and N. Kikuchi, Optimal design of periodic piezocomposites, *Comp. Meth. Appl. Mech. Engng.*, **159**, pp. 49–77, (1998).

37. O. Sigmund, Tailoring materials with prescribed elastic properties, *Mech. Mater.*, **20**, pp. 351–368, (1995).
38. O. Sigmund and S. Torquato, Design of materials with extreme thermal expansion using a three-phase topology optimization method, *J. Mech. Phys. Solid.*, **45**, pp. 1037–1067, (1997).
39. O. Sigmund and J. S. Jensen, Systematic design of photonic band-gap materials and structures by topology optimization, *Phil. Trans. Royal Soc.: Math. Phys. And Eng. Sci.*, **361**, pp. 1011–1019, (2003).
40. S. J. Cox and D. C. Dobson, Maximizing band gaps in two-dimensional photonic crystals, *SIAM J. Appl. Math*, **59**, pp. 2108–2120, (1999).
41. T. Borrvall and J. Petersson, Topology optimization of fluids in Stokes flow, *Int. J. Num. Meth. In Fluids.*, **41**, pp. 77–107, (2003).
42. A. Gersborg-Hansen, O. Sigmund, and R. B. Haber, Topology optimization of channel flow problems, *Struc. Multi. Disc. Optmn.*, **30**, pp. 181–192, (2005).
43. A. Evgrafov, Topology optimization of slightly compressible fluids, *Appl. Math. Optim.*, DOI: 10-1007/s00245-005-0828-z.
44. A. Evgrafov, G. Pingen, and K. Maute, Topology optimization of fluid problems by the Lattice Boltzmann method, *Topological Design Optimization of Structures, Machines and Materials* (eds. M. P. Bendse, N. Olhoff, and O. Sigmund), pp. 599–568, (2006).
45. E. Wadbro and M. Berggren, Topology optimization of wave transducers, *Topological Design Optimization of Structures, Machines and Materials* (eds. M. P. Bendse, N. Olhoff, and O. Sigmund), pp. 301–310, (2006).
46. V. S. S. Srinivas and G. K. Ananthasuresh, Topology optimization of a composite heat-sink involving a phase-change material, *WCSMO-7*, to be presented in Jun. 2007.
47. J. A. Sethian, *Level set methods and fast marching methods*, Cambridge University Press, (1999).
48. M. Y. Wang, X. Wang, and D. Guo, A level set method for structural topology optimization, *Comp. Meth. Appl. Mech. Engng.*, **192**, pp. 227–246, (2003).
49. M. Y. Wang and X. Wang, Structural topology optimization with multiple materials: a multi-phase level set method, *Comp. Meth. Appl. Mech. Engng.*, **193**, pp. 469–496, (2004).
50. G. Allaire and F. Jouve, Coupling the level set method and the topological gradient in structural optimization, *Topological Design Optimization of Structures, Machines and Materials* (eds. M. P. Bendse, N. Olhoff, and O. Sigmund), pp. 3–12, (2006)
51. T. Belytschko, C. Parimi, N. Moes, N. Sukumar, and S. Usui, Structured extended finite element methods for solids defined by implicit surfaces, *Int. J. Num. Meth. Engng.*, **56**, pp. 609–635, (2003).
52. A. Saxena, Synthesis of compliant mechanisms for path generation using genetic algorithms, *J. Mech. Des.*, **127**, pp. 745–752, (2005).
53. T. A. Poulsen, A new scheme for imposing a minimum length scale in topology optimization, *J. Num. Meth. Engng.*, **57**, pp. 741–760, (2003).
54. K.-T. Zhou, L.-P. Chen, Y.-Q. Zhang, and J. Yang., Manufacturing- and machining-based topology optimization, *Int. J. for Adv. In Manuf. Tech.*, **27**, pp. 531–536, (2006).
55. L. Yin and G. K. Ananthasuresh, Design of distributed compliant mechanisms, *Mechanics Based Design of Structures and Machines*, **31**, pp. 151–179, (2003).
56. Multi-User-MEMS Processes, www.memscap.com/memsrus/crmumps.html.

57. A. Alwan and G. K. Ananthasuresh, Topology optimization of micromachined structures with surface micromachining manufacturing constraints, *ASME Design Engineering Technical Conferences*, Philadelphia, paper no. DETC2006-99341 (2006).
58. M. Agrawal and G. K. Ananthasuresh, On including manufacturing constraints in the topology optimization of surface-micromachined Structures, *WCSMO-7*, to be presented in June 2007.
59. G. K. Ananthasuresh, Protein Sequence Design using topology optimization techniques, *Topological Design Optimization of Structures, Machines and Materials* (eds. M. P. Bendse, N. Olhoff, and O. Sigmund), pp. 455–466, (2006).
60. K. A. Dill, S. Bromberg, K. Yue, K. M. Fiebig, D. P. Yee, P. D. Thomas, and H. S. Chen, Principles of protein folding A perspective from simple exact models, *Protein Science*, **4**, pp. 561–602, (1995).
61. S. K. Koh, G. K. Ananthasuresh, and S. Vishveswara, A deterministic optimization approach to protein sequence design using continuous models, *Int. J. Robotics Res.*, **24**, pp. 109–130, (2005).
62. J. G. Saven and P. G. Wolynes, Statistical mechanics of the combinatorial synthesis and analysis of folding macromolecules, *J. Phys. Chem. B.*, **101**, pp. 8375–8389, (1997).
63. S. Miyazawa and R. L. Jernigan, Estimation of effective inter-residue contact energies from protein crystal structures: quasi-chemical approximation, *Macromolecules*, **18**, pp. 534–552, (1985).
64. H. Li, C. Tang, and N. S. Wingreen, Nature of driving force for protein folding: a result from analyzing the statistical potential, *Phys. Rev. Lett.*, **79**, pp. 765–768, (1997).
65. S. K. Koh, G. K. Ananthasuresh, and C. Croke, Design of reduced protein models in continuous sequence space, *J. Mech. Des.*, **127**, pp. 736–738, (2005).

This page intentionally left blank

Chapter 12

Mechanical Characterization of Polysilicon at the Micro-Scale Through On-Chip Tests

Alberto Corigliano, Fabrizio Cacchione and Attilio Frangi

Department of Structural Engineering, Politecnico di Milano
P.za Leonardo da Vinci 32, Milano, Italy
alberto.corigliano@polimi.it

Sarah Zerbini and Marco Ferrera

MEMS Product Division, ST Microlectronics
Cornaredo (Milano), Italy

The issue of mechanical characterization of polysilicon used in Micro Electro Mechanical Systems (MEMS) is discussed in this chapter. An innovative approach based on a fully *on-chip* testing procedure is described; three *ad hoc* designed electrostatically actuated microsystems are here used in order to determine experimentally the Young's modulus and the rupture strength of thin and thick polysilicon. The first device is based on a rotational test structure actuated by a system of comb finger capacitors which load up to rupture a couple of tapered beams under bending in the plane parallel to the substrate. The second microsystem is based on a large plate with holes. It constitutes, with the substrate, a parallel plate capacitor moving in the direction orthogonal to the substrate itself. A couple of tapered beams placed at the center of the plate is loaded up to rupture in bending in the plane orthogonal to the substrate. The third device is again based on a system of comb finger capacitors which load up to rupture a notched specimen of a thick polysilicon layer. Experimental data are obtained which allow for the determination of Young's modulus and rupture strength on the basis of an accurate data-reduction procedure relying on electromechanical numerical simulations. The rupture values are interpreted by means of the Weibull approach; statistical size effects and stress gradient effects are taken into account thus allowing for a direct comparison of the data obtained from the test structures.

Contents

12.1 Introduction 428
12.2 On-Chip Testing with Electrostatic Actuation 430

12.2.1 Fabrication Process 430
12.2.2 Test Structures and Data Reduction Procedure 432
12.3 Weibull Approach 433
12.4 Characterization of Thin Poly-Layers 437
12.4.1 On-Chip Bending Test Through a Comb Finger Rotational Electrostatic Actuator . 437
12.4.2 On-Chip Bending Test Through a Parallel Plate Electrostatic Actuator 439
12.4.3 Experimental Results 442
12.5 Characterization of Thick Polysilicon Layers 445
12.5.1 General Description 445
12.5.2 Data Reduction Procedure 449
12.5.3 Experimental Results 449
12.6 Conclusions 450
References 452

12.1. Introduction

In recent years, there has been a very fast growth in the field of micro electro-mechanical systems (MEMS) and devices. Novel design concepts and new processing techniques are being introduced at a rapid rate, accompanied by the identification of new market opportunities.[1–5]

However, as in other technologies, the ability to exploit materials is limited by our knowledge of their properties. In particular, the successful fabrication and the reliable use of structures with feature sizes in the range 1 μm to 1 mm is strongly contingent on a sufficiently rigorous understanding of their length scale-dependent and process-dependent mechanical properties. In turn, such understanding requires the ability to measure the mechanical properties of microscale structures. The importance of accurate mechanical property measurement was realized early on in the development of microsystems technologies. As a result, there exist today many different microscale mechanical test techniques, as described in several recent papers.[4–23]

In order to measure material properties one should be able to construct a specimen according to a given design, apply an external input in terms of forces or displacements and measure the specimen response by using direct procedures, in the sense that the variable of interest should be (almost) directly measured. All these steps are fully standardised at the macro-scale and are currently applied for testing construction materials like steel and concrete.

Unfortunately, these practices cannot be easily applied at the scale of MEMS. In particular, one has to resort to fully or partially indirect approaches. For example, in order to measure the Young's modulus, cantilever beams in bending are often used; deflection is measured and the material parameter of interest is computed on the basis of an analytical or numerical model of the beam. Even during on-chip tension tests some sort of inverse analysis has to be performed since, in

general, only capacitance variations are measured directly while deformations are obtained on the basis of a numerical model.

Limiting the attention to silicon MEMS, a first general classification of test procedures can be made between off-chip[8,10,12,15,17,20–23] and on-chip devices.[6,10,11,14,18,19,24]

In both cases the micro-device is generally produced by deposition and etching procedures. An off-chip tensile test generally resorts to some sort of external gripping mechanism actuating the force and an external sensor measures the response of the specimen. However, in general, picking a specimen only a few micron thick, place it into a test machine and perform the test is still a challenging task.

On the contrary, on-chip test devices are real MEMS in which actuation and sensing is performed with the same working principles of MEMS. On-chip testing is especially advocated since the thin-film microstructure and the state of residual stress depend strongly on micro fabrication process steps. Nevertheless, it requires accurate modeling and numerical/analytical investigations of the whole device.

In principle, material parameters for MEMS, and in primis the Young's modulus E, can be determined exploiting several test devices. Among others there are tension tests, bending of cantilever beams, resonant devices, bulge tests, buckling tests. Clearly, the most direct approach is the tension test, but unfortunately this is not always applicable since it requires the deployment of considerable forces at the micro-scale in order to produce a significant deformation in the specimen. Hence a wealth of alternative solutions have been proposed in the literature.

The purpose of the present chapter is to discuss some recent results related to a completely *on-chip* approach for the mechanical characterization of polysilicon.

Three different MEMS for on-chip testing have been designed which load up to rupture under bending and tension silicon specimens. The first one is based on a rotational electrostatic actuator which contains a series of interdigitated comb-fingers and loads a couple of specimens in bending in the plane parallel to the substrate. The second one loads the specimens in the plane orthogonal to the substrate thanks to a parallel plate actuator which moves in the direction orthogonal to the substrate. The third device consists of system of comb finger capacitors which load up to rupture a notched specimen of a thick polysilicon layer due to in-plane displacements.

By means of a data reduction procedure based on the measurement of the capacitance variation, it is possible to obtain the value of the Young's modulus of the specimen and that of the maximum stress at rupture.

An outline of the chapter is as follows. Section 12.2 contains a brief description of the fabrication process and of the data reduction procedure adopted in the

experimental tests. Section 12.3 is devoted to the description of Weibull approach for the determination of the failure probability of polysilicon MEMS. Sections 12.4 and 12.5 are, respectively, dedicated to the description of the electrostatic actuators and experimental results. Finally Sec. 12.6 contains some closing remarks.

12.2. On-Chip Testing with Electrostatic Actuation

12.2.1. *Fabrication Process*

The on-chip test devices discussed in the present chapter were produced following the surface micro-machining process ThELMA^{TM} (Thick Epipoly Layer for Microactuators and Accelerometers) which has been developed by STMicroelectronics to realize in-silicon inertial sensors and actuators (see also Refs. 4 and 27 for further details). The ThELMA process permits the realization of suspended structures anchored to the substrate through very compliant parts (springs) and thus capable of moving on a plane parallel to the underlying silicon substrate. The process consists of the phases described concisely hereafter and illustrated schematically in Fig. 12.1.

(1) Substrate thermal oxidation. The silicon substrate is covered by a 2.5 μm thick layer of permanent oxide obtained with a thermal treatment at 1100°C.
(2) Deposition and patterning of horizontal interconnections. The first polysilicon layer is deposited above the thermal oxide; this layer (*poly1*) is used to define the buried runners which are used to bring potential and capacitance signals outside the device and it can be used as structural layer in thin polysilicon devices.
(3) Deposition and patterning of a sacrificial layer. A 1.6 μm thick oxide layer is deposited by means of a Plasma Enhanced Chemical Vapour Deposition (PECVD) process. This layer, together with the thermal oxide layer, forms a 4.1 μm thick layer which separates the moving part from the substrate and which can be considered analogous with the sacrificial layer in a Surface Micromachining process.
(4) Epitaxial growth of the structural layer (thick polysilicon). The polysilicon is made grow in the reactors, thus reaching a thickness of 15 μm.
(5) Structural layer patterning by trench etch. The parts of the mobile structure are obtained by deep trench etch which reaches the oxide layer.
(6) Sacrificial oxide removal and contact metallization deposition The sacrificial oxide layer is removed with a chemical reaction; in order to avoid stiction

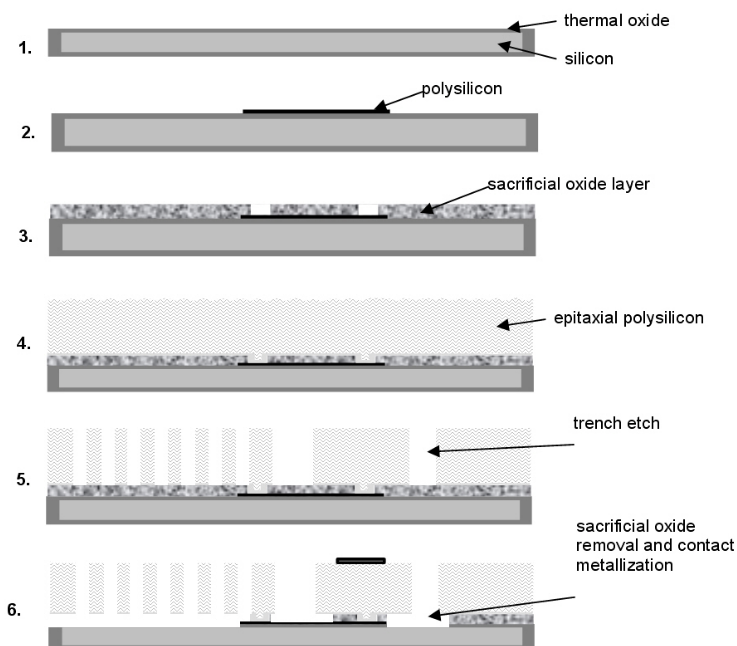

Fig. 12.1. Schematic illustration of Thelma surface micro-machining process. 1) Substrate thermal oxidation. 2) Deposition and patterning of horizontal interconnections. 3) Deposition and patterning of a sacrificial layer. 4) Epitaxial growth of the structural layer (thick polysilicon). 5) Structural layer patterning by trench etch. 6) Sacrificial oxide removal and contact metallization deposition.

due to attractive capillary reactions, this is done in rigorously dry conditions. The contact metallization is deposited; it will be used to make the wire-bonding between the device and the metallic frame.

The focus here is on the mechanical characterization of both the thin polysilicon film named *poly1* and of the thick structural layer (*thick polysilicon*) in the previous brief description of ThELMA process (see phases 2 and 4). The devices for on-chip testing *ad hoc* designed and produced therefore contain 0.7 μm *poly1* and 15 μm *thick polysilicon* specimens, which are suspended on the substrate due to the etching phase which destroy part of the initial oxide layers (phases 3, 5 and 6).

Figure 12.2 presents a cross-section of the layered structure obtained through the ThELMA process. Since the columnar layout strongly depends on the z coordinate orthogonal to the substrate, the *poly1* and *thick polysilicon* specimen

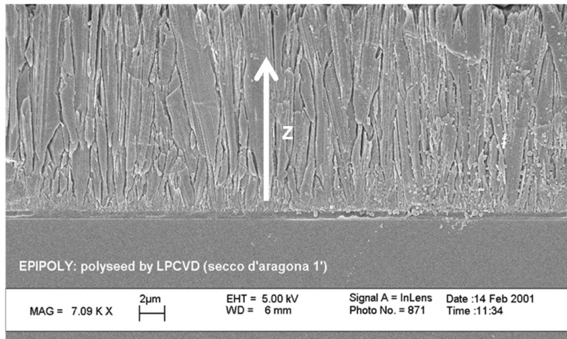

Fig. 12.2. SEM image of thick polysilicon.

addressed herein are expected to display different homogenized material properties.

12.2.2. *Test Structures and Data Reduction Procedure*

In the test devices described in Secs. 12.4 and 12.5, the specimens are co-fabricated with the actuator in order to obtain precise alignment and gripping of the specimens and also to reduce the set up size. The devices have an integrated system of electrostatic actuation: inter-digitated comb-finger actuators in the cases of the bending tests of Sec. 12.4 and of the tension tests of Sec. 12.5; parallel plate actuator in the case of the out of plane bending test of Sec. 12.4.

During the tests an input voltage V is applied to the actuator and a capacitance variation C is measured. The capacitance variation can be related to some significant displacement (or rotation) of the specimen through simplified analytical formulae or through electrostatic finite element simulations of the complete device. The corresponding electrostatic force can then be determined as a function of the displacement by the derivative of the electrostatic energy, which, in turn, is proportional to the derivative of the capacitance. This general scheme for data reduction will be detailed in Secs. 12.4–12.6 for each on-chip test structure. In Fig. 12.3 the meaningful experimental plots used in the data reduction procedure are shown for the case of the rotational device of Sec. 12.4, while Fig. 12.4 shows the final torque versus rotation plots.

Tests were carried out at room temperature and at atmospheric humidity, with a probe station mounted on an optical microscope. A slowly increasing voltage was applied in order to induce quasi-static loading conditions in the specimen. Details on the experimental setup can be found in, *e.g.*, Corigliano *et al.*[27]

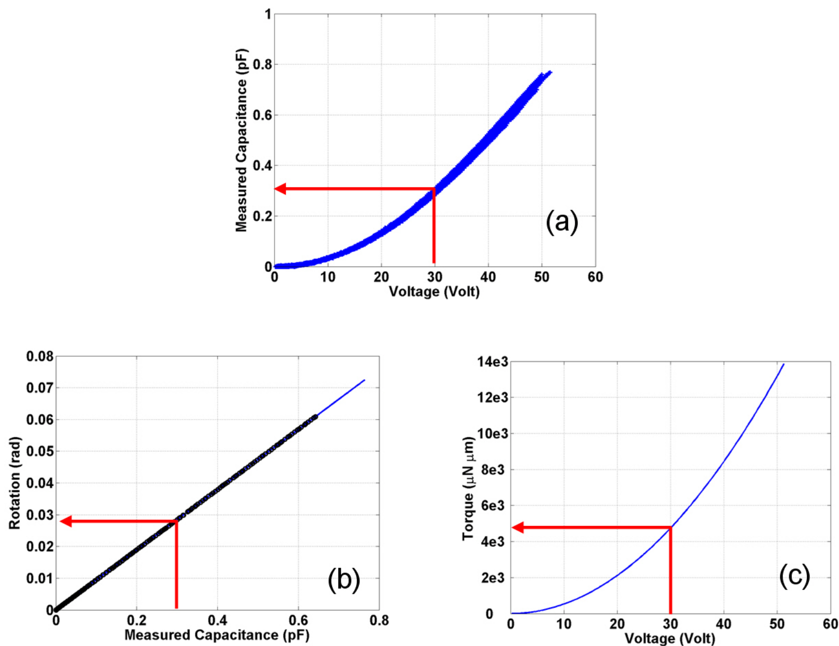

Fig. 12.3. Data reduction procedure applied to the rotational electrostatic actuator. (a) Experimental capacitance versus voltage plots; (b) rotation versus measured capacitance plot; (c) torque versus applied voltage plot.

12.3. Weibull Approach

The Weibull approach,[34–36] is widely applied for the study of brittle materials, like, for example, ceramics. This is the reason why it has been recently applied also to the study of rupture phenomena in polysilicon MEMS.[6,22,23,27] Weibull theory essentially gives a way to estimate the failure probability of a mechanical system, starting from the computation of the probability of failure of its weakest part, the theory is therefore also known as the weakest link approach. The Weibull cumulative distribution function is found, applying the theorem of joint probability, by first computing the probability of survival of a system composed by a large number of elementary parts. This basic idea is extended to a general case, after introduction of limiting hypotheses. The choice of the function giving the survival probability of a single part was not originally based on a precise mechanical interpretation of the rupture process. A recent and interesting discussion on the applicability of Weibull approach can be found in Ref. 36. By means of the Weibull approach it is possible to take into account the experimental scatter of

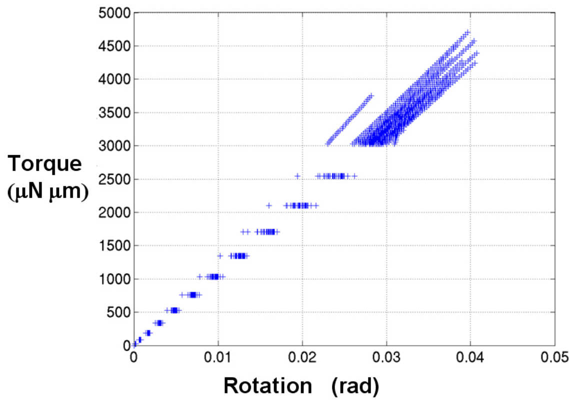

Fig. 12.4. Rotational electrostatic actuator. Experimental torque versus rotation plots.

strength values typical of brittle materials, the statistical size effect and the dependence of the probability of failure on the stress distribution. In this chapter only a brief introduction on Weibull theory applied to MEMS is given.

The application of Weibull approach to a uniformly stressed uniaxial bar gives the following equation for the probability of failure P_{f}:

$$P_{\mathrm{f}} = 1 - \exp\left[-\frac{\Omega}{\Omega_r}\left\langle\frac{\sigma - \sigma_u}{\sigma_0}\right\rangle_+^m\right] \tag{12.1}$$

where: Ω is the volume of the bar, Ω_r is a statistically uniform representative volume, σ_u, σ_0 and m are material parameters, $< \bullet >_+$ denotes the positive part of $\bullet$:

$$< \bullet >_+ = \bullet, \qquad \text{if} \quad \bullet > 0; \qquad < \bullet >_+ = 0 \qquad \text{if} \quad \bullet \leq 0.$$

It is important to recall that Eq. (12.1) is based on the assumption of statistically uniformity of every element Ω_r.

From Eq. (12.1) parameter σ_0 can be interpreted as the increase of the stress level w.r.t. value σ_u to which corresponds a probability of failure of 63.2% in a tensile specimen, uniformly stressed, with a volume Ω_r.

In the case of a multi-axial, non uniform stress state it is usually assumed that cracks form in the planes normal to the principal stresses $\sigma_1(\mathbf{x}), \sigma_2(\mathbf{x}), \sigma_3(\mathbf{x})$; the probability of failure is given by:

$$P_{\mathrm{f}} = 1 - \exp\left[-\frac{1}{\Omega_r}\int_{\Omega}\sum_{i=1}^{3}\left\langle\frac{\sigma_i(\mathbf{x}) - \sigma_u}{\sigma_0}\right\rangle_+^m d\Omega\right] \tag{12.2}$$

Equation (12.2) is obtained from Eq. (12.1) iterating the hypothesis of statistical uniformity of every volume and computing the joint probability of survival for every infinitesimal volume.

The above equation is of general applicability and has been obtained by iterating the hypothesis of statistical equivalence of all elementary parts which constitute the volume Ω. It is also important to notice that the fracture criterion based on principal stresses in a 3D situation is another strong assumption which could be substituted by another one, giving rise to a different stress function in the integral of Eq. (12.2).

The general expression (12.2) is here applied under the assumption that $\sigma_u = 0$, which means that all level of stresses have an influence on the probability of failure. Equation (12.2) is then re-written in a more compact way as:

$$P_{\mathrm{f}} = 1 - \exp\left[-\frac{1}{\Omega_r}\int_{\Omega}\left(\frac{\tilde{\sigma}(\mathbf{x})}{\sigma_0}\right)^m d\Omega\right] \tag{12.3}$$

once the equivalent stress $\tilde{\sigma}(\mathbf{x})$ is defined by:

$$\tilde{\sigma}(\mathbf{x}) \equiv \left(\sum_{i=1}^{3}\langle\sigma_i(\mathbf{x})\rangle_+^m\right)^{1/m} \tag{12.4}$$

The above relations can be used in order to estimate the probability of failure P_{f} of a given structure or solid once the Weibull parameters m and σ_0 are known and the elastic distribution of stresses has been computed via analytical formula or numerical solutions, *e.g.*, the FE method.

Parameters m and σ_0 are usually experimentally determined starting from a series of uniaxially tensile tests on cylindrical specimens of volume Ω and surface area A; in this simple case Eq. (12.3) reduces to:

$$P_{\mathrm{f}} = 1 - \exp\left[-\frac{\Omega}{\Omega_r}\left(\frac{\sigma}{\sigma_0}\right)^m\right] \tag{12.5}$$

Weibull parameters can be identified also from a specimen or structure loaded in a multiaxial situation with a non-uniform stress distribution. Let us re-write Eq. (12.3) in a form similar to Eq. (12.5):

$$P_{\mathrm{f}} = 1 - \exp\left[-\frac{1}{\Omega_r}\int_{\Omega}\left(\frac{\tilde{\sigma}(\mathbf{x})}{\sigma_0}\right)^m d\Omega\right] \equiv 1 - \exp\left[-\frac{\Omega}{\Omega_r}\left(\frac{\sigma_{\mathrm{nom}}}{\sigma_0}\right)^m \beta^m\right] \tag{12.6}$$

where β is defined by

$$\beta^m \equiv \frac{1}{\sigma_{\mathrm{nom}}^m\Omega}\int_{\Omega}\sum_{i=1}^{3}\langle\sigma_i(\mathbf{x})\rangle_+^m d\Omega \equiv \frac{1}{\Omega}\int_{\Omega}(h(\mathbf{x}))^m d\Omega \tag{12.7}$$

and σ_{nom} represents a nominal stress in the non uniformly stressed specimen or structure, which acts as a scaling parameter for the elastic response. Notice that function $h(\mathbf{x})$ defined by Eq. (12.7b) depends only on the normalized stress distribution in the linear elastic response and is therefore independent of the load level.

In order to compare the behaviour of different structures, it is possible to define a critical stress level as the nominal stress level σ_{nom0} evaluated in the structure when the probability of failure is equal to 63.2%, in full equivalence to the interpretation of σ_0 for a uniaxially, uniformly loaded specimen. From Eq. (12.6b) thus follows

$$\sigma_{\text{nom0}} = \frac{\sigma_0}{\beta}\left(\frac{\Omega_r}{\Omega}\right)^{1/m} \tag{12.8}$$

Given two structures (1) and (2), it is therefore possible to write

$$(\sigma_{\text{nom0}})_1 = \frac{\sigma_0}{\beta_1}\left(\frac{\Omega_r}{\Omega_1}\right)^{1/m} \quad (\sigma_{\text{nom0}})_2 = \frac{\sigma_0}{\beta_2}\left(\frac{\Omega_r}{\Omega_2}\right)^{1/m} \quad \frac{(\sigma_{\text{nom0}})_1}{(\sigma_{\text{nom0}})_2} = \frac{\beta_2}{\beta_1}\left(\frac{\Omega_2}{\Omega_1}\right)^{1/m}. \tag{12.9}$$

Relations (12.9) allow for a direct comparison of the behaviour of structures with different volumes and stress distributions. The variation of parameter σ_{nom0} with the volume clarifies the kind of size effect related to the statistical uniform distribution of defects described by a Weibull approach. σ_{nom0} is inversely proportional to the volume and this dependence increases with decreasing m; at the limit, by letting m to infinite, the statistical size effect disappears. Noteworthy is also the dependence of σ_{nom0} on the parameter β, which in turn depends on the stress non-uniformity.

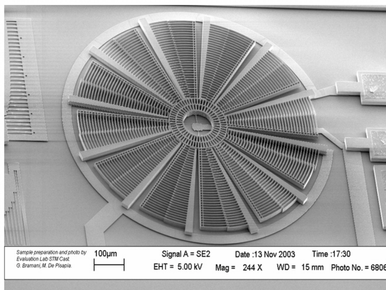

(a)

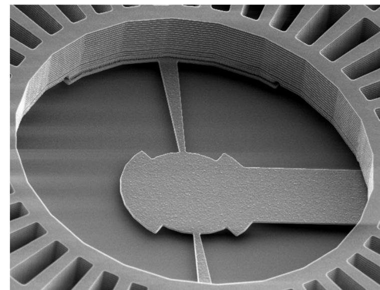

(b)

Fig. 12.5. Rotational electrostatic actuator for on-chip bending tests. (a) General view; (b) detail of the bending specimen.

12.4. Characterization of Thin Poly-Layers

12.4.1. *On-Chip Bending Test Through a Comb Finger Rotational Electrostatic Actuator*

12.4.1.1. *General Description*

The first on-chip device discussed is shown in Fig. 12.5 (see also Refs. 29, 30, and 32). It is made of a central ring connected to the substrate by means of two tapered 0.7 μm thick specimens (Fig. 12.5(b)) which also act as suspension springs of the whole device. Rigidly connected to the central ring are 12 arms with a total of 384 comb fingers capacitors which move, due to the electrostatic attraction, towards the stators connected rigidly to the substrate. When a voltage is applied to the device, the comb fingers develop a force distributed along the 12 arms, equivalent to a torque applied to the central ring. This, in turn, loads the two specimens in bending in the plane parallel to the substrate. The force developed by the system of comb fingers is sufficient to load the specimens up to rupture.

The specimens are a pair of doubly clamped slender beams, with a length of 34 μm and a trapezoidal cross-section. Their width decreases linearly from 5.3 μm to 1.8 μm. This shape was *ad hoc* designed to localize the fracture of the specimen in a specified area through stress concentration.

12.4.1.2. *Data Reduction Procedure*

The rotational on-chip device was tested in order to determine experimentally the Young's modulus and the rupture strength of 0.7 μm thick, thin polysilicon. The general data reduction procedure of Sec. 12.2 was applied; in the present case simplified analytical formulae were used in order to transform the applied voltage in the torque applied by the electrostatic actuator on the rotational device and the measured capacitance variation (with respect to a reference level) in the angle of rotation of the central ring of the rotational device.

The electrostatic attraction of the 32 comb fingers placed along each arm was supposed to be uniformly distributed along the arm, with a resultant F_{arm}; the total torque was therefore evaluated as:

$$M = n\left(l_0 + \frac{l_{\text{arm}}}{2}\right)F_{\text{arm}} = n_a\left(l_0 + \frac{l_{\text{arm}}}{2}\right)n_{\text{cf}}\varepsilon_0\frac{t\,V^2}{g} \qquad (12.10)$$

where n_a is the number of arms, l_0 the distance between the external part of the central ring and the centre of the whole device, l_{arm} the length of each arm, n_{cf} the number of comb fingers for each arm, ε_0 the empty space dielectric constant, t the thickness of the arms in the direction orthogonal to the substrate, g the gap

between the rotor and the stator in each comb finger, V the applied voltage. Equation (12.10) allows us to compute the value of the global torque M for a given voltage V.

Let us consider the 32 comb fingers distributed along each arm defined by index $i = 0, 1, \dots, 31$, being $i = 0$ the finger nearest to the centre. The contribution to the total capacitance of the i-th comb finger is given by

$$C_i = C_{0i} + 2\frac{\varepsilon_0\, t}{g}\, \Delta x_i = 2\frac{\varepsilon_0\, t}{g}\, \theta\, (R_0 + i\, \Delta R) \tag{12.11}$$

where C_{0i} is the capacitance corresponding to the initial configuration, Δx_i the value of the displacement in the direction orthogonal to the arm due to electrostatic attraction, θ is the angle of rotation of the device, R_0 the distance between the rotor finger $i = 0$ and the centre, ΔR the distance between two stator fingers. The total capacitance of the rotational device can be computed by summing the contribution of each finger and of each arm:

$$\begin{aligned} C = n_a \sum_{i=0}^{31} C_i &= n_a \sum_{i=0}^{31} C_{0i} + 2n_a \frac{\varepsilon_0 t}{g} \theta \sum_{i=0}^{31} (R_0 + i\Delta R) \\ &= C_0 + \left[2n_a \frac{\varepsilon_0 t}{g} (32R_0 + 496\Delta R) \right] \theta \end{aligned} \tag{12.12}$$

By means of the equation above, it is possible to compute the rotation of the device from the measured total capacitance C; since only capacitance variations are relevant, the value of C_0 is assumed to be zero.

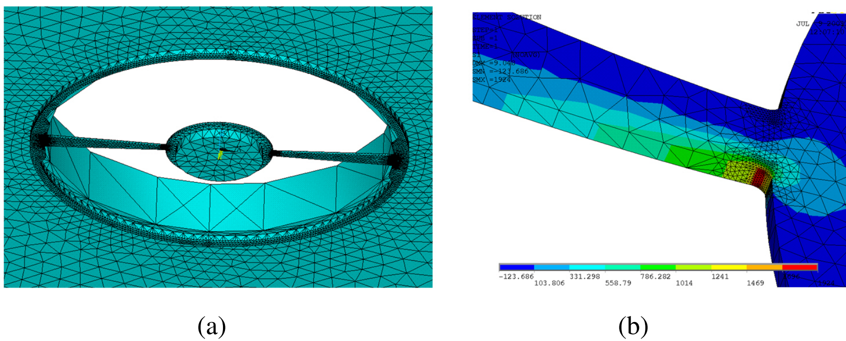

Fig. 12.6. Rotational electrostatic actuator. (a) Detail of the FE mesh; (b) maximum principal stress.

The total torque and the total capacitance were computed starting from experimental values of Voltage and Capacitance variation by introducing in Eqs. (12.10)

and (12.12) the following data:

$$n_a = 12 \quad n_{\text{cf}} = 32 \quad l_0 = 100\ \mu\text{m} \quad l_{\text{arm}} = 307.65\ \mu\text{m} \quad t = 15\ \mu\text{m}$$
$$R_0 = 108\ \mu\text{m} \quad \Delta R = 9.5\ \mu\text{m} \quad \varepsilon_0 = 8.854 \times 10^{-6}\ \frac{\text{pF}}{\mu\text{m}} \tag{12.13}$$

The resulting values are

$$M = 5.18\, V^2 \quad \mu\text{N}\ \mu\text{m}; \qquad C = C_0 + 10.41\,\theta \quad \text{pF}. \tag{12.14}$$

An example of the experimental capacitance versus applied voltage plots and the corresponding torque versus rotation plots obtained after application of relations (12.4) is shown in Figs. 12.3 and 12.4, already discussed.

Starting from the torque versus rotation plot, it was possible to obtain the Young's modulus and the rupture strength of the material (see Sec. 12.6) with the aid of a linear elastic Finite Element (FE) analysis performed on the 3D mesh of Fig. 12.6. This result was achieved after introduction of the following hypotheses: the deformation of the device of Fig. 12.5 is only due to the beam specimens at the centre, *i.e.*, the external part built with a $15\ \mu$m thick polysilicon is assumed to be rigid; the specimen is linear elastic and homogeneous up to rupture; displacements and strains are small; the global behaviour is linear and the global stiffness is proportional to the Young's modulus of the specimen.

It is important to remark that, besides the above mentioned hypotheses, the geometry of the specimen must be carefully reproduced in the FE model. The final FE mesh was therefore obtained after SEM images in order to reproduce the real geometry.

12.4.2. *On-Chip Bending Test Through a Parallel Plate Electrostatic Actuator*

12.4.2.1. *General Description*

The second on-chip device discussed is shown in Fig. 12.7 (see also Cacchione *et al.*[30,32]). Figure 12.7(a) shows the whole device, while Fig. 12.7(b) is a zoom of the central part where the $0.7\ \mu$m thick beam specimens are placed. An holed plate of $15\ \mu$m thick polysilicon is suspended on the substrate by means of four elastic springs placed at the four corners. The holed plate is also connected to the thin polysilicon film specimens placed at the centre, as shown in Fig. 12.7. The two symmetric specimens are in turn connected on one side to the holed plate, while on the other are rigidly connected to the substrate. The two specimens are therefore equivalent to a couple of doubly clamped beams. The holes in the plate are due

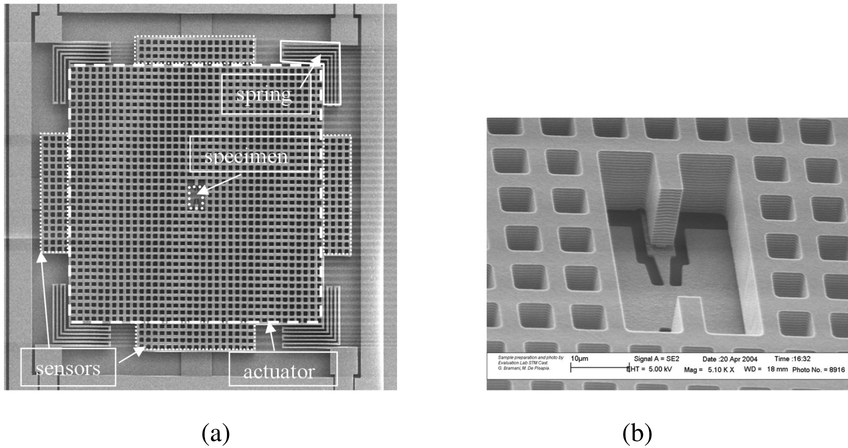

Fig. 12.7. Parallel plate actuator for out of plane bending tests: (a) general view; (b) detail of one of the specimens.

to the etching process for the elimination of the sacrificial layer, thus allowing for movement of the holed plate with respect to the substrate.

The movement in the direction orthogonal to the substrate is obtained by electrostatic attraction of the holed plate towards the substrate. The whole plate and the substrate thus act as a parallel plate electrostatic actuator. When the plate moves towards the substrate, the couple of specimens bend.

It is important to remark that only the squared part of the holed plate acts as an actuator (see Fig. 12.7(a)), while the holed rectangular parts added to each side of the plate act as sensors; these in turn allow for the experimental determination of capacitance variation and vertical movement, as discussed in Sec. 12.2.

The length of each specimen is 7 μm; in order to force the rupture in a section, their cross-section chosen a priori changes with a linearly varying width which decreases from 3 μm to 1 μm (see Fig. 12.7(b)).

12.4.2.2. *Data Reduction Procedure*

As done with the device described in Sec. 12.4, the parallel plate actuator was used to determine experimentally the Young's modulus and the rupture strength of 0.7 μm thick thin polysilicon. The general data reduction procedure of Sec. 12.2 was again applied; the experimentally determined capacitance versus voltage plots are transformed in force versus displacement plots by making use of the relationships between capacitance and displacement and between voltage and electrostatic force, respectively. These relations were obtained by means of accurate

electrostatic BE and FE simulations. In particular, a series of electrostatic BE simulations on one of the lateral sensors allowed for the determination of a capacitance variation versus vertical gap plot, which was directly used in order to transform experimental capacitance variation data in vertical displacements. Figure 12.8(a) shows the BE discretization of one of the sensors.

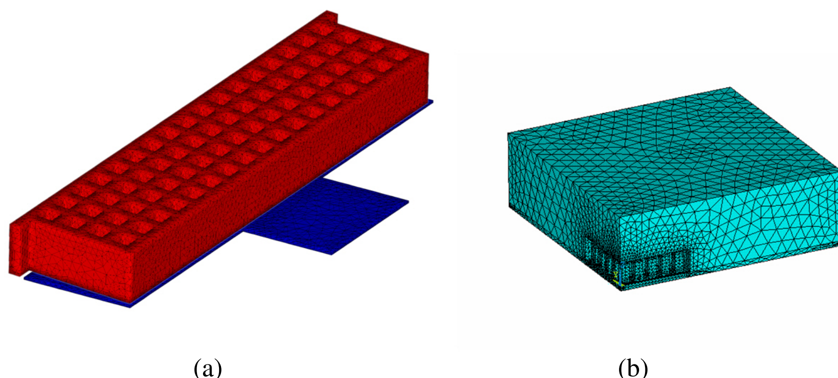

(a) (b)

Fig. 12.8. Parallel plate actuator for out of plane bending tests: (a) BE discretization for one of the sensors; (b) FE discretization of the air sorrounding a part of the actuator.

FE electrostatic simulations were used in order to obtain the vertical force of attraction on the square holed plate acting as a rotor. The 3D model used to this purpose is shown in Fig. 12.8(b): a quarter of a representative volume containing 100 holes was modeled, sorrounded by a large volume of air. The electrostatic field was then evaluated in the air sorrounding the polysilicon plate, applying an imposed voltage as boundary conditions. From the results of FE electrostatic simulations it was deduced that the attractive vertical force can be computed by making use, with negligible error, of the analytical relation for a parallel plate actuator with the same surface and with the correction due to edge effects. Starting from the force-displacement plot, the force acting on the specimens was obtained by subtracting the part equilibrated by the elastic suspension springs in the four corners of the holed plate (see Fig. 12.7(a)). An elastic 3D FE solution of the specimen under bending in the vertical plane (Fig. 12.9) was then used to relate the global stiffness of the specimen to the Young's modulus and the force at rupture to the maximum tensile stress in the specimen. Experimental values of Young's modulus and rupture stress were therefore finally obtained.

A key point in the data reduction procedure, which deserves further study and careful examination, is the sensitivity of the results to the value of the vertical gap

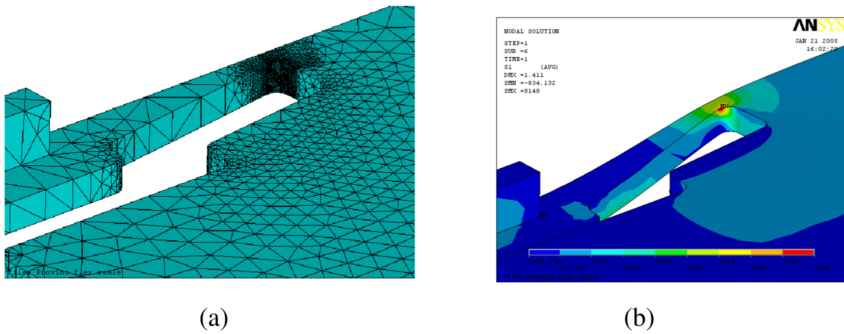

Fig. 12.9. Parallel plate actuator for out of plane bending tests: (a) detail of the Finite Element Mesh; (b) deformed mesh and maximum principal stress.

between the holed plate and the substrate. The vertical gap cannot be easily measured on the real device and it can strongly depend on the quality of the etching process. In the results here presented a mean value of 1.65 μm was used.

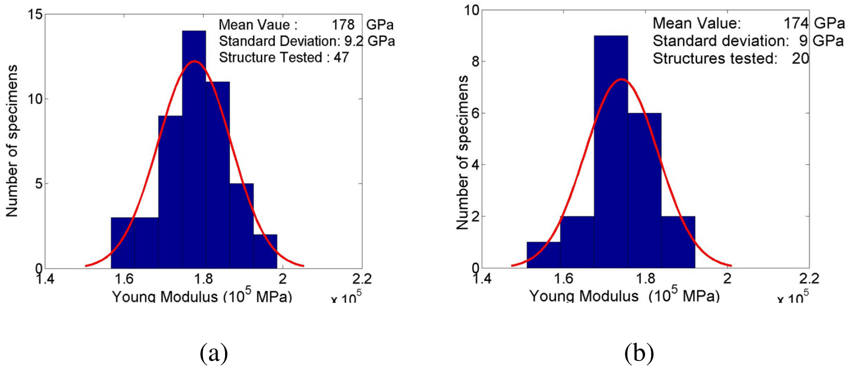

Fig. 12.10. Experimental distribution of Young's modulus. (a) Rotational actuator for in plane bending tests; (b) Parallel plate actuator for out of plane bending tests.

12.4.3. *Experimental Results*

12.4.3.1. *Young's Modulus*

Figure 12.10 shows the experimental distributions of Young's modulus obtained by means of the two devices described in Secs. 12.4 and 12.5. It can be observed that the two mean values (178 GPa and 174 GPa) differ less than the standard deviation of the two distributions; it can therefore be concluded that the two sets

of experimental results give in practice the same value for Young's modulus. The conclusion above implies that the possible non uniformity of the thin polysilicon film along its thickness does not influence sensibly the value of average Young's modulus obtained after the data reduction procedure applied to specimens loaded in different bending planes (in plane and out of plane bending).

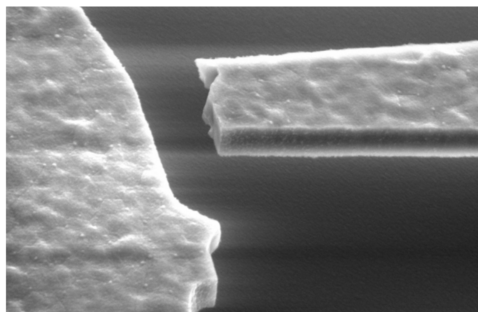

Fig. 12.11. Rotational actuator for in plane bending tests: example of rupture.

12.4.3.2. *Rupture Strength*

An image of a specimen loaded up to rupture in the plane parallel to the substrate by means of the rotational actuator of Sec. 12.4 is shown in Fig. 12.11. The Weibull approach briefly described in Sec. 12.3 was applied to 50 experimental results, computing the volume integral in Eq. (12.7) starting from a linear elastic FE analysis. Volume integrals were computed by means of a numerical Gaussian integration on each FE.

Weibull parameters $\sigma_0 = 1840\,\text{MPa}$; $m = 6.18$ were obtained; the nominal stress value of Eq. (12.8) was $\sigma_{\text{nom}0} = 2894\,\text{MPa}$; these results are shown in Fig. 12.12.

Figures 12.13 and 12.14 have the same meaning of Figs. 12.11 and 12.12 in the case of the parallel plate actuator. The obtained Weibull parameters are $\sigma_0 = 2237\,\text{MPa}$; $m = 5.13$, while the the nominal stress value of Eq. (12.8) is $\sigma_{\text{nom}0} = 3026\,\text{MPa}$.

The remarkable difference between σ_0 and $\sigma_{\text{nom}0}$ obtained with both test structures put in evidence the importance of the stress distribution effect: in a highly non uniformly stressed structure like the ones here tested, the apparent value of rupture is higher than in a uniformly stressed specimen. The difference in Weibull parameters obtained with the two sets of experimental results may be explained in various ways.

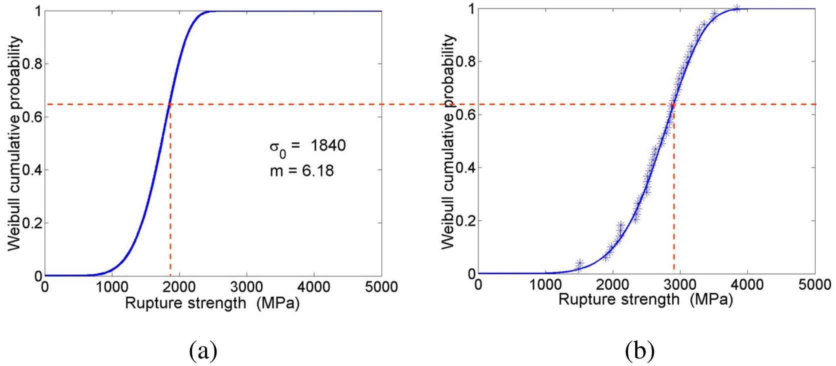

Fig. 12.12. Rotational actuator for in plane bending tests: Weibull cumulative probability densities. (a) Equivalent Weibull plot for a uniaxial, unit volume specimen; (b) experimental data obtained from 50 tests on the rotational structure, $\sigma_{\mathrm{nom}0} = (\sigma_0/\beta)(\Omega_r/\Omega)^{1/m} = 2894$ MPa.

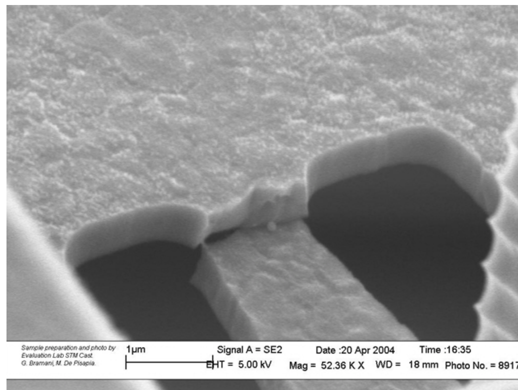

Fig. 12.13. Parallel plate actuator for out of plane bending tests: example of rupture.

A first explanation could be the influence of different loading conditions (in plane and out of plane) which could locally initiate different rupture mechanisms, linked to the anisotropy and non uniformity of distribution of the polysilicon film along its thickness. This conclusion is in partial contrast with the one derived in the previous section with reference to the elastic behaviour.

A second explanation could be linked to the assumption of $\sigma_u = 0$ introduced in Sec. 12.3 in order to simplify the Weibull approach. It is in fact known that a non zero σ_u value influences the final value of identified Weibull parameters σ_0, m. An additional reason for possible discrepances in the results obtained by means of the

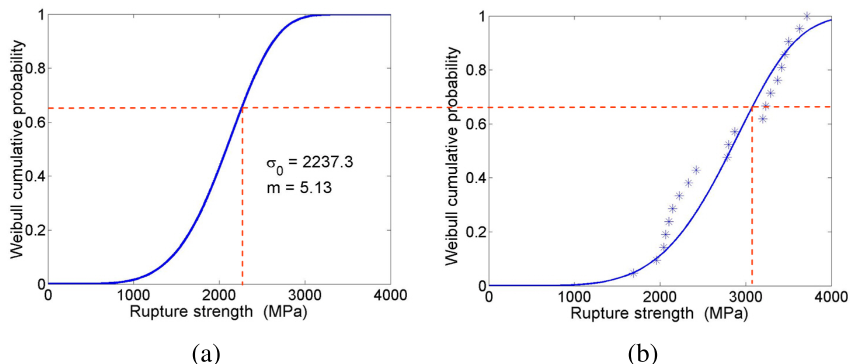

Fig. 12.14. Parallel plate actuator for out of plane bending tests: Weibull cumulative probability densities. (a) Equivalent Weibull plot for a uniaxial, unit volume specimen; (b) experimental data obtained from 21 tests on the parallel plate structure, $\sigma_{\text{nom0}} = (\sigma_0/\beta)(\Omega_r/\Omega)^{1/m} = 3026$ MPa.

two on-chip tests can be found in the influence of geometrical parameters like the gap between stator and holed plate in the device of Sec. 12.4.2.

12.4.3.3. *Prediction of Failure*

As discussed in Sec. 12.3, the probability of failure can in principle be computed starting from the knowledge of Weibull parameters. Figure 12.15 shows the cumulative failure probability of the parallel plate device of Sec. 12.5 predicted starting from the Weibull parameters identified with rupture data of the rotational device of Sec. 12.4. Vice-versa, Fig. 12.16 shows the cumulative failure probability of the rotational device of Sec. 12.4 predicted starting from the Weibull parameters identified with rupture data of the parallel plate device of Sec. 12.5. As expected from the difference in identified Weibull parameters, in Fig. 12.15 an underestimation of the structural resistance is shown, while the contrary occurs in Fig. 12.16.

12.5. Characterization of Thick Polysilicon Layers

12.5.1. *General Description*

The third device designed and then experimentally tested is shown in Fig. 12.17. It has been designed to test the mechanical properties of the epitaxial polysilicon, the thick layer deposited with ThELMA$^{\text{TM}}$ process (see Sec. 12.2). This film is almost twenty times thicker than *poly1* one and therefore a larger force is required to bring the specimen to rupture. This explains the relatively large dimensions of the structure, taking up a 1600 by 2250 μ^2 rectangular area.

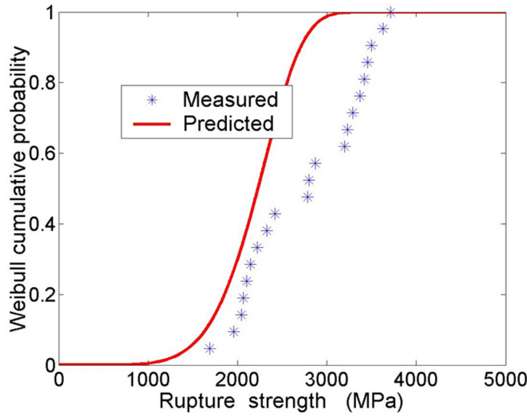

Fig. 12.15. Prediction of failure of the out of plane bending specimen from Weibull parameters identified starting from the rotational structure $\sigma_0 = 1840\,\text{MPa}$; $m = 6.2$.

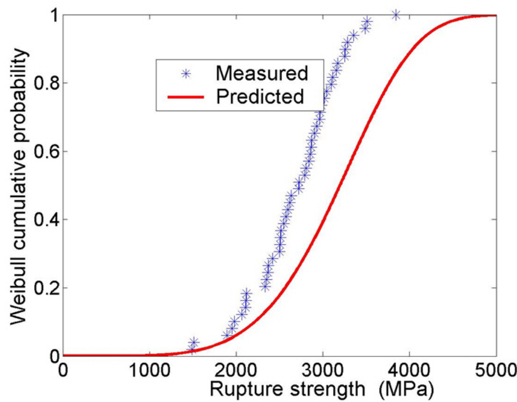

Fig. 12.16. Prediction of failure of the rotational structure from Weibull parameters identified starting from the out of plane bending specimen $\sigma_0 = 2237\,\text{MPa}$; $m = 5.1$.

The electrostatic actuation is realized by over four-thousand comb-finger capacitors. The comb fingers are grouped on specific structures called *arms* each containing 31 comb finger actuators. Its capacitance variation, as a function of the seismic mass displacement *x*, can be estimated from the simple analytic formula:

$$C_{\text{arm}} = 31 \frac{2\varepsilon_0 t}{g} x \tag{12.15}$$

where t is the thickness of the layer and g the gap between different fingers.

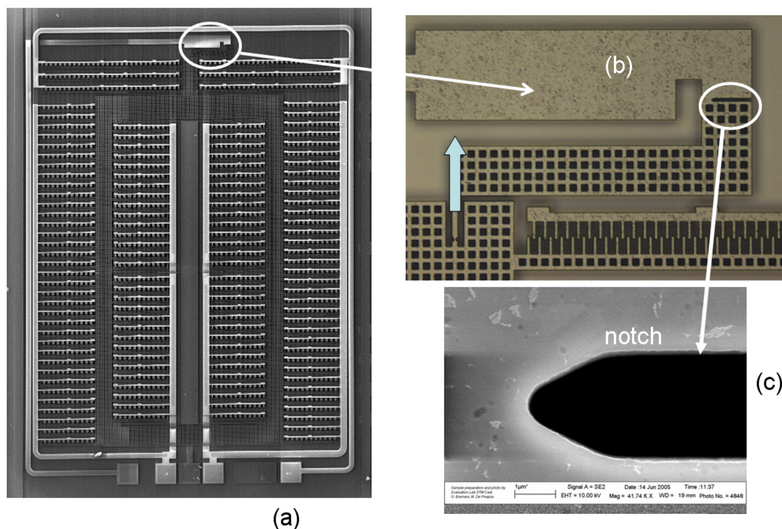

Fig. 12.17. Test structure for thick polysilicon layer.

The total number of arms being $n_a = 130$, the force developed by the actuator can be expressed as:

$$F_{\text{act}} = n_a \frac{1}{2} \frac{\partial C_{\text{arm}}}{\partial x} V^2 = 4030 \frac{\varepsilon_0 t}{g} V^2 \tag{12.16}$$

where V represents the applied voltage.

A stiff frame supports the arms of the movable part and is suspended on the substrate by means of six compliant suspension springs. The upper part of the frame is clamped to the notched specimen (Figs. 12.17(b) and 12.17(c)), that is thus loaded with the force developed by the actuator that is not absorbed by the spring system.

The sensing system is located in the upper part of the frame and again consists of a series of 480 comb finger capacitors. The total sensing capacitance variation, as a function of the displacement of the specimen is:

$$C_{\text{sens}} = 480 \frac{\varepsilon_0 t}{g} x \tag{12.17}$$

With the aid of FE electrostatic analysis a simulation of the sensing system was performed showing that the analytical formula is accurate up to a displacement of 10 μm, which largely overestimates the maximum displacement attainable during the experimental campaign.

The specimen of the structure was designed in order to carry both quasi-static and fatigue testing. It consists in a lever system that causes a stress concentration in a very localized region (Fig. 12.17(c)). The specimen can be divided into four parts (Fig. 12.17(b)): i) a beam that is the physical link between the frame and the specimen; ii) the lever, that transforms the axial action coming from the beam into a bending moment acting in the notched zone; iii) a notch, which is the most stressed part, where the crack starts forming; iv) a part fixed to the substrate.

It is worth stressing that a pure tension test on a thick polysilicon layer has been performed as described by the authors in Ref. 27 employing a different MEMS, where a series of parallel plate capacitors were used to set a thin and long silicon rod in tension (see Fig. 12.18).

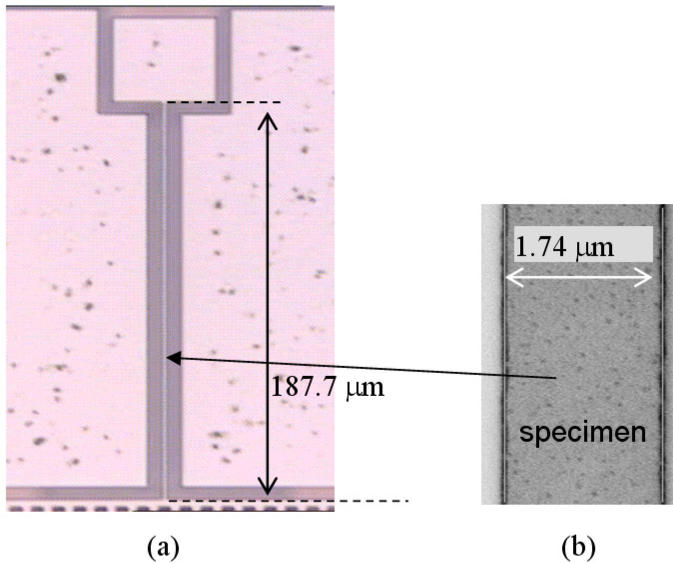

Fig. 12.18. Specimen in tension: (a) overall view of the specimen; (b) zoom on a cross section.

The present layout has been preferred since breaking a specimen in pure tension still remains a formidable task for on-chip tests at the microscale. However, as far as the elastic properties (Young's modulus) are concerned, the two tests provide comparable and reliable results.

12.5.2. *Data Reduction Procedure*

The experimental setup and the instrumentation used is the same as that employed for the thin *poly1* structures. Only the electrical scheme slightly differs since the actuator is used only to load the specimen, while the displacement is measured with the sensing system. This configuration was chosen in order to avoid any interference from the deformation of the frame during the test and to measure the displacement as close as possible to the area of the specimen.

Exploiting Eq. (12.17) the measured capacitance variation is related to the displacement imposed on the extremity of the load beam that causes the rotation of the lever arm; the force produced by the actuator for every imposed voltage is obtained from Eq. (12.16); finally the force versus displacement curves can be plotted (Fig. 12.19). Following the same procedure described in previous sections, a combined use of experimental tests and numerical simulations leads to the identification of the Young's modulus and of the value of the maximum tensile stress at rupture.

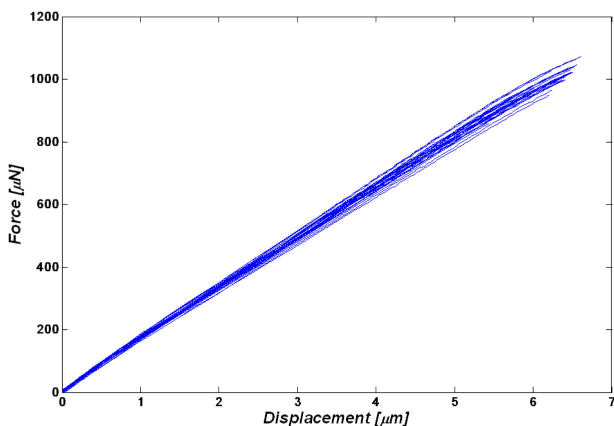

Fig. 12.19. Force versus displacement plots.

12.5.3. *Experimental Results*

A number of 31 structures, deposited on the same wafer, were tested. As it can be appreciated in Fig. 12.20, the measurements were highly repetitive.

The mean value measured for the Young's modulus is of 143 GPa, with a standard deviation of ± 3 GPa. Even in this case, the data concerning rupture of the specimens were interpreted in the framework of Weibull approach, as

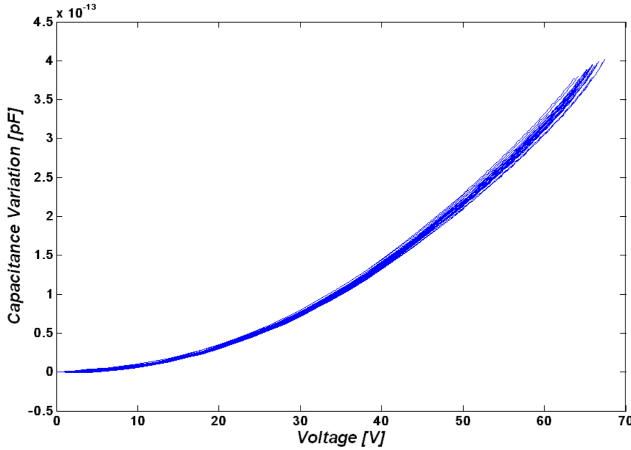

Fig. 12.20. Capacitance variation versus applied voltage plot.

discussed in Sec. 12.2 yielding Weibull modulus $m = 25.76$ and Weibull stress $\sigma_0 = 3622$ MPa.

It is worth recalling that the large differences with analogous data collected on thin *poly1* layers are expected due to the structural differences between the thin and thick layers.

After testing, the specimens were analysed using an optical microscope. Figure 12.21 shows that the fracture starts from the notch as predicted from the FE simulations carried out during the design phase. It is nevertheless to be noticed that: the crack path is often irregular and can be quite different from one structure to another. This can be due to the crystalline structure and grains orientation in the notched area. The grain morphology and orientation is different from one structure to another and has a very important impact on the propagation direction. Moreover the crack starting point is not always the same. This is due to the non-uniform flaw distribution on the notch surface, caused by the fabrication process. Flaws distribution is supposed to be responsible for the scatter of the experimental fracture results.

12.6. Conclusions

The results presented here concern an on-going research activity based on the use of on-chip tests for the mechanical characterization of thin and thick polysilicon films. Three on-chip electrostatic devices were designed and used in order to load 0.7 μm and 15 μm thick beam specimens up to rupture. The obtained values of

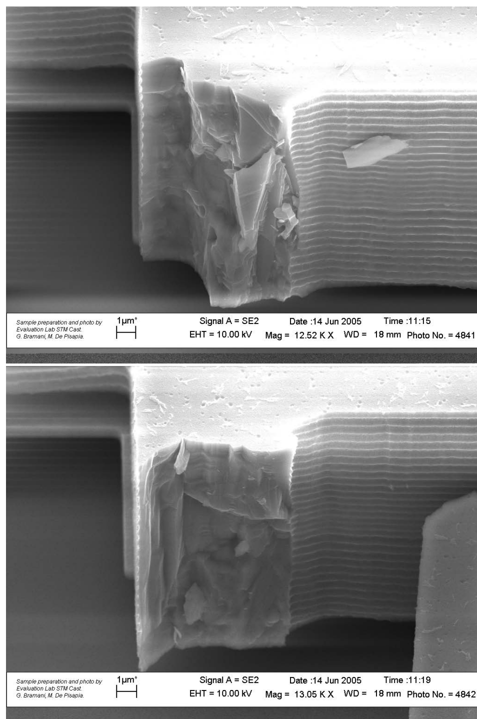

Fig. 12.21. Optical microscope images of broken specimens.

Young's modulus showed a very low dispersion and an apparent independence on the assumed different loading conditions. The large difference in the Young's modulus obtained for the two films was largely expected due to process reasons. The rupture strength was interpreted by means of Weibull theory, thus clarifying the influence of a non uniform stress distribution and of volume size on the probability of failure. A discrepancy in the Weibull parameters obtained with the two devices for *poly1* films was observed and a discussion on possible reasons of this differences was proposed. The results appear to be promising for a full mechanical characterization of polysilicon based on a complete on-chip mechanical characterization.

Acknowledgments

The contribution of EU NoE Design for Micro and Nano Manufacture (PATENT-DfMM), contract no: 507255 and of Cariplo Foundation is gratefully acknowledged.

References

1. S. D. Senturia, *Microsystem Design*, Kluwer Ac. Publ., Dordrecht (2001).
2. J. W. Gardner, V. K. Varadan, and O. O. Awadelkarim, *Microsensors MEMS and Smart Devices*, Wiley, Chichester (2001).
3. S. E. Lyshevski, *MEMS and NEMS. Systems, Devices and Structures*, CRC Press, New York, London (2002).
4. M. J. Madou, *Fundamentals of Microfabrication*, CRC Press, New York, London (2002).
5. B. C. Prorok, Y. Zhu, H. D. Espinosa, Z. Guo, Z. Baant, Y. Zhao, and B. I. Yakobson, Micro and Nanomechanics, in H. S. Nalwa (ed.), *Encyclopedia of Nanoscience and Nanotechnology*, **5**, 555–600 (2004).
6. S. Greek, F. Ericson, S. Johansson, and J. A. Schweitz, In situ tensile strength measurement and Weibull analysis of thick film and thin film micromachined polysilicon structures, *Thin Solid Films*, **292**, 247–254 (1997).
7. P. M. Oostemberg and S. D. Senturia, M-test: a test chip for MEMS material property measurement using electrostatically actuated test structures, *J. Microelectromechanical Systems*, **6**, 107–118 (1997).
8. W. N. Sharpe, Jr., B. Yuan, R. Vaidyanathan, and R. L. Edwards, Measurements of Young's modulus, Poisson's ratio, and tensile strength of polysilicon, Proceedings IEEE. *The Tenth Annual International Workshop on Micro Electro Mechanical Systems*, Nagoya, Japan, 424–429 (1997).
9. R. Ballarini, R. L. Mullen, Y. Yin, H. Kahn, S. Stemmer, and A. H. Heuer, The fracture toughness of polycristalline silicon microdevices: a first report, *J. Materials Research*, **12**, 915–922 (1997).
10. T. Tsuchiya, O. Tabata, J. Sakata, and Y. Taga, Specimen size effect on tensile strength of surface micromachined polycristalline silicon films, *J. Microelectromechanical Systems*, **7**, 106–113 (1998).
11. S. P. Chi and H. Wensyang, A microstructure for in situ determination of residual strain, *J. Microelectromechanical Systems*, **8**, 200–207 (1999).
12. W. N. Sharpe, K. T. Turner, and R. L. Edwards, Tensile testing of polysilicon, *J. Experimental Mechanics*, **39**, 162–170 (1999).
13. G. S. Chen, M. S. Ju, and Y. K. Fang, Effects of monolithic silicon postulated as an isotropic material on design of microstructures, *Sensor and Actuators A*, **86**, 108–114 (2000).
14. H. Kahn, N. Tayebi, R. Ballarini, R. L. Mullen, and A. H. Heuer, Fracture toughness of polysilicon MEMS devices, *Sensor and Actuators A*, **82**, 274–280 (2000).
15. T. Kramer and O. Paul, Surface micromachined ring test structures to determine mechanical properties of compressive thin films, *Sensor and Actuators A*, **92**, 292–298 (2000).
16. T. Yi, L. Li, and C.-J. Kim, Microscale material testing of single crystalline silicon: process effects on surface morphology and tensile strength, *Sensor and Actuators A*, **83**, 172–178 (2000).
17. T. Ando, M. Shikida, and K. Sato, Tensile-mode fatigue testing of silicon films as structural material for MEMS, *Sensor and Actuators A*, **93**, 70–75 (2001).

18. C. L. Muhlstein, S. B. Brown, and R. O. Ritchie, High-cycle fatigue and durability of polycrystalline silicon thin films in ambient air, *Sensor and Actuators A*, **94**, 177–188 (2001).
19. H. Kahn, R. Ballarini, J. J. Bellante, and A. H. Heuer, Fatigue failure in polysilicon not due to simple stress corrosion cracking, *Science*, **298**, 1215–1218 (2002).
20. I. Chasiotis and W. G. Knauss, A new microtensile tester for the study of MEMS materials with the aid of atomic force microscopy, *Experimental Mechanics*, **42**, 51–57 (2002).
21. J. Bagdahn and W. N. Sharpe, Jr., Fracture strength of polysilicon at stress concentrations, *J. Microelectromechanical Systems*, **12**, 302–312 (2003).
22. I. Chasiotis and W. G. Knauss, The mechanical strength of polysilicon films: Part 1. The influence of fabrication governed surface conditions, *J. Mech. Phys. Solids*, **51**, 1533–1550 (2003).
23. I. Chasiotis and W. G. Knauss, The mechanical strength of polysilicon films: Part 2. Size effects associated with elliptical and circular perforations, *J. Mech. Phys. Solids*, **51**, 1551–1572 (2003).
24. R. Ballarini, H. Kahn, A. H. Heuer, M. P. De Boer, and M. T. Dugger, MEMS structures for on-chip testing of mechanical and surface properties of thin films, in I. Milne, R. O. Ritchie, and B. Karihaloo (eds.), *Comprehensive Structural Integrity*, **8**, ch. 9, 325–360 (2003).
25. A. Villa, B. De Masi, A. Corigliano, A. Frangi, and C. Comi, Mechanical characterization of epitaxial polysilicon in MEMS, in K. J. Bathe (ed.), Proceedings *Second MIT Conference on Computational Fluid and Solid Mechanics*, Boston, June 2003, Elsevier, 722–726 (2003).
26. A. Corigliano, A. Frangi, C. Comi, and B. De Masi, Mechanical properties of epitaxial polysilicon at the microscale. Proceedings *XVI Congresso Nazionale AIMETA*, Ferrara, Italy, September 9–12 (2003).
27. A. Corigliano, B. De Masi, A. Frangi, A. Comi, A. Villa, and M. Marchi, Mechanical characterization of polysilicon through on chip tensile tests, *J. Microelectromechanical Systems*, **13**, 200–219 (2004).
28. B. De Masi, A. Villa, A. Corigliano, A. Frangi, C. Comi, and M. Marchi, On chip tensile test for epitaxial polysilicon, Proceedings *MEMS04*, Maastricht, January 25–29 (2004).
29. F. Cacchione, B. De Masi, A. Corigliano, and M. Ferrera, Rupture tests on polysilicon films through on-chip electrostatic actuation. *Sensor Letters*, **4**, 38–45 (2006)
30. F. Cacchione, B. De Masi, A. Corigliano, and M. Ferrera, Material characterization at the micro scale through on-chip tests, Proceedings *ICF11*, Torino, March 20–25 (2005).
31. F. Cacchione, A. Corigliano, B. De Masi, and M. Ferrera, Out of plane flexural behaviour of thin polysilicon films: mechanical characterization and application of the Weibull approach. *Sensor Letters*, **4**, 184–190 (2006).
32. F. Cacchione, A. Corigliano, B. De Masi, and C. Riva, Out of plane versus in plane flexural behaviour of thin polysilicon films: mechanical characterization and application of the Weibull approach. *Microelectronics Reliability*, **45**, 1758–1763, (2005).

33. A. Corigliano, F. Cacchione, B. De Masi, and C. Riva, On-chip electrostatically actuated bending tests for the mechanical characterization of polysilicon at the micro scale. *Meccanica*, **40**, 485–503, (2005).
34. W. Weibull, A statistical distribution of wide applicability, *J. Appl. Mech.*, **18**, 293–297 (1951).
35. P. Stanley and E. Y. Inanc, Assessment of surface strength and bulk strength of a typical brittle material, in *Probabilistic Methods in the Mechanics of Solids and Structures*, Proc. Symposium to the memory of W. Weibull, Stockholm, June 19-21, Springer-Verlag, Berlin (1984).
36. Z. Baant, Y. Xi, and S. Reid, Statistical size effect in quasi brittle structures: I. Is Weibull theory applicable?, *J. Eng. Mech. ASCE*, **117**, 2609–2622, (1991).

Chapter 13

Nano-Scale Testing of Nanowires and Carbon Nanotubes Using a Micro-Electro-Mechanical System

Horacio D. Espinosa, Yong Zhu*, Bei Peng and Owen Loh

Department of Mechanical Engineering, Northwestern University
2145 Sheridan Road, Evanston, IL 60208, USA
espinosa@northwestern.edu

The need to characterize nanometer-scale materials and structures has grown tremendously in the past decade. These structures may behave very differently from their larger counterparts and must be carefully characterized before their full potential is realized. The challenging task of mechanical characterization requires an entirely new set of techniques to achieve the force and displacement resolution needed to accurately characterize these structures. This chapter begins with a brief review of some of the methods used in mechanical characterization of nano-scale specimens, followed by a detailed description of a MEMS-based material testing system. This MEMS-based system allows for continuous observation of specimen deformation and failure with sub-nanometer resolution by scanning or transmission electron microscope while simultaneously measuring the applied load electronically with nano-Newton resolution. Special emphasis is placed on modeling and analysis of a thermal actuator used to apply a displacement-controlled load to the tensile specimen as well as the electrostatic load sensor. Finally, experimental results demonstrating the advantages of the MEMS-based system are presented.

Contents

13.1 Introduction . . . 456
13.2 Mechanical Characterization Techniques . . . 456
  13.2.1 Dynamic Vibration . . . 456
  13.2.2 Bending . . . 457
  13.2.3 Tensile Tests . . . 458
13.3 A MEMS-Based Material Testing Stage . . . 459
  13.3.1 Device Description . . . 460
  13.3.2 Electrothermal Actuator . . . 461

*Currently at Center for Mechanics of Solids, Structures and Materials, University of Texas at Austin, 210 East 24th Street Austin, TX 78712, USA.

13.3.3 Analytical Modeling of the Thermal Actuator 461
13.3.4 Multiphysics FEA of the Thermal Actuator 469
13.3.5 Buckling Analysis 471
13.3.6 Evaluating the Analytic and Finite Element Models 471
13.3.7 Load Sensor 472
13.4 Design Criteria 476
13.5 Material Testing 479
13.5.1 Sample Preparation 479
13.5.2 Tensile Tests 480
13.6 Summary 485
References 485

13.1. Introduction

The emergence of numerous nano-scale materials and structures within the past decade has prompted a need for methods to characterize their unique mechanical properties. For example, nanotubes and nanowires are seen as ideal structures for use in a variety of applications ranging from nanocomposites to nano-electromechanical systems. However, their scale presents a new set of challenges to the mechanics community. Identification of their properties and deformation mechanisms requires techniques of loading, measuring, and imaging with finer resolutions than previously achieved. As a result, these structures demand quantitative *in situ* mechanical testing by scanning or transmission electron microscope, or scanning probe microscope.

13.2. Mechanical Characterization Techniques

The precision required in nano-scale material testing is prohibitive to many techniques used previously on larger scales. This is due to strict requirements in: handling, manipulating, and positioning specimens; applying and measuring forces in the nano-Newton range, and measuring local deformation. Existing material testing techniques intended to overcome these limitations can be roughly categorized into three types: (1) dynamic vibration, (2) bending, and (3) tensile tests.

13.2.1. *Dynamic Vibration*

The Young's modulus of nanostructures can be estimated by observing their vibrations. Treacy *et al.*[1] determined the Young's modulus of multi-walled carbon nanotubes (MWNTs) by measuring the amplitude of their thermal vibrations within a transmission electron microscope (TEM). One end of the MWNT was

attached to the edge of a nickel ring while the other end remained free. The ring and MWNT were then imaged in the TEM. The frequency of the thermal vibration of the MWNT was significantly faster than the integration time required for imaging, causing the free end to appear blurred. The authors used the blurred region to determine an envelope of vibration. This envelope increased significantly with temperature, indicating it was indeed a thermal vibration. The Young's modulus of the MWNT was estimated based on the size of the envelope.

Poncharal *et al.*[2] measured the Young's modulus of MWNTs by inducing resonance within a TEM. Here the MWNTs were attached to a gold wire and an electrode was introduced using a piezo-driven translation stage on the TEM holder. An AC voltage was then applied across the wire and electrode, causing oscillatory deflection of the MWNTs toward the electrode. By increasing the driving frequency to the point of resonance, the authors were able to estimate the Young's modulus based on the measured geometry of the MWNTs and their resonance frequency.

13.2.2. *Bending*

Bending techniques, including force spectroscopy atomic force microscopy (AFM),[3] nanoindentation,[4] and on-chip testing,[5,6] involve application of a known bending force while measuring the resulting displacement. These techniques typically lack the ability to image the specimen during loading. Wong *et al.*[7] measured the Young's modulus, strength, and toughness of MWNTs and SiC nanorods using an atomic force microscope (AFM). The nanostructures were randomly dispersed on a flat substrate and pinned in place by microfabricated patches. The AFM was then used to bend the cantilevered structures transversely. By measuring the lateral force applied to the AFM probe by the nanostructure, the authors were able to obtain force versus deflection data at various locations along the length of the structure.

In the above method, adhesion and friction between the nanostructure and substrate could not be avoided. To avoid these issues, Walters *et al.*[8] suspended MWNTs over a microfabricated trench before bending them laterally with an AFM. Salvetat *et al.*[9] dispersed MWNTs over an alumina ultrafiltration membrane with 200 nm pores. This created similarly suspended nanostructures. The natural adhesion between the MWNTs and membrane was found to be sufficiently strong to fix the MWNTs during testing. The authors then deflected the suspended MWNTs vertically using an AFM probe in contact mode to obtain similar force-displacement measurements.

13.2.3. *Tensile Tests*

The tensile test is perhaps the most direct method of determining the Young's modulus of a material. Some tensile techniques allow for simultaneous load measurement and local imaging by AFM,[10] optical interferometry,[11] or scanning electron microscopy (SEM).[12,13] On a larger scale, Pan *et al.*[14] used a stress-strain rig to load a long (approximately 2 mm) MWNT rope in tension. This rope contained tens of thousands of parallel nanotubes. Sharpe *et al.*[11] loaded thin films in tension while simultaneously measuring displacement using either a capacitance-based displacement probe or laser interferometry, depending on the size of the sample. To use laser interferometry, two closely-spaced reflective gauge markers were patterned on the specimen. When shining a laser on these markers, interference fringes form which move as the spacing between the markers changes. These techniques tend to be better suited to the micrometer scale and not to the study of nanostructures such as nanotubes or nanowires due to their limited resolution.

On a smaller scale, Yu *et al.*[12] and Ding *et al.*[13] used a micro- or nanomanipulator to conduct in situ SEM tensile testing of MWNTs. The authors fixed a single nanotube between two AFM probes by localized electron beam-induced deposition (EBID) of carbonaceous material within the SEM chamber. One of the AFM probes was of low stiffness (less than 0.1 N/m) and used as a load sensor. The other probe was rigid and used to apply tensile load. When the rigid probe was actuated, the soft probe deflected in response to the applied load. The force applied to the nanotube was estimated based on the deflection of the soft cantilever and its known stiffness. The deformation of the nanotube was recorded by the SEM. The Young's modulus and failure strength of the nanotubes were then calculated based on the applied forces and corresponding measured displacements.

Marszalek *et al.*[3] attached a gold nanowire to an AFM probe of known stiffness. By lifting the probe a prescribed amount using the piezoelectric actuators of the AFM and observing the corresponding deflection of the probe, they were able to deduce the force applied to the nanowire and corresponding displacement.

Other techniques combine microfabricated and larger-scale devices. These allow alternating SEM or TEM imaging and load or deformation measurement modes through switching of the imaging electron beam between the specimen and mircofabricated beams used as load sensors.[15,16] During this switching, important local deformation events may go unobserved. Finally, some techniques have been developed to provide real time images of the specimen during loading. However, quantitative measurement of load and deformation are not provided simultaneously.[17,18]

The methods described above represent some of the significant progress made recently in the mechanical testing of nanostructures. However, lack of control in experimental conditions or limited accuracy of force and displacement measurements can limit their applicability. Recent advances in micro-electro-mechanical systems (MEMS) create the potential for material testing systems that overcome some of the described limitations.

13.3. A MEMS-Based Material Testing Stage

MEMS lend themselves naturally to material testing at the nanometer scale. These systems consist of combinations of micromachined elements, including strain sensors and actuators, integrated on a single chip. Due to their intermediate size, MEMS serve as an excellent interface between the macro and nano world. Their extremely fine force and displacement resolution allows accurate measurement and transduction of forces and displacements relevant at the nanometer scale. At the same time, the larger feature sizes and signal levels of MEMS allow handling and addressing by macro-scale tools. Furthermore, many of the sensing and actuation schemes employed in MEMS scale favorably. For example, the time response, sensitivity, and power consumption of electrostatic displacement sensors improves as their dimensions shrink. Electrostatic comb-drive actuators are often used in MEMS-based testing systems to apply time-dependent forces. van Arsdell and Brown[19] repeatedly stressed a micrometer-scale specimen in bending using a comb-drive actuator fixed to one end of the specimen. This comb-drive actuator swept in an arc-like motion while the opposite end of the specimen was fixed, causing bending stresses in the specimen. The comb-drive was also used to measure displacement, allowing for fracture and fatigue data to be collected when testing to the point of failure. Kahn *et al.*[20,21] determined fracture toughness by controlling crack propagation in a notched specimen using a comb-drive. One end of the specimen was fixed while the other was attached to a perpendicularly oriented comb-drive. Electrothermal actuation schemes have also been used to apply loading.[22,23] In these actuators, Joule heating induces localized thermal expansion of regions of the actuators and an overall displacement. The resulting strains are often measured using an integrated capacitive sensor and may be verified through digital image correlation. This section presents a detailed description of the design and modeling of a MEMS-based material testing system[24] for in-situ electron microscopy mechanical testing of nanostructures. This device allows for continuous observation of specimen deformation and failure with sub-nanometer resolution by SEM or TEM while simultaneously measuring the applied load electronically with nano-Newton resolution. To begin, an analytical model of the

thermal actuator used to apply tensile loading includes an electrothermal analysis to determine the temperature distribution in the actuator, followed by a thermo-mechanical analysis to determine the resulting displacement. A coupled-field finite element analysis complements the analytical model. Next, the differential capacitive sensor is analyzed to determine the applied load from the measured electric signals. Finally, a set of design criteria are established based on the analyses as guidelines for design of similar devices.

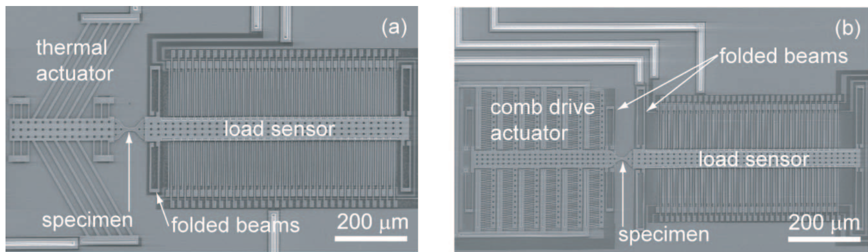

Fig. 13.1. Two variations of the MEMS-based material testing stage. (a) "Displacement controlled" device using a thermal actuator and differential capacitive load sensor. (b) "Force controlled" device using an electrostatic comb-drive actuator and differential capacitive load sensor.

13.3.1. *Device Description*

The MEMS-based tensile loading stage[24–26] consists of a linear actuator and a load sensor with a specimen fixed between them. The actuator is used to apply a tensile load to a specimen attached between the actuator and load sensor, while the load sensor detects the corresponding load. Figure 13.1(a) shows the entire device. The electrothermal actuator acts as a "displacement control" in the sense that it applies a prescribed displacement to the specimen regardless of the force required to achieve this displacement (within the functional range of the device). The load sensor is suspended on a set of folded beams of known stiffness and measures the corresponding tensile force applied to the specimen. Figure 13.1(b) shows an alternative loading stage using an electrostatic rather than a thermal actuator. The electrostatic actuators works as a "force control", applying a prescribed force regardless of the resulting displacement (again within a functional range).

While both the thermal and electrostatic actuators lend themselves nicely to standard microfabrication techniques, the remainder of this chapter focuses on the device using the thermal actuator as a case study in the design and modeling involved in building such a device. Electrostatic actuators have been thoroughly described elsewhere, for example.[5,27,28]

13.3.2. *Electrothermal Actuator*

Electrothermal actuation compliments electrostatic schemes as a compact, stable, high-force actuation technique.[29] It involves coupling of electric, thermal, and structural fields. Typically a resistive heating element is used as a heat input. This invokes thermal expansion of the device, resulting in a displacement. As mentioned above, these actuators are considered a "displacement control" as they displace a specific amount for a given heat input (within the limits of buckling and material stiffness).

Various forms of thermal actuators have been employed in systems ranging from linear and rotary microengines,[30] to two-dimensional nano-scale positioners,[31] optical benches,[32] and instrumentation for material characterization.[33] By incorporating compliant mechanisms, larger displacements can be achieved.[31]

Modeling of thermal actuators generally takes one of two approaches:

(1) A sequential electro-thermal and thermo-structural analysis,[34–36] or;
(2) A complete coupled three-dimensional finite element analysis (FEA).[37]

Additional analyses include characterization of the temperature-dependent electro-thermal properties[29,37] of these devices.

Sections 13.3.3 and 13.3.4 present an analysis of the thermal actuator employed by Zhu *et al.*[24,25] in the MEMS-based material testing system. The description begins with derivation of a set of analytical expressions for the response of the thermal actuator using a structural mechanics approach. This analysis is followed by a three-dimensional finite element multiphysics simulation to assess the temperature distribution within the actuator.

13.3.3. *Analytical Modeling of the Thermal Actuator*

A schematic of the thermal actuator to be analyzed is shown in Fig. 13.2. The thermal actuator consists of a series of inclined polysilicon beams supporting a free-standing shuttle. One end of each of the inclined beams is anchored to the substrate while the opposite end connects to the shuttle. Thermal expansion of the inclined beams, induced by Joule heating, causes the shuttle to move forward. This heating is the result of current flowing through the beams driven by a voltage applied across the two anchor points.[38] Modeling of these actuators requires a two-step analysis; first an electrothermal analysis to determine the temperature distribution in the device, followed by a thermostructural analysis to determine the resulting displacement field.

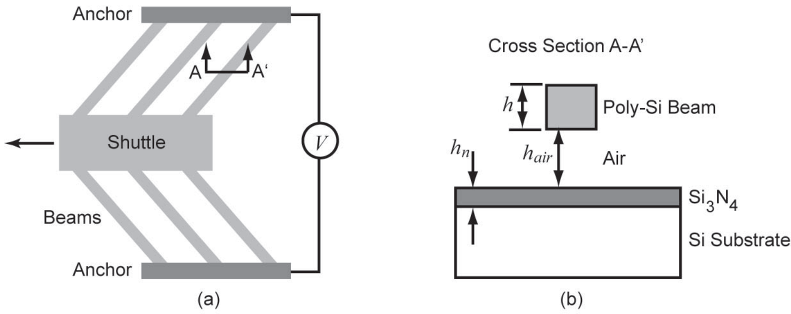

Fig. 13.2. (a) Schematic of the thermal actuator. (b) Cross section of a single beam suspended over the substrate.

13.3.3.1. *Electrothermal Model*

An electrothermal model of the device is developed to determine the temperature distribution as a function of the applied voltage. This is highly dependent upon the operating environment. When operating in air, the dominant heat transfer mechanism is heat conduction between the actuator and substrate through the air-filled gap between them.[35,36,38] In contrast, heat dissipation by conduction through the anchors to the substrate dominates in vacuum.[35,38] Assuming each beam is thermally independent, an electrothermal model based on a single beam is presented.[35] Heat transfer within the beam is treated as a one-dimensional problem since the length dimension is significantly larger than either of the cross-sectional dimensions.

First examine the case in air, where heat conduction through the air-filled gap between the actuator and substrate is the dominant mechanism of heat transfer. Here the governing equation is,

$$k_p \frac{d^2T}{dx^2} + J^2\rho = \frac{S}{h}\frac{T - T_s}{R_T}, \tag{13.1}$$

where k_p and ρ are the thermal conductivity and resistivity respectively of the polysilicon beams; J is the current density; $S = \frac{h}{w}\left(\frac{2h_{air}}{h} + 1\right) + 1$ is a shape factor accounting for the effect of element shape on heat conduction to the substrate; $R_T = \frac{h_{air}}{k_{air}} + \frac{h_n}{k_n} + \frac{h_s}{k_s}$ is the thermal resistance between the polysilicon beam and substrate; h and w are the thickness and width of a single beam respectively; h_{air} is the gap between the beam and silicon nitride layer on the substrate; h_n is the thickness of the silicon nitride; h_s is the representative thickness of the substrate; k_{air}, k_n, k_s are the thermal conductivities of air, silicon nitride, and the substrate respectively; and T_s is the temperature of the substrate.

The thermal conductivities k_p and k_{air} are both temperature dependent. However, the assumption of a constant k_p yields results similar to those using a temperature-dependent value of k_p.[35] Assuming a constant k_p and temperature dependent k_{air}, the finite difference method is implemented to solve Eq. (13.1) by writing the second-order differential equation in the form $\frac{d^2T}{dx^2} = b\,(x, T)$, and approximating it as,

$$\frac{d^2T}{dx^2} \approx \frac{1}{(\Delta x)^2}\,(T_{i+1} - 2T_i + T_{i-1})\,.$$

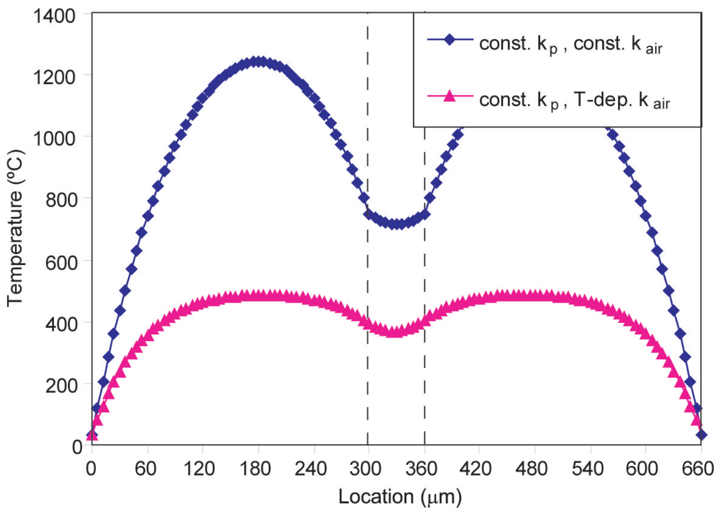

Fig. 13.3. Steady state temperature profile (with respect to the substrate) along a pair of inclined beams and the shuttle operated in air with an input current of 10 mA for both constant and temperature-dependent values of k_{air}. Locations 0–300 μm and 360–660 μm correspond to the beams while locations 300–360 μm correspond to the shuttle between the beams. The beams are anchored to the substrate at locations 0 and 660 μm.

Figure 13.3 shows the steady-state temperature profile obtained for a two-leg (one pair of inclined beams) thermal actuator operating in air. The temperature of the shuttle is significantly lower than that of the majority of each beam. This is due to the relatively low current density in the shuttle, resulting in a lower rate of heat generation as compared to that of the beams. Furthermore, the relatively large area of the shuttle results in greater heat dissipation through the air to the substrate.

The thermal conductivity of the air has a significant effect on the actuator behavior.[35] This strong dependence is clearly seen in Fig. 13.3, where the only difference between the two curves is the temperature dependence of the thermal conductivity of air. k_{air} increases with temperature, increasing the heat flow between the beams and shuttle and the substrate. Consequently, the temperature of the beams and shuttle is lower for a given current flow. Clearly, decreasing heat conduction through the air increases the temperature of the beams. Ultimately, operation in vacuum maximizes the beam temperature for a given current flow, making the device more efficient.

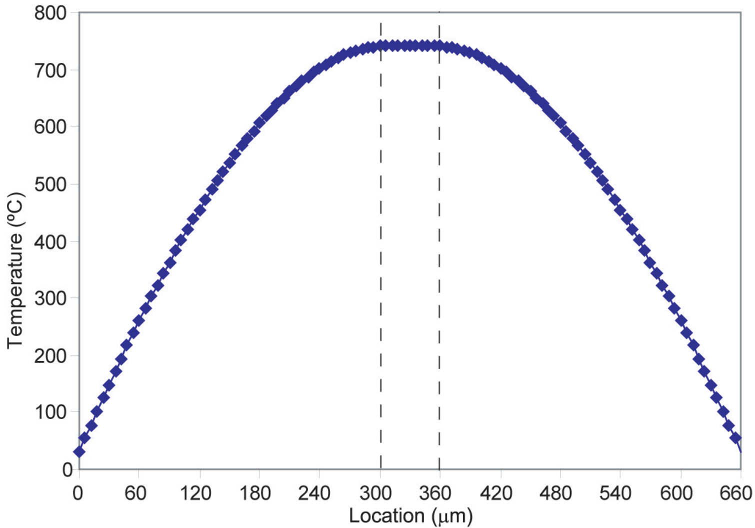

Fig. 13.4. Steady state temperature profile along a pair of inclined beams and the shuttle operated in vacuum with an input current of 3 mA. The thermal conductivity of polysilicon is assumed temperature dependent. Locations 0-300 μm and 360–660 μm correspond to the beams while locations 300-360 μm correspond to the shuttle between the beams. The beams are anchored to the substrate at locations 0 and 660 μm.

To analyze the case where the thermal actuator operates in vacuum, remove the term for heat conduction through the air from Eq. (13.1),

$$k_p \frac{d^2T}{dx^2} + J^2\rho = 0.$$

Figure 13.4 shows that the highest temperature now occurs in the shuttle rather than in the beams. Here the temperature depends most upon the distance from the

anchor points which are now assumed to be the only source of heat dissipation. Since the shuttle is furthest from the anchors, it reaches the highest temperature.

13.3.3.2. *Thermomechanical Model*

With the temperature distribution now known from the electrothermal analysis, the thermomechanical behavior of the actuator is modeled to determine the resulting displacement. The following assumptions are made in the analytical derivation of the thermomechanical behavior:

- the average temperature increase in the inclined beams is known;
- deformation of the central shuttle is negligible compared to that of the inclined beams;
- all strains and displacements are small, and;
- there is negligible shear deformation of the beams.

As in the electrothermal analysis, a single pair of inclined beams is first considered as shown in Fig. 13.5(a). Later the entire device, including the thermal actuator, specimen, and load sensor is analyzed.

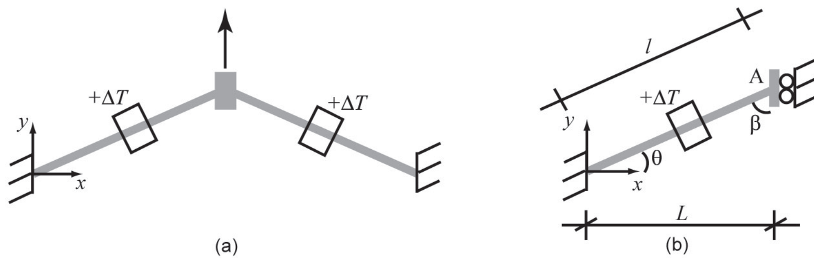

Fig. 13.5. Schematic of a pair of inclined beams subjected to an average increase in temperature ΔT. (a) Two beams joined at the central shuttle; (b) Equivalent mechanical representation of a single beam.

The pair of inclined beams, forming a single V-shaped clamped beam, is subjected to a uniform increase in temperature along its length. While the thermomechanical response of a similar structure was previously approximated,[39] the following analysis follows a rigorous structural mechanics approach.

Exploiting the symmetry of the system, the mechanical response is equivalently computed considering half of the structure as shown in Fig. 13.5(b). To determine the axial force in the beam and the displacement of Node A (Fig. 13.5) in the y-direction, the elastic stiffness matrix of the beam is assembled relative to the displacements in Node A. Before obtaining the stiffness matrix in the global frame, it is first computed in a local reference frame as shown in Fig. 13.6. The

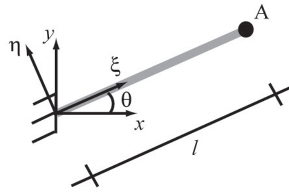

Fig. 13.6. Schematic of an inclined beam in a local reference frame.

governing structural equations for the beam subjected to an average temperature increase ΔT are,[25]

$$\begin{bmatrix} \frac{EA}{l} & 0 \\ 0 & 12\frac{EI}{l^3} \end{bmatrix} \begin{bmatrix} U_\xi^A \\ U_\eta^A \end{bmatrix} = \begin{bmatrix} \alpha \Delta T E A \\ 0 \end{bmatrix} + \begin{bmatrix} R_\xi^A \\ R_\eta^A \end{bmatrix}, \tag{13.2}$$

where E, A, and l are the Young's modulus, cross-sectional area, and length of the beam respectively; I is the moment of inertia of the beam with respect to the out-of-plane axis ζ in the local reference frame; U_ξ^A and U_η^A are the displacements of Node A in the directions ξ and η respectively; α is the coefficient of thermal expansion of the beam material; and R_ξ^A and R_η^A are the reaction forces at Node A in directions ξ and η respectively. The boundary conditions are known in terms of the global x-y reference frame in Fig. 13.5. Thus Eq. (13.2) is transformed to the global system by a rotation matrix relating the local and global degrees of freedom,

$$\begin{bmatrix} U_\xi^A \\ U_\eta^A \end{bmatrix} = \begin{bmatrix} \cos\theta & \sin\theta \\ -\sin\theta & \cos\theta \end{bmatrix} \begin{bmatrix} U_x^A \\ U_y^A \end{bmatrix}.$$

Applying this relation, Eq. (13.2) becomes,

$$\begin{bmatrix} c^2\frac{EA}{l} + s^2\frac{12EI}{l^3} & cs\left(\frac{EA}{l} - \frac{12EI}{l^3}\right) \\ cs\left(\frac{EA}{l} - \frac{12EI}{l^3}\right) & s^2\frac{EA}{l} + c^2\frac{12EI}{l^3} \end{bmatrix} \begin{bmatrix} U_x^A \\ U_y^A \end{bmatrix} = \begin{bmatrix} \alpha \Delta T E A c \\ \alpha \Delta T E A s \end{bmatrix} + \begin{bmatrix} R_x^A \\ R_y^A \end{bmatrix}, \tag{13.3}$$

where $c = \cos\theta$ and $s = \sin\theta$. The boundary conditions reflecting the constraint at Node A are $U_x^A = 0$, $R_x^A \neq 0$, $U_y^A \neq 0$, and $R_y^A = 0$. Applying these to Eq. (13.3) yields the reaction force on Node A in the x-direction and the displacement of Node A in the y-direction for an average increase in temperature ΔT

along the beam, namely;

$$R_x^{\Delta T} \equiv R_x^A = -\alpha \Delta T \, EA \frac{c}{s^2 \frac{Al^2}{12I} + c^2} \equiv -\alpha \Delta T \, EA \frac{c}{s^2 \Psi + c^2} \quad (13.4)$$

$$U^{\Delta T} \equiv U_y^A = \alpha \Delta T \, l \frac{s}{s^2 + c^2 \frac{12I}{Al^2}} \equiv \alpha \Delta T \, l \frac{s}{s^2 + \frac{c^2}{\Psi}}. \quad (13.5)$$

Here the dimensionless parameter $\Psi = Al^2/12I$ represents the ratio of the axial and bending stresses. Using the reaction force R_x^A, it is possible to obtain the compressive axial force N in the beam by projection along the axial direction, $N = R_x^A c$. A similar analysis yields the response of a pair of inclined beams subjected to an external force F applied to the central shuttle acting in the y-direction. In this case, the axial internal force and displacement of Node A are determined using the same system of governing equations (13.3) by replacing the vector on the right hand side that depends on the temperature increase with the external applied force vector $[0 \; F/2]^T$. The axial force and displacement now become,

$$R_x^F \equiv R_x^A = cs \left(\frac{EA}{l} - \frac{12EI}{l^3} \right) U_y^A = F \frac{cs\,(\Psi - 1)}{2\,(s^2 \Psi + c^2)},$$

$$U^F \equiv U_y^A = F \frac{1}{2\left(s^2 \frac{EA}{l} + c^2 \frac{12EI}{l^3}\right)} = \frac{Fl}{EA} \frac{1}{2\left(s^2 + \frac{c^2}{\Psi}\right)}.$$

Using the displacement U^F for a given force F, the stiffness of the V-shaped clamped thermal beam shown in Fig. 13.5 is,

$$K_{tb} \equiv \frac{F}{U^F} = 2\left(s^2 + \frac{c^2}{\Psi}\right) \frac{EA}{l}.$$

A more realistic situation is one where the V-shaped beam experiences both a temperature increase ΔT applied to actuate the device as well as an external force F in reaction to the displacement. This displacement is,

$$U^{\Delta T + F} = U^{\Delta T} + U^F = \frac{2\alpha \Delta T EAs + F}{K_{tb}}.$$

In the MEMS-based tensile loading device, a number of heat sink beams running between the shuttle and substrate are placed near the specimen to reduce the influence of the thermal actuator on the temperature of the specimen (see for example Fig. 13.8). Each pair of heat sink beams has a stiffness in the direction of the shuttle motion of[25]

$$K_{sb} = 2 \frac{12EI_{sb}}{l_{sb}^3} = \frac{2Eb_{sb}^3 h}{l_{sb}^3},$$

where I_{sb}, l_{sb}, and b_{sb} are the moment of inertia, length, and width of the heat sink beams respectively. Finally, combining all these factors to make a thermal actuator with m pairs of thermal beams and n pairs of heat sink beams, the total stiffness and shuttle displacement are:

$$K_{TA} = mK_{tb} + nK_{sb} \tag{13.6}$$

$$U_{TA} = \frac{U^{\Delta T} mK_{tb} + F}{K_{TA}} = \frac{2m\alpha \Delta T E A s + F}{K_{TA}}, \tag{13.7}$$

where $U^{\Delta T}$, given by Eq. (13.5), is the displacement of the actuator in the absence of heat sink beams. Here the relation for the displacement is obtained by imposing compatibility in the kinematics of the systems of the thermal and heat sink beams.

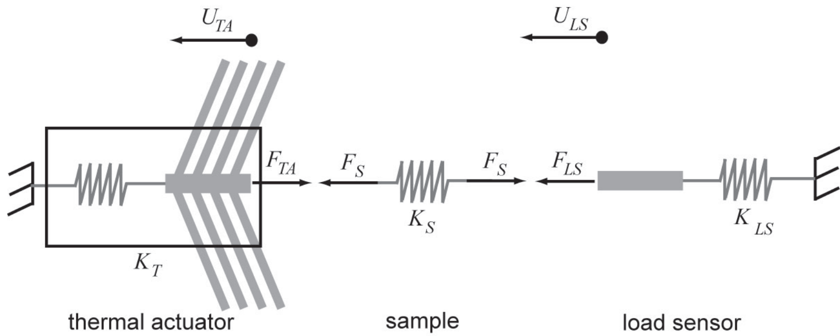

Fig. 13.7. Lumped model of the entire tensile loading device with internal forces and displacements shown in free body form.

13.3.3.3. *Thermomechanical Response of Entire Loading Device*

With the mechanical response of the thermal actuator known for a given current input, it is now possible to formulate a set of equations governing the behavior of the entire device. A lumped model of the entire device is constructed as shown in Fig. 13.7. Here K_S is the stiffness of the tensile specimen, K_{LS} is the stiffness of the load sensor corresponding to the folding beams by which it is suspended, K_{TA} is the stiffness of the thermal actuator computed in Eq. (13.6), and U_{LS} is the displacement of the load sensor. The central shuttle is assumed to be rigid. The governing equations for the lumped system shown in Fig. 13.7 are given by:[25]

$$
\begin{aligned}
\Delta U_S &= U_{TA} - U_{LS} \\
U_{TA} &= \frac{2m\alpha \Delta T E A s - F_{TA}}{K_{TA}} \\
F_{TA} &= F_S = F_{LS} \\
F_S &= K_S \Delta U_S \\
F_{LS} &= K_{LS} U_{LS},
\end{aligned}
\tag{13.8}
$$

where $s = \sin\theta$ and ΔU_S is the elongation of the specimen. Solving the system (13.8), the displacement of the thermal actuator U_{TA}, the tensile force on the specimen F_S, the elongation of the specimen ΔU_S, and the corresponding displacement of the load sensor U_{LS} are obtained:

$$
\begin{aligned}
U_{TA} &= \frac{2m\alpha \Delta T E A s}{K_{TA} + K_{TA}K_{LS}/K_S + K_{LS}} + \frac{2m\alpha \Delta T E A s}{K_{TA} + K_S + K_{TA}K_S/K_{LS}} \\
F_S &= \frac{2m\alpha \Delta T E A s}{K_{TA}/K_S + 1 + K_{TA}/K_{LS}} \\
\Delta U_S &= \frac{2m\alpha \Delta T E A s}{K_{TA} + K_S + K_{TA}K_S/K_{LS}} \\
U_{LS} &= \frac{2m\alpha \Delta T E A s}{K_{TA} + K_{TA}K_{LS}/K_S + K_{LS}}.
\end{aligned}
\tag{13.9}
$$

These represent the critical parameters in obtaining force-displacement data using the MEMS-based tensile loading device.

13.3.4. *Multiphysics FEA of the Thermal Actuator*

While the displacement of the actuator in vacuum is easily characterized experimentally,[25] the temperature distribution is more difficult to obtain. Therefore a coupled-field simulation is particularly necessary. This analysis also helps to assess the temperature at the actuator-specimen interface and to examine the effectiveness of the thin heat sink beams in controlling the temperature increase of the specimen during actuation. The MEMS-based tensile stage is intended to operate within the SEM or TEM. Thus the following finite element electrothermal analysis is carried out for the case where the device operates in vacuum. The actuation voltage applied across the anchor points serves as the input while the output includes both the actuator temperature and displacement fields. Displacements at the anchor points are held fixed in the mechanical boundary conditions. The thermal boundary conditions are zero temperature change at the anchors.

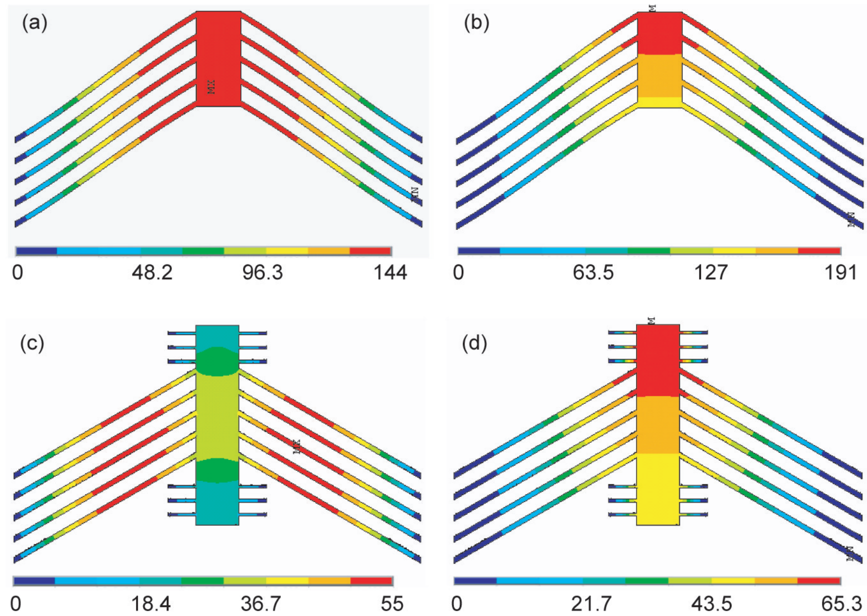

Fig. 13.8. (a) Temperature increase (°C) and (b) displacement field (nm) in the thermal actuator. The displacement component plotted is in the shuttle axial direction. (c) Temperature (°C) and (d) displacement field (nm) in the thermal actuator with three pairs of heat sink beams at the specimen end. In this analysis, the heat sink beams are 40 μm in length and 4 μm wide with 16 μm spacing between them. ANSYS Multiphysics, version 6.1 was used in this analysis.

Figures 13.8(a) and 13.8(b) depict the temperature and displacement in the thermal actuator for an actuation voltage of 1 V. As previously described, heat dissipation through the anchors is the dominant dissipation mechanism. Since the shuttle is furthest from the anchors, the highest temperature occurs in the shuttle. Due to the non-uniformity of the temperature distribution, the displacement is also nonuniform. Heating of the specimen during actuation is unavoidable as a result of the increased temperature of the shuttle to which the sample is attached. However, this effect is minimized with the addition of a series of heat sink beams running between the shuttle and substrate near the shuttle-specimen interface as shown in Figs. 13.8(c) and 13.8(d). To avoid out-of-plane bending, another three pairs of heat sink beams are placed at the opposite end of the shuttle. Comparing this to the case without the heat sink beams (Figs. 13.8(a) and 13.8(b)), this configuration allows for more than twice the displacement at the specimen end of the shuttle for the same allowable temperature increase at the shuttle-specimen interface. The problem of specimen heating can be further mitigated with the

addition of a thermal isolation layer between the actuator and specimen following the custom microfabrication process[38] for highly temperature-sensitive samples.

13.3.5. *Buckling Analysis*

For large tensile loads, buckling of the inclined beams in the thermal actuator is a concern. This occurs in the plane of minimum moment of inertia when the internal force exceeds the critical buckling load. Depending on the beam dimensions, this plane can be either parallel or orthogonal to the surface of the substrate. In this analysis, each beam is assumed to be fixed at the end where it is anchored to the substrate, while it is able to translate along the shuttle's axial direction with no rotation at the other end. The critical axial force at which buckling occurs is:

$$P_{cr} = \pi^2 \frac{EI_{min}}{l^2}. \tag{13.10}$$

For an unloaded thermal actuator (disconnected from the sample and any heat sink beams), the axial internal force is $R_x^{\Delta T} c = \alpha \Delta TEA \frac{c^2}{s^2 \Psi + c^2}$ where $R_x^{\Delta T}$ is given by Eq. (13.4). For an actuator connected to a tensile sample, heat sink beams, and load sensor, the maximum possible axial force achieved is $\alpha \Delta TEA$, *i.e.*, when the actuator is attached to an elastic system of infinite stiffness and cannot translate. The true axial force experienced by the beams during operation falls somewhere between the two extremes.

13.3.6. *Evaluating the Analytic and Finite Element Models*

The thermal actuator is calibrated experimentally to verify the analytical and FEA models described above. Figure 13.9[25] shows a comparison the analytical and FEA predictions of actuator displacement for a given current input with experimentally-measured results. The displacement of the actuator was measured in the SEM,[26] giving spatial resolution of better than 5 nm. Using the analytical model, the displacement is computed based on experimentally-measured temperatures in the actuator.[25] As mentioned in Sec. 13.3.4, the input to the multiphysics model is the voltage applied across the anchor points of the thermal actuator. In order to obtain the resulting current, the resistance of the actuator is computed using the output temperature and a value of resistivity corresponding to the average temperature of the device.[25] The models agree well with the experimentally-measured actuator displacements as shown in Fig. 13.9. This suggests the models are useful in predicting the behavior of thermal actuators of other geometry. At large currents (above approximately 12 mA), both the analytical and FEA models

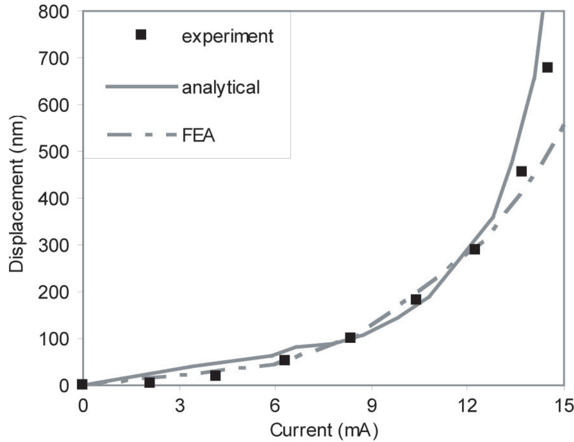

Fig. 13.9. Comparison of displacement at the actuator-specimen interface as predicted by the analytical and FEA models and measured experimentally. Displacement is plotted as a function of the input current. Each experimental point is the average of three experimental measurements obtained from different but geometrically identical thermal actuators.

deviate slightly from the experimental results. This can be explained largely by inaccuracies in material parameters such as resistivity and thermal conductivity at high temperature.[29,35] Furthermore, the microstructure of polysilicon begins to be modified at these high current levels and elevated temperatures.[25]

13.3.7. *Load Sensor*

The load sensor consists of a differential capacitive displacement sensor suspended on a set of elastic members of known stiffness. By calibrating the stiffness of the sensor,[26,40] the load is computed based on the measured displacement. The differential capacitive displacement sensor[41–43] is chosen for its sensitivity and linear behavior over a range of displacements appropriate for tensile testing of nanostructures.

The differential capacitive sensor is comprised of a movable rigid shuttle with electrodes (or "fingers") pointing outward as shown schematically in Fig. 13.10.[26] These fingers are interdigitated between pairs of stationary fingers (Fig. 13.10(b)) fixed to the substrate. Under no load, each movable finger sits centered between the two stationary fingers. Each set of fingers (one movable and a stationary on either side) forms two capacitors, one between the movable finger and each stationary finger. The entire capacitance sensor is equivalent to two combined

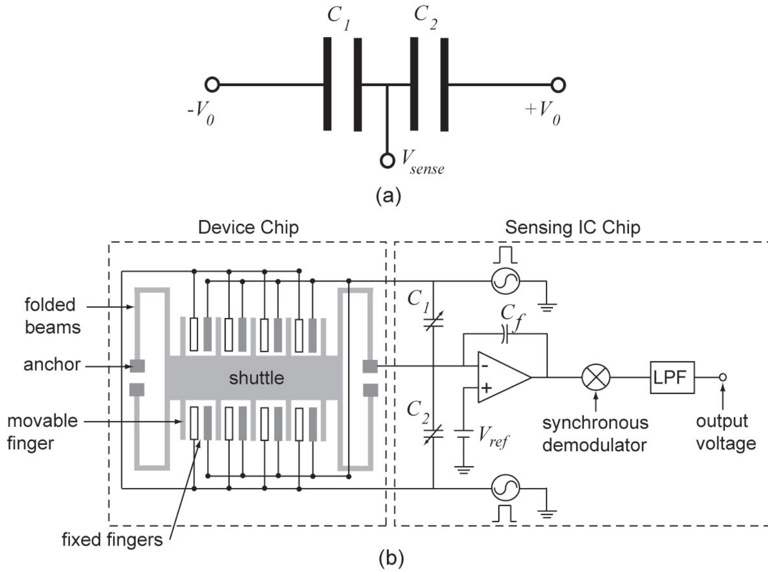

Fig. 13.10. (a) A simple model of the differential capacitor. (b) Double chip architecture used for measuring capacitance change. The capacitance change is proportional to the output voltage change.

capacitances, C_1 and C_2, as shown in Fig. 13.10(a), namely,

$$C_1 = C_2 = C_0 = \epsilon N \frac{A}{d_0} (1 + f),$$

where ϵ is the electric permitivity, N is the number of movable fingers, A and d_0 are the area of overlap and initial gap respectively between the movable finger and each stationary finger, and $f = 0.65 d_0/h$ is the fringing field correction factor with h being the beam height.[44] The movable fingers are attached to the folded beams via the rigid movable shuttle so their displacements are equivalent. This displacement yields a change in capacitance given by,

$$\Delta C = C_1 - C_2 = N\epsilon A \left(\frac{1}{d_0 - \Delta d} - \frac{1}{d_0 + \Delta d} \right) \approx \frac{2N\epsilon A}{d_0^2} \Delta d,$$

where Δd is the displacement of the load sensor. Note the fringing effect factor cancels. For displacements Δd within 50% of the initial gap d_0, the capacitance changes approximately linearly with the sensor displacement. This relatively large range of linear sensing is a major advantage of differential capacitance sensing over direct capacitance sensing which uses a single fixed beam for each movable beam. A variety of circuit configurations may be used in measuring capacitance.[41,42] Figure 13.10 shows schematically the charge sensing method used in

the device described in this chapter. This method mitigates the effects of parasitic capacitances that generally occur in electrostatic MEMS devices. Here the change in output voltage ΔV_{sense} is proportional to the capacitance change,

$$\Delta V_{sense} = \frac{V_0}{C_f} \Delta C,$$

where V_0 is the amplitude of an AC voltage signal applied to the stationary fingers and C_f is the feedback capacitor shown in Fig. 13.10. Minimizing stray capacitance and electromagnetic interference is critical in high resolution capacitance measurements. In this case, integrating the MEMS differential capacitor and sensing electronics on a single chip would minimize these effects, allowing detection of changes in capacitance at the atto-Farad level.[42] However, this would greatly increase fabrication complexity. The double chip architecture depicted in Fig. 13.10 is an alternative to the single chip scheme. Here the MEMS-based system is fabricated on one chip while a commercial integrated circuit chip (for example, Universal Capacitive Readout MS3110, Microsensors, Costa Mesa, CA) is used to measure changes in capacitance. Both chips are housed on a single printed circuit board.

An equivalent circuit for the entire device, including the electrothermal actuator, is shown in Fig. 13.11. The load sensor shuttle is connected electrically to the substrate through the anchor points. The capacitances are given by,

$$C_1 = N\epsilon \left(\frac{A_1}{d_0 + \Delta d} + \frac{A_2}{g} + 0.65 \frac{A_1}{h} \right), \tag{13.11}$$

$$C_2 = N\epsilon \left(\frac{A_1}{d_0 - \Delta d} + \frac{A_2}{g} + 0.65 \frac{A_1}{h} \right), \tag{13.12}$$

$$C_3 = N\epsilon \left(\frac{A_1}{d_3} + 0.65 \frac{A_1}{h} \right), \tag{13.13}$$

where N is the total unit number of differential capacitors, A_1 is the overlapping area of the stationary finger with the movable finger, A_2 is the overlapping area of the stationary finger with the substrate, d_0 is the gap between the stationary finger and the movable finger, Δd is the displacement of the movable finger, d_3 is the gap between the two stationary fingers, g is the gap between the fixed finger and substrate, and h is the finger thickness. In Eqs. (13.11) and (13.12), the first term represents the capacitance between each fixed finger and the corresponding movable finger. The second term is the capacitance between the fixed finger and

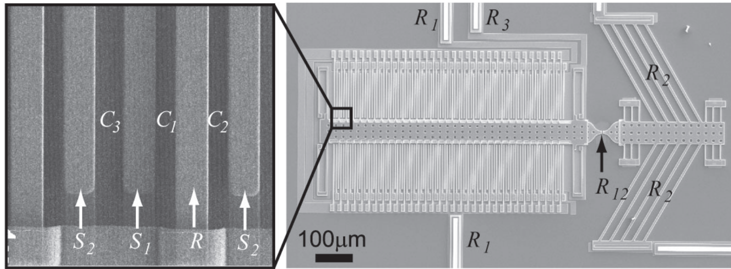

(a)

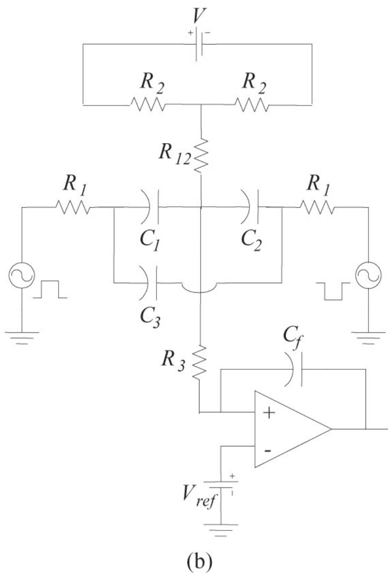

(b)

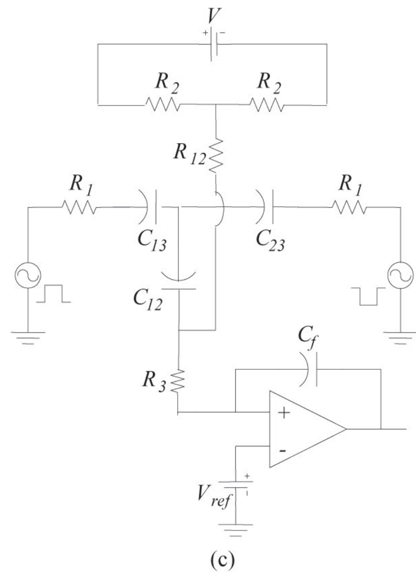

(c)

Fig. 13.11. (a) The device with an electrothermal actuator and corresponding resistances and capacitances. The inset shows details of the movable and stationary fingers. R_2 denotes the resistance of thermal beams, R_{12} the resistance of specimen, R_1 and R_3 the resistances of electric traces, C_1 and C_2 the capacitances between the movable beams and the two stationary beams, respectively, and C_3 the capacitance between two nearby stationary beams. (b) Equivalent electric circuit for the device in (a). (c) Equivalent circuit to that in (b) after a $\Delta - Y$ transformation.

the shield beneath the load sensor which is held at the same potential as the movable finger. The third term considers the fringe effect. Note that when $\Delta d = 0$, $C_1 = C_2 \equiv C_0$. The capacitance term from the fringe effect C_3 cannot be neglected as d_3 is typically comparable to d_0. Figure 13.11(b) shows the circuit used for the device in Fig. 13.11(a) while Fig. 13.11(c) shows the equivalent circuit due to a $\Delta - Y$ transformation.[45] Here the equivalent capacitances are given by,

$$C_{13} = \frac{C_1C_2 + C_2C_3 + C_3C_1}{C_2}$$
$$C_{23} = \frac{C_1C_2 + C_2C_3 + C_3C_1}{C_1} \quad (13.14)$$
$$C_{12} = \frac{C_1C_2 + C_2C_3 + C_3C_1}{C_3}.$$

Combining Eqs. (13.11)–(13.13) and (13.14) gives the difference in capacitance,

$$C_{13} - C_{23} = N\epsilon_0 A_1 \left(1 + \frac{C_1 + C_2}{C_1C_2}\right)\left(\frac{1}{d_0 + \Delta d} - \frac{1}{d_0 - \Delta d}\right)$$
$$\approx 2N\epsilon_0 A_1 \frac{1 + 2C_3/C_0}{d_0^2}\Delta d, \quad (13.15)$$

$$C_{12} = C_1 + C_2 + \frac{C_1C_2}{C_3} \approx 2C_0 + \frac{C_0^2}{C_3} = constant. \quad (13.16)$$

These capacitance values agree well with those obtained in FEA simulation.[46] The quantity $C_{13} - C_{23}$ in Eq. (13.15) is the capacitance that is measured experimentally while using the MEMS tensile loading device. This is approximately five times greater than the quantity $C_1 - C_2$, which is advantageous in measuring sub-femtoFarad capacitances. In practice, the displacement-capacitance relation is calibrated experimentally[26] for improved accuracy.

13.4. Design Criteria

Taking into consideration the above analyses, the following design criteria are set to achieve an effective and reliable material testing system:

(1) Large load sensor displacements to maximize load resolution;
(2) Low temperature at the actuator-specimen interface to avoid artificial heating of the specimen;
(3) The testing system operates as a displacement control, *i.e.*, the stiffness of the thermal actuator is significantly higher than that of the specimen and load sensor, and;
(4) The actuator does not buckle within the operational temperature range.

The specimen stiffness, failure load, and elongation at failure (ΔU_S) dictate the choice of actuator geometry and the number and dimensions of the beams.

Consequently, optimization of the device design requires some preliminary knowledge of the specimen behavior as is customary in experimental mechanics. In choosing the stiffness of the load sensor (K_{LS}), a compromise between the maximum force applied to the specimen and sensor displacement must be reached. The force applied to the specimen is $F_S = F_{LS} = K_{LS}U_{LS}$. For a differential capacitance load sensor, the displacement resolution remains approximately constant.[26] Thus the smaller the stiffness, the greater the load resolution. However, in order to achieve the required elongation of the sample ΔU_S for failure, the displacement of the thermal actuator U_{TA} must increase. This in turn requires higher temperatures resulting in greater heating of the specimen. The displacement of the thermal actuator (unconstrained by heat sink beams or a specimen) depends on the beam length l, beam angle θ, temperature increase, and stiffness ratio Ψ given in Eq. (13.5). The longer the beams, the greater the displacement. However, longer beams are more likely to stick to the substrate during microfabrication and are more prone to buckling. Thus there is a practical limit placed on the length of the inclined beams.

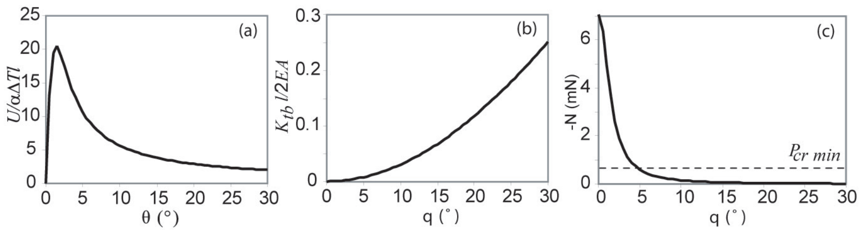

Fig. 13.12. Important parameters in the device design as functions of the thermal beam angle: (a) displacement; (b) stiffness of the thermal actuator; and (c) internal stress. The parameters in (a) and (b) are plotted as dimensionless quantities. Beam dimensions of length $l = 300$ μm, width $b = 8$ μm and height $h = 3.5$ μm were chosen.

Figure 13.12(a)[25] shows the displacement of the thermal actuator as given by Eq. (13.5) as a function of the beam angle. Here the displacement is plotted as a dimensionless quantity ($U^{\Delta T}/\alpha\Delta Tl$) for a fixed stiffness ratio of $\Psi = 1406$. The displacement increases with a decrease in the beam angle in the range $\theta > 2°$. Thus to obtain a given displacement, an actuator with a smaller beam angle ($\theta > 2°$) requires a smaller temperature increase and equivalently a smaller actuation voltage. Regarding the third design criterion, it is desirable to have the thermal actuator operate in displacement control mode. The ability to prescribe the displacement of the tensile specimen is critical in mechanical testing. This allows important mechanical phenomena such as stress softening and fracture to be

captured. In order to achieve true displacement control, the actuator would ideally have infinite stiffness, allowing it to reach the desired displacement regardless of the required force (in theory, it could apply infinite force if given infinite stiffness). In practice, the actuator stiffness must be significantly larger than that of the specimen and load sensor. Figure 13.12(b) plots the stiffness of the thermal actuator as a function of beam angle for the same fixed stiffness ratio ($\Psi = 1406$). Again the quantities are plotted in dimensionless form with the dimensionless stiffness being $K_{tb}l/2EA$. Contrary to the inverse relationship between actuator displacement and beam angle, the actuator stiffness increases with beam angle. Thus there is a trade off between maximizing the displacement and stiffness of the actuator. The final design criterion considers the possibility of buckling. As the temperature of the beams rises, the internal forces build, increasing the possibility of buckling. Figure 13.12(c) plots the internal axial force as a function of the beam angle as well as the critical minimum buckling force for a temperature increase of $\Delta T = 800$ K. Since the recrystallization temperature of polysilicon (the material of the beams) is approximately 800 K,[47] the beams are not expected to buckle within the functional temperature range. The plot shows that the actuator buckles when the beam angle is less than approximately 5° at 800 K.

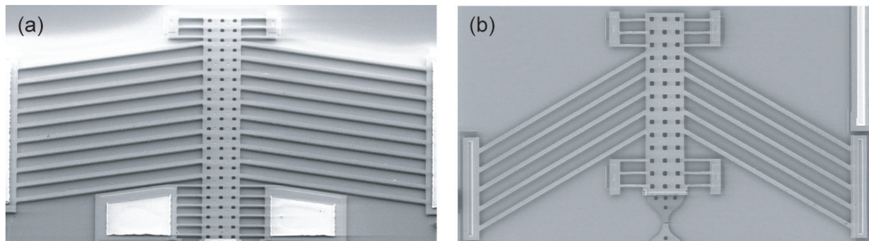

Fig. 13.13. Two types of thermal actuators for testing various types of nanostructures. (a) 10 pairs of thermal beams with beam angle of 10°; (b) 5 pairs of thermal beams with a beam angle of 30°.

To summarize, an actuator with a small beam angle requires the lowest temperature increase for a given displacement. However, the structural stability of the actuator decreases with beam angle. For specimens requiring large actuator displacements, a beam angle of 10° may be selected (Fig. 13.13(a)). For specimens requiring only moderate displacements and greater forces, a beam angle of 30° is more appropriate (Fig. 13.13(b)). In each case, the number of thermal beams is chosen to achieve the desired actuator stiffness-to-load sensor stiffness and actuator stiffness-to-specimen stiffness ratios. Likewise, the load sensor stiffness is chosen according to Eqs. (13.8) and (13.9) once an estimate of the specimen stiffness and elongation at failure is made.

13.5. Material Testing

The MEMS-based tensile stage can be used to test nanometer-scale materials and structures ranging from nanowires and nanotubes to ultra-thin films. As the structures shrink below the sub-micron and into the nanometer scale, new mechanisms dominate their mechanical behavior. For instance, in larger structures, generation and motion of dislocations dictates material behavior. As grain sizes or structural dimensions fall below 50 to 100 nm, surface and intermolecular mechanisms gain influence over material behavior. Nanowires and nanotubes posses a relatively large surface area-to-volume ratio, and small volume compared to that required for the typical dislocation. Consequently, interfaces, interfacial energy, and surface topography play an increasingly important role in their deformation and failure processes. Therefore understanding the mechanics of these new materials and structures is essential. As an example, the following briefly demonstrates the use of the MEMS-based tensile stage for in-situ SEM and TEM of testing nano-scale polysilicon films, palladium nanowires, and multi-walled carbon nanotubes (MWNTs).

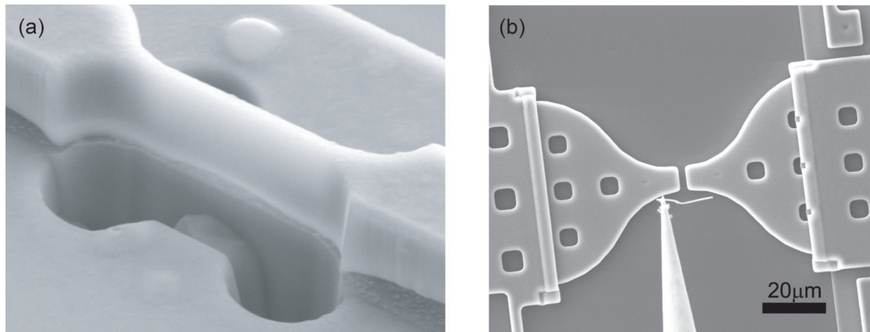

Fig. 13.14. Sample preparation. (a) A polysilicon thin film tensile specimen cofabricated with the MEMS device and further thinned by FIB machining. (b) A palladium nanowire being manipulated into place on the MEMS device using a tungsten probe and nanomanipulator.

13.5.1. *Sample Preparation*

The size and fragile nature of nano-scale materials and structures demands specialized techniques for preparation and mounting on the MEMS device. Thin films may be cofabricated with the MEMS device. This eliminates any handling. For example, freestanding polysilicon films were co-fabricated with the MEMS device between the actuator and the load sensor (Fig. 13.14(a)).[24] Due to limitations

in the resolution of the photolithography used to make the devices, the initial film thickness could not be made thinner than approximately 2 μm. To reduce the thickness dimension, the polysilicon specimen is further machined by focused ion beam (FIB) down to 350-450 nm. Individual nanowires and nanotubes may either be grown across the gap between the actuator and load sensor or placed by nanomanipulator[24] as shown in Fig. 13.14(b). This procedure involves use of a nanomanipulator operated within an SEM to pick up and place an individual nanostructure across the gap, followed by electron beam-induced deposition (EBID) of platinum to weld the ends of the structure in place.

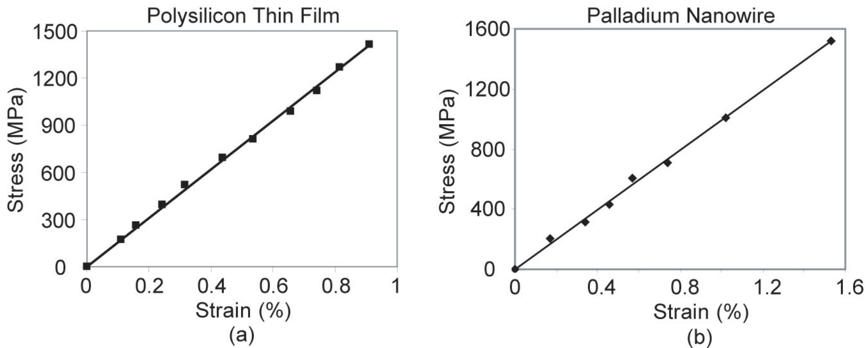

Fig. 13.15. Stress-strain data for (a) a polysilicon thin film specimen[25] and (b) a palladium nanowire.[24]

13.5.2. *Tensile Tests*

13.5.2.1. *Tensile Tests of Polysilicon Thin Films*

Thin film specimens cofabricated with the MEMS device were tested in the SEM. The results of a tensile test of a polysilicon specimen prepared as described in Sec. 13.5.1 are shown in Fig. 13.15(a). Here the stress-strain curve shows strong linearity with a Young's modulus of 156 $\pm$ 17 GPa.[25] This result is consistent other reported values for polysilicon films.[11,46,48]

13.5.2.2. *Tensile Tests of Nanowires*

The tensile test of a palladium nanowire, shown in Fig. 13.15(b),[24] reveals an interesting point. The nanowire was stressed to 1.5 GPa, significantly higher than the yield stress of bulk nanocrystalline Pd,[49] and remained elastic without fracture. This phenomenon, which is attributed to the high stress threshold for the

nucleation of defects,[50,51] confirms that the strength of the material increases as its scale decreases. Ultimately, the strength should tend to approach the theoretical strength of the material (approximately 1/10 of its Young's modulus).[49]

13.5.2.3. *Tensile Tests of Carbon Nanotubes and the Effects of Irradiation*

In-situ SEM and TEM tensile tests of multi-walled carbon nanotubes using the MEMS device allow insight into their failure mechanisms. Figure 13.16 shows sequential SEM images of the in-situ SEM tensile testing of a MWNT. In this case, fracture occurs in a typical "sword-in-sheath" fashion.[12] It is possible that the outermost shell breaks and subsequently the inner concentric shells telescope out. However, the instrument resolution does not permit identification of single or multiple shell failure. As described in Sec. 13.5.1, the two ends of the outermost shell are clamped to the testing device using EBID of platinum.[24] Consequently, it is reasonable to assume that the outermost shell carries the load and breaks under tensile loading as only van der Waals interactions between the concentric inner shells are expected. Based on the assumption that there is minimal load transfer between the outermost shell and subsequent inner shells, stress and strain are often calculated using the measured outer diameter of the MWNT and an assumed shell thickness of 0.34 nm (equal to the interlayer distance of 0.34 nm),[13,52] as opposed to using the combined thickness of multiple concentric shells. In contrast to tests of unmodified MWNTs, in-situ TEM tensile tests of MWNTs exposed to high-energy electron or ion beam irradiation reveal that multiple shells or the entire cross section break simultaneously, resulting in greater stiffness.[40] This observation suggests that the irradiation introduces crosslinks between shells, resulting in load transfer. A series of tests demonstrating this effect were performed using the MEMS device on MWNTs exposed to varying degrees of ion or electron beam radiation, as well as on unexposed MWNTs as a control.[40] These tests are summarized in Fig. 13.17 and Table 13.1. Here it is important to note that the irradiation energy of the electron beam used for SEM imaging during mounting of the MWNTs on the MEMS device is well below the threshold for atomic structure modification and thus is assumed to have negligible effect relative to the high-energy electron and ion beam exposure.

MWNTs exposed to ion irradiation demonstrated significantly greater stiffness than those that were not.[40] In Test 1 (see Table 13.1), the MWNT was irradiated with Ga^{+} ions at a flux of 10^{13} e $cm^{-2}s^{-1}$ for 10 seconds using a 30 kV accelerating voltage. An in-situ TEM tensile test was then performed using the MEMS device. The corresponding inset of Fig. 13.17 shows clearly that the

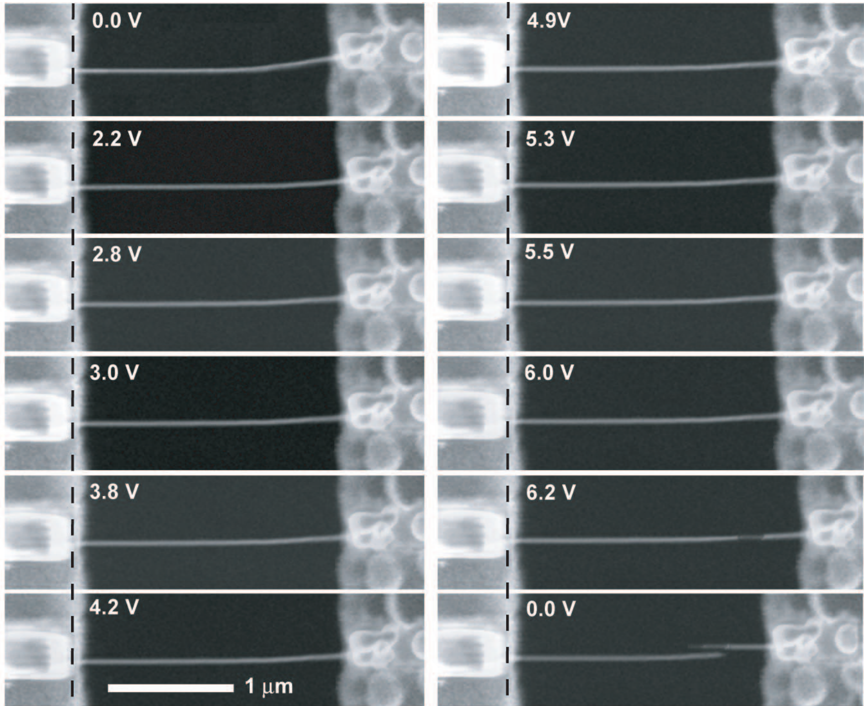

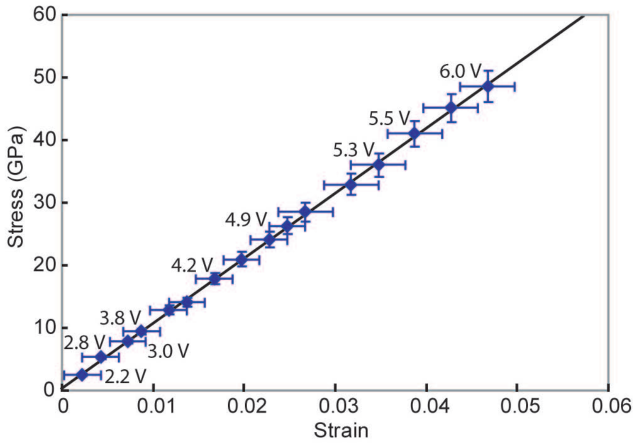

Fig. 13.16. Sequential SEM images and corresponding stress-strain data of a tensile test of a multi-walled carbon nanotube. The nanotube is 2 μm in length and 42 nm in diameter.

Table 13.1. Irradiation conditions and measured mechanical properties of six MWNTs.[40] Shown are the case number, gauge length, outer diameter, applied force at fracture, elongation, tensile strength[a] and Young's modulus[a]. Test 6 corresponds to the images shown in Fig. 13.16.

Test #	Gauge Length [μm]	Outer Dia. [nm]	Ion Radiation Dose [e cm^{-2}]	Electron Radiation Dose [e cm^{-2}]	Breaking Force [μN]	ΔL [nm]	σ_s^a [GPa]	E^a [GPa]
1	6.69	191	10^{14}	—	31.1	195.6	152.5	5,200
2	3.02	142	0.5×10^{14}	—	20.4	101.2	134.5	4,000
3	2.85	169	—	4.5×10^{14}	9.9	143.8	54.8	1,100
4	3.30	108	—	1.5×10^{14}	4.3	97.5	37.3	1,300
5	3.82	96	—	—	1.9	221.9	18.5	300
6	2.06	42	—	—	2.1	156.8	48.5	1,000

[a]Stress and strain are computed under the assumption that only the outermost shell of the MWNT bears the load (*i.e.*, the cross-sectional area is taken to be that of the outermost shell alone).

entire cross section broke as opposed to the typical telescoping, "sword-in-sheath" mechanism. Thus stress and modulus values reported in Table 13.1, which were computed assuming only the outermost shell to be load bearing, appear meaningless in this case. In fact, ion irradiated specimens exhibit values of Young's modulus of 5,200 and 4,000 GPa which are significantly higher than those reported elsewhere in the literature based on quantum mechanics calculations.[53–55] Note also that Ding *et al.*[13] reported moduli ranging from 620 to 1,200 GPa based on the assumption that only the outermost shell is load bearing. However, they do not provide evidence that only the outer shell failed. MWNTs exposed to electron beam irradiation also showed greater stiffness than the unexposed sample, although to a lesser degree. In Test 4 (see Table 13.1), the MWNT was exposed to electron beam radiation with a flux of 1.5×10^{19} e cm^{-2}s^{-1} for 100 seconds within the TEM at an acceleration voltage of 200 kV. In this case, the failure was telescopic in nature as shown in the corresponding inset of Fig. 13.17. However, high-resolution TEM images show that more than one shell broke simultaneously rather than only the outermost shell. Thus again, the computed values of stress and strain based on the outermost shell assumption, do not accurately represent the true material behavior.

In summary, tensile tests of MWNTs exposed to high-energy electron or ion beam irradiation reveal changes in the mode of failure, suggesting that the irradiation introduces crosslinks between shells. Others have reported corroborating evidence based on experiments (for single-walled carbon nanotube bundles) and first principle calculations.[56–58] Above a certain energy threshold, electron and

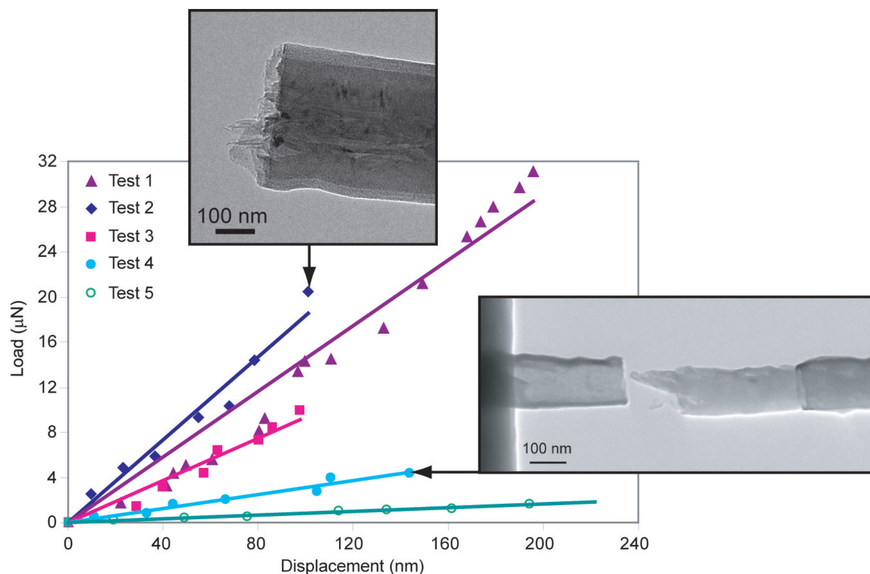

Fig. 13.17. Force-displacement data measured for multi-walled carbon nanotubes exposed to varying degrees and types of radiation. Corresponding irradiation conditions and test parameters are summarized in Table 13.1.

ion beams can produce vacancies in the nanotube shells and corresponding interstitials in the inter-shell spacing.[56] Moreover, molecular dynamics simulations revealed that these interstitial atoms can form stable and covalent bonds between shells.[57] These simulations further demonstrated that the development of covalent bonds under moderate beam irradiation can increase the failure strength of MWNTs while excessive irradiation degrades the mechanical properties due to structural damage (cluster of vacancies) and/or amorphization.[57,58] The experimental observations reported here agree strongly with the predictions of these simulations. These findings show that both electron and ion irradiation could be used to enhance the mechanical properties of MWNTs. However, in light of the observed changes in failure mechanisms, conclusions based on existing stress and strain data computed under the assumption that only the outermost shell bears the load should be drawn with caution. The observations reported here suggest there is some degree of load sharing between shells. For this reason, conclusions inferred from the data reported here focus on the stiffness of the nanostructures, which were measured directly. With advances in TEM image acquisition, the MEMS-based testing technique reported here should allow direct imaging of the the evolution of the failure and the number of shells failing simultaneously.

13.6. Summary

Mechanical characterization of nanometer-scale materials and structures presents a unique set of challenges. The excellent force and displacement resolution of MEMS make them ideal components for material characterization. This chapter presented the modeling and analysis involved in the design of a MEMS-based material testing system allowing simultaneous load-displacement measurement combined with real-time SEM or TEM imaging of the specimen. This system uses a thermal actuator to apply a tensile load and a differential capacitance displacement sensor of known stiffness to determine the applied load. An analytical model of the thermal actuator involved an electrothermal analysis to determine the temperature distribution in the actuator, followed by a thermomechanical analysis to determine the resulting displacement. A coupled-field finite element analysis confirms the analytical model. The differential capacitive load sensor was analyzed to determine the output voltage for a given displacement. A set of design criteria were established based on the analyses as guidelines for design of similar devices. Finally, examples of application of the MEMS-based material testing system to polysilicon thin films, palladium nanowires, and multi-walled carbon nanotubes were presented. Tensile tests of palladium nanowires demonstrated a major strength increase as compared to bulk palladium. Tensile tests of multi-walled carbon nanotubes exposed to varying degrees of electron and ion beam irradiation showed differences in failure mechanisms and an increase in stiffness with the level of irradiation. This is attributed to the formation of crosslinks between shells.

Acknowledgment

The authors thank Alberto Corigliano for his valuable discussions and contributions in the analysis of the thermal actuator.

References

1. M. M. J. Treacy, T. W. Ebbesen, and J. M. Gibson, Exceptionally high Young modulus observed for individual carbon nanotubes, *Nature*. **381**(6584), 678–680, (1996).
2. P. Poncharal, Z. L. Wang, D. Ugarte, and W. A. de Heer, Electrostatic deflections and electromechanical resonances of carbon nanotubes, *Science*. **283**(5407), 1513–1516, (1999).
3. P. E. Marszalek, W. J. Greenleaf, H. Li, A. F. Oberhauser, and J. M. Fernandez. AFM captures quantized plastic deformation in gold nanowires. In ed. 97, *Proceedings of the National Academy of Sciences*, pp. 6282–6286, (2000).

4. W. C. Oliver and G. M. Pharr, An improved technique for determining hardness and elastic-modulus using load and displacement sensing indentation experiments, *Journal of Materials Research*. **7**, 1564, (1992).
5. M. T. A. Saif and N. C. MacDonald, A milli newton microloading device, *Sensors and Actuators A: Physical*. **52**, 65–75, (1996).
6. H. Kahn, R. Ballarini, R. L. Mullen, and A. H. Heuer. Electrostatically actuated failure of microfabricated polysilicon fracture mechanics specimens. In *Proceedings of the Royal Society of London A*, vol. 455, pp. 3807–3823, (1999).
7. E. Wong, P. Sheehan, and C. Lieber, Nanobeam mechanics: elasticity, strength, and toughness of nanorods and nanotubes, *Science*. **277**, 1971–1975, (1997).
8. D. A. Walters, L. M. Ericson, M. J. Casavant, J. Liu, D. T. Colbert, K. A. Smith, and R. E. Smalley, Elastic strain of freely suspended single-wall carbon nanotube ropes, *Applied Physics Letters*. **74**(25), 3803–3805, (1999).
9. J. P. Salvetat, G. A. D. Briggs, J. M. Bonard, R. R. Bacsa, A. J. Kulik, T. Stockli, N. A. Burnham, and L. Forro, Elastic and shear moduli of single-walled carbon nanotube ropes, *Physical Review Letters*. **82**(5), 944–947, (1999).
10. I. Chasiotis and W. G. Knauss, The mechanical strength of polysilicon films: 1. the influence of fabrication governed surface conditions, *Journal of the Mechanics and Physics of Solids*. **51**, 1533–1550, (2003).
11. W. N. Sharpe, K. M. Jackson, and K. J. Hemker, Effect of specimen size on youngs modulus and fracture strength of polysilicon, *Journal of Microelectromechanical Systems*. **10**(3), 317–326, (2001).
12. M.-F. Yu, O. Lourie, M. J. Dyer, K. Moloni, T. F. Kelly, and R. S. Ruoff, Strength and breaking mechanism of multiwalled carbon nanotubes under tensile load, *Science*. **287**, 637, (2000).
13. W. Ding, L. Calabri, K. Kohlhaas, X. Chen, D. Dikin, and R. Ruoff, Modulus, fracture strength, and brittle vs. plastic response of the outer shell of arc-grown multi-walled carbon nanotubes, *Experimental Mechanics*. **online**, (2006).
14. Z. W. Pan, S. S. Xie, L. Lu, B. H. Chang, L. F. Sun, W. Y. Zhou, G. Wang, and D. L. Zhang, Tensile tests of ropes of very long aligned multiwall carbon nanotubes, *Applied Physics Letters*. **74**(21), 3152–3154, (1999).
15. A. Haque and M. T. A. Saif, Novel technique for tensile testing of submicron scale freestanding specimens in SEM and TEM, *Experimental Mechanics*. **42**, 123–128, (2002).
16. A. Haque and M. T. A. Saif, Deformation mechanisms in free-standing nano-scale thin films: A quantitative in-situ TEM study, *Proceedings of the National Academy of Science*. **101**, 6335–6340, (2004).
17. R. C. Hugo, H. Kung, J. Weertman, R. Mitra, J. Knapp, and D. Follstaedt, In-situ TEM tensile testing of dc magnetron sputtered and pulsed laser deposited in thin films, *Acta Materialia*. **51**, 1937–1943, (2003).
18. M. Ke, S. A. Hackney, W. W. Milligan, and E. C. Aifantis, Observation and measurement of grain rotation and plastic strain in nanostructured metal thin films, *Nanostruct. Mater.* **5**(6), 689, (1995).
19. W. van Arsdell and S. Brown, Subcritical crack growth in silicon MEMS, *Journal of Microelectromechanical Systems*. **8**, 319–327, (1999).

20. H. Kahn, N. Tayebi, B. Ballerini, R. Mullen, and A. Heuer, Fracture toughness of polysilicon MEMS devices, *Sensors and Actuators A*. **82**, 274–280, (2000).
21. H. Kahn, B. Ballerini, and A. Heuer, On-chip testing of mechanical properties of MEMS devices, *MRS Bull.* **26**, 300–301, (2001).
22. L. Chu, L. Que, and Y. Gianchandani, Measurements of material properties using differential capacitive strain sensors, *Journal of Microelectromechanical Systems*. **11**, 489–98, (2002).
23. E. Fischer and P. Labossiere. In *Proceedings of the SEM Annual Conference on Exp. and App. Mechanics*, Milwaukee, WI, (2002).
24. Y. Zhu and H. D. Espinosa, An electromechanical material testing system for in situ electron microscopy and applications, *Proceedings of the National Academy of Sciences of the United States of America*. **102**(41), 14503–14508, (2005).
25. Y. Zhu, A. Corigliano, and H. D. Espinosa, A thermal actuator for nanoscale in situ microscopy testing: design and characterization, *Journal of Micromechanics and Microengineering*. **16**, 242–253, (2006).
26. Y. Zhu, N. Moldovan, and H. D. Espinosa, A microelectromechanical load sensor for in situ electron and x-ray microscopy tensile testing of nanostructures, *Applied Physics Letters*. **86**, (2005).
27. W. C. Tang, T. C. H. Nguyen, and R. T. Howe, Laterally driven polysilicon resonant microstructures, *Sensors and Actuators*. **20**(1-2), 25–32, (1989).
28. R. Legtenberg, A. W. Groeneveld, and M. Elwenspoek, Comb-drive actuators for large displacements, *Journal of Micromechanics and Microengineering*. **6**(3), 320–329, (1996).
29. A. A. Geisberger, N. Sarkar, M. Ellis, and G. D. Skidmore, Electrothermal properties and modeling of polysilicon microthermal actuators, *Journal of Microelectromechanical Systems*. **12**(4), 513–523, (2003).
30. J. S. Park, L. L. Chu, A. D. Oliver, and Y. B. Gianchandani, Bent-beam electrothermal actuators — part i: Single beam and cascaded devices, *Journal of Microelectromechanical Systems*. **10**(2), 247–254, (2001).
31. L. L. Chu and Y. B. Gianchandani, A micromachined 2d positioner with electrothermal actuation and sub-nanometer capacitive sensing, *Journal of Micromechanics and Microengineering*. **13**(2), 279–285, (2003).
32. M. F. Pai and N. C. Tien, Low voltage electrothermal vibromotor for silicon optical bench applications, *Sensors and Actuators A-Physical*. **83**(1-3), 237–243, (2000).
33. H. Kapels, R. Aigner, and J. Binder, Fracture strength and fatigue of polysilicon determined by a novel thermal actuator, *IEEE Transactions on Electron Devices*. **47**(7), 1522–1528, (2000).
34. M. Chiao and L. W. Lin, Self-buckling of micromachined beams under resistive heating, *Journal of Microelectromechanical Systems*. **9**(1), 146–151, (2000).
35. C. D. Lott, T. W. Mclain, J. N. Harb, and L. L. Howell, Modeling the thermal behavior of a surface-micromachined linear-displacement thermomechanical microactuator, *Sensors and Actuators A-Physical*. **101**(1-2), 239–250, (2002).
36. Q. A. Huang and N. K. S. Lee, Analytical modeling and optimization for a laterally-driven polysilicon thermal actuator, *Microsystem Technologies-Micro- and Nanosystems-Information Storage and Processing Systems*. **5**(3), 133–137, (1999).

37. N. D. Mankame and G. K. Ananthasuresh, Comprehensive thermal modelling and characterization of an electro-thermal-compliant microactuator, *Journal of Micromechanics and Microengineering*. **11**(5), 452–462, (2001).
38. L. Que, J. S. Park, and Y. B. Gianchandani, Bent-beam electrothermal actuators — part i: Single beam and cascaded devices, *Journal of Microelectromechanical Systems*. **10** (2), 247–254, (2001).
39. Y. B. Gianchandani and K. Najafi, Bent-beam strain sensors, *Journal of Microelectromechanical Systems*. **5**(1), 52–58, (1996).
40. H. D. Espinosa, Y. Zhu, and N. Moldovan, Design and operation of a MEMS-based material testing system for nanomechanical characterization, *To appear in Journal of Microelectromechanical Systems*. (2006).
41. S. D. Senturia, *Microsystem design*. (Kluwer Academic Publishers, Boston, 2002).
42. P. E. Boser. Electronics for micromachined inertial sensors. In *IEEE International Conference on Solid-State Sensors and Actuators*, Chicago (June, 1997).
43. B. E. Boser and R. T. Howe, Surface micromachined accelerometers, *IEEE Journal of Solid-State Circuits*. **31**(3), 366–375, (1996).
44. J. M. Huang, K. M. Liew, C. H. Wong, S. Rajendran, M. J. Tan, and A. Q. Liu, Mechanical design and optimization of capacitive micromachined switch, *Sensors and Actuators A-Physical*. **93**(3), 273–285, (2001).
45. V. Del Toro, *Engineering circuits*. (Prentice Hall, Englewood Cliffs, NJ, 1986).
46. A. Corigliano, B. De Masi, A. Frangi, C. Comi, A. Villa, and M. Marchi, Mechanical characterization of polysilicon through on chip tensile tests, *Journal of Microelectromechanical Systems*. **13**(2), 200–219, (2004).
47. M. Ehmann, P. Ruther, M. von Arx, H. Baltes, and O. Paul, Operation and short-term drift of polysilicon-heated cmos microstructures at temperatures up to 1200 k, *Journal of Micromechanics and Microengineering*. **11**(4), 397–401, (2001).
48. I. Chasiotis and W. G. Knauss, The mechanical strength of polysilicon films: Part 1. the influence of fabrication governed surface conditions, *Journal of the Mechanics and Physics of Solids*. **51**(8), 1533–1550, (2003).
49. T. H. Courtney, *Mechanical Behavior of Materials*. (McGraww-Hill, 2000).
50. H. Espinosa, B. Prorok, and B. Peng, Plasticity size effects in freestanding submicron polycrystalline FCC films subjected to pure tension, *Journal of the Mechanics and Physics of Solids*. **52**, 667–689, (2004).
51. M. Uchic, D. Dimiduk, J. Florando, and N. W., Sample dimensions influence strength and crystal plasticity, *Science*. **305**, 986–989, (2004).
52. A. Barber, I. Kaplan-Ashiri, S. Cohen, R. Tenne, and H. Wagner, Stochastic strength of nanotubes: an appraisal of available data, *Composites Science and Technology*. **65**, 2830–2384, (2005).
53. S. Zhang, S. Mielke, R. Khare, D. Troya, R. Ruoff, G. Schatz, and T. Belytschko, Mechanics of defects in carbon nanotubes: Atomistic and multiscale simulations, *Physical Review B*. **71**, 115403, (2005).
54. S. Mielke, D. Troya, S. Zhang, J. Li, S. Xiao, R. Car, R. Ruoff, G. Schatz, and T. Belutschko, The role of vacancy defects and holes in the fracture of carbon nanotubes, *Chemical Physics Letters*. **390**, 413–420, (2004).

55. D. Troya, S. Mielke, and G. Schatz, Carbon nanotube fracture-differences between quantum mechanical mechanisms and those of empirical potentials, *Chemical Physics Letters*. **382**, 133–141, (2003).
56. W. Smith and D. Luzzi, Electron irradiation effects in single wall carbon nanotubes, *Journal of Applied Physics*. **90**, 3509–3515, (2001).
57. M. Huhtala, A. Krasheninnikov, J. Aittoniemi, S. Stuart, K. Nordlund, and K. Kaski, Improved mechanical load transfer between shells of multiwalled carbon nanotubes, *Physical Review B*. **79**, 045404, (2004).
58. J. Pomoell, A. Krasheninnikov, K. Nordlund, and J. Keinonen, Ion ranges and irradiation-induced defects in multiwalled carbon nanotubes, *Journal of Applied Physics*. **96**(5), 2864–2871, (2004).

This page intentionally left blank

Computational and Experimental Methods in Structures

Editorial Board

Ramon Abascal
Escuela Superior de Ingenieros
Camino de los descubrimientos
Spain

B. Abersek
University of Maribor
Slovenia

K. J. Bathe
Massachusetts Institute of Technology, USA

A. Chan
Department of Engineering
University of Birmingham
UK

P. Dabnichki
Department of Engineering
Queen Mary, University of London
UK

M. Denda
Department of Mechanical and Aerospace Engineering
Rutgers University
USA

Manuel Doblare
Department of Mechanical Engineering
Aragón Institute of Engineering Research
Spain

M. Edirisinghe
Department of Engineering
University College London
UK

H. Espinosa
Mechanical Engineering
Northwestern University
USA

Brian Falzon
Department of Aeronautics
Monash University, Australia

Ugo Galvanetto
Department Engineering
Padova University
Italy

Peter Gudmundson
Department of Solid Mechanics
KTH Engineering Sciences
Sweden

Mario Gugalinao
University of Milan, Italy

David Hills
Lincoln College
Oxford University, UK

R. Huiskes (Rik)
Department of Biomedical Engineering
Eindhoven University of Technology
The Netherlands

Ian Hutchings
Institute for Manufacturing
University of Cambridge
UK

Alojz Ivankovic
Department of Mechanical Engineering
University College Dublin
Ireland

Pierre Jacquot
Nanophotonics and Metrology Laboratory
Swiss Federal Institute of Technology Lausanne
Switzerland

Wing Kam Liu
Department of Mechanical Engineering
Northwestern University
USA

Herbert A. Mang
Technische Universität Wien
Vienna University of Technology
Austria

K. Nikbin
Department of Mechanical Engineering
Imperial College London
UK

Eugenio Onate
CIMNE, UPC, Barcelona
Spain

Spiros Pantelakis
Department of Mechanical Engineering and Aeronautics
University of Patras, Greece

Carmine Pappalettere
Department of Engineering
Bari University, Italy

K. Ravi-Chandar
Department of Aerospace Engineering and Engineering Mechanics
University of Texas at Austin
USA

A. Sellier
LadHyX. Ecole Polytechnique
Palaiseau cedex, France

Jan Sladek
Slovak Academy of Sciences
Slovakia

Paulo Sollero
University of Campinas
Brasil

J. C. F. Telles
COPPE, Brasil

Ole Thybo Thomsen
Department of Mechanical Engineering
Aalborg University
Denmark

Kon-Well Wang
The Pennsylvania State University
USA

J. Woody
Department of Civil and Environmental Engineering
UCLA, USA

Ch. Zhang
University of Siegen
Germany